processes

Special Issue Reprint

Simulation, Modeling, and Decision-Making Processes in Manufacturing Systems and Industrial Engineering

Edited by
Chia-Nan Wang, Nhat Luong Nhieu, Phan Van-Thanh and Hector Tibo

mdpi.com/journal/processes

MDPI

Simulation, Modeling, and Decision-Making Processes in Manufacturing Systems and Industrial Engineering

Simulation, Modeling, and Decision-Making Processes in Manufacturing Systems and Industrial Engineering

Guest Editors

Chia-Nan Wang
Nhat Luong Nhieu
Phan Van-Thanh
Hector Tibo

MDPI

Basel • Beijing • Wuhan • Barcelona • Belgrade • Novi Sad • Cluj • Manchester

Guest Editors

Chia-Nan Wang
Department of Industrial Engineering and Management
National Kaohsiung University of Science and Technology
Kaohsiung
Taiwan

Nhat Luong Nhieu
Department of Industrial Engineering and Management
National Kaohsiung University of Science and Technology
Kaohsiung
Taiwan

Phan Van-Thanh
Vietnam-Korea University of Information and Communication Technology
Danang
Vietnam

Hector Tibo
Department of Electrical Engineering and Technology
Technological University of the Philippines Taguig
Taguig City
Philippines

Editorial Office

MDPI AG
Grosspeteranlage 5
4052 Basel, Switzerland

This is a reprint of the Special Issue, published open access by the journal *Processes* (ISSN 2227-9717), freely accessible at: https://www.mdpi.com/journal/processes/special_issues/MB9NOSECK1.

For citation purposes, cite each article independently as indicated on the article page online and as indicated below:

Lastname, A.A.; Lastname, B.B. Article Title. *Journal Name* **Year**, *Volume Number*, Page Range.

ISBN 978-3-7258-6210-8 (Hbk)
ISBN 978-3-7258-6211-5 (PDF)
https://doi.org/10.3390/books978-3-7258-6211-5

Contents

About the Editors . . . . . **vii**

Van Thanh Phan, Chia Nan Wang, Hector Tibo and Nhat Luong Nhieu
Special Issue on "Simulation, Modeling, and Decision-Making Processes in Manufacturing Systems and Industrial Engineering"
Reprinted from: *Processes* **2025**, *13*, 3767, https://doi.org/10.3390/pr13123767 . . . . . **1**

Julia Nazarejova and Vladimir Modrak
What Role Does Simulation Play in Sustainable Industrial Development?
Reprinted from: *Processes* **2024**, *12*, 1007, https://doi.org/10.3390/pr12051007 . . . . . **7**

Osama A. Marzouk
Reduced-Order Modeling (ROM) of a Segmented Plug-Flow Reactor (PFR) for Hydrogen Separation in Integrated Gasification Combined Cycles (IGCC)
Reprinted from: *Processes* **2025**, *13*, 1455, https://doi.org/10.3390/pr13051455 . . . . . **24**

Chia-Nan Wang, Ming-Hsien Hsueh, Duy-Oanh Tran Thi, Thi Diem-My Le and Quang-Tuyen Dinh
Optimal Maintenance Strategy Selection for Oil and Gas Industry Equipment Using a Combined Analytical Hierarchy Process–Technique for Order of Preference by Similarity to an Ideal Solution: A Case Study in the Oil and Gas Industry
Reprinted from: *Processes* **2025**, *13*, 1389, https://doi.org/10.3390/pr13051389 . . . . . **78**

Ankidim Zinveli, Mihai Dragomir and Diana Dragomir
What's Hot and What's Not—A Simulation-Based Methodology for Fire Risk Assessment in Lead-Acid Battery Manufacturing
Reprinted from: *Processes* **2025**, *13*, 837, https://doi.org/10.3390/pr13030837 . . . . . **99**

Yanqin Li and Dehai Zhang
Toward Efficient Edge Detection: A Novel Optimization Method Based on Integral Image Technology and Canny Edge Detection
Reprinted from: *Processes* **2025**, *13*, 293, https://doi.org/10.3390/pr13020293 . . . . . **121**

Berrin Denizhan, Elif Yıldırım and Öznur Akkan
An Order-Picking Problem in a Medical Facility Using Genetic Algorithm
Reprinted from: *Processes* **2024**, *13*, 22, https://doi.org/10.3390/pr13010022 . . . . . **139**

Jiayang Dai, Peirun Ling, Haofan Shi and Hangbin Liu
A Multi-Step Furnace Temperature Prediction Model for Regenerative Aluminum Smelting Based on Reversible Instance Normalization-Convolutional Neural Network-Transformer
Reprinted from: *Processes* **2024**, *12*, 2438, https://doi.org/10.3390/pr12112438 . . . . . **163**

Kai Zhao, Qiuhua Shi, Shuguang Zhao, Fang Ye and Mohamed Badran
Filling Process Optimization of a Fully Flexible Machine through Computer Simulation and Advanced Mathematical Modeling
Reprinted from: *Processes* **2024**, *12*, 1962, https://doi.org/10.3390/pr12091962 . . . . . **182**

Haiping Tang, Yaping Ding, Guangyou Qiu, Ziguang Liu and Zhibin Deng
Numerical Simulations for the Mechanical Behavior of a Type-B Sleeve under Pipeline Suspension
Reprinted from: *Processes* **2024**, *12*, 1585, https://doi.org/10.3390/pr12081585 . . . . . **202**

Norhidayah Mohamad, Nor Azlina Ab. Aziz, Anith Khairunnisa Ghazali and Mohd Rizal Salleh
Improving Ammonia Emission Model of Urea Fertilizer Fluidized Bed Granulation System Using Particle Swarm Optimization for Sustainable Fertilizer Manufacturing Practice
Reprinted from: *Processes* **2024**, *12*, 1025, https://doi.org/10.3390/pr12051025 . . . . . **223**

Nguyen-Nhu-Y Ho, Phuong Mai Nguyen, Cong Thanh Tran and Huy Hung Ta
Determinants for Supplier Selection Based on Hybrid Grey Theory: Case Study of the Vietnamese Coffee Industry
Reprinted from: *Processes* **2024**, *12*, 901, https://doi.org/10.3390/pr12050901 . . . . . **235**

Yen-Hsing Hung and Fu-Chiang Yang
Northern Lights: Prospecting Efficiency in Europe's Renewable Energy Sector
Reprinted from: *Processes* **2024**, *12*, 618, https://doi.org/10.3390/pr12030618 . . . . . **251**

Walid M. Shewakh and Ibrahim M. Hassab-Allah
Finite Element Simulation of a Multistage Square Cup Drawing Process for Relatively Thin Sheet Metal through a Conical Die
Reprinted from: *Processes* **2024**, *12*, 525, https://doi.org/10.3390/pr12030525 . . . . . **267**

Karolina Czerwińska and Andrzej Pacana
Method of Analyzing Technological Data in Metric Space in the Context of Industry 4.0
Reprinted from: *Processes* **2024**, *12*, 401, https://doi.org/10.3390/pr12020401 . . . . . **280**

Weiguo Liu, Weizhe Dai and Xuyin Wang
Optimizing Production Schedules: Balancing Worker Cooperation and Learning Dynamics in Seru Systems
Reprinted from: *Processes* **2023**, *12*, 38, https://doi.org/10.3390/pr12010038 . . . . . **297**

Xin Feng, Haoyang Li, Jie Huang, Qingfen Ma, Mao Lin, Jingru Li and Zhongye Wu
Structural Design and Analysis of a 100 kW Radial Turbine for an Ocean Thermal Energy Conversion–Organic Rankine Cycle Power Plant
Reprinted from: *Processes* **2023**, *11*, 3341, https://doi.org/10.3390/pr11123341 . . . . . **315**

About the Editors

Chia-Nan Wang

Chia-Nan Wang received the Ph.D. degree from the Department of Industrial Engineering and Management, National Chiao-Tung University, Taiwan, in 2004. He is currently a Professor with the Department of Industrial Engineering and Management, National Kaohsiung University of Science and Technology, Taiwan. He has published around 150 journal articles and 50 patents. He has achieved around 35 projects of research and academy and has some successful cases of technology transfer. He has plenty of practical experience in many industries and provides consulting services for several stock companies in Taiwan. His research interests include manufacturing automation, industrial applications, operations research, management of technology, and systematic innovation. He was a recipient of awards from many international invention competitions, including two Gold Medal Awards, five Silver Medal Awards, and several Bronze Medal Awards.

Nhieu Nhat Luong

Nhieu Nhat Luong is a lecturer and researcher at the Institute of Intelligent and Interactive Technologies, University of Economics Ho Chi Minh City. He received his Ph.D. in Industrial Engineering and Management from National Kaohsiung University of Science and Technology, Taiwan, in 2022. His research interests include data envelopment analysis, fuzzy decision-making methods, sustainable energy systems, supply chain management, and industrial optimization. He has authored more than forty SCI/SSCI-indexed publications in leading journals such as *Renewable Energy*, *Humanities and Social Sciences Communications*, and *Journal of Cleaner Production*. His current work focuses on efficiency assessment, sustainability evaluation, and advanced decision-support modeling, and he served as Academic Editor of *PLoS ONE*.

Van-Thanh Phan

Van-Thanh Phan is currently a lecturer and researcher at Vietnam-Korea University of Information and Communication Technology (VKU). He received the Ph.D. degree from the Department of Industrial Engineering and Management, National Kaohsiung University of Applied Sciences, Taiwan, in 2015. His research interests include gray theory systems, data envelopment analysis, fuzzy time series forecasting, industrial applications, operations research, management of technology, and systematic innovation. He has published around 30 journal articles and patents. He has achieved around 7 projects of research and academy and has some successful cases of technology transfer. His current work focuses on efficiency assessment, sustainability evaluation, operation management, time series forecasting, management of technology, and systematic innovation.

Hector Tibo

Hector Tibo is currently a lecturer at the Technological University of the Philippines, Taguig. He received the Ph.D. degree from the Department of Industrial Engineering and Management, National Kaohsiung University of Science and Technology, Taiwan, in 2022. His research interests and current work focus on data analysis; multi-criteria decision-making; forecasting; information technology; and operations management. He has published around 20 journal articles.

processes

MDPI

Editorial

Special Issue on "Simulation, Modeling, and Decision-Making Processes in Manufacturing Systems and Industrial Engineering"

Van Thanh Phan [1,*], Chia Nan Wang [2,*], Hector Tibo [3] and Nhat Luong Nhieu [2]

[1] Department of Digital Economic and E-Commerce, Vietnam-Korea University of Information and Communication Technology (VKU), Danang 550000, Vietnam
[2] Department of Industrial Engineering and Management, National Kaohsiung University of Science and Technology, Kaohsiung 80778, Taiwan; luongnn@nkust.edu.tw
[3] Department of Electrical Engineering and Technology, Technological University of the Philippines Taguig, Taguig City 1630, Philippines; hector_tibo@tup.edu.ph
* Correspondence: pvthanh.tg@vku.udn.vn (V.T.P.); cn.wang@nkust.edu.tw (C.N.W.); Tel.: +84-915377063 (V.T.P.); +886-7-3814536 (ext. 17109) (C.N.W.)

1. Introduction

The rapid evolution of emerging technologies, the globalization of industrial networks, and the increasing complexity of production ecosystems have fundamentally reshaped the paradigm of modern manufacturing and industrial engineering. The advent of Industry 5.0, characterized by cyber–physical systems, artificial intelligence, big data analytics, and the Internet of Things (IoT), has not only transformed production processes but also redefined the way decisions are made across all levels of manufacturing systems. These transformations have resulted in an unprecedented need for integrating analytical rigor with digital intelligence to ensure system adaptability, operational resilience, and sustainability. Under such a dynamic context, organizations are challenged to respond to volatile market demands, resource constraints, and environmental responsibilities, while maintaining competitiveness and innovation capacity [1,2].

In this evolving industrial landscape, simulation, modeling, and decision-making processes represent the cornerstone of scientific inquiry and managerial practice. Simulation enables researchers and engineers to construct virtual representations of real-world systems, allowing for the exploration of complex interactions among production, logistics, and human factors without the cost or risk associated with physical experimentation. Modeling, both analytical and data-driven, provides a mathematical abstraction to interpret, predict, and optimize system behavior, facilitating the quantification of performance indicators under various operational scenarios. Decision-making processes, built upon these analytical foundations, transform quantitative insights into actionable strategies—supporting evidence-based planning, real-time control, and multi-objective optimization in uncertain environments [3].

Beyond their individual contributions, the integration of simulation, modeling, and decision analytics forms the intellectual core of modern industrial research, driving advances in intelligent manufacturing, digital twins, and sustainable production systems. This triad enables researchers to bridge the gap between theoretical frameworks and industrial realities, linking predictive analytics with prescriptive decision-making to enhance efficiency, flexibility, and competitiveness. Furthermore, as industries progress toward the era of Industry 5.0—emphasizing human-centric design, resilience, and ecological balance—

these methodologies will play an increasingly pivotal role in ensuring that manufacturing systems evolve not only technologically but also socially and environmentally [1].

In light of these developments, this Special Issue, entitled "Simulation, Modeling, and Decision-Making Processes in Manufacturing Systems and Industrial Engineering", aims to provide a comprehensive academic platform for advancing the theoretical foundations, computational methodologies, and empirical applications that define the future of industrial systems research. The Special Issue gathers sixteen carefully selected studies that collectively address how simulation-based approaches, modeling frameworks, and decision-support systems can be seamlessly integrated to improve operational performance, sustainability, and strategic decision-making across diverse manufacturing and industrial contexts. These contributions reflect a global and interdisciplinary perspective, showcasing the synergistic relationship between engineering science, data analytics, and managerial decision-making [4].

From a theoretical standpoint, the papers published in this Special Issue contribute to a deeper understanding of how modeling and simulation interact within complex, multi-layered production systems. They extend classical paradigms by incorporating modern algorithmic techniques, such as machine learning, evolutionary optimization, and digital twin technologies, offering enhanced accuracy, scalability, and adaptability to real-world uncertainties. Methodologically, these studies explore hybrid approaches that combine deterministic and stochastic models, qualitative and quantitative analyses, and computational and behavioral dimensions of decision-making. This multi-method integration provides a richer, more holistic framework for understanding how industrial systems evolve and how managers can make informed decisions in dynamic, uncertain environments [5].

Practically, the contributions emphasize the translation of theoretical insights into applicable solutions that can improve the design, control, and optimization of manufacturing processes. Case studies span a wide range of sectors, including energy conversion, chemical processing, logistics, metal forming, and smart production, demonstrating how simulation and modeling can guide efficiency improvements, resource allocation, and sustainable innovation. For example, data-driven decision-support frameworks are shown to assist policymakers in shaping renewable energy strategies, while optimization-based models enhance the flexibility and reliability of production scheduling, maintenance planning, and quality control systems. Such works exemplify how industrial research can directly contribute to technological advancement and socio-economic sustainability.

Moreover, this Special Issue underscores the importance of integrating human factors, environmental concerns, and digital transformation into industrial decision-making processes. As manufacturing systems increasingly rely on autonomous and intelligent technologies, the role of human cognition, ethics, and collaborative design becomes more critical in ensuring that technological progress aligns with societal and ecological values. By bridging theory, computation, and application, the research featured in this collection not only advances academic understanding but also offers practical pathways toward the realization of resilient, intelligent, and sustainable industrial systems.

2. Three Interrelated Strategic Directions Were Detected by the Set of Contributions Gathered in This Special Issue

The collective insights derived from the papers in this Special Issue reveal a clear trajectory toward three interrelated strategic directions that are reshaping the future of industrial and manufacturing systems—efficiency, resilience, and sustainability. These pillars represent not only operational objectives but also the conceptual foundation for the next generation of industrial transformation. In terms of efficiency, the contributions demon-

strate how advanced simulation and optimization techniques can significantly enhance production throughput, minimize waste, and reduce system variability. The integration of computational intelligence, including metaheuristic optimization and machine learning, enables dynamic process control and predictive analytics, achieving higher productivity with fewer resources. This transition toward "smart efficiency" underscores the value of real-time data integration, digital twins, and adaptive modeling in achieving leaner yet more agile operations.

Equally important is the pursuit of resilience, as modern industries face increasing uncertainty due to supply chain disruptions, market volatility, and environmental fluctuations. The studies presented herein demonstrate how modeling and decision-making frameworks can be employed to design systems that can absorb shocks and maintain functionality under stress. Multi-scenario simulation, probabilistic modeling, and robust optimization methods are emerging as vital tools for developing decision-support systems that can anticipate disturbances, evaluate alternative responses, and facilitate rapid recovery. In this way, these methodologies contribute to building organizations that are not only efficient in steady states but also adaptable and self-correcting in dynamic contexts.

Ultimately, the theme of sustainability pervades the Special Issue as a unifying vision. Several contributions integrate environmental, social, and economic perspectives into the design and assessment of industrial processes, promoting the transition from resource-intensive production models to circular and regenerative systems. Simulation-based environmental assessment, life-cycle modeling, and energy efficiency optimization illustrate how data-driven strategies can reconcile profitability with ecological responsibility. More broadly, these studies affirm that sustainable industrial development requires both technological innovation and strategic governance, ensuring that the evolution of manufacturing systems aligns with global sustainability goals and social well-being.

In synthesis, the cross-pollination of efficiency, resilience, and sustainability reflects a paradigm shift—from isolated process optimization to systemic intelligence and collaborative adaptation. This integrated vision positions simulation, modeling, and decision-making not merely as analytical tools but as enablers of holistic transformation. As industries continue to navigate the convergence of digitalization, globalization, and environmental transition, these three pillars will define the roadmap for advancing industrial excellence in the decades to come [6,7].

3. Conclusions

This Special Issue has delved deeply into the core of contemporary manufacturing and industrial engineering, where simulation, modeling, and decision-making methodologies converge to address the multifaceted challenges of an increasingly complex industrial ecosystem. Collectively, the sixteen papers published in this Special Issue make several significant academic and practical contributions. First, they advance the theoretical understanding of industrial system dynamics by extending classical models toward hybrid and data-driven frameworks that better capture uncertainty, nonlinearity, and interdependence across multiple production layers. Second, they introduce innovative computational approaches—such as machine learning-enhanced optimization, digital twin modeling, and the integration of multi-criteria decision-making—that improve the accuracy, scalability, and adaptability of industrial analysis and control systems. Third, the contributions bridge the long-standing gap between analytical rigor and practical implementation, offering tangible tools for process design, energy management, logistics planning, and predictive maintenance across diverse sectors, including chemical processing, renewable energy, metal manufacturing, and intelligent production systems. Fourth, several studies emphasize the

incorporation of behavioral, social, and environmental dimensions into decision-making frameworks, reflecting a more holistic and sustainable orientation in industrial engineering research, particularly in the era of Industry 5.0 and beyond.

From an editorial perspective, this collection highlights the growing importance of interdisciplinary integration—where engineering science, artificial intelligence, data analytics, and management theory intersect to form new paradigms for industrial innovation. It also reaffirms that the future of manufacturing lies not only in technological sophistication but also in systemic intelligence—the ability of organizations to learn, adapt, and optimize continuously within dynamic environments.

Looking ahead, future research should continue to expand in several promising directions. One avenue involves the fusion of digital twin technologies with real-time decision-making systems, enabling adaptive control and predictive optimization in complex production networks. Another lies in the integration of human-centric and cognitive models into simulation frameworks, ensuring that decision support systems remain aligned with human judgment, ethical considerations, and organizational behavior. Additionally, the application of explainable artificial intelligence (XAI) in industrial modeling deserves greater attention to enhance transparency, interpretability, and trust in automated decision-making processes. Researchers should also pursue cross-disciplinary studies that link industrial engineering with environmental sciences, circular economy, and sustainability assessment, to guide the transition toward carbon-neutral and resource-efficient manufacturing. Finally, the development of standardized benchmarking datasets, open simulation platforms, and reproducible experimental protocols will be crucial to strengthening collaboration and accelerating innovation in this rapidly evolving field.

In conclusion, this Special Issue not only synthesizes the current state of research but also provides a roadmap for future investigations into the intersection of simulation, modeling, and decision-making. It is our hope that the insights presented herein will inspire further academic inquiry and industrial application, fostering the development of resilient, intelligent, and sustainable manufacturing systems that define the next generation of industrial excellence.

Author Contributions: Conceptualization, V.T.P. and C.N.W.; methodology, V.T.P. and C.N.W.; validation, V.T.P., C.N.W., H.T. and N.L.N.; formal analysis, V.T.P.; investigation, V.T.P., C.N.W., H.T. and N.L.N.; resources, C.N.W.; data curation, V.T.P.; writing—original draft preparation, V.T.P.; writing—review and editing, C.N.W.; visualization, H.T. and N.L.N.; supervision, C.N.W.; project administration, C.N.W. All authors have read and agreed to the published version of the manuscript.

Acknowledgments: The authors appreciate the support from the Vietnam-Korea University of Information and Communications Technology, University of Danang, Vietnam, and the National Kaohsiung University of Science and Technology, Taiwan.

Conflicts of Interest: The authors declare no conflicts of interest.

List of Contributions:

1. Nazarejova, J.; Modrak, V. What Role Does Simulation Play in Sustainable Industrial Development? *Processes* **2024**, *12*, 1007. https://doi.org/10.3390/pr12051007.
2. Marzouk, O.A. Reduced-Order Modeling (ROM) of a Segmented Plug-Flow Reactor (PFR) for Hydrogen Separation in Integrated Gasification Combined Cycles (IGCC). *Processes* **2025**, *13*, 1455. https://doi.org/10.3390/pr13051455.
3. Hung, Y.-H.; Yang, F.-C. Northern Lights: Prospecting Efficiency in Europe's Renewable Energy Sector. *Processes* **2024**, *12*, 618. https://doi.org/10.3390/pr12030618.

4. Zinveli, A.; Dragomir, M.; Dragomir, D. What's Hot and What's Not—A Simulation-Based Methodology for Fire Risk Assessment in Lead-Acid Battery Manufacturing. *Processes* **2025**, *13*, 837. https://doi.org/10.3390/pr13030837.
5. Li, Y.; Zhang, D. Toward Efficient Edge Detection: A Novel Optimization Method Based on Integral Image Technology and Canny Edge Detection. *Processes* **2025**, *13*, 293. https://doi.org/10.3390/pr13020293.
6. Wang, C.-N.; Hsueh, M.-H.; Tran Thi, D.-O.; Le, T.D.-M.; Dinh, Q.-T. Optimal Maintenance Strategy Selection for Oil and Gas Industry Equipment Using a Combined Analytical Hierarchy Process–Technique for Order of Preference by Similarity to an Ideal Solution: A Case Study in the Oil and Gas Industry. *Processes* **2025**, *13*, 1389. https://doi.org/10.3390/pr13051389.
7. Denizhan, B.; Yıldırım, E.; Akkan, Ö. An Order-Picking Problem in a Medical Facility Using Genetic Algorithm. *Processes* **2025**, *13*, 22. https://doi.org/10.3390/pr13010022.
8. Dai, J.; Ling, P.; Shi, H.; Liu, H. A Multi-Step Furnace Temperature Prediction Model for Regenerative Aluminum Smelting Based on Reversible Instance Normalization-Convolutional Neural Network-Transformer. *Processes* **2024**, *12*, 2438. https://doi.org/10.3390/pr12112438.
9. Zhao, K.; Shi, Q.; Zhao, S.; Ye, F.; Badran, M. Filling Process Optimization of a Fully Flexible Machine through Computer Simulation and Advanced Mathematical Modeling. *Processes* **2024**, *12*, 1962. https://doi.org/10.3390/pr12091962.
10. Tang, H.; Ding, Y.; Qiu, G.; Liu, Z.; Deng, Z. Numerical Simulations for the Mechanical Behavior of a Type-B Sleeve under Pipeline Suspension. *Processes* **2024**, *12*, 1585. https://doi.org/10.3390/pr12081585.
11. Mohamad, N.; Ab. Aziz, N.A.; Ghazali, A.K.; Salleh, M.R. Improving Ammonia Emission Model of Urea Fertilizer Fluidized Bed Granulation System Using Particle Swarm Optimization for Sustainable Fertilizer Manufacturing Practice. *Processes* **2024**, *12*, 1025. https://doi.org/10.3390/pr12051025.
12. Ho, N.-N.-Y.; Nguyen, P.M.; Tran, C.T.; Ta, H.H. Determinants for Supplier Selection Based on Hybrid Grey Theory: Case Study of the Vietnamese Coffee Industry. *Processes* **2024**, *12*, 901. https://doi.org/10.3390/pr12050901.
13. Shewakh, W.M.; Hassab-Allah, I.M. Finite Element Simulation of a Multistage Square Cup Drawing Process for Relatively Thin Sheet Metal through a Conical Die. *Processes* **2024**, *12*, 525. https://doi.org/10.3390/pr12030525.
14. Czerwińska, K.; Pacana, A. Method of Analyzing Technological Data in Metric Space in the Context of Industry 4.0. *Processes* **2024**, *12*, 401. https://doi.org/10.3390/pr12020401.
15. Liu, W.; Dai, W.; Wang, X. Optimizing Production Schedules: Balancing Worker Cooperation and Learning Dynamics in Seru Systems. *Processes* **2024**, *12*, 38. https://doi.org/10.3390/pr12010038.
16. Feng, X.; Li, H.; Huang, J.; Ma, Q.; Lin, M.; Li, J.; Wu, Z. Structural Design and Analysis of a 100 kW Radial Turbine for an Ocean Thermal Energy Conversion–Organic Rankine Cycle Power Plant. *Processes* **2023**, *11*, 3341. https://doi.org/10.3390/pr11123341.

References

1. Nazarejova, J.; Modrak, V. What Role Does Simulation Play in Sustainable Industrial Development? *Processes* **2024**, *12*, 1007. [CrossRef]
2. Rijwani, T.; Kumari, S.; Srinivas, R.; Abhishek, K.; Iyer, G.; Vara, H.; Dubey, S.; Revathi, V.; Gupta, M. Industry 5.0: A review of emerging trends and transformative technologies in the next industrial revolution. *Int. J. Interact. Des. Manuf. IJIDeM* **2025**, *19*, 667–679. [CrossRef]
3. Liu, Y.; Gupta, H.; Springer, E.; Wagener, T. Linking science with environmental decision making: Experiences from an integrated modeling approach to supporting sustainable water resources management. *Environ. Model. Softw.* **2008**, *23*, 846–858. [CrossRef]
4. Wang, C.-N.; Tsai, T.-T.; Huang, Y.-F. A Model for Optimizing Location Selection for Biomass Energy Power Plants. *Processes* **2019**, *7*, 353. [CrossRef]
5. Sahoo, S.; Kumar, S.; Mukherjee, D.; Kraus, S.; Dabić, M.; Mahto, R.V. Internationalization via industry 4.0 technologies: Application areas and future roadmap for international business. *Manag. Rev. Q.* **2025**, *75*, 3443–3470. [CrossRef]

6. Barbieri, P.; Boffelli, A.; Elia, S.; Fratocchi, L.; Kalchschmidt, M. How does industry 4.0 affect international exposure? The interplay between firm innovation and home-country policies in post-offshoring relocation decisions. *Int. Bus. Rev.* **2022**, *31*, 101992. [CrossRef]
7. Brieger, S.A.; Chowdhury, F.; Hechavarría, D.M.; Muralidharan, E.; Pathak, S.; Lam, Y.T. Digitalization, institutions and new venture internationalization. *J. Int. Manag.* **2022**, *28*, 100949. [CrossRef]

processes

MDPI

Review

What Role Does Simulation Play in Sustainable Industrial Development?

Julia Nazarejova * and Vladimir Modrak

Faculty of Manufacturing Technologies, Technical University of Košice, Bayerova 1, 080 01 Prešov, Slovakia; vladimir.modrak@tuke.sk
* Correspondence: julia.nazarejova@tuke.sk

Abstract: Sustainability as a concept is present in most aspects of our everyday life, and industry is no exception. Likewise, there is no doubt that the necessity to produce goods in a sustainable way and to ensure that products are sustainable is gaining more and more attention from producers, customers, governments, and various organizations. Understandably, there are several ways to increase the sustainable development of industrial production. One effective tool is simulation, which can have a significant impact on improving environmental, economic, and social sustainability. This paper explores the role of simulation as a powerful scientific and engineering solution in advancing sustainability within industrial ecosystems. Its main scope is to map the existing literature on the usage of simulation as a supportive tool for achieving this goal. For this purpose, a bibliometric analysis was conducted, allowing for tailored insights into the use of simulation in sustainable production.

Keywords: simulation; sustainability; industry; economic; environmental

1. Introduction

Sustainable development as a way to understand the interaction of economic, social, and environmental systems, is widely recognized to have its origins in the UN Conference on the Human Environment in Stockholm in 1972. In terms of modern-day problems, sustainability is one of the main domains of interest worldwide. Therefore, even the industrial sector has come to the conclusion that it is necessary to take a stand on this particular issue [1–3]. The question of creating sustainable industry has been raised with the purpose of clarifying the many challenges and problems that businesses are confronted with in the application of this concept. The first time these issues were brought up in an industrial context was in the Brundtland report of 1987 by the World Commission on Environment and Development. This report, concerning industrial matters, focuses on changing how resources and environmental considerations are viewed in industrial planning and decision making [4]. Further elaboration and details are found in the concepts of Industry 4.0, and more recently, in the concept of Industry 5.0. In both concepts, sustainability is divided into three categories: economic, environmental, and social [5,6]. In terms of industrial practice, sustainability is segmented into three categories: corporate sustainability, industrial sustainability, and manufacturing sustainability (MS) [7–10]. This leads us to the conclusion that the concept of sustainability is contemplated in all areas and structural levels of enterprise. It is logical that sustainability cannot be the main goal of a manufacturing company; therefore, there has to be some impetus to participate in this industrial trend.

Some of the main reasons to incorporate sustainability into production, other than sustainable conviction, are as follows [1]:

- Customer demand for sustainable products. Nowadays, the marketing for many companies and products is based on their sustainable characteristics, in terms of how they were produced and how sustainable their usage is in terms of, for example, energy usage, maintenance, and recycling processes. Then, there is the question of

what materials were used in production, where these materials were obtained, and last but not least, who made them and under what conditions.

- Government pressure/support in sustainable production. Individual states can help companies or put pressure on them by implementing laws in the form of bans or, on the other hand, providing financial help if the company innovates in terms of sustainability. The United Nations has set the goal to accomplish seventeen sustainable goals as part of the 2030 Agenda for Sustainable Development [11]. Some of these are aimed directly at the industrial sector.
- Energy and material prices. These commodities are crucial for the functioning of manufacturing companies. According to the latest data from 2021 from Eurostat, the industrial sector consumed 25.6% of all final energy in the EU, making it one of the largest energy consumers. Of the total amount of energy, only 9.7% was made up of renewable sources and biofuels [12]. The prices of these commodities are constantly increasing, and that is why companies should, for their own good, want to reduce their usage.

In addition, it is also necessary to view environmental sustainability through the prism of the reduction of manufacturing waste linked to material inputs. To better understand waste process flows in manufacturing enterprises, a holistic approach is recommended by Ball et al. [13]. The authors developed the input/output flow model of materials, energy, and waste to show how they can interact, using simulation. Their paper also demonstrates how this tool can be used to select appropriate technologies to reduce material and energy consumption as well as the carbon footprint. Moreover, they showed how results of the simulation can be used to redesign manufacturing processes to achieve the above-mentioned effects. In this context, the concept of design for the environment has been introduced to describe design and redesign practices through which products and manufacturing processes are optimized [14]. Therefore, the analysis of the relationships among of materials, energy, and waste is one of the first important steps companies need to take to decrease the consumption of resources and energy and to reduce the emissions of pollutants in line with the Corporate Social Responsibility concept [15–17].

It is crucial for management to think about sustainable production for their company but also a sustainable future for everyone. In connection with sustainable industry, the terms circular and sharing economy are commonly used [18,19]. The main goal of a circular economy is focused on embracing practices that emphasize resource efficiency and waste prevention by promoting close-loop systems in contrast to linear principles [20–22]. Therefore, decision making in terms of sustainability is important but also difficult. A small mistake could lead to a big financial loss. On that note, there are supportive methods and tools that can help management in decision making not just in matters of sustainability but also in the optimalization of various types of processes.

One of these is simulation. Simulation can be described in a simplified form as an imitation of a system [23–25]. From a dynamic point of view, it can be divided into two categories: static simulation and dynamic simulation. All simulations have advantages and disadvantages in terms of their usage [26]. Simulation, as a tool, is used daily in almost all aspects of everyday life. Probably the most well-known everyday simulations include weather forecasting, flight and car simulators, and job position training [27]. It is important to note that simulation is a supportive tool and not a solution for problems. Simulation can help provide a better understanding of the problem or create more possibilities for management or others responsible for decisions. Simulation is not omnipotent; it is only as good as the data that the creator puts into it [28]. In terms of data for simulation, the amount and quality have improved with the implementation of digitalization based on Industry 4.0. The implementation of smart sensors, RFID technologies, the Internet of Things, and cloud technologies brings potential for the usage of simulations with data in real time. In other words, simulation can be used for monitoring and analyzing processes and events in almost real time, which can help with smooth and quick decision making [29–33].

The main research questions (RQs) that this paper addresses can be formulated as follows:

- RQ1: What are possibilities for the utilization of simulation methods for addressing sustainable issues?
- RQ2: What types of simulation methods are most often used for addressing sustainable issues in selected industrial fields?

2. Materials and Methods

To analyze the existing literature on the particular research problem as well as to reach conclusions regarding the stated research questions, the following two approaches were employed. The first one is based on a bibliometric analysis performed with a specialized software that is described below. Two types of bibliometric analyses were applied, namely (1) performance analyses, and (2) science mapping to obtain relevant scientific insights from several angles for the given problem. After the initial step, selected papers were reviewed for deeper analysis. The overall structure of the paper's methodology with some details is depicted in Figure 1.

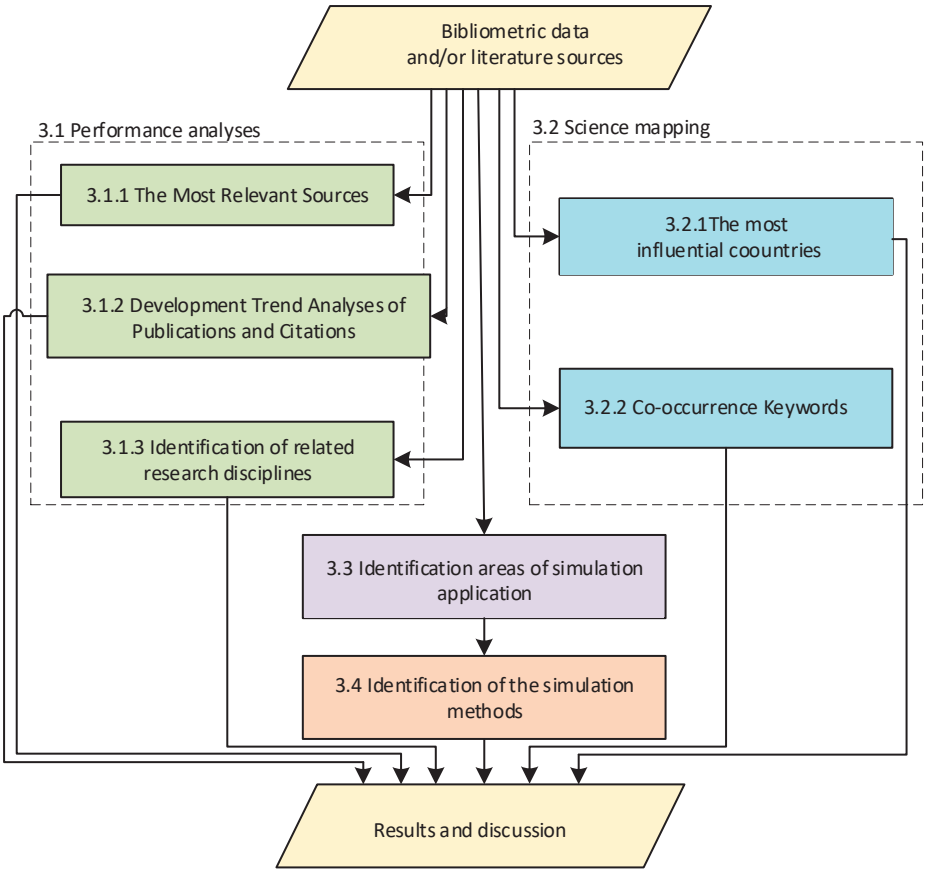

Figure 1. Methodological framework of the study.

3. Bibliometric Analysis and Literature Review

This section describes the results of the bibliometric analysis and the review of selected papers regarding the usage of simulation for ensuring sustainability in industry according to the triple bottom-line construct [34]. To this end, the Web of Science (WoS) database was used to search for specified terms and conditions. The section is divided into two main parts: bibliometric analysis and the review of selected papers. Performance analysis includes categorization of total publications by document type, publication growth, research area, contribution by country, publication title, frequently cited publications, and citation metrics.

Country co-authorship, keyword co-occurrence, and the most used keywords are a part of the science mapping analysis, which is performed using VOSviewer 1.6.20 [35–37].

3.1. Performance Analysis Based on Bibliometric Indicators

The search terms for the purpose of the performance analysis were as follows: simulation (Topic) AND sustainability (Topic) AND industry (Topic) entered on the following day: 25 March 2024. The conditions were also specified by the years, ranging from 2013 to 2023. Together, 1275 documents were identified. Only articles, proceeding papers, review articles, early access documents, and book chapters were analyzed in this study. After removing unrelated documents, a total of 1272 publications were further analyzed. These publications were divided based on their types; see Table 1.

Table 1. Publications based on document types.

Document Types	Total Publications
Article	983
Proceeding paper	199
Review article	107
Early access	24
Book chapters	13

From the previous table, it can be seen that more than 89% of the publications were articles (74.1%) and proceeding papers (15%). Review articles made up 8.1% of the total documents, while early access documents and book chapters contributed 1.8% and 1%, respectively.

3.1.1. The Most Relevant Sources

This subsection is devoted to the evaluation of the publication sources of the papers. There were more than 210 publication sources for this topic, from which the top 10 ones were identified. They are listed in terms of importance in Table 2.

Table 2. The list of the most relevant sources.

Source of the Publications	The Number of Publications
Sustainability	125
Journal of Cleaner Production	73
Energies	26
Applied Sciences	16
Buildings	15
Procedia CIRP	11
ACS Sustainable Chemistry Engineering	10
Applied Energy	10
Biofuels Bioproducts Biorefining	10
Renewable Sustainable Energy Reviews	10

From Table 2, it can be seen that, not surprisingly, the most frequently occurring publication source is Sustainability, with 125 documents. The Journal of Cleaner Production, with 73 publications, took second place. Other documents are distributed across various journals with a similar scope. It is useful to mention some journals not listed in the table above: Buildings, Energy, Polymers, Agricultural Systems, Green Chemistry, and Foods.

3.1.2. Development Trend Analyses of Publications and Citations

The annual publication growth of all the publications in the field, including the number of citations per year and the total number of citations per publications, is shown in Table 3.

Table 3. The number of citations per year and the number of citations per publication.

Year	Total Publications	Percentage (%)	Total Citations	Number of Citations per Publication
2023	233	18.3	5328	22.87
2022	201	15.8	4819	23.98
2021	192	15.1	3629	18.9
2020	119	9.4	2371	19.92
2019	140	11	1458	10.41
2018	99	7.8	949	9.59
2017	74	5.8	546	7.38
2016	70	5.5	310	4.43
2015	64	5	147	2.3
2014	42	3.3	61	1.45
2013	38	3	10	0.26
Total	1272	100	19,628	-

The highest number of total citations was recorded in 2023, with 5328 citations from a total of 19,628 citations. The highest number of citations per paper occurred in 2022. The total annual publications saw an increasing trend from 2013 to 2019. A slight drop occurred in the total annual publications in 2020 due to the COVID-19 pandemic situation. However, the total annual publication number continued to increase until it peaked in 2023, with 233 publications from a total of 1272 publications, as can be seen in Figure 2.

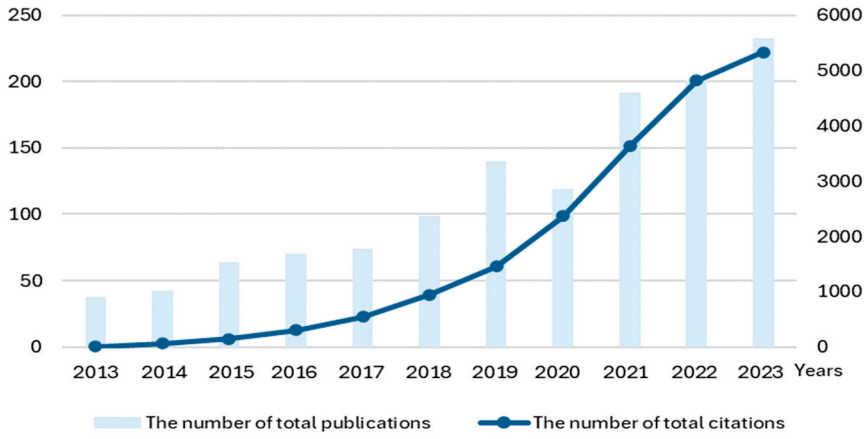

Figure 2. Trend analysis of annual publications and citation growth in a given field.

3.1.3. Identification of Related Research Disciplines

The 1272 publications were subsequently divided into more than 60 research areas. The top 15 research areas are listed in Table 4.

Table 4. The top 15 research areas in the field.

Research Discipline	Number of Publications
Engineering	585
Environmental sciences ecology	333
Science technology and other topics	318
Energy fuels	144
Computer science	139
Business economy	96
Construction building technology	74
Materials science	73
Chemistry	61
Operations research and management science	57
Agriculture	51
Physics	39
Thermodynamics	32
Biotechnology and applied microbiology	27
Telecommunications	27

The highest number of the documents (585) were categorized under the Engineering domain; 333 publications were assigned to the Environmental sciences ecology research area, and 318 publications were from the field of Science technology. The remaining 321 documents were covered by twelve other research areas listed in the lower part of the table. To point out the most important publications on the research topic, Table 5 provides the list of the top 10 cited papers.

Table 5. Selected attributes of the top ten cited publications.

Authors	Year	Number of Citations	Country	Publication Title	Journal Impact Factor
Adil et al. [38]	2017	951	Saudi Arabia	Chemical Society Reviews	46.2
Abubakr et al. [3]	2020	417	China	International Journal of Production Economics	12
Nunes et al. [39]	2020	289	Saudi Arabia/Turkey/Israel/The Netherlands/Canada	Journal of Membrane Science	9.5
Lu et al. [40]	2017	269	China/Singapore	Automation in construction	10.3
Guillard et al. [41]	2018	215	France	Frontiers in nutrition	5
Abanda et al. [42]	2016	202	England	Energy	8.9
Rosin et al. [43]	2020	170	France	International Journal of Production Research	9.2
Chowdhury et al. [44]	2022	134	Australia	Operations management research	9.0
Goodarzian et al. [45]	2021	131	Iran	Engineering applications of artificial intelligence	8.0
Jouzdani et al. [46]	2021	130	Iran	Journal of Cleaner Production	11.1

It is also evident from Table 5 that there is a great interest in this topic in the scientific field, which is supported by the number of citations, a wide range of countries involved in this research, and the number of reputable international journals.

The most cited paper [38], with 951 citations, provides insights into the microscopic mechanisms governing the resultant separation performance, suggesting a plausible correlation between the inherent structural features/topology of metal–organic frameworks and the associated gas/vapor separation performance. The Monte Carlo simulation is used in this publication. The diversity of publication titles and countries within papers is intriguing. Among the ten publications presented in Table 5, three are categorized as review papers and seven as articles.

3.2. Science Mapping Using Bibliometric Networks

Bibliometric mapping or science mapping is used to investigate the interrelations between selected research aspects using a spatial representation of how system elements such as individual documents or authors are related to one another. Such mapping helps to better understand the structure and dynamism of the given research area and to identify research frontiers, leading collaborations, the most relevant sources, and so on. This method was applied in order to identify the most influential countries in this area and the most important sub-domains that can help to uncover connections between different themes within the field of study.

3.2.1. The Most Influential Countries in the Research Field

As was mentioned above, this sub-subsection aims to identify the most important countries and collaboration networks in the research area. This is important because scholars from across the world are collaborating to expand and develop their research interests, which ultimately advances the development of knowledge in a particular domain. This trend can be viewed using VOSviewer software, which allows the creation of a country co-authorship network map. To this end, the input data for VOSviewer was imported

from WoS database; the keywords mentioned in Section 3.1 were used and subsequently transferred into the bibliometric map shown in Figure 3.

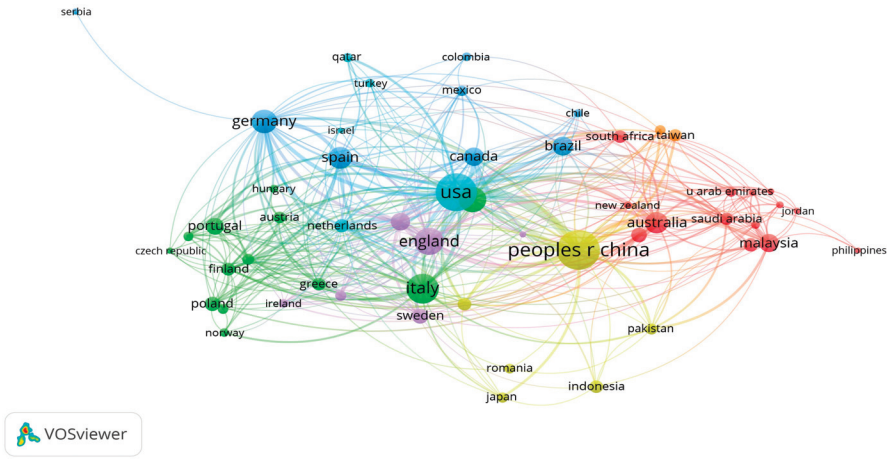

Figure 3. The country co-authorship map in VOSviewer.

The results obtained from VOSviewer showed that country co-authorship analysis identified the USA as having the largest international collaboration, with 151 total link strength, followed by China, England, Germany, and Italy, with 130, 101, 79, and 78 total link strength, respectively. The strongest international collaboration occurs between the USA and China, with 24 link strength. This is followed by cooperation between China and Australia, with 10 total strong links between them. In the third position from this point of view is the cooperation between China–England and China–Canada, with 9 total strong connections.

The publications in the specified fields involve scholars from more than 90 countries. The top 15 countries with the most contributions in the specified field are depicted in Table 6.

Table 6. The top 15 countries with the most contributions in the specified field.

Country	Total Publications	Total Citations	Number of Citations per Publication
China	207	4073	19.7
USA	190	3941	20.7
Italy	122	2363	19.4
England	98	2168	22.1
India	87	1200	13.8
Germany	76	1899	25
Spain	65	997	15.3
Australia	63	1612	25.6
Brazil	50	657	13.1
Canada	48	1107	23
France	46	2461	53.5
Malaysia	46	607	13.2
Portugal	40	541	13.5
Sweden	32	452	14.1
Iran	30	822	27.4

As can be seen from this table, Chinese scholars have the highest number of citations, and French scholars have the greatest number of citations per paper.

3.2.2. Mapping of the Most Important Sub-Domains of the Research Topic

To identify the most important sub-domains of the research topic, the co-occurrence keywords search was used to access scientific manuscripts that were sourced from the WoS database using the same input data as in the previous Section 3.2.1. The keyword co-occurrence map was generated by VOSviewer, and the minimum number of occurrences

of a keyword was set to 15. A total of 85 keywords met the threshold, for which the network shown in Figure 4 was created. The keywords are grouped into five clusters, which are illustrated in different colors. The size of the circle for each keyword emphasizes frequency of the usage of the particular keyword. The bigger the circle, the more frequently the word is used.

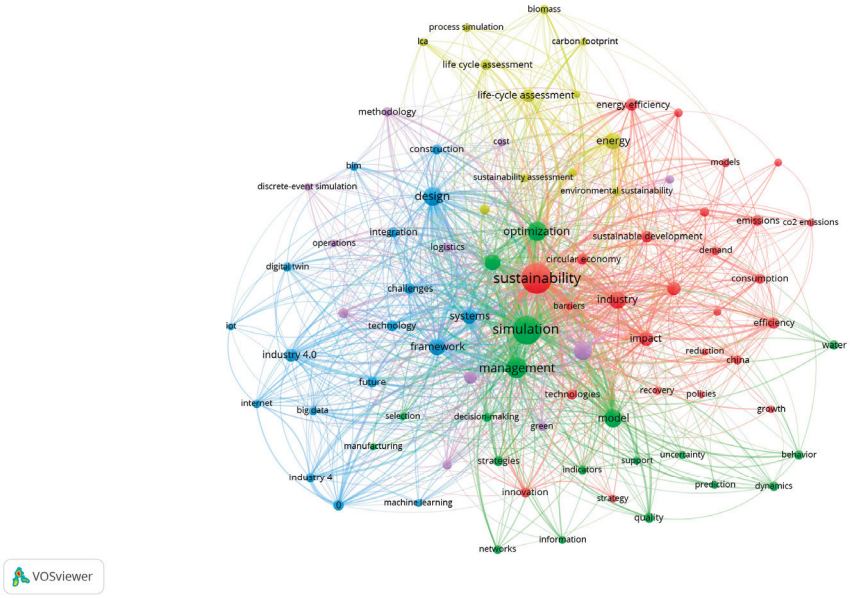

Figure 4. The keyword co-occurrence map.

The most frequent keyword was 'sustainability', which occurred 410 times, with a total link strength of 1378. The second most used keyword was 'simulation', appearing 347 times and having a total link strength of 1284. The third most important was 'management', which occurred 169 times and had a 711 total link strength. From the same figure, it is possible to determine four clusters; the red cluster contains keywords such as sustainability, industry, simulation, impact, circular economy, system dynamics, sustainable development, innovation, etc. This cluster is mostly focused on sustainability topics and its application through the company. The second cluster—the green one—involves the keywords simulation, optimization, management, model, system, strategies, support, indicators, energy, decision making, information, prediction, uncertainty, etc. The listed keywords can help managers direct their activities to correspond with these categories. The third blue cluster includes keywords like design, framework, technology, challenges, future, Industry 4.0, big data, internet, Internet of Things, digital twin, machine learning, etc. The blue cluster highlights the digital transformation of a company using Industry 4.0 tools. The last cluster, purple in color, features the following keywords: performance, supply chain management, waste, implementation, operations, logistics, implementation, etc. This cluster highlights approaches to improve supply chain management and influence the industry towards sustainability by building a responsible supply chain.

Following the results from the previous map, the top ten keywords and their allocation to the clusters are listed in Table 7.

The primary results from bibliometric analysis indicate a significant interest in the topic of simulation usage in sustainable industry. This conclusion is based on the number of publications and the presence of more than 60 research areas under which publications were submitted. These areas encompass a wide range of disciplines, including engineering, chemistry, agriculture, and telecommunications, among others, suggesting that simulation has broad applications across various fields in connection with sustainable industry. Furthermore, interest in this topic is evident across numerous countries, as indicated by the number of publications originating from different regions. As was already mentioned, it is not surprising that the majority of publications are found in reputable journals that focus

on sustainability, such as Sustainability and the Journal of Clean Production. Additionally, strong connections in collaborations between scholars suggest a collective effort to address sustainable industry issues and explore how simulation can contribute to solving this global problem. In terms of the most frequently occurring keywords, sustainability and simulation are closely linked to concepts such as management, optimization, design, performance, and industry as a whole. One could argue that achieving sustainable industry, supported by simulation, can be applied throughout the entire product life cycle.

Table 7. The top 10 keywords and their allocation to the clusters.

Keyword	Appearance	Cluster Color
Sustainability	410	Red
Simulation	347	Green
Management	169	Green
Optimization	142	Green
Design	124	Blue
Performance	118	Purple
Model	111	Green
Industry	102	Red
Framework	97	Blue
Systems	91	Blue

In the next paragraph, a deeper analysis of selected publications will be conducted to gain a better understanding of where and in what contexts simulation is used in terms of sustainable industry.

3.3. Identification of Areas of Simulation Application

The final step in investigation of the published articles is to look at some of them more closely in terms of the areas in which simulations are used for sustainability purpose. For this particular analysis, publications from WoS were used, and papers with 50 and more citations, based on the WOS dataset, were selected for in-depth analysis. This analysis was carried by analyzing the selected publications as distributed over four categories. It is reasonable to assert that almost every paper can by placed in more than one category; thus, the categorization was carried out based on the main field of study.

In the following part, each category is briefly described based on the publications were assigned to it. The two most prominent categories with the most assigned papers are the energy/source category and building/construction category. Manufacturing as a discipline is third in this context.

3.3.1. Energy and Energy Sources

Based on the selected publications, the main topics of this category are how to prevent extensive usage of energy and what can be used for alternative sources of energy. In the publication by Cossu [47], the authors focus on the photovoltaic energy used in the greenhouse industry and focus on identification of strategies to design such greenhouses with a specific agricultural purposes. The authors of [48] used numerical simulation to calculate the light distribution and availability for the main types of photovoltaic greenhouses in the EU. The other publications focused on the usage of photovoltaics include an article by Yang, which emphasizes the usage of simulation in monitoring energy performance [49]. Even if solar energy has great potential, there are many problems with its application as the main source of energy in industry. One of these obstacles is the lack of thermal conversion devices, which have specific parameters for industrial application. In a study by Fernabdez-Garcia, numerical simulation was used for designing such devices [50].

The publication by Jokar is focused on studying the cement industry and its impact on CO_2 pollution, focusing on how more effective methods in processing can help ensure the cement industry is more sustainable in terms of alternative material usage and reduction of

pollution. Simulation carried out by the authors was used to indicate how CO_2 emissions and economical aspects are affected by sustainable decisions [51]. Another publication [52], focused on the usage of alternative sources of energy, namely jet fuel production, was published by Shen. The study in [53] focused on feedstock lignin and cellulosic ethanol. Simulation in this particular publication was conducted via the Aspen Plus simulation tool. In terms of alternative fuels, the publication by Li presents another feedstock opportunity for producing sustainable fuel. In their study, Monte Carlo simulation is used [54]. The review on biomass as a renewable source of energy focused on the biomass supply chain [55]. Another industry affected by sustainable goals is the shipping industry; in the publication by Trivyza, simulation is used for ship energy systems [56]. Another alternative source of energy, namely natural gas hydrate, was more or less successfully tested. One study focused on the exploitation of natural gas hydrate; the investigated methods were thermal simulation and numerical simulation [57]. In another example, natural gas from shale was tested by simulation [58].

3.3.2. Building/Construction

Sustainability has gained much attention in the building and construction sectors. Concerning the building and construction industry, two of the methods that were adopted in various publications were Building Information Modeling [40,42,59–62], with its model-based methods for studying construction through the whole life cycle, and Building Energy Modeling [63–65], bringing opportunities to study construction energy consumption. These models present opportunities to study and analyze construction and the processes that take place [66–68]. In terms of sustainability, it is necessary to look at ways to make the building industry greener in terms of the analysis of existing buildings and possibilities to make them more energy efficient but also regarding new ways to build and which materials are more fitting for sustainability demands [69,70].

3.3.3. Manufacturing and Supply Chain

One of the greatest impacts on the sustainability aspect is undoubtedly manufacturing and the processes connected with it. Therefore, there is a significant demand for solutions to tackle these challenges. Even manufacturing industries themselves are interested in making their systems more sustainable, at least from an economic standpoint. This trend can be noticed in government strategies such as Industry 4.0, Industry 5.0, and Made In China 2025, which focus on processes related to industry, with sustainability being a key topic in these concepts [71–77].

For sustainable manufacturing, it is crucial to examine all levels and processes connected to manufacturing systems. A new perspective on manufacturing sustainability has introduced strategies such as trade-in programs [78], where old products are exchanged for new ones. In this situation, determining the value of the new product is difficult due to the varying condition of the returned product. Simulation proves to be a helpful tool in achieving economic sustainability in such scenarios.

Based on concrete literature, simulations could bring great advantages in designing sustainable manufacturing systems [79]. In many aspects of manufacturing, such as people management, supply chain, and employee management, studies have shown that simulation can be beneficial [80]. For instance, a study by Rehman [81] focuses on the implementation of green manufacturing for organizational performance, for which artificial neural network simulation is utilized. Several publications are based on the implementation of simulation in terms of energy modeling and resource utilization [82–85] In terms of sustainability for workers, 3D modeling and simulation are used; for example, one publication used simulation to set parameters in Delmia Robotics [86] to optimize energy consumption.

A critical component of manufacturing is the supply chain. Numerous studies are dedicated to examining the supply chain through simulation methods across various branches of manufacturing. There is a significant focus on supply chain studies within the food industry [87]. For example, Kamble's [88] paper utilizes a digital twin for studying

the supply chain, which is a simulation-based model of the physical world. Similar studies support the use of simulation in optimizing supply chains, which can help minimize waste, energy consumption, and carbon emissions, as well as evaluate supply chain strategies for more sustainable decision making.

3.3.4. Livestock, Agriculture, and Food Industry

In this section, utilization of simulation is presented in the livestock, agriculture, and food industry. In the context of beef cattle production [89,90], simulation was used to quantify greenhouse gas emissions, fossil energy use, water consumption, and nitrogen loss. Similarly, in the production of aged red wine, a Monte Carlo simulation was employed to address parameter uncertainty, providing confidence intervals for environmental impacts [91]. Additionally, simulation techniques were utilized to analyze land use [92] and food security scenarios [93], using the GlobAgri-AgT model. Studies explored supply chain configurations [44,46,94] and food packaging solutions using mathematical simulation and modeling approaches [41].

3.4. Identification of the Simulation Methods

Simulation methods are modeling approaches that are commonly used for analyzing and optimizing complex systems in operations research. Simulation modeling is frequently defined as the process of creating and experimenting with a computerized mathematical model of physical systems [95]. Simulation methods can be categorized using the taxonomy system model shown in Figure 5.

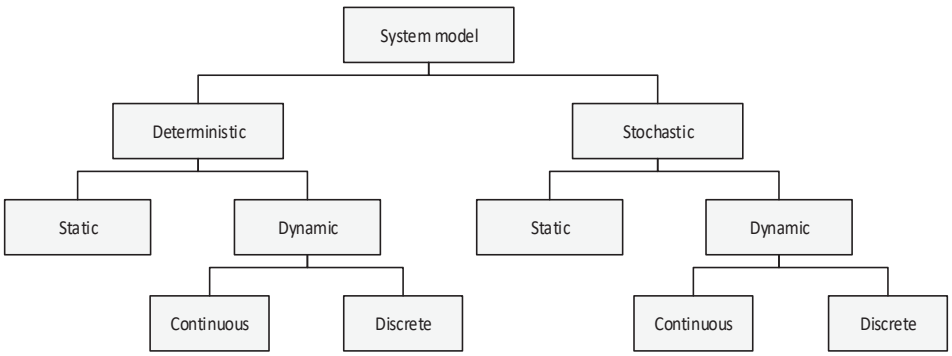

Figure 5. Taxonomy system model (adapted from [96]).

This categorization corresponds to mathematical models that are broadly divided into deterministic and mathematical approaches. Further, in line with RQ2, it is possible to identify actual simulation methods from the above-mentioned literature sources [97]. The simulation methods that are mostly used for solving sustainable issues in the selected industrial field are presented in Table 8.

According to Kelton and Law [96], the most commonly used type of simulation models is the stochastic-dynamic one. The results obtained showed that this type of simulation model is included in 22 publications of the 34 literature sources. Moreover, this table also provides examples of simulation tools used in the articles. Among them, the most frequently used is Building Information Modeling software. This simulation tool is mostly used in building and construction areas to represent the physical and functional aspects of a facility in a digital format. One of the most interesting software programs, which deals specifically with sustainability and the circular economy, is Aspen Plus.

Table 8. The simulation tools used in sustainability.

System Model	Related Documents	Simulation Tool Examples
Deterministic, dynamic, continuous	[50,52–54,58]	Ansys Fluent (https://www.ansys.com/products/fluids/ansys-fluent), Aspen Plus v.10, BioSTEAM (https://biosteam.readthedocs.io/en/latest/), SimaPro Software (https://simapro.com/about/),
Stochastic, static	[3,38,71,79,81]	MATLAB (https://www.mathworks.com/products/matlab.html?s_tid=hp_products_matlab), Monte Carlo simulation (Version 1.1), NOAM calculation software (https://gbs.autodesk.com/gbs)
Deterministic, static	[89,90]	The Integrated Farm System Model (IFSM) (https://www.quantitative-plant.org/model/IntegratedFarmSystemModel)
Stochastic, dynamic, discrete	[40,42,47,51,55,59–66,68,69,78,86–88,91]	Autodesk (https://www.autodesk.com/), Vensim (10.1.4), Arena (https://www.rockwellautomation.com/en-us/products/software/arena-simulation.html), Witness (Version 25.0), Anylogic (https://www.anylogic.com/), ESP-r (https://www.strath.ac.uk/research/energysystemsresearchunit/applications/esp-r/), TRMSYS (https://www.trnsys.com/index.html), EnergyPlus (https://www.3ds.com/products/delmia/industrial-engineering/robotics), Building Information Modeling (https://www.energy.gov/eere/buildings/building-energy-modeling)

4. Results and Discussion

The presented literature review shows the possibility of utilizing simulation in industrial practice. Simulation, as one of the optimization tools, can bring great opportunities for studying and decision making in terms of the sustainability issues that managers face. The results of the presented bibliometric analysis show that interest in this topic is increasing. This can be seen, for example, in the number of nationalities of the scholars involved in this research. Furthermore, there are efforts to address this issue globally. This demonstrates collaborations on various publications involving authors from countries like China, England, Canada, and others. The study then presents a more in-depth analysis of selected papers. From the mentioned analysis, it is valid to declare that simulation has found utilization in creating a more sustainable environment in the industry. By this statement, the first research question is answered; the utilization of simulation in various industries is presented in Section 3.3. As for the second research question, the classification of system models is provided in Section 3.4. Along with this classification, the most-used simulation methods for solving sustainability issues were identified. Moreover, the frequently used system models applied in the simulations were selected according to the taxonomy from Figure 5. From the viewpoint of uncertainty, stochastic models are more often used than deterministic ones, dynamic models prevail over static ones, and discrete models are more common than continuous ones. In addition, the typical simulation software brands for the given purpose were determined from the pertinent publications; these are Building Information Modeling (BIM) and AspenPlus. These simulation tools are in most cases used as a supporting tool in decision making by creating various scenarios and possibilities to achieve the best results. To make the industry sectors sustainable, it is important to achieve accomplishment in three aspects: environmental, economic, and social sustainability. To achieve this kind of implementation in terms of sustainable industry and a sustainable world, the circular economy is viewed as a promising notion. Conceptualization of this approach in relation to sustainable industrial development is outlined in graphic form in Figure 6.

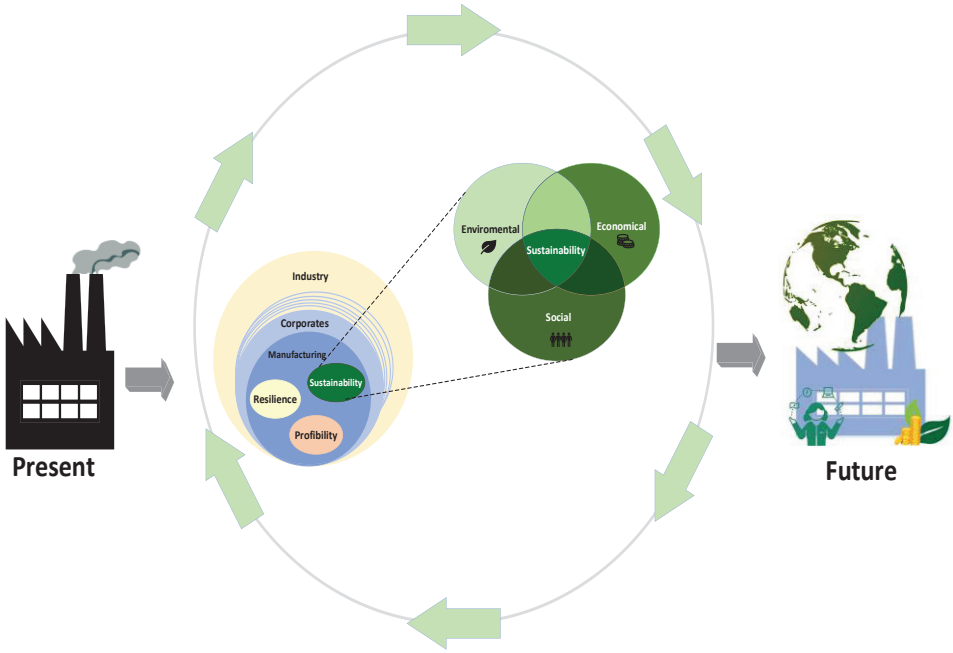

Figure 6. Circular economy as a crucial element of sustainable industrial development.

The concept of circular economy is frequently linked with sustainable manufacturing; both of these concepts highlight the importance of implementing green thinking into industrial sectors in a global perspective. As mentioned in previous sections, the survival of a company can be built solely on sustainable principles. Based on the literature review, it can be stated that simulation can be considered as a valuable tool for sustainable industrial development.

5. Conclusions

It is an indisputable fact that sustainability is a prominent topic not just in the industrial sector but also in every aspect of life. Technological progress brings many opportunities to solve problems in more sophisticated and accurate way. Simulation clearly contributes to the current methods of achieving this effect. It is necessary to say that sustainable production is a key element to achieving competitiveness in the long run. This movement is supported by concepts like Industry 4.0, Industry 5.0, and Made in China 2025, where sustainability is one of the main pillars. Based on research in the literature, the potential of utilization of simulation for sustainability questions is considerable, but there is also great room for improvement in designing new and improving existing simulation methods and tools. With regards to future work and possible improvements in the utilization of simulations for a more sustainable industry, it is necessary to implement sustainability modules into simulation tools for easier implementation of simulations for sustainable industrial development. Also, there appears to be a need for more simulation tools regarding social and employee sustainability.

Author Contributions: Conceptualization, J.N. and V.M.; methodology, J.N. and V.M.; software, J.N.; validation, J.N. and V.M.; formal analysis, J.N. and V.M.; investigation, J.N. and V.M.; writing—original draft preparation, J.N.; writing—review and editing, J.N. and V.M.; visualization, J.N. and V.M.; supervision, V.M.; funding acquisition, V.M. All authors have read and agreed to the published version of the manuscript.

Funding: This research was funded by the KEGA project No. 044TUKE-4/2023 granted by the Ministry of Education of the Slovak Republic and by the project SME 5.0 with funding received from the European Union's research and innovation program under the Marie Skłodowska-Curie grant agreement No. 101086487.

Data Availability Statement: All data are contained within the paper.

Conflicts of Interest: The authors declare no conflicts of interest.

References

1. Herrmann, C.; Schmidt, C.; Kurle, D.; Blume, S.; Thiede, S. Sustainability in manufacturing and factories of the future. *Int. J. Precis. Eng. Manuf.-Green Technol.* **2014**, *1*, 283–292. [CrossRef]
2. Machado, C.G.; Winroth, M.P.; Ribeiro da Silva, E.H.D. Sustainable manufacturing in Industry 4.0: An emerging research agenda. *Int. J. Prod. Res.* **2020**, *58*, 1462–1484. [CrossRef]
3. Abubakr, M.; Abbas, A.T.; Tomaz, I.; Soliman, M.S.; Luqman, M.; Hegab, H. Sustainable and smart manufacturing: An integrated approach. *Sustainability* **2020**, *12*, 2280. [CrossRef]
4. Mondini, G. Sustainability assessment: From Brundtland report to sustainable development goals. *Valori Evalutazioni* **2019**, *23*, 129–137.
5. Bai, C.; Dallasega, P.; Orzes, G.; Sarkis, J. Industry 4.0 technologies assessment: A sustainability perspective. *Int. J. Prod. Econ.* **2020**, *229*, 107776. [CrossRef]
6. Xu, X.; Lu, Y.; Vogel-Heuser, B.; Wang, L. Industry 4.0 and Industry 5.0—Inception, conception and perception. *J. Manuf. Syst.* **2021**, *61*, 530–535. [CrossRef]
7. Neri, A.; Cagno, E.; Di Sebastiano, G.; Trianni, A. Industrial sustainability: Modelling drivers and mechanisms with barriers. *J. Clean. Prod.* **2018**, *194*, 452–472. [CrossRef]
8. Zhivkova, S. Sustainability and the reasons for its adoption in the companies. *Proc. CBU Econ. Bus.* **2022**, *3*, 75–80. [CrossRef]
9. Duić, N.; Urbaniec, K.; Huisingh, D. Components and structures of the pillars of sustainability. *J. Clean. Prod.* **2015**, *88*, 1–12. [CrossRef]
10. Modrak, V.; Soltysova, Z.; Modrak, J.; Behunova, A. Reducing impact of negative complexity on sustainability of mass customization. *Sustainability* **2017**, *9*, 2014. [CrossRef]
11. United Nations. General Assembly Resolution A/RES/70/1. Transforming Our World, the 2030 Agenda for Sustainable Development. Available online: https://sdgs.un.org/2030agenda (accessed on 8 April 2024).
12. Eurostat. Available online: https://ec.europa.eu/eurostat/statistics-explained/index.php?title=Final_energy_consumption_in_industry_-_detailed_statistics (accessed on 8 April 2024).
13. Ball, P.D.; Evans, S.; Levers, A.; Ellison, D. Zero carbon manufacturing facility—Towards integrating material, energy, and waste process flows. *Proc. Inst. Mech. Eng. Part B J. Eng. Manuf.* **2009**, *223*, 1085–1096. [CrossRef]
14. Billatos, S. *Green Technology and Design for the Environment*; CRC Press: Boca Raton, FL, USA, 1997.
15. Shabbir, M.S.; Wisdom, O. The relationship between corporate social responsibility, environmental investments and financial performance: Evidence from manufacturing companies. *Environ. Sci. Pollut. Res.* **2020**, *27*, 39946–39957. [CrossRef] [PubMed]
16. Kitsios, F.; Kamariotou, M.; Talias, M.A. Corporate sustainability strategies and decision support methods: A bibliometric analysis. *Sustainability* **2020**, *12*, 521. [CrossRef]
17. Modrak, V.; Dima, I.C.; Man, M. Methodical approach to corporate sustainability planning. *Pol. J. Manag. Stud.* **2011**, *3*, 156–166.
18. Reuter, M.A.; van Schaik, A.; Gutzmer, J.; Bartie, N.; Abadías-Llamas, A. Challenges of the circular economy: A material, metallurgical, and product design perspective. *Annu. Rev. Mater. Res.* **2019**, *49*, 253–274. [CrossRef]
19. Soltysova, Z.; Modrak, V. Challenges of the sharing economy for SMEs: A literature review. *Sustainability* **2020**, *12*, 6504. [CrossRef]
20. Geissdoerfer, M.; Savaget, P.; Bocken, N.M.; Hultink, E.J. The Circular Economy–A new sustainability paradigm? *J. Clean. Prod.* **2017**, *143*, 757–768. [CrossRef]
21. Ghaithan, A.M.; Alshammakhi, Y.; Mohammed, A.; Mazher, K.M. Integrated impact of circular economy, industry 4.0, and lean manufacturing on sustainability performance of manufacturing firms. *Int. J. Environ. Res. Public Health* **2023**, *20*, 5119. [CrossRef]
22. Salibi, J.G.D.O.R.; Rodrigues, A.L.D.S.M.; Lima, P.A.B.; de Souza, F.B. Lean and the circular economy: A systematic literature review. *J. Lean Syst.* **2022**, *7*, 23–46.
23. Banks, J. *Discrete Event System Simulation*; Pearson Education India: Bangalore, India, 2005.
24. Ingalls, R.G. Introduction to simulation. In Proceedings of the 2011 Winter Simulation Conference, Phoenix, AZ, USA, 11–14 December 2011; pp. 1374–1388.
25. Banks, J. Introduction to simulation. In Proceedings of the 2000 Winter Simulation Conference Proceedings, Orlando, FL, USA, 10–13 December 2000; Volume 1, pp. 9–16.
26. Carson, J.S. Introduction to modeling and simulation. In Proceedings of the Winter Simulation Conference, Orlando, FL, USA, 4 December 2005; p. 8.
27. Robinson, S. *Simulation: The Practice of Model Development and Use*; Bloomsbury Publishing: London, UK, 2014.
28. Maria, A. Introduction to modeling and simulation. In Proceedings of the 29th Conference on Winter Simulation, Atlanta, GA,, USA, 1–7 December 1997; pp. 7–13.
29. De Paula Ferreira, W.; Armellini, F.; De Santa-Eulalia, L.A. Simulation in industry 4.0: A state-of-the-art review. *Comput. Ind. Eng.* **2020**, *149*, 106868. [CrossRef]
30. Khan, A.A.; Abonyi, J. Simulation of sustainable manufacturing solutions: Tools for enabling circular economy. *Sustainability* **2022**, *14*, 9796. [CrossRef]
31. Gunal, M.M. *Simulation for Industry 4.0. Past, Present, and Future*, 1st ed.; Springer Nature: Cham, Switzerland, 2019; pp. 19–36.

32. Parv, A.L.; Deaky, B.A.; Stasiak-Betlejewska, R. Sustainable manufacturing systems–a simulation model. In Proceedings of the IOP Conference Series: Materials Science and Engineering, Brasov, Romania, 7–10 October 2021; Volume 1009, p. 012045.
33. Rocholl, J.; Mönch, L. Simulation-based performance assessment of sustainable manufacturing decisions. In Proceedings of the 2021 Winter Simulation Conference, Phoenix, AZ, USA, 12–15 December 2021; pp. 1–12.
34. Elkington, J.; Rowlands, I.H. Cannibals with forks: The triple bottom line of 21st century business. *Altern. J.* **1999**, *25*, 42. [CrossRef]
35. Donthu, N.; Kumar, S.; Mukherjee, D.; Pandey, N.; Lim, W.M. How to conduct a bibliometric analysis: An overview and guidelines. *J. Bus. Res.* **2021**, *133*, 285–296. [CrossRef]
36. Moral-Muñoz, J.A.; Herrera-Viedma, E.; Santisteban-Espejo, A.; Cobo, M.J. Software tools for conducting bibliometric analysis in science: An up-to-date review. *Prof. Inf. Inf. Prof.* **2020**, *29*. [CrossRef]
37. Chen, C. Science mapping: A systematic review of the literature. *J. Data Inf. Sci.* **2017**, *2*, 1–40. [CrossRef]
38. Adil, K.; Belmabkhout, Y.; Pillai, R.S.; Cadiau, A.; Bhatt, P.M.; Assen, A.H.; Eddaoudi, M. Gas/vapour separation using ultra-microporous metal–organic frameworks: Insights into the structure/separation relationship. *Chem. Soc. Rev.* **2017**, *46*, 3402–3430. [CrossRef] [PubMed]
39. Nunes, S.P.; Culfaz-Emecen, P.Z.; Ramon, G.Z.; Visser, T.; Koops, G.H.; Jin, W.; Ulbricht, M. Thinking the future of membranes: Perspectives for advanced and new membrane materials and manufacturing processes. *J. Membr. Sci.* **2020**, *598*, 117761. [CrossRef]
40. Lu, Y.; Wu, Z.; Chang, R.; Li, Y. Building Information Modeling (BIM) for green buildings: A critical review and future directions. *Autom. Constr.* **2017**, *83*, 134–148. [CrossRef]
41. Guillard, V.; Gaucel, S.; Fornaciari, C.; Angellier-Coussy, H.; Buche, P.; Gontard, N. The next generation of sustainable food packaging to preserve our environment in a circular economy context. *Front. Nutr.* **2018**, *5*, 121. [CrossRef] [PubMed]
42. Abanda, F.H.; BYERS, L. An investigation of the impact of building orientation on energy consumption in a domestic building using emerging BIM (Building Information Modelling). *Energy* **2016**, *97*, 517–527. [CrossRef]
43. Rosin, F.; Forget, P.; Lamouri, S.; Pellerin, R. Impacts of Industry 4.0 technologies on Lean principles. *Int. J. Prod. Res.* **2020**, *58*, 1644–1661. [CrossRef]
44. Chowdhury, M.T.; Sarkar, A.; Paul, S.K.; Moktadir, M.A. A case study on strategies to deal with the impacts of COVID-19 pandemic in the food and beverage industry. *Oper. Manag. Res.* **2022**, *15*, 166–178. [CrossRef]
45. Goodarzian, F.; Taleizadeh, A.A.; Ghasemi, P.; Abraham, A. An integrated sustainable medical supply chain network during COVID-19. *Eng. Appl. Artif. Intell.* **2021**, *100*, 104188. [CrossRef] [PubMed]
46. Jouzdani, J.; Govindan, K. On the sustainable perishable food supply chain network design: A dairy products case to achieve sustainable development goals. *J. Clean. Prod.* **2021**, *278*, 123060. [CrossRef]
47. Cossu, M.; Cossu, A.; Deligios, P.A.; Ledda, L.; Li, Z.; Fatnassi, H.; Poncet, C.; Yano, A. Assessment and comparison of the solar radiation distribution inside the main commercial photovoltaic greenhouse types in Europe. *Renew. Sustain. Energy Rev.* **2018**, *94*, 822–834. [CrossRef]
48. Lv, D.; Shi, R.; Chen, Y.; Wu, Y.; Wu, H.; Xi, H.; Xia, Q.; Li, Z. Selective adsorption of ethane over ethylene in PCN-245: Impacts of interpenetrated adsorbent. *ACS Appl. Mater. Interfaces* **2018**, *10*, 8366–8373. [CrossRef]
49. YANG, R.J. Overcoming technical barriers and risks in the application of building integrated photovoltaics (BIPV): Hardware and software strategies. *Autom. Constr.* **2015**, *51*, 92–102. [CrossRef]
50. Fernández-García, A.; Rojas, E.; Pérez, M.; Silva, R.; Hernández-Escobedo, Q.; Manzano-Agugliaro, F. A parabolic-trough collector for cleaner industrial process heat. *J. Clean. Prod.* **2015**, *89*, 272–285. [CrossRef]
51. Jokar, Z.; Mokhtar, A. Policy making in the cement industry for CO2 mitigation on the pathway of sustainable development-A system dynamics approach. *J. Clean. Prod.* **2018**, *201*, 142–155. [CrossRef]
52. Shen, R.; Tao, L.; Yang, B. Techno-economic analysis of jet-fuel production from biorefinery waste lignin. *Biofuels Bioprod. Biorefining* **2019**, *13*, 486–501. [CrossRef]
53. Morales, M.; Arvesen, A.; Cherubini, F. Integrated process simulation for bioethanol production: Effects of varying lignocellulosic feedstocks on technical performance. *Bioresour. Technol.* **2021**, *328*, 124833. [CrossRef] [PubMed]
54. Li, Y.; Bhagwat, S.S.; Cortés-Peña, Y.R.; Ki, D.; Rao, C.V.; Jin, Y.-S.; Guest, J.S. Sustainable lactic acid production from lignocellulosic biomass. *ACS Sustain. Chem. Eng.* **2021**, *9*, 1341–1351. [CrossRef]
55. Zahraee, S.M.; Shiwakoti, N.; Stasinopoulos, P. Biomass supply chain environmental and socio-economic analysis: 40-Years comprehensive review of methods, decision issues, sustainability challenges, and the way forward. *Biomass Bioenergy* **2020**, *142*, 105777. [CrossRef]
56. Trivyza, N.L.; Rentizelas, A.; Theotokatos, G. A novel multi-objective decision support method for ship energy systems synthesis to enhance sustainability. *Energy Convers. Manag.* **2018**, *168*, 128–149. [CrossRef]
57. Yang, L.; Liu, Y.; Zhang, H.; Xiao, B.; Guo, X.; Wei, R.; Xu, L.; Sun, L.; Yu, B.; Leng, S.; et al. The status of exploitation techniques of natural gas hydrate. *Chin. J. Chem. Eng.* **2019**, *27*, 2133–2147. [CrossRef]
58. Ehlinger, V.M.; Gabriel, K.J.; Noureldin, M.M.B.; El-Halwagi, M.M. Process design and integration of shale gas to methanol. *ACS Sustain. Chem. Eng.* **2014**, *2*, 30–37. [CrossRef]
59. Santos, R.; Costa, A.A.; Silvestre, J.D.; Vandenbergh, T.; Pyl, L. BIM-based life cycle assessment and life cycle costing of an office building in Western Europe. *Build. Environ.* **2020**, *169*, 106568. [CrossRef]

60. Muller, M.F.; Esmanioto, F.; Huber, N.; Loures, E.R.; Canciglieri, O. A systematic literature review of interoperability in the green Building Information Modeling lifecycle. *J. Clean. Prod.* **2019**, *223*, 397–412. [CrossRef]
61. Yin, S.; Li, B.; Xing, Z. The governance mechanism of the building material industry (BMI) in transformation to green BMI: The perspective of green building. *Sci. Total Environ.* **2019**, *677*, 19–33. [CrossRef]
62. Jalaei, F.; Jalaei, F.; Mohammadi, S. An integrated BIM-LEED application to automate sustainable design assessment framework at the conceptual stage of building projects. *Sustain. Cities Soc.* **2020**, *53*, 101979. [CrossRef]
63. Jin, R.; Zhong, B.; Ma, L.; Hashemi, A.; Ding, L. Integrating BIM with building performance analysis in project life-cycle. *Autom. Constr.* **2019**, *106*, 102861. [CrossRef]
64. Pezeshki, Z.; Soleimani, A.; Darabi, A. Application of BEM and using BIM database for BEM: A review. *J. Build. Eng.* **2019**, *23*, 1–17. [CrossRef]
65. Chen, Y.; Tong, Z.; Malkawi, A. Investigating natural ventilation potentials across the globe: Regional and climatic variations. *Build. Environ.* **2017**, *122*, 386–396. [CrossRef]
66. Aste, N.; Manfren, M.; Marenzi, G. Building Automation and Control Systems and performance optimization: A framework for analysis. *Renew. Sustain. Energy Rev.* **2017**, *75*, 313–330. [CrossRef]
67. Dong, L.; Liang, H.; Zhang, L.; Liu, Z.; Hu, M. Highlighting regional eco-industrial development: Life cycle benefits of an urban industrial symbiosis and implications in China. *Ecol. Model.* **2017**, *361*, 164–176. [CrossRef]
68. Gan, V.J.; Lo, I.M.; Ma, J.; Tse, K.T.; Cheng, J.C.; Chan, C.M. Simulation optimization towards energy efficient green buildings: Current status and future trends. *J. Clean. Prod.* **2020**, *254*, 120012. [CrossRef]
69. Kaewunruen, S.; Xu, N. Digital twin for sustainability evaluation of railway station buildings. *Front. Built Environ.* **2018**, *4*, 77. [CrossRef]
70. Riley, B. The state of the art of living walls: Lessons learned. *Build. Environ.* **2017**, *114*, 219–232. [CrossRef]
71. Marsono, A.K.B.; Balasbaneh, A.T. Combinations of building construction material for residential building for the global warming mitigation for Malaysia. *Constr. Build. Mater.* **2015**, *85*, 100–108. [CrossRef]
72. Giret, A.; Trentesaux, D.; Prabhu, V. Sustainability in manufacturing operations scheduling: A state of the art review. *J. Manuf. Syst.* **2015**, *37*, 126–140. [CrossRef]
73. Li, L. China's manufacturing locus in 2025: With a comparison of "Made-in-China 2025" and "Industry 4.0". *Technol. Forecast. Soc. Chang.* **2018**, *135*, 66–74. [CrossRef]
74. Takakuwa, S.; Veza, I.; Celar, S. "Industry 4.0" in Europe and East Asia. *Ann. DAAAM Proc.* **2019**, *29*, 61–69.
75. Maddikunta, P.K.R.; Pham, Q.V.; Prabadevi, B.; Deepa, N.; Dev, K.; Gadekallu, T.R.; Liyanage, M. Industry 5.0: A survey on enabling technologies and potential applications. *J. Ind. Inf. Integr.* **2020**, *26*, 100257. [CrossRef]
76. Wu, Y.A.; Ng, A.W.; Yu, Z.; Huang, J.; Meng, K.; Dong, Z. A review of evolutionary policy incentives for sustainable development of electric vehicles in China: Strategic implications. *Energy Policy* **2021**, *148*, 111983. [CrossRef]
77. Modrak, V.; Soltysova, Z.; Onofrejova, D. Complexity assessment of assembly supply chains from the sustainability viewpoint. *Sustainability* **2019**, *11*, 7156. [CrossRef]
78. Tozanli, Ö.; Kongar, E.; Gupta, S.M. Trade-in-to-upgrade as a marketing strategy in disassembly-to-order systems at the edge of blockchain technology. *Int. J. Prod. Res.* **2020**, *58*, 7183–7200. [CrossRef]
79. Sathish, T. Modeling of Support Vector Mechanism for Green Manufacturability Quantification of Production. In Proceedings of the Advances in Manufacturing Technology: Select Proceedings of ICAMT 2018; Springer: Singapore, 2019; pp. 391–397.
80. Lugert, A.; Batz, A.; Winkler, H. Empirical assessment of the future adequacy of value stream mapping in manufacturing industries. *J. Manuf. Technol. Manag.* **2018**, *29*, 886–906. [CrossRef]
81. Rehman, M.A.; Seth, D.; Shrivastava, R.L. Impact of green manufacturing practices on organisational performance in Indian context: An empirical study. *J. Clean. Prod.* **2016**, *137*, 427–448. [CrossRef]
82. Garwood, T.L.; Hughes, B.R.; Oates, M.R.; O'Connor, D.; Hughes, R. A review of energy simulation tools for the manufacturing sector. *Renew. Sustain. Energy Rev.* **2018**, *81*, 895–911. [CrossRef]
83. May, G.; Stahl, B.; Taisch, M. Energy management in manufacturing: Toward eco-factories of the future–A focus group study. *Appl. Energy* **2016**, *164*, 628–638. [CrossRef]
84. Giampieri, A.; Ling-Chin, J.; Ma, Z.; Smallbone, A.; Roskilly, A.P. A review of the current automotive manufacturing practice from an energy perspective. *Appl. Energy* **2020**, *261*, 114074. [CrossRef]
85. Meike, D.; Pellicciari, M.; Berselli, G. Energy efficient use of multirobot production lines in the automotive industry: Detailed system modeling and optimization. *IEEE Trans. Autom. Sci. Eng.* **2013**, *11*, 798–809. [CrossRef]
86. Gadaleta, M.; Pellicciari, M.; Berselli, G. Optimization of the energy consumption of industrial robots for automatic code generation. *Robot. Comput.-Integr. Manuf.* **2019**, *57*, 452–464. [CrossRef]
87. Kazancoglu, Y.; Ekinci, E.; Mangla, S.K.; Sezer, M.D.; Kayikci, Y. Performance evaluation of reverse logistics in food supply chains in a circular economy using system dynamics. *Bus. Strategy Environ.* **2021**, *30*, 71–91. [CrossRef]
88. Kamble, S.S.; Gunasekaran, A.; Parekh, H.; Mani, V.; Belhadi, A.; Sharma, R. Digital twin for sustainable manufacturing supply chains: Current trends, future perspectives, and an implementation framework. *Technol. Forecast. Soc. Change* **2022**, *176*, 121448. [CrossRef]
89. Rotz, C.A.; Asem-Hiablie, S.; Place, S.; Thoma, G. Environmental footprints of beef cattle production in the United States. *Agric. Syst.* **2019**, *169*, 1–13. [CrossRef]

90. Asem-Hiablie, S.; Battagliese, T.; Stackhouse-Lawson, K.R.; Rotz, C.A. A life cycle assessment of the environmental impacts of a beef system in the USA. *Int. J. Life Cycle Assess.* **2019**, *24*, 441–455. [CrossRef]
91. Meneses, M.; Torres, C.M.; Castells, F. Sensitivity analysis in a life cycle assessment of an aged red wine production from Catalonia, Spain. *Sci. Total Environ.* **2016**, *562*, 571–579. [CrossRef]
92. Niswonger, R.G.; Morway, E.D.; Triana, E.; Huntington, J.L. Managed aquifer recharge through off-season irrigation in agricultural regions. *Water Resour. Res.* **2017**, *53*, 6970–6992. [CrossRef]
93. Mora, O.; Le Mouël, C.; de Lattre-Gasquet, M.; Donnars, C.; Dumas, P.; Réchauchère, O.; Brunelle, T.; Manceron, S.; Marajo-Petitzon, E.; Moreau, C.; et al. Exploring the future of land use and food security: A new set of global scenarios. *PLoS ONE* **2020**, *15*, e0235597. [CrossRef]
94. Jonkman, J.; Barbosa-Póvoa, A.P.; Bloemhof, J.M. Integrating harvesting decisions in the design of agro-food supply chains. *Eur. J. Oper. Res.* **2019**, *276*, 247–258. [CrossRef]
95. Chung, C.A. *Simulation Modeling Handbook: A Practical Approach*; CRC Press: Boca Raton, FL, USA, 2003.
96. Kelton, W.D.; Law, A.M. *Simulation Modeling and Analysis*; McGraw Hill: Boston, MA, USA, 2000.
97. Soleymani Shishvan, M.; Benndorf, J. Operational decision support for material management in continuous mining systems: From simulation concept to practical full-scale implementations. *Minerals* **2017**, *7*, 116. [CrossRef]

processes

MDPI

Article

Reduced-Order Modeling (ROM) of a Segmented Plug-Flow Reactor (PFR) for Hydrogen Separation in Integrated Gasification Combined Cycles (IGCC)

Osama A. Marzouk

College of Engineering, University of Buraimi, Al Buraimi 512, Oman; osama.m@uob.edu.om

Abstract: In an integrated gasification combined cycle (IGCC), a gasification process produces a gas stream from a solid fuel, such as coal or biomass. This gas (syngas or synthesis gas) resulting from the gasification process contains carbon monoxide, molecular hydrogen, and carbon dioxide (other gaseous components may also be present depending on the gasified solid fuel and the gasifying agent). Separating hydrogen from this syngas stream has advantages. One of the methods to separate hydrogen from syngas is selective permeation through a palladium-based metal membrane. This separation process is complicated as it depends nonlinearly on various variables. Thus, it is desirable to develop a simplified reduced-order model (ROM) that can rapidly estimate the separation performance under various operational conditions, as a preliminary stage of computer-aided engineering (CAE) in chemical processes and sustainable industrial operations. To fill this gap, we present here a proposed reduced-order model (ROM) procedure for a one-dimensional steady plug-flow reactor (PFR) and use it to investigate the performance of a membrane reactor (MR), for hydrogen separation from syngas that may be produced in an integrated gasification combined cycle (IGCC). In the proposed model, syngas (a feed stream) enters the membrane reactor from one side into a retentate zone, while nitrogen (a sweep stream) enters the membrane reactor from the opposite side into a neighbor permeate zone. The two zones are separated by permeable palladium membrane surfaces that are selectively permeable to hydrogen. After analyzing the hydrogen permeation profile in a base case (300 °C uniform temperature, 40 atm absolute retentate pressure, and 20 atm absolute permeate pressure), the temperature of the module, the retentate-side pressure, and the permeate-side pressure are varied individually and their influence on the permeation performance is investigated. In all the simulation cases, fixed targets of 95% hydrogen recovery and 40% mole-fraction of hydrogen at the permeate exit are demanded. The module length is allowed to change in order to satisfy these targets. Other dependent permeation-performance variables that are investigated include the logarithmic mean pressure-square-root difference, the hydrogen apparent permeance, and the efficiency factor of the hydrogen permeation. The contributions of our study are linked to the fields of membrane applications, hydrogen production, gasification, analytical modeling, and numerical analysis. In addition to the proposed reduced-order model for hydrogen separation, we present various linear and nonlinear regression models derived from the obtained results. This work gives general insights into hydrogen permeation via palladium membranes in a hydrogen membrane reactor (MR). For example, the temperature is the most effective factor to improve the permeation performance. Increasing the absolute retentate pressure from the base value of 40 atm to 120 atm results in a proportional gain in the permeated hydrogen mass flux, with about 0.05 kg/m^2.h gained per 1 atm increase in the retentate pressure, while decreasing the absolute permeate pressure from the base value of 20 bar to 0.2 bar causes the hydrogen mass flux to increase exponentially from 1.15 kg/m^2.h. to 5.11 kg/m^2.h. This study is linked with the United Nations Sustainable Development Goal (SDG) numbers 7, 9, 11, and 13.

Keywords: hydrogen; palladium; membrane; permeate; retentate; syngas; reduced-order model; IGCC; chemical; processes

1. Introduction

1.1. General Overview

Gasification is a thermochemical process in which a carbonaceous solid fuel (such as coal or biomass) is converted into a synthesis gas, which is known as "syngas" [1–3], using a gasification agent, also called "gasifying reagent" or "gasification medium" (such as steam, oxygen, carbon dioxide, or a mixture of them) under a controlled gasification environment (such as the residence time, heating rate, pressure, and temperature) within a facility called a "gasifier" [4–8]. In other words, gasification is a partial oxidation (substoichiometric) process consisting of physical processes, such as pyrolysis, and chemical reactions, such as gasification using steam [9,10]. Syngas is a mixture of gases, primarily carbon monoxide (CO) and hydrogen (H_2), with possible additional impurities such as carbon dioxide (CO_2), methane (CH_4), water vapor (H_2O), and nitrogen (N_2) [11]. Syngas is also produced from natural gas or light crude oil fractions through steam reforming [12]. The molar ratio of molecular hydrogen (H_2) to carbon monoxide increases as the ratio of hydrogen atoms to carbon atoms in the feedstock increases. Thus, ideal steam reforming of one mole of carbon gives a molar ratio of H_2:CO equal to 1:1, given the following reaction:

$$C + H_2O \rightarrow H_2 + CO \quad (1)$$

which has one mole of hydrogen and one mole of carbon monoxide as the products. On the other hand, the ideal steam reforming of one mole of methane (as an approximation for natural gas) gives a molar ratio of H_2:CO equal to 3:1, given the following reaction:

$$CH_4 + H_2O \rightarrow 3H_2 + CO \quad (2)$$

which has three moles of hydrogen and one mole of carbon monoxide as the products [13].

Syngas has multiple uses beyond being a gaseous fuel that can be used in gas turbines or boilers [14,15]. For example, syngas is also a feedstock for the production of methanol, ammonia, synthetic gasoline, and hydrogen [16,17] in alignment with SDG 9 "Industry, innovation and infrastructure" [18–24]. Syngas-based hydrogen, particularly, is of special environmental importance, as it enables the production of electricity through fuel cells without harmful carbon dioxide emissions [25,26]. This is aligned with the United Nation's seventh Sustainable Development Goal (SDG) "Goal 7: Affordable and Clean Energy" [27–32]. Syngas-based hydrogen also can be used as an alternative fuel for sustainable mobility [33–35] in alignment with SDG 11 "Sustainable Cities and Communities" [36–41], leading to reduced greenhouse gas (GHG) emissions in the transportation sector and thus mitigating global warming effects [42–44] in alignment with SDG 13 "Climate Action" [45–47], and also leading to improved air quality in the built environment [48,49] in alignment with SDG 11 "Sustainable Cities and Communities" [50–53], since the combustion of hydrogen does not lead to carbon dioxide or toxic products [54,55] (but undesired nitrogen oxides or NOx "NO and NO_2" are still possible due to the oxidizing air [56]). In the power sector, nitrogen-diluted syngas-based hydrogen can be used in hydrogen-fueled gas turbines, with no harmful carbon dioxide emissions [57,58]. This dilution allows for reducing the combustion temperatures, and thus reducing the NOx emissions [59]. A nitrogen-diluted hydrogen flame with a fuel mixture having a chemical composition of 60% nitrogen and 40% hydrogen (mole fractions) was experimentally studied, and it was shown that this nitrogen dilution is effective in adjusting the flame length [60]. Separating hydrogen from syngas increases the concentration of carbon dioxide in the remaining

content [61], thereby facilitating the carbon capture process afterward [62,63], which is similar to how using pure oxygen (rather than air) as an oxidizer in oxy-fuel combustion [64–67] causes the combustion products to be rich in carbon dioxide and this makes its capture easier [68,69]. The impurity carbon dioxide can be captured from the syngas, preventing its release into the atmosphere [70,71]. The captured carbon dioxide may be stored underground and it may be utilized commercially to achieve economic gains in different applications [72–74]. This carbon capture scenario is classified as a pre-combustion capture because carbon dioxide is segregated from the fuel stream (syngas in this case) before it is sent to the combustion facility [75,76].

Hydrogen separation from a hydrogen-containing gas mixture can be accomplished by various methods, including membrane separation [77,78]. Palladium-based (Pd-based) membranes allow the production of high-purity hydrogen [79–81], which is important for the effective operation of proton exchange membrane (PEM) fuel cells [82–86]. Palladium-based membranes are known for selectively separating hydrogen from a gas stream [87], which undergoes a dehydrogenation process as hydrogen is removed and is made to pass across the membrane. Compared to pressure swing adsorption (PSA), where adsorbing the impurities is used for hydrogen separation, membrane-based hydrogen separation allows for higher hydrogen recovery [88]. The term "hydrogen recovery" means the fraction of hydrogen mass in a gaseous mixture that is extracted (separated) from that mixture acting as the source of hydrogen [89–94]. Thus, if all the hydrogen content in a mixture of gases is extracted, the hydrogen recovery reaches its highest value of 100% or 1.0. Pressure swing adsorption is a process used for separating a gas (such as hydrogen) from a mixture of gases, or for purifying a gas mixture by removing present gas impurities in it [95–100]. Although this is the same purpose as the palladium membrane in the current study, the mechanism is very different. In PSA, selective adsorption–desorption takes place. When PSA is used in separating or purifying hydrogen, a mixture of gases containing hydrogen is pressurized, and then it passes through a reactor with an adsorbent material in the form of solid particles, which selectively attract the molecules of the impurities (the gases other than hydrogen) from the mixture onto their surface, as an adsorption stage, leaving hydrogen atoms at a high level of purity. Then, the pressure is decreased, which causes bound molecules of the impurities (the adsorbed non-hydrogen gases) to be released from the adsorbent surface, as a desorption stage [101]. Compared to cryogenic distillation, where impurities are condensed at low temperatures for purifying hydrogen; membrane purification is less energy-intensive [102]. The cryogenic separation of hydrogen uses a refrigeration system to cool a gaseous mixture containing hydrogen [103]. Because the constituent gases of the mixture typically condense and change from a gaseous state into a liquid state at different temperatures (at different boiling points), non-hydrogen gases in the mixture condense first, leaving only the hydrogen in a purified gaseous form [104–110]. Among all elements, hydrogen has the second lowest boiling point of any pure substance, which is about 20.3 K (−252.85 °C) at normal atmospheric pressures [111–114], while helium has the lowest one, which is about 4.2 K (−268.95 °C) at a normal atmospheric pressure [115,116]. Similarly, hydrogen has the second lowest melting point of any element, while helium has the lowest melting point [117–123]. Membrane-based hydrogen purification here refers to a pressure-driven process, where the selective permeation of hydrogen through the palladium membrane is stimulated by a difference in the partial pressure of hydrogen as it is transferred from the retentate side (before the hydrogen separation, where hydrogen has a higher partial pressure) to the permeate side (after the hydrogen separation, where hydrogen has a lower partial pressure). It may be worth mentioning that the carbon capture process (such as pre-combustion capture as demonstrated in the current study, or post-combustion carbon capture and oxy-fuel carbon capture) is a retrofitting action to mitigate carbon dioxide (CO_2) emissions from existing energy systems or other industrial facilities [124,125]. For better environmental aspects, a total switch to renewable energy sources (particularly solar energy [126,127] and wind energy [128,129]) and harvested energy [130,131]

is preferred because, in such scenarios, no carbon dioxide is produced [132–134]. However, such an energy transition toward renewable and sustainable resources may not be readily easy for existing conventional energy plants, whereas carbon capture strategies may remain suitable solutions for low-emission energy and process systems [135].

1.2. The Objectives of the Study

This work considers metal membranes that are unsupported (bulk), relatively thick, dense (non-porous) palladium foils for hydrogen separation. Catalytic reactors with dense metallic membranes for hydrogen production have shown a potential to overcome limitations on the yield that are associated with chemical equilibrium [136]. The mechanism of permeation through the membrane involves the dissociation of molecular hydrogen at the surface of the palladium membrane as hydrogen atoms, which then diffuse into the palladium membrane [137]. An isothermal hydrogen separation module (thus, having a uniform temperature) is adopted here. The spatial variation in the chemical composition of the permeate stream and retentate stream is modeled numerically as a plug-flow reactor. The permeation performance is examined under a reference set of representative conditions, as well as when each of the three control (design) variables is changed from the reference (base) case. These control variables are as follows: (1) the reactor temperature; (2) the retentate-side pressure; (3) the permeate-side pressure. Our study is based on simplified system-level computational modeling using principles of membrane-based hydrogen permeation. The interested reader can find some information about modeling a continuous plug-flow reactor in Appendix A.

1.3. Novelty and Added Knowledge

The contributions of this work include the following: (1) the detailed step-by-step numerical model algorithm for membrane-based hydrogen permeation; (2) the regression models that qualitatively show the impact of three operational conditions on membrane-based hydrogen permeation; (3) the contrasting profiles of hydrogen recovery and mole fractions in an isothermal membrane reactor at a base case and three other extreme cases. Although reduced-order modeling (ROM) is a new concept, and it has been used in several fields of engineering and physics [138–142]; our study proposes a detailed reduced-order model for plug-flow reactors (PFRs) when viewed as membrane reactors for mass transfer. This unique model is helpful in computer-aided design (CAD) and computer-aided engineering (CAE) in important applications under chemical engineering (CAE) and industrial processes, as an early-stage analysis without formidable three-dimensional computational fluid dynamics (CFD) models [143–147] and expensive experimental testing [148,149]. For high-fidelity analysis, these sophisticated CFD models or experimental prototypes may be utilized while guided by the finding of our ROM. In addition, all the results and regression models presented here are novel, thereby expanding our knowledge about palladium-based hydrogen production.

1.4. The Structure of the Manuscript

In the next section, the research method is described. Then, details about the geometric and inlet parameters are provided. Most of these settings remain fixed throughout the entire study. Then, the modeling procedure is described for the hydrogen permeation in the reactor. After this, five quantitative scalar quantities are introduced as criteria for evaluating the overall permeation performance. This is followed by a presentation of results for a base case, combined with a discretization-sensitivity analysis that confirms the adequacy of the spatial resolution utilized. Then, the influence of three control variables is explored, with some regression models relating the value of each control variable (as an independent or explanatory variable) to the five permeation metrics of the hydrogen permeation (as dependent or response variables). Finally, concluding remarks are provided.

2. Research Method

The research conducted here is computational in principle, and it relies on the modeling of hypothetical units for the permeation of hydrogen from a feedstock (feed) gas stream to a destination stream called permeate.

2.1. Connection to Real-Life Application

The feed stream is representative of a realistic syngas flow in an integrated gasification combined cycle (IGCC), in which coal is converted into syngas (mainly carbon monoxide "CO", molecular hydrogen "H_2", and carbon dioxide "CO_2") [150–159]. In the IGCC power plant, this syngas drives gas turbines as the first method of electric power generation [160–168]. Then, the heat content in the exhaust gases is partially recovered to produce steam as a working fluid for steam turbines that form the second method of electric power generation [169–177]. An IGCC power plant has an efficiency (with respect to the lower heating value, LHV) of about 48%, which means it has a higher efficiency (10–15% increase) and lower harmful emissions (10–15% reduction) compared to a conventional steam power plant operating by burning coal as a fuel [178–181].

2.2. Computer Modeling Tool

We performed the computational modeling through spreadsheets (Microsoft Excel software program, Version (2019)), where the mathematical equations governing the hydrogen permeation along the membrane length were implemented as dependent formulas. The built-in tool "Goal Seek" within the Microsoft Excel desktop application (under the Microsoft Windows operating system) was utilized for solving the nonlinear algebraic equation relating the unknown membrane length to the specified hydrogen recovery target (95%) [182,183]. Obtaining a solution using this nonlinear solver tool is nearly immediate on a personal computer. This is a big advantage compared to multi-dimensional detailed computational fluid dynamics (CFD) models, which not only take more time and require more computing power, but also require advanced skills and specialized software for setting the model and running a computer solver [184–190]. While such detailed CFD models allow for more realistic solutions (such as three-dimensional flow fields), for a preliminary design stage, a quick and convenient tool may be advantageous for exploring the approximated impact of the quantities of interest, particularly when only system-level operational parameters are desired. Such reduced-order modeling allows for rapid preliminary design, benchmarking, optimization and control, parametric sensitivity analysis, and investigating the validity of wide ranges of operating conditions [191–194].

2.3. Controllable Variables

The variables that are subject to change in this work as independent parameters are (1) the temperature of the membrane reactor (while keeping the retentate-side pressure and the permeate-side pressure at reference values of a base case), (2) the retentate-side pressure (while keeping the temperature and the permeate-side pressure at reference values of a base case), and (3) the permeate-side pressure (while keeping the temperature and the retentate-side pressure at reference values of a base case).

For each of the three scenarios listed above, the influence of the isolated design variable on the hydrogen permeation and fluid flow was investigated.

2.4. Simplifying Assumptions and Their Implications

Some assumptions were made in the present work, which reduces the interaction of factors and makes the interpretation of cause–effect dependence more evident. Such assumptions include the uniformity of the temperature and ignoring the effect of permeation on the

pressures [195]. It is acknowledged that these assumptions limit the generality of the results and introduce deviations from real-world systems. However, the study focuses on trends and patterns of relational dependence between variables for a simplified configuration. Thus, the results presented here can be useful when regarded as broad guides rather than firm facts.

The assumption of constant temperature (isothermal environment) seems proper since the modeled dehydrogenation process does not involve internal heat sources, combustion, coolants, or external heat exchange [196].

The assumption of fixed total pressure in either the retentate zone or the permeate zone during the hydrogen transfer from the retentate zone to the permeate zone was relaxed given that it is the partial pressure of hydrogen (not the total pressure of the gas mixture) that effectively drives this mass transfer. The variations in the partial hydrogen pressure during the hydrogen transfer were captured in our simplified model through the variation in the hydrogen mole fraction.

The detailed steps of the numerical modeling procedure for the proposed palladium-based hydrogen separation are presented in Appendix B.

2.5. Flow Setup

Figure 1 is a sketch of the stream directions and the compositions of the feed (inlet of the retentate side, in the shell) and the sweep (inlet of the permeate side, inside the tubes). Instead of showing all eight tubes (which can make the sketch unclear), only the central tube is shown. The coordinate (x) is the longitudinal distance measured from the left edge of the membrane reactor. The feed syngas enters the shell from the left, and the sweep nitrogen enters the tubes from the right.

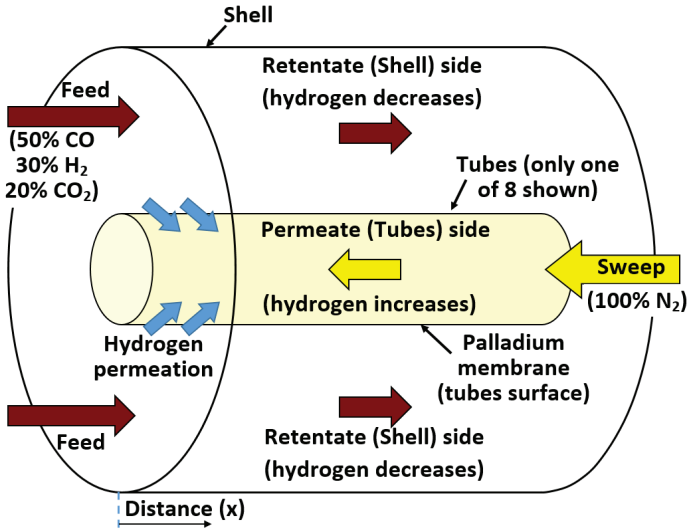

Figure 1. Inlet conditions and flow directions for retentate and permeate streams.

The counter-flow profile used here for the streams (where the two streams enter from the opposite ends of the membrane reactor) is preferred over the parallel or co-flow profile (when the two streams enter the membrane reactor from the same edge and exit from the same edge). This is due to a more even distribution of the driving force for the mass transfer of hydrogen from the retentate side to the permeate side. This advantage of counter-flow design over parallel flow (co-flow) design also exists in the field of heat exchangers, where heat transfer rather than mass transfer is sought [197–199].

3. General Model Settings

3.1. Fixing Common Parameters

This section illustrates various elements of the hydrogen separation modeling that remained unchanged for all simulation cases. They may be classified into two groups: (1) geometric parameters; (2) flow parameters. It should be noted that this work is not primarily intended to solve a particular problem or recommend a specific design. Instead, more value is provided by examining variations in permeation parameters when three operational variables are changed. Thus, any reasonable selection of settings was considered satisfactory here to establish a starting design point in the design space.

3.2. Underlying Geometry

All the imagined hydrogen separation modules investigated in this study share the same presumed geometric configuration except for the length. Such a proposed module is in the form of a shell-and-tube reactor, with eight cylindrical tubes placed inside a cylindrical shell. The sum of the cross-sectional areas of the tubes is 50% of the cross-sectional area of the outer enclosing cylinder, which forms the outer boundary of the shell. In the current work, the term "shell" means the part of the outer enclosing cylinder that remains after subtracting the tubes. Thus, it refers to the passage available for the gaseous stream to flow around the tubes but within the outer enclosing cylinder. This stream is referred to as the shell stream or the retentate. It is the fluid stream where the syngas feedstock enters and loses hydrogen during a dehydrogenation process to the other stream located inside the tubes. The retentate stream entering the shell is referred to as the feed, which means the raw syngas that is supplied before any processing by the hydrogen permeation membranes.

The other stream located inside the eight tubes is the tube-side stream or the permeate. It is the destination of the hydrogen that is transported from the retentate through the palladium membranes. At the inlet of the permeate, a non-hydrogen gas of molecular nitrogen (N_2) is supplied in the current model. This intentionally added nitrogen (or other gas) is referred to as the sweep gas or the sweep [200–205], and this is common in membrane-based separation or distillation processes [206–212]. While the use of such sweep gas is, strictly speaking, optional, it helps improve the permeation process by ensuring that the permeate side can never be saturated with hydrogen, and it increases the difference in the hydrogen partial pressures across the membrane, leading to an increased hydrogen permeation flux [213–216]. The added sweep gas can play another function of controlling the temperature [217], but this is not considered here as we assume the membrane reactor to be isothermal for simplicity. Other gases can also be used as a sweep gas, such as argon, Ar [218–221]; steam, H_2O [222–225]; helium, He [226–229]; or a mixture of gases [230–235]. The use of nitrogen here seems adequate [236,237].

The shell-and-tube reactor configuration was used in another study [238] while computationally modeling the propane steam reforming process under high temperatures (between 750 K and 900 K). In the propane steam reforming process, propane (C_3H_8) reacts with steam (H_2O) to produce molecular hydrogen (H_2) and carbon dioxide (CO_2). This reformation reaction takes place within a porous medium acting as a catalyst. Unlike the present study, the model in that external study did not include hydrogen separation. The tubes in the reactor were used in that external study to heat the surrounding porous shell through passing hot gases.

Another computational study for propane steam reforming (as a method for producing hydrogen from propane) used the shell-and-tube configuration [239–242]. There is a difference between the modeled reactor in that study and the modeled reactor in the present work. The reactor in the external study was a reformer with a catalytic chemical reaction taking place inside it, while here it is a separator with selective permeance (selective mass

transport) but without a chemical reaction between gaseous species. However, there are some similarities between the two studies. One similarity is that both modeling methods assumed a steady flow (no change with time). Also, the flow entering the tubes (heating gas) and the flow entering the shell (reactant propane and steam) in the other study flow in opposite directions longitudinally, which is the same situation here for the retentate stream and the permeating stream.

Outside the field of hydrogen generation or separation (purification), shell-and-tube reactors can be used for heat transfer processes, when the fluid in the tubes is used to heat or change the phase of the fluid in the shell (or vice versa) without direct contact. The heat transfer performance can be improved by adding baffles of different geometries that alter the path of the fluid in the shell and control its level of mixing through intensified turbulence [243–245]. The shell-and-tube configuration is also viable in multi-phase flows [246–248].

In other research work, a palladium-based membrane reactor of steam methane reforming (MR-SMR) was optimized with two objectives, which are (1) minimum heat exchange and (2) minimum power consumption—through reducing the pressure gradient that should be counteracted by an external compressor unit [249,250]. In that reported work, by controlling the exterior wall temperature, it was found possible to achieve a saving of 5.1% for the power consumption and a drop of 1.4% in the rate of heat exchange. The membrane reactor was tubular (a single tube inside a single tube). It was treated as a plug-flow reactor, given the high aspect ratio (large length compared to the diameter). The outer annular tube is the reaction zone (where methane reacts with steam to produce hydrogen), while the inner circular tube is the permeation zone (hydrogen permeates from the outer tube to the inner tube through a separating palladium membrane). The outer annular tube has a catalyst in the form of particles uniformly filling the outer annular tube, making it a porous 'packed bed'. The palladium membrane was dense.

Figure 2 shows a proposed cross-section of the membrane reactor, indicating the areas of the eight tubes (yellow color) and the area of the shell (white color). To obtain more uniform gaps between walls, one of the tubes was placed exactly at the center of the shell. The remaining seven tubes were arranged with equal circumferential spacing. It should be mentioned that the plug-flow reactor modeling conducted here utilized the details about the layout of tubes when calculating the total perimeter of the palladium membranes (but the shell outer diameter was not utilized in the permeation calculation). In addition, such a layout provides justification for the adopted membrane perimeter, and also helps the reader envision how the membrane reactor looks in a real situation.

Table 1 shows some details about the shell-and-tube geometry. The tubes and shell are assumed to have zero thickness, and the palladium membranes cover the entire surface of each tube. Being a reduced-order one-dimensional model, there are no baffles in the membrane reactor [251–253].

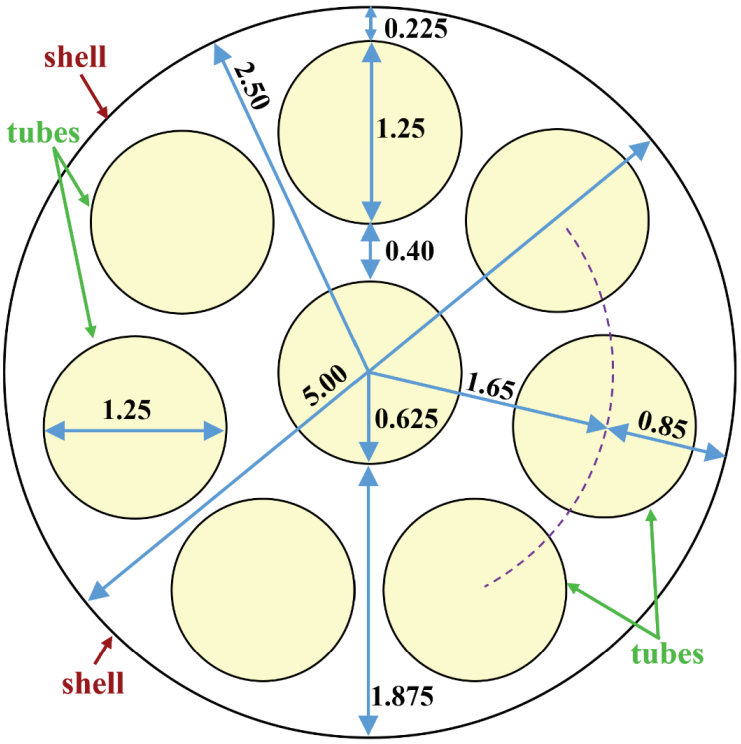

Figure 2. The proposed cross-section of the shell-and-tube membrane reactor (all dimensions are in cm).

Table 1. Some fixed geometric details about the proposed shell-and-tube membrane reactor.

Geometric Feature	Value
Shell diameter	5.000 cm (1.969 in)
Tube diameter	1.250 cm (0.4921 in)
Number of tubes	8
Shell cross-section area (excluding tubes)	9.817 cm^2 (1.522 in^2)
Tubes cross-section area (all 8 tubes)	9.817 cm^2 (1.522 in^2)
Shell-to-tubes area ratio	1:1
Tube cross-section area (single tube)	1.227 cm^2 (0.1902 in^2)

3.3. Fixed Conditions

Table 2 shows some details about the retentate stream, whose inlet conditions correspond to the raw syngas (the feed) supplied to the membrane reactor. The temperature and pressure are considered uniform in that stream. The temperature and pressure values are not specified because they are not common in all simulation cases, but are varied and their influences are studied later in multiple simulations.

Table 2. Some common fixed properties of the retentate stream.

Condition	Value
Inlet mole fraction, H_2	30% [254]
Inlet mole fraction, CO	50% [255]
Inlet mole fraction, CO_2	20% [256,257]
Molecular weight, H_2	2.01588 kg/kmol [258]

Table 2. *Cont.*

Condition	Value
Molecular weight, CO	28.0101 kg/kmol [259]
Molecular weight, CO_2	44.0095 kg/kmol [260]
Molecular weight, mixture	23.412 kg/kmol
Inlet mass fraction, H_2	0.025832
Inlet mass fraction, CO	0.598207
Inlet mass fraction, CO_2	0.375961
Inlet mass flow rate	60 kg/h (132.28 lbm/h)
Inlet standard volume flow rate	970,068 sccm (standard cubic centimeters per minute)
Target hydrogen recovery	95% (by mass, by mole, or by standard volume—identical)

The mixture molecular weight of the feed (MW_{mix}) is calculated as a mole-weighted average of the molecular weights of the constituent gases, according to [261–267].

$$\mathrm{MW_{mix}} = \mathrm{MW_{H2}}\ X_{H2} + \mathrm{MW_{CO}}\ X_{CO} + \mathrm{MW_{CO2}}\ X_{CO2} \tag{3}$$

where (MW) refers to the molecular weight, (X) refers to the mole fraction, and the subscripts refer to the individual gases.

The mass fraction (Y) for each constituent gas in the feed is dependent upon its mole fraction (X) according to [268].

$$Y_i = \frac{\mathrm{MW_i}\ X_i}{\mathrm{MW_{mix}}} \tag{4}$$

where the subscript (i) refers to any gas of the constituent gases in the feed.

The standard volume flow rate [269–273] of a gas (as a compressible medium whose volume is considerably sensitive to pressure and temperature) is the virtual volume flow if the temperature and pressure are at specified reference standard values [274–278]. These standard conditions are taken here as T_{stnd} = 0 °C (32 °F, 273.15 K) and P_{stnd} (absolute pressure) = 10^5 Pa (0.9869 atm, 14.504 psi). These two standard values of temperature and pressure are based on the International Union of Pure and Applied Chemistry (IUPAC) [279–285].

An ideal gas is a gas that obeys the ideal-gas equation of state, which can be expressed as

$$P\ V = N\ \overline{R}\ T \tag{5}$$

where (P) is the pressure, (V) is the volume, (N) is the number of moles, ($\overline{R}$) is the universal gas constant, and (T) is the absolute temperature, expressed in kelvins. For an ideal gas, each mole occupies a volume of 22,711 cm^3 (22.711 L) at the standard pressure and temperature mentioned earlier. Thus, the standard volume is directly proportional to the number of moles, which in turn (and assuming no change occurs in the chemical composition of the gas) is directly proportional to the mass. This value can be obtained from the ideal-gas equation of state by solving for the standard volume per mole (V_{stnd}/N) as follows:

$$\frac{V_{stnd}}{N} = \overline{R}\frac{T_{snd}}{P_{stnd}} = \left(10^6\right)\left(8.3145\frac{\mathrm{J}}{\mathrm{mol.K}}\right)\left(\frac{273.15\ \mathrm{K}}{10^5\ \mathrm{Pa}}\right) = 22,711\frac{\mathrm{cm^3}}{\mathrm{mol}} \tag{6}$$

where the multiplier (10^6) is inserted to convert the volume unit from cubic meters (m^3) to cubic centimeters (cm^3), and the value of the universal gas constant ($\overline{R}$) is a physical constant taken from the U.S. National Institute of Standards and Technology [286]. The

value shown in the above equation is a truncated version of the published one used in the computation, which is 8.314462618 J/mol.K.

Table 3 shows some details about the permeate stream, whose inlet conditions correspond to the sweep gas supplied to the membrane reactor. The temperature and pressure are considered uniform in that stream.

Table 3. Some common fixed properties of the permeate stream.

Condition	Value
Inlet gas	100% N_2
Molecular weight, N_2	28.0134 kg/kmol [287]
Inlet mass flow rate	30.692 kg/h (67.664 lbm/h)
Inlet standard volume flow rate	414,704 sccm (standard cubic centimeters per minute)
Target outlet mole fraction of H_2	40%

The flow rate of the sweep gas is decided based on the target mole fraction of hydrogen in the permeate outlet ($X_{H2,per-out}$), the mass flow rate of hydrogen in the syngas ($\dot{m}_{H2,feed}$), and the target hydrogen recovery (β) according to

$$\dot{m}_{sweep} = \frac{MW_{N2}\left(1 - X_{H2,per-out}\right)}{MW_{H2}\, X_{H2,per-out}}\, \beta\, \dot{m}_{H2,feed} \tag{7}$$

The above relation can be used under the condition that there is only nitrogen in the sweep gas (which is true in all the simulations in the present work). It is a special relation and should not be used in other configurations, such as when the sweep gas is a mixture.

In the present work, β = 0.95, $X_{H2,per-out}$ = 0.4, and $\dot{m}_{H2,feed}$ = 1.5499 kg/h (this is the product of the feed mass flow of 60 kg/h, and the mass fraction of hydrogen in the feed of 0.025832). With the previously mentioned molecular weights of hydrogen (Table 2) and nitrogen (Table 3), we obtain $\dot{m}_{sweep}$ = 30.692 kg/h as mentioned in Table 3.

The mass flow rates (and the standard volume flow rates) and the chemical compositions of the sweep gas and the feed gas are fixed in all the simulations of this work.

4. Hydrogen Permeation Metrics

After performing a complete steady-state simulation for the palladium membrane permeation of hydrogen in a segmented plug-flow reactor, the assessment of the overall permeation process is facilitated using a number of quantitative scalar quantities (referred to here as performance metrics or permeation metrics) that are convenient to utilize for comparing the performance of different simulations. The use of quantitative metrics is an effective way of concisely assessing and benchmarking the performance of two processes or systems, and they are adopted in many fields [288,289]. In this section, five performance metrics for hydrogen separation are discussed.

4.1. Membrane Length

The first permeation performance metric adopted here was the membrane length needed to achieve the target hydrogen recovery (β = 95%). This is designated by the symbol (L).

A smaller membrane length was desired, because it means a shorter membrane reactor, which is a better design due to reduced cost and space.

4.2. Average Hydrogen Permeation Mass Flux

The second permeation performance metric adopted here was the average mass flux (mass flow rate per unit area) of the permeated hydrogen through the membrane. It is designated by the symbol ($\overline{M}_{H2}$). Since the local mass flux of the permeated hydrogen is subject to variation from one segment to another in the membrane reactor model, the average of all segmental values is used. This metric is related to the corrected (second-iteration) segment-level molar flux of permeating hydrogen through the palladium membrane ($J_{H2,i}$) as

$$\overline{M}_{H2} = 3.6\ MW_{H2} \frac{1}{n} \sum_{i=1}^{n} J_{H2,i} \tag{8}$$

where (MW_{H2} = 2.01588 kg/kmol) is the molecular weight of the molecular hydrogen, and the factor (3.6) appears to enable unit conversion such that the average mass flux is expressed in (kg/m^2.h) when the segmental mole flux ($J_{H2,i}$) is expressed in (mol/m^2.s).

A higher average mass flux is desired, as it shows more intense utilization of the membrane surface (better use of each unit area).

In the present study, because the total permeated hydrogen is fixed (by fixing the inlet mass flow of hydrogen in the syngas feed and fixing the target hydrogen recovery), and the membrane perimeter is also fixed, the average hydrogen mass flux ($\overline{M}_{H2}$) and the membrane length (L) are not independent. Instead, they are inversely proportional to each other, and their product should be invariant.

4.3. Log Mean Pressure-Square-Root Difference

The third permeation performance metric adopted here is a global (membrane-level, not a segment-level) pressure-square-root difference, which is a membrane-level difference in the hydrogen partial pressure raised to the power of 0.5, between the retentate stream (higher value) and the permeate stream (lower value). It is designated here by the symbol (LMPsrD), or simply (LMPD), and is called log (or logarithmic) mean pressure-square-root difference. This difference in the square root of the hydrogen partial pressure (PsrD) stimulates the permeation through the palladium membrane. Because this stimulus driving force can vary along the membrane segments, an average value was sought. Instead of a simple arithmetic average over all segments, a logarithm-based average was used, which takes into account the differences at the left end and at the right end of the entire membrane reactor (where the flow inlets and outlets are located). Unlike computing a simple average of the driving force (the difference in the square root of the hydrogen partial pressure, or PsrD) along the membrane, the LMPD is related to the change in this driving force between the two ends of the hydrogen separation modules only, and this makes this metric simpler to compute without the need to know the details of the driving force between the two side ends of the hydrogen separation module. This resembles an approach of calculating an overall temperature difference in the field of heat transfer within heat exchangers, which is called log mean temperature difference (or LMTD); and this is a representative temperature difference between the colder stream and the hotter stream [290–296]. The global log mean pressure-square-root difference is calculated as follows:

$$\text{LMPD} = \frac{\left(\Delta P_{H2}^{0.5}\right)_{LHS,1} - \left(\Delta P_{H2}^{0.5}\right)_{RHS,n}}{ln\left(\left(\Delta P_{H2}^{0.5}\right)_{LHS,1}\right) - ln\left(\left(\Delta P_{H2}^{0.5}\right)_{RHS,n}\right)} \tag{9}$$

where $(\Delta P_{H2}{}^{0.5})_{LHS,1}$ is the driving force at the left end of the membrane reactor (at x = 0), $(\Delta P_{H2}{}^{0.5})_{RHS,n}$ is the driving force at the right end of the membrane reactor (at x = L), and the (ln) function is the natural logarithm. The LMPD should lie between $(\Delta P_{H2}{}^{0.5})_{LHS,1}$ and $(\Delta P_{H2}{}^{0.5})_{RHS,n}$, regardless of which of them is larger than the other.

A higher log mean pressure-square-root difference (LMPD) is desired, as it is an indicator of the average driving force for hydrogen permeation between the left end and the right end of the membrane reactor, and is interpreted in a similar way to the LMTD in heat exchanges, being the driving force for heat transfer [297].

4.4. Global Apparent Permeance

The fourth permeation performance metric adopted here is the global apparent permeance (k'_{app}), which is a solution-dependent variable that represents the effective permeance based on the obtained profile of hydrogen permeation in the membrane reactor. It has the same unit of the actual (ideal) permeance (k′), which is an input parameter that depends on the temperature and the membrane length, and thus can be computed before the numerical simulation of the plug-flow reactor. To explain the usefulness and significance of the global apparent permeance (k'_{app}), it should be noted that the actual permeance (k′) is a local value, corresponding to a specific segment (or even a specific point), and it depends on the temperature and the membrane thickness, as in Equation (A14). However, the apparent permeance is computed based on the overall performance of the membrane reactor as a whole, as follows:

$$k'_{app} = \frac{\frac{1}{n}\sum_{i=1}^{n} J_{H2,i}}{\text{LMPD}} \tag{10}$$

Therefore, two dehydrogenation palladium membrane reactors may have the same actual permeance because they have the same uniform temperature and the same uniform thickness, but due to variations in the dehydrogenation performance, they can have different global apparent permeance values. This makes the global apparent permeance a good metric for assessing the dehydrogenation process.

The numerator in the above equation is the arithmetic average of the molar flux of permeating hydrogen through the palladium membrane (average of the n segmental values), while the denominator is the log mean pressure-square-root difference (LMPD).

A higher apparent permeance is desired, as it shows that the membrane reactor yields a higher useful output (hydrogen molar flux) for a given average input (hydrogen pressure driving force).

4.5. Efficiency Factor

The fifth and last permeation performance metric adopted here is the efficiency factor (η_k), which is simply the ratio of the global apparent permeance to the local actual permeance, expressed as a percentage. Therefore,

$$\eta_k = \frac{k'_{app}}{k'} \tag{11}$$

The efficiency factor is the only permeation metric presented here that is non-dimensional, which makes it unambiguous and identical in any system of units.

The “efficiency factor” is not strictly an efficiency as used in energy conversion by a heat engine or an energy conversion process [298–303], being a useful output energy that is a fraction of an input heat energy, and this case the efficiency is limited to an upper ceiling value of 100% [304]. Instead, the “efficiency factor” is a ratio between two quantities that have the same dimensional units but have different meanings, and either of them is allowed to exceed the other. Thus, the “efficiency factor” used here can exceed 100%. This is somehow similar to the concept of the Octane Number or the Research Octane Number (RON) as a quality scale for gasoline (petrol) automotive fuels, where this rating is not strictly bound by an upper limit of 100 [305–315].

A higher efficiency factor is desired, as it is directly proportional to the global apparent permeance; thus, it is related to the goodness of the membrane reactor operation with regard to hydrogen permeation.

5. Results

5.1. Base Case and Spatial Resolution Test

The first implementation of the plug-flow membrane reactor model is referred to as the base case or reference simulation. To run a simulation, three thermodynamic properties that describe the two flowing streams in the reactor are needed. These three properties are as follows: (1) temperature (assumed uniform in the entire reactor); (2) retentate pressure (assumed uniform in the retentate stream); (3) permeate pressure (assumed uniform in the permeate stream).

The uniform-temperature assumption avoids ambiguity when computing the actual (ideal) permeance of the palladium membrane, which is temperature-dependent. Thus, the actual permeance is also uniform in the entire membrane, and this eliminates an undesirable distracting influence from varying permeance.

The three aforementioned thermodynamic properties are to be varied individually later, deviating from their base values. The influence of each of them on the hydrogen permeation is examined.

The base case is considered to have representative (realistic) values of the membrane streams [316–318], which are summarized in Table 4.

Table 4. Temperature and pressures of base case (reference simulation).

Fluid Property	Value
Temperature	300 °C (572.00 °F)
Absolute retentate pressure	40.0 atm (587.84 psia)
Absolute permeate pressure	20.0 atm (293.92 psia)

The local actual hydrogen permeance (k') for the base temperature of (300 °C, 573.15 K) is 10.263×10^{-4} mol/m^2.s.Pa$^{0.5}$.

Table 5 gives numerical results for the base case after a complete simulation of the segmented plug-flow reactor. The normal resolution of 200 segments is compared with another resolution with twice the number of segments (400 segments) having the same membrane length found necessary for the 200-segment case.

Table 5. Some results obtained for the base case with 200 segments (normal resolution) and 400 segments (refined resolution for testing only).

Result	Value		Absolute Percentage Change
	n = 200 Segments	n = 400 Segments	$\frac{\lvert \text{Value}(200) - \text{Value}(400) \rvert}{\text{Value}(200)}$
Membrane length (cm)	407.359	407.359	0% (identical)
Average hydrogen permeation mass flux (kg/m^2.h)	1.151	1.150	0.01%
Pressure-square-root difference at left end (Pa$^{0.5}$)	202.345	202.345	0% (identical)
Pressure-square-root difference at right end (Pa$^{0.5}$)	260.655	268.896	3.16%
Log mean pressure-square-root difference (Pa$^{0.5}$)	230.271	234.05	1.64%
Global apparent hydrogen permeance (mol/m^2.s.Pa$^{0.5}$)	6.8849×10^{-4}	6.7732×10^{-4}	1.62%
Efficiency factor (%)	67.09%	66.00%	1.62%
Hydrogen recovery (%)	95.000%	94.991%	0.01%

Also, the absolute percentage deviations of these results between the two resolutions are shown in the table. Such comparison reveals small deviations not exceeding 2% in all four permeation performance metrics other than the membrane length, which was forced to be identical in the two simulations. Namely, these metrics are (1) average hydrogen permeation mass flux, (2) log mean pressure-square-root difference, (3) global apparent hydrogen permeance, (4) efficiency factor.

For the hydrogen recovery, it was a specified input in the case of using 200 segments, where the membrane length was a computed output. In the case of using 400 segments, the membrane length was the specified input (to ensure geometric consistency between the two simulations), while the hydrogen recovery was computed from the segmented plug-flow reactor model, in an inverse simulation mode. There is an insignificant difference (0.01% absolute change) in the two values of the hydrogen recovery.

In addition to the demonstrated quantitative agreement between the normal-resolution simulation with 200 segments and the high-resolution validation simulation with 400 segments, the qualitative agreement can also be observed in Figure 3. This figure compares the cumulative hydrogen recovery along the base-case plug-flow reactor model, for the 200-segment resolution and the 400-segment resolution. The profiles under both resolutions are visually indistinguishable.

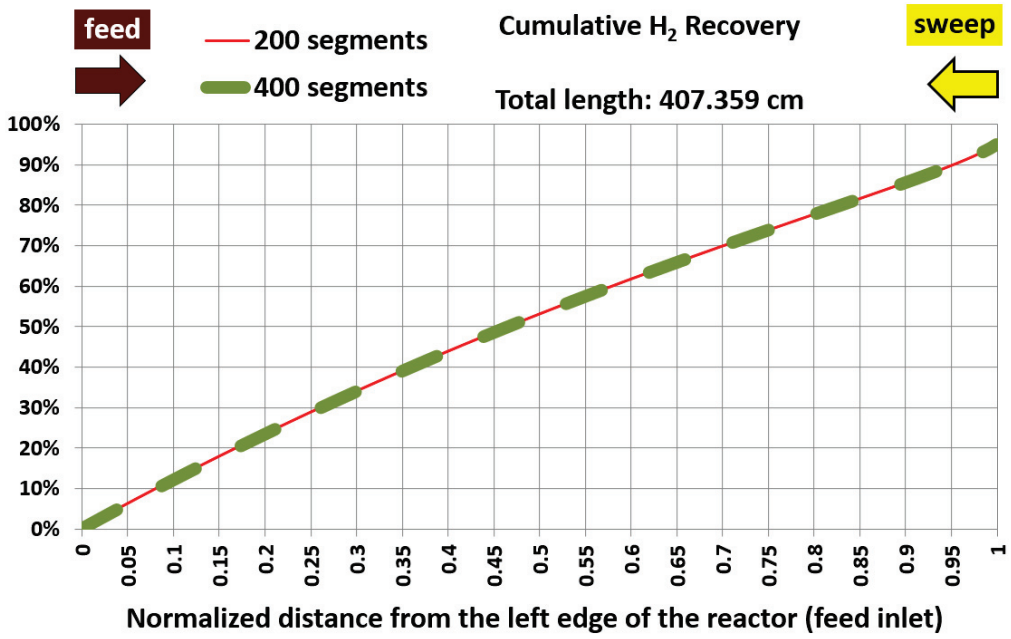

Figure 3. Commutative hydrogen recovery for the base case, with two spatial resolutions (the 200 segments represent the normal resolution adopted in the study; the 400 segments represent the finer resolution for testing the resolution insensitivity).

Figure 4 shows the segmental hydrogen recovery profile (contribution of each reactor segment to the total hydrogen recovery). The normal resolution (200 segments) corresponds to nearly twice the values of the high resolution (400 segments). Although this may indicate a mismatch between the two simulations, it is actually appropriate because each segment under the normal resolution has twice the membrane area of a segment under the high resolution. For a meaningful visual comparison, a third curve was added to the figure by doubling the segmental hydrogen recovery obtained under high resolution (because each data point, in this case, represents only half of what a data point represents in the case of normal resolution). When the added curve (the adjusted high-resolution curve) is compared with the normal resolution curve, it is seen that both curves are visually identical.

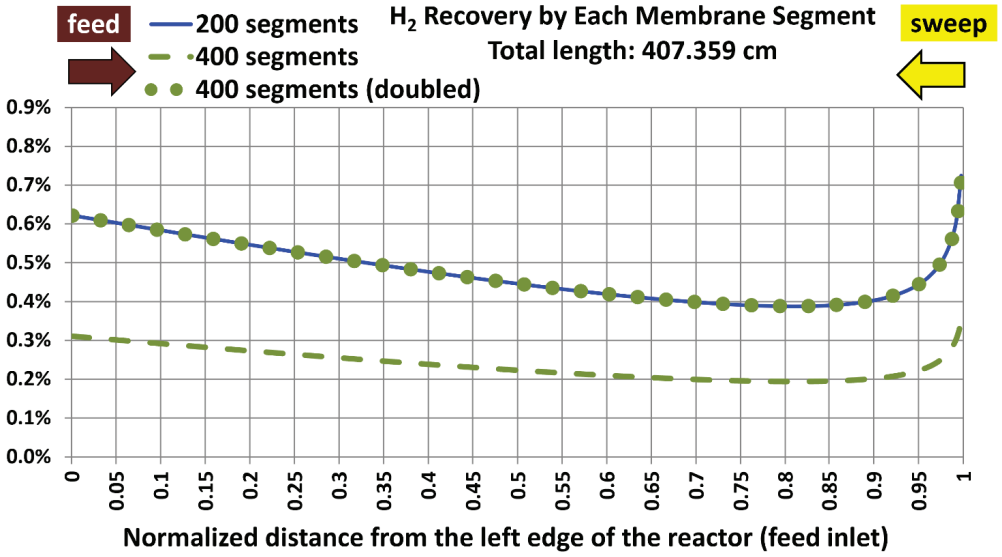

Figure 4. Segmental hydrogen recovery for the base case, with two spatial resolutions (the 200 segments represent the normal resolution). There is a third curve added, with the segmental recovery values in the case of 400 segments being doubled.

The nonlinear profile of the segmental recovery is attributed to the underlying variation in the driving force for the segmental hydrogen permeation (the segmental pressure-square-root difference), which is a nonlinear function of the hydrogen mole fraction in the permeate stream and the hydrogen mole fraction in the retentate stream.

The variations in the hydrogen mole fraction in the retentate stream as the retentate gas traverses the membrane reactor from the left to the right are shown in Figure 5. It decreases from 30% at the left end corresponding to x/L = 0 to 2.10% at the right end corresponding to x/L = 1. The variation is weakly nonlinear with the distance. The exit mole fraction is not exactly zero, but this is consistent with the target hydrogen recovery of 95%. The value of the exit mole fraction of hydrogen (2.10%) and the longitudinal pattern of that mole fraction for the normal resolution (200 segments) are consistent with those for the validation resolution (400 segments).

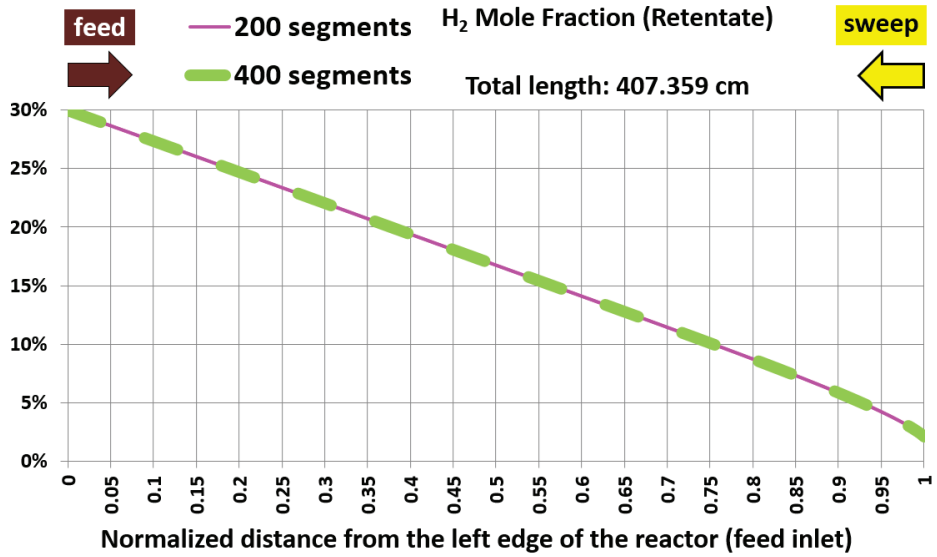

Figure 5. Hydrogen mole fraction in the retentate stream for the base case, with two spatial resolutions (the 200 segments represent the normal resolution).

The variations in the hydrogen mole fraction in the permeate stream as the permeate gas traverses the membrane reactor from the right to the left are shown in Figure 6. It increases from 0% at the right end corresponding to x = L (a normalized variable x/L = 1 is used in the figure) to the target 40% at the left end corresponding to x = 0. The variation is weakly nonlinear with the distance, as in the case of the retentate stream. Comparing the mole fraction patterns with 200 segments and with 400 segments suggests independence of the results on the spatial resolution. Thus, using 200 segments is adequate and there is no need to use a higher resolution.

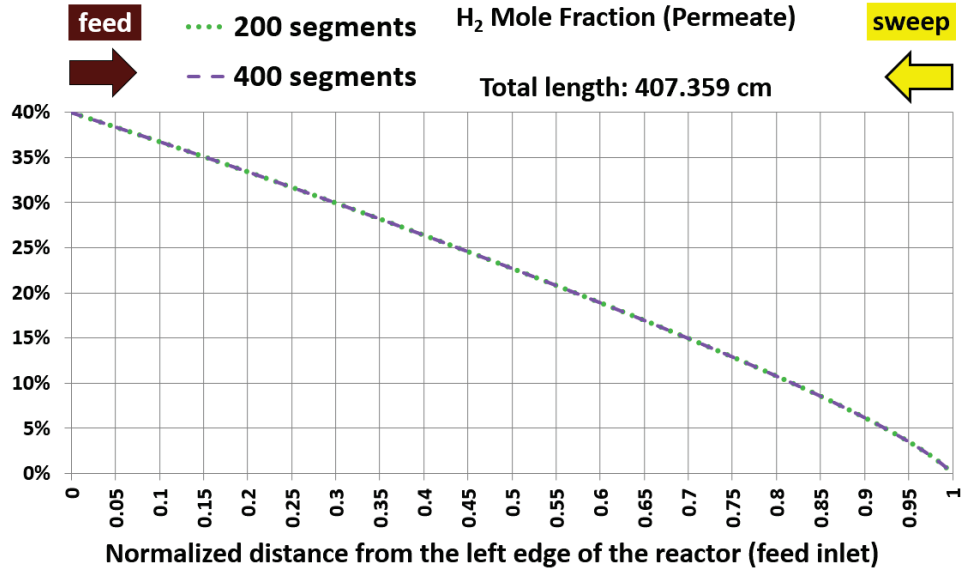

Figure 6. The hydrogen mole fraction in the permeate stream for the base case, with two spatial resolutions (the 200 segments represent the normal resolution).

With such good observed agreement between the normal spatial resolutions and the high testing resolution, the choice of 200 segments (normal resolution) was considered satisfactory and was adopted in all remaining simulations.

5.2. Influence of Temperature

After completing the segmented flow reactor under a set of representative operational conditions, the temperature of the flows in the membrane reactor was varied in a discrete manner, leading to seven temperature values that are higher than the base value of 300 °C. The base value and the six additional temperatures are as follows:

1. 300 °C (base);
2. 350 °C;
3. 400 °C;
4. 500 °C;
5. 600 °C;
6. 700 °C;
7. 800 °C.

It is understood that high temperatures may pose practical challenges for the materials and the process feasibility. Despite this, the model allows for exploring the change in the permeation performance due to elevated temperatures. This is achieved by monitoring the changes in the five performance metrics due to the changes in the temperature alone. The other two design variables (retentate pressure and permeate pressure) are kept at their base values (40 atm absolute and 20 atm absolute, respectively).

Figure 7 shows the influence of the temperature on the first hydrogen permeation metric, which is the membrane length. The figure shows a monotonic nonlinear decline in the needed membrane length as the temperature increases. This dependence can be described by a nonlinear power-type regression model, which is also shown in the figure. In the equation shown within the figure, (x) refers to the temperature in degrees Celsius, T (°C), while (y) refers to the membrane length in meters, L (cm). Therefore,

$$L(\text{cm}) = 3.0364 \times 10^6 \; T(^\circ\text{C})^{-1.5676} \tag{12}$$

Thus, the temperature is an instrumental variable in limiting the membrane length (for a given target hydrogen recovery) to less than 25% of its base value. Thus, it is equally instrumental to increase the hydrogen recovery for a given geometric length.

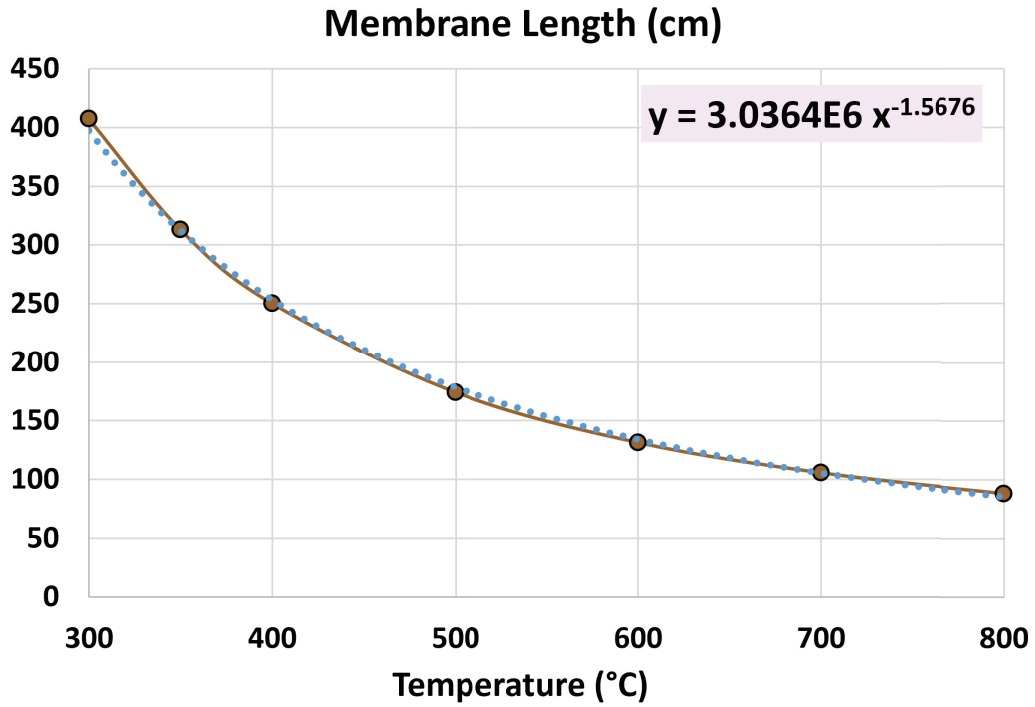

Figure 7. The membrane length as a function of the temperature in the membrane reactor.

Figure 8 shows the influence of the temperature on the second hydrogen permeation metric, which is the average hydrogen permeation mass flux. There is an almost linear increase with temperature, which can be described by the following linear regression model:

$$\overline{M}_{H2}\left(\text{kg/m}^2\text{.h}\right) = -1.4491 + 0.0084087 \; T(^\circ\text{C}) \tag{13}$$

with an (R^2) value of 0.9990. This value that accompanies the linear regression equation is called the coefficient of determination. It helps in evaluating the goodness of the regression fit, with a perfect fit having a value of 1.0, which means that the data points lie exactly on a straight line [319–328]. Therefore, the provided regression model is almost perfect within the examined range of temperatures.

Thus, the temperature is an instrumental variable to improve the permeation flux. This is justified by the increase in the actual local permeance when the temperature increases, following an Arrhenius-type dependence, which actually appears in different fields other than the current application of hydrogen permeation (such as chemical reaction rates [329]).

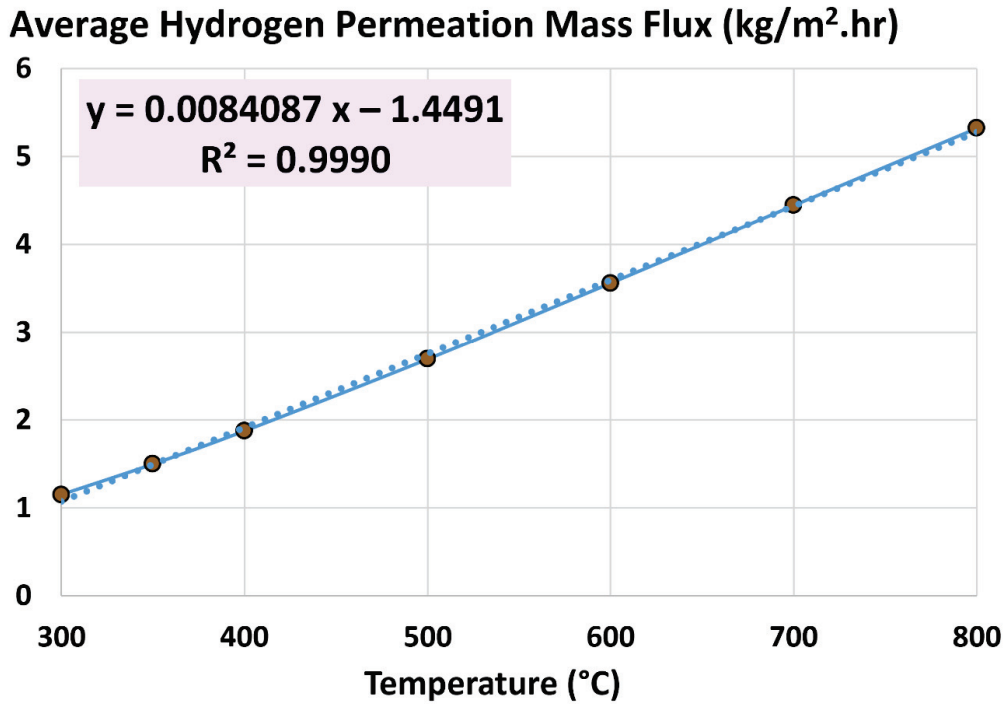

Figure 8. The average hydrogen permeation mass flux as a function of the temperature in the membrane reactor.

The third hydrogen permeation metric, which is the logarithmic mean pressure-square-root difference (LMPD), maintains its base values due to fixed inlet and outlet pressures. Therefore, its implicit dependence on the temperature is not manifested. Similarly, the left-end pressure-square-root difference, $(\Delta P_{H2}{}^{0.5})_{LHS,1}$, and the right-end pressure-square-root difference, $(\Delta P_{H2}{}^{0.5})_{RHS,n}$ remain the same when the temperature of the membrane reactor is varied while fixing the inlet and outlet pressures. Thus, they maintain their base values. Therefore, there is no need to visualize these three variables in a dedicated figure with the temperature being the independent variable (because they would simply appear as three straight horizontal lines in such a figure).

The lack of influence of temperature on this permeation metric is valid, due to fixing the pressures in all the cases while changing only the temperatures.

Figure 9 shows how the fourth and fifth hydrogen permeation metrics change as the temperature increases. These metrics are the global apparent permeance and the efficiency factor, respectively. In addition, the figure also includes the actual local permeance. While both the actual (local) permeance and the global apparent permeance increase nonlinearly with the temperature, their ratio remains constant at the base value of 67.09%. Because their ratio is, by definition, the efficiency factor, the efficiency factor remains constant at its base value when the operational temperature of the palladium membrane reactor module increases. The increase in the permeance values exactly follows an exponential function of the following form:

$$k' \text{ or } k'_{app}\left(\text{mol/m}^2\text{.s.Pa}^{0.5}\right) \propto e^{-\mu/(T(^\circ C)+273.15)} \quad (14)$$

where (μ) is a constant, being the activation energy divided by the universal gas constant ($E/\overline{R}$).

Therefore, while increasing the temperature leads to better permeance, it is useless for improving the efficiency factor.

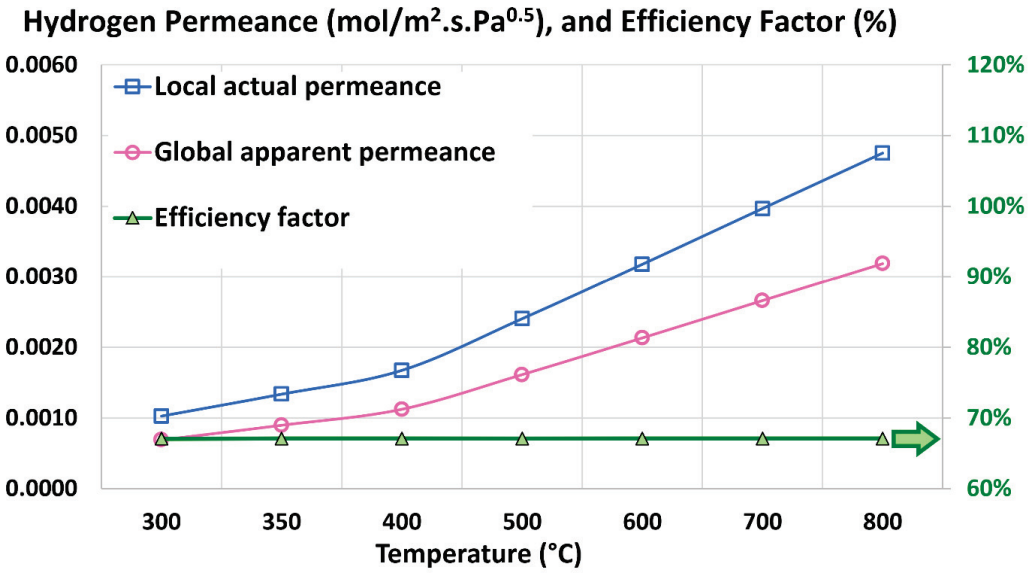

Figure 9. Local actual permeance, global apparent permeance, and efficiency factor as functions of temperature in membrane reactor.

5.3. Influence of Retentate Pressure

After exploring the role of the temperature as a design variable to improve permeation in a membrane reactor, this subsection explores the similar role of the retentate pressure. The retentate pressure was varied in a discrete manner, leading to a number of pressures higher than the base value of 40 atm (absolute). The base value and seven additional absolute retentate pressures are as follows:

1. 40 atm (base);
2. 45 atm;
3. 50 atm;
4. 60 atm;
5. 70 atm;
6. 80 atm;
7. 100 atm;
8. 120 atm.

The goal here is to investigate the relation between this retentate pressure and the five performance metrics. The other two design variables (temperature and permeate pressure) are kept at their base values (300 °C and 20 atm absolute, respectively).

Figure 10 shows the influence of the retentate pressure on the first hydrogen permeation metric, which is the membrane length. Similarly to the observed relation with the temperature, there is a favorable nonlinear decline in the membrane length as the retentate pressure increases. This relation can be described by the following fifth-order polynomial:

$$L(\text{cm}) = 4.43331 \times 10^{-5}\, r^4 - 0.015423\, r^3 + 2.0356\, r^2 - 119.74\, r + 2812.2 \qquad (15)$$

where (r) refers to the retentate absolute pressure, expressed in atm, P_{Ret} (atm, absolute). The retentate pressure was found to be an instrumental variable in limiting the membrane length (for a given target hydrogen recovery) to less than 25% of its base value at about 110 atm (absolute). In other words, it can be utilized to increase the hydrogen recovery for a given geometric length.

Figure 11 shows the influence of the retentate pressure on the second hydrogen permeation metric, which is the average hydrogen permeation mass flux. There is an

approximate linear increase with pressure, which can be described by the following linear regression model:

$$\overline{M}_{H2}\left(\mathrm{kg/m^2.h}\right) = -0.75288 + 0.051720\ P_{Ret}(\mathrm{atm, absolute}) \quad (16)$$

with an (R^2) value of 0.9931, which is close to the perfect value of 1.0. Thus, the retentate pressure is useful for improving the permeation flux. This is justified by the increase in the driving force for permeation when the retentate pressure increases, due to the resulting proportional increase in the hydrogen partial pressure in the retentate stream.

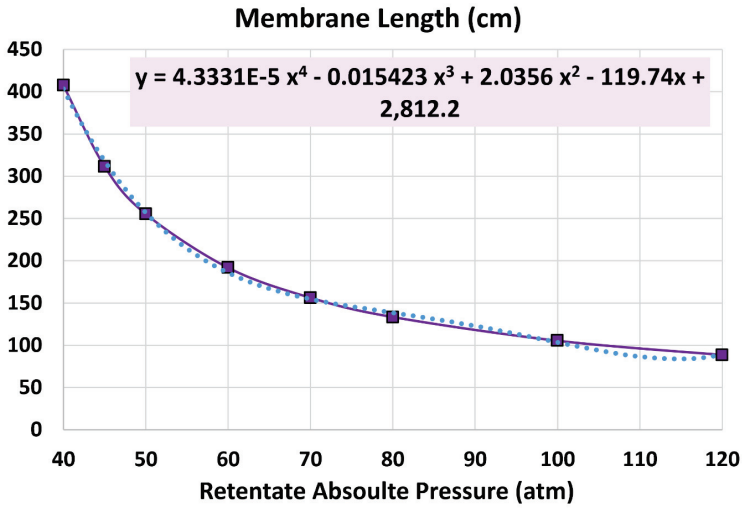

Figure 10. The membrane length as a function of the retentate pressure in the membrane reactor.

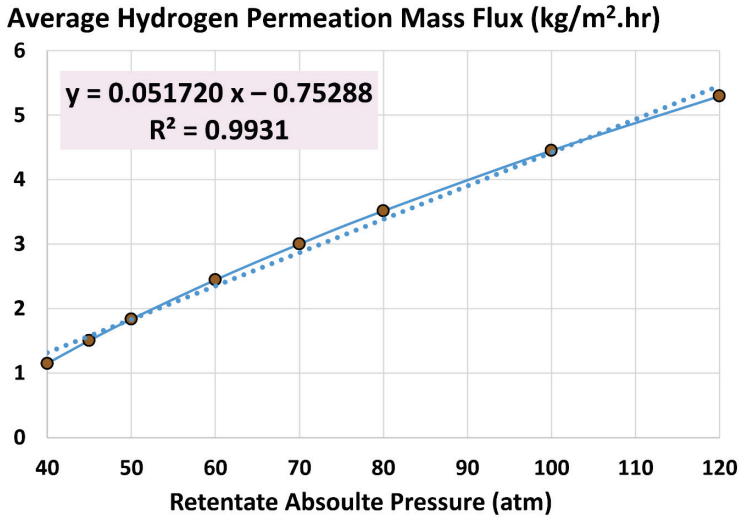

Figure 11. The average hydrogen permeation mass flux as a function of the retentate pressure in the membrane reactor.

Figure 12 shows that the third hydrogen permeation metric (log mean pressure-square-root difference—LMPD) increases logarithmically with the retentate pressure. The relation between the log mean pressure-square-root difference and the absolute pressure of the retentate stream over the range of considered pressures can be approximated as the following logarithmic function:

$$\mathrm{LMPD}\left(\mathrm{Pa^{0.5}}\right) = 442.40\ \ln\left(P_{Ret}(\mathrm{atm, absolute})\right) - 1412.6 \quad (17)$$

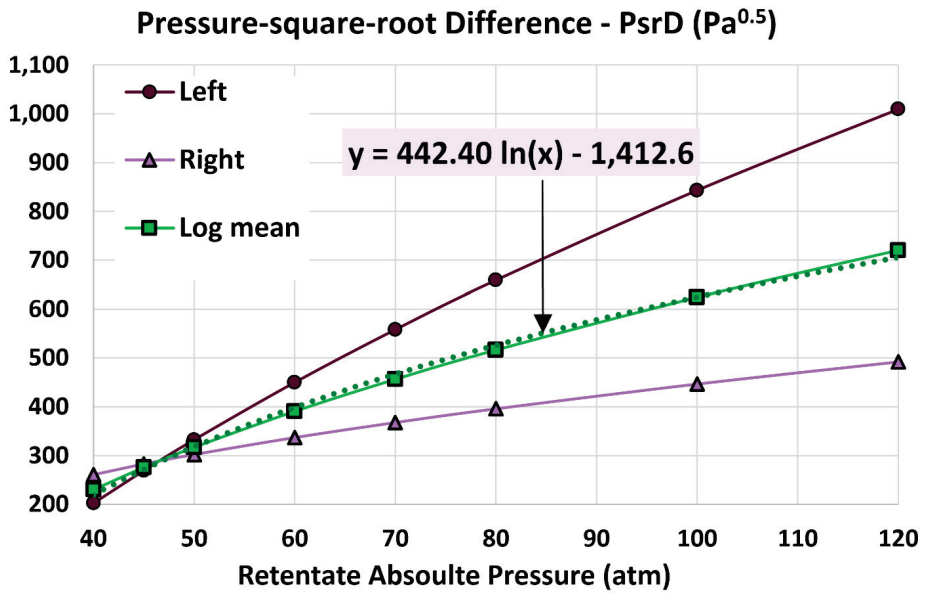

Figure 12. The pressure-square-root difference at the left end of the membrane reactor (x = 0), the pressure-square-root difference at the right end of the membrane reactor (x = L), and the log mean pressure-square-root difference (LMPD) as functions of the retentate pressure in the membrane reactor.

At an absolute retentate pressure of about 47 atm, the left-end pressure-square-root difference and the right-end pressure-square-root difference are equal, and become matching with the log mean pressure-square-root difference. The gap between the left-end and right-end pressure-square-root difference becomes larger as the retentate pressure increases.

Figure 13 shows how the global apparent permeance and the efficiency factor change as the retentate pressure increases. The actual local permeance is fixed at its base value of 10.263×10^{-4} mol/m^2.s.Pa$^{0.5}$, but the apparent global permeance increases slightly as the retentate pressure increases, and it approaches the actual local permeance at high retentate pressure. The efficiency factor increases from its base value of 67.09% at 40 atm (absolute) to 98.71% at 120 atm (absolute).

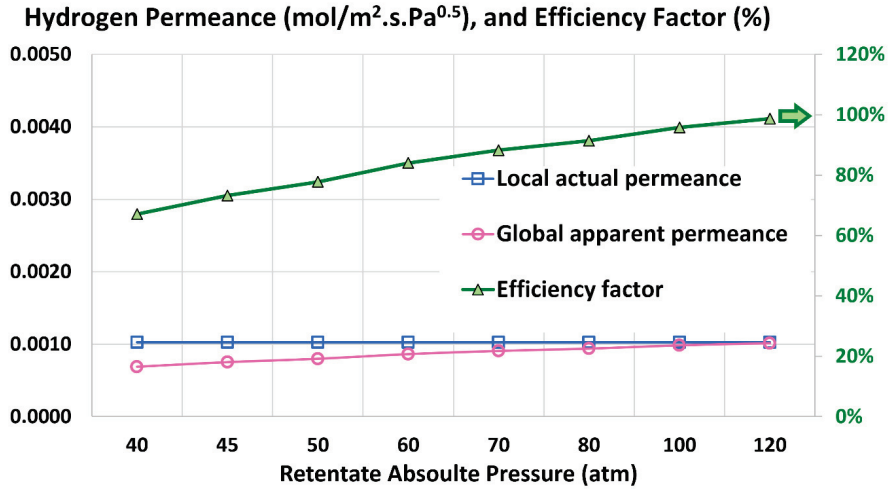

Figure 13. Local actual permeance, global apparent permeance, and efficiency factor as functions of retentate pressure in membrane reactor.

5.4. Influence of Permeate Pressure

In this subsection, the impact of the permeate pressure (the last design variable considered in this study) on the permeation metrics is discussed. Seven additional simulations with different values of the absolute permeate pressure were conducted with the aim of capturing

the trend of the permeation performance when the permeate pressure decreased from the base value of 20 atm (absolute) to a small value near the absolute vacuum (zero atm absolute) [330–332]. The base value and seven additional absolute permeate pressures are as follows:

1. 20 atm (base);
2. 17.5 atm;
3. 15 atm;
4. 10 atm;
5. 5 atm;
6. 1 atm;
7. 0.5 atm;
8. 0.2 atm.

The other two design variables (temperature and retentate pressure) are kept at their base values (300 °C and 40 atm absolute, respectively). Unlike the temperature and the retentate pressure, where larger values than the base values were investigated, smaller values of permeate pressures are investigated here to seek better permeation, since this permeation pressure has a resistive effect for permeation (not a supportive effect as the temperature and the retentate pressure).

Figure 14 shows the influence of the permeate pressure on the first hydrogen permeation metric, which is the membrane length. There is a nonlinear (nearly exponential) increase in the membrane length as the retentate pressure increases. This relation can be described by the following regression model:

$$L(\text{cm}) = 93.105\, e^{0.07192 P_{Per}(\text{atm,absolute})} \quad (18)$$

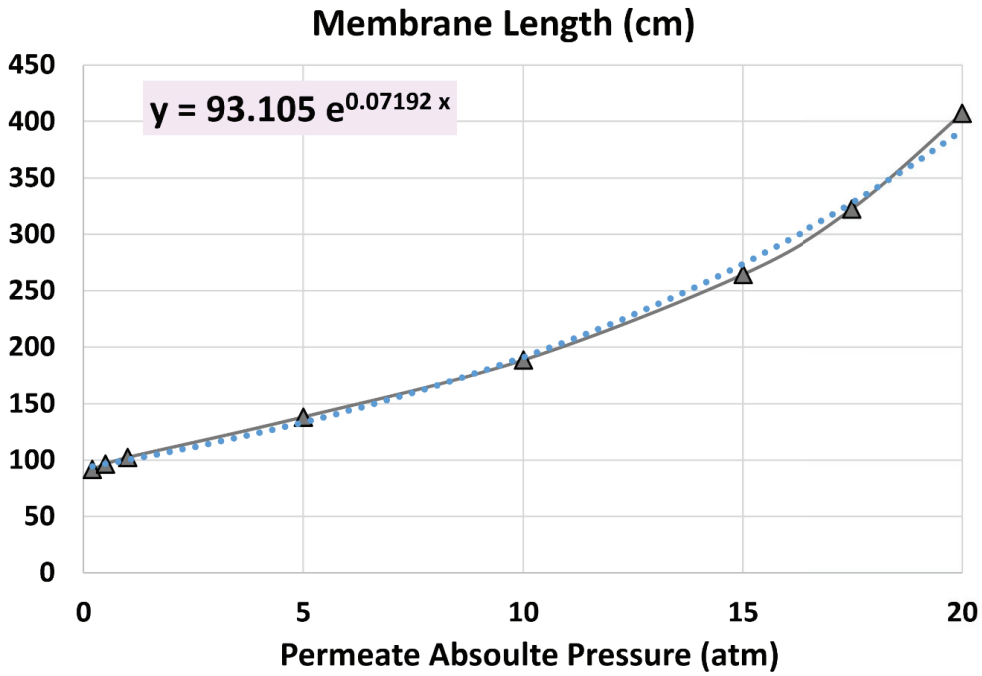

Figure 14. The membrane length as a function of the permeate pressure in the membrane reactor.

Although manipulating the permeate pressure can reduce the membrane length (for a given target hydrogen recovery) to less than 25% of its base value (which was also achievable by manipulating the temperature or the retentate pressure), a partial vacuum is needed to achieve this, with pressures below the normal atmospheric pressure of 1 atm. This imposes complications and expense, and may not be acceptable. However, the reduction in the permeate pressure within more realistic values (like 10 atm, absolute)

has still a favorable effect, and the membrane length can decrease to less than half of its base value by halving the absolute permeate pressure.

Figure 15 shows the influence of the permeate pressure on the second hydrogen permeation metric, which is the average hydrogen permeation mass flux. There is approximately an exponential decline in the average hydrogen permeation mass flux as the permeate pressure increases. This can be described by the following nonlinear regression model:

$$\overline{M}_{H2}\left(\mathrm{kg/m^2.h}\right) = 5.0339\, e^{-0.07192 P_{Per}(\mathrm{atm,absolute})} \quad (19)$$

If the absolute permeate pressure can be reduced to half of its base value, the average hydrogen permeation mass flux can be intensified to more than twice its base value. In the base case (with the base absolute permeate pressure of 20 bar), the average hydrogen permeation mass flux is 1.15054 kg/m^2.h. This increases to 2.48568 kg/m^2.h at an absolute permeate pressure of 10 bar (which is an increase by a multiplicative factor of 2.160 compared to the base case), and increases further to 5.10756 kg/m^2.h at an absolute permeate pressure of 0.2 bar (which is an increase by a multiplicative factor of 4.439 compared to the base case).

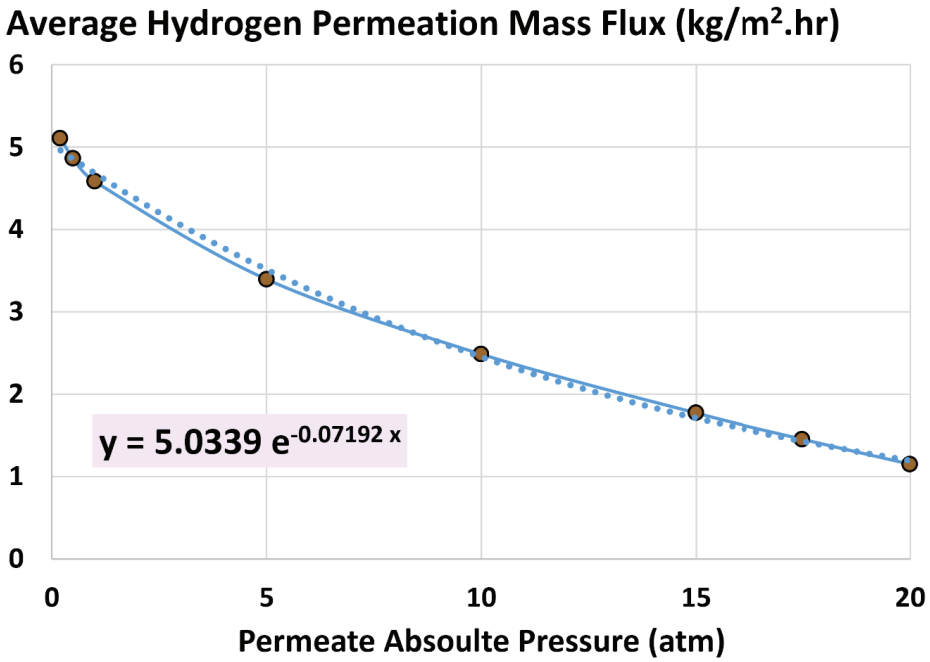

Figure 15. The average hydrogen permeation mass flux as a function of the permeate pressure in the membrane reactor.

Figure 16 shows that the third hydrogen permeation metric (log mean pressure-square-root difference) increases logarithmically with retentate pressure. The relation between the pressure-square-root (LMPD) and the absolute pressure of the permeate stream over the range of considered pressures can be approximated as an exponential function as

$$\mathrm{LMPD}\left(\mathrm{Pa}^{0.5}\right) = 571.05\, e^{-0.04471\ P_{Per}(\mathrm{atm,absolute})} \quad (20)$$

Below the absolute permeate pressure of about 17.5 atm, the left-end pressure-square-root difference is larger than the right-end pressure-square-root difference, which is reversed at higher permeate pressures.

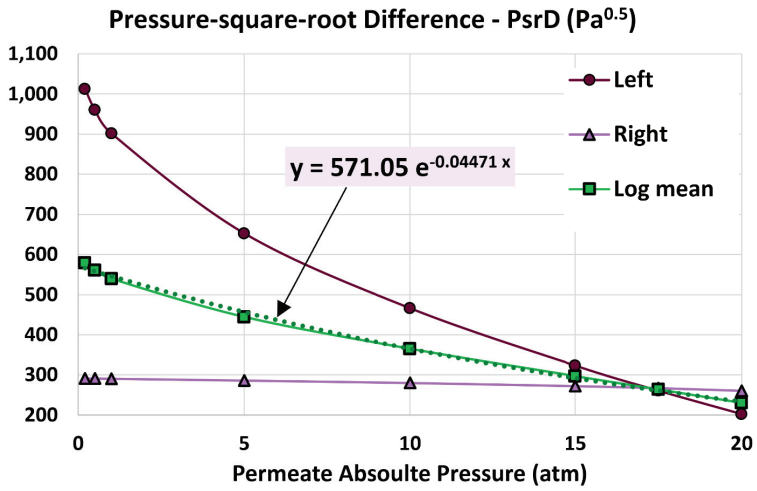

Figure 16. The pressure-square-root difference at the left end of the membrane reactor (x = 0), the pressure-square-root difference at the right end of the membrane reactor (x = L), and the log mean pressure-square-root difference (LMPD) as functions of the permeate pressure in the membrane reactor.

Figure 17 shows how the global apparent permeance and the efficiency factor decrease as the permeate pressure increases. The actual local permeance is fixed at its base value of 10.263×10^{-4} mol/m^2.s.Pa$^{0.5}$, but the apparent global permeance decreases from a value higher than the actual local permeance (thus, an efficiency factor above 100%) at very low permeate pressures to a value smaller than the actual local permeance as the permeate pressure increases (thus, an efficiency factor below 100%) as the absolute permeate pressure is increases beyond about 5 atm. Specifically, the efficiency factor reaches 102.53% and 118.43% at absolute permeate pressures of 5 atm and 0.2 atm, respectively (compared to the base value of 67.09% at 20 atm, absolute).

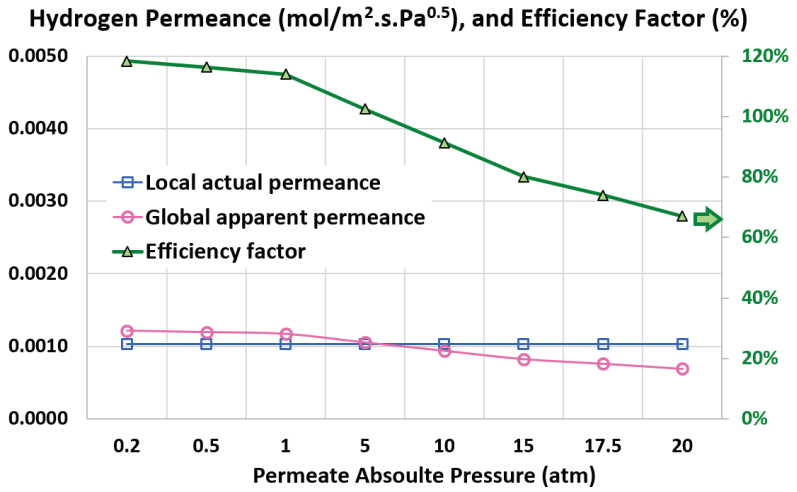

Figure 17. Local actual permeance, global apparent permeance, and efficiency factor as functions of permeate pressure in membrane reactor.

5.5. Profiles with Extreme Design Variables

The final method to highlight the general impacts of the three design variables (temperature, retentate pressure, and permeate pressure) on the hydrogen permeation within a generic palladium membrane reactor is contrasting some longitudinal profiles when the membrane reactor operates at the extreme values (of the ranges considered in the current study) assigned to each design variable while keeping the other two design variables at their base values.

This means contrasting results from three different simulations with the following conditions in Table 6.

Table 6. Some details about the extreme cases.

Extreme Case Number	Temperature	Absolute Retentate Pressure	Absolute Permeate Pressure
1	800 °C (1472.00 °F)	40.0 atm (587.84 psia)	20.0 atm (293.92 psia)
2	300 °C (572.00 °F)	120.0 atm (1763.5 psia)	20.0 atm (293.92 psia)
3	300 °C (572.00 °F)	40.0 atm (587.84 psia)	0.20 atm (2.9392 psia)

The cumulative hydrogen recovery profiles for the three extreme cases are contrasted in Figure 18. The left-end value (0%) and the right-end value (95%) are implicitly imposed by the enforced inlet or outlet conditions. Thus, all profiles should coincide at both the left and right edges of the membrane reactor, but they can deviate in the intermediate zone. The cumulative hydrogen recovery for the extreme temperature shows more linearity than the other two profiles, with the extreme permeate pressure corresponding to a curved profile, resembling a second-order function of the normalized membrane coordinate (x/L), with a gradually declining slope as x/L increases. The extreme retentate pressure simulation shows an intermediate behavior between the other two extreme cases, in terms of the cumulative hydrogen recovery profiles.

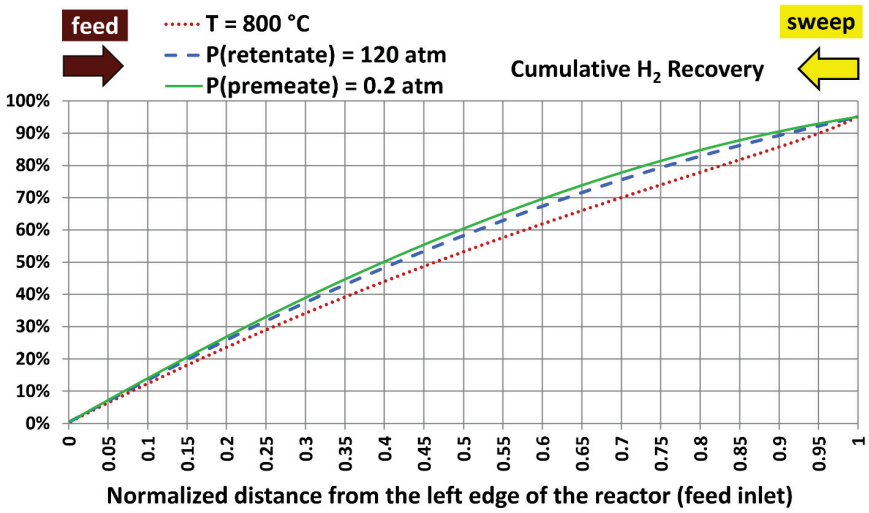

Figure 18. Commutative hydrogen recovery with the extreme values considered for the temperature, absolute retentate pressure, and absolute permeate pressure.

This behavior is better explained by visualizing the segmental contribution to the total hydrogen recovery for these three extreme cases in Figure 19. While the profile for the extreme temperature is not horizontal, it first decreases and then increases, making it behave as if changing around a uniform mean value. Thus, the cumulative value (integration of the profile) should be close to a straight upward line as shown earlier. On the other hand, the extreme permeate pressure causes a nearly linear declining profile for the segmental hydrogen recovery, which when integrated, gives a nearly quadratic profile as shown before. The extreme retentate pressure simulation shows an intermediate behavior between the other two extreme cases, as noted earlier.

The hydrogen mole fractions in the retentate stream and the permeate stream for the three extreme cases are contrasted in Figures 20 and 21, respectively. The simulation with the extreme permeate pressure shows a regular variation for both streams. The simulation with the extreme temperature shows an accelerated decline in the hydrogen mole fractions in both streams as the coordinate x approaches the right end (permeate inlet, retentate exit). This can be attributed to the rapidly elevated segmental hydrogen recovery in this region,

after steadily declining in the left part of the membrane reactor. Again, the extreme retentate pressure simulation shows an intermediate behavior between the other two extreme cases.

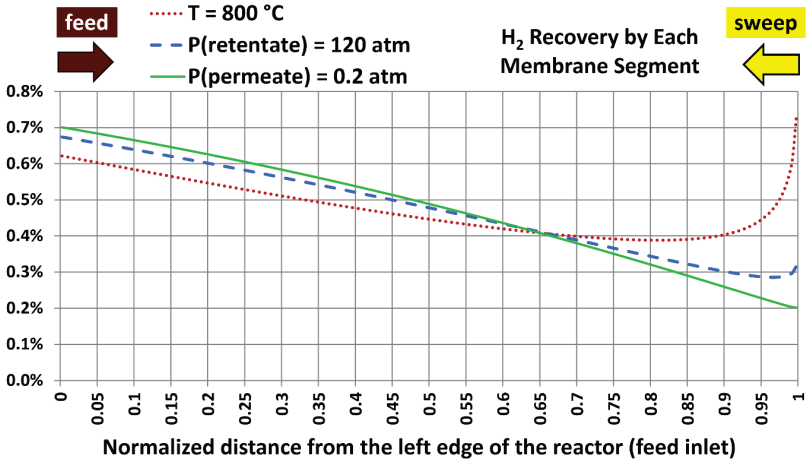

Figure 19. Segmental hydrogen recovery with the extreme values considered for the temperature, absolute retentate pressure, and absolute permeate pressure.

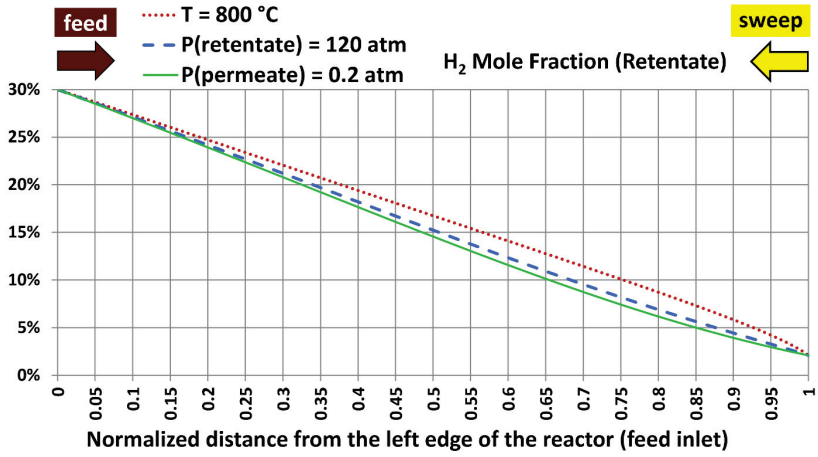

Figure 20. The hydrogen mole fraction in the retentate stream with the extreme values considered for the temperature, absolute retentate pressure, and absolute permeate pressure.

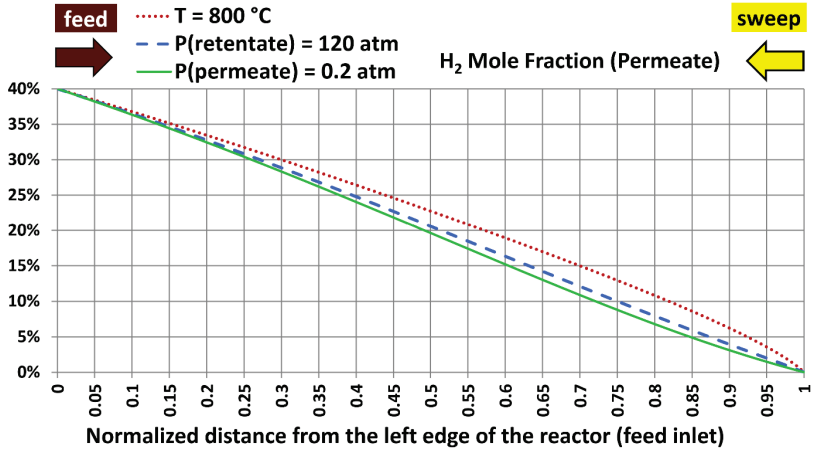

Figure 21. The hydrogen mole fraction in the permeate stream with the extreme values considered for the temperature, absolute retentate pressure, and absolute permeate pressure.

6. Discussion

This section addresses four topics. First, it briefly discusses how some of the presented components in this study can add new insight to the literature and fill a potential gap in it.

Second, it addresses the question of whether or not the results are limited to ideal gases. Third, it comments on the type of validation used for the presented reduced-order model. Fourth, we provide a visual summary that compares the influence levels of the three design variables examined in this study.

6.1. The Contributions of the Study

The contribution of this work to the fields of energy systems, computational modeling, hydrogen production, and carbon capture includes presenting a simple plug-flow reactor computational model for the membrane-based hydrogen separation, which takes a short time to give rough predictions as a precursor of time-consuming three-dimensional computational fluid dynamics (CFD) models performed using specialized computer programs [333–337]. The simple plug-flow reactor model developed here can be automated using spreadsheet software without resorting to complicated computer programming or expensive simulation packages. The model was checked by comparing cases with different spatial resolutions. The model uses a predictor-corrector approach in the computation, where an initial value (in a predictor step) is refined (in a corrector step) to yield the final value at each segment of the segmented reactor. An apparent lack of such a model in the literature is one of the motivations for disseminating this study. The present study also demonstrates examples of consolidated metrics for comparing and judging the permeation performance of hydrogen. This can guide researchers when analyzing or interpreting similar problems. In addition, the study describes the impact of three different design variables on the hydrogen permeation performance, accompanied by good-fit regression models. This step helps in having a broad estimation of the advantage of manipulating each of these variables, which can be weighed against the expenses or practical difficulty in a realistic setting, thus helping in selecting optimum operational conditions. Aside from the technical aspect of the current study, the study may also be viewed as an educational asset for diversifying and enriching teaching content in various courses (modules), such as chemical engineering, material science, energy systems, industrial processes, or numerical methods [338–342]. The simplicity of our proposed reduced-order model (ROM) becomes particularly advantageous here, where students can be exposed to the covered modeling concepts without having a deep background in many subjects. The students can replicate the presented simulations to ensure their understanding of the problem and can even expand this work through innovative projects.

6.2. Ideal-Gas Law and Compressibility Factor

While inspecting the steps of the proposed numerical membrane-based permeation model for hydrogen, confusion may arise regarding any restriction of applicability to gases that obey the ideal-gas law (ideal-gas equation of state). This can occur because the proposed model has steps (steps e and j) where the molar flux of permeating hydrogen through the palladium membrane (with the unit mol/m^2.s, which is moles per square meter per second) was expressed as a standard-temperature–pressure volume flow rate (with the unit scc/min or sccm, which is standard cubic centimeters per minute). In particular, in step e, the conversion constant (22,711 scc/mol) was explicitly utilized, and it was derived earlier in Equation (6) using the ideal-gas equation of state. However, such restriction does not exist. The standard cubic centimeter (scc) for a gas is simply another unit of the amount of substance, like the mole (mol) unit and the kilomole (kmol) unit. All the numerical values used to derive the conversion constant (22,711 scc/mol) represent universal constants themselves. These values are the universal gas constant ($\overline{R}$ = 8.3145 J/mol.K), the units multiplier (10^6 cm^3/m^3), the standard absolute temperature (273.15 K), and the standard pressure (10^5 Pa). Therefore, the unit (scc) is always linearly related to the unit (mol) through a fixed multiplication factor that is independent of the type of gas, the operating temperature, and the operating pressure. The

use of scc in the model (rather than mol for example) can be viewed as an arbitrary choice for compliance with others who use this unit for gaseous flow rates in academic, commercial, or governmental sectors [343–346], and for convenience due to dealing with larger numbers having many significant digits before the decimal point.

Some studies may adopt slightly different values for the standard temperature and standard pressure than those adopted here. For example, the pressure value of 1 atm (101,325 Pa) may be considered the standard pressure instead of 10^5 Pa [347–351]. In such a case, the conversion constant (22,711 scc/mol) derived here consequently should change slightly to 22,414 scc/mol (after multiplying 22,711 by 10^5 and dividing it by 101,325), but this does not invalidate the fact that the scc and the mol are two related units.

In relation to the aforementioned remark, Table 2 in the present study provides the inlet standard volume flow rate (in sccm) for the retentate stream. This value is what is needed as a boundary condition to start using the proposed numerical hydrogen permeation model. The same table also provides the equivalent mass flow rate (in kg/h and lbm/h). This mass flow rate is auxiliary information. It is not directly utilized in the proposed permeation model.

The deviation from the ideal gas condition (which is utilized in the current study) is expressed in terms of a non-dimensional number called compressibility factor or deviation factor, Z [352–358], defined as

$$Z = \frac{P}{\rho\, R\, T} = \frac{P\, v}{R\, T} \tag{21}$$

where (P) is the absolute pressure, (ρ) is the density, (R) is the specific gas constant, (T) is the absolute temperature, and (v) is the specific volume (the reciprocal of the density).

For ideal gases, the compressibility factor has the value of $Z = 1$ [359–366]. The more the deviation from the unity compressibility factor, the more the error resulting from using the ideal-gas law. The compressibility factor depends on the type of the gas, its temperature, and its pressure. Each gas has a characteristic temperature called the critical temperature or T_c [367–372], above which a vapor-liquid phase change becomes no longer observable. When the temperature of the gas is well above its critical point, this gas generally does not deviate significantly from being ideal, over a wide range of pressure [373,374]. All the simulations presented in the current study are at relatively high temperatures (from 300 °C to 800 °C, or 573.15 K to 1073.15 K), which are much more than the critical temperature of all the four gases (H_2, CO, CO_2, N_2) included in all the simulations in the current study. The critical temperature of these gases ranges from 33.2 K for H_2 to 304.2 K for CO_2 [375–379]. Therefore, these gases are not expected to deviate largely from the ideal gas behavior in the performed simulations. For example, experiments showed that the compressibility factor for hydrogen at 75 °C (348.15 K) varies from 1.0024 at an absolute pressure of 4.5400 atm to 1.0455 at an absolute pressure of 85.269 atm [380]. As another example to support the ideal-gas assumption adopted in the current study, reported calculations based on the Reference Fluid Thermodynamic and Transport Properties Database or (REFPROP) [381–384] of the United States National Institute of Standards and Technology (NIST) [385–389] showed that the compressibility factor for hydrogen at 125 °C (398.15 K) varies from 1.0005 at an absolute pressure of 0.9869 atm to 1.0481 at an absolute pressure of 98.69 atm [390].

6.3. Self-Validation

In the current study, we presented self-validation by comparing results from our proposed reduced-order model (ROM) at a normal spatial resolution with results from the same ROM but at a higher spatial resolution. The outcome of this validation was very promising and satisfactory. Although further validation through comparisons with experimental results or three-dimensional computational fluid dynamics (CFD) tools may appear to add value to our study, we do not

incorporate such high-fidelity validations. This should not harm the objectives of the study, which were fully accomplished. The study still presents a novel ROM for a membrane-type plug-flow reactor (PFR) as a preliminary stage before proceeding with a more-detailed computational modeling or an experimental prototype. Our ROM is not intended to replace such a more detailed analysis. Rather, it is aimed to assist it by providing a quick and convenient pre-analysis step that does not require specialized CFD software or prohibitive laboratory work (either of them can be extremely costly, time-consuming, and available only to institutionally backed researchers). In addition, our ROM is largely built upon first principles in chemistry and physics rather than unproven or complex concepts. Thus, the performed self-validation is considered sufficient for supporting the success of our ROM algorithm. We point out that our ROM is favorably made simple and easy to implement, but this also means it lacks the ability to capture some features that appear in a high-fidelity analysis. Such features include heat transfer effects, eddy structures, and temporal unsteadiness [391–393]. On the other hand, a three-dimensional CFD simulation is expected to have a lot of uncertainty given the large number of options and user-defined parameters that need to be selected during the simulation. Added to the different geometric and physical phenomena involved in a CFD model but not involved in our ROM, it is felt that a comparison with such CFD results is not a critical element of this study and can be skipped without major harm.

6.4. Priority Design Chart

Based on the findings of our study, the temperature of the membrane reactor for the palladium-based hydrogen separation is the most influential design variable affecting the hydrogen permeation performance, while the permeate pressure is the least influential, and the retentate pressure has an intermediate level of importance. We depict this variation among the three control variables in Figure 22, taking the shape of an inverted triangle. The relative importance of each variable in this figure is designated by the font size as well as by the area it occupies within the triangle. We refer to this sketch as a "priority design chart".

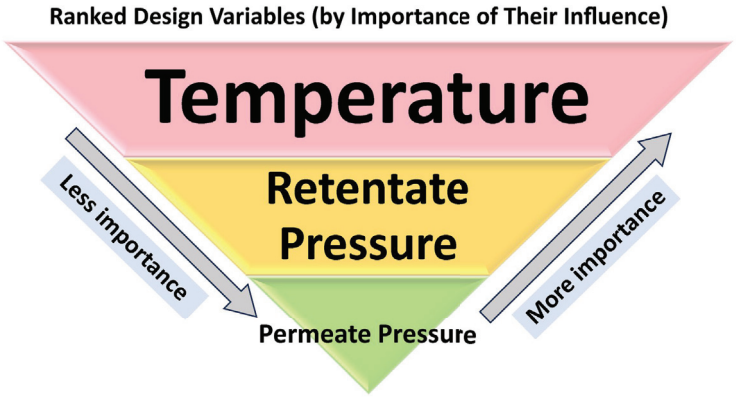

Figure 22. A visualization of the importance of the three design variables covered in the current study (a priority design chart) showing that the temperature has the highest priority, while the permeate pressure has the least priority.

7. Conclusions

A discrete plug-flow reactor model was established for simulating the one-dimensional isothermal permeation of hydrogen through palladium membranes, and was applied for separating hydrogen from a pressurized hot syngas stream. The model assumed a shell-and-tube cross-section for estimating the exact membrane area. A set of inlet conditions for the feed syngas and an inlet sweep nitrogen were established. Also, a target hydrogen recovery of 95% and a target hydrogen mole fraction of 40% at the permeate exit were enforced. The required membrane length was computed to achieve these targets. The

model consisted of 200 segments, with each segment having a length of about 2 cm. After a validity test, it was found that this spatial segmentation was adequate.

Then, the impact of three operational variables was investigated, when varied individually starting from the reference values such that better hydrogen permeation can be obtained. These design variables are the temperature, retentate-side pressure, and permeate-side pressure. For quantitative evaluation of the hydrogen permeation improvement, five assessment metrics were discussed, including the apparent global permeance and the efficiency factor. Linear or nonlinear regression models were provided for the membrane length, the average permeation mass flux, and the log mean pressure-square-root difference. In addition, the one-dimensional profiles of some permeation-related quantities (such as the segmental hydrogen recovery) at the extreme value of each design variable were contrasted. The present study can serve as a rough guide for palladium-based hydrogen separation, showing designers some potential gains in hydrogen permeation by manipulating some operational conditions. The designers may then seek an optimum compromise between the expected gain and the incurred complications or implementation costs.

Considering the relative changes in the three investigated design variables and the dependent hydrogen permeation metrics in 21 simulations (one reference simulation and 20 additional ones), temperature is the most effective variable for improving the permeation performance. The retentate pressure comes in second place. The permeate pressure is the least powerful way to improve hydrogen permeation.

Funding: This research received no funding.

Data Availability Statement: Data elements and parameters used in this study are described and contained within the manuscript itself.

Conflicts of Interest: The author declares no conflicts of interest.

Appendix A. Continuous Plug-Flow Reactor Modeling

This appendix gives a brief description of modeling a continuous plug-flow reactor (PFR).

The Center for Chemical Process Safety (CCPS) within the American Institute of Chemical Engineers (AIChE) defines a plug-flow reactor (PFR) as "A tubular reactor where the feed is continuously introduced at one end and the products continuously removed from the other end. The concentration/temperature in the reactor is not uniform" [394]. This definition is commended for being generic enough to cover different varieties of the PFR model, based on specific sets of assumptions implied. It can be added that in a plug-flow reactor, the plug-like flow of substance does not have any mixing along the axial direction (no axial mixing between different 'plugs' of material) [395].

If the axial (longitudinal) axis is denoted by (x), the concentration of the ith species is denoted by (C_i), the volumetric reaction rate is denoted by (r), the linear velocity is denoted by (u), and the stoichiometric coefficient of the ith species is denoted by (ν_i), then the following partial differential equation governs the temporal and spatial evolution of the concentration along the PFR [396]:

$$\frac{\partial C_i}{\partial t} + \frac{\partial C_i}{\partial x} = \frac{1}{u}\,\nu_i\,r \tag{A1}$$

If the flow is assumed to be steady, the above partial differential equation (PDE) is reduced to an ordinary differential equation (ODE):

$$\frac{dC_i}{dx} = \frac{1}{u}\,\nu_i\,r \tag{A2}$$

Furthermore, if the reaction is first-order, which means that the reaction rate depends linearly on the concentration of only one reactant [397], then the axial gradient of the concentration (C) of that reacting species in the PFR becomes

$$\frac{dC}{dx} = -\frac{1}{u}\, k\, C \tag{A3}$$

where (k) is the rate coefficient of the reaction, which can depend on the absolute temperature (T) following an exponential profile [398], such that

$$k = k_0\, e^{-\varepsilon\, T} \tag{A4}$$

where (k_0) and (ε) are constants.

Appendix B. Modeling Hydrogen Permeation

Appendix B.1. Segmental Plug-Flow Reactor

Hydrogen permeation through a palladium membrane is a nonlinear phenomenon [399], which can be understood and investigated through numerical simulations rather than simple symbolic expressions [400]. For simulating the hydrogen permeation in the simplified hydrogen membrane reactor (HMR), piece-wise constant profiles are utilized to replace the continuous distributions along the membrane reactor, and no partial differential equations or sources of unsteadiness are involved. The membrane reactor is divided into (n) segments, having a small thickness and a constant cross-section. Each segment is assumed to have a uniform gas composition in either the permeate stream or in the retentate stream, and a uniform permeation flux. The flow is steady (time-independent), with a feed syngas entering the reactor from the left end (and leaving the reactor from the right end after losing 95% of its hydrogen moles), and a sweep gas entering the reactor from the right end (and leaving the reactor from the left end after gaining the same amount of hydrogen lost from the syngas, reaching a composition of 40% hydrogen and 60% nitrogen, by mole or volume). Such a segmental approach for handling the one-dimensional evolution of the permeation process along the membrane reactor resembles a discretized version of a plug-flow reactor, PFR [401]. Instead of having infinitely small segments (or plugs) in a true PFR, these segments here are finite. Also, instead of solving ordinary differential equations to find the composition distribution as a function of the longitudinal coordinate as in true PFR problems [402], a numerical approach based on a nonlinear mathematical framework involving scalar algebraic equations only, without a need to solve vector equations or to process matrices [403] is used to describe that composition in adjacent segments, by ensuring continuity of the permeate flow and the retentate flow at the interfaces of each pair of adjacent segments. The hydrogen permeation occurs through the palladium membranes from the retentate to the permeate, with the permeation rate approximated as being uniform (having the same value) within each segment, but it can change from one segment to another. In other words, the smoothly changing permeation rate is discretized and approximated as a piecewise-constant function. Similarly, the driving force for hydrogen permeation (which stems from the partial pressures of hydrogen in the retentate and the permeate sides) is also approximated as a piecewise-constant function.

Appendix B.2. Modeling Algorithm

Figure A1 explains the segmentation of the hypothetical hydrogen membrane reactor (HMR). It shows a portion of its left end, with the two most-left segments. The left end of the membrane reactor is where the coordinate (x) is assigned the value zero. Because the segmental plug-flow reactor (PFR) model is aimed to capture the hydrogen permeation with no consideration of the flow pattern, only the membrane surface is of concern here, because it is where permeation occurs. No gradients are allowed in the direction perpendicular

to the longitudinal axis (thus, no gradients perpendicular to the membrane surface). The membrane is simplified in the figure as a cylindrical surface, separating the permeate stream (inside) from the retentate stream (outside).

The left-hand side (LHS) of the first segment is the left end of the entire membrane (where x = 0).

The LHS of the other segments (all segments except the first one) is the right-hand side (RHS) of the previous segment located to its left.

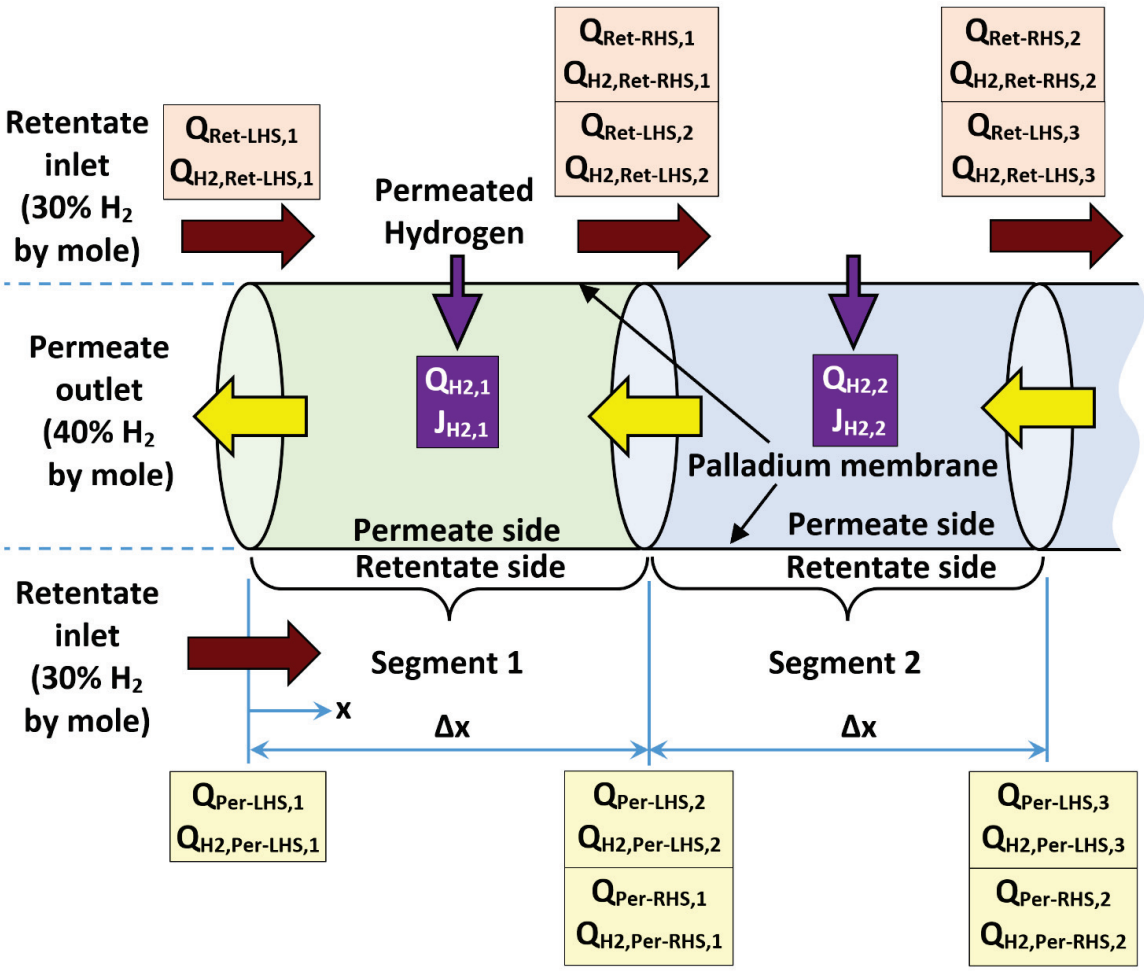

Figure A1. An illustration of the segments of the membrane reactor near its left end.

The index number (i) for a segment can take the value from (1) for the first segment at the left edge of the membrane reactor to (n) for the last segment at the right edge of the membrane reactor. The algorithm for calculating the segment-wise composition in the permeate and the retentate streams for a generic segment is provided below.

(a) Start with a known hydrogen mole fraction in the retentate at the LHS ($X_{H2,Ret\text{-}LHS,i}$), standard volume flow rate of retentate at the LHS ($Q_{Ret\text{-}LHS,i}$), hydrogen mole fraction of permeate at the LHS ($X_{H2,Per\text{-}LHS,i}$), and standard volume flow rate of permeate at the LHS ($Q_{Per\text{-}LHS,i}$) of the segment (say segment number i).

For this step, there are two routes of calculations.

For the first segment (i = 1), implement the inlet conditions and the target mole fraction as follows:

$$X_{H2,Ret-LHS,1} = 30\% \text{ (specified inlet condition)} \quad \text{(A5)}$$

$$Q_{Ret-LHS,1} = 970,068 \text{ sccm (specified inlet condition)} \quad \text{(A6)}$$

$$Q_{H2,Ret-LHS,1} = X_{H2,Ret-LHS,1}\ Q_{Ret-LHS,1} \tag{A7}$$

In the last equation, the product ($X_{H2,Ret-LHS,1}$ $Q_{Ret-LHS,1}$) gives the standard volume flow rate of the hydrogen content in the feed syngas.

$$X_{H2,Per-LHS,1} = 40\% \text{ (specified target)} \tag{A8}$$

$$Q_{Per-LHS,1} = \frac{\beta\ Q_{H2,Ret-LHS,1}}{X_{H2,Per-LHS,1}} \tag{A9}$$

In the last equation, multiplying the standard volume flow rate of the hydrogen content in the feed syngas ($Q_{H2,Ret-LHS,1}$) by the target hydrogen recovery (β) gives the target standard volume flow rate of the hydrogen content in the permeate stream as it exits the membrane reactor from its left end. Dividing this value further by the target mole fraction of the exiting permeate stream ($X_{H2,Per-LHS,1}$) gives the target standard volume flow of the exiting permeate stream ($Q_{Per-LHS,1}$), which is composed of molecular hydrogen and molecular nitrogen. Performing these calculations gives $Q_{Per-LHS,1}$ = 691,173 sccm.

For other segments except the first one (i = 2, 3, . . . n), the connectivity condition of the segments (interfacing condition) can be used as follows:

$$X_{H2,Ret-LHS,i} = X_{H2,Ret-RHS,i-1} \tag{A10}$$

$$Q_{Ret-LHS,i} = Q_{Ret-RHS,i-1} \tag{A11}$$

$$Q_{H2,Ret-LHS,i} = Q_{H2,Ret-RHS,i-1} \tag{A12}$$

$$X_{H2,Per-LHS,i} = X_{H2,Per-RHS,i-1} \tag{A13}$$

$$Q_{Per-LHS,i} = Q_{Per-RHS,i-1} \tag{A14}$$

where the values of ($X_{H2,Ret-RHS,i-1}$), ($Q_{Ret-RHS,i-1}$), ($Q_{H2,Ret-RHS,i-1}$), ($X_{H2,Per-RHS,i-1}$), and ($Q_{Ret-RHS,i-1}$) should be available from the analysis of the previous segment (numbered i − 1).

(b) Compute ($Q_{H2,Per-LHS,i}$), which is the standard volume flow rate of the hydrogen content in the permeate stream at the LHS of the current segment being analyzed (say segment i), as follows:

$$Q_{H2,Per-LHS,i} = X_{H2,Per-LHS,i}\ Q_{Per-LHS,i} \tag{A15}$$

(c) Compute $(\Delta {P_{H2}}^{0.5})_{LHS,i}$, which is the difference in the partial pressures of hydrogen raised to the power of 0.5 (this difference is the driving force for hydrogen permeation through the palladium membrane) at the LHS of the current segment being analyzed (say segment i), as follows:

$$\left(\Delta P_{H2}^{0.5}\right)_{LHS,i} = \left(X_{H2,Ret-LHS,i}\ P_{Ret}\right)^{0.5} - \left(X_{H2,Per-LHS,i}\ P_{Per}\right)^{0.5} \tag{A16}$$

where (P_{Ret}) is the absolute pressure of the retentate stream, and (P_{Per}) is the absolute pressure of the permeate stream. Since the retentate stream is assumed to have a constant pressure, there is no need to add details (a subscript index) about the location for its value to be used in the above equation. The same reason justifies not specifying a particular location for the permeate pressure.

(d) Compute ($J_{H2,i}$), which is a predicted (first-iteration) segment-level molar flux of permeating hydrogen through the palladium membrane based on the conditions at LHS of the current segment being analyzed (say segment i), as follows:

$$J_{H2,i} = k' \left(\Delta P_{H2}^{0.5} \right)_{LHS,i} \tag{A17}$$

This predicted flux value is an initial estimation, based on LHS conditions only. In a subsequent step of the present algorithm, it is refined by including the effects of RHS conditions of the segment.

The above equation is referred to as the Richardson equation [404,405]. It is based on applying both Fick's law for diffusion of hydrogen atoms across the metal membrane, and Sieverts' law relating the concentration of the hydrogen atoms in the metal membrane (the equilibrium between gaseous hydrogen molecules next to the metal membrane and dissociated hydrogen atoms in the metal membrane) to the square root of the partial pressure of the adjacent molecular hydrogen gas [406–408]. The factor (k') is an ideal (or local, or actual) permeance for hydrogen permeation. It is the product of the Fick's diffusion coefficient (for the hydrogen atoms' diffusion across the metal membrane) and the Sieverts' solubility constant (the Sieverts' law constant for the dissociation of a H_2 molecule into two H atoms), and divided by the thickness of the metal membrane. In the current model, the factor (k') is calculated as

$$k' = \frac{A}{\delta} e^{-E/(\overline{R}T)} \tag{A18}$$

where (A) is a pre-exponential factor for hydrogen permeation, (δ) is the thickness of the palladium membrane, (E) is an activation energy for hydrogen permeation, and (T) is the absolute temperature (in kelvins). The values of (A) and (E) used here are [409,410].

$$A = 2.2 \times 10^{-7} \text{ mol/m/s/Pa}^{0.5} \tag{A19}$$

$$\boldsymbol{E} = 15{,}670 \text{ J/mol} \tag{A20}$$

with $\overline{R}$ = 8.3145 J/mol.K, the value of (E/$\overline{R}$) in the above equation becomes 1884.7 K.

The thickness of the palladium membrane is set to 80 μm, which is considered a reasonable value [411,412].

(e) Convert the LHS-based first-iteration molar flux ($J_{H2,i}$) to a predicted (first-iteration) segment-level standard volume flow rate of permeating hydrogen ($Q_{H2,i}$) for the current segment being analyzed (say segment i).

This temporary standard volume flow rate value is an initial estimation, based on LHS conditions only. In a subsequent step of the present algorithm, it is refined by including the effect of RHS conditions. It is computed as follows:

$$Q_{H2,i} = \lambda \, J_{H2,i} \, A_{seg} \tag{A21}$$

where (A_{seg}) is the membrane surface area in one segment, and (λ) is a constant that arises from a necessary unit conversion, as follows:

$$\lambda = 22{,}711 \frac{\text{scc}}{\text{mol}} \, 60 \frac{\text{s}}{\text{min}} \tag{A22}$$

where (scc) stands for (standard cubic centimeters). This gives λ = 1.36266 × 10^6 scc.s/mol.min.

When computing the segmental membrane area, the envisioned tube layout in the shell-and-tube design and its specified dimensions become necessary.

If the tube diameter is designated by the symbol (d), and the length of the entire membrane reactor is designated by the symbol (L), then for eight tubes and (n) segments, the length of a single segment is

$$\Delta x = \frac{L}{n} \tag{A23}$$

and the membrane area within a single segment is

$$A_{seg} = 8\Delta x\ \pi\ d \tag{A24}$$

where (π = 3.14159) is the traditional mathematical constant.

(f) Compute ($\bar{X}_{H2,Ret\text{-}RHS,i}$) and ($\bar{X}_{H2,Per\text{-}RHS,i}$), which are predicted (first-iteration) mole fractions of hydrogen in the retentate stream and the permeate stream, respectively, at the RHS of the current segment being analyzed (say segment i), as follows:

$$\bar{X}_{H2,Ret-RHS,i} = \frac{Q_{H2,Ret-LHS,i} - \bar{Q}_{H2,i}}{Q_{Ret-LHS,i} - \bar{Q}_{H2,i}} \tag{A25}$$

$$\bar{X}_{H2,Per-RHS,i} = \frac{Q_{H2,Per-LHS,i} - \bar{Q}_{H2,i}}{Q_{Per-LHS,i} - \bar{Q}_{H2,i}} \tag{A26}$$

(g) Compute $(\Delta P_{H2}{}^{0.5})_{RHS,i}$, which is the difference in the partial pressures of hydrogen raised to the power of 0.5 (as the driving force for hydrogen permeation) at the RHS of the current segment being analyzed (say segment i), as follows:

$$\left(\Delta P_{H2}^{0.5}\right)_{RHS,i} = \left(X_{H2,Ret-RHS,i}\ P_{Ret}\right)^{0.5} - \left(X_{H2,Per-RHS,i}\ P_{Per}\right)^{0.5} \tag{A27}$$

(h) Compute $(\Delta P_{H2}{}^{0.5})_{i}$, which is the difference in the partial pressures of hydrogen raised to the power of 0.5 assigned to the current segment being analyzed (say segment i). It is taken as the arithmetic average of the LHS value and the RHS value, as follows:

$$\left(\Delta P_{H2}^{0.5}\right)_{i} = 0.5\left(\left(\Delta P_{H2}^{0.5}\right)_{LHS,i} + \left(\Delta P_{H2}^{0.5}\right)_{RHS,i}\right) \tag{A28}$$

(i) Compute ($J_{H2,i}$), which is a corrected (second-iteration) segment-level molar flux of permeating hydrogen through the palladium membrane, which includes driving forces for permeation at both sides of the current segment being analyzed (say segment i), as follows:

$$J_{H2,i} = k'\left(\Delta P_{H2}^{0.5}\right)_{i} \tag{A29}$$

(j) Convert the corrected, segment-level molar flux ($J_{H2,i}$) to a corresponding updated (refined) segment-level standard volume flow rate of permeating hydrogen ($Q_{H2,i}$) for the current segment being analyzed (say segment i), as follows:

$$Q_{H2,i} = \lambda J_{H2,i}\ A_{seg} \tag{A30}$$

This is considered the final representation of the segment-level permeation of hydrogen.

(k) Compute ($R_{H2,i}$), which is the hydrogen recovery due to the current segment being analyzed (say segment i), as follows:

$$R_{H2,i} = Q_{H2,i} / Q_{H2,Ret-LHS,1} \tag{A31}$$

The denominator ($Q_{H2,Ret\text{-}LHS,1}$) in the previous equation is basically the standard volume flow rate of hydrogen in the inlet feed syngas. Thus, it is the standard volume flow of hydrogen available for permeation.

The segmental contribution to the overall recovery ($R_{H2,i}$) can help in studying the distribution of the permeation, and thus identifying portions of the membrane reactor that are more effective than others.

(l) Optional: Compute ($\hat{R}_{H2,i}$), which is the cumulative hydrogen recovery, due to all previous segments of the membrane reactor in addition to the current segment being analyzed (say segment i), as follows:

$$\hat{R}_{H2,i} = \sum_{m=1}^{i} R_{H2,i} \tag{A32}$$

While this value is not necessary for continuing the calculation process, it is part of the data visualization of results here. It is thus beneficial to explain how it is obtained.

(m) Compute ($Q_{Ret\text{-}RHS,i}$) and ($Q_{H2,Ret\text{-}RHS,i}$), which are the standard volume flow rate of the retentate stream and the hydrogen content in that retentate stream, respectively, at the RHS of the current segment being analyzed (say segment i), as follows:

$$Q_{Ret-RHS,i} = Q_{Ret-LHS,i} - Q_{H2,i} \tag{A33}$$

$$Q_{H2,Ret-RHS,i} = Q_{H2,Ret-LHS,i} - Q_{H2,i} \tag{A34}$$

(n) Compute ($X_{H2,Ret\text{-}RHS,i}$), which is the corrected (second-iteration) mole fraction of hydrogen in the retentate stream at the RHS of the current segment being analyzed (say segment i), as follows:

$$X_{H2,Ret-RHS,i} = Q_{H2,Ret-RHS,i} / Q_{Ret-RHS,i} \tag{A35}$$

(o) Compute ($Q_{Per\text{-}RHS,i}$) and ($Q_{H2,Per\text{-}RHS,i}$), which are the standard volume flow rate of the permeate stream and the hydrogen content in that permeate stream, respectively, at the RHS of the current segment being analyzed (say segment i), as follows:

$$Q_{Per-RHS,i} = Q_{Per-LHS,i} - Q_{H2,i} \tag{A36}$$

$$Q_{H2,Per-RHS,i} = Q_{H2,Per-LHS,i} - Q_{H2,i} \tag{A37}$$

(p) Compute ($X_{H2,Per\text{-}RHS,i}$), which is the corrected (second-iteration) mole fraction of hydrogen in the permeate stream at the RHS of the current segment being analyzed (say segment i), as follows:

$$X_{H2,Per-RHS,i} = Q_{H2,Per-RHS,i} / Q_{Per-RHS,i} \tag{A38}$$

(q) Set the obtained RHS conditions of the current segment being analyzed (say segment i) as LHS conditions at the next adjacent segment to be analyzed (segment i + 1), and repeat the computation procedure sequentially for all remaining segments until the last membrane segment (segment n).

The following values should be obtained for each segment:

- $(\Delta P_{H2}{}^{0.5})_{LHS,i}$;
- ~~J~~$_{H2,i}$;
- ~~Q~~$_{H2,i}$;
- ~~X~~$_{H2,Ret\text{-}RHS,i}$ and ~~X~~$_{H2,Per\text{-}RHS,i}$;
- $(\Delta P_{H2}{}^{0.5})_{RHS,i}$;
- $(\Delta P_{H2}{}^{0.5})_{i}$;
- $J_{H2,i}$;

- $Q_{H2,i}$;
- $R_{H2,i}$;
- Optional: $\hat{R}_{H2,i}$
- $Q_{Ret\text{-}RHS,i}$ and $Q_{H2,Ret\text{-}RHS,i}$;
- $X_{H2,Ret\text{-}RHS,i}$;
- $Q_{Per\text{-}RHS,i}$ and $Q_{H2,Per\text{-}RHS,i}$;
- $X_{H2,Per\text{-}RHS,i}$.

(r) Compute ($\hat{R}_{H2,n}$), which is the cumulative hydrogen recovery at the last segment. It is the overall hydrogen recovery by the entire membrane reactor, and it is obtained by simply adding the segment-level hydrogen recovery ($R_{H2,i}$) for all the (n) segments of the membrane reactor. The total cumulative value is the target hydrogen recovery (β). Therefore,

$$\beta \text{ or } \hat{R}_{H2,n} = \sum_{m=1}^{n} R_{H2,i} \quad \text{(A39)}$$

The hydrogen recovery is an important success criterion not only from the chemical perspective, but also from an economic perspective. A higher hydrogen recovery leads to a lower cost per unit mass of hydrogen produced [413,414].

In the presented algorithm, the length of the entire membrane (L) is a nonlinear function of the overall hydrogen recovery (β). Since (β) is fixed at a desired value of 95% (in all the simulation cases of this study), a matching membrane length (L) should be obtained. Solving such a nonlinear system of equations is achieved here using the Goal Seek tool in the Microsoft Excel software program Version (2019). This tool is useful only when the equation or system of equations relates a single independent variable to a single dependent variable [415]. This condition is satisfied in the segmented plug-flow reactor problems here, with the independent variable being the membrane length, and the dependent variable being the hydrogen recovery.

References

1. Bell, D.A.; Towler, B.F.; Fan, M. *Coal Gasification and Its Applications*; William Andrew/Elsevier: Oxford, UK, 2011; ISBN 978-1-4377-7851-9.
2. Marzouk, O.A.; Huckaby, E.D. Assessment of Syngas Kinetic Models for the Prediction of a Turbulent Nonpremixed Flame. In Proceedings of the Fall Meeting of the Eastern States Section of the Combustion Institute 2009, College Park, ML, USA, 18–21 October 2009; pp. 726–751. [CrossRef]
3. Couto, N.; Rouboa, A.; Silva, V.; Monteiro, E.; Bouziane, K. Influence of the Biomass Gasification Processes on the Final Composition of Syngas. *Energy Procedia* **2013**, *36*, 596–606. [CrossRef]
4. Żogała, A. Equilibrium Simulations of Coal Gasification—Factors Affecting Syngas Composition. *J. Sustain. Min.* **2014**, *13*, 30–38. [CrossRef]
5. Wagner, N.J.; Coertzen, M.; Matjie, R.H.; van Dyk, J.C. Chapter 5—Coal Gasification. In *Applied Coal Petrology*; Suárez-Ruiz, I., Crelling, J.C., Eds.; Elsevier: Burlington, NJ, USA, 2008; pp. 119–144, ISBN 978-0-08-045051-3.
6. Guo, X.; Tang, Y.; Wang, Y.; Eble, C.F.; Finkelman, R.B.; Li, P. Evaluation of Carbon Forms and Elements Composition in Coal Gasification Solid Residues and Their Potential Utilization from a View of Coal Geology. *Waste Manag.* **2020**, *114*, 287–298. [CrossRef]
7. Wang, Z.; Yang, J.; Li, Z.; Xiang, Y. Syngas Composition Study. *Front. Energy Power Eng. China* **2009**, *3*, 369–372. [CrossRef]
8. Al-Zareer, M.; Dincer, I.; Rosen, M.A. Influence of Selected Gasification Parameters on Syngas Composition from Biomass Gasification. *J. Energy Resour. Technol.* **2018**, *140*, 041803. [CrossRef]
9. Jayanarasimhan, A.; Pathak, R.M.; Shivapuji, A.M.; Rao, L. Tar Formation in Gasification Systems: A Holistic Review of Remediation Approaches and Removal Methods. *ACS Omega* **2024**, *9*, 2060–2079. [CrossRef]
10. NETL, [National Energy Technology Laboratory of the United States Department of Energy]. Reactions & Transformations. Available online: https://netl.doe.gov/research/coal/energy-systems/gasification/gasifipedia/reaction-transformations (accessed on 5 May 2022).

11. Frolov, S.M.; Panin, K.S.; Smetanyuk, V.A. Gasification of Liquid Hydrocarbon Waste by the Ultra-Superheated Mixture of Steam and Carbon Dioxide: A Thermodynamic Study. *Energies* **2024**, *17*, 2126. [CrossRef]
12. Talmadge, M.; Biddy, M.; Dutta, A.; Jones, S.; Meyer, A. *Syngas Upgrading to Hydrocarbon Fuels Technology Pathway*; National Renewable Energy Laboratory (NREL), and Pacific Northwest National Laboratory (PNNL) of the United States Department of Energy (DoE): Richland, WA, USA, 2013.
13. Lin, S.; Harada, M.; Suzuki, Y.; Hatano, H. Hydrogen Production from Coal by Separating Carbon Dioxide during Gasification. *Fuel* **2002**, *81*, 2079–2085. [CrossRef]
14. Vow (ETIA SAS) | Syngas-High Energy Pyrolysis Gas for Power Applications. Available online: https://www.biogreen-energy.com/syngas (accessed on 6 May 2025).
15. Suxing, S.; Yu, X.; Li, J.; Liu, X.; Sui, L.; Zhang, J.; Fu, Z.; Shao, Y. Effects of Hydrogen Addition on the Thermal Performance and Emissions of Biomass Syngas Combustion in a Horizontal Boiler. *Energies* **2024**, *17*, 2632. [CrossRef]
16. Marzouk, O.A. Portrait of the Decarbonization and Renewables Penetration in Oman's Energy Mix, Motivated by Oman's National Green Hydrogen Plan. *Energies* **2024**, *17*, 4769. [CrossRef]
17. Timilsina, M.S.; Chaudhary, Y.; Shah, A.K.; Lohani, S.P.; Bhandari, R.; Uprety, B. Syngas Composition Analysis for Waste to Methanol Production: Techno-Economic Assessment Using Machine Learning and Aspen Plus. *Renew. Energy* **2024**, *228*, 120574. [CrossRef]
18. Costa, E. Industry 5.0 and SDG 9: A Symbiotic Dance towards Sustainable Transformation. *Sustain. Earth Rev.* **2024**, *7*, 4. [CrossRef]
19. Marzouk, O.A.; Nayfeh, A.H. Mitigation of Ship Motion Using Passive and Active Anti-Roll Tanks. In Proceedings of the ASME 2007 International Design Engineering Technical Conferences and Computers and Information in Engineering Conference (IDETC-CIE 2007), ASME [American Society of Mechanical Engineers]. Las Vegas, NV, USA, 20 May 2009; pp. 215–229. [CrossRef]
20. TGG, [The Global Goals] SDG 9 | Goal 9: Industry, Innovation and Infrastructure. Available online: https://globalgoals.org/goals/9-industry-innovation-and-infrastructure (accessed on 3 May 2025).
21. Marzouk, O.A.; Nayfeh, A.H. Control of Ship Roll Using Passive and Active Anti-Roll Tanks. *Ocean Eng.* **2009**, *36*, 661–671. [CrossRef]
22. Kynčlová, P.; Upadhyaya, S.; Nice, T. Composite Index as a Measure on Achieving Sustainable Development Goal 9 (SDG-9) Industry-Related Targets: The SDG-9 Index. *Appl. Energy* **2020**, *265*, 114755. [CrossRef]
23. Marzouk, O.A. Summary of the 2023 (1st Edition) Report of TCEP (Tracking Clean Energy Progress) by the International Energy Agency (IEA), and Proposed Process for Computing a Single Aggregate Rating. *E3S Web Conf.* **2025**, *601*, 00048. [CrossRef]
24. Küfeoğlu, S. (Ed.) SDG-9: Industry, Innovation and Infrastructure. In *Emerging Technologies: Value Creation for Sustainable Development*; Springer International Publishing: Cham, Switzerland, 2022; pp. 349–369, ISBN 978-3-031-07127-0.
25. Cavo, M.; Rivarolo, M.; Gini, L.; Magistri, L. An Advanced Control Method for Fuel Cells—Metal Hydrides Thermal Management on the First Italian Hydrogen Propulsion Ship. *Int. J. Hydrogen Energy* **2023**, *48*, 20923–20934. [CrossRef]
26. Marzouk, O.A. Expectations for the Role of Hydrogen and Its Derivatives in Different Sectors through Analysis of the Four Energy Scenarios: IEA-STEPS, IEA-NZE, IRENA-PES, and IRENA-1.5 °C. *Energies* **2024**, *17*, 646. [CrossRef]
27. Villavicencio Calzadilla, P.; Mauger, R. The UN's New Sustainable Development Agenda and Renewable Energy: The Challenge to Reach SDG7 While Achieving Energy Justice. *J. Energy Nat. Resour. Law* **2018**, *36*, 233–254. [CrossRef]
28. Marzouk, O.A. Power Density and Thermochemical Properties of Hydrogen Magnetohydrodynamic (H2MHD) Generators at Different Pressures, Seed Types, Seed Levels, and Oxidizers. *Hydrogen* **2025**, *6*, 31. [CrossRef]
29. Estevão, J.; Lopes, J.D. SDG7 and Renewable Energy Consumption: The Influence of Energy Sources. *Technol. Forecast. Soc. Change* **2024**, *198*, 123004. [CrossRef]
30. Marzouk, O.A. *Jatropha Curcas* as Marginal Land Development Crop in the Sultanate of Oman for Producing Biodiesel, Biogas, Biobriquettes, Animal Feed, and Organic Fertilizer. *Rev. Agric. Sci.* **2020**, *8*, 109–123. [CrossRef] [PubMed]
31. Marcillo-Delgado, J.C.; Ortego, M.I.; Pérez-Foguet, A. A Compositional Approach for Modelling SDG7 Indicators: Case Study Applied to Electricity Access. *Renew. Sustain. Energy Rev.* **2019**, *107*, 388–398. [CrossRef]
32. Marzouk, O.A. Facilitating Digital Analysis and Exploration in Solar Energy Science and Technology through Free Computer Applications. *Eng. Proc.* **2022**, *31*, 75. [CrossRef]
33. Halder, P.; Babaie, M.; Salek, F.; Haque, N.; Savage, R.; Stevanovic, S.; Bodisco, T.A.; Zare, A. Advancements in Hydrogen Production, Storage, Distribution and Refuelling for a Sustainable Transport Sector: Hydrogen Fuel Cell Vehicles. *Int. J. Hydrogen Energy* **2024**, *52*, 973–1004. [CrossRef]
34. Marzouk, O.A. Growth in the Worldwide Stock of E-Mobility Vehicles (by Technology and by Transport Mode) and the Worldwide Stock of Hydrogen Refueling Stations and Electric Charging Points between 2020 and 2022. In *Construction Materials and Their Processing*; Key Engineering Materials; Trans Tech Publications Ltd.: Bäch, Switzerland, 2023; Volume 972, pp. 89–96, ISBN 978-3-0364-0498-1. [CrossRef]

35. Jayakumar, A.; Madheswaran, D.K.; Kannan, A.M.; Sureshvaran, U.; Sathish, J. Can Hydrogen Be the Sustainable Fuel for Mobility in India in the Global Context? *Int. J. Hydrogen Energy* **2022**, *47*, 33571–33596. [CrossRef]
36. Mahadevia, D.; Mukhopadhyay, C.; Lathia, S.; Gounder, K. The Role of Urban Transport in Delivering Sustainable Development Goal 11: Learning from Two Indian Cities. *Heliyon* **2023**, *9*, e19453. [CrossRef] [PubMed]
37. Marzouk, O.A. Toward More Sustainable Transportation: Green Vehicle Metrics for 2023 and 2024 Model Years. In *Intelligent Sustainable Systems*; Nagar, A.K., Jat, D.S., Mishra, D.K., Joshi, A., Eds.; Lecture Notes in Networks and Systems; Springer Nature: Singapore, 2024; Volume 817, pp. 261–272, ISBN 978-981-9978-85-4. [CrossRef]
38. DESA, [United Nations Department of Economic and Social Affairs]. Sustainable Transport (SDG 11). Available online: https://sdgs.un.org/topics/sustainable-transport (accessed on 3 May 2025).
39. Marzouk, O.A. Recommended LEED-Compliant Cars, SUVs, Vans, Pickup Trucks, Station Wagons, and Two Seaters for Smart Cities Based on the Environmental Damage Index (EDX) and Green Score. In *Innovations in Smart Cities Applications Volume 7*; Ben Ahmed, M., Boudhir, A.A., El Meouche, R., Karaş, İ.R., Eds.; Lecture Notes in Networks and Systems; Springer Nature: Cham, Switzerland, 2024; Volume 906, pp. 123–135, ISBN 978-3-031-53823-0. [CrossRef]
40. Franco, S. Sustainable Cities and Communities: The Road towards SDG 11. *TeMA—J. Land Use Mobil. Environ.* **2022**, *15*, 341–344. [CrossRef]
41. Mulibana, L.; du Toit, J. Transport Planning Research Toward Implementing SDG 11 in South Africa. In *SDGs in Africa and the Middle East Region*; Leal Filho, W., Abubakar, I.R., da Silva, I., Pretorius, R., Tarabieh, K., Eds.; Springer International Publishing: Cham, Switzerland, 2022; pp. 1–24, ISBN 978-3-030-91260-4.
42. Marzouk, O.A. Zero Carbon Ready Metrics for a Single-Family Home in the Sultanate of Oman Based on EDGE Certification System for Green Buildings. *Sustainability* **2023**, *15*, 13856. [CrossRef]
43. Liu, H.; Lu, H.; Hu, H. CO_2 Capture and Mineral Storage: State of the Art and Future Challenges. *Renew. Sustain. Energy Rev.* **2024**, *189*, 113908. [CrossRef]
44. Marzouk, O.A. Assessment of Global Warming in Al Buraimi, Sultanate of Oman Based on Statistical Analysis of NASA POWER Data over 39 Years, and Testing the Reliability of NASA POWER against Meteorological Measurements. *Heliyon* **2021**, *7*, e06625. [CrossRef]
45. Doni, F.; Gasperini, A.; Soares, J.T. What Is the SDG 13? In *SDG13—Climate Action: Combating Climate Change and Its Impacts*; Emerald Publishing Limited: Leeds, UK, 2020; pp. 21–30, ISBN 978-1-78756-915-7.
46. Marzouk, O.A. Evolution of the (Energy and Atmosphere) Credit Category in the LEED Green Buildings Rating System for (Building Design and Construction: New Construction), from Version 4.0 to Version 4.1. *J. Infrastruct. Policy Dev.* **2024**, *8*, 5306. [CrossRef]
47. TGG, [The Global Goals] SDG 13 | Goal 13: Climate Action. Available online: https://globalgoals.org/goals/13-climate-action (accessed on 3 May 2025).
48. Bakirci, M. Smart City Air Quality Management through Leveraging Drones for Precision Monitoring. *Sustain. Cities Soc.* **2024**, *106*, 105390. [CrossRef]
49. Marzouk, O.A. Compilation of Smart Cities Attributes and Quantitative Identification of Mismatch in Rankings. *J. Eng.* **2022**, *2022*, 5981551. [CrossRef]
50. Akuraju, V.; Pradhan, P.; Haase, D.; Kropp, J.P.; Rybski, D. Relating SDG11 Indicators and Urban Scaling—An Exploratory Study. *Sustain. Cities Soc.* **2020**, *52*, 101853. [CrossRef]
51. Marzouk, O.A. Urban Air Mobility and Flying Cars: Overview, Examples, Prospects, Drawbacks, and Solutions. *Open Eng.* **2022**, *12*, 662–679. [CrossRef]
52. Abastante, F.; Lami, I.M.; Gaballo, M. Pursuing the SDG11 Targets: The Role of the Sustainability Protocols. *Sustainability* **2021**, *13*, 3858. [CrossRef]
53. Marzouk, O.A. Aerial E-Mobility Perspective: Anticipated Designs and Operational Capabilities of eVTOL Urban Air Mobility (UAM) Aircraft. *Edelweiss Appl. Sci. Technol.* **2025**, *9*, 413–442. [CrossRef]
54. Marzouk, O.A. Adiabatic Flame Temperatures for Oxy-Methane, Oxy-Hydrogen, Air-Methane, and Air-Hydrogen Stoichiometric Combustion Using the NASA CEARUN Tool, GRI-Mech 3.0 Reaction Mechanism, and Cantera Python Package. *Eng. Technol. Appl. Sci. Res.* **2023**, *13*, 11437–11444. [CrossRef]
55. Jamrozik, A.; Grab-Rogaliński, K.; Tutak, W. Hydrogen Effects on Combustion Stability, Performance and Emission of Diesel Engine. *Int. J. Hydrogen Energy* **2020**, *45*, 19936–19947. [CrossRef]
56. Xie, T.; Wang, P. Analysis of NO Formation in Counter-Flow Premixed Hydrogen-Air Flame. *Trans. Can. Soc. Mech. Eng.* **2013**, *37*, 851–859. [CrossRef]
57. Marzouk, O.A. Hydrogen Utilization as a Plasma Source for Magnetohydrodynamic Direct Power Extraction (MHD-DPE). *IEEE Access* **2024**, *12*, 167088–167107. [CrossRef]
58. Goldmeer, J.; Catillaz, J.; Donohue, J. *Hydrogen as a Fuel for Gas Turbines—A Pathway to Lower CO_2*; General Electric (GE): Boston, MA, USA, 2022.

59. Javoy, S.; Mevel, R.; Paillard, C.E. A Study of N_2O Decomposition Rate Constant at High Temperature: Application to the Reduction of Nitrous Oxide by Hydrogen. *Int. J. Chem. Kinet.* **2009**, *41*, 357–375. [CrossRef]
60. Weiland, N.T.; Strakey, P.A. *Global NOx Measurements in Turbulent Nitrogen-Diluted Hydrogen Jet Flames*; National Energy Technology Laboratory (NETL): San Diego, CA, USA, 2007.
61. Marzouk, O.A. Dataset of Total Emissivity for CO_2, H_2O, and H_2O-CO_2 Mixtures; over a Temperature Range of 300–2900 K and a Pressure-Pathlength Range of 0.01–50 Atm.m. *Data Brief* **2025**, *59*, 111428. [CrossRef] [PubMed]
62. Ghiat, I.; Al-Ansari, T. A Review of Carbon Capture and Utilisation as a CO_2 Abatement Opportunity within the EWF Nexus. *J. CO2 Util.* **2021**, *45*, 101432. [CrossRef]
63. Madejski, P.; Chmiel, K.; Subramanian, N.; Kuś, T. Methods and Techniques for CO_2 Capture: Review of Potential Solutions and Applications in Modern Energy Technologies. *Energies* **2022**, *15*, 887. [CrossRef]
64. Ruan, R.; Wang, G.; Li, S.; Wang, M.; Lin, H.; Tan, H.; Wang, X.; Liu, F. The Effect of Alkali and Alkaline Earth Metals (AAEMs) on Combustion and PM Formation during Oxy-Fuel Combustion of Coal Rich in AAEMs. *Energy* **2024**, *293*, 130695. [CrossRef]
65. Marzouk, O.A. Radiant Heat Transfer in Nitrogen-Free Combustion Environments. *Int. J. Nonlinear Sci. Numer. Simul.* **2018**, *19*, 175–188. [CrossRef]
66. Rajabloo, T.; Valee, J.; Marenne, Y.; Coppens, L.; De Ceuninck, W. Carbon Capture and Utilization for Industrial Applications. *Energy Rep.* **2023**, *9*, 111–116. [CrossRef]
67. Marzouk, O.A. Temperature-Dependent Functions of the Electron–Neutral Momentum Transfer Collision Cross Sections of Selected Combustion Plasma Species. *Appl. Sci.* **2023**, *13*, 11282. [CrossRef]
68. Donskoy, I. Techno-Economic Efficiency Estimation of Promising Integrated Oxyfuel Gasification Combined-Cycle Power Plants with Carbon Capture. *Clean Technol.* **2023**, *5*, 215–232. [CrossRef]
69. Marzouk, O.A. Detailed and Simplified Plasma Models in Combined-Cycle Magnetohydrodynamic Power Systems. *Int. J. Adv. Appl. Sci.* **2023**, *10*, 96–108. [CrossRef]
70. Dinca, C.; Slavu, N.; Cormoş, C.-C.; Badea, A. CO_2 Capture from Syngas Generated by a Biomass Gasification Power Plant with Chemical Absorption Process. *Energy* **2018**, *149*, 925–936. [CrossRef]
71. Marzouk, O.A. Technical Review of Radiative-Property Modeling Approaches for Gray and Nongray Radiation, and a Recommended Optimized WSGGM for CO_2/H_2O-Enriched Gases. *Results Eng.* **2025**, *25*, 103923. [CrossRef]
72. Bhavsar, A.; Hingar, D.; Ostwal, S.; Thakkar, I.; Jadeja, S.; Shah, M. The Current Scope and Stand of Carbon Capture Storage and Utilization ∼ A Comprehensive Review. *Case Stud. Chem. Environ. Eng.* **2023**, *8*, 100368. [CrossRef]
73. Dziejarski, B.; Krzyżyńska, R.; Andersson, K. Current Status of Carbon Capture, Utilization, and Storage Technologies in the Global Economy: A Survey of Technical Assessment. *Fuel* **2023**, *342*, 127776. [CrossRef]
74. Tomasko, D.L.; Li, H.; Liu, D.; Han, X.; Wingert, M.J.; Lee, L.J.; Koelling, K.W. A Review of CO_2 Applications in the Processing of Polymers. *Ind. Eng. Chem. Res.* **2003**, *42*, 6431–6456. [CrossRef]
75. Singh, A.; Saini, V.; Jain, S.; Gour, A. Techno-Economic, Environmental, and Policy Perspectives of Carbon Capture to Fuel Technologies. *Int. Res. J. Adv. Eng. Hub.* **2024**, *2*, 1387–1403. [CrossRef]
76. Bukar, A.M.; Asif, M. Technology Readiness Level Assessment of Carbon Capture and Storage Technologies. *Renew. Sustain. Energy Rev.* **2024**, *200*, 114578. [CrossRef]
77. Shabbani, H.J.K.; Othman, M.R.; Al- Janabi, S.K.; Barron, A.R.; Helwani, Z. H2 Purification Employing Pressure Swing Adsorption Process: Parametric and Bibliometric Review. *Int. J. Hydrogen Energy* **2024**, *50*, 674–699. [CrossRef]
78. Singh, A.P.; Singh, S.; Ganguly, S.; Patwardhan, A.V. Steam Reforming of Methane and Methanol in Simulated Macro & Micro-Scale Membrane Reactors: Selective Separation of Hydrogen for Optimum Conversion. *J. Nat. Gas Sci. Eng.* **2014**, *18*, 286–295. [CrossRef]
79. Kassi, A.H.; Al-Hattab, T.A. A Review: Membrane Reactor for Hydrogen Production: Modeling and Simulation. *Eng. Chem.* **2023**, *4*, 17–31. [CrossRef]
80. Omidifar, M.; Akbar Babaluo, A.; Jamshidi, S. H_2 Permeance and Surface Characterization of a Thin (2 Mm) Pd-Ni Composite Membrane Prepared by Electroless Plating. *Chem. Eng. Sci.* **2024**, *283*, 119370. [CrossRef]
81. Zito, P.F.; Brunetti, A.; Barbieri, G. Hydrogen Concentration and Purification by Membrane Process: A Multistage Analysis. *Renew. Energy* **2023**, *218*, 119243. [CrossRef]
82. Piemonte, V.; Di Paola, L.; De Falco, M.; Iulianelli, A.; Basile, A. Hydrogen Production Using Inorganic Membrane Reactors. In *Advances in Hydrogen Production, Storage and Distribution*; Elsevier: Amsterdam, The Netherlands, 2014; pp. 283–316, ISBN 978-0-85709-768-2.
83. Li, Y.; Yuan, H.; Wang, X.; Wei, X.; Zhu, J.; Ma, R.; Gao, L.; Dai, H. Insight into Resistance Relaxation Characteristics of Proton Exchange Membrane Fuel Cell in Purge Operation: Experiment, Application, and Mechanisms. *J. Clean. Prod.* **2025**, *496*, 145118. [CrossRef]
84. Marzouk, O.A. 2030 Ambitions for Hydrogen, Clean Hydrogen, and Green Hydrogen. *Eng. Proc.* **2023**, *56*, 14. [CrossRef]

85. Huang, T.; Zou, P.; Xiao, Y.; Ding, W.; Ke, R.; Zhang, Y.; Wan, Z.; Tu, Z.; Tang, S.; Zeng, W. Comprehensive Analysis of Half-Wave Continuous Cooling Channels in Performance of Proton Exchange Membrane Fuel Cells. *Int. J. Heat Mass Transf.* **2025**, *244*, 126971. [CrossRef]
86. Irshad, H.M.; Shahgaldi, S. Comprehensive Review of Bipolar Plates for Proton Exchange Membrane Fuel Cells with a Focus on Materials, Processing Methods and Characteristics. *Int. J. Hydrogen Energy* **2025**, *111*, 462–487. [CrossRef]
87. Peters, T.; Caravella, A. Pd-Based Membranes: Overview and Perspectives. *Membranes* **2019**, *9*, 25. [CrossRef]
88. Marcantonio, V.; De Falco, M.; Capocelli, M.; Bocci, E.; Colantoni, A.; Villarini, M. Process Analysis of Hydrogen Production from Biomass Gasification in Fluidized Bed Reactor with Different Separation Systems. *Int. J. Hydrogen Energy* **2019**, *44*, 10350–10360. [CrossRef]
89. Park, S.-J.; Lee, D.-W.; Yu, C.-Y.; Lee, K.-Y.; Lee, K.-H. Hydrogen Production from a DME Reforming-Membrane Reactor Using Stainless Steel-Supported Knudsen Membranes with High Permeability. *J. Membr. Sci.* **2008**, *318*, 123–128. [CrossRef]
90. Lee, D.-W.; Park, S.-J.; Yu, C.-Y.; Ihm, S.-K.; Lee, K.-H. Remarkable Improvement in Hydrogen Recovery and Reaction Efficiency of a Methanol Reforming−Membrane Reactor by Using a Novel Knudsen Membrane. *Ind. Eng. Chem. Res.* **2008**, *47*, 1392–1397. [CrossRef]
91. Lee, D.-W.; Nam, S.-E.; Sea, B.; Ihm, S.-K.; Lee, K.-H. Preparation of Pt-Loaded Hydrogen Selective Membranes for Methanol Reforming. *Catal. Today* **2006**, *118*, 198–204. [CrossRef]
92. Barg, C.; Ferreira, J.M.P.; Trierweiler, J.O.; Secchi, A.R. Simulation and Optimization of an Industrial PSA Unit. *Braz. J. Chem. Eng.* **2000**, *17*, 695–704. [CrossRef]
93. Damle, A.S. Hydrogen Production by Reforming of Liquid Hydrocarbons in a Membrane Reactor for Portable Power Generation—Model Simulations. *J. Power Sources* **2008**, *180*, 516–529. [CrossRef]
94. Lee, D.-W.; Park, S.-J.; Yu, C.-Y.; Ihm, S.-K.; Lee, K.-H. Study on Methanol Reforming–Inorganic Membrane Reactors Combined with Water–Gas Shift Reaction and Relationship between Membrane Performance and Methanol Conversion. *J. Membr. Sci.* **2008**, *316*, 63–72. [CrossRef]
95. Sircar, S. Pressure Swing Adsorption. *Ind. Eng. Chem. Res.* **2002**, *41*, 1389–1392. [CrossRef]
96. Ruthven, D.M.; Farooq, S.; Knaebel, K.S. *Pressure Swing Adsorption*; John Wiley & Sons: Hoboken, NJ, USA, 1996; ISBN 978-0-471-18818-6.
97. Zhang, R.; Shen, Y.; Tang, Z.; Li, W.; Zhang, D. A Review of Numerical Research on the Pressure Swing Adsorption Process. *Processes* **2022**, *10*, 812. [CrossRef]
98. Wiheeb, A.D.; Helwani, Z.; Kim, J.; Othman, M.R. Pressure Swing Adsorption Technologies for Carbon Dioxide Capture. *Sep. Purif. Rev.* **2016**, *45*, 108–121. [CrossRef]
99. Ko, D.; Siriwardane, R.; Biegler, L.T. Optimization of Pressure Swing Adsorption and Fractionated Vacuum Pressure Swing Adsorption Processes for CO_2 Capture. *Ind. Eng. Chem. Res.* **2005**, *44*, 8084–8094. [CrossRef]
100. Grande, C.A. Advances in Pressure Swing Adsorption for Gas Separation. *Int. Sch. Res. Not.* **2012**, *2012*, 982934. [CrossRef]
101. Liemberger, W.; Groß, M.; Miltner, M.; Harasek, M. Experimental Analysis of Membrane and Pressure Swing Adsorption (PSA) for the Hydrogen Separation from Natural Gas. *J. Clean. Prod.* **2017**, *167*, 896–907. [CrossRef]
102. Vermaak, L.; Neomagus, H.W.J.P.; Bessarabov, D.G. Hydrogen Separation and Purification from Various Gas Mixtures by Means of Electrochemical Membrane Technology in the Temperature Range 100–160 °C. *Membranes* **2021**, *11*, 282. [CrossRef]
103. Chang, K.; Li, Q.; Li, Q. Refrigeration Cycle for Cryogenic Separation of Hydrogen from Coke Oven Gas. *Front. Energy Power Eng. China* **2008**, *2*, 484–488. [CrossRef]
104. Naeiji, E.; Noorpoor, A.; Ghanavati, H. Energy, Exergy, and Economic Analysis of Cryogenic Distillation and Chemical Scrubbing for Biogas Upgrading and Hydrogen Production. *Sustainability* **2022**, *14*, 3686. [CrossRef]
105. Kowalczyk, P.; Gauden, P.A.; Terzyk, A.P. Cryogenic Separation of Hydrogen Isotopes in Single-Walled Carbon and Boron-Nitride Nanotubes: Insight into the Mechanism of Equilibrium Quantum Sieving in Quasi-One-Dimensional Pores. *J. Phys. Chem. B* **2008**, *112*, 8275–8284. [CrossRef]
106. Lazar, A.; Brad, S.; Vijulie, M.; Oubraham, A. Cryogenic Distillation Experimental Stands for Hydrogen Isotopes Separation. *Fusion Eng. Des.* **2019**, *146*, 1998–2001. [CrossRef]
107. Bogdan, C.; Brad, S.; Necula, H.; Sirosh, O.; Brill, C.; Vijulie, M.; Lazar, A.; Grafov, A. Design, Fabrication, and Test of a Prototype of Matrix Heat Exchanger for Cryogenic Distillation of Hydrogen Isotopes. *Fusion Sci. Technol.* **2024**, *80*, 443–454. [CrossRef]
108. Naquash, A.; Riaz, A.; Yehia, F.; Chaniago, Y.D.; Lim, H.; Lee, M. Hydrogen Purification through a Membrane–Cryogenic Integrated Process: A 3 E's (Energy, Exergy, and Economic) Assessment. *Gases* **2023**, *3*, 92–105. [CrossRef]
109. Cavaliere, P. Hydrogen Separation and Purification. In *Water Electrolysis for Hydrogen Production*; Cavaliere, P., Ed.; Springer International Publishing: Cham, Switzerland, 2023; pp. 509–541, ISBN 978-3-031-37780-8.
110. Yang, X.; Xu, Q. Product Loss Minimization of an Integrated Cryogenic Separation System. *Chem. Eng. Technol.* **2012**, *35*, 635–645. [CrossRef]
111. Kangwanpongpan, T.; Makarov, D.; Cirrone, D.; Molkov, V. LES Model of Flash-Boiling and Pressure Recovery Phenomena during Release from Large-Scale Pressurised Liquid Hydrogen Storage Tank. *Int. J. Hydrogen Energy* **2024**, *50*, 390–405. [CrossRef]

112. Ohira, K. Study of Nucleate Boiling Heat Transfer to Slush Hydrogen and Slush Nitrogen. *Heat Trans. Asian Res.* **2003**, *32*, 13–28. [CrossRef]
113. Pereira, R.; Monteiro, V.; Afonso, J.L.; Teixeira, J. Hydrogen Refueling Stations: A Review of the Technology Involved from Key Energy Consumption Processes to Related Energy Management Strategies. *Energies* **2024**, *17*, 4906. [CrossRef]
114. Ozawa, A.; Inoue, M.; Kitagawa, N.; Muramatsu, R.; Anzai, Y.; Genchi, Y.; Kudoh, Y. Assessing Uncertainties of Well-To-Tank Greenhouse Gas Emissions from Hydrogen Supply Chains. *Sustainability* **2017**, *9*, 1101. [CrossRef]
115. Harris, P.D.; Barnes, R. The Uses of Helium and Xenon in Current Clinical Practice. *Anaesthesia* **2008**, *63*, 284–293. [CrossRef]
116. Xie, Y.; Zhong, K. Investigation on the Performances of Vuilleumier Cycle Heat Pump Adopting Mixture Refrigerants. *Entropy* **2017**, *19*, 446. [CrossRef]
117. Moldrik, P.; Sebesta, R. Hydrogen Fuel Cells as a Part of the System for Accumulation of Electric Energy. In Proceedings of the 2009 10th International Conference on Electrical Power Quality and Utilisation, Lodz, Poland, 15–17 September2009; pp. 1–6.
118. Ubic, R. Covalent, Metallic, and Secondary Bonding. In *Crystallography and Crystal Chemistry*; Ubic, R., Ed.; Springer International Publishing: Cham, Switzerland, 2024; pp. 257–303, ISBN 978-3-031-49752-0.
119. Soejima, M.; Tanaka, N.; Oshima, T.; Kinoshita, H.; Koda, Y. Detection of Helium in a Fire Victim: A Case Report. *Forensic Sci. Int.* **2021**, *318*, 110613. [CrossRef]
120. Li, Y.; Zhang, W.; Wang, L.; Zhao, F.; Han, W.; Chen, G. Henry's Law and Accumulation of Weak Source for Crust-Derived Helium: A Case Study of Weihe Basin, China. *J. Nat. Gas Geosci.* **2017**, *2*, 333–339. [CrossRef]
121. Qin, S.; Dou, L.; Tao, G.; Li, J.; Qi, W.; Li, X.; Guo, B.; Zhao, Z.; Wang, J. Helium Enrichment Theory and Exploration Ideas for Helium-Rich Gas Reservoirs. *Pet. Explor. Dev.* **2024**, *51*, 1340–1356. [CrossRef]
122. Lu, C.; Wang, B.; Zhu, D.; Liu, Q.; Zhang, X.; He, H. High-Spatial-Resolution Helium Detection and Its Implications for Helium Accumulation Mechanisms. *Appl. Sci.* **2024**, *14*, 3453. [CrossRef]
123. NCBI, [National Center for Biotechnology Information] PubChem | Melting Point (Periodic Table of Elements). Available online: https://pubchem.ncbi.nlm.nih.gov/periodic-table/melting-point (accessed on 6 May 2025).
124. Usas, S.A.; Ricardez-Sandoval, L. An Optimal Sustainable Planning Strategy for National Carbon Capture Deployment: A Review on the State of CO 2 Capture in Canada. *Can. J. Chem. Eng.* **2024**, *102*, 2332–2351. [CrossRef]
125. Marzouk, O.A. Subcritical and Supercritical Rankine Steam Cycles, under Elevated Temperatures up to 900 °C and Absolute Pressures up to 400 Bara. *Adv. Mech. Eng.* **2024**, *16*, 16878132231221065. [CrossRef]
126. Nijsse, F.J.M.M.; Mercure, J.-F.; Ameli, N.; Larosa, F.; Kothari, S.; Rickman, J.; Vercoulen, P.; Pollitt, H. The Momentum of the Solar Energy Transition. *Nat. Commun.* **2023**, *14*, 6542. [CrossRef]
127. Marzouk, O.A. Land-Use Competitiveness of Photovoltaic and Concentrated Solar Power Technologies near the Tropic of Cancer. *Sol. Energy* **2022**, *243*, 103–119. [CrossRef]
128. Magar, V.; Peña, A.; Hahmann, A.N.; Pacheco-Rojas, D.A.; García-Hernández, L.S.; Gross, M.S. Wind Energy and the Energy Transition: Challenges and Opportunities for Mexico. *Sustainability* **2023**, *15*, 5496. [CrossRef]
129. Marzouk, O.A. Wind Speed Weibull Model Identification in Oman, and Computed Normalized Annual Energy Production (NAEP) From Wind Turbines Based on Data From Weather Stations. *Eng. Rep.* **2025**, *7*, e70089. [CrossRef]
130. Priya, S.; Inman, D.J. (Eds.) *Energy Harvesting Technologies*; Springer: Boston, MA, USA, 2009; ISBN 978-0-387-76463-4.
131. Marzouk, O.A. Thermoelectric Generators versus Photovoltaic Solar Panels: Power and Cost Analysis. *Edelweiss Appl. Sci. Technol.* **2024**, *8*, 406–428. [CrossRef]
132. Marzouk, O.A. Tilt Sensitivity for a Scalable One-Hectare Photovoltaic Power Plant Composed of Parallel Racks in Muscat. *Cogent Eng.* **2022**, *9*, 2029243. [CrossRef]
133. Shang, Y.; Sang, S.; Tiwari, A.K.; Khan, S.; Zhao, X. Impacts of Renewable Energy on Climate Risk: A Global Perspective for Energy Transition in a Climate Adaptation Framework. *Appl. Energy* **2024**, *362*, 122994. [CrossRef]
134. Marzouk, O.A. Energy Generation Intensity (EGI) of Solar Updraft Tower (SUT) Power Plants Relative to CSP Plants and PV Power Plants Using the New Energy Simulator "Aladdin". *Energies* **2024**, *17*, 405. [CrossRef]
135. Chipangamate, N.S.; Nwaila, G.T. Assessment of Challenges and Strategies for Driving Energy Transitions in Emerging Markets: A Socio-Technological Systems Perspective. *Energy Geosci.* **2024**, *5*, 100257. [CrossRef]
136. Murmura, M.A.; Cerbelli, S.; Annesini, M.C. Transport-Reaction-Permeation Regimes in Catalytic Membrane Reactors for Hydrogen Production. The Steam Reforming of Methane as a Case Study. *Chem. Eng. Sci.* **2017**, *162*, 88–103. [CrossRef]
137. Oh, D.-K.; Lee, K.-Y.; Park, J.-S. Hydrogen Purification from Compact Palladium Membrane Module Using a Low Temperature Diffusion Bonding Technology. *Membranes* **2020**, *10*, 338. [CrossRef] [PubMed]
138. Lucia, D.J.; Beran, P.S.; Silva, W.A. Reduced-Order Modeling: New Approaches for Computational Physics. *Prog. Aerosp. Sci.* **2004**, *40*, 51–117. [CrossRef]
139. Marzouk, O.A. A Nonlinear ODE System for the Unsteady Hydrodynamic Force—A New Approach. *World Acad. Sci. Eng. Technol.* **2009**, *39*, 948–962. [CrossRef]

140. Masoumi-Verki, S.; Haghighat, F.; Eicker, U. A Review of Advances towards Efficient Reduced-Order Models (ROM) for Predicting Urban Airflow and Pollutant Dispersion. *Build. Environ.* **2022**, *216*, 108966. [CrossRef]
141. Marzouk, O.; Nayfeh, A. Differential/Algebraic Wake Model Based on the Total Fluid Force and Its Direction, and the Effect of Oblique Immersed-Body Motion on 'Type-1' and 'Type-2' Lock-In. In Proceedings of the 47th AIAA Aerospace Sciences Meeting including The New Horizons Forum and Aerospace Exposition, AIAA [American Institute of Aeronautics and Astronautics]. Orlando, FL, USA, 5–8 January 2009; p. AIAA 2009-1112. [CrossRef]
142. Keiper, W.; Milde, A.; Volkwein, S. (Eds.) *Reduced-Order Modeling (ROM) for Simulation and Optimization*; Springer International Publishing: Cham, Switzerland, 2018; ISBN 978-3-319-75318-8.
143. Han, G.; Li, G.; Sun, Y. Electrocatalytic Hydrogenation Using Palladium Membrane Reactors. *JACS Au* **2024**, *4*, 328–343. [CrossRef]
144. Marzouk, O.A.; Nayfeh, A.H. Loads on a Harmonically Oscillating Cylinder. In Proceedings of the ASME 2007 International Design Engineering Technical Conferences and Computers and Information in Engineering Conference (IDETC-CIE 2007), ASME [American Society of Mechanical Engineers]. Las Vegas, NV, USA, 20 May 2009; pp. 1755–1774. [CrossRef]
145. Khosravi, M.; Jafari, M.; Ghasemzadeh, K.; Iulianelli, A. Enhancing Styrene Production: CFD Analysis of a Pd-Based Membrane Reactor to Carry out Ethylbenzene Dehydrogenation. *Fuel Process. Technol.* **2025**, *270*, 108191. [CrossRef]
146. Marzouk, O.A.; Nayfeh, A.H. Reduction of the Loads on a Cylinder Undergoing Harmonic In-Line Motion. *Phys. Fluids* **2009**, *21*, 083103. [CrossRef]
147. Ghasemzadeh, K.; Ghahremani, M.; Yousefi Amiri, T.; Basile, A.; Iulianelli, A. Hydrogen Production by Silica Membrane Reactor during Dehydrogenation of Methylcyclohexane: CFD Analysis. *Int. J. Hydrogen Energy* **2021**, *46*, 19768–19777. [CrossRef]
148. Yang, W.-W.; Tang, X.-Y.; Ma, X.; Cao, X.E.; He, Y.-L. Synergistic Intensification of Palladium-Based Membrane Reactors for Hydrogen Production: A Review. *Energy Convers. Manag.* **2025**, *325*, 119424. [CrossRef]
149. Chompupun, T.; Limtrakul, S.; Vatanatham, T.; Kanhari, C.; Ramachandran, P.A. Experiments, Modeling and Scaling-up of Membrane Reactors for Hydrogen Production via Steam Methane Reforming. *Chem. Eng. Process.—Process Intensif.* **2018**, *134*, 124–140. [CrossRef]
150. Berstad, D.; Nekså, P.; Gjøvåg, G.A. Low-Temperature Syngas Separation and CO_2 Capture for Enhanced Efficiency of IGCC Power Plants. *Energy Procedia* **2011**, *4*, 1260–1267. [CrossRef]
151. Brdar, R.D.; Jones, R.M. *GE IGCC Technology and Experience with Advanced Gas Turbines*; General Electric (GE) Power Systems: Schenectady, NY, USA, 2021.
152. Krishnan, G.; Steele, D.; O'Brien, K.; Callahan, R.; Berchtold, K.; Figueroa, J. Simulation of a Process to Capture CO_2 From IGCC Syngas Using a High Temperature PBI Membrane. *Energy Procedia* **2009**, *1*, 4079–4088. [CrossRef]
153. Gazzani, M.; Macchi, E.; Manzolini, G. CO_2 Capture in Integrated Gasification Combined Cycle with SEWGS—Part A: Thermodynamic Performances. *Fuel* **2013**, *105*, 206–219. [CrossRef]
154. Jin, H.; Xu, Y.; Lin, R.; Han, W. A Proposal for a Novel Multi-Functional Energy System for the Production of Hydrogen and Power. *Int. J. Hydrogen Energy* **2008**, *33*, 9–19. [CrossRef]
155. Park, S.H.; Chung, S.W.; Lee, S.K.; Choi, H.K.; Lee, S.H. Thermo-Economic Evaluation of 300 MW Class Integrated Gasification Combined Cycle with Ash Free Coal (AFC) Process. *Appl. Therm. Eng.* **2015**, *89*, 843–852. [CrossRef]
156. Zhang, Z.; Zhu, L.; Yu, J.; Liu, H.; Hao, Q.; Huang, Y. Feasibility and Performance Analysis of a Dual-Regulation System in the Process of Methanol and Electricity Coproduction by Coal Gasification. *Energy Technol.* **2024**, *12*, 2300718. [CrossRef]
157. Boruah, A.; Phukan, A.; Singh, S. Utilization of Coal for Hydrogen Generation. *Int. J. Coal Prep. Util.* **2024**, 1–22. [CrossRef]
158. Zhao, L.; Etezadi, R.; Tsotsis, T. Chapter 15—Syngas from Coal. In *Advances in Synthesis Gas : Methods, Technologies and Applications*; Rahimpour, M.R., Makarem, M.A., Meshksar, M., Eds.; Elsevier: Amsterdam, The Netherlands, 2023; Volume 1, pp. 363–377, ISBN 978-0-323-91871-8.
159. Vairakannu, P. Clean Coal Technologies. In *Sustainable Utilization of Natural Resources*; CRC Press: Boca Raton, FL, USA, 2017; ISBN 978-1-315-15329-2.
160. Gräbner, M.; von Morstein, O.; Rappold, D.; Günster, W.; Beysel, G.; Meyer, B. Constructability Study on a German Reference IGCC Power Plant with and without CO_2-Capture for Hard Coal and Lignite. *Energy Convers. Manag.* **2010**, *51*, 2179–2187. [CrossRef]
161. Aineto, M.; Acosta, A.; Rincón, J.M.; Romero, M. Thermal Expansion of Slag and Fly Ash from Coal Gasification in IGCC Power Plant. *Fuel* **2006**, *85*, 2352–2358. [CrossRef]
162. Melchior, T.; Madlener, R. Economic Evaluation of IGCC Plants with Hot Gas Cleaning. *Appl. Energy* **2012**, *97*, 170–184. [CrossRef]
163. Siefert, N.S.; Narburgh, S.; Chen, Y. Comprehensive Exergy Analysis of Three IGCC Power Plant Configurations with CO_2 Capture. *Energies* **2016**, *9*, 669. [CrossRef]
164. Pérez-Fortes, M.; Bojarski, A.D.; Velo, E.; Nougués, J.M.; Puigjaner, L. Conceptual Model and Evaluation of Generated Power and Emissions in an IGCC Plant. *Energy* **2009**, *34*, 1721–1732. [CrossRef]
165. Valero, A.; Usón, S. Oxy-Co-Gasification of Coal and Biomass in an Integrated Gasification Combined Cycle (IGCC) Power Plant. *Energy* **2006**, *31*, 1643–1655. [CrossRef]

166. Casella, F.; Colonna, P. Dynamic Modeling of IGCC Power Plants. *Appl. Therm. Eng.* **2012**, *35*, 91–111. [CrossRef]
167. Merkel, T.C.; Zhou, M.; Baker, R.W. Carbon Dioxide Capture with Membranes at an IGCC Power Plant. *J. Membr. Sci.* **2012**, *389*, 441–450. [CrossRef]
168. Oh, H.-T.; Lee, W.-S.; Ju, Y.; Lee, C.-H. Performance Evaluation and Carbon Assessment of IGCC Power Plant with Coal Quality. *Energy* **2019**, *188*, 116063. [CrossRef]
169. Wang, T. An Overview of IGCC Systems. In *Integrated Gasification Combined Cycle (IGCC) Technologies*; Elsevier: Amsterdam, The Netherlands, 2017; pp. 1–80, ISBN 978-0-08-100167-7.
170. Wolfersdorf, C.; Meyer, B. 25—The Current Status and Future Prospects for IGCC Systems. In *Integrated Gasification Combined Cycle (IGCC) Technologies*; Wang, T., Stiegel, G., Eds.; Woodhead Publishing: Sawston, UK, 2017; pp. 847–889, ISBN 978-0-08-100167-7.
171. Siefert, N.S.; Litster, S. Exergy and Economic Analyses of Advanced IGCC–CCS and IGFC–CCS Power Plants. *Appl. Energy* **2013**, *107*, 315–328. [CrossRef]
172. Descamps, C.; Bouallou, C.; Kanniche, M. Efficiency of an Integrated Gasification Combined Cycle (IGCC) Power Plant Including CO_2 Removal. *Energy* **2008**, *33*, 874–881. [CrossRef]
173. Ståhl, K.; Neergaard, M. IGCC Power Plant for Biomass Utilisation, Värnamo, Sweden. *Biomass Bioenergy* **1998**, *15*, 205–211. [CrossRef]
174. Hossein Sahraei, M.; McCalden, D.; Hughes, R.; Ricardez-Sandoval, L.A. A Survey on Current Advanced IGCC Power Plant Technologies, Sensors and Control Systems. *Fuel* **2014**, *137*, 245–259. [CrossRef]
175. Sofia, D.; Coca Llano, P.; Giuliano, A.; Iborra Hernández, M.; García Peña, F.; Barletta, D. Co-Gasification of Coal–Petcoke and Biomass in the Puertollano IGCC Power Plant. *Chem. Eng. Res. Des.* **2014**, *92*, 1428–1440. [CrossRef]
176. Buttler, A.; Kunze, C.; Spliethoff, H. IGCC–EPI: Decentralized Concept of a Highly Load-Flexible IGCC Power Plant for Excess Power Integration. *Appl. Energy* **2013**, *104*, 869–879. [CrossRef]
177. Omell, B.P.; Chmielewski, D.J. IGCC Power Plant Dispatch Using Infinite-Horizon Economic Model Predictive Control. *Ind. Eng. Chem. Res.* **2013**, *52*, 3151–3164. [CrossRef]
178. Pruschek, R.; Oeljeklaus, G.; Kloster, R. *Enhancement of the Efficiency of Coal-Fired Power Generation Systems: Final Report*; Institute for Process Engineering and Power Plant Technology, University of Stuttgart: Stuttgart, Germany, 1998.
179. Marzouk, O.A. Condenser Pressure Influence on Ideal Steam Rankine Power Vapor Cycle Using the Python Extension Package Cantera for Thermodynamics. *Eng. Technol. Appl. Sci. Res.* **2024**, *14*, 14069–14078. [CrossRef]
180. Mitsubishi Power. *IGCC Integrated Coal Gasification Combined Cycle Power Plants*; Mitsubishi Power, a brand of Mitsubishi Heavy Industries, Ltd.: Kanagawa, Japan, 2021.
181. Marzouk, O.A. Chronologically-Ordered Quantitative Global Targets for the Energy-Emissions-Climate Nexus, from 2021 to 2050. In Proceedings of the 2022 International Conference on Environmental Science and Green Energy (ICESGE), Shenyang, China, 25–27 December 2022; pp. 1–6. [CrossRef]
182. Zhao, Y.; Ying, D.; Liu, Y.; Wentao, R. Relative Stability Analysis Method of Systems Based on Goal Seek. In Proceedings of the 2021 3rd International Conference on Industrial Artificial Intelligence (IAI), Shenyang, China, 8–11 November 2021; pp. 1–5.
183. Guerrero, H. Solver, Scenarios, and Goal Seek Tools. In *Excel Data Analysis: Modeling and Simulation*; Guerrero, H., Ed.; Springer International Publishing: Cham, Switzerland, 2019; pp. 311–346, ISBN 978-3-030-01279-3.
184. Tian, Y.; Qin, C.; Yang, Z.; Hao, D. Numerical Simulation Study on the Leakage and Diffusion Characteristics of High-Pressure Hydrogen Gas in Different Spatial Scenes. *Int. J. Hydrogen Energy* **2024**, *50*, 1335–1349. [CrossRef]
185. Marzouk, O.A. Contrasting the Cartesian and Polar Forms of the Shedding-Induced Force Vector in Response to 12 Subharmonic and Superharmonic Mechanical Excitations. *Fluid Dyn. Res.* **2010**, *42*, 035507. [CrossRef]
186. Ghasemzadeh, K.; Torabi, T.; Yousefi Amiri, T.; Fortunelli, A.; Iulianelli, A. Parametric and Sensitive Analysis of Pd-Ag Membrane Reactor Performance in Biogas Reforming to Generate Decarbonized Hydrogen by Computational Fluid Dynamic-Response Surface Methodology. *Fuel* **2024**, *365*, 131205. [CrossRef]
187. Marzouk, O.A. Characteristics of the Flow-Induced Vibration and Forces With 1- and 2-DOF Vibrations and Limiting Solid-to-Fluid Density Ratios. *J. Vib. Acoust.* **2010**, *132*, 041013. [CrossRef]
188. Kassi, A.H.; Al-Hattab, T.A. A CFD Model of Natural Gas Steam Reforming in a Catalytic Membrane Reactor: Effect of Various Operating Parameters on the Performance of CMR. *Int. J. Hydrogen Energy* **2024**, *56*, 780–796. [CrossRef]
189. Marzouk, O.A.; Nayfeh, A.H. Characterization of the Flow over a Cylinder Moving Harmonically in the Cross-Flow Direction. *Int. J. Non-Linear Mech.* **2010**, *45*, 821–833. [CrossRef]
190. Zakeri, R.; Fazeli, A. CFD Modeling of Hydrogen Production from Glycerol Steam Reforming in Tesla Microchannel Reactor. *Fuel* **2024**, *357*, 129646. [CrossRef]
191. Li, X.; Zhao, Y.; Liu, Z.; Chen, H. A New Methodology for Preliminary Design of Centrifugal Impellers with Prewhirl. *Proc. Inst. Mech. Eng. Part A J. Power Energy* **2020**, *234*, 251–262. [CrossRef]

192. Marzouk, O.A. Evolutionary Computing Applied to Design Optimization. In Proceedings of the Volume 2: 27th Computers and Information in Engineering Conference, Parts A and B, Las Vegas, NV, USA, 4–7 September 2007; ASMEDC: Las Vegas, NV, USA, 2007; pp. 995–1003. [CrossRef]
193. Zhang, Z. Understanding and Exploiting the Nonlinear Behavior of Tuned Liquid Dampers (TLDs) for Structural Vibration Control by Means of a Nonlinear Reduced-Order Model (ROM). *Eng. Struct.* **2022**, *251*, 113524. [CrossRef]
194. Marzouk, O.A. Flow Control Using Bifrequency Motion. *Theor. Comput. Fluid Dyn.* **2011**, *25*, 381–405. [CrossRef]
195. Marzouk, O.A. A Two-Step Computational Aeroacoustics Method Applied to High-Speed Flows. *Noise Control Eng. J.* **2008**, *56*, 396. [CrossRef]
196. San, J.Y.; Worek, W.M.; Lavan, Z. Entropy Generation in Convective Heat Transfer and Isothermal Convective Mass Transfer. *J. Heat Transf.* **1987**, *109*, 647–652. [CrossRef]
197. DOE, [United States Department of Energy]. *Department of Energy Fundamentals Training Handbook, Thermodynamics, Heat Transfer, and Fluid Flow, Volume 2 of 3*; United States Department of Energy (DOE): Washington, DC, USA, 1992.
198. Enerquip What's the Difference between Parallel Flow, Counter Flow and Crossflow Heat Exchangers? Available online: https://www.enerquip.com/whats-the-difference-between-parallel-flow-counter-flow-and-crossflow-heat-exchangers (accessed on 7 May 2022).
199. Thermex Why Counter Flow Heat Exchangers Are More Efficient. Available online: http://www.thermex.co.uk/news/blog/605-why-counter-flow-heat-exchangers-are-more-efficient (accessed on 7 May 2022).
200. Pinacci, P.; Drago, F. Influence of the Support on Permeation of Palladium Composite Membranes in Presence of Sweep Gas. *Catal. Today* **2012**, *193*, 186–193. [CrossRef]
201. Skoulidas, A.I.; Sholl, D.S. Multiscale Models of Sweep Gas and Porous Support Effects on Zeolite Membranes. *AIChE J.* **2005**, *51*, 867–877. [CrossRef]
202. Akamatsu, K.; Ohta, Y.; Sugawara, T.; Kanno, N.; Tonokura, K.; Hattori, T.; Nakao, S. Stable High-Purity Hydrogen Production by Dehydrogenation of Cyclohexane Using a Membrane Reactor with Neither Carrier Gas nor Sweep Gas. *J. Membr. Sci.* **2009**, *330*, 1–4. [CrossRef]
203. Moussaddy, S.; Maisonneuve, J. Energy from Carbon Dioxide: Experimental and Theoretical Analysis of Power Generation from Membrane-Based Sweep Gas Permeation. *J. Membr. Sci.* **2022**, *644*, 120053. [CrossRef]
204. Li, Z.; Zhang, P.; Guan, K.; Gonzales, R.R.; Ishigami, T.; Xue, M.; Yoshioka, T.; Matsuyama, H. An Experimental Study on Recovering and Concentrating Ammonia by Sweep Gas Membrane Distillation. *Process Saf. Environ. Prot.* **2023**, *171*, 555–560. [CrossRef]
205. Gobina, E.; Hou, K.; Hughes, R. Ethane Dehydrogenation in a Catalytic Membrane Reactor Coupled with a Reactive Sweep Gas. *Chem. Eng. Sci.* **1995**, *50*, 2311–2319. [CrossRef]
206. Xie, Z.; Duong, T.; Hoang, M.; Nguyen, C.; Bolto, B. Ammonia Removal by Sweep Gas Membrane Distillation. *Water Res.* **2009**, *43*, 1693–1699. [CrossRef] [PubMed]
207. Yoon, H.; Lee, J.; Lee, G.; Shin, W.; Min, T. Membrane Degassing with the Combination of Sweep Gas and Vacuum Pressure for Ammonia Removal. *Environ. Sci. Water Res. Technol.* **2023**, *9*, 467–473. [CrossRef]
208. Shukla, S.; Benes, N.E.; Vankelecom, I.; Méricq, J.P.; Belleville, M.P.; Hengl, N.; Marcano, J.S. Sweep Gas Membrane Distillation in a Membrane Contactor with Metallic Hollow-Fibers. *J. Membr. Sci.* **2015**, *493*, 167–178. [CrossRef]
209. Nordio, M.; Soresi, S.; Manzolini, G.; Melendez, J.; Van Sint Annaland, M.; Pacheco Tanaka, D.A.; Gallucci, F. Effect of Sweep Gas on Hydrogen Permeation of Supported Pd Membranes: Experimental and Modeling. *Int. J. Hydrogen Energy* **2019**, *44*, 4228–4239. [CrossRef]
210. Lee, C.H.; Hong, W.H. Effect of Operating Variables on the Flux and Selectivity in Sweep Gas Membrane Distillation for Dilute Aqueous Isopropanol. *J. Membr. Sci.* **2001**, *188*, 79–86. [CrossRef]
211. Franz, J.; Schiebahn, S.; Zhao, L.; Riensche, E.; Scherer, V.; Stolten, D. Investigating the Influence of Sweep Gas on CO_2/N_2 Membranes for Post-Combustion Capture. *Int. J. Greenh. Gas Control* **2013**, *13*, 180–190. [CrossRef]
212. Jiménez-Robles, R.; Gabaldón, C.; Martínez-Soria, V.; Izquierdo, M. Simultaneous Application of Vacuum and Sweep Gas in a Polypropylene Membrane Contactor for the Recovery of Dissolved Methane from Water. *J. Membr. Sci.* **2021**, *617*, 118560. [CrossRef]
213. Ben-Mansour, R.; Haque, M.A.; Habib, M.A.; Paglieri, S.; Harale, A.; Mokheimer, E.M.A. Effect of Temperature and Heat Flux Boundary Conditions on Hydrogen Production in Membrane-Integrated Steam-Methane Reformer. *Appl. Energy* **2023**, *346*, 121407. [CrossRef]
214. Barbieri, G. Sweep Gas in a Membrane Reactor. In *Encyclopedia of Membranes*; Drioli, E., Giorno, L., Eds.; Springer: Berlin/Heidelberg, Germany, 2015; pp. 1–2, ISBN 978-3-642-40872-4.
215. Li, Z.; Polfus, J.M.; Xing, W.; Denonville, C.; Fontaine, M.-L.; Bredesen, R. Factors Limiting the Apparent Hydrogen Flux in Asymmetric Tubular Cercer Membranes Based on $LaCO_{27}WCO_{3.5}MoCO_{1.5}O_{55.5-\delta}$ and $La_{0.87}Sr_{0.13}CrO_{3-\delta}$. *Membranes* **2019**, *9*, 126. [CrossRef]

216. Xie, D.; Yu, J.; Wang, F.; Zhang, N.; Wang, W.; Yu, H.; Peng, F.; Park, A.-H.A. Hydrogen Permeability of Pd–Ag Membrane Modules with Porous Stainless Steel Substrates. *Int. J. Hydrogen Energy* **2011**, *36*, 1014–1026. [CrossRef]
217. Chein, R.Y.; Chen, Y.C.; Chung, J.N. Sweep Gas Flow Effect on Membrane Reactor Performance for Hydrogen Production from High-Temperature Water-Gas Shift Reaction. *J. Membr. Sci.* **2015**, *475*, 193–203. [CrossRef]
218. Balachandran, U.; Dorris, S.E.; Emerson, J.E.; Lee, T.H.; Lu, Y.; Park, C.Y.; Picciolo, J.J. *Hydrogen Separation Membranes*; Argonne National Laboratory (ANL) of the United States Department of Energy: Lemont, IL, USA, 2011.
219. Bidica, N.; Ghimis, N.; Monea, B. Experimental Results of Deuterium/Hydrogen Co-Current Permeation through Nickel Membrane, in Non-Steady-State Surface Limited Regime. *Fusion Eng. Des.* **2023**, *194*, 113718. [CrossRef]
220. Escolástico, S.; Ivanova, M.; Solís, C.; Roitsch, S.; Meulenberg, W.A.; Serra, J.M. Improvement of Transport Properties and Hydrogen Permeation of Chemically-Stable Proton-Conducting Oxides Based on the System $BaZr_{1-x-y}Y_xM_yO_{3-\delta}$. *RSC Adv.* **2012**, *2*, 4932. [CrossRef]
221. Longhurst, G.R.; Kratville, A. A Simple System for Measuring Permeation of Hydrogen Through Stainless Steel. *Fusion Sci. Technol.* **2014**, *66*, 385–393. [CrossRef]
222. Chen, W.-H.; Lin, C.-H.; Lin, Y.-L.; Tsai, C.-W.; Chein, R.-Y.; Yu, C.-T. Interfacial Permeation Phenomena of Hydrogen Purification and Carbon Dioxide Separation in a Non-Isothermal Palladium Membrane Tube. *Chem. Eng. J.* **2016**, *305*, 156–168. [CrossRef]
223. Chiesa, P.; Romano, M.C.; Kreutz, T.G. Use of Membranes in Systems for Electric Energy and Hydrogen Production from Fossil Fuels. In *Handbook of Membrane Reactors*; Elsevier: Amsterdam, The Netherlands, 2013; pp. 416–455, ISBN 978-0-85709-415-5.
224. Marín, P.; Patiño, Y.; Díez, F.V.; Ordóñez, S. Modelling of Hydrogen Perm-Selective Membrane Reactors for Catalytic Methane Steam Reforming. *Int. J. Hydrogen Energy* **2012**, *37*, 18433–18445. [CrossRef]
225. Park, Y.; Cha, J.; Oh, H.-T.; Lee, T.; Lee, S.H.; Park, M.G.; Jeong, H.; Kim, Y.; Sohn, H.; Nam, S.W.; et al. A Catalytic Composite Membrane Reactor System for Hydrogen Production from Ammonia Using Steam as a Sweep Gas. *J. Membr. Sci.* **2020**, *614*, 118483. [CrossRef]
226. Brunetti, A.; Caravella, A.; Drioli, E.; Barbieri, G. CHAPTER 1. Membrane Reactors for Hydrogen Production. In *Membrane Engineering for the Treatment of Gases: Volume 2: Gas-Separation Issues Combined with Membrane Reactors*; The Royal Society of Chemistry: London, UK, 2017; pp. 1–29.
227. Li, X.; Li, A.; Lim, C.J.; Grace, J.R. Hydrogen Permeation through Pd-Based Composite Membranes: Effects of Porous Substrate, Diffusion Barrier and Sweep Gas. *J. Membr. Sci.* **2016**, *499*, 143–155. [CrossRef]
228. Meng, X.; Shang, Y.; Meng, B.; Yang, N.; Tan, X.; Sunarso, J.; Liu, S. Bi-Functional Performances of $BaCe_{0.95}Tb_{0.05}O_{3-\delta}$-Based Hollow Fiber Membranes for Power Generation and Hydrogen Permeation. *J. Eur. Ceram. Soc.* **2016**, *36*, 4123–4129. [CrossRef]
229. Roberts, R.M.; Elleman, T.S.; Iii, H.P.; Verghese, K. Hydrogen Permeability of Sintered Aluminum Oxide. *J. Am. Ceram. Soc.* **1979**, *62*, 495–499. [CrossRef]
230. Escolástico, S.; Solís, C.; Kjølseth, C.; Serra, J.M. Outstanding Hydrogen Permeation through CO_2 -Stable Dual-Phase Ceramic Membranes. *Energy Environ. Sci.* **2014**, *7*, 3736–3746. [CrossRef]
231. Qi, X. Electrical Conduction and Hydrogen Permeation through Mixed Proton–Electron Conducting Strontium Cerate Membranes. *Solid State Ion.* **2000**, *130*, 149–156. [CrossRef]
232. Sakbodin, M.; Schulman, E.; Oh, S.C.; Pan, Y.; Wachsman, E.D.; Liu, D. Dual Utilization of Greenhouse Gases to Produce C_{2+} Hydrocarbons and Syngas in a Hydrogen-Permeable Membrane Reactor. *J. Membr. Sci.* **2020**, *595*, 117557. [CrossRef]
233. Smith, J.B.; Aasen, K.I.; Wilhelmsen, K.; Käka, D.; Risdal, T.; Berglund, A.; Stenersen Østby, A.; Budd, M.; Bruun, T.; Werswick, B. Recent Development in the HMR Pre-Combustion Gas Power Cycle. *Energy Procedia* **2009**, *1*, 343–351. [CrossRef]
234. Tan, X.; Tan, X.; Yang, N.; Meng, B.; Zhang, K.; Liu, S. High Performance $BaCe_{0.8}Y_{0.2}O_{3-a}$ (BCY) hollow fibre membranes for hydrogen permeation. *Ceram. Int.* **2014**, *40*, 3131–3138. [CrossRef]
235. Unruh, D.; Pabst, K.; Schaub, G. Fischer−Tropsch Synfuels from Biomass: Maximizing Carbon Efficiency and Hydrocarbon Yield. *Energy Fuels* **2010**, *24*, 2634–2641. [CrossRef]
236. GTI, [Gas Technology Institute]. *Direct Hydrogen Production from Biomass Gasifier Using Hydrogen-Selective Membrane*; Gas Technology Institute (GTI), In Collaboration with Natural Resources Research Institute University of Minnesota at Duluth: Des Plaines, IL, USA, 2007.
237. Kinouchi, K.; Katoh, M.; Horikawa, T.; Yoshikawa, T.; Wada, M. Hydrogen permeability of palladium membrane for steam-reforming of bio-ethanol using the membrane reactor. *Int. J. Mod. Phys. Conf. Ser.* **2012**, *6*, 7–12. [CrossRef]
238. Barnoon, P. Modeling of a High Temperature Heat Exchanger to Supply Hydrogen Required by Fuel Cells through Reforming Process. *Energy Rep.* **2021**, *7*, 5685–5699. [CrossRef]
239. Barnoon, P.; Toghraie, D.; Mehmandoust, B.; Fazilati, M.A.; Eftekhari, S.A. Comprehensive Study on Hydrogen Production via Propane Steam Reforming inside a Reactor. *Energy Rep.* **2021**, *7*, 929–941. [CrossRef]
240. Fornarelli, F.; Dambrosio, L.; Terlizzi, L.; Camporeale, S.M. Performance and Cost Multi Objective Optimisation of a Shell-and-Tube LHTES Device for Mid-Temperature Applications. *J. Energy Storage* **2024**, *99*, 113134. [CrossRef]

241. Kirincic, M.; Trp, A.; Lenic, K.; Torbarina, F. Numerical Analysis of the Influence of Geometry Parameters on Charging and Discharging Performance of Shell-and-Tube Latent Thermal Energy Storage with Longitudinal Fins. *Appl. Therm. Eng.* **2024**, *236*, 121385. [CrossRef]
242. Li, C.; Li, Q.; Ge, R. Comparison of Performance Enhancement in a Shell and Tube Based Latent Heat Thermal Energy Storage Device Containing Different Structured Fins. *Renew. Energy* **2023**, *206*, 994–1006. [CrossRef]
243. Marzouk, O.A. Direct Numerical Simulations of the Flow Past a Cylinder Moving With Sinusoidal and Nonsinusoidal Profiles. *J. Fluids Eng.* **2009**, *131*, 121201. [CrossRef]
244. Daneshparvar, M.R.; Beigzadeh, R. Multi-Objective Optimization of Helical Baffles in the Shell-and-Tube Heat Exchanger by Computational Fluid Dynamics and Genetic Algorithm. *Energy Rep.* **2022**, *8*, 11064–11077. [CrossRef]
245. Marzouk, O.A. One-Way and Two-Way Couplings of CFD and Structural Models and Application to the Wake-Body Interaction. *Appl. Math. Model.* **2011**, *35*, 1036–1053. [CrossRef]
246. Marzouk, O.A.; Huckaby, E.D. Simulation of a Swirling Gas-Particle Flow Using Different k-Epsilon Models and Particle-Parcel Relationships. *Eng. Lett.* **2010**, *18*, 1.
247. Saldanha, W.H.; Arrieta, F.R.P.; Soares, G.L. State-of-the-Art of Research on Optimization of Shell and Tube Heat Exchangers by Methods of Evolutionary Computation. *Arch Comput. Methods Eng* **2021**, *28*, 2761–2783. [CrossRef]
248. Marzouk, O.A.; Huckaby, E.D. Modeling Confined Jets with Particles and Swril. In *Machine Learning and Systems Engineering*; Ao, S.-I., Rieger, B., Amouzegar, M.A., Eds.; Lecture Notes in Electrical Engineering; Springer: Dordrecht, The Netherlands, 2010; Volume 68, pp. 243–256, ISBN 978-90-481-9418-6. [CrossRef]
249. Li, P.; Chen, L.; Xia, S.; Zhang, L. Entropy Generation Rate Minimization for Methanol Synthesis via a CO_2 Hydrogenation Reactor. *Entropy* **2019**, *21*, 174. [CrossRef] [PubMed]
250. Li, P.; Chen, L.; Xia, S.; Kong, R.; Ge, Y. Multi-Objective Optimal Configurations of a Membrane Reactor for Steam Methane Reforming. *Energy Rep.* **2022**, *8*, 527–538. [CrossRef]
251. Bichkar, P.; Dandgaval, O.; Dalvi, P.; Godase, R.; Dey, T. Study of Shell and Tube Heat Exchanger with the Effect of Types of Baffles. *Procedia Manuf.* **2018**, *20*, 195–200. [CrossRef]
252. Pal, E.; Kumar, I.; Joshi, J.B.; Maheshwari, N.K. CFD Simulations of Shell-Side Flow in a Shell-and-Tube Type Heat Exchanger with and without Baffles. *Chem. Eng. Sci.* **2016**, *143*, 314–340. [CrossRef]
253. Salahuddin, U.; Bilal, M.; Ejaz, H. A Review of the Advancements Made in Helical Baffles Used in Shell and Tube Heat Exchangers. *Int. Commun. Heat Mass Transf.* **2015**, *67*, 104–108. [CrossRef]
254. Jamsran, N.; Park, H.; Lee, J.; Oh, S.; Kim, C.; Lee, Y.; Kang, K. Influence of Syngas Composition on Combustion and Emissions in a Homogeneous Charge Compression Ignition Engine. *Fuel* **2021**, *306*, 121774. [CrossRef]
255. Kousheshi, N.; Yari, M.; Paykani, A.; Saberi Mehr, A.; de la Fuente, G.F. Effect of Syngas Composition on the Combustion and Emissions Characteristics of a Syngas/Diesel RCCI Engine. *Energies* **2020**, *13*, 212. [CrossRef]
256. Ribeiro, A.M.; Santos, J.C.; Rodrigues, A.E. PSA Design for Stoichiometric Adjustment of Bio-Syngas for Methanol Production and Co-Capture of Carbon Dioxide. *Chem. Eng. J.* **2010**, *163*, 355–363. [CrossRef]
257. Giuliano, A.; Freda, C.; Catizzone, E. Techno-Economic Assessment of Bio-Syngas Production for Methanol Synthesis: A Focus on the Water–Gas Shift and Carbon Capture Sections. *Bioengineering* **2020**, *7*, 70. [CrossRef]
258. NIST, [United States National Institute of Standards and Technology]. NIST Chemistry WebBook—Hydrogen. Available online: https://webbook.nist.gov/cgi/cbook.cgi?Name=h2&Units=SI (accessed on 7 May 2022).
259. NIST, [United States National Institute of Standards and Technology]. NIST Chemistry WebBook—Carbon Monoxide. Available online: https://webbook.nist.gov/cgi/cbook.cgi?Name=CO&Units=SI (accessed on 7 May 2022).
260. NIST, [United States National Institute of Standards and Technology]. NIST Chemistry WebBook—Carbon Dioxide. Available online: https://webbook.nist.gov/cgi/cbook.cgi?ID=C124389&Units=SI (accessed on 7 May 2022).
261. Kuo, K.K. *Principles of Combustion*, 2nd ed.; John Wiley: Hoboken, NJ, USA, 2005; ISBN 978-0-471-04689-9.
262. Shi, L.; Liu, X.-J.; Wang, X.; Zhu, M.-S. Prediction Method for Liquid Thermal Conductivity of Refrigerant Mixtures. *Fluid Phase Equilibria* **2000**, *172*, 293–306. [CrossRef]
263. Agathou, M.S.; Kyritsis, D.C. An Experimental Comparison of Non-Premixed Bio-Butanol Flames with the Corresponding Flames of Ethanol and Methane. *Fuel* **2011**, *90*, 255–262. [CrossRef]
264. Marzouk, O.A. Estimated Electric Conductivities of Thermal Plasma for Air-Fuel Combustion and Oxy-Fuel Combustion with Potassium or Cesium Seeding. *Heliyon* **2024**, *10*, e31697. [CrossRef] [PubMed]
265. Mills, P.L. Analysis of Multiphase Polycarbonate Polymerization in a Semibatch Reactor. *Chem. Eng. Sci.* **1986**, *41*, 2939–2952. [CrossRef]
266. Hudebine, D.; Verstraete, J.J. Molecular Reconstruction of LCO Gasoils from Overall Petroleum Analyses. *Chem. Eng. Sci.* **2004**, *59*, 4755–4763. [CrossRef]

267. Bell, D.; Heyne, J.S.; Won, S.H.; Dryer, F.; Haas, F.M.; Dooley, S. On the Development of General Surrogate Composition Calculations for Chemical and Physical Properties. In Proceedings of the 55th AIAA Aerospace Sciences Meeting, Grapevine, TX, USA, 9–13 January 2017; p. AIAA 2017-0609.
268. Poinsot, T.; Veynante, D. *Theoretical and Numerical Combustion*, 2nd ed.; Edwards: Philadelphia, PA, USA, 2005; ISBN 978-1-930217-10-2.
269. Shikida, M.; Yoshikawa, K.; Iwai, S.; Sato, K. Flexible Flow Sensor for Large-Scale Air-Conditioning Network Systems. *Sens. Actuators A Phys.* **2012**, *188*, 2–8. [CrossRef]
270. Heselmann, M.; Dämgen, U.; Brümmer, A. Experimental Investigation of the Distribution of Two-Phase Flow in Oil-Injected Twin-Screw Compressors. In Proceedings of the 13th International Conference on Compressors and Their Systems, London, UK, 11–13 September 2023; Read, M., Rane, S., Ivkovic-Kihic, I., Kovacevic, A., Eds.; Springer Nature: Cham, Switzerland, 2024; pp. 61–76.
271. Johansson, P.S.; Valle, A.; Holm, H.T. Model-Uncertainty-Estimation Methodology Used on High-Flow-Rate Field Cases. *SPE J.* **2017**, *22*, 1254–1260. [CrossRef]
272. Carrington, C.G.; Liu, Q. Calorimeter Measurements of a Heat Pump Dehumidifier: Influence of Evaporator Air Flow. *Int. J. Energy Res.* **1995**, *19*, 649–658. [CrossRef]
273. Stoppel, L.; Fehling, T.; Geißler, T.; Baake, E.; Wetzel, T. Carbon Dioxide Free Production of Hydrogen. *IOP Conf. Ser. Mater. Sci. Eng.* **2017**, *228*, 012016. [CrossRef]
274. Wang, X.; Zhao, Y.; Yu, H.; Liu, Y. Research on Dynamic Characteristics of Laminar Flow Meter. *Flow Meas. Instrum.* **2024**, *97*, 102619. [CrossRef]
275. Murgia, S.; Valenti, G.; Contaldi, G.; Valenti, A. Experimental Investigation on Materials and Lubricants for Sliding-Vane Air Compressors. *IOP Conf. Ser. Mater. Sci. Eng.* **2015**, *90*, 012039. [CrossRef]
276. Wiederkehr, R.S.; Salvadori, M.C.; Degasperi, F.T.; Cattani, M. Development of Microvalves for Gas Flow Control in Micronozzles Using PVDF Piezoelectric Polymer. *J. Phys. Conf. Ser.* **2008**, *100*, 052046. [CrossRef]
277. Rönsch, S.; Auer, B.; Kinateder, M.; Gleichmann, K. Zeolite Heat Storage: Key Parameters from Experimental Results with Binder-Free NaY. *Chem. Eng. Technol.* **2020**, *43*, 2530–2537. [CrossRef]
278. Dierks, S.; Kroll, A. Quantification of Methane Gas Leakages Using Remote Sensing and Sensor Data Fusion. In Proceedings of the 2017 IEEE Sensors Applications Symposium (SAS), Glassboro, NJ, USA, 13–15 March 2017; pp. 1–6.
279. IUPAC, [International Union of Pure and Applied Chemistry]. IUPAC Compendium of Chemical Terminology, 3rd Ed. Online Version 3.0.1. Available online: https://doi.org/10.1351/goldbook.S06036 (accessed on 1 June 2024).
280. Klinger, R.; Kolářik, C.; Fluck, J.; Hofmann-Apitius, M.; Friedrich, C.M. Detection of IUPAC and IUPAC-like Chemical Names. *Bioinformatics* **2008**, *24*, i268–i276. [CrossRef] [PubMed]
281. Kuhn, H.J.; Braslavsky, S.E.; Schmidt, R. Chemical actinometry (IUPAC Technical Report). *Pure Appl. Chem.* **2004**, *76*, 2105–2146. [CrossRef]
282. Pettit, L.D. The IUPAC Stability Constants Database. *Chem. Int.—Newsmag. IUPAC* **2006**, *28*, 14–15. [CrossRef]
283. Jenkins, A.D.; Kratochvíl, P.; Stepto, R.F.T.; Suter, U.W. Glossary of basic terms in polymer science (IUPAC Recommendations 1996). *Pure Appl. Chem.* **1996**, *68*, 2287–2311. [CrossRef]
284. Guthrie, R.D.; Jencks, W.P. IUPAC Recommendations for the Representation of Reaction Mechanisms. Available online: https://pubs.acs.org/doi/pdf/10.1021/ar00166a001 (accessed on 4 May 2025).
285. Buck, R.P.; Rondinini, S.; Covington, A.K.; Baucke, F.G.K.; Brett, C.M.A.; Camoes, M.F.; Milton, M.J.T.; Mussini, T.; Naumann, R.; Pratt, K.W.; et al. Measurement of pH. Definition, Standards, and Procedures (IUPAC Recommendations 2002). *Pure Appl. Chem.* **2002**, *74*, 2169–2200. [CrossRef]
286. NIST, [United States National Institute of Standards and Technology]. CODATA [Committee on Data for Science and Technology] Value: Molar Gas Constant. Available online: https://physics.nist.gov/cgi-bin/cuu/Value?r (accessed on 7 May 2022).
287. NIST, [United States National Institute of Standards and Technology]. NIST Chemistry WebBook—Nitrogen. Available online: https://webbook.nist.gov/cgi/cbook.cgi?Name=n2 (accessed on 7 May 2022).
288. Mallette, M.D. Sustainable Development Through the Use of Bio-Fuels and Quantitative Metrics—Blacklight. Master of Science, Environmental Pollution Control; Pennsylvania State University: Pennsylvania, PA, USA, 2008.
289. Marzouk, O.A. Benchmarks for the Omani Higher Education Students-Faculty Ratio (SFR) Based on World Bank Data, QS Rankings, and THE Rankings. *Cogent Educ.* **2024**, *11*, 2317117. [CrossRef]
290. Utamura, M.; Nikitin, K.; Kato, Y. A Generalised Mean Temperature Difference Method for Thermal Design of Heat Exchangers. *Int. J. Nucl. Energy Sci. Technol.* **2008**, *4*, 11. [CrossRef]
291. Cao, Y. Equivalent Enthalpy Model and Log-Mean Enthalpy Difference Method for Heat-Mass Transfer in Cooling Towers. *ASME J. Heat Mass Transf.* **2024**, *146*, 104501. [CrossRef]
292. Hurd, N.L. Mean Temperature Difference in the Field or Bayonet Tube. *Ind. Eng. Chem.* **1946**, *38*, 1266–1271. [CrossRef]
293. Fakheri, A. Alternative Approach for Determining Log Mean Temperature Difference Correction Factor and Number of Shells of Shell and Tube Heat Exchangers. *JEH(T)* **2003**, *10*, 407–420. [CrossRef]

294. Lu, G.; Wang, J.; Li, Z. *Investigation on Calculating Methods of Mean Temperature Differences*; American Society of Mechanical Engineers Digital Collection: New York, NY, USA, 2009; pp. 33–36.
295. Bowman, R.A.; Mueller, A.C.; Nagle, W.M. Mean Temperature Difference in Design. *Trans. Am. Soc. Mech. Eng.* **2023**, *62*, 283–293. [CrossRef]
296. Almeshaal, M.A.; Choubani, K. Using the Log Mean Temperature Difference (LMTD) and ε-NTU Methods to Analyze Heat and Mass Transfer in Direct Contact Membrane Distillation. *Membranes* **2023**, *13*, 588. [CrossRef] [PubMed]
297. Lienhard, J.H., IV; Lienhard, J.H., V. *A Heat Transfer Textbook (Fifth Edition)*, 5th ed.; Phlogiston Press: Cambridge, MA, USA, 2019.
298. Quade, K.L.; Jöst, D.; Sauer, D.U.; Li, W. Understanding the Energy Potential of Lithium-Ion Batteries: Definition and Estimation of the State of Energy. *Batter. Supercaps* **2023**, *6*, e202300152. [CrossRef]
299. Kanoğlu, M.; Çengel, Y.A.; Dinçer, İ. Energy Conversion Efficiencies. In *Efficiency Evaluation of Energy Systems*; Kanoğlu, M., Çengel, Y.A., Dinçer, İ., Eds.; Springer: New York, NY, USA, 2012; pp. 55–68, ISBN 978-1-4614-2242-6.
300. Yin, L.; Ingesson, G.; Tunestal, P.; Johansson, R.; Johansson, B. *An Experimental Investigation of a Multi-Cylinder Engine with Gasoline-Like Fuel towards a High Engine Efficiency*; SAE Technical Paper: Detroit, MI, USA, 2016; p. 2016–01–0763.
301. Marzouk, O.A. Energy Generation Intensity (EGI) for Parabolic Dish/Engine Concentrated Solar Power in Muscat, Sultanate of Oman. *IOP Conf. Ser. Earth Environ. Sci.* **2022**, *1008*, 012013. [CrossRef]
302. Idris, K.A.; Ramdan, M.I.; Idroas, M.Y. Optimising the Performance of 110cc Engines for Fuel-Efficient Vehicle Design in the Shell Eco-Marathon. *Politek. Kolej Komuniti J. Eng. Technol.* **2024**, *9*, 125–135.
303. Caton, J.A. Maximum Efficiencies for Internal Combustion Engines: Thermodynamic Limitations. *Int. J. Engine Res.* **2018**, *19*, 1005–1023. [CrossRef]
304. Bandyopadhyay, S. All Forms of Energy Are Equal, but Some Forms of Energy Are More Equal than Others. *Clean Technol. Env. Policy* **2021**, *23*, 2775–2776. [CrossRef]
305. Demirbas, A.; Balubaid, M.A.; Basahel, A.M.; Ahmad, W.; Sheikh, M.H. Octane Rating of Gasoline and Octane Booster Additives. *Pet. Sci. Technol.* **2015**, *33*, 1190–1197. [CrossRef]
306. Kubesh, J.; King, S.R.; Liss, W.E. *Effect of Gas Composition on Octane Number of Natural Gas Fuels*; SAE Technical Paper: San Francisco, CA, USA, 1992; p. 922359.
307. Salgado-Conrado, L.; Lopez-Montelongo, A.; Alvarez-Macias, C.; Hernadez-Jaquez, J. Review of Heliodon Developments and Computational Tools for Building Shadow Analysis. *Buildings* **2022**, *12*, 627. [CrossRef]
308. Ramadhan, O.M.; Al-Hyali, E.A. New Experimental and Theoretical Relation to Determine the Research Octane Number (Ron) of Authentic Aromatic Hydrocarbons Could Be Present in the Gasoline Fraction. *Pet. Sci. Technol.* **1999**, *17*, 623–635. [CrossRef]
309. Wu, Z.; Zhang, G.; Wang, C.; Jin, S.; Ji, M.; Hu, C.; Shang, Q. Numerical Investigation on the Flame Propagation Process of Ammonia/Hydrogen Blends under Engine-Related Conditions. *Int. J. Hydrogen Energy* **2024**, *60*, 1041–1053. [CrossRef]
310. Muhammed, T.; Tokay, B.; Conradie, A. Raising the Research Octane Number Using an Optimized Simulated Moving Bed Technology towards Greater Sustainability and Economic Return. *Fuel* **2023**, *337*, 126864. [CrossRef]
311. Liu, H.; Wang, Z.; Wang, J.; He, X. Effects of Gasoline Research Octane Number on Premixed Low-Temperature Combustion of Wide Distillation Fuel by Gasoline/Diesel Blend. *Fuel* **2014**, *134*, 381–388. [CrossRef]
312. Nikolaou, N.; Papadopoulos, C.E.; Gaglias, I.A.; Pitarakis, K.G. A New Non-Linear Calculation Method of Isomerisation Gasoline Research Octane Number Based on Gas Chromatographic Data. *Fuel* **2004**, *83*, 517–523. [CrossRef]
313. Daly, S.R.; Niemeyer, K.E.; Cannella, W.J.; Hagen, C.L. Predicting Fuel Research Octane Number Using Fourier-Transform Infrared Absorption Spectra of Neat Hydrocarbons. *Fuel* **2016**, *183*, 359–365. [CrossRef]
314. Luecke, J.; Zigler, B.T. Rapid Prediction of Fuel Research Octane Number and Octane Sensitivity Using the AFIDA Constant-Volume Combustion Chamber. *Fuel* **2021**, *301*, 120969. [CrossRef]
315. Sun, X.; Zhang, F.; Liu, J.; Duan, X. Prediction of Gasoline Research Octane Number Using Multiple Feature Machine Learning Models. *Fuel* **2023**, *333*, 126510. [CrossRef]
316. Leonzio, G. Methanol Synthesis: Optimal Solution for a Better Efficiency of the Process. *Processes* **2018**, *6*, 20. [CrossRef]
317. Tan, E.C.D.; Talmadge, M.; Dutta, A.; Hensley, J.; Schaidle, J.; Biddy, M.; Humbird, D.; Snowden-Swan, L.J.; Ross, J.; Sexton, D.; et al. *Process Design and Economics for the Conversion of Lignocellulosic Biomass to Hydrocarbons via Indirect Liquefaction Thermochemical Research Pathway to High-Octane Gasoline Blendstock Through Methanol/Dimethyl Ether Intermediates*; National Renewable Energy Laboratory (NREL) and Pacific Northwest National Laboratory (PNNL) of the United States Department of Energy: Richland, WA, USA, 2015.
318. Vita, A.; Italiano, C. Fuel and Hydrogen Related Problems for Conventional Steam Reforming of Natural Gas. In *Current Trends and Future Developments on (Bio-) Membranes*; Elsevier: Amsterdam, The Netherlands, 2020; pp. 71–89, ISBN 978-0-12-816778-6.
319. Najjar, R.P.; Teikari, P.; Cornut, P.-L.; Knoblauch, K.; Cooper, H.M.; Gronfier, C. Heterochromatic Flicker Photometry for Objective Lens Density Quantification. *Investig. Ophthalmol. Vis. Sci.* **2016**, *57*, 1063–1071. [CrossRef] [PubMed]
320. Herbst, R.S.; Peterman, D.R.; Tillotson, R.D.; Delmau, L.H. Aspects of the Fundamental Chemistry of Cesium Extraction from Acidic Media by Hccd. *Czech J. Phys.* **2006**, *56*, D477–D482. [CrossRef]

321. Marzouk, O.A. Lookup Tables for Power Generation Performance of Photovoltaic Systems Covering 40 Geographic Locations (Wilayats) in the Sultanate of Oman, with and without Solar Tracking, and General Perspectives about Solar Irradiation. *Sustainability* **2021**, *13*, 13209. [CrossRef]
322. Heumann, C.; Schomaker, M. *Shalabh Introduction to Statistics and Data Analysis: With Exercises, Solutions and Applications in r*, 2nd ed.; Springer: Cham, Switzerland, 2023; ISBN 978-3-031-12025-1.
323. Hamilton, D.F.; Ghert, M.; Simpson, A.H.R.W. Interpreting Regression Models in Clinical Outcome Studies. *Bone Jt. Res.* **2015**, *4*, 152–153. [CrossRef]
324. Kim, Y.; van der Pol, E.; Arafa, A.; Thapa, I.; Britton, C.J.; Kosti, J.; Song, S.; Joshi, V.B.; Erickson, R.M.; Ali, H.; et al. Calibration and Standardization of Extracellular Vesicle Measurements by Flow Cytometry for Translational Prostate Cancer Research. *Nanoscale* **2022**, *14*, 9781–9795. [CrossRef] [PubMed]
325. Kulik, M.M.; Yaklich, R.W. Evaluation of Vigor Tests in Soybean Seeds: Relationship of Accelerated Aging, Cold, Sand Bench, and Speed of Germination Test to Field Performance. *Crop Sci.* **1982**, *22*, 766–770. [CrossRef]
326. Lewis-Beck, M.S.; Skalaban, A. The R-Squared: Some Straight Talk. *Political Anal.* **1990**, *2*, 153–171. [CrossRef]
327. Jenkins, D.G.; Quintana-Ascencio, P.F. A Solution to Minimum Sample Size for Regressions. *PLoS ONE* **2020**, *15*, e0229345. [CrossRef]
328. Menard, S. Coefficients of Determination for Multiple Logistic Regression Analysis. *Am. Stat.* **2000**, *54*, 17–24. [CrossRef]
329. Marzouk, O.A.; Huckaby, E.D. A Comparative Study of Eight Finite-Rate Chemistry Kinetics for CO/H_2 Combustion. *Eng. Appl. Comput. Fluid Mech.* **2010**, *4*, 331–356. [CrossRef]
330. Wang, S.; Lei, X.; Xu, B.; Jiang, W.; Kong, L.; Yang, B.; Tian, Y.; Liu, Y. Vacuum Evaporation and Condensation Thermodynamics and Evaporation Kinetics of Pure Silver. *Next Mater.* **2024**, *4*, 100189. [CrossRef]
331. Han, X.; Li, G.; Xu, M.; Guo, C.; Wang, Y.; Feng, Y.; Li, D. Miniature Capacitance Diaphragm Gauge for Absolute Vacuum Measurement. *Measurement* **2022**, *194*, 110851. [CrossRef]
332. Bello, I. *Vacuum and Ultravacuum: Physics and Technology*; CRC Press: Boca Raton, FL, USA, 2017; ISBN 978-1-315-15536-4.
333. Adam, T.; Hashim, U. COMSOL Multiphysics Simulation in Biomedical Engineering. *Adv. Mater. Res.* **2014**, *832*, 511–516. [CrossRef]
334. Zimmerman, W.B.J. Introduction to Comsol Multiphysics. In *Multiphysics Modeling with Finite Element Methods*; Series on Stability, Vibration and Control of Systems, Series A.; World Scientific: Singapore, 2006; Volume 18, pp. 1–26, ISBN 978-981-256-843-4.
335. Marzouk, O.A.; Nayfeh, A.H. Fluid Forces and Structure-Induced Damping of Obliquely-Oscillating Offshore Structures. In Proceedings of the the Eighteenth (2008) International Offshore and Polar Engineering Conference (ISOPE-2008), Vancouver, BC, Canada, 6 July 2008; Volume 3, pp. 460–468. [CrossRef]
336. Rybdylova, O.; Qubeissi, M.A.; Braun, M.; Crua, C.; Manin, J.; Pickett, L.M.; de Sercey, G.; Sazhina, E.M.; Sazhin, S.S.; Heikal, M. A Model for Droplet Heating and Its Implementation into ANSYS Fluent. *Int. Commun. Heat Mass Transf.* **2016**, *76*, 265–270. [CrossRef]
337. Ekambara, K.; Sanders, R.S.; Nandakumar, K.; Masliyah, J.H. Hydrodynamic Simulation of Horizontal Slurry Pipeline Flow Using ANSYS-CFX. *Ind. Eng. Chem. Res.* **2009**, *48*, 8159–8171. [CrossRef]
338. McLure, F.I.; Tang, K.-S.; Williams, P.J. What Do Integrated STEM Projects Look like in Middle School and High School Classrooms? A Systematic Literature Review of Empirical Studies of iSTEM Projects. *Int. J. STEM Educ.* **2022**, *9*, 73. [CrossRef]
339. Hall, A.; Miro, D. A Study of Student Engagement in Project-Based Learning Across Multiple Approaches to STEM Education Programs. *Sch. Sci. Math.* **2016**, *116*, 310–319. [CrossRef]
340. Marzouk, O.A. Globalization and Diversity Requirement in Higher Education. In Proceedings of the 11th World Multi-Conference on Systemics, Cybernetics and Informatics (WMSCI 2007)—The 13th International Conference on Information Systems Analysis and Synthesis (ISAS 2007), Orlando, FL, USA, 8–11 July 2007; Volume III, pp. 101–106. [CrossRef]
341. Mun, R.U.; Hertzog, N.B. Teaching and Learning in STEM Enrichment Spaces: From Doing Math to Thinking Mathematically. *Roeper Rev.* **2018**, *40*, 121–129. [CrossRef]
342. Boelter, C.; Link, T.C.; Perry, B.L.; Leukefeld, C. Diversifying the STEM Pipeline. *J. Educ. Stud. Placed Risk (JESPAR)* **2015**, *20*, 218–237. [CrossRef]
343. *Alicat Scientific Alicat Flow Controller—MC · MCW · MCR · MCV*; Alicat Scientific, Inc. (a Halma Company): Tucson, AZ, USA, 2020.
344. Arshi, N.; Lu, J.; Joo, Y.K.; Lee, C.G.; Yoon, J.H.; Ahmed, F. Study on Structural, Morphological and Electrical Properties of Sputtered Titanium Nitride Films under Different Argon Gas Flow. *Mater. Chem. Phys.* **2012**, *134*, 839–844. [CrossRef]
345. Ralchenko, V.; Sychov, I.; Vlasov, I.; Vlasov, A.; Konov, V.; Khomich, A.; Voronina, S. Quality of Diamond Wafers Grown by Microwave Plasma CVD: Effects of Gas Flow Rate. *Diam. Relat. Mater.* **1999**, *8*, 189–193. [CrossRef]
346. Rombouts, C.; Bair, M.; Barbe, J.; Wright, J.D.; Kramer, R.; Krajicek, Z. A Comparison of Primary Gas Flow Standards Spanning the Range from 10 Sccm N_2 to 10 Slm N_2. *NCSLI Meas.* **2014**, *9*, 46–54. [CrossRef]
347. Ahmadi, A.; Hadipour, N.L.; Kamfiroozi, M.; Bagheri, Z. Theoretical Study of Aluminum Nitride Nanotubes for Chemical Sensing of Formaldehyde. *Sens. Actuators B Chem.* **2012**, *161*, 1025–1029. [CrossRef]

348. Berg, R.F.; Gooding, T.; Vest, R.E. Constant Pressure Primary Flow Standard for Gas Flows from 0.01cm^3/Min to 100cm^3/Min (0.007–74 μmol/s). *Flow Meas. Instrum.* **2014**, *35*, 84–91. [CrossRef]
349. Fillet, R.; Nicolas, V.; Celzard, A.; Fierro, V. Solar Evaporation Performance of 3D-Printed Concave Structures Filled with Activated Carbon under Low Convective Flow. *Chem. Eng. J.* **2023**, *457*, 141168. [CrossRef]
350. Jing, J.; Yang, L.; Tang, X.; He, P.; Tang, K. Numerical Simulation of Multiphase Flow Erosion in the Gas Well Relief Line Elbow under Supercritical Conditions. *J. Pipeline Syst. Eng. Pract.* **2023**, *14*, 04023031. [CrossRef]
351. Shahid, M.; Chambers, B.; Sankarasubramanian, S. Methane and Oxygen from Energy-efficient, Low Temperature in Situ Resource Utilization Enables Missions to Mars. *AIChE J.* **2023**, *69*, e18010. [CrossRef]
352. Cao, Y.; Liang, W.; Law, C.K. Real Gas Effects in High-Pressure Ignition of *n* -Dodecane/Air Mixtures. *J. Phys. Chem. A* **2024**, *128*, 3604–3612. [CrossRef]
353. Ding, H.; Zhang, Y.; Dong, Y.; Wen, C.; Yang, Y. High-Pressure Supersonic Carbon Dioxide (CO_2) Separation Benefiting Carbon Capture, Utilisation and Storage (CCUS) Technology. *Appl. Energy* **2023**, *339*, 120975. [CrossRef]
354. Gaganis, V.; Homouz, D.; Maalouf, M.; Khoury, N.; Polychronopoulou, K. An Efficient Method to Predict Compressibility Factor of Natural Gas Streams. *Energies* **2019**, *12*, 2577. [CrossRef]
355. Kartal, M.A.; Atakök, G.; Ersoy, S. Cooling and Multiphase Analysis of Heated Environmentally Friendly R152A (C2H4F2) Fluid Coming from the Production Process According to Nist Indicators. *Appl. Sci.* **2024**, *14*, 4143. [CrossRef]
356. Manfredi, M.; Persico, G.; Spinelli, A.; Gaetani, P.; Dossena, V. Design and Commissioning of Experiments for Supersonic ORC Nozzles in Linear Cascade Configuration. *Appl. Therm. Eng.* **2023**, *224*, 119996. [CrossRef]
357. Ruiz Maraggi, L.M.; Moscardelli, L.G. Modeling Hydrogen Storage Capacities, Injection and Withdrawal Cycles in Salt Caverns: Introducing the GeoH$_2$ Salt Storage and Cycling App. *Int. J. Hydrogen Energy* **2023**, *48*, 26921–26936. [CrossRef]
358. Srinivasan, N.; Zhang, H.; Yang, S. VLE-Based Phase Field Method to Simulate High-Pressure Diffuse Interface with Phase Change. In Proceedings of the AIAA SCITECH 2024 Forum, Orlando, FL, USA, 8 January 2024.
359. Mahmoud, M. Development of a New Correlation of Gas Compressibility Factor (Z-Factor) for High Pressure Gas Reservoirs. *J. Energy Resour. Technol.* **2013**, *136*, 012903. [CrossRef]
360. Jung, H.-Y.; Kim, M.S.; Ko, A.-R.; Lee, J.I. Investigation of CO_2 Leak Accident in SFR Coupled with S-CO_2 Brayton Cycle. *Ann. Nucl. Energy* **2017**, *103*, 212–226. [CrossRef]
361. Marzouk, O.A. The Sod Gasdynamics Problem as a Tool for Benchmarking Face Flux Construction in the Finite Volume Method. *Sci. Afr.* **2020**, *10*, e00573. [CrossRef]
362. Kim, M.S.; Oh, B.S.; Jung, H.-Y.; Bae, S.J.; Lee, J.I. *Experimental and Numerical Study of Critical Flow Model Development for Supercritical CO_2 Power Cycle Application*; American Society of Mechanical Engineers Digital Collection: New York, NY, USA, 2018.
363. Kim, M.S.; Bae, S.J.; Son, S.; Oh, B.S.; Lee, J.I. Study of Critical Flow for Supercritical CO_2 Seal. *Int. J. Heat Mass Transf.* **2019**, *138*, 85–95. [CrossRef]
364. Yan, P.; Gori, G.; Zocca, M.; Guardone, A. SU2-COOL: Open-Source Framework for Non-Ideal Compressible Fluid Dynamics. *Comput. Phys. Commun.* **2025**, *307*, 109394. [CrossRef]
365. Kandula, M.; Nufer, B.M.; Felt, A.M.; Hicks, N.G.; Aranyos, T.J.; Webster, G.K.; Coll, G.T. Compressibility, Reynolds Number and Thermal Effects in Pressure-Decay Based Leak Detection Systems. In Proceedings of the AIAA Aviation 2019 Forum, Dallas, TX, USA, 17–21 June 2019; p. AIAA 2019-3437.
366. Sarmast, S.; Rouindej, K.; Fraser, R.A.; Dusseault, M.B. Sizing-Design Method for Compressed Air Energy Storage (CAES) Systems: A Case Study Based on Power Grid in Ontario. *Energy Convers. Manag.* **2023**, *277*, 116656. [CrossRef]
367. Bischoff, J.L.; Rosenbauer, R.J.; Pitzer, K.S. The System NaCl-H_2O: Relations of Vapor-Liquid near the Critical Temperature of Water and of Vapor-Liquid-Halite from 300° to 500 °C. *Geochim. Cosmochim. Acta* **1986**, *50*, 1437–1444. [CrossRef]
368. Dauchot, J.-P.; Dath, J.-P. Oxidation of Carbon Monoxide on Thin Film Catalysts: Characterization by a Critical Temperature Measurement. *J. Catal.* **1984**, *86*, 373–383. [CrossRef]
369. Guo, G.; Wang, F.; Liu, G.-Q.; Luo, S.-J.; Guo, R.-B. Calculation on the Phase Equilibrium and Critical Temperature of CH_4/CO_2. *Process Saf. Environ. Prot.* **2018**, *113*, 369–377. [CrossRef]
370. Ingebritsen, S.E.; Hayba, D.O. Fluid Flow and Heat Transport near the Critical Point of H $_2$ O. *Geophys. Res. Lett.* **1994**, *21*, 2199–2202. [CrossRef]
371. Karnaukhov, V.A.; Oeschler, H.; Avdeyev, S.P.; Duginova, E.V.; Rodionov, V.K.; Budzanowski, A.; Karcz, W.; Bochkarev, O.V.; Kuzmin, E.A.; Chulkov, L.V.; et al. Critical Temperature for the Nuclear Liquid-Gas Phase Transition. *Phys. Rev. C* **2003**, *67*, 011601. [CrossRef]
372. Kestin, J.; Korfali, Ö.; Sengers, J.V. Density Expansion of the Viscosity of Carbon Dioxide near the Critical Temperature. *Phys. A Stat. Mech. Its Appl.* **1980**, *100*, 335–348. [CrossRef]
373. Dincer, I.; Zamfirescu, C. 1.5 Thermodynamic Aspects of Energy. In *Comprehensive Energy Systems*; Elsevier: Amsterdam, The Netherlands, 2018; pp. 153–211, ISBN 978-0-12-814925-6.

374. Tiab, D.; Donaldson, E.C. Introduction to Petroleum Geology. In *Petrophysics*; Elsevier: Amsterdam, The Netherlands, 2016; pp. 23–66, ISBN 978-0-12-803188-9.
375. Sankar Behera, U.; Kumar Prasad, S.; Byun, H.-S. Experimental Validation on the Phase Separation for the 2-(Diisopropylamino)Ethyl Methacrylate and Poly[2-(Diisopropylamino)Ethyl Methacrylate] in Supercritical CO_2. *J. Mol. Liq.* **2024**, *393*, 123553. [CrossRef]
376. Shang, Z.; Yang, Y.; Zhang, L.; Sun, H.; Zhong, J.; Zhang, K.; Yao, J. Hydrogen Adsorption and Diffusion Behavior in Kaolinite Slit for Underground Hydrogen Storage: A Hybrid GCMC-MD Simulation Study. *Chem. Eng. J.* **2024**, *487*, 150517. [CrossRef]
377. Shen, Y.; Qiu, C.; Liu, D.; Tao, X.; Wan, A.; Zhang, Z.; Gan, Z. Experimental Study on a Closed-Cycle Joule-Thomson Cryocooler Working at Liquid Hydrogen Temperature. *Appl. Therm. Eng.* **2023**, *234*, 121291. [CrossRef]
378. Wei-yu, C.; Sun, L.; Zhou, J.; Li, X.; Huang, L.; Xia, G.; Meng, X.; Wang, K. Toward Predicting Interfacial Tension of Impure and Pure CO_2-Brine Systems Using Robust Correlative Approaches. *ACS Omega* **2024**, *9*, 7937–7957. [CrossRef]
379. Xie, Y.; Dong, H.; Zhang, S.; Lu, X.; Ji, X. Solubilities of CO_2, CH_4, H_2, CO and N_2 in Choline Chloride/Urea. *Green Energy Environ.* **2016**, *1*, 195–200. [CrossRef]
380. Mihara, S.; Sagara, H.; Arai, Y.; Saito, S. The Compressibility Factors of Hydrogen-Methane, Hydrogen-Ethane and Hydrogen-Propane Gaseous Mixtures. *J. Chem. Eng. Jpn./JCEJ* **1977**, *10*, 395–399. [CrossRef]
381. White, C.W.; Weiland, N.T. Evaluation of Property Methods for Modeling Direct-Supercritical CO_2 Power Cycles. *J. Eng. Gas Turbines Power* **2017**, *140*, 011701. [CrossRef]
382. Seneviratne, K.N.; Hughes, T.J.; Johns, M.L.; Marsh, K.N.; May, E.F. Surface Tension and Critical Point Measurements of Methane + Propane Mixtures. *J. Chem. Thermodyn.* **2017**, *111*, 173–184. [CrossRef]
383. Rane, S.; Kovačević, A.; Stošić, N.; Smith, I. Analysis of Real Gas Equation of State for CFD Modelling of Twin Screw Expanders with R245fa, R290, R1336mzz(Z) and R1233zd(E). *Int. J. Refrig.* **2021**, *121*, 313–326. [CrossRef]
384. Clementoni, E.M.; Cox, T.L. *Comparison of Carbon Dioxide Property Measurements for an Operating Supercritical Brayton Cycle to the REFPROP Physical Property Database*; American Society of Mechanical Engineers Digital Collection: New York, NY, USA, 2014.
385. Obein, G.; Bousquet, R.; Nadal, M.E. New NIST Reference Goniospectrometer. In *Optical Diagnostics*; SPIE: Pune, India, 2005; Volume 5880, pp. 241–250.
386. Pearce, N.J.G.; Perkins, W.T.; Westgate, J.A.; Gorton, M.P.; Jackson, S.E.; Neal, C.R.; Chenery, S.P. A Compilation of New and Published Major and Trace Element Data for NIST SRM 610 and NIST SRM 612 Glass Reference Materials. *Geostand. Newsl.* **1997**, *21*, 115–144. [CrossRef]
387. Lafarge, T.; Possolo, A. The NIST Uncertainty Machine. *NCSLI Meas.* **2015**, *10*, 20–27. [CrossRef]
388. Ferraiolo, D.F.; Sandhu, R.; Gavrila, S.; Kuhn, D.R.; Chandramouli, R. Proposed NIST Standard for Role-Based Access Control. *ACM Trans. Inf. Syst. Secur.* **2001**, *4*, 224–274. [CrossRef]
389. Linstrom, P.J.; Mallard, W.G. The NIST Chemistry WebBook: A Chemical Data Resource on the Internet. *J. Chem. Eng. Data* **2001**, *46*, 1059–1063. [CrossRef]
390. PNNL, [Pacific Northwest National Laboratory of the United States Department of Energy]. H2 Tools—Hydrogen Compressibility at Different Temperatures and Pressures. Available online: https://h2tools.org/hyarc/hydrogen-data/hydrogen-compressibility-different-temperatures-and-pressures (accessed on 20 September 2022).
391. Todić, B.; Pravilović, R.; Nikačević, N. Design and Simulations of a Helical Oscillatory Baffled Reactor for Biochemical Reactions. *Chem. Eng. Process. -Process Intensif.* **2024**, *203*, 109895. [CrossRef]
392. Marzouk, O.A.; Nayfeh, A.H. Hydrodynamic Forces on a Moving Cylinder with Time-Dependent Frequency Variations. In Proceedings of the 46th AIAA Aerospace Sciences Meeting and Exhibit, Reno, NV, USA, 7–10 January 2008; p. AIAA 2008-680. [CrossRef]
393. Wang, J.; Shen, L.; Wang, L.; Sundén, B. Effect of Hydrogen Permeation and Operating Parameters on Thermochemical Performance of Solar-Driven Steam Methane Reforming Membrane Reactor. *Chem. Eng. Sci.* **2024**, *295*, 120157. [CrossRef]
394. CCPS, [Center for Chemical Process Safety of the American Institute of Chemical Engineers]. Plug Flow Reactor (PFR). Available online: https://www.aiche.org/ccps/resources/glossary/process-safety-glossary/plug-flow-reactor-pfr (accessed on 20 September 2022).
395. Ming, D.; Glasser, D.; Hildebrandt, D.; Glasser, B.; Metzer, M. *Attainable Region Theory: An Introduction to Choosing an Optimal Reactor*; Wiley: Hoboken, NJ, USA, 2016; ISBN 978-1-119-24470-7.
396. Rosa, D.; Goes, P.; Manzi, J. Steady-State Plug Flow Reactor Analysis by Means of Minimum Entropy. In *Computer Aided Chemical Engineering*; Elsevier: Amsterdam, The Netherlands, 2017; Volume 40, pp. 1165–1170, ISBN 978-0-444-63965-3.
397. Curtis, R.; Nguyen, C.; Lower, S. 2.3: First-Order Reactions. Available online: https://chem.libretexts.org/Bookshelves/Physical_and_Theoretical_Chemistry_Textbook_Maps/Supplemental_Modules__(Physical_and_Theoretical_Chemistry)/Kinetics/02:_Reaction_Rates/2.03:_First-Order_Reactions (accessed on 20 September 2022).
398. Phuakpunk, K.; Chalermsinsuwan, B.; Assabumrungrat, S. Comparison of Chemical Reaction Kinetic Models for Corn Cob Pyrolysis. *Energy Rep.* **2020**, *6*, 168–178. [CrossRef]

399. Marzouk, O.A.; Nayfeh, A.H. New Wake Models with Capability of Capturing Nonlinear Physics. In Proceedings of the ASME 2008 27th International Conference on Offshore Mechanics and Arctic Engineering (OMAE 2008), Estoril, Portugal, 27 July 2009; pp. 901–912. [CrossRef]
400. Marzouk, O.A.; Nayfeh, A.H. A Study of the Forces on an Oscillating Cylinder. In Proceedings of the ASME 2007 26th International Conference on Offshore Mechanics and Arctic Engineering (OMAE 2007), San Diego, CA, USA, 20 May 2009; pp. 741–752. [CrossRef]
401. AIChE, [American Institute of Chemical Engineers]. Continuous Reactors. Available online: https://www.aiche.org/ccps/resources/glossary/process-safety-glossary/continuous-reactors (accessed on 6 May 2025).
402. Tuckerman, M.E. Lecture 25: Plug Flow Reactors and Comparison to Continuously Stirred Tank Reactors. Available online: https://chem.libretexts.org/Courses/New_York_University/CHEM-UA_652:_Thermodynamics_and_Kinetics/Lecture_25:_Plug_flow_reactors_and_comparison_to_continuously_stirred_tank_reactors (accessed on 9 May 2022).
403. Marzouk, O.A. Coupled Differential-Algebraic Equations Framework for Modeling Six-Degree-of-Freedom Flight Dynamics of Asymmetric Fixed-Wing Aircraft. *Int. J. Appl. Adv. Sci.* **2025**, *12*, 30–51. [CrossRef]
404. Brencio, C.; Fontein, F.W.A.; Medrano, J.A.; Di Felice, L.; Arratibel, A.; Gallucci, F. Pd-Based Membranes Performance under Hydrocarbon Exposure for Propane Dehydrogenation Processes: Experimental and Modeling. *Int. J. Hydrogen Energy* **2022**, *47*, 11369–11384. [CrossRef]
405. Campo, M.; Tanaka, A.; Mendes, A.; Sousa, J.M. Characterization of Membranes for Energy and Environmental Applications. In *Advanced Membrane Science and Technology for Sustainable Energy and Environmental Applications*; Elsevier: Amsterdam, The Netherlands, 2011; pp. 56–89, ISBN 978-1-84569-969-7.
406. Caravella, A.; Hara, S.; Drioli, E.; Barbieri, G. Sieverts Law Pressure Exponent for Hydrogen Permeation through Pd-Based Membranes: Coupled Influence of Non-Ideal Diffusion and Multicomponent External Mass Transfer. *Int. J. Hydrogen Energy* **2013**, *38*, 16229–16244. [CrossRef]
407. Olander, D.; Konashi, K.; Yamawaki, M. Uranium–Zirconium Hydride Fuel. In *Comprehensive Nuclear Materials*; Elsevier: Amsterdam, The Netherlands, 2012; pp. 313–357, ISBN 978-0-08-056033-5.
408. Suzuki, A.; Yukawa, H. A Review for Consistent Analysis of Hydrogen Permeability through Dense Metallic Membranes. *Membranes* **2020**, *10*, 120. [CrossRef] [PubMed]
409. Koffler, S.A.; Hudson, J.B.; Ansell, G.S. Hydrogen Permeation through Alpha-Palladium. *Trans. Metall. Soc. Am. Inst. Min. Metall. Pet. Eng.* **1969**, *245*, 1735–1740.
410. Morreale, B.D.; Ciocco, M.V.; Enick, R.M.; Morsi, B.I.; Howard, B.H.; Cugini, A.V.; Rothenberger, K.S. The Permeability of Hydrogen in Bulk Palladium at Elevated Temperatures and Pressures. *J. Membr. Sci.* **2003**, *212*, 87–97. [CrossRef]
411. Yuan, M.; Lee, K.; Van Campen, D.G.; Liguori, S.; Toney, M.F.; Wilcox, J. Hydrogen Purification in Palladium-Based Membranes: An Operando X-Ray Diffraction Study. *Ind. Eng. Chem. Res.* **2019**, *58*, 926–934. [CrossRef]
412. Marzouk, O.A. Performance Analysis of Shell-and-Tube Dehydrogenation Module. *Int. J. Energy Res.* **2017**, *41*, 604–610. [CrossRef]
413. Nordio, M.; Wassie, S.A.; Van Sint Annaland, M.; Pacheco Tanaka, D.A.; Viviente Sole, J.L.; Gallucci, F. Techno-Economic Evaluation on a Hybrid Technology for Low Hydrogen Concentration Separation and Purification from Natural Gas Grid. *Int. J. Hydrogen Energy* **2021**, *46*, 23417–23435. [CrossRef]
414. Marzouk, O.A. Levelized Cost of Green Hydrogen (LCOH) in the Sultanate of Oman Using H2A-Lite with Polymer Electrolyte Membrane (PEM) Electrolyzers Powered by Solar Photovoltaic (PV) Electricity. *E3S Web Conf.* **2023**, *469*, 00101. [CrossRef]
415. Microsoft Corporation Use Goal Seek to Find the Result You Want by Adjusting an Input Value. Available online: https://support.microsoft.com/en-us/office/use-goal-seek-to-find-the-result-you-want-by-adjusting-an-input-value-320cb99e-f4a4-417f-b1c3-4f369d6e66c7 (accessed on 11 May 2022).

processes

MDPI

Article

Optimal Maintenance Strategy Selection for Oil and Gas Industry Equipment Using a Combined Analytical Hierarchy Process–Technique for Order of Preference by Similarity to an Ideal Solution: A Case Study in the Oil and Gas Industry

Chia-Nan Wang [1], Ming-Hsien Hsueh [1], Duy-Oanh Tran Thi [1,2,*], Thi Diem-My Le [1,2,*] and Quang-Tuyen Dinh [3]

[1] Department of Industrial Engineering and Management, National Kaohsiung University of Science and Technology, Kaohsiung 807618, Taiwan; cn.wang@nkust.edu.tw (C.-N.W.); mhhsueh@nkust.edu.tw (M.-H.H.)
[2] Department of Economics and Industrial Management, Cantho University of Technology, Can Tho 901163, Vietnam
[3] Quality Management Department, Orient Oil & Gas Joint Stock Company, Can Tho 901163, Vietnam; tuyen.dinhquang@orientoil.com.vn
* Correspondence: ttdoanh@ctuet.edu.vn (D.-O.T.T.); ltdiemmy160695@gmail.com (T.D.-M.L.)

Abstract: Maintenance plays a key role in oil and gas enterprises, especially in the process of increasing pressure to improve equipment efficiency, reduce costs, and comply with environmental protection requirements towards sustainable production. This study proposes an optimal maintenance strategy based on the overall equipment effectiveness (OEE) index, using a multi-criteria decision-making method (MCDM) integrating an Analytical Hierarchy Process (AHP) and a Technique for Order of Preference by Similarity to an Ideal Solution (TOPSIS). The study evaluates five maintenance strategies—preventive maintenance (PM), risk-based maintenance (RBM), condition-based maintenance (CBM), reliability-centered maintenance (RCM), and predictive maintenance (PdM)—based on four key criteria: maintenance cost, safety, efficiency, and flexibility. The comparison of each pair of criteria and the maintenance strategy choices was carried out systematically to ensure consistency in the decision-making process. The Evaluation Distance to the Mean Solution (EDAS) method was used as a cross-validation tool to strengthen the reliability of the results. The results showed that RCM is the optimal maintenance strategy, providing superior equipment performance and reliability. The study expands the theoretical basis in industrial maintenance, providing a structured and data-driven decision support tool. The method can be flexibly applied in many industries to optimize maintenance strategies and promote sustainable production.

Keywords: oil refinery; maintenance strategy selection; overall equipment efficiency (OEE); multi-criteria decision-making; Vietnam oil and gas industry

1. Introduction

The petrochemical industry is essential to each country's economic, energy, transportation, and defense development. In particular, the maintenance of production equipment is vital to ensure continuous operation, stable product quality, and minimize leakage and negative environmental impacts. Production lines and equipment in oil refineries are the most significant assets of the enterprise, acting as the "heart" in maintaining continuous and efficient production operations. According to many previous studies, effective maintenance strategies help to reduce machine downtime, improve system reliability, optimize

costs, and improve overall productivity [1–3]. Maintenance costs can account for up to 15–70% of total production costs [4], the second largest category after energy costs [5]. Therefore, choosing the correct maintenance strategy is an essential problem in industrial production management.

Modern maintenance models such as reliability-based maintenance (RCM), total productive maintenance (TPM), predictive maintenance (PdM), condition-based maintenance (CBM), and risk-based maintenance (RBM) have been widely applied [6–9]. However, these methods share the fact that they require the evaluation of many different factors, such as cost, safety, efficiency, flexibility, and practicality. Therefore, the optimal strategy selection must be based on a systematic, quantitative approach that can handle conflicting criteria. A popular indicator for evaluating maintenance effectiveness is the OEE, which analyzes losses related to availability, performance, and product quality [10]. In practice, OEE has been applied to identify the causes of major losses in critical equipment systems, typically the injection pump system at an oil field of the Pertamina group in Indonesia [11]. Despite many studies addressing different maintenance policies and methods, there is still a gap in building a systematic decision-making framework that integrates qualitative and quantitative factors to support selecting appropriate maintenance strategies. Particularly in the petrochemical industry complex and high-risk production environments, a structured decision support model with multi-criteria evaluation capabilities is extremely necessary.

The MCDM, which integrates two methods, namely the Analytical Hierarchy Process (AHP) and Technique for Order of Preference by Similarity to an Ideal Solution (TOPSIS), was proposed to address this gap. This combination allows for a systematic evaluation of maintenance options, based on both expert opinion (AHP determines the weighting of criteria) and real-world data to rank options (TOPSIS) [12–17].

However, through a survey of existing documents, there have not been many studies that systematically integrate AHP and TOPSIS to select the optimal maintenance strategy based on the OEE index in the real context of oil refineries. This is the research gap that this paper aims to overcome. Specifically, the study proposes an integrated AHP-TOPSIS model to select the optimal maintenance strategy for equipment in the oil and gas industry. The OEE index is used as the basis for measuring the overall efficiency of the equipment, combined with multidimensional evaluation criteria such as cost, safety, efficiency, flexibility, and deployment capability. The methodology is systematically built through defining objectives, creating a criteria system, evaluating weights through AHP, and ranking options using TOPSIS, ensuring objectivity and scientificity in decisions.

2. Literature Review

2.1. Equipment Maintenance Strategies in the Oil and Gas Industry

The maintenance of equipment in the oil and gas industry has garnered significant attention due to its critical role in enhancing operational efficiency, minimizing costs, and adhering to environmental regulations. Traditional maintenance strategies, such as preventive maintenance (PM) and corrective maintenance (CM), have been widely adopted; however, the evolving complexities of industrial operations necessitate the exploration of more dynamic and effective maintenance methodologies.

Over time, many new maintenance strategies have been developed, each with advantages and limitations. Abdel Bayoumi et al. [18] proposed a predictive maintenance (PdM) model based on sensor data collection and data analysis to support maintenance decision-making. Similarly, Hameed and Khan [19] developed a risk-based maintenance (RBM) model to effectively plan inspection and maintenance, significantly improving safety and cost and reducing downtime. Condition-based maintenance (CBM), as presented in [20], is based on condition monitoring data used to perform maintenance when there

are signs of failure. They integrate real-time data to assess asset condition and predict potential failures, thereby taking timely maintenance actions, minimizing unnecessary interventions, and improving reliability. TPM and RCM are third-generation maintenance methods that help increase operational efficiency and maintain equipment stability [21]. Studies have also shown that the effectiveness of maintenance strategies can be evaluated through performance indicators such as OEE. For example, a study at the PEP field Bunyu injection system showed that measuring and analyzing OEE combined with the "six major losses" model significantly improved operating performance and reduced the risk of environmental pollution [11].

2.2. Application of the MCDM in Selecting Maintenance Strategies

Since each maintenance strategy has advantages and disadvantages, selecting the appropriate strategy requires the consideration of many factors simultaneously. The MCDM is an effective tool for selecting the optimal solution. Many studies have applied MCDM in the industrial field, including the AHP-Delphi-PROMETHEE method, which is applied to select the optimal maintenance solution for each marine engine part based on fuzzy reliability and many criteria [13]. The combined FAHP and TOPSIS model has been used in the paper industry to select the optimal pump maintenance strategy [14,15]. The studies of Hemmati et al. and Jamali et al. have demonstrated the effectiveness of combining AHP and TOPSIS in a fuzzy environment to make optimal maintenance decisions [16,17].

2.3. Criteria for Evaluating Maintenance Strategies

To ensure the effectiveness of maintenance strategy selection, the criteria commonly considered include cost, safety, efficiency, and flexibility. Studies have shown the following:

Cost: The implementation of PdM and RCM reduces unplanned downtime and maintenance costs by 15% to 25% [22,23].

Safety: The application of CBM reduces accidents due to equipment failures by up to 20% [24,25].

Effectiveness: Combining RCM and CBM increases OEE by up to 15%, while PdM can improve equipment performance by 18% [26,27].

Flexibility: PdM and RCM improve flexible planning by 20% to 25%, adapting to changing operating conditions [28–30].

In addition to the four main criteria, recent studies have expanded to 18 sub-criteria: spare parts, personnel training, outsourcing costs, machine downtime, CMMS system, reliability, product productivity, employee acceptance, and flexible scheduling. These criteria provide a more comprehensive and realistic evaluation framework in the decision-making process for selecting the optimal maintenance strategy. [27,28,30–33].

The selection and weighting of these sub-criteria, derived from expert consultation and literature synthesis, form the foundation for applying the AHP-TOPSIS model in this study. This comprehensive approach ensures the selection of a maintenance strategy that is not only cost-effective but also safe, efficient, and adaptable to operational demands.

2.4. Research Gap

Although many studies have applied MCDM models when selecting maintenance strategies in various industrial sectors, such as manufacturing, marine, and paper industries, the number of in-depth studies using these models in the oil and gas industry, especially for equipment in oil refining plants, is still limited. Building a systematic decision-making framework that integrates qualitative and quantitative factors to support selecting appropriate maintenance strategies is extremely necessary.

The MCDM that integrates two methods, AHP and TOPSIS, was proposed to address this gap. This combination allows for a systematic evaluation of maintenance options, based

on the use of expert opinion (AHP determines the weighting of criteria) and real-world data to rank options (TOPSIS). In addition, the OEE index has been proven to be a useful tool for measuring equipment performance; the integration of OEE as an evaluation criterion in MCDM models for selecting maintenance strategies has not been studied. This novel combination is essential when businesses increasingly focus on optimizing equipment performance to improve productivity and reduce maintenance costs.

Therefore, this study aims to fill this gap by developing an AHP-TOPSIS-integrated model incorporating OEE as a performance measure to ensure that strategy selection reflects actual operational outcomes in the oil and gas industry. It supports the decision-making process of selecting the optimal maintenance strategy for equipment in complex and constrained operating environments.

3. Methods and Materials

3.1. Methodology

The research methodology is designed with an integrated approach to evaluate equipment performance and propose optimal maintenance strategies in the petrochemical refining sector. The research process includes two main stages, as described in Figure 1 below.

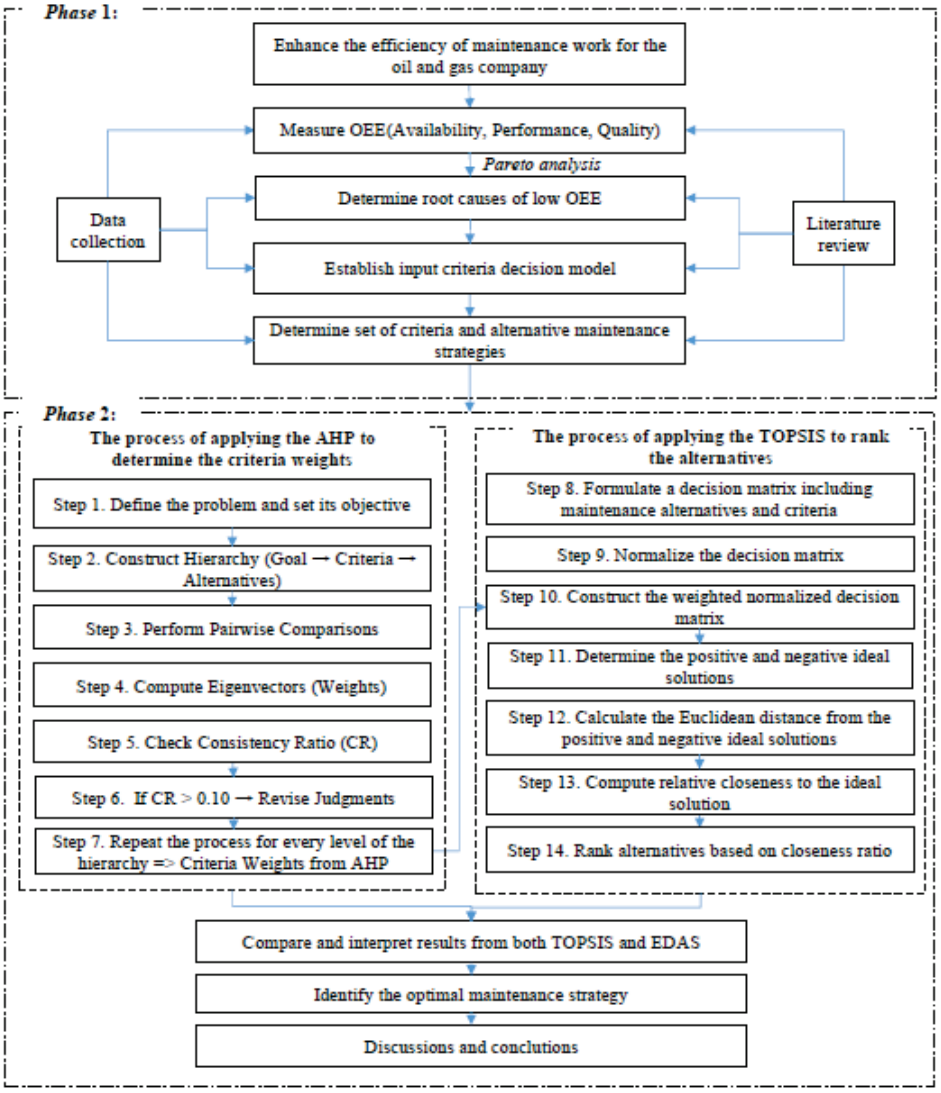

Figure 1. Research methodology diagram.

3.1.1. Phase 1: Analyze Equipment Status Based on OEE Index and Identify Root Causes

The first phase focuses on measuring manufacturing equipment performance through the OEE index, which includes three components: availability, performance, and quality.

Overall equipment efficiency (OEE) is developed based on the TPM concept introduced by Nakajima in 1988. OEE has been widely applied in industrial production to measure equipment performance [34]. OEE has been applied in the semiconductor industry to evaluate and remove loss in manufacturing [35,36]. In another paper, Hwang et al. developed a new manufacturing performance model to measure real-time performance metrics based on the IoT and OEE [37]. Previous studies have found that the OEE index is a popular tool used to calculate the overall performance of equipment. OEE performs loss identification and the measurement of significant aspects of production in terms of three key factors: availability, operational efficiency, and quality ratio. The following equations calculate the OEE value:

$$\text{OEE} = \text{Availability (A)} \times \text{Performance efficiency (PE)} \times \text{Rate of quality (Qr)} \quad (1)$$

World-class OEE is a standard used to compare a company's OEE. Studies worldwide show that the average OEE rate in manufacturing plants is 60%. Therefore, there is potential to improve OEE in many plant areas. World-class OEE is considered 85% or better [38].

After calculating the OEE for all equipment, Pareto analysis (80/20) is applied to identify the group of necessary equipment that accounts for most production losses. These types of equipment are subjected to in-depth analysis to propose appropriate maintenance strategies.

Next, to identify the root causes affecting the OEE index, a fishbone (Ishikawa) diagram is created based on combining real-world data and expert consultation.

OEE is an essential tool to evaluate the performance of equipment, including three main components:

Availability: The time in which the equipment is ready to operate compared to the planned time.
Performance: The actual speed of the equipment compared to the standard speed.
Quality: The rate of products meeting quality requirements compared to the total number of products produced.

After analysis, the study identifies that the factors affecting OEE can be transformed into maintenance strategy evaluation criteria, creating a logical and practical input foundation for the AHP model, which helps to link qualitative data with the systematization of quantitative criteria. The requirements that are consistent with the enterprise's actual goals were identified, ensuring that each AHP criterion accurately reflects the root cause affecting OEE. This bridges the current status analysis of OEE and maintenance strategy decisions, helping the decision-making model to be highly applicable.

3.1.2. Phase 2—Multi-Criteria Decision-Making Using the AHP–TOPSIS Integrated Method and Verifying the Optimal Results

The hybrid optimization method has become helpful in addressing complex decision-making problems, especially in MCDM tasks, where single methods may not be effective enough. This method combines the strengths of various techniques to achieve better optimization results, overcoming the limitations of single methods. AHP determines the weights of essential criteria in evaluating alternatives [39,40], while TOPSIS helps analyze these alternatives based on their distances to the ideal and negative ideal solutions.

Although other methods like PROMETHEE and VIKOR can be applied in MCDM situations, the combination of AHP and TOPSIS offers several advantages. PROMETHEE compares criteria-based alternatives and identifies the best solutions through a scoring

system. However, PROMETHEE lacks a precise mechanism to systematically determine the criteria weights and ensure consistency in these weights, which AHP does very well.

On the other hand, VIKOR is primarily used to identify the "best" solution based on benefit or cost criteria. Still, it depends on establishing a system of weights and priorities for the requirements. VIKOR lacks a straightforward method for determining these weights, whereas AHP offers a rigorous process for calculating and ensuring the consistency of these weights. Moreover, VIKOR may face challenges in handling conflicting or unclear criteria, while AHP addresses these issues through pairwise comparisons and consistency checks. Therefore, the combination of AHP and TOPSIS helps overcome the drawbacks of PROMETHEE and VIKOR, while providing a more transparent, systematic, and efficient decision-making process. This method accurately determines the criteria weights, and then uses them to evaluate and rank alternatives objectively, leading to better decision outcomes.

a. The process of applying the AHP analytical hierarchy method is presented as follows:

Step 1: Define the problem and set its objective.

Step 2: Create a hierarchy from the top (objectives) down to the lower levels (criteria and alternatives).

Step 3: Create pairwise comparison matrices (size $m \times n$) for each lower-level element compared to every other level component immediately above, using the relative scale measurement outlined in [39,40]. The comparisons should indicate which element dominates the other in terms of importance. A total of $n \times (n-1)/2$ udgments are needed to construct the set of matrices in step 3. Reciprocals are automatically assigned in each pair-wise comparison.

Step 4: Hierarchical synthesis weights eigenvectors by criteria weight, summing over all corresponding entries at the next lower level of the hierarchy.

Step 5: After completing all pair-wise comparisons, consistency is assessed using the eigenvalue, λ max, to compute the consistency index (CI) as follows: $CI = (\lambda_{max} - n)/(n-1)$. The size of the matrix, denoted by n determines the consistency. The consistency ratio (CR) of the consistency index (CI) should be compared to the values in [39,40].

Step 6: An acceptable (CR) does not surpass 0.10. If it exceeds this threshold, the judgment matrix is inconsistent. It is necessary to review and enhance the judgments to ensure consistency.

Step 7: Steps 3 to 6 are carried out for every level within the hierarchy.

b. After determining the criteria weights using AHP, TOPSIS ranks the alternatives based on their distance from the ideal and negative ideal solutions.

The main steps in the TOPSIS approach are as follows [41,42]:

Step 8: Based on m alternatives and n criteria, a B matrix with elements b_{ij} is made, where each element denotes the rating of the ith decision maker (DM) with respect to the jth criteria. The matrix is known as the decision matrix, denoted by B:

$$B = (b_{ij})_{m \times n} = \begin{bmatrix} b_{11} & b_{12} & \dots & b_{1n} \\ b_{21} & b_{22} & \dots & b_{2n} \\ \dots & \dots & \dots & \dots \\ b_{m1} & b_{m2} & \dots & b_{mn} \end{bmatrix} \quad (2)$$

Step 9: Normalization of the evaluation matrix:

$$h_{ij} = \frac{b_{ij}}{\sqrt{\sum_i^m b_{ij}^2}} \; i = 1, 2, 3 \; \dots \; \dots \; m, \; j = 1, 2, 3 \; \dots \; \dots \; n \quad (3)$$

This is denoted by H as follows:

$$H = (h_{ij})_{m\times n} = \begin{bmatrix} h_{11} & h_{12} & \dots & h_{1n} \\ h_{21} & h_{22} & \dots & h_{2n} \\ \vdots & \vdots & \vdots & \vdots \\ h_{m1} & h_{m2} & \dots & h_{mn} \end{bmatrix} \quad (4)$$

where m is the number of feasible alternatives and n is the number of criteria.

Step 10: Construction of the weight-normalized decision matrix, which is denoted by Q:

$$Q = (w_j h_{ij})_{m\times n} \quad (5)$$

The weights (w_j) were calculated using the AHP method.

Step 11: Determining the positive ideal solution q_j^+ and negative ideal solution q_j^- by finding the maximum and minimum values of weighted normalized elements in each column for benefit criteria and reverse for cost criteria.

Step 12: Calculate the Euclidean distance for each alternative.

The Euclidean distance from the positive ideal solution is represented by Q_i^+:

$$Q_i^+ = \sqrt{\sum_{i=1}^{n} (q_{ij} - q_j^+)^2},\ i \in \{1, 2, \dots, m\} \quad (6)$$

where $i = 1, 2, \dots, m$; $j = 1,\ 2, \dots,\ n$.

Q_i^- represents the Euclidean distance from the negative ideal solution.

$$Q_i^- = \sqrt{\sum_{i=1}^{n} (q_{ij} - q_j^-)^2},\ i \in \{1, 2, \dots, m\} \quad (7)$$

Step 13: Calculate the relative closeness to the ideal solutions C_I^*. If it is closest to 1, then it depicts the best solution:

$$C_I^* = \frac{Q_i^-}{Q_i^+ + Q_i^-},\ i \in \{1, 2, \dots, m\} \quad (8)$$

Q_i^+ represents the distance from the positive ideal solution, and Q_i^- represents the distance from a negative ideal solution.

Step 14: Rank the alternatives based on their closeness ratio C_I^* in order of preference. The alternative with the shortest distance to the ideal solution is considered the best. The shortest distance to the ideal solution indicates the longest distance from the negative ideal solution.

Next, the reasonableness and reliability of the selected maintenance strategy must be ensured. The EDAS method (Evaluation based on Distance from Average Solution) was chosen as a comparison tool. EDAS evaluates the plans based on the distance to the average value, providing a different perspective to compare with the TOPSIS method. If the rankings are similar, this confirms the stability and reliability of the selected optimal choice.

3.2. Materials

A case study was conducted at an oil and gas company in Vietnam [43] to collect data. The company has come into operation after many years of having maintenance problems with the following issues: reduced production efficiency, increased maintenance costs, and challenges with pressure to improve machinery and equipment maintenance for sustainable production with the environment. Observations are performed on the machine operations,

and the performance data available are recorded. The meeting discussions were conducted to contextualize staff responses and experts' opinions regarding the observations made during the data collection process in the company's maintenance department. The textual data of three years were collected from available historical records, such as downtime, failure time, output, and other data, to determine the OEE of the petrochemical refinery production company.

3.2.1. OEE Measurement and Identify Root Causes

The production line operates daily for 24 h, being evenly divided into three 8 h shifts. The number of working days a week is seven days (including Sundays), and the number of working hours per year is 8760. The research team collected data for the last three years, including defects during each shift, corrective actions to correct errors, downtime, and the exact failure time. Common types of damage in each workstation are damage to the valve system, electrical, mechanical, pneumatic pressure, etc.. . . There may be the same failure mode in different workstations. In each case, the record also includes the failure type, machine, and failed workstation. To serve the process of preparing petroleum, the leading equipment in the plant includes seven devices: towers, heating furnaces, pumping equipment, containers, reaction towers, and valve systems. The process of mixing petroleum will be shown in detail through the technology diagram shown in Figure 2 below.

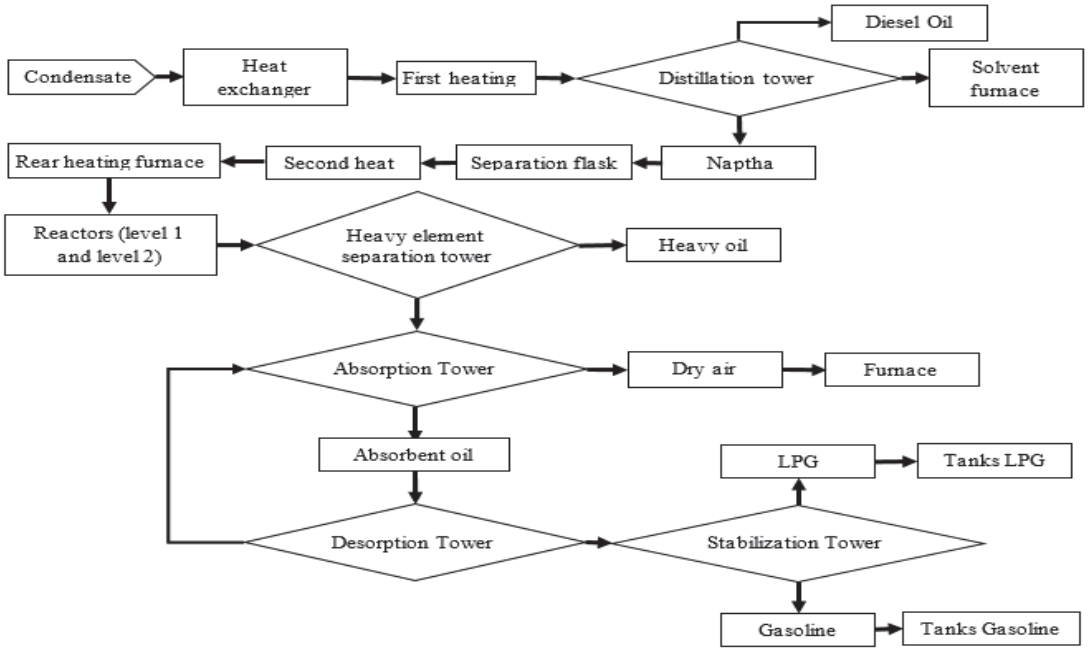

Figure 2. Diagram of the process of mixing petroleum at company.

Research data are collected directly from maintenance department personnel and maintenance department statistics. The factory is divided into 30 leading equipment systems. During data collection, systems that have never been damaged are ignored. Therefore, only 24 systems will be selected for discussion in this study. According to the design, the maximum wattage of the plant is 130,000 tons/year. The real operating time of the equipment in each year is calculated as the sum of operating time in a year of 8760 h minus the number of downtime hours (the number of failures multiplied by the time each failure occurs). The real operation of the machinery is the availability of machinery and equipment. The time when the machinery and equipment are down and the availability time are shown in Table 1.

Table 1. Data of downtime and availability time.

No.	Device System Name	Mean Downtime (MDT) (h/time)			Mean Time Between Failures (MTBF) (h)			Availability (A)		
		2021	2022	2023	2021	2022	2023	2021	2022	2023
1	PRS-1	23.75	25.17	30.05	241.70	355.70	227.60	91.05	93.39	88.34
2	PRS-2	21.67	22.58	28.39	328.73	290.28	263.61	93.82	92.78	90.28
3	PRS-3	16.75	19.25	23.80	233.54	246.20	200.82	93.31	92.75	89.40
4	PRS-4	25.70	25.67	31.93	324.70	339.33	292.51	92.67	92.97	90.16
5	PRS-5	20.75	23.58	25.92	261.83	226.71	324.48	92.66	90.58	92.60
6	PRS-6	20.58	21.62	27.74	222.75	315.30	322.66	91.54	93.58	92.08
7	PRS-8	25.67	26.75	32.89	339.33	265.25	304.03	92.97	90.84	90.24
8	PRS-9	23.75	24.67	29.62	278.32	232.98	195.00	92.14	90.42	86.81
9	PRS-10	17.75	18.67	24.91	284.32	263.91	287.95	94.12	93.39	92.04
10	PRS-11	18.75	20.30	25.14	273.25	216.46	339.86	93.58	91.43	93.11
11	PRS-13	17.75	19.25	24.10	347.25	238.40	200.52	95.14	92.53	89.27
12	PRS-15	18.75	20.22	25.15	231.54	216.54	287.71	92.51	91.46	91.96
13	PRS-16	19.67	22.25	24.95	304.77	260.33	311.97	93.94	92.13	92.59
14	PRS-17	25.67	25.67	30.98	266.33	311.25	271.09	91.21	92.38	89.74
15	PRS-18	18.58	20.17	25.98	273.42	344.83	266.02	93.64	94.47	91.10
16	PRS-19	33.83	32.76	41.92	303.09	240.99	223.53	89.96	88.03	84.21
17	PRS-20	18.58	19.63	25.98	283.49	245.82	239.47	93.85	92.61	90.21
18	PRS-21	17.58	19.26	24.26	319.34	246.19	300.18	94.78	92.74	92.52
19	PRS-22	21.67	22.63	28.96	291.19	227.66	228.69	93.07	90.96	88.76
20	PRS-23	21.67	24.23	28.89	243.78	356.64	308.03	91.84	93.64	91.43
21	PRS-24	23.70	25.22	30.10	278.37	355.65	235.35	92.15	93.38	88.66
22	PRS-25	21.75	22.73	28.48	221.58	259.85	295.96	91.06	91.96	91.22
23	PRS-26	23.67	23.61	28.95	241.78	289.25	195.67	91.08	92.45	87.11
24	PRS-30	32.53	32.78	33.97	291.91	259.22	231.48	89.97	88.77	87.20

The production department has an annual registration of 80–85% of the capacity as a landmark for operation. On the other hand, for the quality ratio, due to the specificity of the oil and gas industry, the input materials through the separation process and the production system will be controlled on the computer by the DCS system, including adjusting the temperature, pressure, and flow rate of semi-finished products during production. When preparing to enter the final stage of exporting finished products, the chemical laboratory staff will be responsible for taking samples for testing. If the test does not pass, the finished product will be transferred to the reflux system for reprocessing. At this time, the parameters of the pressure and temperature conditions will be changed according to the results of the chemistry laboratory. The data on the pressure and temperature of the first flow will be based on experience and standard parameters to adjust until it runs through the finished tank system. Because the process does not have a forecast system for defective products, this causes a waste of raw materials and time and increases production costs. Additionally, the factory inevitably damaged machinery and equipment during production, affecting product quality. The summary table includes the availability index, equipment efficiency, and the ratio of product quality collected directly at the company in the past three years, as shown in Table 2.

Formula 1 is applied to calculate the OEE index shown in Table 3. According to world standards, the standard value of the OEE index must reach 85% or more. The performance of OEE values from 2021 to 2023 is shown in Table 3, indicating that OEE values for the past three years are below the set requirements. More importantly, the company's OEE index tends to decrease over 2021, 2022, and 2023. This signals that the problem of maintenance activities has not been researched, paid attention to, or implemented correctly from the

start. Based on the analysis of the current state of maintenance at the company, many causes still need to be resolved to improve the maintenance work effectively. According to the Pareto principle, this maintenance strategy will be applied at the company for 19 pieces of equipment that affect 80% of the manufacturing downtime. The list is shown in the red frame in Figure 3.

Table 2. Results of overall equipment effectiveness at Orient Oil, Vietnam.

Time	Target Amount of Product	Actual Amount of Product	Total Amount of Quality	Processed Quantity	Availability Index (A) (%)	Performance Efficiency (PE) (%)	Quality Rate (Qr) (%)	OEE (%)
2021	117,000	107,640	102,530.4	110,032	92.59	92.00	93.18	79.37
2022	115,700	104,130	101,334.4	107,640	92.07	90.00	94.14	78.01
2023	118,300	107,653	101,394.2	108,836	90.04	91.00	93.16	76.34

Table 3. Description of leading causes and their impact on OEE components.

Leading Causes	Impact on OEE Components	Detailed Description
Man	Availability, Performance, Quality	Lack of training, incorrect operation, incorrect operating habits, lack of skills
Machine	Availability, Performance	Equipment damage, no spare parts, long repair time
Method	Performance, Quality	Poor maintenance planning, lack of standard procedures, no PM/CMMS
Cost/Material	Availability, Quality	Lack of maintenance budget, no investment in improvement, ineffective use of external services
Environment	Quality, Availability	Temperature, humidity, dust, unsafe working environment, affect product reliability and quality

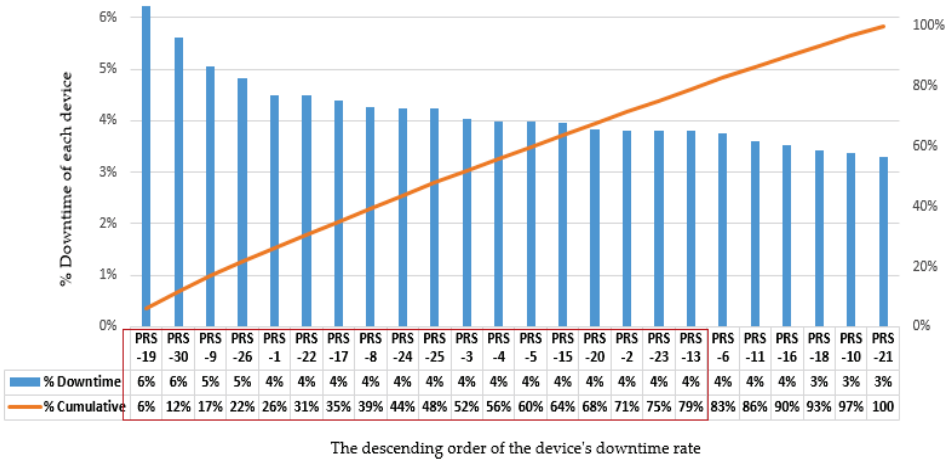

Figure 3. The list of 19 pieces of equipment affects 80% of the manufacturing's downtime.

The study grouped the causes into five main groups, commonly found in industrial manufacturing environments: man, machine, method, cost/material, and environment. To identify the root causes of low OEE, each group of causes was directly linked to the three components that make up the OEE index, namely availability, performance, and quality, to clarify the mechanism that affects the overall operational efficiency of the equipment. This relationship is presented in Table 3.

Next, the Ishikawa method was used to analyze the root cause of low OEE (Fishbone diagram). This diagram is often used for "digging up" the cause after rearranging the causal relationships [44]. The resulting diagram, shown in Figure 4, highlights the five aforementioned categories as the company's principal sources of OEE degradation.

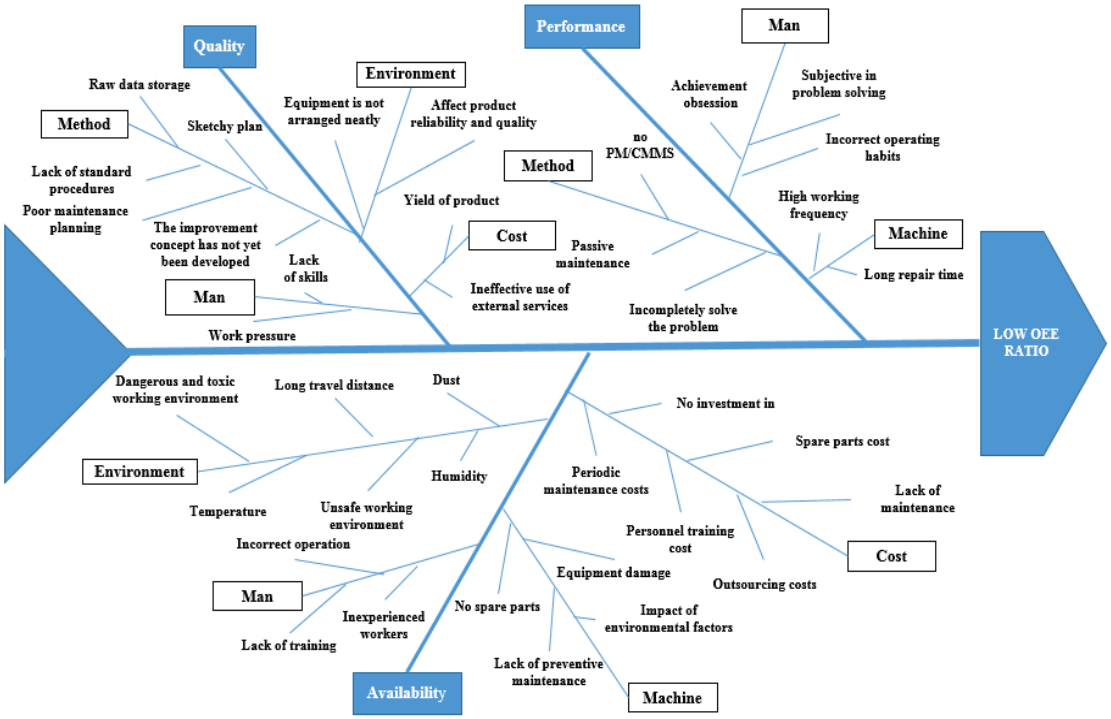

Figure 4. Fishbone chart analysis of the causes affecting OEE.

Through this root cause analysis, the study effectively established a causal pathway linking OEE decline to the company's current maintenance inefficiencies. The next objective is to define criteria to select optimal maintenance strategies. These criteria must comprehensively reflect the underlying causes of poor OEE performance, ensuring that strategic decisions are evidence-based and practically applicable.

Accordingly, a hierarchical structure of decision criteria was developed using the AHP. The model consists of four primary criteria groups, namely cost, safety, efficiency, and flexibility, and eighteen sub-criteria, all directly derived from the root cause categories identified in the Fishbone diagram. This structured framework ensures alignment between observed performance issues and strategy selection. The mapping between the AHP criteria and their associated OEE impacts is presented in Table 4.

Table 4. Relationship between AHP criteria and OEE root causes.

AHP Criteria Group	Detailed Criteria (Link from Fishbone)	Impact on OEE
Cost	- Spare parts availability - Training cost - Outsourced maintenance cost - Productivity loss due to downtime	Availability, Quality
Safety	- Human safety - Equipment safety - Environmental safety	Quality, Availability
Efficiency	- Preventive/prognostic maintenance - Reliability - Investment capacity - Output per hour (UPH) - Operator habit/routine - Repair time/downtime	Availability, Performance, Quality

Table 4. *Cont.*

AHP Criteria Group	Detailed Criteria (Link from Fishbone)	Impact on OEE
Flexibility	- Use of CMMS - Improvement cost - Product variety - Labor acceptance - Maintenance planning flexibility	Performance, Availability

The factors affecting the OEE index have been transformed into input criteria for the decision-making model to select a maintenance strategy. Each AHP criterion reflects the root cause while ensuring that it is consistent with the goals and actual conditions of the enterprise. This transition bridges the current status analysis of OEE and maintenance strategy planning, helping the decision-making model achieve feasibility and high applicability in the industrial environment.

3.2.2. Choosing a Maintenance Strategy

a. Maintenance strategy

After the analysis process, the results are combined with the data collection from the maintenance department managers' needs and related studies. The set input consists of 4 main criteria, and 18 sub-criteria were determined to select the maintenance strategies, including PM, CBM, RBM, RCM, and PdM, as shown in Figure 5.

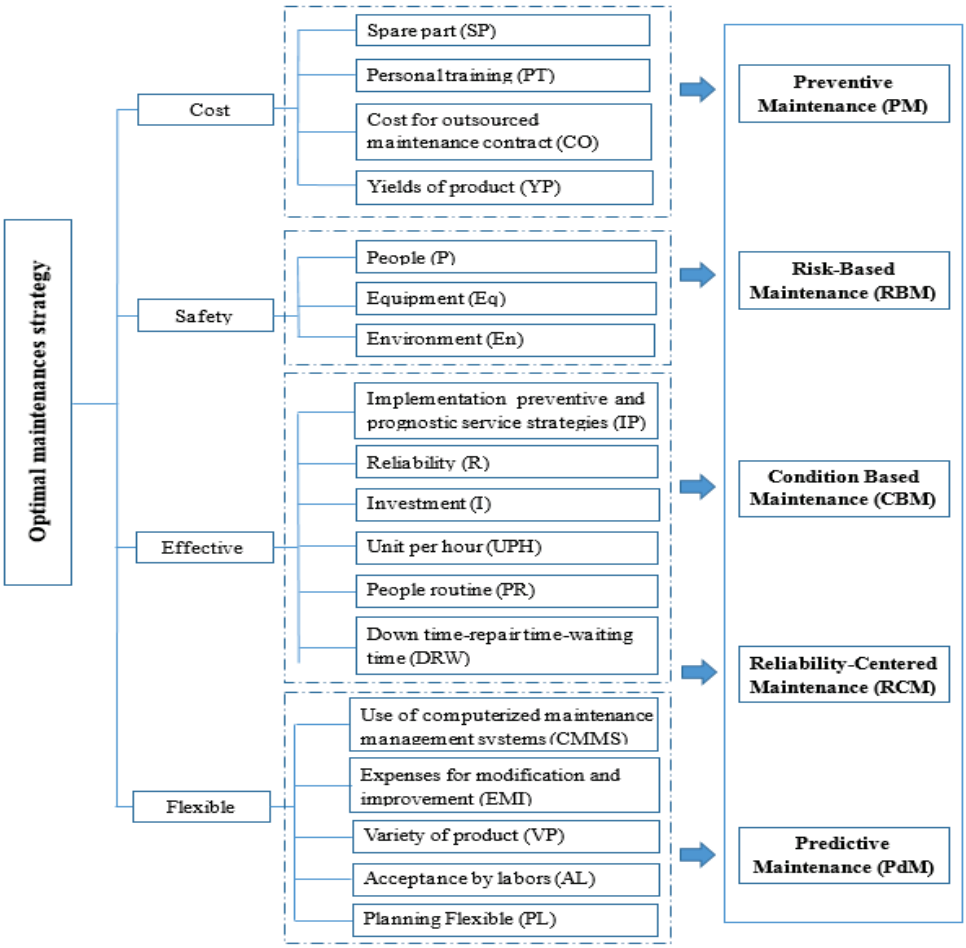

Figure 5. A hierarch of the criteria and maintenance strategy.

4. Results

The maintenance strategy for the refinery is determined using a model that combines the AHP and TOPSIS methods. The AHP method will be used first to assess the weights of the main criteria. From there, the weights for the sub-criteria are calculated based on the weights of the main criteria. After performing pairwise comparisons of the main criteria, the resulting weights are as follows: cost (0.055), safety (0.586), efficiency (0.256), and flexibility (0.102). The evaluation results show that the weight of safety and efficiency criteria is higher than that of cost and flexibility. This result is entirely consistent with the characteristics of the oil and gas industry because safety and efficiency factors will be given more special attention during the production process. The consistency ratio (CR) value was also tested to be 0.04, which is within the acceptable threshold of 0.1.

After determining the relationship between the overall goal and the main criteria, the sub-criteria related to the main criteria will be shown in the pairwise comparison process. The pairwise comparison matrix of the sub-criteria is built by synthesizing the experts' assessments. After standardization, the initial pairwise comparison matrix of the sub-criteria will provide the local weights. Next, the local weights were multiplied by the main criteria weight in Table 5 to find the global weight. The CR for each sub-criteria group is also determined and presented in Table 5.

Table 5. Comparison of each pair of sub-criteria.

			Local Weights					**Global Weights**	**CR**
Cost	SP	PT	CO	YP			0.055		
SP	1.000	0.333	4.000	0.333			0.175	0.010	0.079
PT	3.000	1.000	5.000	2.000			0.459	0.025	
CO	0.250	0.200	1.000	0.333			0.075	0.004	
YP	3.000	0.500	3.000	1.000			0.290	0.016	
Safety	P	Eq	En				0.586		
P	1.000	5.000	2.000				0.556	0.326	0.052
Eq	0.200	1.000	0.200				0.090	0.053	
En	0.500	5.000	1.000				0.354	0.207	
Effective	IP	R	I	UPH	PR	DRW	0.256		
IP	1.000	2.000	1.000	1.000	2.000	2.000	0.218	0.056	0.082
R	0.500	1.000	2.000	1.000	0.500	1.000	0.145	0.037	
I	1.000	0.500	1.000	0.333	2.000	2.000	0.161	0.041	
UPH	1.000	1.000	3.000	1.000	1.000	2.000	0.213	0.055	
PR	0.500	2.000	0.500	1.000	1.000	2.000	0.165	0.042	
DRW	0.500	1.000	0.500	0.500	0.500	1.000	0.097	0.025	
Flexible	CMMS	EMI	VP	AL	PL		0.102		
CMMS	1.000	0.500	0.500	0.333	1.000		0.108	0.011	0.084
EMI	2.000	1.000	0.333	0.333	2.000		0.152	0.016	
VP	2.000	3.000	1.000	3.000	2.000		0.359	0.037	
AL	3.000	3.000	0.333	1.000	3.000		0.273	0.028	
PL	1.000	0.500	0.500	0.333	1.000		0.108	0.011	

Following this, the TOPSIS method was utilized to evaluate and compare the maintenance alternatives based on the weighted criteria obtained from the AHP method. A decision matrix is created based on five alternatives and eighteen criteria, with each element representing the rating of the people surveyed. In the TOPSIS method, the weight of each option related to each criterion is shown in Table 6.

Table 6. The weights of the alternatives and criteria are aggregated using the arithmetic mean.

Main Criteria	Sub Criteria	Maintenance Strategy				
		PM	RBM	CBM	RCM	PdM
Cost	SP	70	50	50	80	70
	PT	90	90	70	90	90
	CO	60	30	50	40	30
	YP	30	20	40	40	20
Safety	P	20	40	50	80	40
	EQ	50	50	50	80	90
	EN	20	40	30	80	60
Effective	IP	20	60	70	90	80
	R	20	50	40	90	60
	I	70	70	60	90	80
	UPH	50	50	30	50	20
	PR	20	50	40	80	40
	DRW	70	40	30	40	20
Flexible	CMMS	20	60	60	90	90
	EMI	20	60	60	90	90
	VP	20	40	30	60	60
	AL	30	40	50	70	50
	PL	20	50	40	80	80

The elements of the decision matrix in Table 6 will be normalized to create the evaluation matrix. This step is performed according to Formulas (3) and (4) of the Methodology Section. After normalizing the elements in Table 7, the weight-normalized decision matrix will be constructed following Formula (5), where the weight (w_j) is calculated using the AHP method. Apply Formulas (6) and (7) to calculate the Euclidean distance for each alternative. The positive ideal solution (q_j^+) and negative ideal solution (q_j^-) are identified by finding the maximum and minimum values of the weighted normalized elements in each column. The results in Table 7 are as follows:

Table 7. Weighted normaliabilized decision matrix.

No.	Criteria	Maintenance Strategy						q_j^+	q_j^-
		PM	RBM	CBM	RCM	PdM	WEIGHT		
1	SP	0.005	0.003	0.003	0.005	0.005	0.010	0.005	0.003
2	PT	0.012	0.012	0.009	0.012	0.012	0.025	0.012	0.009
3	CO	0.003	0.001	0.002	0.002	0.001	0.004	0.003	0.001
4	YP	0.007	0.005	0.009	0.009	0.005	0.016	0.009	0.005
5	P	0.058	0.117	0.146	0.233	0.117	0.326	0.233	0.058
6	EQ	0.018	0.018	0.018	0.029	0.032	0.053	0.032	0.018
7	EN	0.037	0.073	0.055	0.146	0.110	0.207	0.146	0.037
8	IP	0.007	0.022	0.026	0.033	0.029	0.056	0.033	0.007
9	R	0.006	0.015	0.012	0.026	0.018	0.037	0.026	0.006
10	I	0.017	0.017	0.015	0.022	0.020	0.041	0.022	0.015
11	UPH	0.029	0.029	0.017	0.029	0.012	0.055	0.029	0.012
12	PR	0.008	0.019	0.015	0.030	0.015	0.042	0.030	0.008
13	DRW	0.018	0.010	0.008	0.010	0.005	0.025	0.018	0.005
14	CMMS	0.002	0.005	0.006	0.006	0.005	0.011	0.006	0.002
15	EMI	0.002	0.006	0.006	0.009	0.009	0.016	0.009	0.002
16	VP	0.007	0.015	0.011	0.022	0.022	0.037	0.022	0.007
17	AL	0.008	0.010	0.013	0.018	0.013	0.028	0.018	0.008
18	PL	0.002	0.004	0.003	0.007	0.007	0.011	0.007	0.002

The Euclidean distance from the positive ideal solution (Q_i^+) and negative ideal solution (Q_i^-) is calculated for each alternative. The relative closeness to the ideal solutions, denoted as C_I^*, is calculated for each alternative to determine the best solution. Finally, the alternatives are ranked based on their closeness ratio C_I^*. This methodology calculates the close distance ratio (C_I^*) as in Formula (8), with the alternative closest to 1 being considered the best option.

The research results in Table 8 show that RCM is the most optimal maintenance strategy among the five strategies considered, with the ranking order of maintenance strategies being RCM > PdM > CBM > RBM > PM. The results have been verified and compared with the EDAS method; both methods provide the same results, with RCM being the most optimal maintenance strategy. The TOPSIS method will find the difference between the positive ideal value (Q_i^+) and the negative ideal value (Q_i^-), from which the ranking results are provided. From the ranking table, it is found that RCM has the highest score and shows the suitability of this strategy with the optimization criteria set by the company. The results from EDAS also provide similar ranking results, proving the consistency and high accuracy of RCM in optimizing maintenance strategies.

Table 8. The results of optimal maintenance strategy by TOPSIS method.

Maintenance Strategy	TOPSIS Method Results				EDAS Method Results			
	Q_i^+	Q_i^-	C_I^*	RANK	NSPi	NSNi	ASi	RANK
PM	0.212	0.022	0.095	5	0.049	0	0.024	5
RBM	0.141	0.075	0.347	4	0.044	0.364	0.204	4
CBM	0.131	0.092	0.414	3	0.120	0.461	0.291	3
RCM	0.009	0.212	0.961	1	1	0.854	0.927	1
PdM	0.126	0.100	0.443	2	0.257	0.469	0.363	2

The EDAS is a method for comparing and evaluating alternatives based on their distance from the average solution. This method was chosen to verify the results from TOPSIS because EDAS provides an independent approach with a more intuitive assessment of the suitability of maintenance strategies in real environments. Compared with TOPSIS, EDAS can be more flexible in handling heterogeneous and complex factors in production systems. The application of EDAS has demonstrated that the ranking results of RCM are stable and accurate in evaluating maintenance strategies, increasing the reliability of the research results. Both methods provide consistent results, indicating the rationality and high applicability of the RCM strategy. In addition to the verification by the EDAS method, the study also provides insight into the combination of AHP and TOPSIS methods in evaluating and comparing maintenance strategies. This method helps to determine the optimal strategy and clarifies the relationship between the criteria and the priority level of each factor. The result is a clear, reasonable, and convenient ranking that supports managers in making accurate and optimal decisions for the company. Another critical factor is the cost and feasibility of implementation. Hybrid methods such as GA or SA require significant computational resources and may require a long time to find the optimal solution. Meanwhile, TOPSIS can be implemented more easily in manufacturing companies, helping to save costs and reduce implementation time while ensuring maintenance efficiency. More importantly, TOPSIS considers each criterion separately and analyzes the relationship between the factors and the overall system, helping to optimize production performance and reduce maintenance costs comprehensively.

Moreover, RCM is theoretical and very practical when applied to industrial environments. Implementing the RCM strategy helps minimize failures, improve system reliability, and reduce overall maintenance costs, thanks to focusing on the most critical factors in the

maintenance process and ensuring that maintenance resources are allocated reasonably. RCM is suitable for the company in the study and has broad applicability in the petrochemical refining industry. The petrochemical refining systems are highly complex and require excellent operational reliability and stability. The application of RCM helps optimize maintenance for these systems, minimize unexpected incidents, improve performance, and reduce maintenance costs. Therefore, RCM is an ideal choice for industries with complex maintenance requirements and high stability requirements, such as petrochemical refining.

Thus, this study provides a powerful tool to help the company choose the most optimal maintenance strategy and demonstrates the high practical applicability of the TOPSIS method in the petrochemical refining and production industry. Implementing an RCM strategy in the company will contribute to stable operation, improve maintenance efficiency, minimize incidents, optimize maintenance resources, and reduce overall costs for the business.

5. Discussion

The results of this study have emphasized the importance and necessity of maintenance activities in improving operational efficiency, minimizing downtime, and improving OEE in the oil blending sector of the oil and gas industry. The OEE measurement results of the enterprise show that the operational efficiency has been on a continuous downward trend over the past three years, with a value lower than the global standard of 85%. This situation further highlights the urgency of developing and applying a more effective maintenance strategy based on practical data.

To address this pressing issue, the study proposed applying the AHP-TOPSIS combined methodology framework in the MCDM system to evaluate and select the optimal maintenance strategy. It should be noted that the AHP-TOPSIS-integrated approach was first applied in the oil and gas sector to choose a maintenance strategy based on the criteria: safety, cost, efficiency, and flexibility. The application of AHP-TOPSIS allows for the systematic evaluation of multiple criteria at the same time, thereby enhancing consistency in the decision-making process in the oil and gas industry.

The outstanding contribution of the study is the construction of a comprehensive evaluation framework, including a detailed decision matrix and quantitative analysis of the criteria, ensuring that the evaluation process is based on real data and can be reproduced in subsequent studies.

Moreover, to bridge the gap between theoretical analysis and practical application, the study conducted compares the potential suitability of maintenance strategies by analyzing the advantages and disadvantages of each option in the actual context of the oil and gas industry, as shown in Table 9.

Although all five maintenance strategies have advantages, the company's long-term goal is to enhance the OEE index and reduce production losses due to equipment failures. Meanwhile, the RCM strategy balances operational efficiency, safety, and cost-effectiveness. Notably, compared with the existing literature [25,45], the study also shows consistent results: RCM is often favored in environments that require operational excellence but have not yet achieved a complete digital transformation. This indicates that the recommendation of RCM in this study is based on data and the context of the Vietnamese oil and gas industry.

The study is based on the AHP-TOPSIS results and was reconfirmed by the EDAS method, showing high consistency and reliability throughout the strategy selection process. This cross-validation confirms that RCM consistently outperforms other strategies, providing scientific rigor and additional credibility to the results.

Table 9. Comparison of maintenance strategies for the oil and gas industry.

Strategy	Advantages	Disadvantages
RCM (Reliability-Centered Maintenance)	- Focuses on critical failure modes for optimal resource allocation - Balances cost, safety, and reliability - Proactively reduces unexpected breakdowns - Improves system reliability and availability	- Requires extensive data analysis and system knowledge - High initial implementation effort (e.g., training, FMEA tools)
PdM (Predictive Maintenance)	- Enables real-time failure prediction using advanced sensors and data analytics - Reduces unnecessary maintenance and extends equipment life - Supports better planning and resource use	- High initial investment in technology and infrastructure - Requires technical expertise for data interpretation
CBM (Condition-Based Maintenance)	- Avoids over-maintenance by acting only when the conditions warrant it - Effective in preventing unexpected breakdowns - Improves spare parts and labor utilization	- Demands continuous condition monitoring - Requires skilled personnel and adds system complexity
RBM (Risk-Based Maintenance)	- Prioritizes high-risk assets, ensuring efficient allocation of resources - Supports decision-making under uncertainty	- Lacks real-time condition monitoring - Can overlook lower-risk assets, leading to eventual inefficiencies
PM (Preventive Maintenance)	- Simple to implement and widely understood - Reduces chances of sudden equipment failure through scheduled checks	- Based on time/usage intervals, not actual equipment condition - Can lead to unnecessary downtime and increased cost

In terms of practical implementation, although PdM and CBM strategies also demonstrate modernity and are ranked higher after RCM, the significant technological investment costs and operational complexity barriers make mass adoption difficult, especially for companies with limited infrastructure.

Meanwhile, RCM allows for a more systematic implementation roadmap, starting with training personnel in the analysis process and applying computerized maintenance management systems (CMMSs) and failure analysis tools such as FMEA. Furthermore, staying ahead of emerging technologies like IoT and machine learning can enhance the predictive capabilities of RCM, moving the strategy closer to real-time, intelligent maintenance ecosystems.

However, the study still has some limitations:

Reliance on manual data: Data collection from personnel and manual recording can lead to bias or inconsistencies.

Limited data scope: The data were collected from a single enterprise, while operational and maintenance factors can vary significantly across manufacturing facilities or industries.

Limitations in applying modern technology: Although advanced strategies such as PdM or CBM have potential, they have not been widely deployed due to high investment and infrastructure requirements.

In conclusion, the study provides a quantitative, transparent, and scalable approach to maintenance strategy selection. It promotes operational efficiency, reduces costs, and increases sustainability in oil and gas production. Adopting RCM as a central strategy can be a practical solution for many businesses in the industry to achieve sustainable development and long-term competitiveness.

6. Conclusions

6.1. Findings

The findings of this study show the integrated model of the MCDM techniques (AHP, TOPSIS) along with the OEE index and verification using EDAS, which is useful specifically within the unique operational context and challenges of the oil and gas industry. This integrated framework provides a systematic, quantitative approach to maintenance strategy selection, which was previously limited in detailed studies within this sector. The structured process, from analyzing OEE and identifying root causes via the Fishbone diagram, defining the criteria and sub-criteria linked to these causes, determining criteria weights using AHP, evaluating and ranking strategies with TOPSIS based on these weighted criteria, to finally verifying the results with EDAS, represents the novel comprehensive methodology applied to the oil and gas industry-specific problem. This model uses a data-based decision, ensuring alignment with the company's goals and conditions.

The study shows that RCM is theoretical and practical when applied to industrial environments. RCM is the optimal choice based on a systematic, data-driven, multi-criteria evaluation tailored to the specific context of the oil and gas industry. Additionally, implementing RCM helps minimize failures, improve system reliability, and reduce maintenance costs by focusing on critical factors and allocating resources reasonably. RCM is highlighted as suitable for the company in this study and has broad applicability in the petrochemical refining industry due to its complexity and requirement for high reliability and stability.

6.2. Contributions

The study proposed several significant contributions to both academic research and industrial practice.

The scholarly contributions include proposing a novel hybrid approach combining AHP and TOPSIS for maintenance strategy selection in the oil and gas industry and expanding the theoretical foundation in industrial maintenance. It marks the first application of the AHP-TOPSIS method to maintenance strategy selection within this sector, using safety, cost, efficiency, and flexibility as evaluation criteria. The study also validates the EDAS method as a cross-validation tool. It provides a structured, data-driven decision support tool applicable across various industries. Moreover, the research emphasizes the significance of the OEE index as a metric for evaluating performance and identifying maintenance needs. It employs a Fishbone diagram to analyze the primary factors impacting OEE in oil and gas companies. It offers a detailed analysis and comparison of five maintenance strategies (PM, RBM, CBM, RCM, and PdM) within the oil and gas industry context. It explores four main criteria and their eighteen sub-criteria for selection. The study also proposes future research directions and demonstrates the application of the AHP-TOPSIS model in an honest company. It quantitatively presents criteria weights and TOPSIS/EDAS results, explicitly highlighting its novelty in applying these techniques tailored to the oil and gas industry's unique challenges.

In addition, industrial contributions include providing oil and gas enterprises with a systematic, data-driven methodology for selecting the optimal maintenance strategy and facilitating consistent and efficient decision-making. It emphasizes the crucial role of the correct maintenance strategy in enhancing OEE, reducing downtime, and lowering costs. The case study results indicate that RCM is the most optimal strategy for the studied company, offering superior performance and reliability. It provides a feasibility analysis for RCM in real industrial settings, highlighting its potential benefits and comparing different strategies regarding cost-effectiveness and implementation. The study underscores RCM's alignment with the oil and gas industry's high emphasis on safety and efficiency and suggests concrete steps for RCM's implementation. It highlights RCM's broad applicability

in complex petrochemical refining systems and quantitatively indicates the company's declining OEE, emphasizing the urgency for improved strategies.

6.3. Future Research Directions

Future research could develop a predictive maintenance model that integrates advanced technologies, building a predictive maintenance framework incorporating advanced technologies such as the Industrial Internet of Things (IIoT), artificial intelligence (AI), and machine learning. This model could provide real-time data analysis, the early detection of failure signals, and automatically recommend an optimal maintenance plan for each piece of equipment in the oil blending system.

In addition, the study may extend to test the sensitivity of changing the weight of each criterion to consider how the results depend on the criterion weights, especially safety and cost, which might influence the rankings of different maintenance strategies.

Moreover, the research may also compare maintenance strategies across the automotive, electronics, and chemical manufacturing industries. Evaluating similarities and differences in the selection and implementation of maintenance strategies would help identify each industry's best way to implement and provide a basis for the flexible adaptation and application of RCM or a hybrid approach.

Author Contributions: The authors confirm their contribution to the paper as follows: study conception and design: C.-N.W. and M.-H.H.; data collection: Q.-T.D. and T.D.-M.L.; analysis and interpretation of results: D.-O.T.T. and C.-N.W.; draft manuscript preparation: T.D.-M.L. and D.-O.T.T. All authors have read and agreed to the published version of the manuscript.

Funding: This article is partially supported by the NSTC 113-2622-E-992-012 project.

Data Availability Statement: The authors confirm that the data supporting the findings of this study are available within the article.

Conflicts of Interest: Author Q.-T.D. was employed by the company Orient Oil and Gas Joint Stock Company. The remaining authors declare that the research was conducted in the absence of any commercial or financial relationships that could be construed as a potential conflict of interest. The Orient Oil and Gas Joint Stock Company, in affiliation and funding, had no role in the design of the study; in the collection, analyses, or interpretation of data; in the writing of the manuscript, or in the decision to publish the results.

References

1. Velmurugan, R.S.; Dhingra, T. Maintenance strategy selection and its impact in maintenance function: A conceptual framework. *Int. J. Oper. Prod. Manag.* **2015**, *35*, 1622–1661. [CrossRef]
2. Zhong, D.; Xia, Z.; Zhu, Y.; Duan, J. Overview of predictive maintenance based on digital twin technology. *Heliyon* **2023**, *9*, e14534. [CrossRef] [PubMed]
3. Vyasa, V.; Xu, Z. Maintenance in automotive and aerospace applications—An overview. *Int. J. Adv. Sci. Trans.* **2024**, *3*, 349–361.
4. Alsyouf, I. The role of maintenance in improving companies' productivity and profitability. *Int. J. Prod. Econ.* **2007**, *105*, 70–78. [CrossRef]
5. Dowlatshahi, S. The role of industrial maintenance in the maquiladora industry: An empirical analysis. *Int. J. Prod. Econ.* **2008**, *114*, 298–307. [CrossRef]
6. Oluwatoyin, O.A.; Afolalu, S.A.; Monye, S.I. Maintenance Impact on Production Profitability in Industry—An Overview. In Proceedings of the 2024 International Conference on Science, Engineering and Business for Driving Sustainable Development Goals (SEB4SDG), Omu-Aran, Nigeria, 2–4 April 2024; IEEE: Piscataway, NJ, USA, 2024.
7. Mostafa, S.; Lee, S.-H.; Dumrak, J.; Chileshe, N.; Soltan, H. Lean thinking for a maintenance process. *Prod. Manuf. Res.* **2015**, *3*, 236–272. [CrossRef]
8. Kothamasu, R.; Huang, S.H. Adaptive Mamdani fuzzy model for condition-based maintenance. *Fuzzy Sets Syst.* **2007**, *158*, 2715–2733. [CrossRef]
9. Pinjala, S.K.; Pintelon, L.; Vereecke, A. An empirical investigation on the relationship between business and maintenance strategies. *Int. J. Prod. Econ.* **2006**, *104*, 214–229. [CrossRef]

10. Yang, L.; Zhao, Y.; Peng, R.; Ma, X. Opportunistic maintenance of production systems subject to random wait time and multiple control limits. *J. Manuf. Syst.* **2018**, *47*, 12–34. [CrossRef]
11. Jaqin, C.; Alimudin, D.; Purba, H.H.; Aisyah, S. Performance Improvement of Injection Pump Machines Based on Overall Equipment Effectiveness: Case Study in Oil Company. In Proceedings of the 2019 1st International Conference on Engineering and Management in Industrial System (ICOEMIS 2019), Malang, Indonesia, 8–9 August 2019; Atlantis Press: Dordrecht, The Netherlands, 2019.
12. Emovon, I.; Norman, R.A.; Murphy, A.J. Hybrid MCDM based methodology for selecting the optimum maintenance strategy for ship machinery systems. *J. Intell. Manuf.* **2018**, *29*, 519–531. [CrossRef]
13. Seiti, H.; Hafezalkotob, A. Developing the R-TOPSIS methodology for risk-based preventive maintenance planning: A case study in rolling mill company. *Comput. Ind. Eng.* **2019**, *128*, 622–636. [CrossRef]
14. Kirubakaran, B.; Ilangkumaran, M. Selection of optimum maintenance strategy based on FAHP integrated with GRA–TOPSIS. *Ann. Oper. Res.* **2016**, *245*, 285–313. [CrossRef]
15. Wang, C.-N.; Pan, C.-F.; Nguyen, H.-P.; Fang, P.-C. Integrating fuzzy AHP and TOPSIS methods to evaluate operation efficiency of daycare centers. *Mathematics* **2023**, *11*, 1793. [CrossRef]
16. Hemmati, N.; Rahiminezhad Galankashi, M.; Imani, D.; Mokhatab Rafiei, F. An integrated fuzzy-AHP and TOPSIS approach for maintenance policy selection. *Int. J. Qual. Reliab. Manag.* **2020**, *37*, 1275–1299. [CrossRef]
17. Jamali, N.; Feylizadeh, M.R.; Liu, P. Prioritization of aircraft maintenance unit strategies using fuzzy Analytic Network Process: A case study. *J. Air Transp. Manag.* **2021**, *93*, 102057. [CrossRef]
18. Bayoumi, A.; McCaslin, R. Internet of things–a predictive maintenance tool for general machinery, petrochemicals and water treatment. In *Advanced Technologies for Sustainable Systems: Selected Contributions from the International Conference on Sustainable Vital Technologies in Engineering and Informatics, Proceedings of the BUE ACE1 2016, Cairo, Egypt, 7–9 November 2016*; Springer: Berlin/Heidelberg, Germany, 2017.
19. Hameed, A.; Khan, F. A framework to estimate the risk-based shutdown interval for a processing plant. *J. Loss Prev. Process Ind.* **2014**, *32*, 18–29. [CrossRef]
20. Cai, Y.; Teunter, R.H.; de Jonge, B. A data-driven approach for condition-based maintenance optimization. *Eur. J. Oper. Res.* **2023**, *311*, 730–738. [CrossRef]
21. Braglia, M.; Castellano, D.; Frosolini, M. An integer linear programming approach to maintenance strategies selection. *Int. J. Qual. Reliab. Manag.* **2013**, *30*, 991–1016. [CrossRef]
22. Zhang, W.; Yang, D.; Wang, H. Data-driven methods for predictive maintenance of industrial equipment: A survey. *IEEE Syst. J.* **2019**, *13*, 2213–2227. [CrossRef]
23. Alfahdi, K.; Gultekin, H.; Summad, E. A Novel Prognostics and Health Management Framework to Extract System Health Requirments in the Oil and Gas Industry. *Int. J. Progn. Health Manag.* **2024**, *15*, 2213–2227. [CrossRef]
24. Prajapati, A.; Bechtel, J.; Ganesan, S. Condition based maintenance: A survey. *J. Qual. Maint. Eng.* **2012**, *18*, 384–400. [CrossRef]
25. Zeinalnezhad, M.; Chofreh, A.G.; Goni, F.A.; Klemeš, J.J. Critical success factors of the reliability-centred maintenance implementation in the oil and gas industry. *Symmetry* **2020**, *12*, 1585. [CrossRef]
26. Ylipää, T.; Skoogh, A.; Bokrantz, J.; Gopalakrishnan, M. Identification of maintenance improvement potential using OEE assessment. *Int. J. Product. Perform. Manag.* **2017**, *66*, 126–143. [CrossRef]
27. Theissler, A.; Pérez-Velázquez, J.; Kettelgerdes, M.; Elger, G. Predictive maintenance enabled by machine learning: Use cases and challenges in the automotive industry. *Reliab. Eng. Syst. Saf.* **2021**, *215*, 107864. [CrossRef]
28. Einabadi, B.; Mahmoodjanloo, M.; Baboli, A.; Rother, E. Dynamic predictive and preventive maintenance planning with failure risk and opportunistic grouping considerations: A case study in the automotive industry. *J. Manuf. Syst.* **2023**, *69*, 292–310. [CrossRef]
29. Arinze, C.A.; Izionworu, V.O.; Isong, D.; Daudu, C.D.; Adefemi, A. Predictive maintenance in oil and gas facilities, leveraging ai for asset integrity management. *Int. J. Front. Eng. Technol. Res.* **2024**, *6*, 16–26. [CrossRef]
30. Mallioris, P.; Aivazidou, E.; Bechtsis, D. Predictive maintenance in Industry 4.0: A systematic multi-sector mapping. *CIRP J. Manuf. Sci. Technol.* **2024**, *50*, 80–103. [CrossRef]
31. Faghihinia, E.; Mollaverdi, N. Building a maintenance policy through a multi-criterion decision-making model. *J. Ind. Eng. Int.* **2012**, *8*, 14. [CrossRef]
32. Pei, Y.; Liu, Z.; Xu, J.; Qi, B.; Cheng, Q. Grouping preventive maintenance strategy of flexible manufacturing systems and its optimization based on reliability and cost. *Machines* **2023**, *11*, 74. [CrossRef]
33. Liu, X.-W.; Li, C.-Y.; Dang, S.; Wang, W.; Qu, J.; Chen, T.; Wang, Q.-L. Research on training effectiveness of professional maintenance personnel based on virtual reality and augmented reality technology. *Sustainability* **2022**, *14*, 14351. [CrossRef]
34. Ng Corrales, L.d.C.; Lambán, M.P.; Hernandez Korner, M.E.; Royo, J. Overall equipment effectiveness: Systematic literature review and overview of different approaches. *Appl. Sci.* **2020**, *10*, 6469. [CrossRef]

35. Prasetyo, Y.T.; Veroya, F.C. An application of overall equipment effectiveness (OEE) for minimizing the bottleneck process in semiconductor industry. In Proceedings of the 2020 IEEE 7th International Conference on Industrial Engineering and Applications (ICIEA), Bangkok, Thailand, 16–18 April 2020; IEEE: Piscataway, NJ, USA, 2020.
36. Dovere, E.; Cavalieri, S.; Ierace, S. RFId systems for moveable asset management: An assessment model. *Int. J. Prod. Res.* **2017**, *55*, 1336–1349. [CrossRef]
37. Hwang, G.; Lee, J.; Park, J.; Chang, T.-W. Developing performance measurement system for Internet of Things and smart factory environment. *Int. J. Prod. Res.* **2017**, *55*, 2590–2602. [CrossRef]
38. Gupta, A.K.; Garg, R. OEE improvement by TPM implementation: A case study. *Int. J. IT Eng. Appl. Sci. Res.* **2012**, *1*, 115–124.
39. Pant, S.; Kumar, A.; Ram, M.; Klochkov, Y.; Sharma, H.K. Consistency indices in analytic hierarchy process: A review. *Mathematics* **2022**, *10*, 1206. [CrossRef]
40. Rios, R.; Duarte, S. Selection of ideal sites for the development of large-scale solar photovoltaic projects through Analytical Hierarchical Process–Geographic information systems (AHP-GIS) in Peru. *Renew. Sustain. Energy Rev.* **2021**, *149*, 111310. [CrossRef]
41. Chakraborty, S. TOPSIS and Modified TOPSIS: A comparative analysis. *Decis. Anal. J.* **2022**, *2*, 100021. [CrossRef]
42. Madanchian, M.; Taherdoost, H. A comprehensive guide to the TOPSIS method for multi-criteria decision making. *Sustain. Soc. Dev.* **2023**, *1*, 2220. [CrossRef]
43. Orient Oil and Gas Joint Stock Company. Available online: https://www.topcv.vn/cong-ty/cong-ty-co-phan-dau-khi-dong-phuong/103004.html (accessed on 20 April 2025).
44. Luo, T.; Wu, C.; Duan, L. Fishbone diagram and risk matrix analysis method and its application in safety assessment of natural gas spherical tank. *J. Clean. Prod.* **2018**, *174*, 296–304. [CrossRef]
45. Van Nguyen, T. Research on solutions for connecting to marginal fields at Cuu Long basin to process and transport the products basing on existing petroleum technology and equipment. *J. Min. Earth Sci. Vol.* **2021**, *62*, 65–75. [CrossRef]

processes

MDPI

Article

What's Hot and What's Not—A Simulation-Based Methodology for Fire Risk Assessment in Lead-Acid Battery Manufacturing

Ankidim Zinveli *, Mihai Dragomir * and Diana Dragomir

Department of Design Engineering and Robotics, Faculty of Industrial Engineering, Robotics and Production Management, Technical University of Cluj-Napoca, 400641 Cluj-Napoca, Romania; diana.dragomir@muri.utcluj.ro

* Correspondence: ankidim.zinveli@muri.utcluj.ro (A.Z.); mihai.dragomir@muri.utcluj.ro (M.D.)

Abstract: The present paper addresses dynamic risks in automotive industry factories, specifically in the car lead-acid battery manufacturing area. The main analyzed risk is fire risk. The battery manufacturing process is described and analyzed from this perspective, and the hazard areas are identified. The investigation methodology uses case studies for different lead-acid battery formation processes, combined with 3D simulations using the PyroSim platform, and it is based on our practical experience in the battery manufacturing field. The results of the case studies are compared using the same inputs but specific process conditions, and conclusions are formulated. To avoid fires and mitigate the risk, a series of actions are proposed in the discussion section. As a general conclusion, the current research demonstrates that the complex and dynamic risks in the automotive industry, associated with Industry 5.0 technologies, must be analyzed using combined methods, both quantitative and qualitative, including 3D simulations.

Keywords: risk assessment; fire risk; battery manufacturing; automotive industry; lead-acid batteries

1. Introduction

In our previous research and articles, we found that automotive industry companies adopting digitization and technologies specific to the fourth and fifth industrial revolutions face dynamic risks that are complex and difficult to control and mitigate [1,2]. After analyzing and testing various risk assessment methods, we concluded that developing a specific generic model for the automotive industry is essential, considering emerging technologies. Organizations should combine qualitative and quantitative analysis methods to discover and mitigate risks effectively [3]. Considering these aspects, this research aims to carry out validation case studies on complex dynamic risks in automotive industry companies, with the most relevant being fires in various phases of the manufacturing process, which are unpredictable and impactful. We chose the manufacturing of lead-acid batteries, considering the future market trend of these batteries and the industry's development towards efficiency and sustainability. Although in recent years, the main focus of automotive battery manufacturing has been on lithium-based batteries and related technologies such as $LiFePO_4$ and Nickel Cadmium, lead-acid technology batteries still have and will continue to have a significant demand, reflected in the total number of batteries produced worldwide, as shown in the statistics by GS Yuasa in Figure 1 [4]. Their reliability and proven track record make these batteries a necessity even for electric vehicles. Their manufacturing is expected to improve to keep up with changing customer expectations and the evolving regulatory landscape.

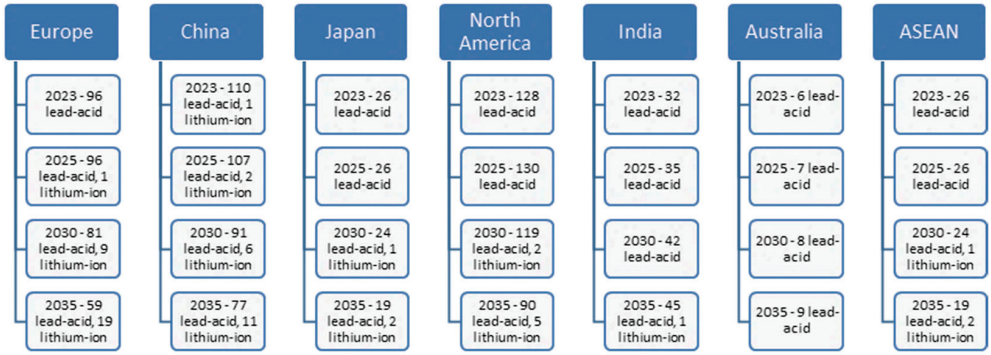

Figure 1. Worldwide car battery demand forecast, 2023–2035, in million units [4].

The significant demand for lead-acid batteries is due to the continued manufacturing of conventional cars with combustion engines until 2035 and possibly beyond. Additionally, most hybrid and fully electric cars still use a lead-acid battery as an auxiliary battery for backup and stationary consumption support, because these batteries are much cheaper, electrically efficient, and more stable than lithium technologies. Even though the switch to electric cars aims to reduce the carbon footprint and achieve zero emissions by 2035 [5], the reality is that lithium-based batteries are currently more polluting and have a lower recycling rate, which also involves higher costs. According to Romanian battery manufacturer Rombat's official website, the recycling rate of lead from wasted batteries is about 99% [6], and based on our experience, the overall recycling rate of all battery materials can reach 84%. The significant advantage of lead is that it can be infinitely recycled and reused with minimal loss.

Within the current research, we aim to test the methodology proposed in our previous studies and to apply a combined analysis model to a real automotive company that uses a 360-degree battery manufacturing process, located in Romania. The manufacturer has implemented automated processes with collaborative robots, IIoT (Industrial Internet of Things) processes, and monitoring and planning using SCADA (Supervisory Control and Data Acquisition) and SAP ERP (Enterprise Resource Planning). Most of the production is concentrated on lead-based batteries, but it also sells lithium-based batteries dedicated solely to energy storage in small volumes at this time.

Lithium-based batteries are more often associated with fires, due to the "thermal runaway" phenomenon that occurs during use (in the car or at the storage site) caused by internal manufacturing defects or exploitation problems [7]. However, such incidents are very rare at the production plant due to strictly supervised processes. The literature provides several research studies and case studies on fire risk causes and mitigation solutions, including fire extinction methods, as can be seen in articles [8–10] and others. Compared with lithium batteries, lead-based batteries are much safer and more stable during use because of the reduced possibility of generating a fire, as the battery itself is smaller in size. However, we focused on lead-based technologies because there are many manufacturers worldwide, and the risks are more associated with the manufacturing process than with the product itself. Additionally, for sustainable development, the safety of employees is critical.

2. Materials and Methods

At the beginning of the study, we created the research methodology based on best practices specific to the field of engineering management (Figure 2).

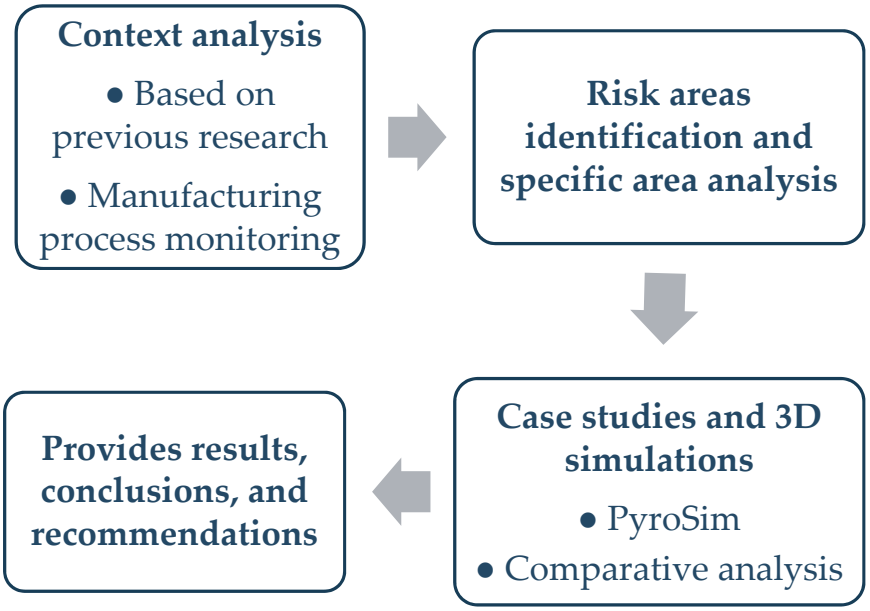

Figure 2. Research methodology.

The introduction is based on our previous research and experience in lead-acid battery manufacturing. We decided to analyze fire risk using case studies and 3D simulations. To provide a proper context, we first describe car lead-acid batteries and then present the complete manufacturing process. Next, we identify and present the risk areas. These risks are analyzed in the case studies by presenting the theoretical background for each specific area, and 3D simulations are performed using PyroSim software to test the hypotheses and demonstrate their effects. The simulation results are analyzed using graphs and numerical data, forming the basis for pertinent conclusions and recommendations for manufacturers in this field. The research instruments include case studies, SolidWorks Premium 2020 SP01 software for modeling some parts, PyroSim 3D fire simulation software, and graphs and tables for comparative analyses. The most complex instrument is the PyroSim software, version 2023.3.1312 X64, provided to the team through a six-month free license by Thunderhead Engineering Software House, Manhattan, KS, USA. This software offers a 3D interface, as shown in Figure 3, allowing users to model the desired areas and objects and generate numeric results and graphs based on fire knowledge and user inputs [11].

Objects can be modeled directly in the application or imported from other programs such as Autodesk or SolidWorks. For this study, we modeled the production area to create a realistic simulation. All the specific points, such as access doors, windows, vents, and exhaust systems, were defined, along with input parameters like dimensions, airflow, the materials involved, and burning areas. The burning areas were defined using the software library and were represented in our research by polypropylene and a gas mix of hydrogen and oxygen. Default parameters can be used or modified based on user experience. Additionally, the simulation time, frame number, display mode, and other parameters can be set. Depending on these settings, the simulation can take from a few minutes to several hours, allowing for a detailed investigation of phenomena.

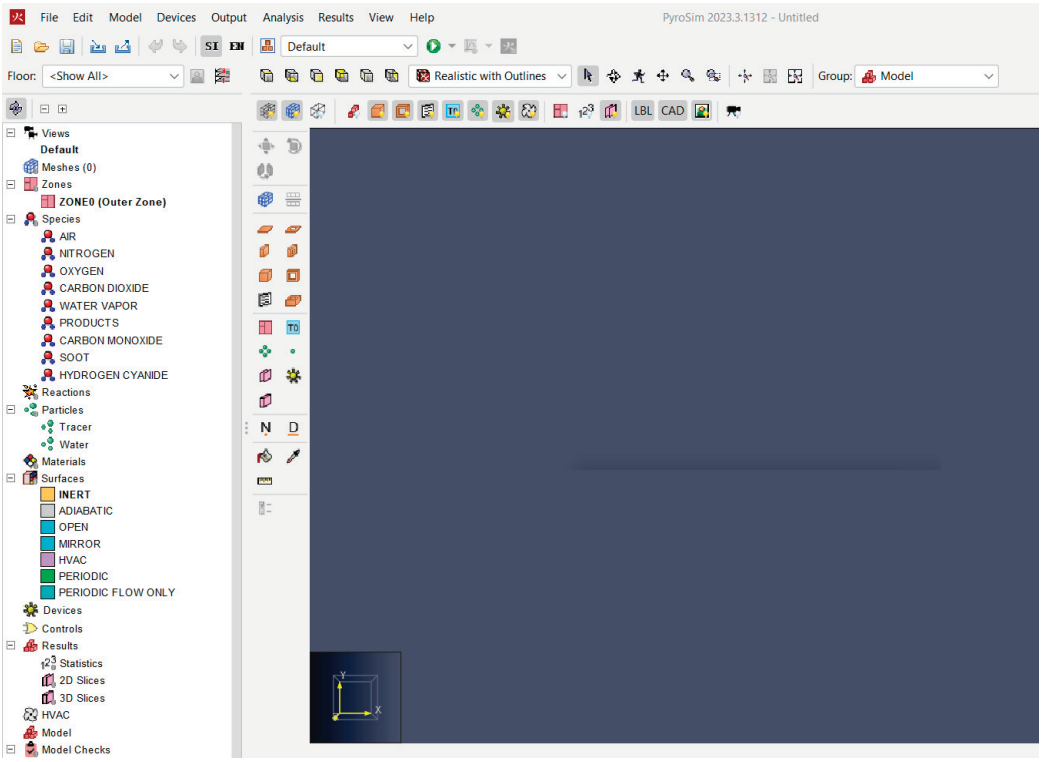

Figure 3. PyroSim Start Interface (screenshot from [12]).

3. Results

3.1. Lead-Acid Batteries and Manufacturing Process Description

3.1.1. Car Lead-Acid Batteries—Overview

Lead-acid batteries for cars are a type of battery that quickly charges and discharges, providing energy for starting the engine and supporting consumption while the engine is off. This is why they are called SLI batteries (Starting, Lighting, Ignition). These batteries have a long history of about 150 years and were invented by Gaston Plante in 1859 [13,14]. Initially, they were developed to provide a nominal OCV (Open Circuit Voltage) of 6 volts. However, after 1950, they switched to 12 volts due to higher consumption and engines that required a higher power supply [15]. Modern batteries provide 12 volts and are built with six individual cells. Each cell contains groups of positive and negative plates that provide a nominal voltage of 2 volts and are connected in series, as shown in Figure 4. The most basic parts are the positive and negative grids, made of lead and alloyed with different materials according to the manufacturer's specifications. These grids are produced using various technologies such as punching, expanding, and continuous casting. A paste made of lead oxide is applied to the grids to create positive plates, while metallic lead is used for negative plates. The positive and negative plates are connected separately with a lead strap called the Cast On Strap, which is cast into a mold with melted lead alloy, forming the terminals on the sides. The plates are separated using different separators, such as polyethylene bags or glass mat foil, depending on the battery technology. Inside the box or separator, there is an electrolyte liquid containing approximately 35% sulfuric acid and distilled water. The groups, known as element sets, are connected in series (positive plates from one cell connected to negative plates from the next cell) and react with the electrolyte to generate lead sulfate and electrons, providing the energy needed for the car. For proper battery operation, other components not mentioned in Figure 4 include the polypropylene battery box, lid, plugs, handle, positive and negative terminals, terminal protection and covers, and specific labels for recycling, safety, and battery parameters.

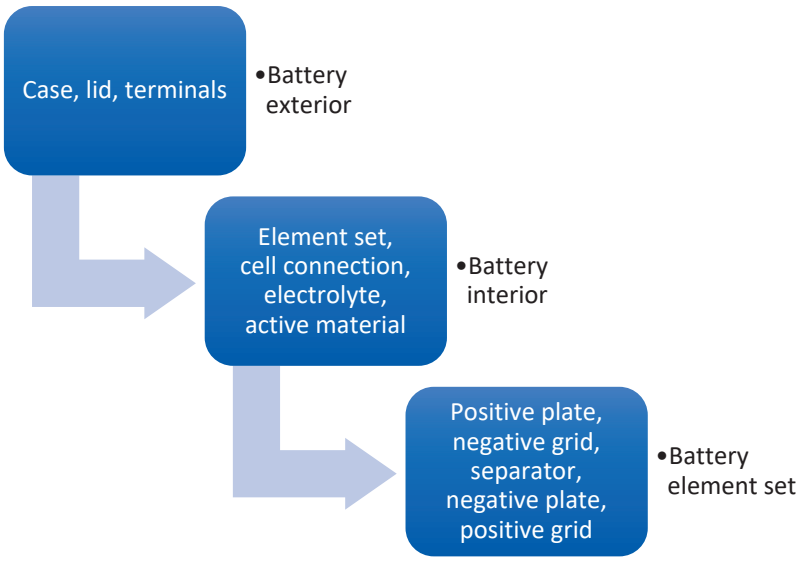

Figure 4. Lead-acid battery construction [16].

The main parameters of the battery are as follows:

- OCV—(Open Circuit Voltage);
- Battery Capacity—defined as the amount of energy provided over a specific time period [17]. This is rated at 20 h (C_{20}) and measured in ampere-hours (Ah), according to ISO EN 50342 standards [18]. The battery's capacity is linked to the quantity of active mass applied to the plates and is determined by the manufacturer during the development phase;
- CCA (Cold Cranking Amps)—defined as the maximum amount of current that the battery can provide at a temperature of −18 °C for 30 s [19]. The starting current is linked to the active surface area that reacts during the electrochemical process. This theoretically means that the more plates a battery contains, the higher its CCA value.

The dimensions of the batteries (length, height, width, terminal positions, etc.) and the requirements for testing the parameters are specified in the ISO EN 50342 standards. These standards also define the current technologies, including the Standard Flooded battery, and other technologies such as EFB (Enhanced Flooded Battery [20]), which has almost the same construction as the Flooded battery but is enhanced to withstand higher numbers of charging and discharging cycles; EFB + C; and VRLA (Valve-Regulated Lead-Acid battery [20]), which can use AGM (Absorbent Glass Mat [21]) technology or GEL (where the electrolyte is not liquid but a gel). EFB and VRLA batteries are dedicated to cars with a Start and Stop System.

3.1.2. Manufacturing Process Description

To better understand the risks, Figure 5 presents the manufacturing process of lead-acid batteries. The process starts with lead preparation, using either pure lead (99.998% Pb) or lead alloy, depending on the process. The lead bars are melted and transformed into strips or grids using various methods (continuous casting, punching, expanding, etc.). The melted lead is also shaped into molds to create cylinders, which are then introduced into a mill. Through continuous rotation and friction, a thin dust called lead oxide is obtained.

Next, the lead oxide is mixed with electrolyte, distilled water, and other elements to create the positive and negative paste. Using pasting machines, the paste is applied to the grid strips, pressed, and dried with special paper to ensure optimal adherence. The plates are cut from the strips, stacked on special pallets, and prepared for the next step: plate formation. The plates are placed in automatic chambers with climate and humidity

control for several hours, as prescribed. The plates are then stored, awaiting stacking, enveloping (only the positive plates), and the preparation of plate groups. A robot takes the groups, stores them in a buffer, and transfers them into molds, where connection strips are built using melted lead. Another robot extracts the groups, places them into battery boxes, and performs an electrical test to detect possible short circuits. If the battery passes the test, it proceeds to group welding (creating series connections). Another electrical test is conducted to detect internal defects. The lid and box are fitted using a thermal welding process, and the terminals are built using an oxy-acetylene flame and molds. To ensure proper welding, a leakage test is performed. The batteries are then weighed, and manufacturing codes are engraved on the lid. Finally, an industrial robot stacks the batteries on pallets and transfers them to the warehouse, awaiting the next phases.

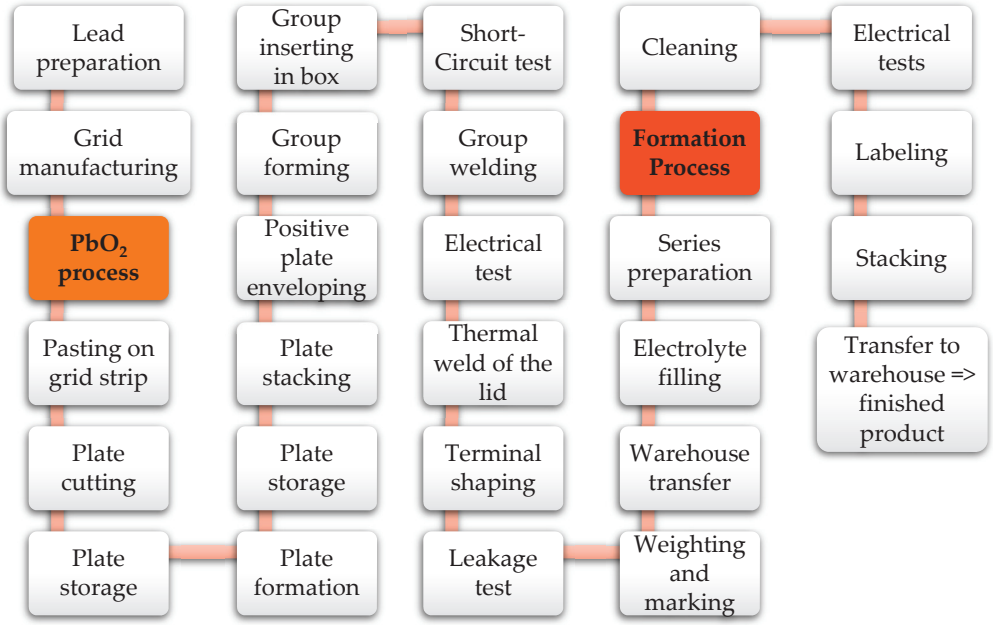

Figure 5. Lead-acid battery manufacturing process.

Based on the orders, the semi-finished batteries are transferred to the finishing line, where they are filled with electrolyte, connected in series, and introduced into the formation process (charging process). The charging time depends on the formation technology used, the battery type, and the battery capacity. The charged batteries then go through the washing step, electrical tests to detect any defects, manufacturing code engraving, and labeling according to customer requirements. Terminal protections are fitted, and a robot places the batteries on pallets. The pallets are wrapped, labeled, registered into the ERP, and transferred to the warehouse, awaiting delivery.

3.2. Case Studies for the Fire Risk Areas

In Figure 5, the areas where fire risks can occur are highlighted in orange/red, specifically during the lead oxide manufacturing process and the formation step. According to previous experience, the formation process presents the highest fire risk. In the lead-acid battery industry, three types of formation processes are used:

- Formation in open air, on shelves—the most basic and least efficient type;
- Formation in tank cells with water cooling;
- Formation with electrolyte recirculation—the most advanced one.

These three formation processes are the most common worldwide in lead-acid battery manufacturing. Based on industrial experience within a real-world battery factory in

Romania, it is inferred that fire risk is one of the most significant cause of disasters, when compared with other process and product risks (e.g., worker safety or logistical errors).

The root causes of the fire may seem to be in common, but due to process specificity, they will be treated separately.

The generic root causes of fires during formation are as follows:

- Internal battery defect;
- Electrolyte filling problems;
- Empty battery or empty battery cells due to formation process problems;
- Foaming on the cooling water surface;
- Cooling water level problems;
- Electrolyte recirculation system problems;
- Cables or connection worn or wrongly connected.

Usually, these are automated processes controlled by computerized systems, and operators only need to supervise the parameters without being physically present in the workplace.

There is another risk area in the complementary processes—the air aspiration area (exhaust system). Occasionally, and under extraordinary conditions, the filters can burn, but the effects are less significant. The risks are analyzed in detail below, and the important ones are simulated using PyroSim.

3.2.1. Fire Risks in the Battery Formation Process—In Open Air, on Shelves

As the name suggests, the batteries are placed on metal shelves, connected with cables for electricity transfer, and cooled solely by airflow, as shown in the 3D model in Figure 6.

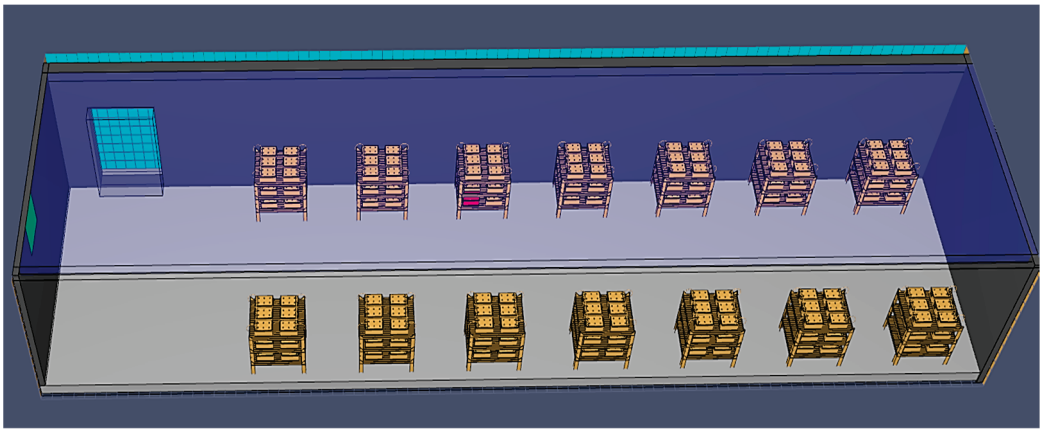

Figure 6. A 3D model of formation on shelves in open air using PyroSim.

This process is the slowest, and due to high temperatures, various complications can occur. The cooling method can cause the temperature to rise quickly, leading to fires if there are any process problems, especially in the summertime when outside temperatures are also high. For example, if one of the batteries has electrolyte level problems (a lack or low level) due to the filling process or other causes, the temperature in the problematic cell will rise significantly due to the applied electrical current. The plates come into contact due to grid growth and separator wear, generating short circuits. The battery box and lid will slowly melt and eventually burn. If the fire is not quickly detected, it will spread to other batteries through the air or connection cables, as shown in Figure 7.

An internal battery defect due to manufacturing processes, such as short circuits or interruption problems, can cause sparks, local heating, water loss, and gas release, resulting in the same effects as described above. Moreover, because the gases generated during the formation process are oxygen and hydrogen, any spark or fire can cause the battery to

explode, increasing the fire's intensity and propagation. This can cause significant trouble and injuries to firefighters, as the hot and corrosive electrolyte is splashed around the area. The smoke is also dangerous for workers and firefighters.

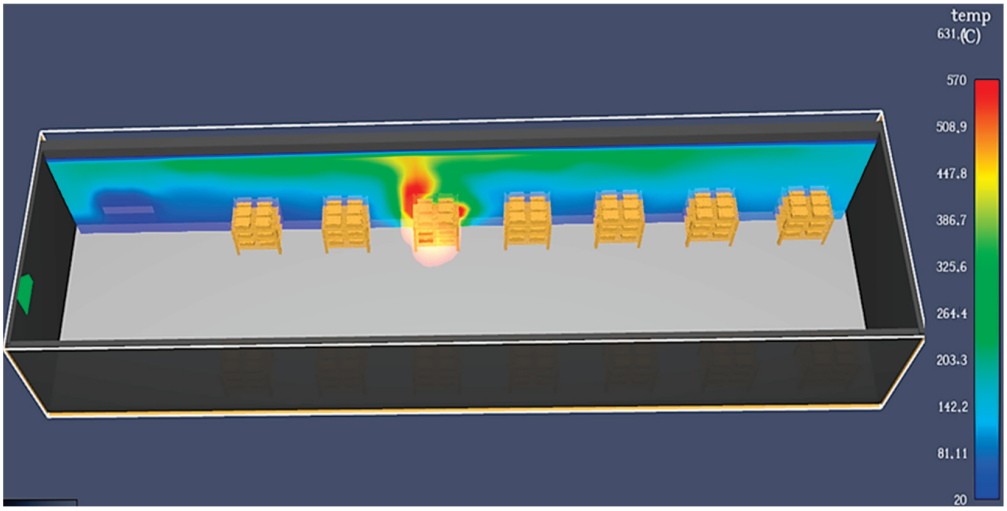

Figure 7. Fire simulation for formation on the shelves in open air using PyroSim.

3.2.2. Fire Risks in the Battery Formation Process—Formation in Tanks with Water Cooling

The batteries are placed in special tanks made of stainless steel or plastic base materials. They are connected to each other and to the chargers with cables (series connection) and continuously cooled with water, as shown in the 3D model created in PyroSim (Figure 8).

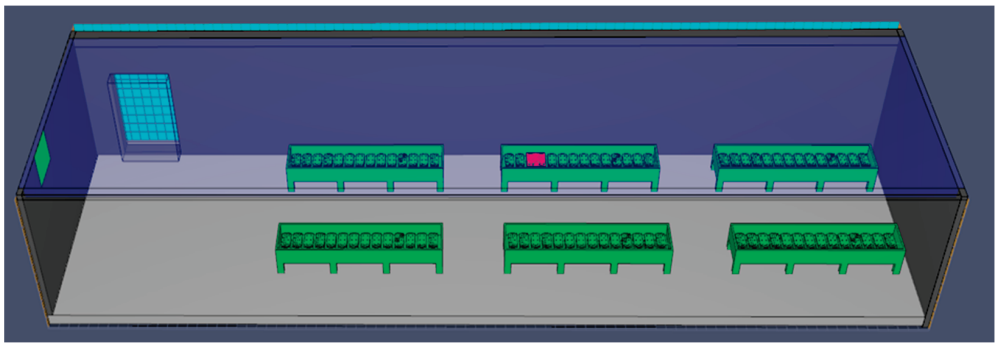

Figure 8. A 3D model of formation in tanks cooled with water, using PyroSim.

Water pumps are used to continuously recirculate the water. These pumps are computer-controlled using information from the PLC, level sensors, and temperature sensors. The water is supplied from the municipal network or the internal neutralization station. While this process ensures good cooling and involves water, making it theoretically safer from a fire risk perspective, problems can still occur. If the cooling process fails, the water level is inadequate, or the batteries have internal defects or level issues as previously described, a fire can still occur, as shown in Figure 9.

Additionally, in this process, the "foaming phenomenon" can occur on the water's surface, causing electrical contact between the positive and negative battery terminals through the foam, leading to lids melting or burning, fire, and even explosions. Other problems can arise after the formation process, during battery resting (e.g., on weekends), with or without the water drained from the tanks. If one or more batteries have internal defects (usually a short circuit), especially if the tanks are made of plastic, fires can occur. Similar to the previous case, the plastic materials used in battery construction can cause the fire to escalate quickly, leading to explosions and splashing, which are dangerous for

operators and firefighters. Usually, the fire is isolated to one formation tank, but without a proper response, it can spread to others. The smoke is also hazardous.

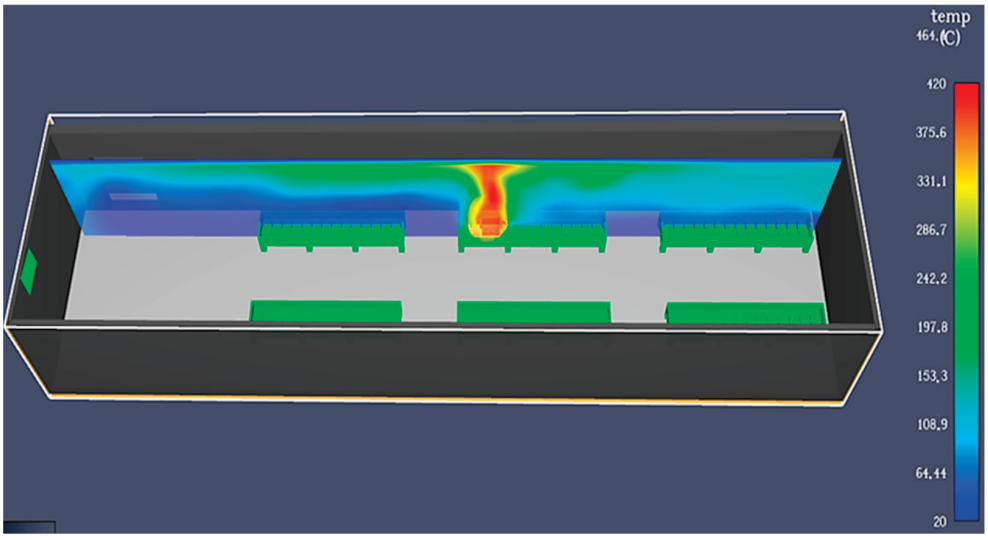

Figure 9. Fire simulation in the case of formation in tanks, using PyroSim.

3.2.3. Fire Risks in the Battery Formation Process—Formation with Electrolyte Recirculation

This is the most advanced formation process today, but it is also the most challenging from a fire safety perspective. The batteries are placed in modules integrated into the formation cell, as shown in Figure 10. They are connected with cables for electricity and hoses to the acid recirculation system. The electrolyte is continuously recirculated using special pumps and a tank to ensure cooling and cleanliness.

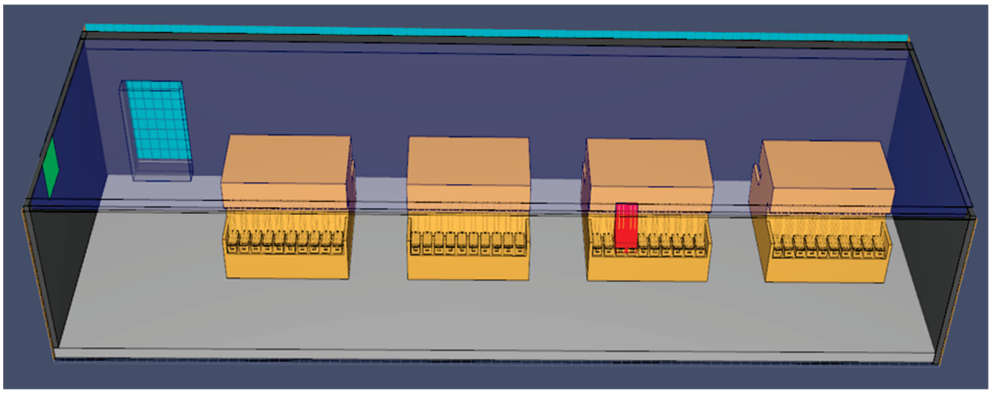

Figure 10. A 3D model of formation with electrolyte recirculation, using PyroSim.

Most of the components of the formation modules are made of plastic and rubber because they need to resist the corrosive effect of the electrolyte. Unfortunately, this also facilitates the propagation of fire. If there are batteries with electrolyte level problems, including issues caused by the recirculation system (such as clogged hoses), excessive heating can occur, causing the battery lid to ignite. The fire spreads rapidly due to the connecting hoses, which conduct it to the top of the module and the rest of the batteries, as shown in Figure 11.

Due to the various plastic-based materials used in the modules' construction, fires can spread quickly. If not detected urgently, the consequences can be disastrous, which is why every manufacturer using this technology takes precautions. Moreover, when the connection hoses burn and melt, a large amount of electrolyte leaks and splashes onto

the floor and factory. Similar to the other two processes, explosions can occur, but in this case, the electrolyte splashing can make the firefighters' work harder. The smoke is also dangerous for the workers.

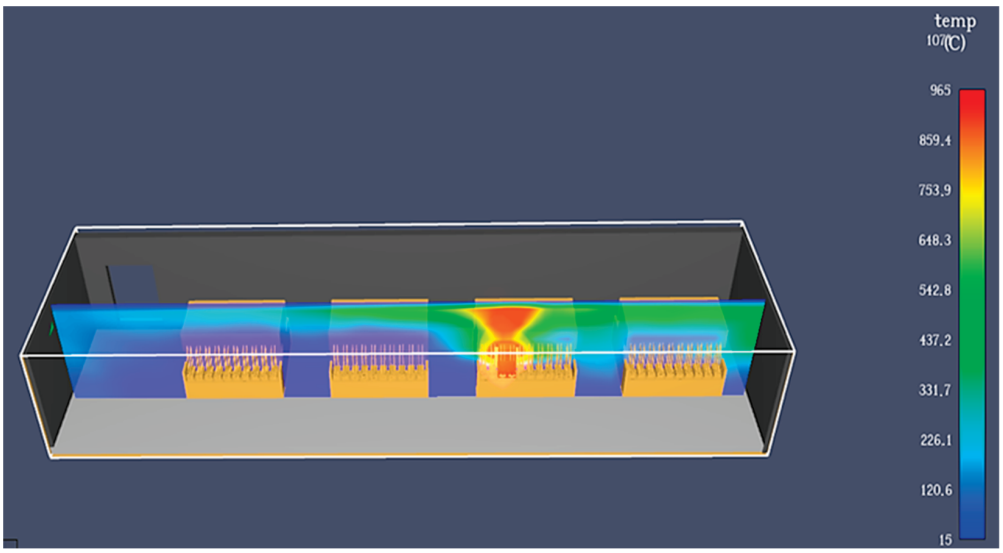

Figure 11. Fire simulation in the case of formation with electrolyte recirculation, using PyroSim.

3.2.4. Fire Risks in the Lead Oxide Manufacturing Process

Depending on the type of lead oxide desired, various methods are available. The process usually involves a rotary mill loaded with lead cylinders or slices. The lead parts are introduced into a spinning metal drum, and due to the friction between them, a thin dust of oxide is generated. This dust is then aspirated into tanks based on the airflow introduced from outside. The airflow, containing oxygen and water, plays a role in the superficial oxidation of the lead. If rough lead particles with a lower oxidation grade are generated and aspirated by the airflow, an exothermic reaction can occur due to the humidity and air, causing the filters to burn. This is specific to mills with low-grade oxidation processes. The fire remains inside the mill, typically damaging only the filters and lead oxide, and usually does not spread outside. Modern mills use an automated and controlled process of water supply and oxygenation that theoretically prevents fires, though small, localized fires can still occur. Because this risk is considered very low and the effects are not significant, only causing material damage, we decided not to treat it the same way as the other three cases above and not to perform a 3D simulation. We applied the same reasoning to the next risk as well.

3.2.5. Fire Risks in the Auxiliary Processes

Separate from the manufacturing processes, there are also places with fire risks. These are linked to auxiliary processes, one of which is the vent system that eliminates and filters the polluted air from the factory, especially from the lead oxide manufacturing area, pasting area, and assembly area. Special textile bags are used, which can generate a fire under certain conditions, such as when low-oxidized lead oxide dust accumulates, humidity is present, or small parts of the pasting paper are aspirated from the process. This can cause local fires and filter burning. The filters are located outside on the roof of the factory, and theoretically, the fire effects are reduced and limited to air quality and system efficiency.

3.2.6. Fire Risks in the Recycling Process

The recycling process is quite safe from a fire perspective because there are strict regulations and supervised processes. Scrap batteries (out of use) are collected from the

market by authorized distributors. The batteries are stored in dedicated containers that prevent leakage, usually made of plastic-based materials. Transport from dealers to the recycling factory is performed according to legislation and only by companies that hold environmental licenses. Only trucks equipped with ADR (Agreement concerning the International Carriage of Dangerous Goods by Road) certification are allowed to carry the scrap batteries. The route of the truck must be declared to the authorities and strictly followed. Because most of the scrap batteries are discharged or deeply discharged, the voltage and current values are low, resulting in a very low risk of fire during storage or transport. According to our experience (more than 10 years), no incidents have been reported in Romania directly linked to batteries as the root cause. As a precaution, to prevent any short circuits or possible fires, new batteries that are fully charged must have terminal protections (made of plastic), should be stacked in a vertical position to prevent leakage, and properly wrapped.

As we mentioned, the batteries have an 85% recycling rate for the materials they are made of, and specifically, the lead can be recovered at a rate of up to 99%. At the recycling unit, the batteries are processed to give new life to future batteries, as shown in Figure 12.

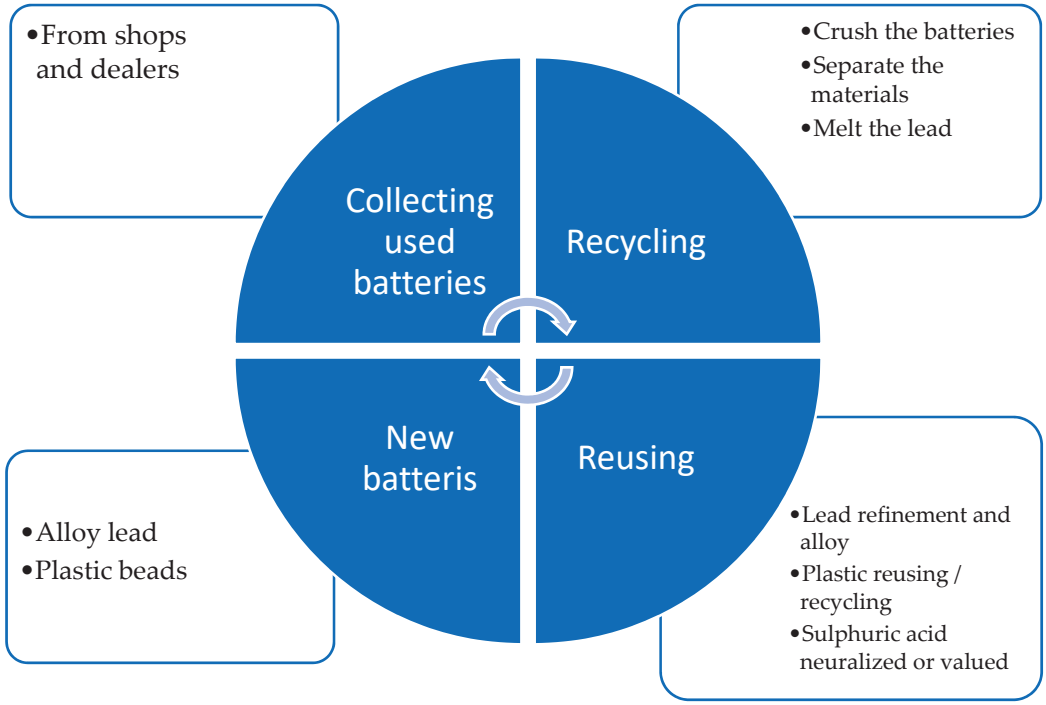

Figure 12. Battery recycling process [9].

The first step is unloading the batteries from the truck directly into a large collector. To prevent any fire risks, continuous watering is implemented. Using a conveyor belt, the batteries are transported to a mill that crushes them. There is a risk of fire if lithium- or nickel metal-based batteries arrive at the mill, because they can explode and catch fire. The damage could cause a prolonged production breakdown and high repair costs. The easiest and cheapest way to prevent this is to collect the batteries very carefully and strictly. To ensure this, the collectors are trained, and handbooks can be prepared for them. For some batteries, metal detectors installed on the conveyor might be sufficient for detection, but they are not 100% effective. We suggest implementing a robust action plan that involves AI technologies to detect battery types. Cameras can be used to detect labels and battery shapes, and X-ray detectors can also be employed. The solutions must be adapted to the

company's budget because complex ones, such as those involving X-rays, can cost over 1 million Euros.

The materials are separated by the mill and transported separately using special conveyors to the next steps. The lead parts (plates, terminals, etc.) are transferred to a rotary furnace that melts them at 1100 °C. The lead is then refined to achieve 99.98% purity and used to create alloys such as lead–calcium and lead–antimony. The casting machine creates ingots of these materials, which will be used to manufacture new batteries.

At this step, fires can occur if water meets the hot melted material. This will react and may even cause explosions. To avoid this, the process should be supervised, and any unauthorized actions should be prevented. The box and lid of the battery are ground, and the resulting material is reused in other battery parts or sold for use in other industries. Sulfuric acid is neutralized or repurposed in other industrial fields. To avoid any operator injuries, the processes that involve crushing and hot materials, such as melting and casting, are automated. For other processes, the operators are properly equipped with PPE (personal protective equipment) like dedicated visors, gloves, aprons, etc.

4. Discussion

4.1. Discussions of the Case Studies

Based on a theoretical analysis and validation case studies, the most hazardous formation process used in the company, from a fire perspective, is formation with electrolyte recirculation. This is also confirmed by the 3D simulations. The comparative analysis starts with the input data and conditions used for the three simulations:

- The same surface of the manufacturing area: 26,000 × 6200 × 4000 mm^3 (L × W × H);
- The same type of batteries: Heavy Duty batteries, C type (M16);
- The same battery box and lid materials: polypropylene;
- The same simulation end time: 60 s;
- The same ramp-up time on the burning area: t2 = 20 s;
- The same Heat Release Rate Per Area: 1000 kW/m^2;
- The same maximum air debit of the exhaust system: 15 m^3/h;
- The same geometry of the vents: circular with a radius of 200 mm;
- The same position of the vent;
- The same positions and dimensions of the access doors—important for the air flow.

In all scenarios, the building is equipped with exhaust systems, and the ambient temperature is not taken into account, as the only process that can involve higher ambient temperatures is formation on shelves. Other parameters, such as humidity, influence only the lead-oxide process and auxiliary processes where they can truly cause problems—see Sections 3.2.4 and 3.2.5. Humidity is problematic for lithium-based batteries, but in the case of lead-acid batteries, it does not have a significant effect on fire hazard. We chose the parameters to provide proper results that can be adequately compared and to ensure that the simulations can be performed in a reasonable time. The time needed can vary from minutes to hours, depending on the inputs. Of course, there are also differences based on the process specificity, such as the following:

- Cooling type: with air (natural flow)/with recirculated water (in tanks)/with recirculated electrolyte;
- Burning surface: complete battery and neighbors/the part of the battery from the water surface/the battery, the neighbors, the connection hoses, and the formation module;
- The position, the arrangement of batteries, and their number in the production area.

However, the process conditions are specific to each formation process. Due to this specificity, there can be a larger or a smaller burning area, the materials around the batteries are more or less flammable, the amount of the batteries could be different, etc. For example, in the case of tanks cooled with water, the fire cannot go under the water and will arrive in a longer time to the neighbor batteries, but in the case of the other two formation processes the batteries are on shelves, without any water around, and more batteries stay together, thus heightening the risks, etc.

For a clear overview of the 3D simulation results using PyroSim, we decided to perform an analysis using graphs and diagrams, as seen in Figures 13 and 15–17, and numerically in Table 1. As shown in Figure 13a–c, the Heat Release Rate resulting from the burning process varies between these three types of processes. The most hazardous is formation with electrolyte recirculation (almost 2000 kW), while the least problematic is formation in tanks cooled with water (almost 400 kW).

Table 1. Parameter values that resulted from PyroSim simulations [12].

Parameter	Formation on Shelves	Formation in Tanks Cooled with Water	Formation with Electrolyte Recirculation
Maximum temperature	570 [°C]	420 [°C]	965 [°C]
Maximum air velocity	5.5 [m/s]	4.5 [m/s]	4 [m/s]
Soot visibility	29.18 [m]	28.82 [m]	28.71 [m]
Maximum HRR (Heat Release Rate)	1366 [KW]	373 [KW]	2000 [KW]
Maximum Q_radi (heat radiated)	2621 [KW]	1805 [KW]	4613 [KW]
Maximum Q_Conv (heat convection)	5.8 [KW]	2.95 [KW]	107 [KW]
Minimum Q_Conv (heat convection)	−1667 [KW]	−987 [KW]	−1620 [KW]
Minimum Q_Cond (heat conducted)	−1097 [KW]	−703 [KW]	−1160 [KW]
Q_Total (total heat)	2671 [KW]	1666 [KW]	4568 [KW]
MLR_air (Mass Loss Rate—Air)	−14.4 [Kg/s]	−15.83 [Kg/s]	−10.25 [Kg/s]
MLR_Polypropylene (Mass Loss Rate—Polypropylene)	2.88 [Kg/s]	1.51 [Kg/s]	4.63 [Kg/s]
Simulation time (until the whole material is burned)	60 [s]	60 [s]	20.4 [s]

Moreover, the graphs show a quick increase in the HRR in the first 20 s and a stabilization, with small variations around the maximum value, for the cases of formation in tanks cooled with water and on shelves. However, in the case of formation with electrolyte recirculation, there is a quick increase up to 20.4 s, when the maximum value is reached, and the battery material is completely burned, leaving no lasting effects, as seen in Figure 14.

Another relevant graph represents the total quantity of heat released (Q_TOTAL) during burning, as seen in Figure 15. All three graphs show a very quick increase in the parameter in the first 5 s, followed by a decrease with small variations until the end of the simulation. In this case, the formation with electrolyte recirculation has the highest value (4500 kW)—almost double compared with the one on shelves and almost triple compared with the one in tanks cooled with water. Similar to the HRR case, the process stops at 20 s and about 1500 kW. The other two processes have smaller values at the end, around 200–300 kW.

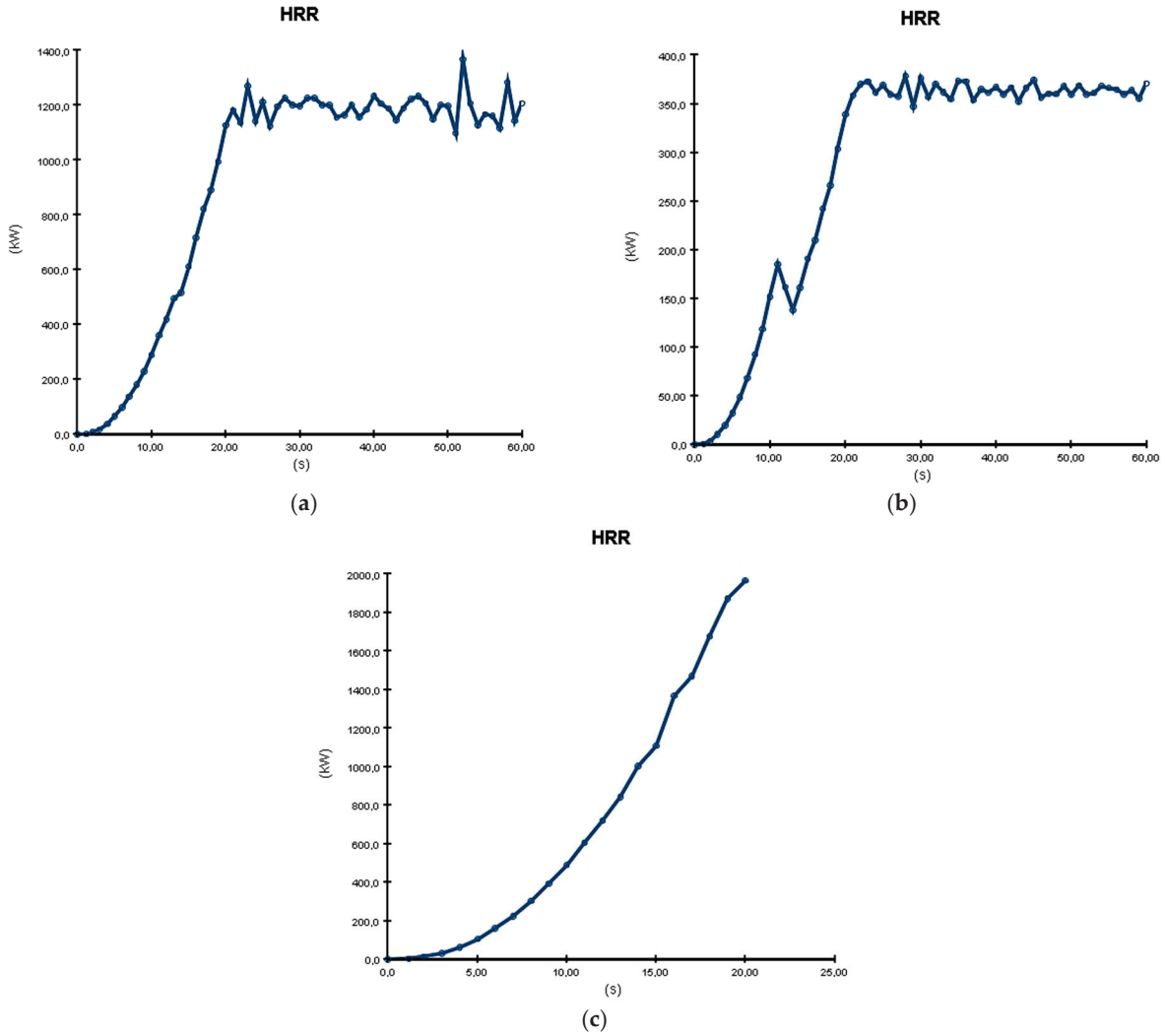

Figure 13. HRR (Heat Release Rate) graphs resulting from PyroSim simulation: (**a**) formation on shelves, in open air; (**b**) formation in tanks cooled with water; (**c**) formation with electrolyte recirculation.

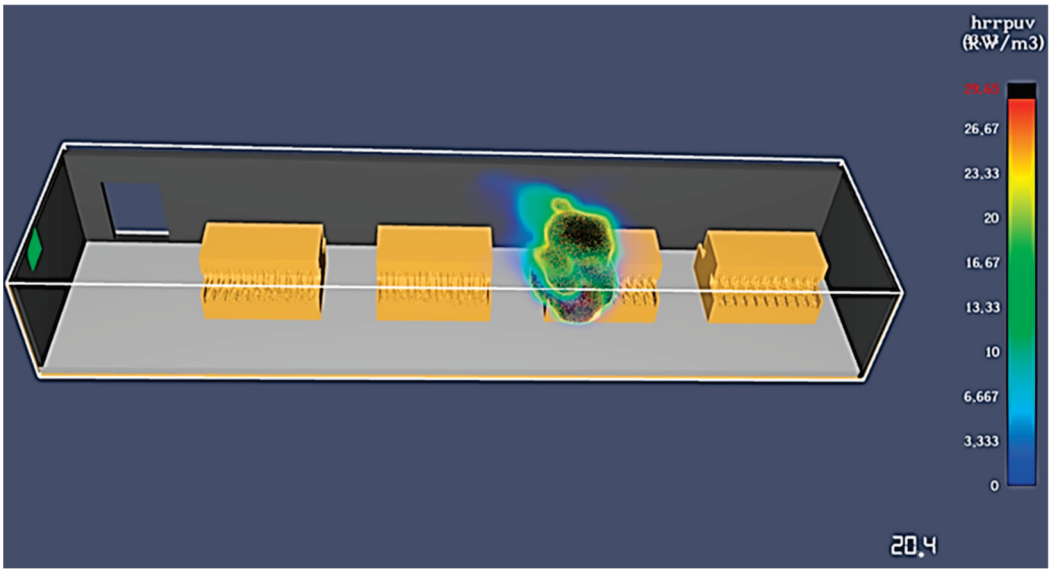

Figure 14. Simulation end time for formation with acid recirculation.

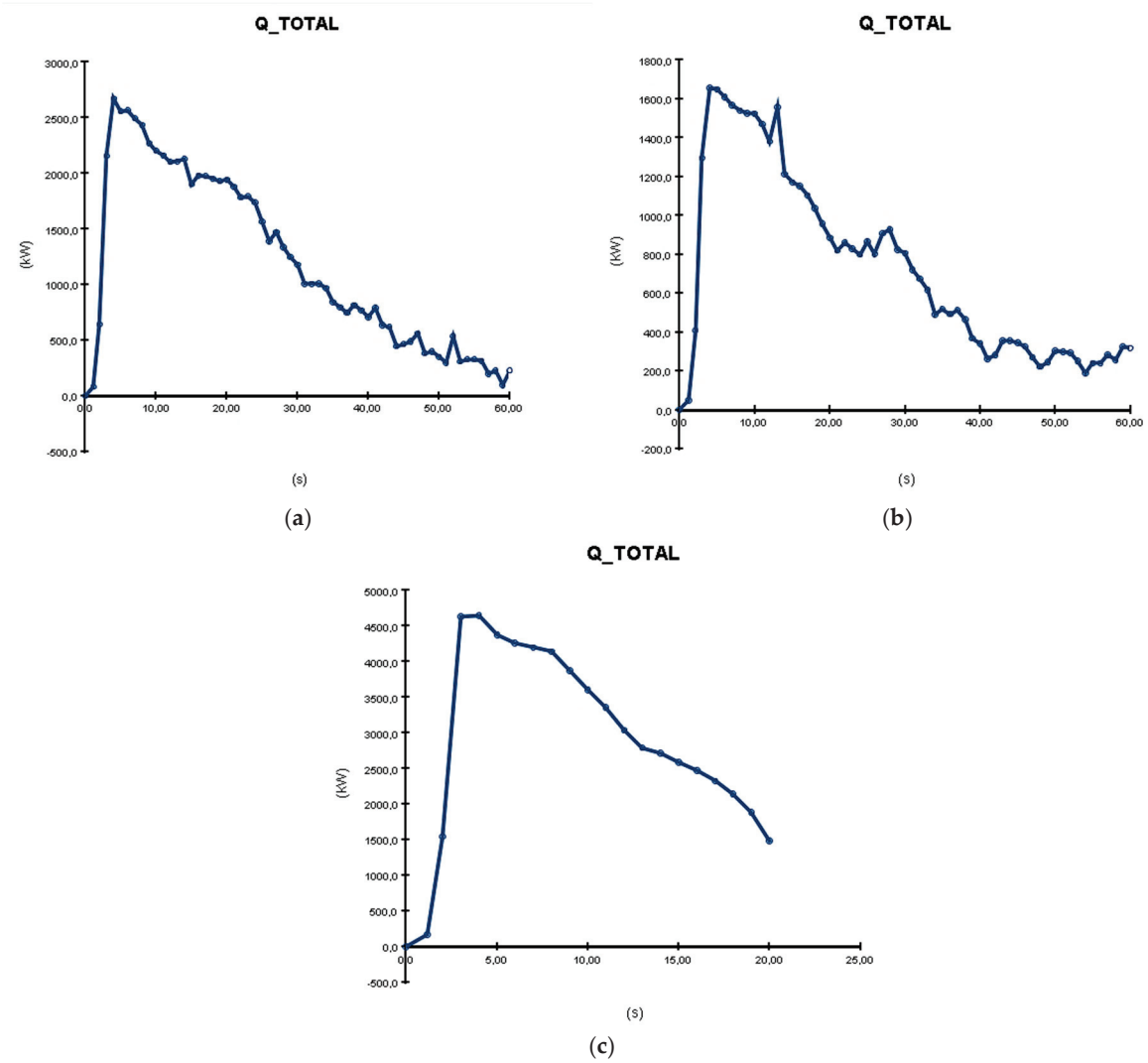

Figure 15. Q_TOTAL graphs resulting from PyroSim simulation: (**a**) formation on shelves in open air; (**b**) formation in tanks cooled with water; (**c**) formation with electrolyte recirculation.

In the graphs from Figure 16, the Mass Loss Rate (MLR) of the battery material selected as combustible (polypropylene) is analyzed. This presents the amount of material burned per second. As shown, in the case of formation on shelves (a) and in tanks cooled with water (b), there is a loss of material in the first 15 s, followed by a linear loss until the end of the simulation. However, for the formation with recirculation, there is a continuous mass loss that suddenly ends at 20 s because the entire material is burned. The lost mass value differs for all three processes, with that of formation with electrolyte recirculation being three times greater than that of formation on shelves and almost double that of formation in tanks cooled with water.

The amount of material burned per second indicates how quickly the batteries and surrounding materials will ignite. This helps stakeholders understand the potential speed and devastation of the fire's spread. It is also crucial for determining response times and intervention strategies.

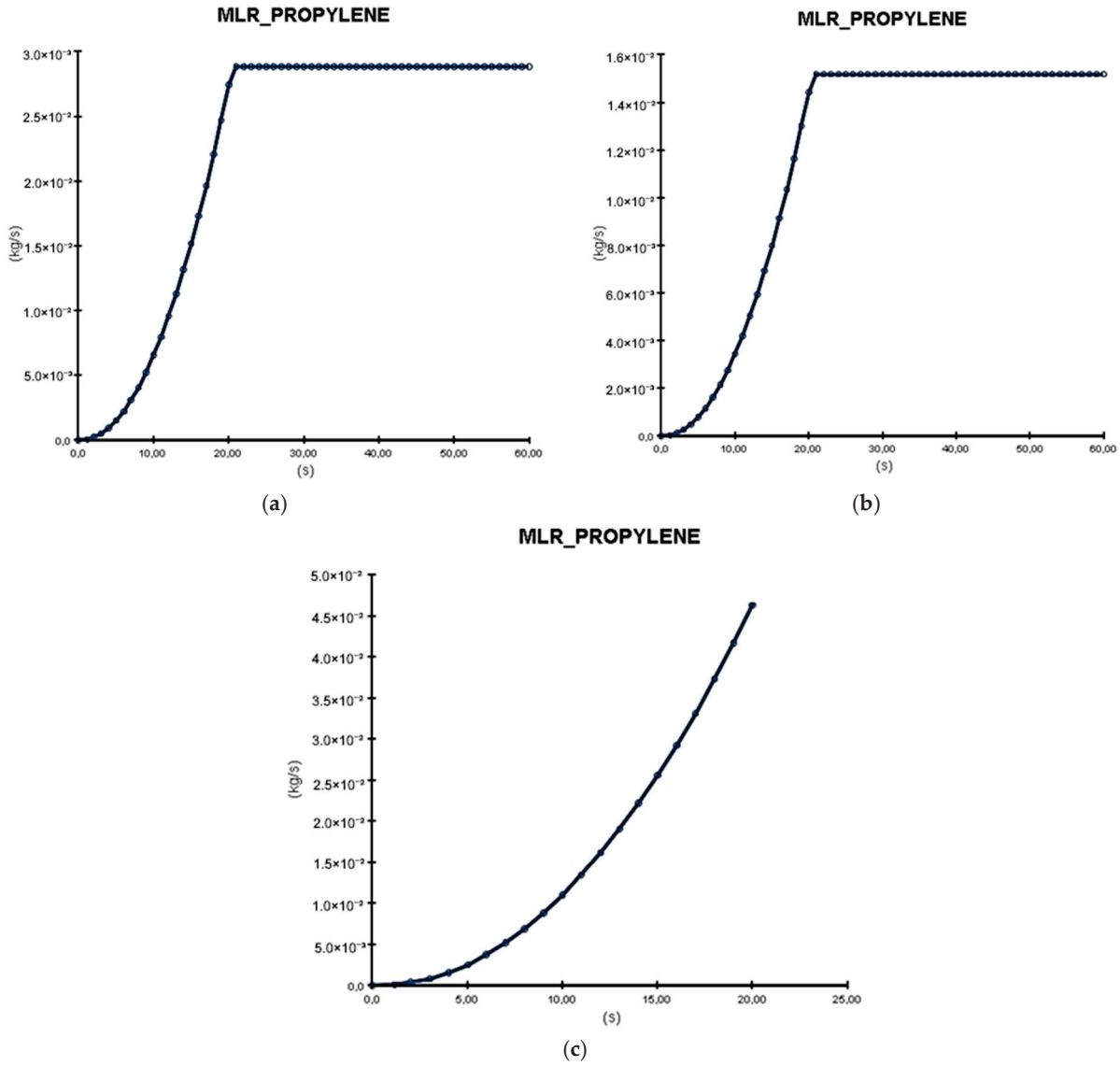

Figure 16. Mass Loss Rate resulted from PyroSim simulation: (**a**) formation on shelves in open air; (**b**) formation in tanks cooled with water; (**c**) formation with electrolyte recirculation.

The last analyzed parameter is MLR_AIR (Mass Loss Rate for Air), based on the graphs from Figure 17. This represents the volume of air from the manufacturing building that is lost per second due to the burning process, which is why the values in the graphs are negative. As shown in the case of formation on shelves (a) and in tanks cooled with water (b), there is a quick air mass loss in the first 20 s, followed by an almost linear loss around -12 to -14 kg/s until the end of the simulation. In the case of formation with electrolyte recirculation, there is a linear air loss that stops at 20 s, similar to the other parameters monitored. The mass loss at the end of the simulation is almost the same for all three types of formation, about -10 kg/s, with the difference being smaller than in the other cases. The Mass Loss Rate has two components: the materials involved in the burning process and the air. The amount of the material that is burned per second shows how quickly the batteries and materials around will burn. This will help the stakeholders understand how quickly the fire can expand and how devastating it can be. Also, this is very important for response time and intervention. Air loss is important for the risk of harm to operators and the propagation of dangerous gases resulting from the burning.

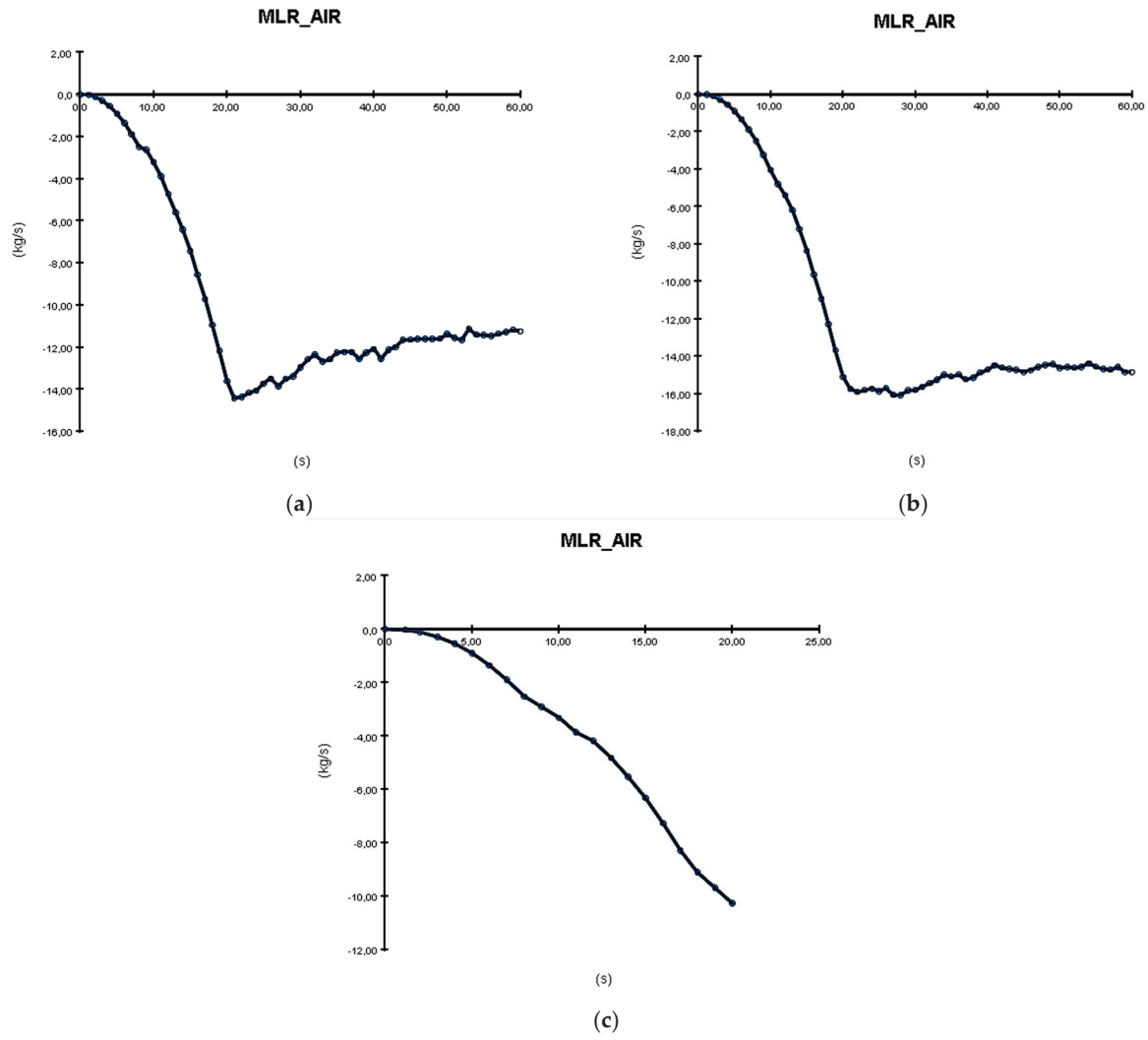

Figure 17. MLR—Air (Mass Loss Rate—Air) graphs resulting from PyroSim simulation: (**a**) formation on shelves in open air; (**b**) formation in tanks cooled with water; (**c**) formation with electrolyte recirculation.

PyroSim software provides several graphs at the end of the simulation regarding the pressure values at different workspace points, as well as other heat and material losses. The minimum and maximum values of these parameters, along with other important values, are presented in Table 1.

The inferences based on the graph analyses from Figures 12 and 14–16 are confirmed by the data from Table 1. The battery formation process with electrolyte recirculation is the most hazardous from a fire perspective, followed by formation on shelves with air cooling.

4.2. Discussions of Fire Safety Regulations

In Romania, fire safety legislation is primarily governed by Law No. 307/2006. This law sets the legal framework for preventing and managing fires, including measures and obligations for building owners, business administrators, and other entities. Other laws include Law No. 481/2004 on Civil Protection and Emergency Ordinance No. 21/2004. As can be seen, the regulation has not been updated over time, but the processes have become more and more complex.

The international standards regarding fire safety include the EN 54 series [22–25], ISO 45001 [26] (not directly linked), and the previous OHSAS 18001 [27] (not directly linked). The EN 54 series is a comprehensive set of European standards that cover various aspects of

fire detection and fire alarm systems, such as control and indicating equipment, fire alarm devices, power supply equipment, heat detectors, smoke detectors, manual call points, voice alarm systems, and visual alarm devices.

According to these laws and standards, companies have to adopt preventive actions such as the following:

- Performing periodic training for all employees, based on working procedures and safety regulations;
- Conducting practical exercises with employees;
- Designing evacuation plans and making them available in all rooms;
- Installing emergency lighting;
- Installing manual triggers and alarm systems
- Installing fire and smoke detection systems, depending on the company type and size;
- Installing fire extinguishers on all floors and in all production areas;
- Installing vents for smoke control;
- Installing automated fire-extinguishing systems (mandatory only for large companies);
- Installing fire hydrants (mandatory only for large companies);
- Having their own firefighting team (mandatory only for large companies);
- Hiring dedicated and qualified employees in charge of fire safety.

5. Conclusions

Risk assessment in automated processes within automotive companies involves facing dynamic risks, as we presented in the current research focused on analyzing fire risks. This study addresses fire risks in lead-acid battery factories by using case studies and simulations to identify hazardous areas and analyze the main causes, effects, and outcomes. Fire risk is one of the most hazardous risks because its effects can be catastrophic, involving material loss, human injuries or deaths, and even company bankruptcy in extreme cases, if the company lacks appropriate resilience plans.

Avoiding fires in lead-acid battery manufacturing is challenging, and the fires are also difficult to control if they are not quickly detected in the initial phase. The regulations provide a generic set of rules, but to ensure proper fire safety, companies should identify specific risks as accurately as possible and adopt appropriate actions. Therefore, our recommendations for companies wishing to adopt efficient preventive actions include the following:

- Automated fire management systems;
- Fire sensors for smoke detection in problematic areas—these sensors send a signal to the fire management system and trigger an alarm at the fire station;
- Thermal detection cameras connected to the fire management system—these issue an alert when maximum temperature values are exceeded and are useful for formation with electrolyte recirculation;
- Water temperature sensors—useful for formation in tanks cooled with water;
- AI systems for fire detection in the initial phase;
- Automated fire-extinguishing systems mounted on the ceiling.

The cost may be a problem for smaller manufacturers, but when comparing these costs with the costs of the resulting effects in case of a fire, such as manufacturing breakdown, replacing the formation cells and annexes, the lack of delivery to car manufacturers, and rebuilding the formation in extreme cases, the cost of automation will be lower. Moreover, some basic solutions that are not very expensive can be adopted with a smaller budget, such as temperature sensors, smoke detection sensors, and standard alarms.

This analysis is a comprehensive one, addressing qualitative issues through a safety audit, followed by the evaluation and quantification of risks for the hazardous areas and

the implementation of robust actions based on immersive 3D visualization studies. For a proper analysis and risk mitigation, we recommend that companies use and combine classical methods, both qualitative and quantitative, as listed in the ISO 31000 standard [28], with complex and modern instruments such as 3D simulations and AI.

The outputs, such as values, graphs, and videos with 3D simulations, are invaluable as inputs for management review, process and product development, and other analyses. Top management and other stakeholders can properly understand the risks and effects without needing special knowledge, making them more oriented toward and open to supporting the team in controlling and eliminating those risks. Using PyroSim or other 3D software, the risk manager can easily present the evolution of the fire, the influence of the involved factors and materials, the time of escalation, the losses, the resulting polluting gases, the visibility of the manufacturing area, the airflow, etc.

The authors' recommendations regarding hazard identification and mitigation can apply to any kind of automotive company, including lithium-based battery manufacturers. Lithium-based batteries use very different technologies compared to lead-acid batteries. The manufacturing process, chemical technology, and cell types are different in lithium batteries. The most hazardous risk in lithium-based batteries is the thermal runaway phenomenon, and the problem is that containment is not as easy as with lead batteries. In this case, automated water systems are not suitable, because water can cause short circuits and other problems. However, our recommendations regarding fire detection in the initial phases can be successfully applied to lithium batteries as well.

Lithium batteries use complex technologies, some of which are more stable than others. For example, LiFePO4 cells are much safer from the perspective of thermal runaway risk than NMC batteries (Lithium Nickel Manganese Cobalt Oxide). In the future, we will consider expanding our research scope to encompass this area further.

The methodology presented is oriented towards the technical benefits of improving the fire risk assessment process, but consideration should be given also to the economic aspects that can influence investment decisions based on cost–benefit considerations. For the three types of formation presented, the mitigation of risk should include costs for the following: smoke detectors, thermal tracking cameras, fire suppression systems, personal protective equipment, smoke ventilation systems, fire extinguishers, chemical spill sensors, infrastructure upgrades (e.g., emergency showers, diversion channels), personnel training and drills, the overhauling of safety procedures, simulation and data analytics software, AI solutions, etc. For one production unit, the costs estimated by the company are ca. 1.5 million Euros over a period of 2 years, with 100,000 Euros/year operational costs for an active life of 10 years. However, the benefits of continued production and facility uptime, and avoiding medical and insurance costs for injured personnel, are estimated to be at least five times that value during the same period.

A cursory sensitivity analysis was conducted, using a modified correlation matrix combined with a risk analysis protocol, using Qualica QFD software, version 2.5. The most important input and output parameters of the simulations have been considered, ensuring their robustness and continued relevance (Figure 18). Based on industrial experience and the simulation findings, the analysis revealed that the most important inputs are related to material composition and surface features (summing ca. 60%) that influence the potential fire, while the most relevant outputs are related to the maximum temperature and the Heat Release Rate from the incident (also summing ca. 60%).

The second analysis, considering scores for impact, sensitivity and mitigability on decimal scales, classifies all the output parameters as being critical ones, which require intervention plans and the stabilization of inputs through environment control on tem-

perature and humidity and material composition control through chemical and physical analysis of the raw materials.

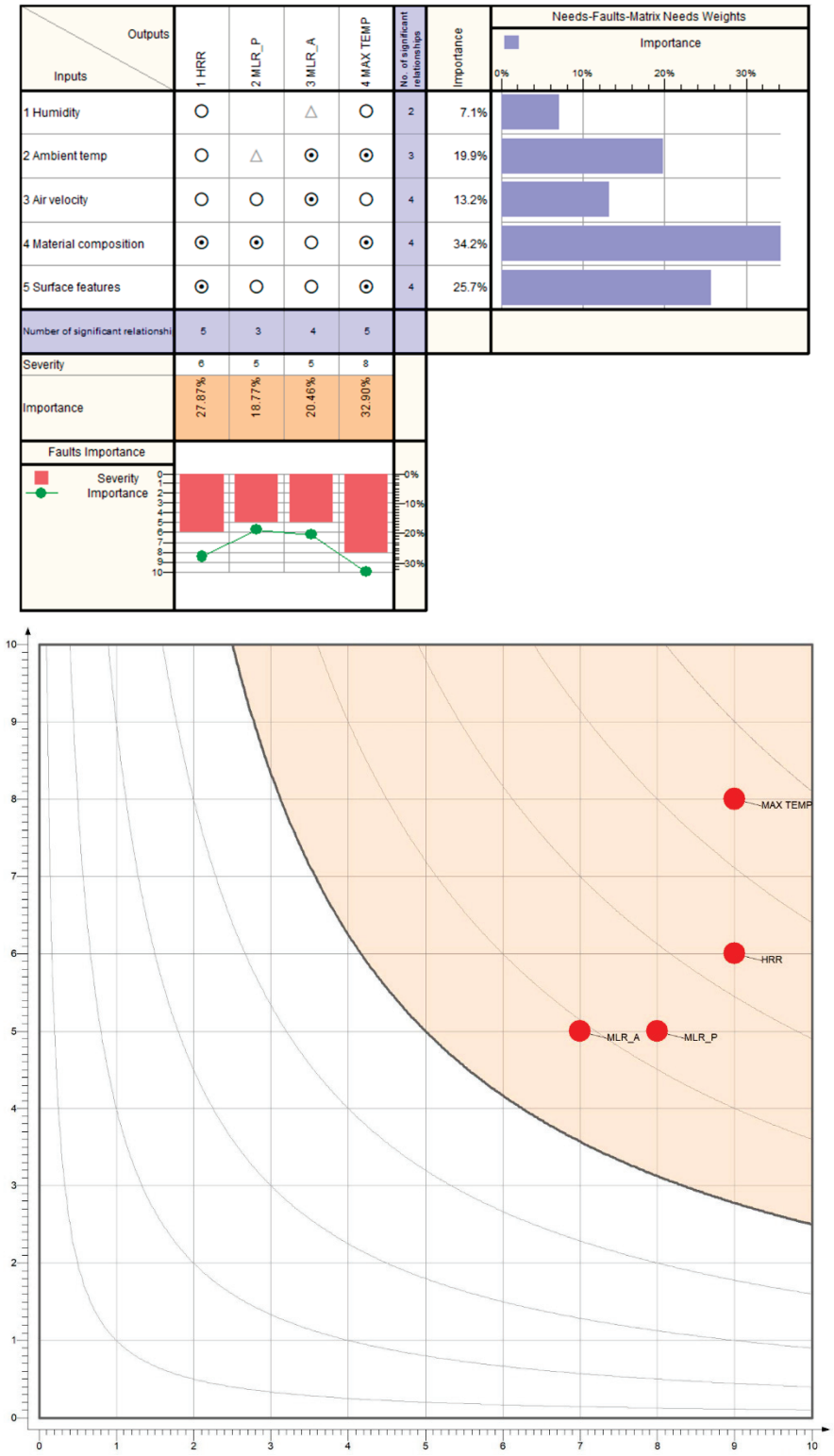

Figure 18. Sensitivity analysis carried out for input–output relationships using correlation (**above**) and risk influences (**below**).

We conclude that the approach presented in this paper is feasible because, by applying this methodology, we conducted a complex analysis of the risks in battery manufacturing companies. In this way, one can understand not only the causes but also their effects

very well and offer recommendations to other similar companies. The risk hierarchization is much more accurate compared to current practices, and the mitigation actions are more efficient.

Author Contributions: Conceptualization, M.D.; Methodology, M.D.; Software, D.D.; Validation, A.Z.; Formal analysis, A.Z.; Investigation, A.Z.; Data curation, D.D.; Writing—original draft, A.Z., M.D. and D.D.; Writing—review & editing, A.Z., M.D. and D.D.; Supervision, M.D. All authors have read and agreed to the published version of the manuscript.

Funding: This research received no external funding.

Data Availability Statement: The original contributions presented in this study are included in the article. Further inquiries can be directed to the corresponding authors.

Acknowledgments: The authors would like to thank Thunderhead Engineering Consultants, Inc. for generously providing access to the PyroSim software for research purposes.

Conflicts of Interest: The authors declare no conflict of interest.

References

1. Zinveli, A.; Tareq, S.; Popescu, S. Literature review concerning safety risk assessment in collaborative environments. In Proceedings of the 22nd International Conference of Nonconventional Technologies, Bistrita, Romania, 16–18 November 2023.
2. Zinveli, A.; Dragomir, M. A case study in improving the safety of collaborative tasks in the automotive industry. In Proceedings of the 22nd International Conference of Nonconventional Technologies, Bistrita, Romania, 16–18 November 2023.
3. Zinveli, A.; Dragomir, M. Risk assessment in collaborative tasks: A comparative analysis—Qualitative method and quantitative method. In *Advances in Manufacturing IV*; Springer Nature: Cham, Switzerland, 2024; pp. 68–79. [CrossRef]
4. Yuasa Bullish on Future Global Auto Market for Lead Batteries, Batteries International Magazine. Available online: https://www.batteriesinternational.com/2024/03/21/yuasa-bullish-on-future-global-auto-market-for-lead-batteries/# (accessed on 21 March 2024).
5. EU Ban on the Sale of New Petrol and Diesel Cars from 2035 Explained. Available online: https://www.europarl.europa.eu/topics/en/article/20221019STO44572/eu-ban-on-sale-of-new-petrol-and-diesel-cars-from-2035-explained (accessed on 25 March 2024).
6. Recycling Process. Available online: https://www.rombat.ro/en/company/rebat/ (accessed on 26 March 2024).
7. Feng, X.; Zhang, F.; Feng, J.; Jin, C.; Wang, H.; Xu, C.; Ouyang, M. Propagation dynamics of the thermal runaway front in large-scale lithium-ion batteries: Theoretical and experiment validation. *Int. J. Heat Mass Transf.* **2024**, *225*, 125393. [CrossRef]
8. Chen, M.; Liu, J.; He, Y.; Yuen, R.; Wang, J. Study of the fire hazards of lithium-ion batteries at different pressures. *Appl. Therm. Eng.* **2017**, *125*, 1061–1074. [CrossRef]
9. Funk, E.; Flecknoe-Brown, K.W.; Wijesekere, T.; Husted, B.P.; Andres, B. Fire extinguishment tests of electric vehicles in an open sided enclosure. *Fire Saf. J.* **2023**, *141*, 103920. [CrossRef]
10. Hodges, J.L.; Salvi, U.; Kapahi, A. Design fire scenarios for hazard assessment of modern battery electric and internal combustion engine passenger vehicles. *Fire Saf. J.* **2024**, *146*, 104145. [CrossRef]
11. Thunderhead Egnineering. Faster FDS Modeling with Professional Results. Available online: https://www.thunderheadeng.com/pyrosim (accessed on 10 April 2024).
12. PyroSim Software by Thunderhead Engineering, version 2023.3.1312, X64. Available online: https://support.thunderheadeng.com/release-notes/pyrosim/2023/2023-3-1312/ (accessed on 10 January 2025).
13. Buchmann, I. Can the Lead-Acid Battery Compete in Modern Times? Available online: https://batteryuniversity.com/article/can-the-lead-acid-battery-compete-in-modern-times (accessed on 15 April 2024).
14. Buchmann, I. BU-1501 Battery History. Available online: https://batteryuniversity.com/article/bu-1501-battery-history (accessed on 15 April 2024).
15. Continental Battery Systems, Car Battery Evolution—From Old-Tech to MIXTECH. Available online: https://www.continentalbattery.com/blog/car-battery-evolution-from-old-tech-to-mixtech (accessed on 15 April 2024).
16. Yakup, Ş.; Yıldırım, E.; Çağatay, A.; Enes, D.; Emre, K. Lead Acid Batteries for Micro Hybrid Electrical Vehicles—Influence of Different Type Expanders on the Performance of the negative plates. In Proceedings of the 5th International Anatolian Energy Symposium, Karadeniz Technical University, Trabzon, Turkey, 24–26 March 2021; Available online: https://www.researchgate.net/publication/357673614 (accessed on 15 April 2024).

17. Buchmann, I. BU-904: How to Measure Capacity. Available online: https://batteryuniversity.com/article/bu-904-how-to-measure-capacity (accessed on 15 April 2024).
18. *EN 50342-1:2015*; Lead Acid Starter Batteries—Part 1: General Requirements and Test Methods. CENELEC: Brussels, Belgium, 2015.
19. Buchmann, I. BU-902a: How to Measure CCA. Available online: https://batteryuniversity.com/article/bu-902a-how-to-measure-cca (accessed on 15 April 2024).
20. Buchmann, I. BU-1102: Abbreviations. Available online: https://batteryuniversity.com/article/bu-1102-abbreviations (accessed on 15 April 2024).
21. EUROBAT. EUROBAT Battery Innovation Roadmap 2030 White Paper. Available online: https://www.eurobat.org/wp-content/uploads/2022/03/EUROBAT_Battery_Innovation_Roadmap_2030_White_Paper.pdf (accessed on 15 April 2024).
22. *EN 54-1:2021*; Fire Detection and Fire Alarm Systems. Introduction. CENELEC: Brussels, Belgium, 2021.
23. *EN 54-7:2001*; Smoke Detectors. Point Detectors Using Scattered Light, Transmitted Light, or Ionization. CENELEC: Brussels, Belgium, 2001.
24. *EN 54-22:2015*; Resettable Line-Type Heat Detectors. CENELEC: Brussels, Belgium, 2015.
25. *EN 54-23:2010*; Fire Alarm Devices. Visual Alarm Devices. CENELEC: Brussels, Belgium, 2010.
26. *ISO 45001:2018*; Occupational Health and Safety Management Systems—Requirements with Guidance for Use. International Organization for Standardization: Geneva, Switzerland, 2018.
27. *OHSAS 18001:2007*; Occupational Health and Safety Management Systems—Requirements. British Standards Institution: London, UK, 2007.
28. *ISO 31000:2018*; Risk Management—Guidelines. International Organization for Standardization: Geneva, Switzerland, 2018.

processes

MDPI

Article

Toward Efficient Edge Detection: A Novel Optimization Method Based on Integral Image Technology and Canny Edge Detection

Yanqin Li [1] and Dehai Zhang [1,2,*]

[1] Mechanical and Electrical Engineering Institute, Zhengzhou University of Light Industry, Zhengzhou 450002, China; yqli@zzuli.edu.cn
[2] Henan Key Laboratory of Intelligent Manufacturing of Mechanical Equipment, Zhengzhou 450002, China
* Correspondence: zhangdehai0318@163.com; Tel.: +86-187-6885-6978

Abstract: The traditional SIFT (Scale Invariant Feature Transform) registration algorithm is highly regarded in the field of image processing due to its scale invariance, rotation invariance, and robustness to noise. However, it faces challenges such as a large number of feature points, high computational demand, and poor real-time performance when dealing with large-scale images. A novel optimization method based on integral image technology and canny edge detection is presented in this paper, aiming to maintain the core advantages of the SIFT algorithm while reducing the complexity involved in image registration computations, enhancing the efficiency of the algorithm for real-time image processing, and better adaption to the needs of large-scale image handling. Firstly, Gaussian separation techniques were used to simplify Gaussian filtering, followed by the application of integral image techniques to accelerate the construction of the entire pyramid. Additionally, during the feature point detection phase, an innovative feature point filtering strategy was introduced by combining Canny edge detection with dilation operations alongside the traditional SIFT approach, aiming to reduce the number of feature points and thereby lessen the computational load. The method proposed in this paper takes 0.0134 s for Image type a, 0.0504 s for Image type b, and 0.0212 s for Image type c. In contrast, the traditional method takes 0.1452 s for Image type a, 0.5276 s for Image type b, and 0.2717 s for Image type c, resulting in reductions of 0.1318 s, 0.4772 s, and 0.2505 s, respectively. A series of comparative experiments showed that the time taken to construct the Gaussian pyramid using our proposed method was consistently lower than that required by the traditional method, indicating greater efficiency and stability regardless of image size or type.

Keywords: SIFT algorithm; canny edge detection; image registration; Gaussian separation; integral image

1. Introduction

In numerous fields, such as medical image processing, remote sensing technology, pattern recognition, and defect detection, the crucial role of image registration technology is increasingly evident [1–4]. It involves computing the transformation model between different images to establish their corresponding geometric relationships, aligning the overlapping parts. Existing image registration methods can be classified into two main categories: intensity-based and feature-based methods [5,6]. Intensity-based image registration is renowned for its simplicity, intuitiveness, and computational efficiency, primarily relying on the pixel intensity information of images for registration. However, it is less effective when dealing with images with excessive noise or indistinct structures [7–9]. In contrast, feature-based registration methods precisely extract key features in images, such

as edges and corners, and combine similarity measures with various constraints to ascertain the geometric transformation relationships between images. This leads to more accurate image registration, effectively overcoming the limitations of intensity-based methods. It demonstrates superior performance in complex scenarios with significant lighting changes or the need for multisensory data analysis, as illustrated in ref. [10,11].

The development of feature-based matching algorithms has led to many classic methods. In 1988, the Harris algorithm proposed by Harris et al. emerged as a classic feature point detection algorithm [12]. This algorithm extracts a moderate number of feature points with low computational load, robustness to image rotation, and changes in viewing angle, and has good noise resistance. However, it detects feature points at a single scale and lacks scale invariance, making it unsuitable for applications with significant image scale variations. In 2004, Lowe introduced the Scale Invariant Feature Transform (SIFT) algorithm, characterized by its ability to extract distinct features with scale invariance and robustness to noise and other interferences, hence its widespread use in the field of image processing. However, the SIFT algorithm generates a large number of feature points, requires extensive computation, and has long processing times, consuming substantial system resources, and resulting in poor real-time performance [13–15].

To address the issue of long computation time and poor real-time performance of the SIFT algorithm, Ke et al. introduced the PCA-based SIFT (PCA-SIFT) algorithm in the same year. Initially, for each image path, the gradient image vector is computed and reduced to a lower-dimensional feature vector using Principal Component Analysis (PCA). Based on the sub-pixel location, scale, and dominant orientation of keypoints provided by the SIFT algorithm, a 41×41 image block is extracted from the image, rotated to a canonical orientation, and projected onto the computed feature vector space to obtain a smaller and more compact feature vector. The Euclidean distance between two feature vectors is calculated to determine if they correspond to the same keypoint in different images. Although PCA-SIFT excels in computational efficiency and reduced storage requirements, it has some drawbacks. First, the PCA dimensionality reduction process, by selecting principal components (main directions of variance) in data, reduces dimensions but may overlook certain details and features, leading to information loss and affecting the algorithm's robustness. Second, PCA is sensitive to outliers, diminishing matching performance in the presence of noise or anomalies. To better ensure uniform distribution of features in terms of location and scale, and to enhance the stability and accuracy of matching, Sedaghat et al. proposed the uniformly processed SIFT algorithm in 2011. The core idea of this algorithm is a novel SIFT feature selection strategy based on uniform distribution in location and scale, isolating feature quality through stability and uniqueness constraints. Initially, SIFT features with good distribution characteristics are extracted through the feature selection strategy. Then, a preliminary cross-matching process is introduced, and consistency is checked using a projective transformation model. However, the introduced uniform processing increases computational complexity in handling large-scale image data, resulting in poor real-time performance. Additionally, the uniformly processed SIFT algorithm is limited if the image has significant non-rigid deformations. In 2022, Yu et al. proposed a heterologous image matching algorithm based on an improved SIFT algorithm. Firstly, during feature point detection, grids are set for each layer in the scale space with weight coefficients, and a quadtree method is used in conjunction with the image's phase response intensity map to select uniformly distributed and stable feature points. Secondly, descriptors are reconstructed, and standardized Euclidean distance is used to measure feature descriptors, employing a bidirectional matching strategy for coarse matching. Finally, the Random Sample Consensus (RANSAC) algorithm is used for refinement. Due to the introduction of multi-level processing and the quadtree method, the

algorithm's computational complexity is relatively high, posing challenges for large-scale image processing [16–19].

The above methods often involve global optimization techniques and many require high-performance computing environments to achieve reasonable processing times. However, they face challenges such as a large number of feature points, high computational demand, and poor real-time performance when dealing with large-scale images. A novel optimization method based on integral image technology and canny edge detection presented by this paper, its goal aims to maintain the core advantages of the SIFT algorithm while reducing the complexity involved in image registration computations, enhancing the efficiency of the algorithm for real-time image processing, and better adapting it to the needs of large-scale image handling. Firstly, Gaussian separation techniques were used to simplify Gaussian filtering, followed by the application of integral image techniques to accelerate the construction of the entire pyramid. Additionally, during the feature point detection phase, an innovative feature point filtering strategy was introduced by combining Canny edge detection with dilation operations alongside the traditional SIFT approach, aiming to reduce the number of feature points and thereby lessen the computational load. A series of comparative experiments showed that the time taken to construct the Gaussian pyramid using the improved SIFT method was consistently lower than that required by the traditional SIFT approach, indicating greater efficiency and stability regardless of image size or type.

Section 2, titled "Related Work", synthesizes existing literature and identifies gaps that our research aims to address. Section 3, "Methodology", details the theoretical framework and procedural steps of our study. Section 4, "Experimental Evaluation", presents the results of our experiments and a thorough analysis. Finally, Section 5, which we have titled "Conclusion", summarizes our findings, discusses their implications, and suggests avenues for future research.

2. Related Work

In order to simultaneously preserve the advantages of the SIFT algorithm, such as scale invariance, rotational invariance, illumination invariance, rich feature descriptors, high robustness, and resistance to noise interference, and to enhance the computational efficiency of image registration, this paper effectively optimizes two key stages within the SIFT algorithm, as shown in Figure 1.

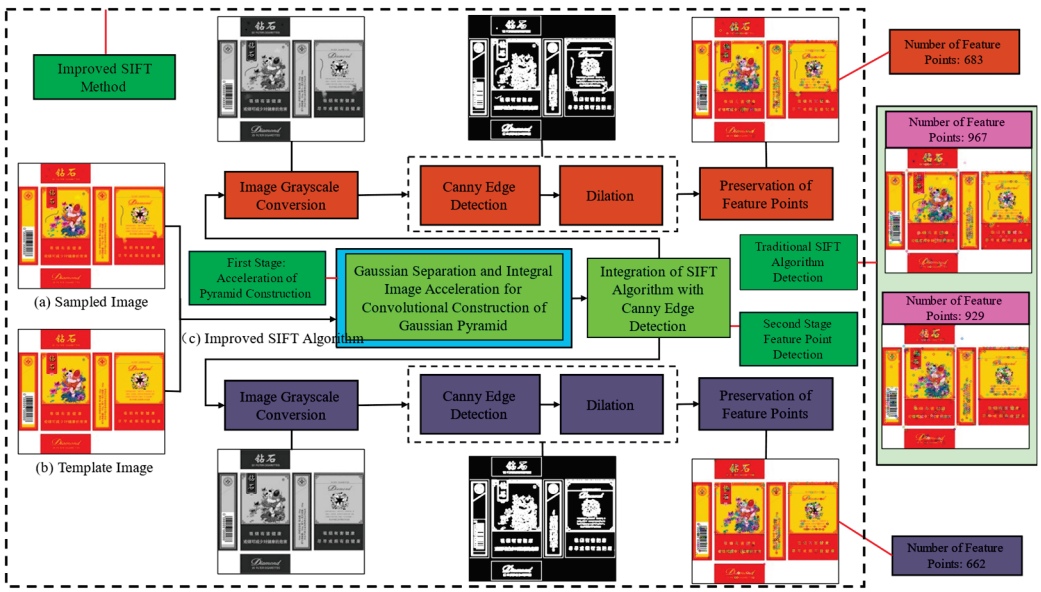

Figure 1. Improved SIFT Algorithm.

Initially, in the Gaussian pyramid construction phase, the separability of Gaussian filtering and the characteristics of integral images were utilized to successfully accelerate the construction of the Gaussian pyramid. This not only preserves the advantages of the SIFT algorithm but also enhances computational efficiency, making the algorithm more suitable for processing large-scale images. Subsequently, in the feature point detection phase, the combination of Canny edge detection and dilation operations was employed to filter feature points, effectively improving the accuracy and reliability of the feature points. This not only enables the SIFT algorithm to more precisely locate feature points in images but also reduces unnecessary redundant calculations, thereby further optimizing computational efficiency.

Table 1 shows the differences between both methods.

Table 1. The differences between the traditional SIFT method and the improves SIFT method [20–24].

	The Traditional SIFT Gaussian Pyramid Construction Method with Images of Different Sizes	**The Improved SIFT Gaussian Pyramid Construction Method**
feature point generation	generates a large number of feature points, robust but computationally expensive	reduces the number of feature points using Canny edge detection and dilation, maintaining robustness.
Gaussian pyramid construction	computationally intensive, involving multiple scales and octaves.	simplified using Gaussian separation techniques and accelerated with integral image technology
real-time performance	struggles to achieve real-time performance, especially for large-scale images	significantly improved real-time performance, suitable for large-scale images
time efficiency	high computational demand, long processing times.	reduced time for constructing the Gaussian pyramid and detecting feature points
accuracy	high accuracy in feature point detection and image registration.	maintains high accuracy while reducing computational load.
comparative experiments	consistently slower, especially for large images	consistently faster, regardless of image size or type

The proposed method, which combines SIFT with Canny edge detection and integral image technology, addresses the challenges of the traditional SIFT algorithm by reducing computational complexity and improving real-time performance. The use of Gaussian separation techniques, integral image technology, and an innovative feature point filtering strategy makes the method more efficient and suitable for large-scale image processing and real-time applications.

3. Methodology

3.1. Improved Gaussian Pyramid Construction Based on SIFT

The SIFT algorithm is broadly divided into four steps: construction of the scale space, keypoint detection, determination of the main orientation of feature points, and generation of feature descriptors [25–27]. In the construction of the Difference in Gaussian (DOG) scale space, the first step is to construct the Gaussian scale space. The Gaussian scale space of an image can be obtained through convolution of the image with Gaussian kernels of varying

scales. The convolution operation of a two-dimensional image $I(x, y)$ with a convolution kernel can be represented as follows:

$$L(x, y, \sigma) = G(x, y, \sigma) * I(x, y), \tag{1}$$

where $L(x, y, \sigma)$ represents the Gaussian smoothed image at a specific scale σ in the Gaussian pyramid, obtained by convolving the original image $I(x, y)$ with a two-dimensional Gaussian kernel. is the two-dimensional Gaussian kernel, and the two-dimensional Gaussian distribution is defined as follows,

$$G(x, y, \sigma) = \frac{1}{2\pi\sigma^2} e^{-\frac{x^2+y^2}{2\sigma^2}}, \tag{2}$$

where x and y denote the offset from the mean in each of the two dimensions and σ is the standard deviation.

However, constructing the Gaussian pyramid often involves numerous convolution operations, leading to high computational complexity. To enhance computational efficiency, the construction of the Gaussian pyramid is accelerated by leveraging the separability of Gaussian filtering and the properties of integral images. The Gaussian filtering is first decomposed into horizontal and vertical directions, followed by the use of integral images to expedite the convolution process.

3.1.1. Gaussian Separation

The one-dimensional Gaussian distribution is given as follows:

$$G(x, \sigma) = \frac{1}{\sqrt{2\pi}\sigma} e^{-\frac{x^2}{2\sigma^2}}, \tag{3}$$

where x is the offset from the mean and σ is the standard deviation.

The definition of the one-dimensional Gaussian distribution is extended to two dimensions, forming a two-dimensional Gaussian distribution. For simplicity, it is assumed that the standard deviation is equal in both directions. $(\sigma_x = \sigma_y = \sigma)$.

To separate variables from the two-dimensional Gaussian filter kernel, two one-dimensional Gaussian distributions are introduced as follows:

$$\begin{array}{l} G(x, \sigma) = \frac{1}{\sqrt{2\pi}\sigma} e^{-\frac{x^2}{2\sigma^2}} \\ G(y, \sigma) = \frac{1}{\sqrt{2\pi}\sigma} e^{-\frac{y^2}{2\sigma^2}} \end{array}, \tag{4}$$

Representing the two-dimensional Gaussian distribution as the product of two one-dimensional Gaussian distributions:

$$G(x, y, \sigma) = G(x, \sigma) \cdot G(y, \sigma), \tag{5}$$

3.1.2. Accelerated Convolution of Integral Images

Convolution operation for 2D images with 2D Gaussian filter kernel:

$$R(x, y) = \sum_{i=-k}^{k} \sum_{j=-k}^{k} G(i, j, \sigma) \cdot I(x - i, y - j), \tag{6}$$

where $R(x, y)$ denotes the convolution result, $G(i, j, \sigma)$ denotes the value at position (i, j) in the two-dimensional Gaussian kernel, $I(x - i, y - j)$ denotes the value of the original

image at position $(x-i, y-j)$, i, j denotes the index within the Gaussian kernel, and k is the radius of the Gaussian kernel determined based on σ.

Now, first a one-dimensional convolution is performed in the horizontal direction,

$$R_x(t, y, \sigma) = \sum_{i=-k}^{k} G(i, \sigma) \cdot I(t-i, y), \tag{7}$$

where t denotes the index in the horizontal direction

Next, a one-dimensional convolution is performed in the vertical direction as follows:

$$R_x(y, x, \sigma) = \sum_{\mathrm{j}=-k}^{k} G(j, \sigma) \cdot R_x(x, y-j), \tag{8}$$

An integral image is the cumulative sum of the pixel values of a two-dimensional image. Its definition is as follows:

$$S(x, y) = \sum_{i=0}^{x} \sum_{j=0}^{y} I(i, j), \tag{9}$$

Recursion of the integral image:

For the first line ($y = 0$):

$$S(x, 0) = \sum_{i=0}^{x} I(i, 0), \tag{10}$$

For the first column ($x = 0$):

$$S(0, y) = \sum_{j=0}^{y} I(0, j), \tag{11}$$

For a general case of $S(x, y)$, the calculation involves summing all the pixel values to the left and above the current point, and then subtracting the part that was double-counted in the upper-left corner. The formula is expressed as follows:

$$S(x,\ y) = S(x,\ y-1) + S(x-1,\ y) - S(x-1,\ y-1) + I(x,\ y), \tag{12}$$

In the formula,$S(x,\ y-1)$ and $S(x-1,\ y)$ are the integral image values to the left and above the current point, respectively. $S(x-1,\ y-1)$ is the integral image value of the overlapping part in the upper-left corner, and $I(x,\ y)$ is the pixel value of the current point.

Assuming that the sum of a rectangular area needs to be calculated, with the upper-left corner coordinates as (A, B) and the lower-right corner coordinates as (C, D), then the sum of this rectangular area can be calculated using the following formula:

$$Sum = S(C, D) - S(C, B-1) - S(A-1, D) + S(A-1, B-1), \tag{13}$$

3.2. Based on the Traditional SIFT Algorithm Integrated with Canny Edge Detection

The SIFT algorithm detects feature points in images and extracts their descriptors, enabling the identification of similar feature targets across different images. However, in complex scenes, images may contain a large amount of detail and texture, leading to an excessive number of feature points detected by SIFT, which can slow down the registration process [28–30]. To enhance the performance of SIFT in registering images in complex scenes, this paper utilizes Canny edge detection to extract edge information from images and employs dilation operations. By reducing the number of feature points while ensuring

registration accuracy, the speed of the algorithm is increased, and more stable image registration is achieved in complex settings.

The Canny edge detection algorithm operates by locating the local maxima of image gradients, using high and low thresholds to differentiate between strong and weak edges. This approach effectively minimizes the effects of noise and ensures the detection of genuine weak edges. The core process involves using an approximate Gaussian function with $f_s = f(x,y) \times G(x,y)$ for smoothing the image, followed by employing a directional first-order derivative operator to pinpoint where the derivatives are maximized. After the smoothing process, the image gradients $f_s(x,y)$ are approximated using a 2×2 first-order finite difference formula, as detailed in Equation (14).

$$\begin{array}{l} P[i,j] \approx (f_s[i,j+1] - f_s[i,j] + f_s[i+1,j+1] - f_s[i+1,j])/2 \\ Q[i,j] \approx (f_s[i,j] - f_s[i+1,j] + f_s[i,j+1] - f_s[i+1,j+1])/2n \end{array}, \tag{14}$$

By calculating the average of finite differences within a 2×2 square region, the partial derivatives of the gradients in the x and y directions at the same point in the image are obtained. The magnitude and angle of the gradient are then calculated by converting from Cartesian coordinates to polar coordinates.

$$\begin{array}{l} M[i,j] = \sqrt{P[i,j]^2 + Q[i,j]^2} \\ \theta[i,j] = \arctan(Q[i,j]/P[i,j]) \end{array}, \tag{15}$$

where $M[i,\ j]$ represents the edge strength in the image. $\theta(i,j)$ denotes the orientation of the edges. $M[i,\ j]$ achieves a local maximum value at the direction angle $\theta(i,j)$, which indicates the direction of the edge.

Next, the gradient magnitudes are subjected to Non-Maxima Suppression (NMS), which extracts pixels that have the greatest gradient magnitude along their respective gradient directions.

$$\begin{array}{l} \xi[i,j] = \text{Sector}(\theta[i,j]) \\ N[i,j] = \text{NMS}(M[i,j], \xi[i,j]) \end{array}, \tag{16}$$

where $\xi[i,j]$ calibrates the gradient direction, dividing it into four ranges based on the size of the directional angle $\theta(i,j)$, which can be labeled as 0, 1, 2, or 3. Non-maxima suppression is applied for each direction. If the gradient magnitude of a pixel's neighboring pixels along its gradient direction is greater than that of the pixel itself, the pixel's value will be set to zero.

Next, edge detection and connection are performed using a dual-threshold algorithm. This process involves applying two different threshold values to the image.

$$\tau_2 = 2\tau_1, \tag{17}$$

where τ_2 determines the edges, while τ_1 tracks breaks in the edges. Pixels with gradient magnitudes greater than τ_2 are definitively edges; those less than τ_1 are definitively not edges; for pixels with gradient magnitudes between τ_1 and τ_2, the decision to classify them as edges depends on whether there are neighboring pixels with values exceeding the higher threshold.

The process of integrating Canny edge detection with an improved traditional SIFT algorithm is illustrated in Figure 2. Initially, an image is loaded, followed by the detection of feature points using an algorithm that builds on the improved Gaussian pyramid construction of SIFT. Subsequently, the loaded image is converted to grayscale, and Canny edge detection is applied. The edges are then expanded through dilation operations. Finally, only those SIFT feature points located within the white areas of the Canny edge detection

results are retained, effectively filtering out feature points from other areas. These filtered feature points are then plotted on the original image.

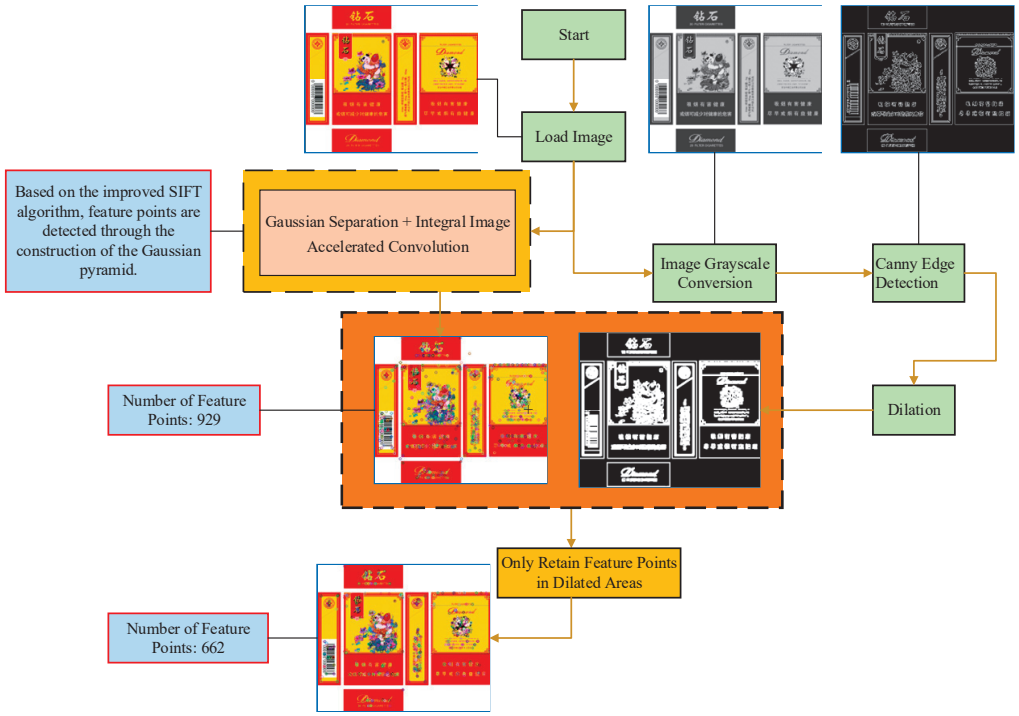

Figure 2. Integration of Traditional SIFT Algorithm with Canny Edge Detection.

3.3. Image Alignment

Utilizing the improved SIFT algorithm, feature points of the original image, as well as rotated or translated images, are identified. For each feature point, the gradient magnitude and direction of its surrounding area are calculated. Then, based on the orientation and scale of the feature point, its feature descriptor is computed. The Euclidean geometric distance between two sets of feature descriptors is determined, as shown in Equation (18).

$$D(r,s) = \|D_r - D_s\| = \sqrt{\sum_{i=1}^{n}(D_r[i] - D_s[i])^2} \tag{18}$$

where r and s represent the feature points of the rotated or translated image and the original image, respectively, while D_r and D_s represent the n-dimensional feature descriptors.

The two feature points with the smallest Euclidean geometric distance are selected, and their distance ratio r is calculated, as shown in Equation (19).

$$r = \frac{d_1}{d_2} < T, \tag{19}$$

where d_1 and d_2 are the Euclidean distances of the feature point to its nearest and next nearest neighbors, respectively, and T is the threshold. If the ratio r exceeds a specific threshold T, it is identified as an incorrect match and filtered out. Conversely, if the ratio r is less than the threshold T, it is deemed a correct match and retained.

The primary concept of the RANSAC algorithm is to obtain the optimal solution through iterative computation [31]. In image registration, the RANSAC algorithm is used

to determine the coordinates of matching point pairs between images, thereby establishing the transformation relationship between the two images:

$$\begin{bmatrix} x \\ y \\ 1 \end{bmatrix} = \begin{bmatrix} h_0 & h_1 & h_2 \\ h_3 & h_4 & h_5 \\ h_6 & h_7 & 1 \end{bmatrix} \begin{bmatrix} x^* \\ y^* \\ 1 \end{bmatrix}, \tag{20}$$

In the equation, (x, y) and (x^*, y^*) represent the feature points extracted from the two images, respectively. The steps of the algorithm are as follows:

1. Initialization of Matched Pair Set: Start by forming a set from the feature point pairs of the two local images, labeled as N; then randomly select four matched pairs from N.
2. Random Sample Selection: Since at least four points are needed to estimate an affine or perspective transformation, randomly choose four matched pairs from the set N.
3. Model Parameter Solution: Based on these four pairs of points, calculate the eight unknown parameters in transformation Equation (20) to form a preliminary transformation matrix H.
4. Error Calculation for Other Samples in Set N: Calculate the error η for the other sample points in the set using the preliminary transformation matrix H. Set a threshold T; if the error η is less than or equal to T, these points are identified as inliers, i.e., correct matches. Conversely, matches that do not meet this criterion are considered outliers.
5. Inlier Set Formation: Group the matched pairs with an error less than T into the inlier set S and recalculate the transformation matrix H* using the least squares method from Equation (20).
6. Iterative Optimization: Repeat the above process K times, retaining the transformation matrix with the highest number of inliers from each iteration. This matrix is considered the optimal spatial transformation model.

Use the RANSAC algorithm to further process the matched points after the first round of filtering, removing mismatched points and ensuring that at least four remaining matched points are available. With these four feature points, the transformation matrix between the two images can be calculated. The transformation matrix, as specified in Equation (20), uses affine transformation to map all pixels of the sampled image to the template image, thereby achieving registration between the two images.

4. Experimental Evaluation

To validate the effectiveness of the algorithm, the experiment will be conducted on a computer equipped with an Intel Core i5-10400F CPU, which is manufactured by Intel. Intel is headquartered in Santa Clara, CA, USA. 16 GB of memory, and an NVIDIA GeForce GTX 1660, which is manufactured by NVIDIA Corporation. NVIDIA is headquartered in Santa Clara, CA, USA.

4.1. Experiment on the Efficiency of the Improved SIFT Gaussian Pyramid Construction

The purpose of the experiment is to compare the performance of the improved SIFT Gaussian pyramid construction method with the traditional SIFT Gaussian pyramid construction method. The main parameters affecting the efficiency of Gaussian pyramid construction are σ (sigma), levels, and image size.

In the OpenCV implementation of the SIFT algorithm, the parameters for σ and levels are typically fixed. According to the official documentation, the default setting for σ is 1.6, and each octave in the scale space usually contains three levels. Therefore, the experiments adhere to this standard, setting σ = 1.6 and $levels = 3$. Another significant parameter that affects the efficiency of Gaussian pyramid construction is the image size. To further

verify the effectiveness of the algorithm, experiments were conducted with three different types and sizes of images: Image a (924 × 785 pixels), Image b (1405 × 1985 pixels), and Image c (1252 × 976 pixels), as shown in Figure 3. To more comprehensively assess the impact of image size on the efficiency of Gaussian pyramid construction, each type of image underwent resizing operations at 0.3 times, 0.1 times, the original size 1 times, 1.5 times, and 1.7 times to generate datasets of various image sizes. This allows for a more comprehensive comparison between the performance of the traditional SIFT method for constructing Gaussian pyramids and the improved method under these varying image sizes, as shown in Table 2.

(**a**) (**b**) (**c**)

Figure 3. Images of three different types and sizes. (**a**) Image a (924 × 785 pixels); (**b**) Image b (1405 × 1985 pixels); (**c**) Image c (1252 × 976 pixels).

Table 2. Performance of the Improved SIFT Gaussian Pyramid Construction Method and the Traditional SIFT Gaussian Pyramid Construction Method with Images of Different Sizes.

Image Type	Image Resolution Size (pixel)	Time for the Improved SIFT Gaussian Pyramid Construction Method				Time for the Traditional SIFT Gaussian Pyramid Construction Method			
		1	2	3	Average Time (s)	1	2	3	Average Time (s)
a	277 × 235	0.0010	0.0010	0.0010	0.0010	0.0121	0.0127	0.0127	0.0125
	462 × 392	0.0020	0.0020	0.0020	0.0020	0.0307	0.0301	0.0314	0.0307
	924 × 785	0.0090	0.0099	0.0110	0.0100	0.1108	0.1099	0.1099	0.1102
	1386 × 1177	0.0239	0.0239	0.0239	0.0239	0.2481	0.2559	0.2471	0.2504
	1570 × 1334	0.0299	0.0309	0.0299	0.0302	0.3196	0.3186	0.3287	0.3223
	Average Time for Image Type a				0.0134	Average Time for Image Type a			0.1452
b	421 × 595	0.0021	0.0023	0.0020	0.0021	0.0396	0.0379	0.0399	0.0391
	702 × 992	0.0174	0.0160	0.0177	0.0170	0.1042	0.1029	0.1016	0.1029
	1405 × 1985	0.0383	0.0374	0.0313	0.0357	0.4054	0.4116	0.4214	0.4128
	2107 × 2977	0.0937	0.0937	0.0816	0.0897	0.9129	0.9247	0.9347	0.9241
	2388 × 3374	0.1094	0.1038	0.1094	0.1075	1.1615	1.1656	1.1499	1.1593
	Average Time for Image Type b				0.0504	Average Time for Image Type b			0.5276
c	375 × 292	0.0010	0.0011	0.0010	0.0010	0.0214	0.0213	0.0224	0.0217
	626 × 488	0.0022	0.0022	0.0031	0.0025	0.0537	0.0534	0.0533	0.0535
	1252 × 976	0.0284	0.0288	0.0293	0.0288	0.2070	0.2075	0.2091	0.2079
	1878 × 1464	0.0312	0.0306	0.0327	0.0315	0.4668	0.4778	0.4733	0.4726
	2128 × 1659	0.0402	0.0433	0.0424	0.0420	0.6038	0.6032	0.6013	0.6028
	Average Time for Image Type c				0.0212	Average Time for Image Type c			0.2717

In the experiments with three different image types (a, b, c), based on Table 1 and Figure 4, it was observed that the time taken to construct the Gaussian pyramid using the improved SIFT method was generally lower than that of the traditional SIFT method. This

indicates that the improved method is more efficient and stable regardless of image size or type. The specific analysis is as follows:

1. Impact of Scaling Ratio: For both methods, as the scaling ratio increased from 0.3 times to 1.7 times, the processing time also increased, reflecting the increased complexity in building the Gaussian pyramid due to more pixels in enlarged images. However, the growth in construction time for the Gaussian pyramid in large images was more gradual with the improved SIFT method, demonstrating its efficiency in processing large images.
2. Algorithm Adaptability and Stability: The improved SIFT method showed stable time growth across different image types and scaling ratios, indicating the adaptability and stability of the algorithm. In contrast, the traditional SIFT method had more significant time increases with specific image types and higher scaling ratios.
3. Suitability for Application Scenarios: Due to its high efficiency and stability, the improved SIFT method is particularly well-suited for scenarios requiring fast and efficient processing, such as real-time image processing or in resource-limited environments.

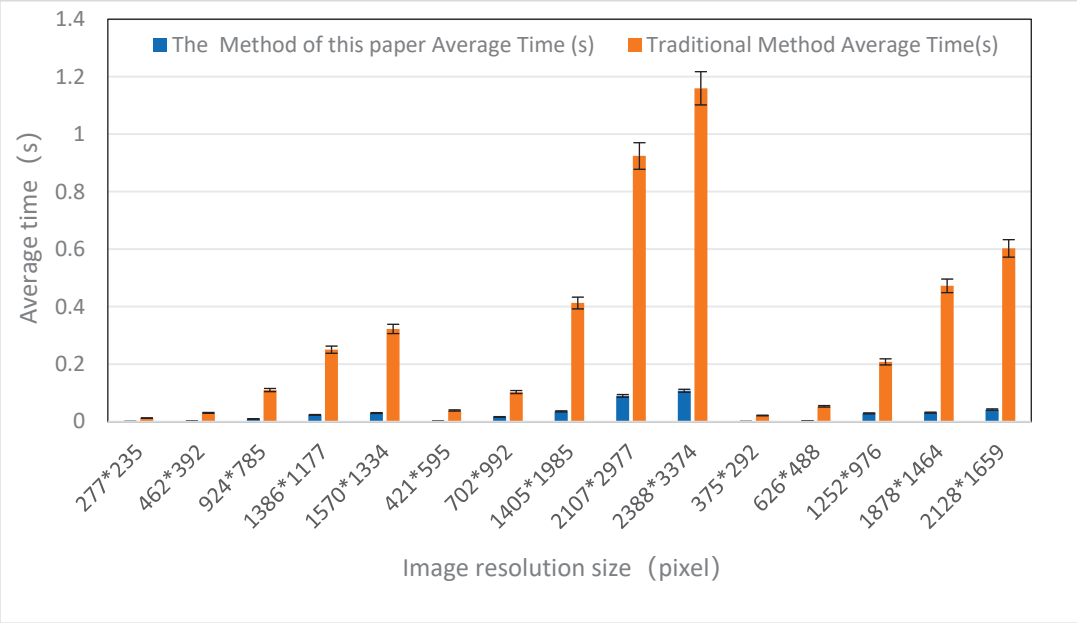

Figure 4. Performance of the improved SIFT Gaussian pyramid construction method and traditional SIFT Gaussian pyramid construction with images of different sizes.

4.2. Experiment on Improved Keypoint Filtering Based on SIFT

The differences between the original sampled image and the registered image were quantitatively assessed using pixel-level comparisons, Structural Similarity Index (SSIM), Mean Squared Error (MSE), and histogram intersection indices. The total time taken from feature point detection to completion of registration was recorded for both the traditional SIFT method and the method combining traditional SIFT with Canny edge detection. These times were used to evaluate the efficiency of these methods in image registration, with the registration processes illustrated in Figures 5 and 6.

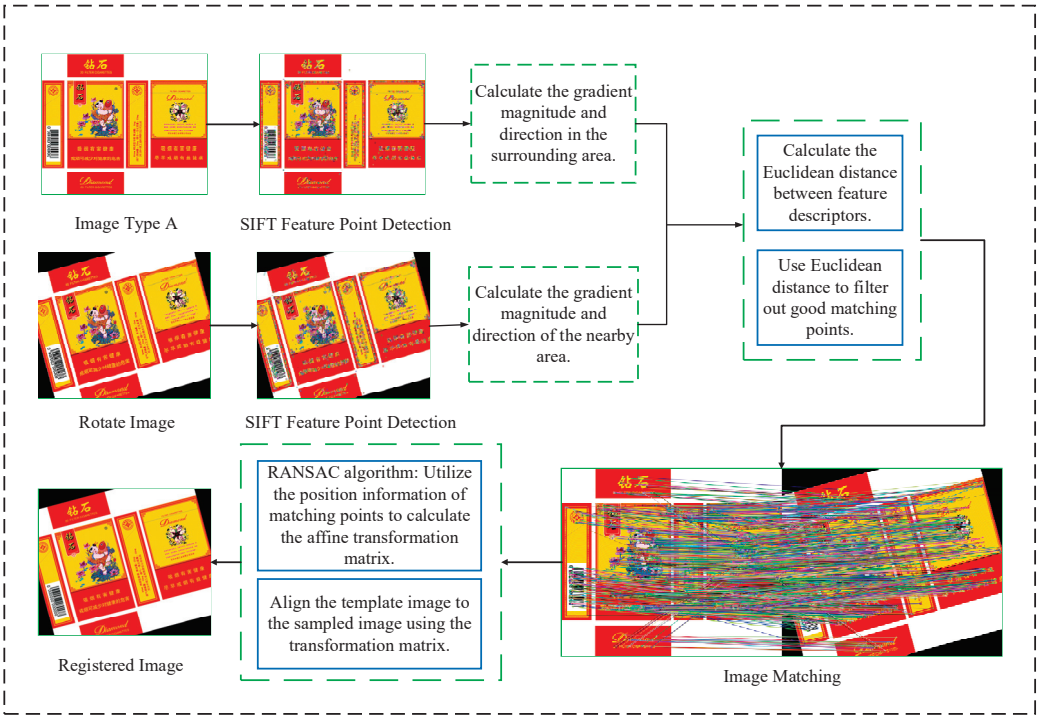

Figure 5. Image registration using the traditional SIFT algorithm.

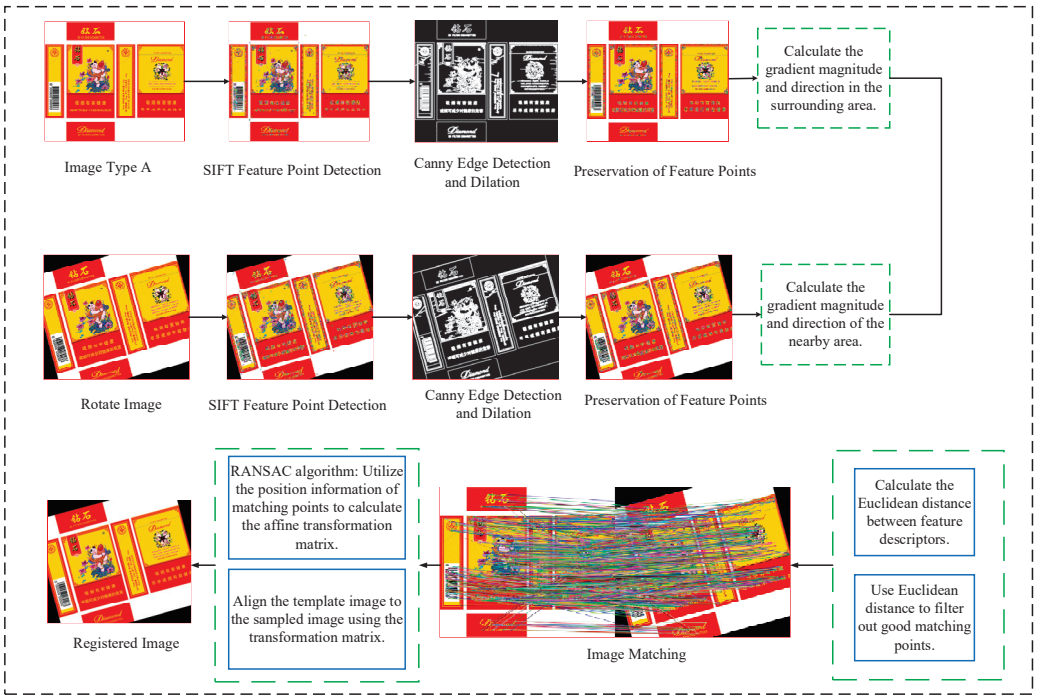

Figure 6. Image registration using the SIFT algorithm combined with canny edge detection.

Pixel-level Comparison: This involves calculating the absolute pixel differences between the rotated image and the post-registration image. Lower pixel difference values indicate better registration results.

$$\mathrm{F}_{(I_1,I_2)} = |I_1 - I_2|, \tag{21}$$

Structural Similarity Index (SSIM): SSIM is a metric that measures the visual similarity between two images. The closer the SSIM value is to 1, the better the image registration effect. The formula for SSIM is as follows:

$$\mathrm{SSIM}(x,y) = \frac{(2\mu_x\mu_y + c_1)(2\sigma_{xy} + c_2)}{\left(\mu_x^2 + \mu_y^2 + c_1\right)\left(\sigma_x^2 + \sigma_y^2 + c_2\right)}, \tag{22}$$

where u_x and u_y are the mean values of images x and y, respectively. σ_x^2 and σ_y^2 are the variances of images x and y, respectively. σ_{xy} is the covariance of x and y. c_1 and c_2 are small constants added to avoid division by zero, typically taken as $c_1 = (k_1 L)^2$ and $c_2 = (k_2 L)^2$, where L represents the dynamic range of the pixel values $k_1 = 0.01$ and $k_2 = 0.03$.

Mean Squared Error (MSE): MSE is a commonly used method for measuring the difference between two images. The lower the MSE value, the better the registration effect. The formula for MSE is as follows:

$$\mathrm{MSE}(I_1, I_2) = \frac{1}{MN}\sum_{i=1}^{M}\sum_{j=1}^{N}(I_1(i,j) - I_2(i,j))^2, \tag{23}$$

where M and N are the dimensions of the image, $I_1(i,j)$ and $I_2(i,j)$ are the pixel values of the two images at position (i,j).

Histogram Analysis: Histogram analysis typically involves comparing the histograms of two images. The higher the similarity, the better the registration effect. Histogram intersection is a common method for this analysis, and its calculation formula is as follows:

$$(H_1, H_2) = \sum_{i=1}^{K}\min(H_1(i), H_2(i)), \tag{24}$$

where H_1 and H_2 are the histograms of the two images, and K is the number of bins in the histogram.

Experiment 3.1 demonstrates that the improved SIFT Gaussian pyramid construction method offers a significant speed advantage over the traditional SIFT algorithm. To further illustrate the enhancements of the improved feature point selection based on SIFT compared to the traditional SIFT algorithm, this experiment involved applying translation and rotation transformations to image a, as shown in Figure 7.

(**a**) (**b**) (**c**)

Figure 7. *Cont.*

(**d**) (**e**) (**f**)

Figure 7. Displays a comparative illustration of image keypoints before and after filtering: (**a**) Number of keypoints before filtering in image type a (3165). (**b**) Number of keypoints after filtering in image type a (2480). (**c**) Number of keypoints before filtering in 15-degree rotated image (3685). (**d**) Number of keypoints after filtering in 15-degree rotated image (2994). (**e**) Number of keypoints before filtering in the (15, 15) translated image (3124). (**f**) Number of keypoints after filtering in the (15, 15) translated image (2429).

The analysis of Table 3, along with Figures 7–9, reveals that the feature point filtering strategy employed in this study, which combines the SIFT algorithm with Canny edge detection for processing image a (924 × 785 pixels), focuses on selecting the most representative feature points while eliminating those that have a minimal impact on image registration. This selection mechanism significantly reduces the total number of feature points, thereby decreasing the data processing requirements for feature point matching and image registration steps. Consequently, this approach effectively shortens the processing time from feature point detection to image registration and enhances overall efficiency.

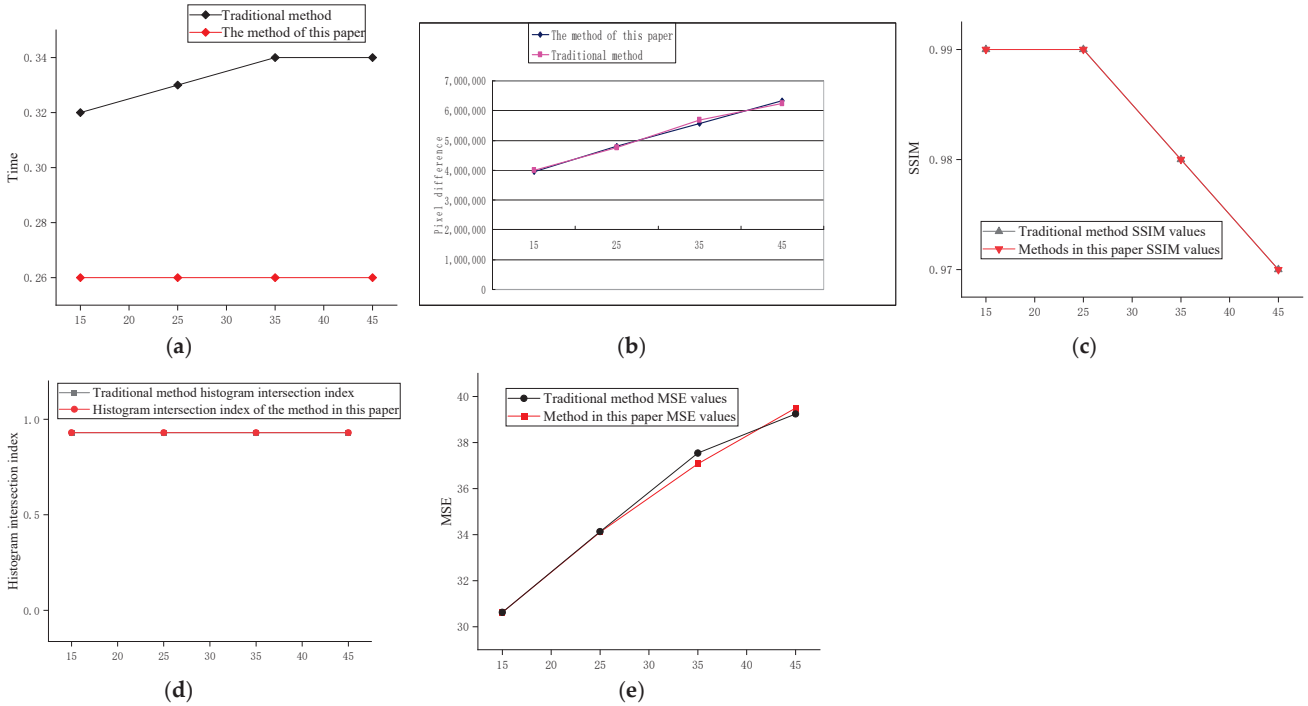

Figure 8. Comparison of rotation parameters in images: (**a**) Comparison of registration time consumption between the method in this paper and traditional methods. (**b**) Comparison of difference values between this paper's method and traditional methods. (**c**) Comparison of SSIM between this paper's method and traditional methods. (**d**) Comparison of histogram intersection index between this paper's method and traditional methods. (**e**) Comparison of MSE between this paper's method and traditional methods.

Table 3. Data comparison between improved keypoint selection based on SIFT and traditional methods in rotation and translation.

Rotation Angle (°)		15	25	35	45	Translation Distance (mm)	(15, 15)	(35, 35)	(−15, −15)	(−35, −35)
Number of keypoints after filtering	Image a	2994	2900	2957	3071		2429	2358	2382	2317
Number of keypoints before filtering	Image a	3685	3604	3638	3689		3124	3031	3087	2974
Time from feature point detection to image registration	The method of this paper	0.26	0.26	0.26	0.26		0.24	0.23	0.23	0.24
	Traditional method	0.32	0.33	0.34	0.34		0.31	0.30	0.30	0.30
Pixel difference	The method of this paper	3,953,015	4,800,217	5,569,518	6,336,485		0	0	0	0
	Traditional method	4,000,647	4,762,046	5,671,722	6,241,591		10,853	23,716	0	0
SSIM	The method of this paper	0.99	0.99	0.98	0.97		1.0	1.0	1.00	1.00
	Traditional method	0.99	0.99	0.98	0.97		1.0	1.0	1.00	1.00
MSE	The method of this paper	30.62	34.11	37.07	39.50		0.0	0.0	0	0
	Traditional method	30.62	34.13	37.54	39.24		0.11	0.16	0	0
Index	The method of this paper	0.93	0.93	0.93	0.93		1.00	1.00	1.00	1.00
	Traditional method	0.93	0.93	0.93	0.93		1.00	1.00	1.00	1.00

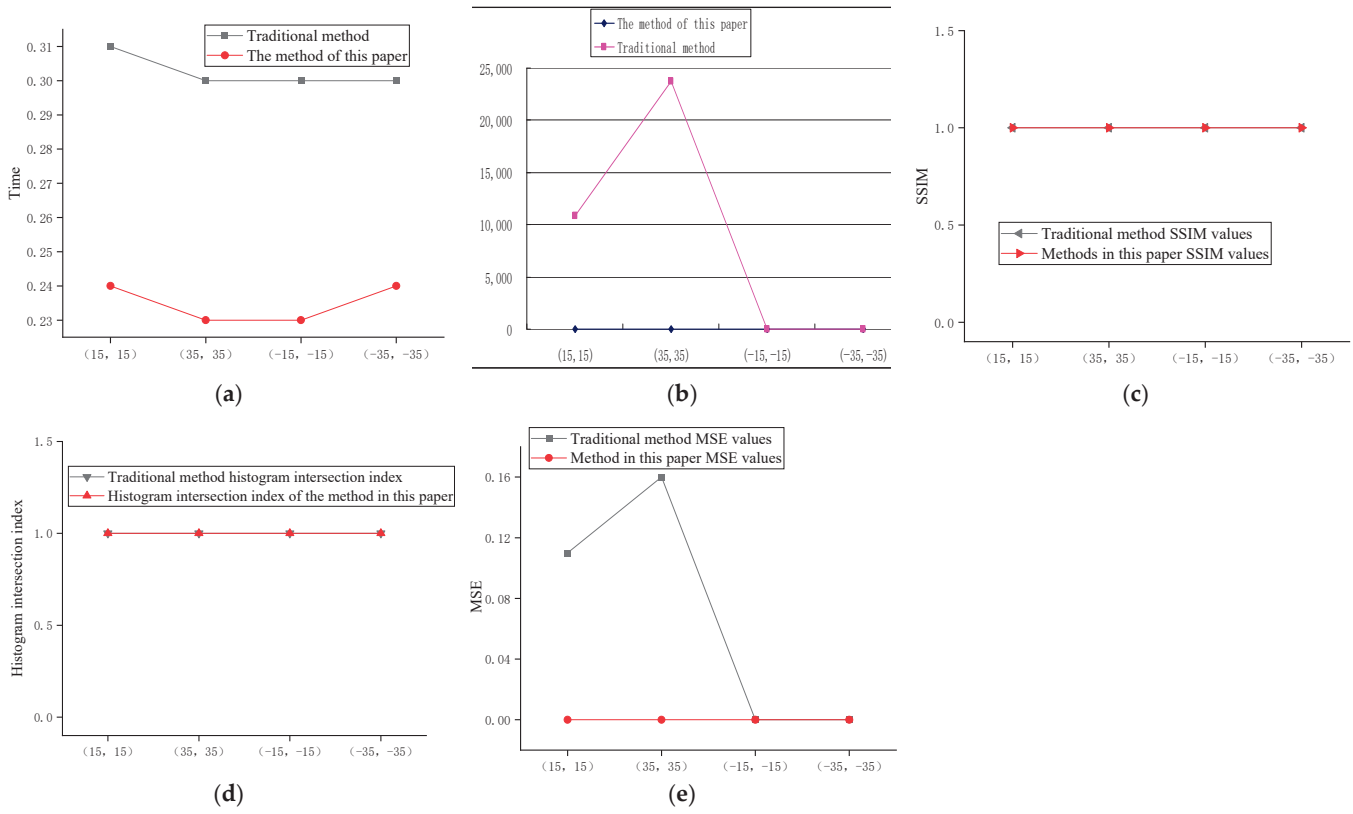

Figure 9. Translation image parameter comparison: (**a**) Registration time consumption comparison between this paper's method and traditional methods. (**b**) Difference value comparison between this paper's method and traditional methods. (**c**) SSIM comparison between this paper's method and traditional methods. (**d**) Histogram intersection index comparison between this paper's method and traditional methods. (**e**) MSE comparison between this paper's method and traditional methods.

4.3. Discussion

It is noteworthy that even with a reduced number of feature points, the method presented in this study still demonstrates high standards on key performance indicators such as Structural Similarity Index (SSIM), pixel differences, Mean Squared Error (MSE), and histogram intersection indices, compared to traditional methods. Particularly in experiments involving translation distances, pixel differences were significantly reduced, while performance indices remained at optimal levels, highlighting the improvements in image registration accuracy achieved by this method. This finding indicates that despite reducing the volume of data processed, the quality and accuracy of image registration have not been compromised by using selectively chosen feature points.

The study in question employs a feature point filtering strategy that combines the SIFT algorithm with Canny edge detection for processing images. This approach is particularly applied to an image of size 924×785 pixels. The primary goal of this strategy is to select the most representative feature points while eliminating those that have minimal impact on image registration. This selection mechanism significantly reduces the total number of feature points, thereby decreasing the data processing requirements for feature point matching and image registration steps. Consequently, this approach effectively shortens the processing time from feature point detection to image registration and enhances overall efficiency.

Overall, this study successfully demonstrates how to optimize the image registration process by precisely reducing the number of feature points without sacrificing quality. This approach is crucial for handling large-scale image data, especially in applications such as real-time video analysis or high-speed image processing systems, where it shows immense potential for application.

5. Conclusions

This paper successfully implements improvements to the SIFT algorithm, specifically through the optimization of Gaussian pyramid construction and the effective integration of Canny edge detection in feature point filtering. These enhancements not only speed up the construction of the Gaussian pyramid and increase the overall computational efficiency of the algorithm but also effectively reduce the number of feature points, thereby decreasing computational complexity and enhancing registration accuracy. Experimental results demonstrate that compared to the traditional SIFT algorithm, our method exhibits higher efficiency and better performance in the construction phase of the Gaussian pyramid when processing image registration tasks of varying sizes and types. Moreover, in the feature point detection phase, the combination of Canny edge detection and dilation operations effectively improves the accuracy and reliability of the feature points. This not only allows the SIFT algorithm to more precisely locate feature points within images but also reduces unnecessary redundant calculations, thereby increasing efficiency.

Overall, the results of this research not only enrich the theoretical applications of the SIFT algorithm but also hold significant practical value, particularly in fields requiring fast and accurate image registration, such as real-time video analysis and high-speed image processing systems. We plan to further optimize the performance of the algorithm by exploring more advanced techniques for Gaussian pyramid construction and feature point filtering. This includes the integration of deep learning techniques to enhance the robustness of feature detection and the use of hardware acceleration to speed up the image registration process.

These future directions will continue to advance the field of image registration and make the SIFT algorithm more applicable to a wider range of real-world scenarios.

Author Contributions: Conceptualization, D.Z. and Y.L.; D.Z. software, Y.L.; data curation. All authors have read and agreed to the published version of the manuscript.

Funding: This research was funded by the National Natural Science Foundation of China, grant number No. 52006201; Henan Provincial Science and Technology Research Project under Grant number No. 242102230034.

Data Availability Statement: The original contributions presented in this study are included in the article. Further inquiries can be directed to the corresponding author.

Acknowledgments: This work was supported by the National Natural Science Foundation of China under Grant number No. 52006201, and the Henan Provincial Science and Technology Research Project under Grant number No. 242102230034.

Conflicts of Interest: The authors declare no conflicts of interest.

References

1. Yang, H.; Li, X.R.; Zhao, L.Y.; Chen, S.H. A Novel Coarse-to-Fine Scheme for Remote Sensing Image Registration Based on Sift and Phase Correlation. *Remote Sens.* **2019**, *11*, 1833. [CrossRef]
2. Li, J.W.; Wu, X.Y.; Liao, P.H.; Song, H.H.; Yang, X.M.; Zhang, Z.R. Robust Registration for Infrared and Visible Images Based on Salient Gradient Mutual Information and Local Search. *Infrared Phys. Technol.* **2023**, *131*, 104711. [CrossRef]
3. Liang, H.D.; Liu, C.L.; Li, X.G.; Wang, L.N. A Binary Fast Image Registration Method Based on Fusion Information. *Electronics* **2023**, *12*, 4475. [CrossRef]
4. Lu, J.Y.; Jia, H.G.; Li, G.; Li, Z.Q.; Ma, J.Y.; Zhu, R.F. An Instance Segmentation Based Framework for Large-Sized High-Resolution Remote Sensing Images Registration. *Remote Sens.* **2021**, *13*, 1657. [CrossRef]
5. Liu, J.L.; Bu, F.L. Improved RANSAC Features Image-Matching Method Based on SURF. *J. Eng.-JoE* **2019**, *23*, 9118–9122. [CrossRef]
6. Lazar, E.; Bennett, K.S.; Hurtado Carreon, A.; Veldhuis, S.C. An Automated Feature-Based Image Registration Strategy for Tool Condition Monitoring in CNC Machine Applications. *Sensors* **2024**, *24*, 7458. [CrossRef] [PubMed]
7. Li, B. Application of Machine Vision Technology in Geometric Dimension Measurement of Small Parts.EURASIP. *J. Image Video Proc.* **2018**, *127*, 1–8. [CrossRef]
8. Xin, Z.H.; Wang, H.Y.; Qi, P.Y.; Du, W.D.; Zhang, J.; Chen, F.H. Printed Surface Defect Detection Model Based on Positive Samples. *Comput. Mater. Contin.* **2022**, *72*, 5925–5938. [CrossRef]
9. Ben-Zikri, Y.K.; Helguera, M.; Fetzer, D.; Shrier, D.A.; Aylward, S.R.; Chittajallu, D.; Niethammer, M.; Cahill, N.D.; Linte, C.A. A Feature-based Affine Registration Method for Capturing Background Lung Tissue Deformation for Ground Glass Nodule Tracking. Computer methods in biomechanics and biomedical engineering. *Imaging Vis.* **2022**, *10*, 521–539. [CrossRef]
10. Kuppala, K.; Banda, S.; Barige, T.R. An Overview of Deep Learning Methods for Image Registration with Focus on Feature-Based Approaches. *Int. J. Image Data Fusion* **2020**, *11*, 113–135. [CrossRef]
11. Razaei, M.; Rezaeian, M.; Derhami, V.; Khorshidi, H. Local Feature Descriptor using Discrete First and Second Fun-Damental Forms. *J. Electron. Imaging* **2021**, *30*, 023008. [CrossRef]
12. Chang, H.-H.; Chan, W.-C. Automatic Registration of Remote Sensing Images Based on Revised Sift with Trilateral Computation and Homogeneity Enforcement. *IEEE Trans. Geosci. Remote Sens.* **2021**, *59*, 7635–7650. [CrossRef]
13. Harris, C.G.; Stephens, M. A Combined Corner and Edge Detector. In Proceedings of the Alvey Vision Conference, Manchester, UK, 1 January 1988; pp. 147–151. [CrossRef]
14. Lowe, D.G. Distinctive Image Features from Scale-Invariant Keypoints. *Int. J. Comput. Vis.* **2004**, *60*, 91–110. [CrossRef]
15. Zheng, S.Y.; Zhang, Z.X.; Zhang, J.Q. Image Relaxation Matching Based on Feature Points for DSM Generation. *Geo-Spat* **2004**, *7*, 243–248. [CrossRef]
16. Ke, Y.; Sukthankar, R. PCA-SIFT: A More Distinctive Representation for Local Image Descriptors. In Proceedings of the 2004 IEEE Computer Society Conference on Computer Vision and Pattern Recognition CVPR 2004, Washington, DC, USA, 27 June–2 July 2004. [CrossRef]
17. Alhwarin, F.; Ristić-Durrant, D.; Gräser, A. VF-SIFT: Very Fast SIFT Feature Matching. In *Pattern Recognition (DAGM 2010)*; Lecture Notes in Computer Science, Volume 6376; Goesele, M., Roth, S., Kuijper, A., Schiele, B., Schindler, K., Eds.; Springer: Berlin/Heidelberg, Germany, 2010. [CrossRef]
18. Sedaghat, A.; Mokhtarzade, M.; Ebadi, H. Uniform Robust Scale-Invariant Feature Matching for Optical Remote Sensing Images. *IEEE Trans. Geosci. Remote Sens. IEEE* **2011**, *49*, 4516–4527. [CrossRef]
19. Yu, Z.W.; Zhang, N.; Pan, Y.; Zhang, Y.; Wang, Y.X. Heterogeneous Image Matching Based on Improved SIFT Algorithm. *Laser Optoelectron. Prog.* **2022**, *59*, 1211002. [CrossRef]

20. Zhu, F.; Zheng, S.; Wang, X.; He, Y.; Gui, L.; Gong, L. Real-Time Efficient Relocation Algorithm Based on Depth Map for Small-Range Textureless 3D Scanning. *Sensors* **2019**, *19*, 3855. [CrossRef] [PubMed]
21. Yang, J.; Xiao, Y.; Cao, Z. Toward the Repeatability and Robustness of the Local Reference Frame for 3D Shape Matching: An Evaluation. *IEEE Trans. Image Process* **2018**, *27*, 3766–3781. [CrossRef]
22. Bonnaffe, W.; Coulson, T. Fast fitting of neural ordinary differential equations by Bayesian neural gradient matching to infer ecological interactions from time-series data. *Methods Ecol. Evol.* **2023**, *14*, 1543–1563. [CrossRef]
23. Yang, J.; Zhang, Q.; Xiao, Y.; Cao, Z. TOLDI: An effective and robust approach for 3D local shape description. *Pattern Recognit.* **2017**, *65*, 175–187. [CrossRef]
24. Petrelli, A.; Di Stefano, L. Pairwise registration by local orientation cues. *Comput. Graph. Forum* **2016**, *35*, 59–72. [CrossRef]
25. Liu, Y.Y.; He, M.; Wang, Y.Y.; Sun, Y.; Gao, X.B. Fast Stitching for The Farmland Aerial Panoramic Images Based on Optimized SIFT Algorithm. *Trans. CSAE* **2023**, *39*, 117–125. [CrossRef]
26. Paul, S.; D., U.; Naidu, Y.; Reddy, Y. An Efficient SIFT-based Matching Algorithm for Optical Remote Sensing Images. *Remote Sens. Lett.* **2022**, *13*, 1069–1079. [CrossRef]
27. Gao, S.P.; Xia, M.; Zhuang, S.J. Automatic Mosaic Method of Remote Sensing Images Based on Machine Vision. *Comput. Opt.* **2024**, *48*, 705–713. [CrossRef]
28. Liu, Y.Y.; He, M.; Wang, Y.Y.; Sun, Y.; Gao, X.B. Farmland Aerial Images Fast-Stitching Method and Application Based on Improved SIFT Algorithm. *IEEE Access* **2022**, *10*, 95411–95424. [CrossRef]
29. Tang, L.; Ma, S.H.; Ma, X.C.; You, H.R. Research on Image Matching of Improved Sift Algorithm Based on Stability Factor and Feature Descriptor Simplification. *Appl. Sci.* **2022**, *12*, 8448. [CrossRef]
30. Sundani, D.; Widiyanto, S.; Karyanti, Y.; Wardani, D.T. Identification of Image Edge Using Quantum Canny Edge Detection Algorithm. *J. ICT Res. Appl.* **2019**, *13*, 133–144. [CrossRef]
31. Niedfeldt, P.C.; Beard, R.W. Convergence and Complexity Analysis of Recursive-RANSAC: A New Multiple Target Tracking Algorithm. *IEEE Trans. Autom. Control* **2016**, *61*, 456–461. [CrossRef]

processes

MDPI

Article

An Order-Picking Problem in a Medical Facility Using Genetic Algorithm

Berrin Denizhan *, Elif Yıldırım and Öznur Akkan

Department of Industrial Engineering, Engineering Faculty, Sakarya University, 54050 Sakarya, Türkiye; elifyildirim@sakarya.edu.tr (E.Y.)

* Correspondence: denizhan@sakarya.edu.tr

Abstract: Storage operations, order-picking, and product-handling processes have become increasingly important in today's industrial environment. These operations are a huge burden for businesses in terms of time and cost, but they often do not add direct value to products or services. Therefore, it has become essential to improve the storage operations to the highest quality, reduce the costs arising from storage, and increase customer satisfaction. This study compared genetic algorithm (GA) and simulated annealing (SA) methods with existing real results and operations in order to minimize the distance traveled by the picker in order-picking systems, optimize routes, and increase operational efficiency in the medical textile industry. In the analyses conducted on product-based, list-based, and order-based strategies, real data sets were used to examine the performance of both methods in detail. The study results revealed that GA reduced the total travel distance by 50% and reduced the total number of tours from 51 to 32. In addition, the SA method provided efficient results in certain scenarios, but GA showed superior performance in terms of minimizing the distance and number of tours. While the product-based strategy provided the best results regarding travel distance and number of tours, the list-based approach showed a balanced performance. The study offers significant improvement potential in logistics operations by reducing distances by up to 37% and increasing operational efficiency by up to 50% in order-picking processes.

Keywords: travel distance optimization; warehouse operations; order picking optimization; genetic algorithm; simulated annealing

1. Introduction

Order picking constitutes a vital element of warehouse operations, representing roughly 50% to 55% of the total time utilization and 65% of overall operational costs [1]. Healthcare systems worldwide face mounting pressure to minimize waste and cut unnecessary costs while enhancing the quality of patient care. For instance, the supply chain function oversees most of a health system's external spending, which accounts for up to 40 percent of total costs [2]. As a result, healthcare logistics and supply chain management are increasingly scrutinized by both practitioners and researchers [3–6]). Manual order picking is employed in small and medium enterprises. The storage process is overseen by warehouse personnel who manually choose items from shelves and generate orders. Despite technological advancements, many firms have favored manual order selection due to its diminished technological requirements and lower costs. There are several categories of order-picking systems. Picker-to-parts systems are the most common, where workers move through shelves to pick products. This system can include low-level picking and

high-level picking, where workers use lifting mechanisms to reach high shelves. Order picking is divided into and detailed as picking operations performed by humans or machines. For humans, picking policies are determined according to who is moving in the picking area (picker or product) and whether a conveyor system is used. In cases where a picker moves, picking can be performed according to the order or product, while in cases where a conveyor system is used, order, product or piece-based picking policies are applied. There are also automatic picking methods for operations performed by machines. This type of classification helps to select an appropriate picking method to increase the efficiency of warehouse operations [7].

The types of order picking, which are tailored to different operational scales and efficiency goals, include single order picking, best suited for small businesses where individual orders are processed independently [8]; batch order picking, ideal for consolidating multiple orders to minimize picker travel [9–11]; zone order picking, designed for large businesses to divide picking tasks by warehouse zones [12,13]; pick-and-pass, where items are sequentially picked and passed along a predefined route [14]; cluster order picking, focused on grouping similar orders to optimize picking time [15]; and wave order picking, used to coordinate picking schedules with outbound shipping times [16]. Order-picking systems have also been categorized, including sorting systems for the automated organization of items [17]; pick-to-box systems, which streamline the packing process by picking items directly into order-specific boxes [18–20]; picker-to-part systems, where pickers move to retrieve items from storage locations (this study); and part-to-picker systems, where items are brought to pickers via automated solutions for increased efficiency [21,22].

Given these classifications, order picking can be performed by humans or machines, and each system offers different operational benefits and barriers. According to the literature, four main sub-problems are identified in order picking: order grouping, group assignment, group sorting, and picker routing [23]. Optimizing order picking is crucial for improving a company's logistics performance. Careful planning and execution are necessary to avoid inefficiencies and to reduce costs [24]. Otherwise, inefficient order picking can lead to wasted time and under-utilization of resources [25].

In this study, the manual order-picking process of medical textile products operating as a labor-intensive factory in Türkiye is discussed. Our aim is to improve the manual order-picking process and develop a fast, forward-looking solution that can be adapted to all similar applications by optimizing it with meta-heuristic techniques.

Moreover, recent research has explored advanced optimization techniques for improving order picking. He and Chen [26] proposed a dynamic routing algorithm for manual order picking that adapts to real-time changes in the warehouse environment, reducing overall travel time. In a study by Petersen and Aase [27], the effects of slotting optimization were analyzed, revealing that well-planned product placement can significantly enhance order-picking efficiency. Additionally, Grosse et al. [28] discussed the integration of autonomous robots in parts-to-picker systems, highlighting the potential of collaborative robots (cobots) in reducing human workload and increasing operational speed. Finally, Boysen et al. [29] explored the benefits of zone-picking systems, where workers focus on specific warehouse areas, leading to better workload distribution and increased throughput.

This study focuses on the picker-to-parts system, specifically low-level picking. However, this approach has drawbacks, such as higher error rates, slower processes, and reduced productivity. Factors such as workforce fatigue and incorrect order selection negatively impact productivity. Businesses can improve manual order picking by improving inventory organization, providing employee training, and developing optimization strategies, especially in industries such as textiles, which still rely heavily on manual labor for manufacturing and warehouse tasks.

Coruzzolo et al. [30] developed a joint model for batching, assignment, sequencing, and routing in order picking to minimize completion time and tardiness in picker-to-part systems. Using multi-start heuristics, iterated local search, and constructive heuristics, their study demonstrated a 57% reduction in picking time compared to the single-order strategy, contributing significantly to the literature on integrated optimization in order-picking systems. Similarly, Czerniachowska et al. [31] introduced a model for order picking using a one-way conveyor system with buffer zones to optimize travel and resource allocation in high-demand e-commerce environments. Their study employed a CPLEX solver, which effectively optimized small instances but revealed limitations in medium and large-scale scenarios. Focusing on ergonomics in manual order picking, Kapou et al. [32] proposed a slot allocation algorithm designed to improve layout and storage assignments, reducing physical fatigue for workers. The study achieved a 14.9% increase in productivity and a 31% reduction in the order-picking difficulty index, emphasizing the importance of ergonomic considerations in warehouse operations. Li, Zhang, and Jiang [33] provided a literature review summarizing advancements in picker-to-parts and parts-to-picker systems, focusing on e-commerce warehouses.

As seen in the literature, rigid mathematical models reduce flexibility and become difficult or impossible to solve as the number of parts increases—they are called NP-hard problems. However, order picking is a problem with a dynamic structure, and techniques that will increase this dynamism and flexibility are needed. In this context, meta-heuristic algorithms like genetic algorithm (GA) and simulated annealing algorithm (SA) provide an advantage that can be integrated into computer systems and data in today's conditions, providing dynamism and flexibility. It also contributes to the data-driven decision-making process. It is emphasized that smart methods must be utilized to organize tasks effectively, ensuring that orders can be easily located when placed [34]. This study addresses critical gaps in current order-picking optimization research by combining GA and SA with real-world data and provides a practical, scalable approach to logistics efficiency. It provides travel length, pallet utilization rate, and picking mode flexibility in the context of real orders.

By Ou et al. [35], a literature review from 2018 to 2023 has closely examined how GA has been applied to optimize order-picking systems in picker-to-part environments. It has been further investigated that various optimization techniques such as GA, meta-heuristics, cluster analysis, and hybrid approaches have been proposed to address order assignment, grouping, and sorting problems. Some of these studies have partially developed GA-based methods targeting efficiency improvements in different warehouse systems through storage location assignment. In most studies, GA is applied to optimize multiple objectives, such as travel distance and resource utilization.

Casella et al. [36] studied 269 journal papers published between 2007 and 2022, and the studies focused primarily on trends in order-picking research, particularly in manual picker-to-parts systems, identifying the minimization of travel distance and ergonomic considerations as key priorities. Real-world applications in e-commerce and warehousing are emphasized, with suggestions for integrating emerging technologies to optimize picking systems. While traditional research prioritizes reducing travel distances and ergonomic improvements in manual picking systems, our study uniquely integrates GA with adaptive constraints, emphasizing real-world warehouse operations and focusing on dynamic order clustering to enhance practical applicability and efficiency.

Our study stands out by applying GA to optimize order picking in a real-world medical warehouse across three distinct picking scenarios, thereby advancing practical solutions in warehouse management as seen in Figure 1.

Classical metrics such as "travel distances", "ergonomic pickers' movements", "number of orders" and "storage space limitations" have been frequently studied in the literature. We minimize the travel distance and number of tours of the pickers, while also increasing the pallet usage. In this respect, it offers a multi-purpose solution. In addition, by considering the order change dynamically and probabilistically, it can produce solutions even if the order list becomes more complex or increases in volume, and thus aims to contribute to the literature. In particular, the interaction between pallet management and order grouping, which is usually addressed individually or in a limited scope in the existing literature, has been analyzed comprehensively and flexibly by using GA and SA in accordance with the structure of the real problem, taking into account high order diversity.

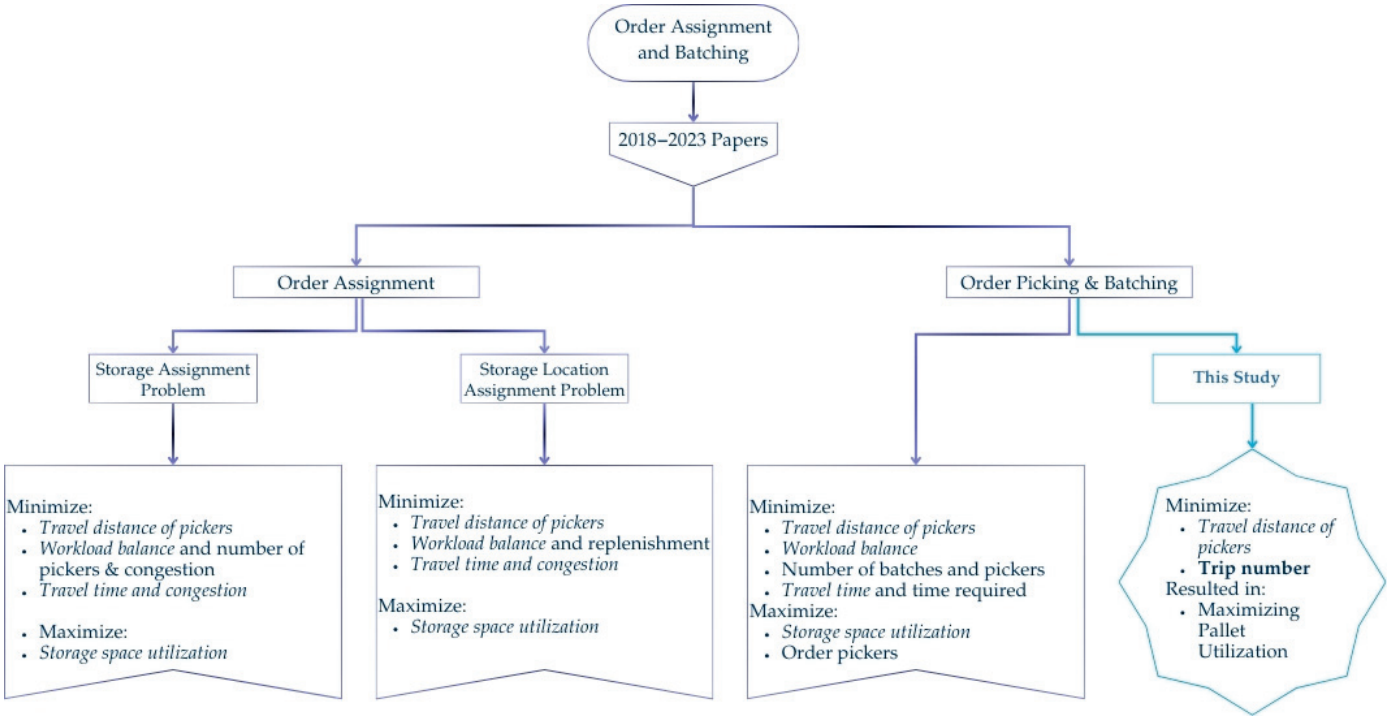

Figure 1. Classification of order-picking systems (OPS). Adapted from [36].

2. Materials and Methods

Order picking involves retrieving items from the warehouse to fulfill customer orders. The process includes receiving and processing customer orders, determining product placement and priority, selecting items in sequence, packing the selected products, and shipping them to customers. Efficient order picking is critical for both customer satisfaction and business success [37]. The order lists of a medical textile manufacturer described above were searched for best performance using genetic algorithm (GA) and simulation annealing algorithm (SA). The Manhattan distance was used to calculate the circulation distance of the orders. In this section, information about GA and SA, their reasons for use in the research, and Manhattan distance will be given, respectively.

2.1. Genetic Algorithm and Simulated Annealing

Genetic algorithm (GA) optimization techniques are inspired by the principles of natural selection and evolutionary biology [38] firstly introduced by Holland in 1975 [39]. These algorithms simulate the process of natural evolution to solve complex optimization problems [40]. The fundamental concept involves representing potential solutions as "chromosomes" and iterative improving these solutions through genetic operators such as selection, crossover, and mutation. The GA approach has been successfully applied to

various optimization problems, including vehicle routing, scheduling, and network design, particularly in scenarios where traditional optimization methods are computationally infeasible [41].

This paper presents an artificial intelligence approach using a multi-objective GA solution. The proposed GA method's performance is compared with the traditional method using real data from a medical textile manufacturer. The two primary research questions are: (1) Can a better order-picking sequence be created beyond the fixed lists? and (2) How does the new GA approach affect the number of tours and distance traveled? Which algorithm is better for this problem, SA or GA, to meet optimum results?

Although approaches vary, the GA has been used to address order-picking challenges. For example, GA can optimize make-span in manual order-picking operations. Dalle Mura and Dini [42] utilized GA to address the order-picking problem, emphasizing its application in optimizing worker health by accounting for variations in energy expenditure influenced by individual characteristics such as gender, age, and weight. GA has optimized worker assignments in order-picking systems by considering worker fatigue and spatial characteristics of order groups [43]. Additionally, GA has been applied to balance workloads and minimize the number of batches required in the picking process [44]. Other GA were also used to reduce congestion and waiting times during order picking and sorting [45].

Some combined storage location assignment problems with order picking involve using multi-objective GA to improve warehouse management efficiency. Other methods, such as meta-heuristics and cluster analysis, have also been tried to improve picker routing, grouping, and delivery scheduling. It involves the combined problems of order-picking and sorting problems in low-level picker-to-part systems, where the potential for simplifying operations using GA-based solutions has been revealed. Overall, this study addresses the flexibility and efficiency of GA in solving relevant problems related to order-picking problems. SA and GA are both prominent optimization techniques that can be effectively combined to enhance their performance in various applications. The SA approach has been shown to significantly enhance storage assignment strategies, yielding a 21% reduction in total retrieval times compared to traditional frequency-based methods in multi-level warehouses [46]. On the other hand, GA has been explored in various contexts, including optimizing order-picking strategies through simulations that compare multiple algorithms, including hlGA and ant colony optimization [47]. Furthermore, Ardjmand et al. [48] demonstrated the effectiveness of combining list-based SA with GA for order batching and picker routing, leading to improved efficiency in put wall picking systems. Similarly, Nathania [49] highlights the joint optimization of order batching and picker routing through the SA algorithm, effectively circumventing local optima to achieve superior solutions. Additionally, Castier and Martínez-Toro [50] applied a modified SA method for storage allocation, integrating advanced computational tools to tackle the pick-to-parts problem. Collectively, these studies underscore the potential of SA and GA in enhancing operational efficiency in order-picking systems.

Simulated annealing (SA) is an optimization technique inspired by the annealing process in materials science and engineering and first introduced by Kirkpatrick in 1983. This technique carefully heats and cools a material to form the desired structure. The method uses probabilistic navigation of the solution space from a computational perspective to address complex optimization problems [51].

SA has been acknowledged for effectively addressing many optimization problems, including the traveling salesman problem, workshop planning, etc. For example, SA was successfully used in order picking aimed at reducing CO2 emissions [52]. The method is convenient in scenarios where the search space is significantly large and complex, and traditional optimization methods are less applicable. Atmaca et al. [53] demonstrated

that SA is a viable method for solving complex warehouse management problems by effectively minimizing costs and improving efficiency in the storage system. Also, in their paper, Kostrzewski et al. [54] employed SA to optimize order-picking policies in automated storage/retrieval systems. By applying SA, the authors [54] aim to minimize order picking times and costs, enhance process reliability, and support warehouse managers in decision-making. Kucuksari [55] is another study that successfully solves the SA algorithm in minimizing congestion and travel distance in an automated warehouse. The SA method was used to obtain an optimal solution, which then, in combination with the COMET method, provided satisfactory results by determining the relationship between the preferences of the initial alternatives and newly identified alternatives [56].

This study implements the SA alongside the GA due to the challenges associated with identifying the optimal solution using conventional approaches in complicated and expansive solution spaces within warehouse systems. The research categorizes the issue of manual order picking in a manufacturing facility producing medical textile items, along with the minimization of trip time and rounds, as NP-hard due to the wide variety of orders. In this scenario, where identifying the optimal solution inside extensive solution spaces becomes mathematically infeasible, the SA algorithm was employed as a metaheuristic strategy.

In recent years, the SA algorithm has been employed in the literature for warehouse placement and picking challenges, owing to its capacity to yield results near the global optimal solution while avoiding entrapment in local optima [51]. The SA algorithm was employed in the study for its capacity to dynamically optimize order selection strategies. The program generates an appropriate order list of materials based on three distinct scenarios and product categories. The SA algorithm operated iteratively across varying temperatures, generating distinct solutions at each temperature, and assessed these solutions using a probabilistic method. In accepting lower-cost solutions, it also demonstrated the capability to evade local minima, allowing for the exploration of higher-cost yet broader solution spaces. GA emulate the mechanisms of diversity and adaptation using genetic operators like crossover and mutation among individuals (solutions) in a population, drawing inspiration from natural evolutionary processes [39,41]. By evaluating several solutions concurrently (population), GA possess the capacity to enhance diversity while progressing toward the global optimum. They can offer a wider view on certain issues by concurrently assessing various solution alternatives [51,57]. Consequently, the issue was examined using two methodologies.

The benefits and contributions can be described as follows:

1. This study concentrates on lightweight and essential medical textile items, particularly utilizing empirical data.
2. It enhances the literature by comparing the performance of GA and SA optimization techniques, addressing the complexities inherent in real-world scenarios characterized by a variety of products and orders.
3. By including actual warehouse data, the research enhances the practical relevance of its findings and bridges the divide between theoretical models and real-world implementations.
4. The paper examines the performance of three scenarios classified by dataset size and order selection procedures, specifically product-based, list-based, and order-based approaches, offering a comprehensive comparison of GA and SA methodologies.
5. Concurrently, the order lists in these three scenarios indicate variations regarding products, volume, and order quantity in alignment with reality.

6. Incorporating adaptive pallet capacity limits, the model accurately represents real-world fluctuations in resource availability and operating requirements, hence enhancing its adaptability to dynamic contexts.
7. Sensitivity evaluations examine the impacts of variations in order volume and adjustments to genetic algorithm parameters, illustrating the scalability and adaptability of the offered methodologies.

2.2. Manhattan Distance

The Manhattan distance, also known as the city block distance, Taxicab distance or L1 norm, is a metric used to measure the distance between two points on a rectangular grid. This method is named after the Manhattan borough of New York City, characterized by its grid-like street layout. Because the forklifts have to navigate between and around shelves, determining the Euclidean distance cannot be feasible because it requires maneuvering over the racks, which is not practicable. As shown in Figure 2, the Manhattan distance is a more suitable distance metric in this situation.

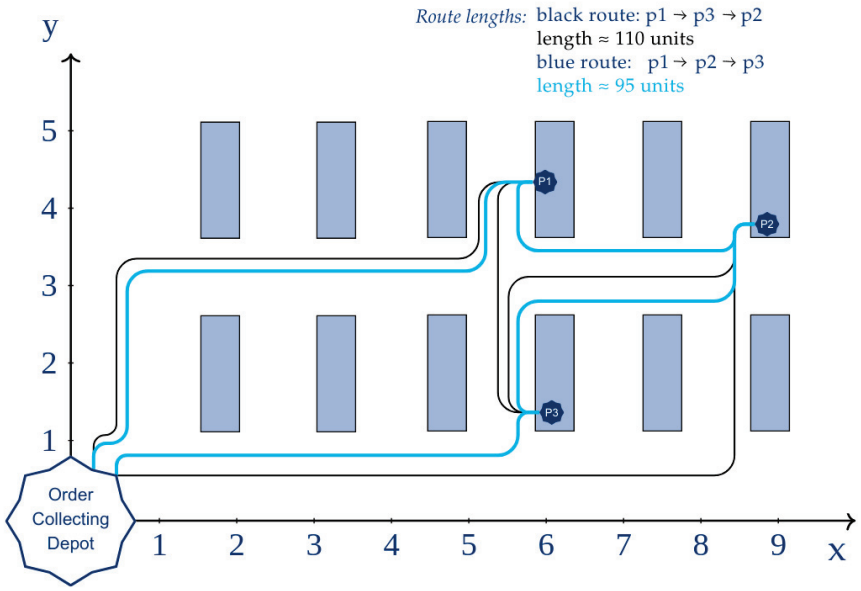

Figure 2. Possible calculations for picking two consecutive products in the warehouse.

The Manhattan distance is calculated as the sum of the absolute differences between the coordinates of two points. It represents the path between points using only right-angle turns, analogous to navigating city blocks [58]. Also it calculates the absolute differences between coordinates of a pair of objects [59].

Specifically, let $A = (a_1, a_2, \ldots, a_m)$ and $B = (b_1, b_2, \ldots, b_m)$ be two points in $\mathbb{R}^m$. Then the multi-dimensional Manhattan distance can be written as:

$$D_{AB} = \sum_{k=1}^{m} |a_k - b_k| \tag{1}$$

where $|\cdot|$ denotes the absolute value function, m is the total dimension number, and D_{XY} is the Manhattan distance between the two points.

For two points such as a and b, which are from the products to be collected, a(x_1, y_1) and b(x_2, y_2) in a two-dimensional plane, the Manhattan distance is calculated in Equation (9).

3. Problem Definition

The company's order fulfillment process involves multiple interrelated activities that significantly impact operational efficiency and customer satisfaction. The current system follows a two-tiered approach, depending on the type and volume of incoming orders:

1. High-volume orders: A production order is generated, and production begins to meet the demand;
2. Low-volume orders: The company fulfills demand using existing inventory from the central warehouse while maintaining production efficiency.

The warehouse management system is the foundation of the order fulfillment process, which oversees product selection, packaging, and distribution. When an order arrives, the production planning engineer checks inventory availability through the Enterprise Resource Planning (ERP) system. If the products are in stock, the warehouse staff initiates a transfer of goods.

However, the current picking strategy (product-based, list-based, or order-based) lacks systematic optimization, leading to inefficiencies in travel distances, under-utilized pallet capacities, and excessive travel times within the warehouse. These inefficiencies directly affect the speed and accuracy of order fulfillment, ultimately impacting customer satisfaction.

Three primary picking techniques are discussed as potential solutions to these challenges, as seen in Figure 3.

1. Product-based picking: Products are arranged and collected based on their proximity within the warehouse to minimize travel distances. This method emphasizes grouping items by location while considering capacity constraints, resulting in 169 distinct groups.
2. List-based picking: Products are picked according to predefined selection lists that came directly from the company, yielding 10 groups. The company uses this list as a stable order-picking method for collecting orders.
3. Order-based picking: Products are gathered based on order sequences to fulfill multiple orders in a single trip, minimizing overall travel distances and maximizing efficiency, resulting in 29 groups.

The experiment utilized a dataset from a medical textile company's actual data, comprising 169 unique products with varying quantities, volumes, and spatial coordinates within a warehouse. Each product was associated with a specific list number and order name.

After the input data containing the necessary details for the process calculations are loaded by the genetic algorithm, a random sequence of routes is generated to create the initial population. The efficiency of each route is evaluated by calculating the route distances. The first route is created and changed with genetic operations such as crossover and mutation (addition, replacement, or substitution of genes), and selection is performed. Termination criteria determine whether the algorithm should stop after finding a feasible solution or after a predetermined number of iterations, which is 1000 in our study. Pallet capacity is managed throughout the process to keep track of picked volumes.

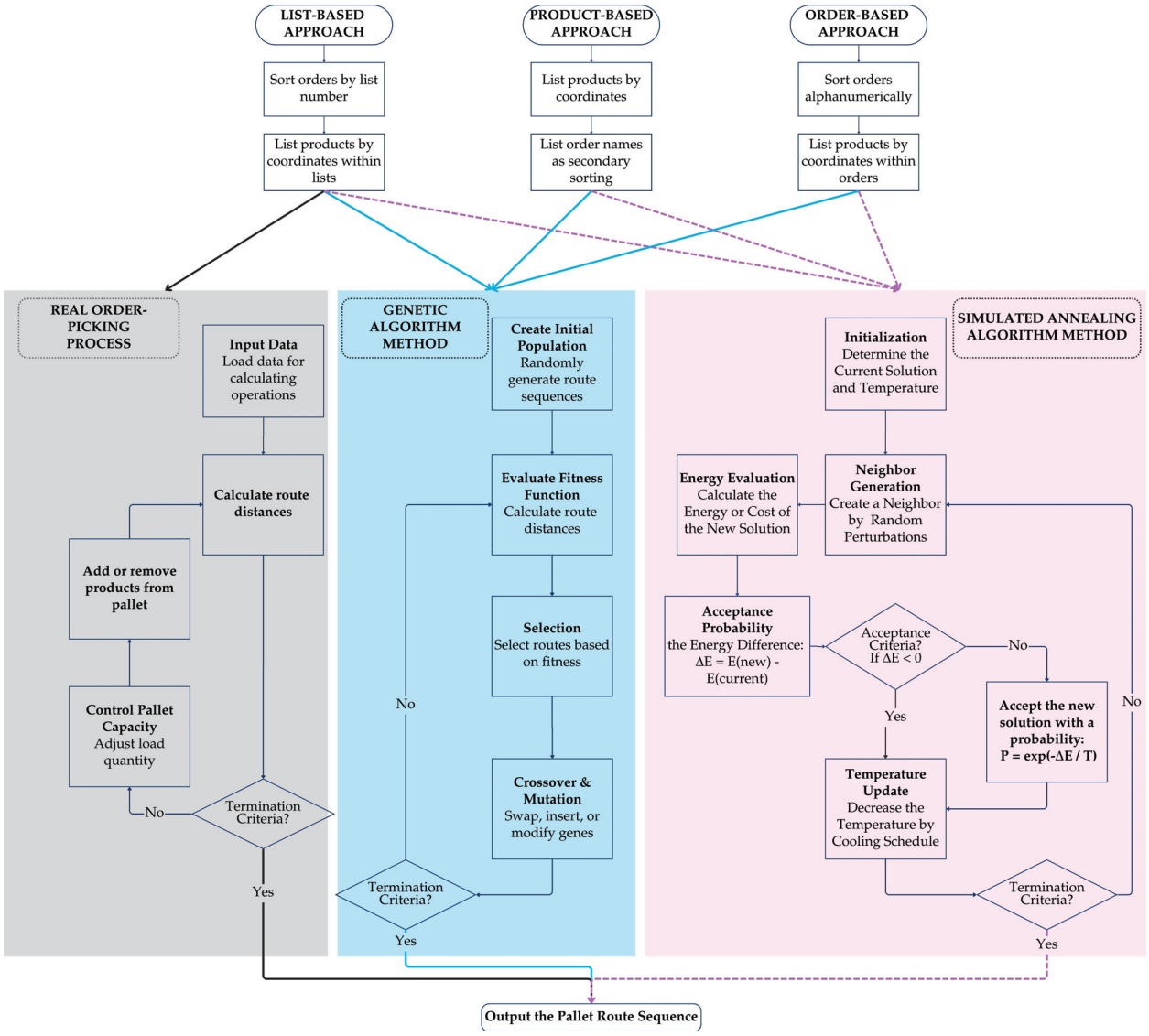

Figure 3. The flowchart of the picking strategies of this study.

This study implemented three different order-picking strategies by using Python 3.12: product-based, list-based, and order-based approaches. Each strategy was evaluated based on its performance in terms of the number of trips required, total trip distance, total volume picked, total products collected, and pallet utilization efficiency, as shown in Table 1. The study was formulated as a multi-objective optimization model, where the objectives were first to minimize the total trip distance, and subsequently to minimize the number of trips. Each trip utilized a single pallet that traversed the warehouse to collect orders, with a maximum pallet capacity of 1.2 m^3. A simulated order-picking process was executed for each strategy, recording key performance indicators during the collection process.

Table 1. Outline of the parameters of the study.

Symbol	Description	Type
T	Set of trips	Index
P	Set of products	Index
O	Set of orders	Index
i, j	Product indices (specific products in P)	Index
k	Order index (specific order in O)	Index
x_i, y_i	Coordinates of product i in the warehouse	Parameter
x_0, y_0	Coordinates of the starting and ending point in the warehouse	Parameter
V_i	Volume of product i	Parameter
C	Maximum capacity per trip	Parameter
d_{ij}	Manhattan distance between products i and j	Parameter
d_{i0}	Manhattan distance between the starting point and product i	Parameter
$X_{t,i}$	Binary variable indicating if product i is collected in trip t	Decision Variable
$Y_{t,k}$	Binary variable indicating if order k is included in trip t	Decision Variable
$S_{k1,k2}$	Set of shared products between orders k_1, k_2	Set

Fitness Functions:

$$\min \sum_{t \in T} Distance_t \tag{2}$$

$$\min |T| \tag{3}$$

Distance Calculation:

$$Distance_t = \sum_{i=1}^{|P|-1} (|x_i - x_{i+1}| + |y_i - y_{i+1}|) + (|x_{|P|} - x_0| + |y_{|P|} - y_0|) \tag{4}$$

Capacity Constraint:

$$\sum_{i \in P} X_{t,i} V_i \leq C, \quad \forall t \in T \tag{5}$$

Order Inclusion Constraint:

$$Y_{t,k} \geq X_{t,i}, \quad \forall i \in P, \forall k \in O \tag{6}$$

Product Collection Constraint:

$$\sum_{t \in T} X_{t,i} = 1, \quad \forall i \in P \tag{7}$$

Shared Product Constraint:

$$\sum_{i \in S_{k_1,k_2}} V_i \leq C, \quad \forall k_1, k_2 \in O \tag{8}$$

Manhattan Distance Definition:

$$d(a, b) = |x_1 - x_2| + |y_1 - y_2| \tag{9}$$

Output Metrics:

$$\sum_{t \in T} Distance_t \quad \text{(Total Distance)} \tag{10}$$

$$|T| \quad \text{(Total Number of Trips)} \tag{11}$$

$$\text{Pallet Utilization} = \frac{\text{Total Volume}}{|T| \times C} \tag{12}$$

The proposed product-based collection model has been applied to a simulated warehouse environment to validate its effectiveness in addressing the order-picking problem. The warehouse layout comprises a double block of parallel racks with four bays. This setup is in accordance with the product allocation and capacity constraints established in the model. The process, which involves three distinct orders, is executed manually without the aid of automated tools. During this process, the picker traverses the warehouse, starting and ending at a predefined position (x_0, y_0). This point, also known as the order-picking point or depot, is located in the front left corner of the warehouse.

The travel distances from this starting point to each product i (denoted as d_{i0}) and between consecutive products i and j (denoted as d_{ij}) are determined using the Manhattan distance metric, as described in objective functions (Equations (2) and (3)). The objective, defined by Equations (2) and (3), is to minimize both the total distance traveled and the number of trips made. Equations (4) and (5) address distance calculations and capacity constraints, ensuring that the total volume of products collected per trip does not exceed capacity C. Furthermore, Equations (6) and (7) establish order and product inclusion rules, while Equation (8) manages shared products across multiple orders. Equation (9) defines the distance metric between any two given points. Finally, the overall performance and utilization metrics are summarized by Equations (10)–(12).

4. Results

The study environment of this paper consists of a double block of parallel racks with four bays, as seen in Figure 4a. The pallet used for collecting orders is shown in Figure 4b. The warehouse layout and order placement for List 1 can be seen in Figure 4c.

Through these considerations, the application ensures that the constraints and assumptions align with real-world scenarios, providing a robust framework for minimizing travel distance while respecting operational constraints.

(a)

(b)

Figure 4. *Cont.*

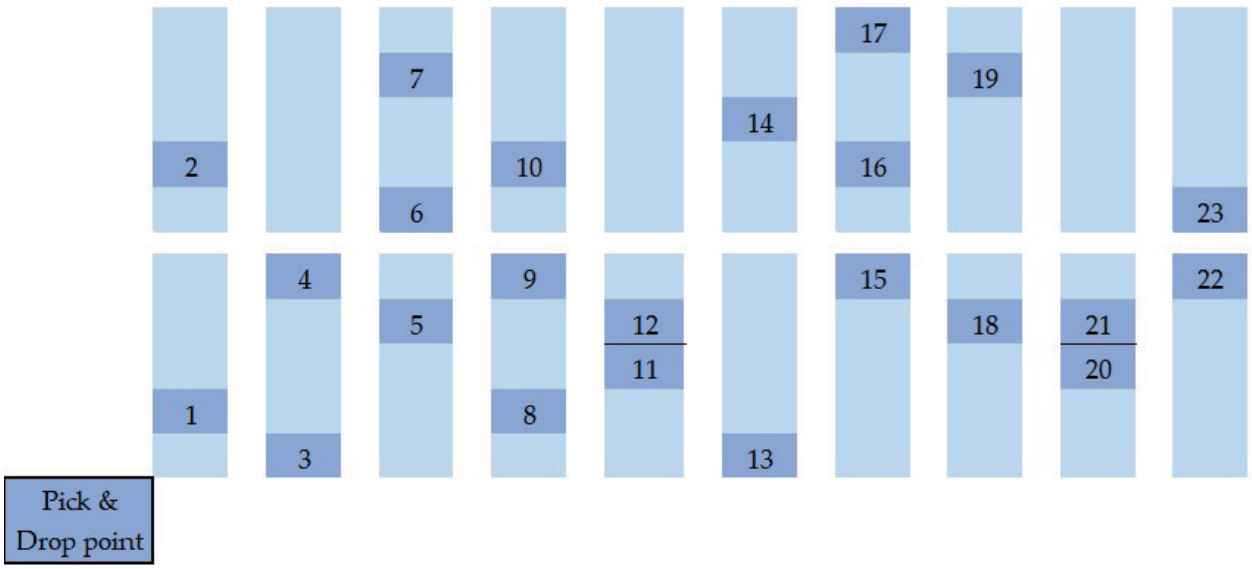

(c)

Figure 4. (**a**) Shelves of the warehouse. (**b**) Pallet used in order picking. (**c**) Product layout of List 1 in the facility.

4.1. The Real-World Dataset

The total number of separate orders for each list varies between 2 and 6, totaling 29 different orders. The number of unique items varies between 16 and 67 per list, totaling 169 unique items, as shown in Table 2.

Table 2. The study environment of algorithms.

Scenario: List ID	Problem Size	Count of Unique Orders	Count of Unique Products	Total Products	Total Volume	Min Expected Trip Number
1	Large	6	23	2837	4.017125	4
2	Medium	3	51	920	3.41414	4
3	Medium	2	45	1976	3.67986	4
4	Medium	2	35	660	2.26585	3
5	Large	2	67	2663	9.95921	9
6	Medium	2	39	558	2.53745	3
7	Small	4	24	339	1.664875	2
8	Small	3	23	724	1.6945	2
9	Medium	3	16	1240	4.0205	4
10	Medium	2	34	1605	4.4378	5
11	Very Large	29	169	13,522	37.69131	32

Case studies were studied by considering 11 datasets with unique order configurations to evaluate the efficiency of the proposed approaches in solving the order-picking optimization problem. Table 2 provides an overview of the datasets, ranging from small-, medium-, and large-scale problems, based on the number of orders, volume, and items, which enables the comparison of the proposed methods in various complexities. Lists 1 through 10 for different scenarios range in scale from small to medium, while List 11 combines all lists into one large-sized dataset.

Each of the lists possesses different characteristics and can provide insight into how changes in order and the number of items, along with volume, affect the performance of the optimization. Problem instances with small sizes, like List 7, have only four distinct orders and 24 distinct items. These are representatives of sparse picking environments with

small volumes. One large-scale set is List 11, a merged dataset that forms the base on which one will witness the scalability and robustness of the order-picking strategy with high volumes. Diversity in the design of the dataset is structured in such a way that it allows robust testing of the proposed GA-based solutions across different warehouse scenarios, providing insights into both performance scalability and adaptability under varying levels of operational demand. Through these considerations, the application ensures that the constraints and assumptions align with real-world scenarios, providing a robust framework for minimizing travel distance while respecting operational constraints.

4.2. Comparative Results

This research evaluates the effectiveness of three picking scenarios using GA and SA algorithms and real models. The methodologies cover product-based, list-based, and order-based approaches. The evaluation focused on basic operational data such as the total number of trips, trip distances, total volume picked, and pallet usage rates. In the application phase, data were collected from a medical device manufacturer. The studies were carried out by considering the company's current operational workflow. The results of the study are summarized in Table 3. Table 3 details the results of various order-picking techniques. The company's calculated solutions are also provided for comparison.

The performance of the GA was assessed concerning the current warehouse operations procedure through several scenarios and a comparison. The current method in the company generates fresh lists with every order arrival without dynamically adjusting to continuous changes, so it is rather strict. This rigidity causes ineffective grouping and routing as well as more trips and pallet capacity under-utilization.

Using three different approaches—product-based, order-based, and list-based—the evaluation concentrated on three key performance indicators (Total Distance Traveled, Total Number of Trips, and Pallet Utilization) to compare against the actual process and ascertain relative effectiveness.

In situations with lower order volumes and fewer products, such as Lists 7 and 8, the GA method found ideal solutions quickly by lowering the number of trips and the distance covered by over 30% compared to the current process, producing efficiency gains visible through shortened travel distances. Conversely, the rigidity of the current method resulted in a doubling of trips due to its tight order processing and long travel paths, reducing pallet utilization rates.

For medium-sized scenarios, such as Lists 2 and 6, the GA regularly showed efficiency improvements when handling moderate complexity by achieving a 20–30% reduction in the number of trips and travel distance, highlighting its capacity to dynamically optimize routes even with a modest increase in complexity.

In large-scale scenarios, such as Lists 5 and 9, the GA showed its full potential by minimizing travel distances while maintaining high pallet usage, attaining a 22–35% reduction in trips and a 10–15% decrease in travel distances compared to the existing process, which remained limited by its fragmented list generating, resulting in a higher number of trips, increased travel distances, and lower pallet utilization.

Scenario 11, which shows the joining of all lists into a single daily order set, demonstrated the scalability and flexibility of the GA as it dynamically adapted to the large-scale scenario, achieving a 37.3% reduction in trips and a 12.7% decrease in total travel distance while maintaining a high pallet utilization rate of 98% compared to 61.5% for the existing process.

Table 3. Results of GA, SA, and company's real process.

Scenario	Approach	Method	Total Distance (m)	Total Trips
1	List-Based	GA	420	4
	Order-Based	GA	430	4
	Product-Based	GA	240	4
	List-Based	Real Process	487	7
	List-Based	SA	439.5	5
	Order-Based	SA	435	4
	Product-Based	SA	288	4
2	List-Based	GA	85	3
	Order-Based	GA	119	3
	Product-Based	GA	89	3
	List-Based	Real Process	137.5	5
	List-Based	SA	124	4
	Order-Based	SA	130	4
	Product-Based	SA	124	4
3	List-Based	GA	153	4
	Order-Based	GA	158	4
	Product-Based	GA	150	4
	List-Based	Real Process	165.5	5
	List-Based	SA	150	4
	Order-Based	SA	174	4
	Product-Based	SA	126	4
4	List-Based	GA	78	2
	Order-Based	GA	79	2
	Product-Based	GA	74	2
	List-Based	Real Process	94.5	3
	List-Based	SA	103	2
	Order-Based	SA	95	2
	Product-Based	SA	93	2
5	List-Based	GA	342	9
	Order-Based	GA	419	9
	Product-Based	GA	347	9
	List-Based	Real Process	378.5	11
	List-Based	SA	359	10
	Order-Based	SA	347	11
	Product-Based	SA	359	10
6	List-Based	GA	146	3
	Order-Based	GA	178	3
	Product-Based	GA	145	3
	List-Based	Real Process	152.5	3
	List-Based	SA	154.5	3
	Order-Based	SA	188.5	3
	Product-Based	SA	156.5	3
7	List-Based	GA	75	2
	Order-Based	GA	78	2
	Product-Based	GA	74	2
	List-Based	Real Process	90	4
	List-Based	SA	79	2
	Order-Based	SA	83	2
	Product-Based	SA	81	2
8	List-Based	GA	120	2
	Order-Based	GA	165	2
	Product-Based	GA	118	2
	List-Based	Real Process	154.5	3
	List-Based	SA	127	2
	Order-Based	SA	125	2
	Product-Based	SA	123	2

Table 3. *Cont.*

Scenario	Approach	Method	Total Distance (m)	Total Trips
8	List-Based	GA	120	2
	Order-Based	GA	165	2
	Product-Based	GA	118	2
	List-Based	Real Process	154.5	3
	List-Based	SA	127	2
	Order-Based	SA	125	2
	Product-Based	SA	123	2
9	List-Based	GA	210	4
	Order-Based	GA	240	4
	Product-Based	GA	215	4
	List-Based	Real Process	215.5	5
	List-Based	SA	213.5	5
	Order-Based	SA	234	4
	Product-Based	SA	225.5	5
10	List-Based	GA	125	4
	Order-Based	GA	132	4
	Product-Based	GA	124	4
	List-Based	Real Process	133.5	5
	List-Based	SA	132.5	5
	Order-Based	SA	124.2	4
	Product-Based	SA	126.2	4
11	List-Based	GA	1754	32
	Order-Based	GA	1998	32
	Product-Based	GA	980	32
	List-Based	Real Process	2009	51
	List-Based	SA	1992	36
	Order-Based	SA	1998	36
	Product-Based	SA	1723.5	37

With fast convergence to optimal solutions observed in small-scope lists, therefore reducing travel distances and trips, the size of each list, the number of orders, and the degree of complexity were fundamental factors of GA efficiency. Simultaneously, the GA showed steady efficiency improvements with increasing scenario complexity, indicating its versatility throughout various logistical settings.

Under different conditions, each of the three GA techniques showed capabilities; the product-based approach was most successful in situations involving many unique items by lowering the total journey distance through spatial grouping. By contrast, the list-based approach offered balanced performance for medium-to-large lists. When maintaining order integrity was a top concern, and enormous order quantities were involved, the order-based approach performed exceptionally well, providing a flexible toolkit for optimizing logistics operations depending on scenario-specific criteria.

Where the GA regularly achieved lower distances, fewer trips, and more pallet utilization rates than the actual process across all scenarios, the visual analysis evaluated the impact of each strategy on total journey distance, number of trips, and pallet usage.

With particularly marked reductions in large-numbered lists, including List 5, List 9, and Scenario 11, where total distance dropped by over 50% compared to the current process (98,000 cm), the GA approach resulted in significantly reduced travel distances compared to the existing process in almost every scenario, demonstrating its capacity to optimize routes and lower travel time, thus generating significant operational cost savings and enhanced efficiency.

Although the GA method concentrated on reducing journey distance, it kept a similar or lower number of visits than conventional methods, so it efficiently grouped orders and reduced unnecessary trips without running afoul of capacity limits.

The GA order-picking strategy shows great promise for high usage rates despite less operational predictability and more variance in journey distances. Consistency is essential; the list-based GA performs consistently for realistic journey distances. Although the order-based GA shows effective pallet use, generally it results in longer journey distances. A GA may be appropriate for flexibility and adaptability due to managing variability. For typical applications that require consistent and predictable results, list-based GA approaches offer a balanced solution with satisfactory performance across various criteria. Future work could focus on combining hybrid methodologies that combine the adaptability of GA with the robustness of real models, thus achieving optimal travel times and high utilization rates in various logistics contexts. Moreover, creating complex algorithms that dynamically adapt to changing layout configurations could increase efficiency and operational robustness. In contrast, the existing process required additional journeys due to its fragmented processing of incoming orders, resulting in excessive trips.

Depending on the scenario, the GA consistently achieved higher pallet utilization, ranging between 70% and 98%. In comparison, the existing process showed significant under-utilization with rates ranging from 35% to 60%, with higher utilization rates indicating improved load management, reducing the number of trips required and minimizing empty pallet spaces, as the GA achieved nearly 98% utilization in the combined scenario compared to 61.5% for the actual process.

The GA outperforms the current company process in all performance metrics (total trips, travel distances, and pallet usage), optimizing routes and combining orders efficiently despite fluctuations in order composition and volumes. This practical applicability in real-world logistics is demonstrated in this study, with a 37.3% reduction in trips and a 12.7% reduction in distance in the combined scenario. Furthermore, GA is a preferable solution for contemporary logistics with high pallet usage rates.

Minimizing the travel distance primarily relies on the manual product-based method. On the other hand, the intuitive order-based strategy maintains a suitable number of trips and a balanced performance, maintaining a short travel time overall. Regarding travel distance, the manual order-based strategy outperforms other methods, indicating that it is unsuitable for reducing travel time even if excellent pallet utilization is achieved. The results of our study reveal that approach selection can improve warehouse operations. The goal might be to reduce travel distance, reduce trips, or balance both.

Since the GA product-based approach has the shortest travel distances, the results prove the success of this method. The study reveals that optimization techniques applied beyond the organization's baseline can significantly increase logistics efficiency with comprehensive analysis and strategic selection.

The datasets were classified into fuzzy categories (Small, Medium, Large, and Very Large [only for list 11/combined list]) based on Total Volume Size, Number of Discrete Items, and Number of Discrete Orders. The performance of the datasets divided into these categories, SA, GA, and the real process, was compared in three approaches: list-based, order-based, and product-based, as shown in the Figures below.

For example, in Figure 5a, List 7 in the small category showed the minimum total distance of 74 m from the product-based GA approach, about an 18% reduction from the real process that took 90 m. All the approaches by both SA and GA recorded two trips, while the real process made four trips—an indication of how inefficient the real process is. In general, it was seen that in both approaches, GA provided more efficient distance reductions than those obtained with SA.

For example, the minimum total distance of 126 m in the Medium List of Scenario 3 was obtained through product-based GA, which achieved about a 24% gain compared to the real process as shown in Figure 5b. The SA method found the same number of trips but a slightly higher total distance than GA. GA provided better optimization than SA, with a consistent reduction in total distance while maintaining comparable trip counts.

For the Large List shown in Figure 5c the best performance was from the product-based GA approach; it trimmed the total distance by 50% from 487 m, as executed by the real list-based process, to 240 m. For the instances in which comparable distances were available, GA was always consistently superior to SA at minimizing distances. The greatest gap occurred with the product-based approach. All heuristics resulted in fewer trips compared to the real process. In the Very Large List (Scenario 11), which was created by combining all the lists, the product-based GA approach showed the highest efficiency, resulting in a total distance of 980 m, a reduction of over 51% from the real list-based process of 2009 m. The number of trips was also minimized; GA and SA methods required only 32 to 37 trips in all approaches, which is significantly fewer than the 51 trips of the real process. When all the lists were combined, the product-based GA method achieved an overall minimum distance of 2556 m; this represented a 36% reduction compared to the actual list-based process (4018 m). GA achieved significantly shorter distances than SA, particularly in the product-based approach, where the difference exceeded 43%. These findings demonstrate that the product-based GA approach consistently offers superior efficiency in minimizing both total distance and trips across all list categories as shown in Figure 5d. GA demonstrated overall superiority across all approaches, with notable efficiency gains in reducing both total distance and the number of trips compared to SA.

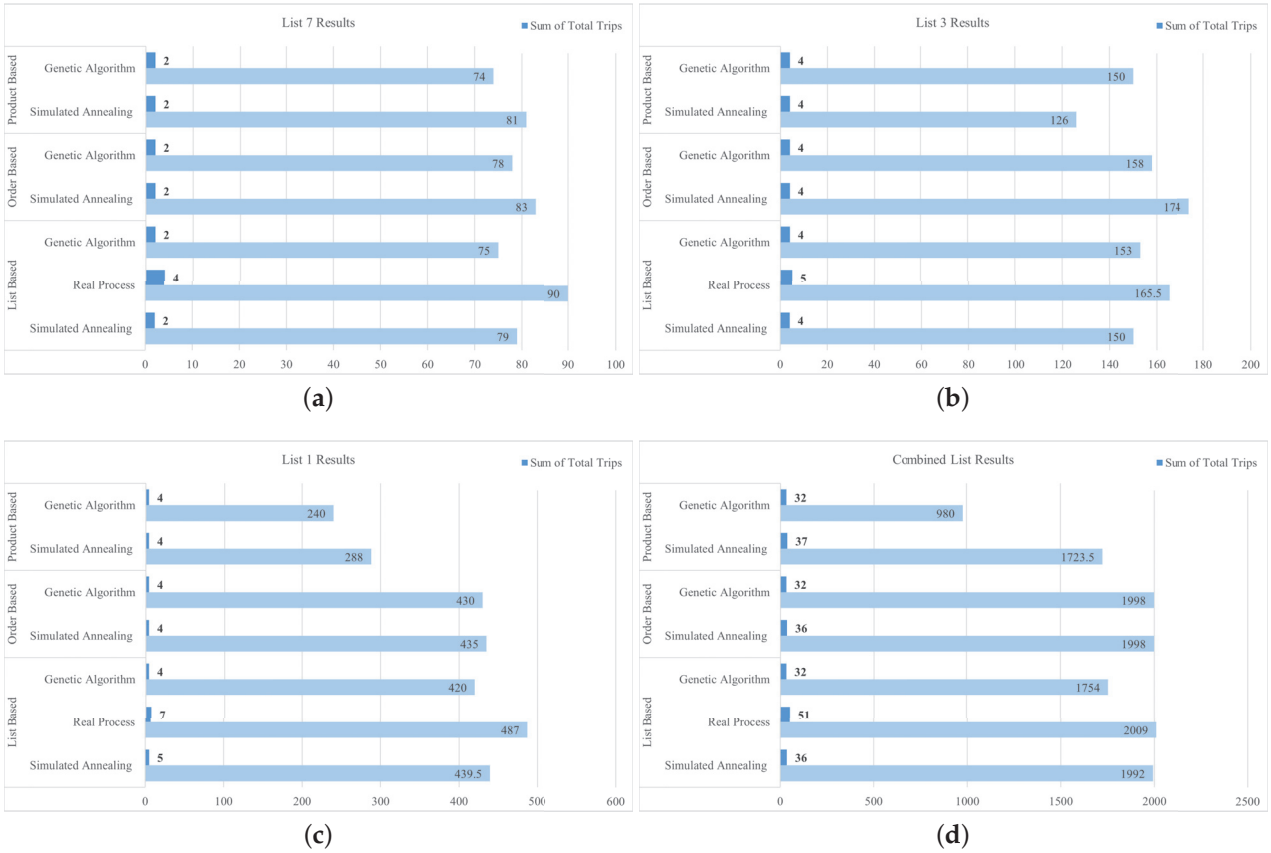

Figure 5. Results for various lists: (**a**) Small list: List 7 results, (**b**) Medium list: List 3 results, (**c**) Large list: List 1 results, (**d**) Combined list (Very Large List): List 11 results.

4.3. Sensitivity Analysis Made by Order Amount Increased

Sensitivity analysis shows how each picking strategy adapts to increased order volumes, showing scalability and operational strengths or limitations.

4.3.1. Order-Based Strategy

As shown in Figure 6a, for combined List 11, the distance increases drastically as more and more orders increase, reflecting the inefficiency in processing each order individually at high demand levels. From this, it can be seen that since this strategy necessitates a separate pass through the warehouse for every order, it presupposes lower efficiency in picking and higher costs of time and labor, as can be seen from notable distance growth in List 5 as orders increase. Sensitivity analysis underlines that this strategy scales poorly with demand in the case of high-order periods.

As such, it is best averaged for smaller order quantities where the accuracy of each order individually is more important than travel efficiency.

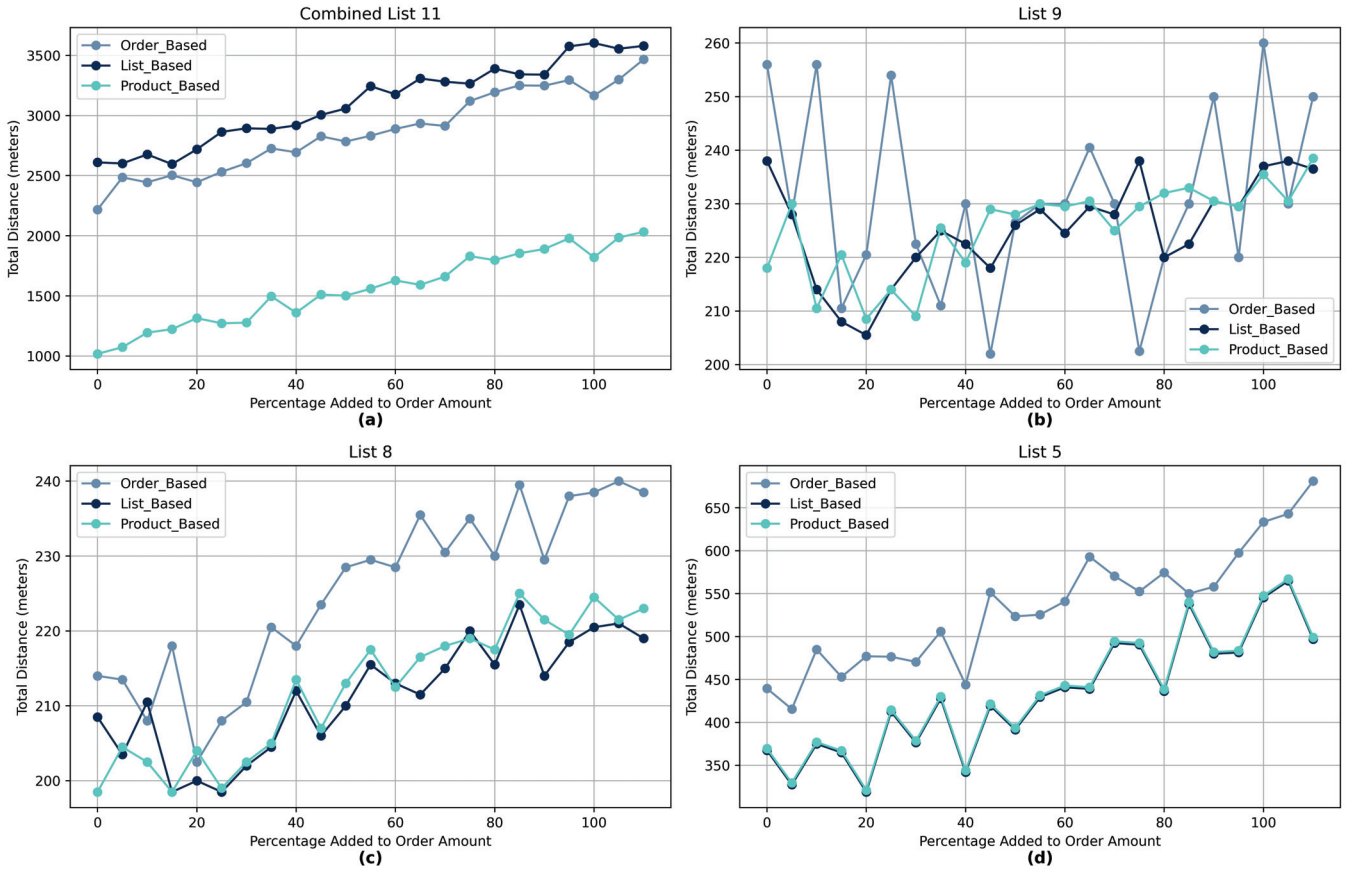

Figure 6. Sensitivity Analysis on (**a**) List 9. (**b**) List 8. (**c**) Combined List 11. (**d**) List 5 results.

4.3.2. List-Based Strategy

First, the list-based approach saves travel time by clumping orders together to minimize routes taken. However, as order volumes increase, this approach becomes less flexible. That can be understood from the list, wherein larger volumes of orders disrupt the planned routes and cause small inefficiencies in travel. Another weakness of this strategy is its potential to generate shortages of items when high-demand products have to be shared among orders, as shown in the list, where the increased order amounts include slight variability in travel distances. The sensitivity analysis results show that, though effective under stable demand conditions, the list-based strategy cannot maintain efficiency when volumes increase substantially. It is more appropriate in moderate and predictable demand.

4.3.3. Product-Based Strategy

The product-based strategy is resilient to higher volumes because the items would be collected by product location; this means travel distances would remain relatively constant even at high demand. As shown in Figure 6a–d, distance remains efficient in the various sized lists despite added orders, underlining the strategy's capability for effective scaling. On the other hand, this method needs more significant inventory management since the shortest travel relies on well-stocked product locations.

The difficulty represented by sorting the items into individual orders after collective picking for more orders is increased in the combined List 11 profile. Sensitivity analysis reveals that under the product-based strategy, travel efficiency is advantageous but needs robust stock control to prevent congestion bottlenecks, especially in high-demand environments.

Sensitivity analysis indicates that the product-based strategy behaves well with increased demand but requires strong inventory practices. By contrast, the order-based and list-based strategies are more challenged by increased order amounts due to higher travel distances and reduced flexibility. By understanding these dynamics, warehouses can choose strategies that match travel efficiency, labor costs, and flexibility for expected demand variability.

4.4. Sensitivity Analysis of Population Size—Genetic Algorithm Parameter

A sensitivity analysis of the GA concerning the population size is performed in this work to study the variations in the solution quality. Overall, population sizes ranged from 10 to 150 across multiple lists of complexities described by attributes like distinct orders, distinct items, total volume, and problem size. The main goal of this analysis is to search for an appropriate population size that will yield a good balance between the accuracy of the solution and time efficiency for various scenarios.

4.4.1. Population Size Impact

As can be gathered from Table 1, the objective function values and computation times generated by GA are sensitive to changes in the size of the population. For small problem sizes such as Lists 7 and 8, for instance, population size in the 50–70 range gave the optimum solution with a limited increase in computation time, whereas further increases have resulted in diminishing returns. Medium-sized problems—exact Lists 1 and 2—have shown a 10–15% improvement of objective function after increasing the population size to 70–100 while computation time increases remained manageable. Population size in the range of 100–150 yielded the best solution quality with as much as a 28% objective function improvement at large and very large problem sizes, such as lists 5 and 11, respectively. These gains in solution accuracy had to be weighed against increased computation times, double or triple those found with smaller populations, indicating an apparent solution accuracy and computation time trade-off.

4.4.2. Correlation Analysis

Figure 7 presents the correlation matrix of the critical parameters. From this figure, it is observed that computation time is highly correlated with population size (0.89), shown in the red circle, implying that high population sizes increase computational requirements significantly. Problem Size is highly correlated with Total Volume 0.85 and Number of Distinct Items 0.75, implying that these factors together increase complexity. The other correlations of Best Fitness remain low, testifying to the robustness of the performance of GA across a wide range of configurations.

Changes in population size led to statistically significant objective improvements, especially related to complex scenarios. For example, Lists 3 and 5 had solution quality gains of 20-28% going from baseline to optimal population sizes, which suggests gains from larger population sizes when dealing with more complex scenarios.

The sensitivity analysis identified general effective population sizes based on the problem complexities: 50–100 for small- to medium-sized problems, while larger ones see significant improvements with increased population sizes up to 100–150, although at increased computational costs. These findings give insights into the more practical tuning of the parameters of GA in balancing the solution quality with the availability of resources in adaptable optimization for real applications.

Figure 7. Correlation matrix of the critical parameters.

5. Conclusions

Manual order picking and optimization is an NP-hard problem in real life and leads to an increase in time and distance to the user as product variety and complexity increase. In this study, meta-heuristic solutions are proposed to the problem of a medical textile manufacturer where manual order picking is quite intensive.

In the solution phase, 3 different scenarios and different order lists were run in both algorithms and the results were compared for GA and SA. In addition, detailed sensitivity analyses were performed. According to the findings obtained, in cases where GA was used, the product-based strategy reduced the pallet usage rate by offering the lowest total distance in many scenarios, and in addition, orders in the entire list were collected with fewer trips. For example, in Scenario 1, when GA is used, the product-based solution offers the lowest distance with 240 m, while list-based remains at 420 m and order-based remains at 430 m. When we look at SA, the product-based approach is still in a relatively advantageous position with a result of 288 m. List-based SA falls behind with 439.5 m, and order-based SA falls behind with 435 m. According to the real process results, it is seen that the list-based application remains at 487 m, which further emphasizes the superiority of

GA and SA-based product-based solutions in this scenario. This superiority is also evident in different scenarios.

In Scenario 3, the product-based approach with GA is better or at a similar level when compared to both list-based (GA: 153 m) and order-based (GA: 158 m) solutions with a result of 150 m. When we look at the SA results, product-based provides a significant advantage with 126 m (list-based SA: 150 m, order-based SA: 174 m). Here, the real process falls behind other methods with 165.5 m.

In Scenario 4, while product-based is 74 m, list-based is 78 m, and order-based is 79 m among the GA results; SA and product-based remains at 93 m, list-based SA is 103 m, and order-based SA is 95 m. The real process, on the other hand, offers a longer distance compared to GA and SA solutions, with 94.5 m. This table shows that when GA is applied, the product-based approach has a slight advantage, while when SA is applied, it maintains its competitive position.

Scenario 11 reflects a larger volume and a more complex structure. Here, when GA is used, the product-based strategy provides a remarkable advantage with a total distance of 980 m. While list-based GA is 1754 m, order-based GA is 1998 m, and the real process is far behind with 2009 m. In the SA application, product-based is also better than list-based (1992 m) and order-based (1998 m) solutions with 1723.5 m. This shows that the product-based approach can produce strong results with GA and SA, even in complex and large-scale scenarios.

In general, it is understood that the product-based approach can offer stable advantages in terms of both distance and number of trips in different scenarios, especially when GA is used. When compared with SA and real process data, the competitive position of the product-based strategy is clearly revealed. GA maximizes the potential of the product-based approach by effectively scanning a multidimensional and dynamic decision space, but this also brings costs such as increased computational time, software/hardware requirements, and operational planning requirements.

As a result, the table data shows that the product-based strategy, when supported by GA and SA, can show high performance even in different and challenging scenarios and provide significant distance and time savings compared to real processes. In future studies, it should be aimed to make the product-based approach more sustainable and effective in both theoretical and practical terms by integrating human factors, equipment limitations, cost, energy consumption, and environmental effects into the process.

In this context, we advocate the importance of heuristic algorithms that adaptively evaluate the optimal picking approach based on the descriptive characteristics of the orders and warehouse design and metrics obtained from real-time interaction. Capturing this flexibility with the GA is much easier and more adaptable than mathematical models. For example, even if the lists change in the study, the algorithm can work and produce the best ordering. In addition, since a single and fixed-sized pallet was used in our problem, the model was solved accordingly. Still, researchers can produce alternatives that can reduce the number of rounds in the solution by adding multiple pallets to the model. More refined picking strategies can be created by comprehensively integrating machine learning techniques and SA. Doing so can focus on optimizing order-picking operations in a more balanced and sustainable way through approaches that go beyond a single performance indicator and include energy consumption, environmental footprint, and labor cost issues. For new studies, ergonomic considerations and personnel costs can be fully integrated into the optimization process. Although simulation and theoretical models have guided the research, and the practical applicability of the proposed strategies is high, companies may have to pick priorities they can implement. These priorities can be expanded by adding them to the model.

Author Contributions: Methodology, E.Y.; software, E.Y.; investigation, E.Y.; data curation, Ö.A.; writing—review and editing, B.D. and E.Y. All authors have read and agreed to the published version of the manuscript.

Funding: This research received no external funding

Data Availability Statement: The data are unavailable due to privacy restrictions.

Conflicts of Interest: The authors declare no conflicts of interest.

References

1. Coyle, J.J.; Bardi, E.J.; Langley, C.J. *The Management of Business Logistics*; West Publishing Company: St. Paul, MN, USA, 1992.
2. Bowen, B.; Galceran Borja, C.; Karim, S.; Weinstein, W. *Optimizing Health System Supply Chain Performance*; McKinsey & Company: Chicago, IL, USA, 2023. Available online: https://www.mckinsey.com/industries/healthcare/our-insights/optimizing-health-system-supply-chain-performance (accessed on 24 November 2024).
3. Bradley, P. Taking on the Health Care Supply Chain. Available online: https://www.proquest.com/trade-journals/taking-on-health-care-supply-chain/docview/205962882/se-2 (accessed on 24 November 2024).
4. Chandra, C. The case for healthcare supply chain management: Insights from problem-solving approaches. *Int. J. Procure. Manag.* **2008**, *1*, 261. [CrossRef]
5. Battini, D.; Faccio, M.; Persona, A.; Sgarbossa, F. Healthcare supply chain modeling: A conceptual framework. In Proceedings of the POMS (Production and Operations Management Society) 20th Annual Conference, Orlando, FL, USA, 1–4 May 2009.
6. Lewczuk, K.; Kłodawski, M.; Gepner, P. Energy consumption in a distributional warehouse: A practical case study for different warehouse technologies. *Energies* **2021**, *14*, 2709. [CrossRef]
7. Dallari, F.; Marchet, G.; Melacini, M. Design of order picking system. *Int. J. Adv. Manuf. Technol.* **2008**, *42*, 1–12. [CrossRef]
8. Pan, J.C.H.; Shih, P.H. Evaluation of the throughput of a multiple-picker order picking system with congestion consideration. *Comput. Ind. Eng.* **2008**, *55*, 379–389. [CrossRef]
9. Yener, F.; Yazgan, H.R.; Cömert, S.E.; Kır, S.; Kaya, Y. Solution of Order Batching Problem with Association Rules and Genetic Algorithm: A Case Study in Pharmacy Warehouse. *J. Transp. Logist.* **2016**, *1*, 129–142. [CrossRef]
10. Yang, J.; Zhou, L.; Liu, H.; Wang, Y. Hybrid genetic algorithm-based optimisation of the batch order picking in a dense mobile rack warehouse. *PLoS ONE* **2021**, *16*, e0249543. [CrossRef]
11. Yousefi Nejad Attari, M.; Ebadi Torkayesh, A.; Malmir, B.; Neyshabouri Jami, E. Robust possibilistic programming for joint order batching and picker routing problem in warehouse management. *Int. J. Prod. Res.* **2021**, *59*, 4434–4452. [CrossRef]
12. Ho, Y.-C.; Lin, J.-W. Improving order-picking performance by converting a sequential zone-picking line into a zone-picking network. *Comput. Ind. Eng.* **2017**, *113*, 241–255. [CrossRef]
13. Yu, M.; de Koster, R. The impact of order batching and picking area zoning on order picking system performance. *Eur. J. Oper. Res.* **2009**, *198*, 480–490. [CrossRef]
14. Yu, M.; de Koster, R. Performance approximation and design of pick-and-pass order picking systems. *IIE Trans.* **2008**, *40*, 1054–1069. [CrossRef]
15. Lorenc, A.; Burinskiene, A. Improve the orders picking in eCommerce by using WMS data and BigData analysis. *FME Trans.* **2021**, *49*, 233–243. [CrossRef]
16. Saylam, S.; Çelik, M.; Süral, H. The min–max order picking problem in synchronised dynamic zone-picking systems. *Int. J. Prod. Res.* **2023**, *61*, 2086–2104. [CrossRef]
17. Yener, F.; Yazgan, H.R. Green order sorting problem in cold storage solved by genetic algorithm. *Sustainability* **2024**, *16*, 9062. [CrossRef]
18. Yener, F. Determination of Picking Policies in Robotic Compact bin Picking Storage Systems with Artificial Bee Colony Algorithm. Ph.D. Thesis, Sakarya University, Sakarya, Turkey, 2023. Available online: https://acikerisim.sakarya.edu.tr/bitstream/handle/20.500.12619/101079/T10387.pdf (accessed on 27 November 2024).
19. Tutam, M. Optimizing order-picking warehouse designs using collaborative robots. *Gazi Üniversitesi Mühendislik Mimarlık Fakültesi Dergisi* **2023**, *39*, 203–216. [CrossRef]
20. Pan, J.C.H.; Wu, M.H. A study of storage assignment problem for an order picking line in a pick-and-pass warehousing system. *Comput. Ind. Eng.* **2009**, *57*, 261–268. [CrossRef]
21. Yener, F.; Yazgan, H.R. Simulation of Re-Arrangement and Healing in Robotic Compact Bin-Storage System. *Int. J. Simul. Model.* **2023**, *22*, 100–109. [CrossRef]
22. Bolu, A.; Korçak, Ö. Adaptive Task Planning for Multi-Robot Smart Warehouse. *IEEE Access* **2021**, *9*, 27346–27358. [CrossRef]
23. Ardjmand, E.; Ghalehkhondabi, I.; Young II, W.A.; Sadeghi, A.; Shakeri, H. A hybrid artificial neural network, GA, and column generation for minimizing makespan in manual order-picking operations. *Expert Syst. Appl.* **2020**, *159*, 113566. [CrossRef]

24. Kumar, S.; Sheu, J.B.; Kundu, T. Planning a parts-to-picker order-picking system with consideration of the impact of perceived workload. *Transp. Res. Part E Logist. Transp. Rev.* **2023**, *173*, 103088. [CrossRef]
25. Loske, D.; Klumpp, M.; Grosse, E.H.; Modica, T.; Glock, C.H. Storage systems' impact on order-picking time: An empirical economic analysis of flow-rack storage systems. *Int. J. Prod. Econ.* **2023**, *261*, 108887. [CrossRef]
26. He, W.; Chen, J. Dynamic routing algorithm for manual order-picking systems with real-time adjustment. *Transp. Res. Part C Emerg. Technol.* **2018**, *96*, 392–407. [CrossRef]
27. Petersen, C.; Aase, G. Effects of slotting optimization in warehouse order-picking. *Eur. J. Oper. Res.* **2021**, *290*, 1051–1063. [CrossRef]
28. Grosse, E.H.; Glock, C.H.; Sadrnia, A.; Modica, T. Collaborative robots in parts-to-picker systems: A simulation study. *Comput. Ind. Eng.* **2019**, *131*, 597–605. [CrossRef]
29. Boysen, N.; Emde, S.; Hoeck, M.; Kauderer, L. Zone-picking systems: A survey of conceptual variants and their optimization approaches. *Eur. J. Oper. Res.* **2020**, *284*, 799–818. [CrossRef]
30. Coruzzolo, A.M.; Lolli, F.; Balugani, E.; Magnani, E.; Sellitto, M.A. Order-picking problem: A model for the joint optimisation of order batching, batch assignment sequencing, and picking routing. *Logistics* **2023**, *7*, 61. [CrossRef]
31. Czerniachowska, K.; Wichniarek, R.; Żywicki, K. A model for an order-picking problem with a one-directional conveyor and buffer. *Sustainability* **2023**, *15*, 13731. [CrossRef]
32. Kapou, V.; Ponis, S.T.; Plakas, G.; Aretoulaki, E. An innovative layout design and storage assignment method for manual order-picking with respect to ergonomic criteria. *Logistics* **2022**, *6*, 83. [CrossRef]
33. Li, Y.; Zhang, R.; Jiang, D. Order-picking efficiency in e-commerce warehouses: A literature review. *J. Theor. Appl. Electron. Commer. Res.* **2022**, *17*, 1812–1830. [CrossRef]
34. Çil, İ.; Pınar, D.; Araslı, A.; Kurt, A.; Topcan, A.N. Creating a Lean and Sustainable Warehouse with 5S in E-Commerce Operations Center: Trendyol Case Study. *Int. J. Behav. Sustain. Manag. (JOBESAM)* **2023**, *10*, 131–150. [CrossRef]
35. Ou, S.; Ismail, Z.H.; Sariff, N. Hybrid Genetic Algorithms for Order Assignment and Batching in Picking System: A Systematic Literature Review. *IEEE Access* **2024**, *12*, 23029–23042. [CrossRef]
36. Casella, G.; Volpi, A.; Montanari, R.; Tebaldi, L.; Bottani, E. Trends in order picking: A 2007–2022 review of the literature. *Prod. Manuf. Res.* **2023**, *11*, 2191115. [CrossRef]
37. Yazgan, H.R.; Kir, S.; Yener, F.; Comert, S.E. A new collecting and management proposal under logistics 4.0 and green concept. In *Logistics 4.0: Digital Transformation of Supply Chain Management*; Paksoy, T., Kochan, C.G., Ali, S.S., Eds.; CRC Press: Boca Raton, FL, USA, 2020; pp. 320–337. [CrossRef]
38. Holland, J.H. *Adaptation in Natural and Artificial Systems: An Introductory Analysis with Applications to Biology, Control, and Artificial Intelligence*; MIT Press: Cambridge, MA, USA, 1992.
39. Holland, J.H. *Adaptation in Natural and Artificial Systems*; University of Michigan Press: Ann Arbor, MI, USA, 1975.
40. Yıldırım, E.; Denizhan, B. A Two-Echelon Pharmaceutical Supply Chain Optimization via Genetic Algorithm. In *Recent Advances in Intelligent Manufacturing and Service Systems*; Sen, Z., Oztemel, E., Erden, C., Eds.; Springer: Singapore, 2022; pp. 77–87.. [CrossRef]
41. Goldberg, D.E. *Genetic Algorithms in Search, Optimization, and Machine Learning*; Addison-Wesley: Reading, MA, USA, 1989.
42. Dalle Mura, M.; Dini, G. Optimizing ergonomics in assembly lines: A multi-objective genetic algorithm. *CIRP J. Manuf. Sci. Technol.* **2019**, *27*, 31–45. [CrossRef]
43. Gabellini, M.; Calabrese, F.; Regattieri, A.; Loske, D.; Klumpp, M. A hybrid approach integrating GA and machine learning to solve the order-picking batch assignment problem considering learning and fatigue of pickers. *Comput. Ind. Eng.* **2024**, *191*, 110175. [CrossRef]
44. Pan, J.C.H.; Shih, P.H.; Wu, M.H. Order batching in a pick-and-pass warehousing system with group genetic algorithm. *Omega* **2015**, *57*, 238–248. [CrossRef]
45. Jiang, X.; Sun, L.; Zhang, Y.; Hu, X. Order batching and sequencing for minimizing the total order completion time in pick-and-sort warehouses. *Expert Syst. Appl.* **2022**, *187*, 115943. [CrossRef]
46. Eckrot, A. A Simulated Annealing Approach to Optimal Storing in a Multi-Level Warehouse. *arXiv* **2017**, arXiv:1704.01049.
47. Jin, H.; Wang, W.; Cai, M.; Wang, G.; Chen, Y. Ant colony optimization model with characterization-based speed and multi-driver for the refilling system in hospital. *Adv. Mech. Eng.* **2017**, *9*, 168781401771370. [CrossRef]
48. Ardjmand, E.; Bajgiran, O.; Youssef, E. Using list-based simulated annealing and genetic algorithm for order batching and picker routing in put wall-based picking systems. *Appl. Soft Comput.* **2019**, *75*, 106–119. [CrossRef]
49. Nathania, F. An Efficient Simulated Annealing Algorithm for the Joint Order Batching and Picker Routing Problem in Manual Order Picking Systems. In Proceedings of the 8th North American Conference on Industrial Engineering and Operations Management, Houston, TX, USA, 12–15 June 2023. [CrossRef]
50. Castier, M.; Martínez-Toro, E. Planning and picking in small warehouses under industry-relevant constraints. *Prod. Eng.* **2022**, *17*, 575–590. [CrossRef]

51. Kirkpatrick, S.; Gelatt, C.D.; Vecchi, M. Optimization by simulated annealing. *Science* **1983**, *220*, 671–680. [CrossRef]
52. Küçükoğlu, İ.; Ene, S.; Aksoy, A.; Öztürk, N. A memory structure adapted simulated annealing algorithm for a green vehicle routing problem. *Environ. Sci. Pollut. Res.* **2015**, *22*, 3279–3297. [CrossRef] [PubMed]
53. Atmaca, E.; Ozturk, A. Defining order picking policy: A storage assignment model and a simulated annealing solution in AS/RS systems. *Appl. Math. Model.* **2013**, *37*, 5069–5079. [CrossRef]
54. Kostrzewski, M. Sensitivity Analysis of Selected Parameters in the Order Picking Process Simulation Model, with Randomly Generated Orders. *Entropy* **2020**, *22*, 423. [CrossRef] [PubMed]
55. Kucuksari, Z. Optimal Order Batching for Automated Warehouse Picking. Ph.D. Thesis, University of Waterloo, Waterloo, ON, Canada, 2023. Available online: http://hdl.handle.net/10012/19869 (accessed on 27 November 2024).
56. Więckowski, J.; Kizielewicz, B.; Kołodziejczyk, J. Finding an approximate global optimum of characteristic objects preferences by using simulated annealing. *Intell. Decis. Technol.* **2020**, *193*, 365–375. [CrossRef]
57. Michalewicz, Z.; Fogel, D. B. *How to Solve It: Modern Heuristics*; Springer: Berlin/Heidelberg, Germany, 2004. [CrossRef]
58. Zhao, Y. Manufacturing cell integrated layout method based on RNS-FOA algorithm in smart factory. *Processes* **2022**, *10*, 1759. [CrossRef]
59. Can, Z.; Colak, Z.; Yıldırım, K.; Gelişgen, O. A Note on Some Distance Formulae in 3-Dimensional Maximum Space. *J. Mahani Math. Res.* **2021**, *10*, 95–102. [CrossRef]

processes

MDPI

Article

A Multi-Step Furnace Temperature Prediction Model for Regenerative Aluminum Smelting Based on Reversible Instance Normalization-Convolutional Neural Network-Transformer

Jiayang Dai, Peirun Ling *, Haofan Shi and Hangbin Liu

School of Electrical Engineering, Guangxi University, Nanning 530004, China;
daijiayang@gxu.edu.cn (J.D.); shihaofan@st.gxu.edu.cn (H.S.); liuhangbin@st.gxu.edu.cn (H.L.)
* Correspondence: peirunling@st.gxu.edu.cn

Abstract: In the regenerative aluminum smelting process, the furnace temperature is critical for the quality and energy consumption of the product. However, the process requires protective sensors, making real-time furnace temperature measurement costly, while the strong nonlinearity and distribution drift of the process data affect furnace temperature prediction. To handle these issues, a multi-step prediction model for furnace temperature that incorporates reversible instance normalization (RevIN), convolutional neural network (CNN), and Transformer is proposed. First, the self-attention mechanism of the Transformer is combined with CNN to extract global and local information in the furnace temperature data, thus addressing the strong nonlinear characteristics of the furnace temperature. Second, RevIN with learnable affine transformation is utilized to address the distribution drift in the furnace temperature data. Third, the temporal correlation of the prediction model is enhanced by a time-coding method. The experimental results show that the proposed model demonstrates higher prediction accuracy for furnace temperature at different prediction steps in the regenerative aluminum smelting process compared to other models.

Keywords: reversible instance normalization (RevIN); convolutional neural network (CNN); Transformer; time coding

1. Introduction

Aluminum has good malleability, reflectivity, and recyclability. Based on its excellent physical and chemical properties, aluminum is widely used in the automobile, aviation, and military industries. The regenerative aluminum smelting process is an important stage for the production of aluminum, and it directly affects product quality and energy consumption [1,2]. The challenge of accurately measuring temperature is compounded by the heterogeneity of the environment in the regenerative aluminum smelting furnace and the aging of the sensors at high temperatures [3]. At present, because the real-time measurement of the furnace temperature is costly, it is common to use models to predict furnace temperature in a single step. The single-step prediction of the furnace temperature is easy to implement but sometimes does not provide sufficient information for the operators. By providing a multi-step prediction of the furnace temperature, operators have plenty of time to make adjustments compared to using a single-step prediction, resulting in increased productivity [4–7]. Therefore, researching multi-step prediction of furnace temperature is of practical significance for monitoring the state of the regenerative aluminum smelting process.

In recent years, the existing time-series prediction models have primarily been categorized into mechanism-based models, statistical models, and artificial intelligence models. Mechanism-based models require detailed analysis and simulation of the structure and production process of equipment. On this basis, mechanism-based models of industrial

processes are constructed for prediction using physical or chemical principles [8]. Although mechanism-based models are characterized by strong interpretability due to their foundation in actual physical or chemical processes, the complexity of these processes often makes the construction of such models challenging. Mechanism-based models are typically reliant on idealized assumptions, which may not always hold true in practical applications, thus inevitably introducing errors that impact the accuracy of prediction results [9]. Historical features of the data are utilized by statistical models to forecast future data. Commonly used statistical models include the autoregressive model (AR) [10], autoregressive moving average model (ARMA) [11], and autoregressive integrated moving average model (ARIMA) [12]. When faced with incomplete data or data distribution drift, the accuracy of statistical models is often reduced, making it challenging to meet practical requirements [13]. With the rapid advancement of artificial intelligence technology, the research and application of artificial intelligence models in time-series prediction have garnered significant attention [14,15]. In particular, powerful tools for modeling time-series data are provided by the rise of machine learning and deep learning. The nonlinear mapping capabilities of machine learning are utilized to effectively address multivariate coupling issues within data, thus significantly improving prediction accuracy [16–18]. Huang et al. [19] employed kernel principal component analysis (KPCA) to extract the principal components of network inputs and optimized the extreme learning machine (ELM) using the harmony search algorithm (HS) to predict the furnace temperature in a regenerative aluminum smelting furnace. Liu et al. [20] developed a stable furnace temperature model by incorporating a restricted Boltzmann machine to enhance the stochastic initialization of input weights and hidden layer thresholds in ELM. Although multivariate coupling relationships within data are uncovered by machine learning, limitations are present in addressing the strong nonlinear characteristics of the data, resulting in prediction accuracy that often falls short of ideal levels.

With strong feature extraction and learning capabilities, deep learning is significantly superior to machine learning in processing high-dimensional data and time-series tasks [21]. Over the years, deep-learning models such as convolutional neural network (CNN), long short-term memory network (LSTM), and Transformer [22] have provided strong technical support for time-series prediction [23]. Based on deep learning, many scholars have studied the single-step prediction of time series. Duan et al. [24] proposed a single-step furnace temperature prediction model by combining working condition classification and local sample weighting LSTM. A single-step prediction model was established based on the gated recurrent unit (GRU), which used the time series of fuel and air to predict the temperature in a heating furnace [25]. A single-step prediction model for boiler temperature and oxygen content was proposed by combining CNN, bidirectional long short-term memory network (biLSTM), and squeezing and excitation (SE) network [26]. This work utilized the advantages of various deep-learning networks and significantly improved the prediction accuracy of oxygen content and boiler temperature. Ma et al. [27] proposed a single-step prediction model of temperature in an intermediate frequency furnace smelting process based on Transformer. Han et al. [28] proposed a CNN-based Transformer model that integrates the Boruta algorithm, which can effectively predict the liquefied petroleum gas output in industrial processes. By combining CNN and Transformer, local features extracted by CNN and global features captured by Transformer can be utilized to improve the accuracy of single-step prediction. These studies have provided a basic idea for the work of this paper. The advantage of these single-step prediction models is that they can maintain high prediction accuracy and stability in a short time. However, single-step prediction models often fail to effectively capture the long-term dependence in the time series, resulting in the prediction error increasing with the increase of the prediction time step. Tan et al. [29] proposed an LSTM model for the boiler of a 660 MW coal-fired power station, which effectively realized the multi-step prediction of the reheated steam temperature in the boiler. A multi-step prediction model based on Transformer is proposed for lithium-ion battery temperature [30]. The lithium-ion battery temperature, multi-step

prediction model predicted 24 times more data than a single-step prediction model, and despite it having six times more running time, the prediction accuracy of the multi-step model did not decrease much. Chen et al. [31] proposed a hybrid model based on CNN and Transformer to predict ozone concentration. In the hybrid model, CNN compensates for the limited ability of Transformer to mine information from multivariable datasets, thereby improving the accuracy of multi-step prediction. However, both single-step prediction and multi-step prediction need to deal with data distribution drift in time series. Data distribution drift refers to changes in the statistical information of data over time [32]. Du et al. [33] proposed an adaptive recurrent neural network to deal with the data distribution drift of non-stationary time series. The method first characterized the data distribution information by dividing the training data into different time periods, and it then generalized the model by matching the data distribution information of these time periods. Jin et al. [34] proposed a simple and effective reversible instance normalization (RevIN) technique, which can solve the problem of data distribution drift in time series. Unlike adaptive recurrent neural networks, which were computationally expensive, RevIN was simple and effective. Although the RevIN technique has provided an important reference for this paper, the multi-step prediction of temperature for a regenerative aluminum smelting furnace, which considers both strong nonlinear characteristics and data distribution drift, cannot directly apply the results of the above research and needs further study.

Inspired by the above literature, a prediction model named RevIN-CNN-Transformer has been proposed to improve the multi-step prediction accuracy of temperature for a regenerative aluminum smelting furnace. The prediction model considers the key factors affecting furnace temperature prediction and enhances temporal correlation through time coding. The strong nonlinear characteristics and data distribution drift effects of furnace temperature data are effectively addressed through the integration of RevIN, CNN, and Transformer, resulting in accurate and stable multi-step furnace temperature predictions. The rest of this paper is structured as follows: In Section 2, the process of regenerative aluminum smelting is first introduced, and the main factors affecting furnace temperature are analyzed. In Section 3, the proposed RevIN-CNN-Transformer model is described in detail. Then, in Section 4, the proposed model is applied to furnace temperature prediction at an aluminum plant to verify its effectiveness. Finally, a summary of the entire paper is provided.

2. Regenerative Aluminum Smelting Process Analysis

2.1. Structure and Working Principle of Regenerative Aluminum Smelting Furnace

The working process of a regenerative aluminum smelting furnace is regarded as a complex industrial process. The internal structure and operational principles of an industrial regenerative aluminum smelting furnace are illustrated in Figure 1. The regenerative aluminum smelting furnace is primarily composed of a furnace chamber, ceramic sphere accumulator, reversing valve, and exhaust pipe. The regenerative burners are arranged in pairs, with two opposing burners (A and B) forming a group. After the normal temperature air discharged from the blower enters burner B through the reversing valve, it is heated to near-furnace temperature as it passes through the ceramic sphere accumulator. After being heated, the normal temperature air enters the furnace, entraining the surrounding flue gas inside the furnace to form a high-temperature, oxygen-depleted gas stream with an oxygen content lower than 21%. The high-temperature, oxygen-depleted gas stream is mixed with the injected fuel to achieve oxygen-poor combustion of the fuel. Meanwhile, the high-temperature flue gas inside the furnace chamber is stored in the ceramic sphere accumulator and then discharged through burner A. Subsequently, an exhaust flue gas temperature below 150 °C is expelled through the reversing valve. When the heat stored in the ceramic sphere accumulator reaches saturation, the direction of the reversing valve is changed, causing burners A and B to operate alternately between combustion and heat storage states. The process of alternating between combustion and heat storage states by burners A and B is repeated cyclically, resulting in energy savings and emission reduction.

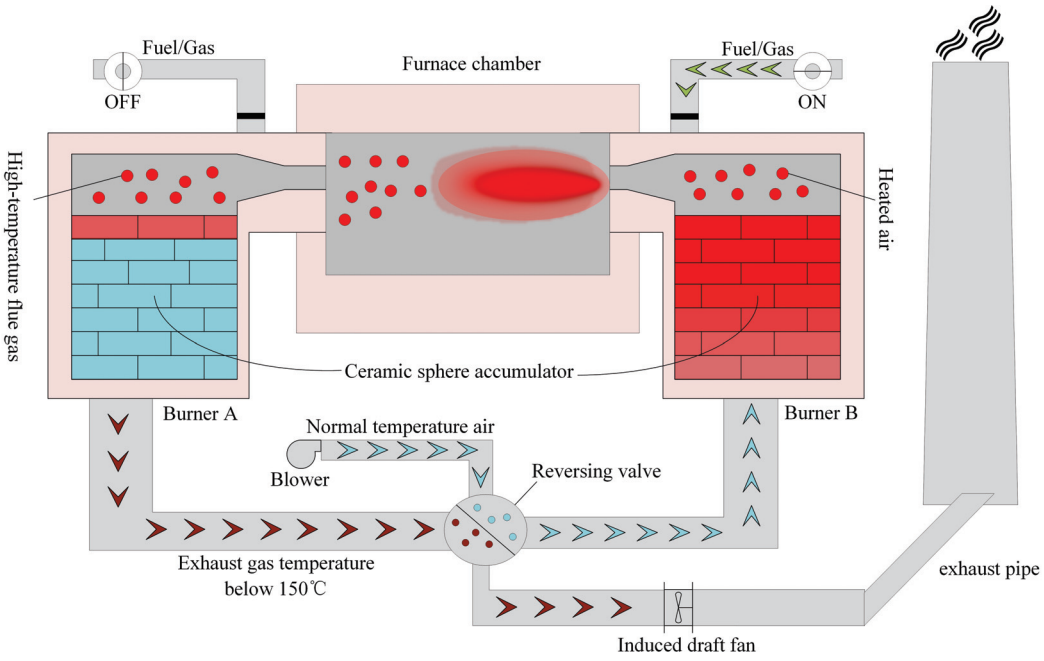

Figure 1. Structure and working principle of regenerative aluminum smelting furnace.

2.2. Analysis of Factors Affecting Furnace Temperature

The furnace temperature is considered a crucial index in the working process of the regenerative aluminum smelting furnace, influencing both the time and quality of aluminum smelting production. The regenerative aluminum melting process is very complex, and the furnace temperature is dynamically influenced by various factors. The main factors affecting the furnace temperature are gas flow rate, combustion air flow rate, combustion air pressure differential, combustion air valve opening, and exhaust temperature, which have a significant effect on temperature variations. Some influence on the furnace temperature is also exerted by burner switching time and combustion air temperature, but the impact is relatively small. When analyzing the factors affecting furnace temperature, burner switching time and combustion air temperature are considered secondary factors and can be ignored. Additionally, the difficulty of predicting the furnace temperature is further increased by changes in external environmental conditions and equipment aging. To better predict the furnace temperature, it is necessary that the main factors influencing the furnace temperature are analyzed in detail. Auxiliary variables affecting furnace temperature are presented in Table 1. By analyzing the working principle of the regenerative aluminum smelting furnace, it can be established that the factors influencing furnace temperature are primarily comprised of two aspects.

(a) Combustion aspect: The gas flow rate and the combustion air flow rate are identified as the primary factors influencing furnace temperature. The ratio of gas flow rate to combustion air flow rate is directly influenced by the combustion efficiency. If the combustion air flow rate is excessive, the surplus air will be expelled in the form of smoke, resulting in significant heat loss and a direct reduction in furnace temperature. If the gas flow rate is excessive, insufficient combustion of the gas will be caused, and increased costs will also be incurred. The air resistance and flow entering the furnace are reflected by the combustion air pressure differential. Excessive combustion air pressure differential results in an insufficient supply of combustion air, which affects combustion efficiency and furnace temperature. On the contrary, if the combustion air pressure differential is too small, excess air is present, which increases heat loss from the furnace. The amount of air entering the furnace is determined by the combustion air valve opening. If the combustion air valve opening is too large, it can lead to excess combustion air, resulting in a significant amount of unburned gas and heat loss. On the contrary, if the combustion air valve opening is

too small, insufficient air supply is experienced, leading to incomplete combustion, which affects the furnace temperature.

(b) Exhaust aspect: High-temperature flue gas is first gradually cooled by passing through the ceramic sphere regenerator, and it is then directed by the reversing valve to be discharged through the exhaust pipe. In this exhaust process, a significant amount of heat is directly removed from the furnace chamber by the high-temperature flue gas, resulting in a significant loss of energy for the process. Consequently, the exhaust temperature is considered a critical auxiliary variable in the exhaust process and must be strictly monitored and regulated to effectively reduce energy loss and improve thermal efficiency.

Table 1. Auxiliary variables for furnace temperature.

Variable	Unit	Description
Gas flow rate	Nm^3/h	Volume flow rate of the gas entering the furnace
Combustion air flow rate	Nm^3/h	Volume flow rate of air entering the furnace for combustion
Combustion air pressure differential	Pa	The pressure differential between the air before entering the furnace and the pressure in the furnace
Combustion air valve opening	%	Valve opening for adjusting the air flow rate
Exhaust temperature	°C	Temperature of the flue gas upon exit from the furnace

3. The RevIN-CNN-Transformer Prediction Model

To establish a multi-step prediction model for the furnace temperature in the regenerative aluminum smelting process, a RevIN-CNN-Transformer model is proposed by combining RevIN, CNN, and Transformer. Global information from the furnace temperature data is acquired through the self-attention mechanism of the Transformer, while sensitivity to local information in the furnace temperature data is improved by combining CNN. The issue of distribution drift in furnace temperature data is addressed through RevIN. Additionally, the time dependency of furnace temperature data is augmented through time coding by the proposed prediction model.

3.1. Time Coding Based CNN-Transformer

Transformer is described as a deep-learning model based on the self-attention mechanism, with the structure shown in Figure 2. Unlike traditional RNN, the recursive operations in sequence processing are discarded by the Transformer, which relies on the self-attention mechanism to handle the global dependencies of the input data. The recursive operations in sequence processing are discarded by the Transformer, with the self-attention mechanism relied upon to handle the global dependencies of the input sequence. The core structure of the Transformer model includes an encoder and a decoder, with features extracted from the input sequence by the encoder and the output generated by the decoder. The encoder is composed of multiple similar layers, each primarily consisting of a multi-head attention mechanism and a feed-forward network. The decoder is also composed of multiple similar layers, with each layer primarily including a multi-head attention mechanism, masked multi-head attention, and feed-forward network.

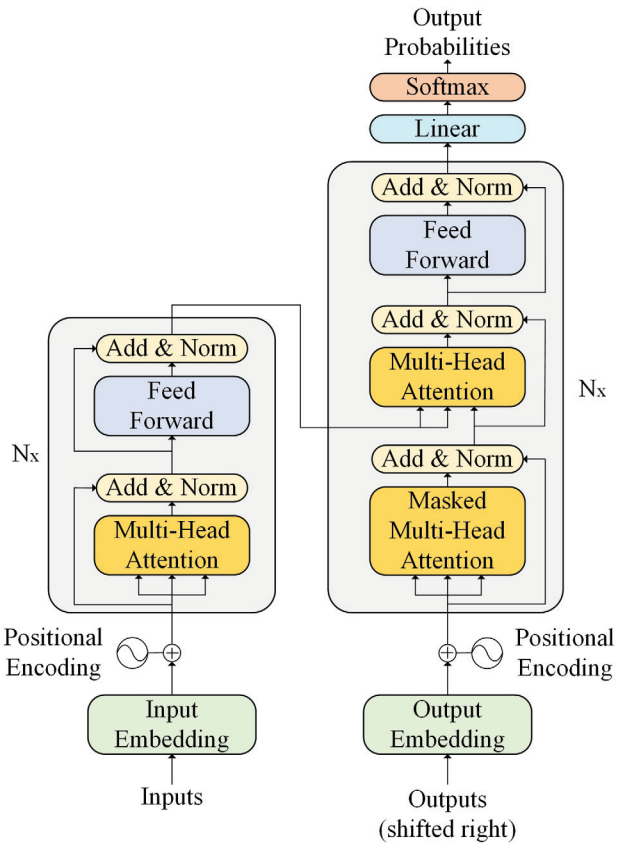

Figure 2. The structure of the Transformer model.

The self-attention mechanism is utilized by the Transformer model to handle dependencies between different positions in the input sequence, thereby allowing for better capture of long-range dependencies. The attention mechanism of the Transformer is illustrated in Figure 3. The structure of the self-attention mechanism is depicted in Figure 3a, while the structure of the multi-head attention mechanism is depicted in Figure 3b. Attention scores are calculated by the self-attention mechanism to assign weights to each position in the input sequence. The self-attention mechanism is defined as Equation (1):

$$\text{Attention}(Q, K, V) = \text{softmax}\left(\frac{Q \cdot K^{\text{T}}}{\sqrt{d_k}}\right) \cdot V \tag{1}$$

where Attention(·) is the function for self-attention calculation; Q, K, and V are the query, key, and value matrices, respectively; T denotes the matrix transpose operation; d_k denotes the dimension of the K; and softmax(·) is the normalization function used to convert scores into probabilities.

The outputs of different attention heads are concatenated by the multi-head attention mechanism, and the final multi-head attention output is obtained through linear transformations. The computation process of the multi-head attention mechanism is described as follows:

$$\text{MultiHead}(Q, K, V) = \text{Concat}(\text{Head}_1, \cdots, \text{Head}_h) \cdot W^O \tag{2}$$

$$\text{Head}_i = \text{Attention}\left(Q \cdot W_i^Q, K \cdot W_i^K, V \cdot W_i^V\right) \tag{3}$$

where MultiHead(·) is the function for multi-head self-attention calculation, Head_i denotes the output of the i attention head, h denotes the total number of attention heads, and Concat(·) denotes the vector concatenation operation. W_i^Q, W_i^K, and W_i^V are mapping matrices used to project Q, K, and V into a higher-dimensional representation. W^O is

the mapping matrix used to project the multi-head attention results back to the original lower-dimensional representation.

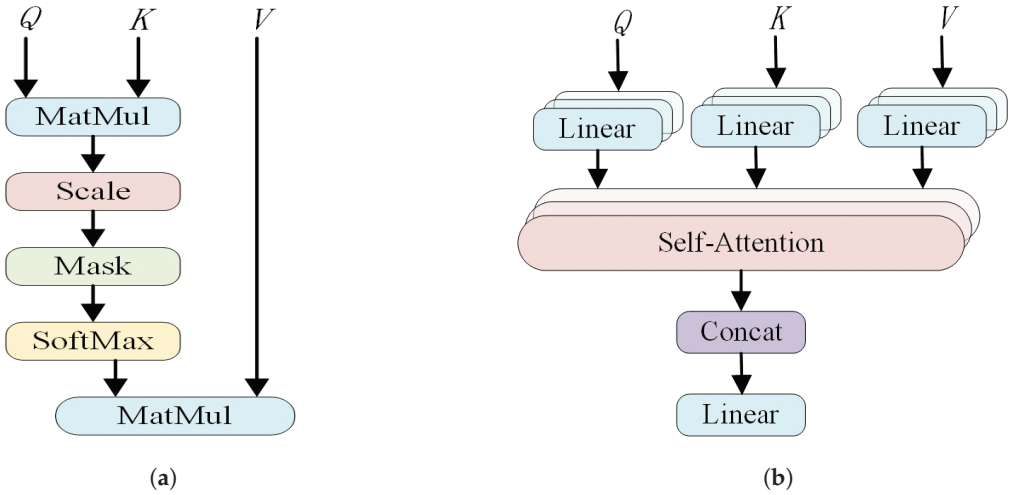

(**a**) (**b**)

Figure 3. Attention mechanisms: (**a**) Self-attention mechanism. (**b**) Multi-head attention mechanism.

Compared to the self-attention mechanism, multiple subspaces are generated by the multi-head attention mechanism, allowing different aspects of the input sequence to be simultaneously attended to by the attention mechanism. Richer and more diverse features are captured in different subspaces by the multi-head attention mechanism.

Global features are captured from the input sequence by the Transformer model through the multi-head attention mechanism. However, the attention to local information within the input sequence and the perception of time-related information are found to be insufficient in the Transformer model. To more effectively extract the time-related information and local features from the furnace temperature data, embedding operations are needed. Embedding operations are comprised of positional encoding, time coding, and multi-feature embedding.

Positional information on furnace temperature data is provided by positional encoding to help the prediction model understand the relative positions of the furnace temperatures, thereby addressing the issue of lost positional information. Since time steps are not included in Transformer models as they are in RNN, positional encoding is employed to capture the relative positions of furnace temperature data. The definition of positional encoding is shown in Equation (4):

$$\begin{cases} PE(pos, 2n) = \sin\left(\dfrac{pos}{10000^{\frac{2n}{d_{\text{model}}}}}\right) \\ PE(pos, 2n+1) = \cos\left(\dfrac{pos}{10000^{\frac{2n}{d_{\text{model}}}}}\right) \end{cases} \tag{4}$$

where pos denotes the index of the current position and n denotes the index of the dimension in the position embedding vector.

By encoding time, the ability of the prediction model to capture time-related information is significantly enhanced, leading to improved prediction accuracy. Time coding is used to convert the data from the time channel into specific time features, thus assisting the prediction model in better understanding and utilizing the time-related information within the time series. Time coding is performed by converting the time point into corresponding $minute\_number$, $hour\_number$, $day\_of\_the\_week$, and $day\_of\_the\_month$, and then scaling the values to the range $[-0.5, 0.5]$. The computation process of time coding is described as follows:

$$\begin{cases} minute\_number = \frac{minute}{59} - 0.5 \\ hour\_number = \frac{hour}{23} - 0.5 \\ day\_of\_week = \frac{weekday}{6} - 0.5 \\ day\_of\_month = \frac{days\_passed-1}{total\_days\_in\_month-1} - 0.5 \end{cases} \quad (5)$$

where *minute* represents the number of minutes at the current time point (from 0 to 59), *hour* represents the number of hours at the current time point (from 0 to 23), *weekday* represents the day of the week at the current time point (from 0 to 6), and *days_passed* represents the day of the month at the current time point.

The CNN is used for multi-feature embedding, and the local features of furnace temperature data are able to be captured. The CNN is primarily composed of an input layer, convolutional layers, pooling layers, fully connected layers, and an output layer, and is depicted as a typical feedforward neural network, with the structure shown in Figure 4. Key information in the furnace temperature data is captured by applying convolution operations over different time periods by the CNN. Important details of furnace temperature variations are revealed through the extraction of local features by the CNN. By introducing the CNN module into the Transformer model to extract local features, the strong nonlinear characteristics of the furnace temperature data are effectively addressed, leading to an enhancement in the performance of the proposed model.

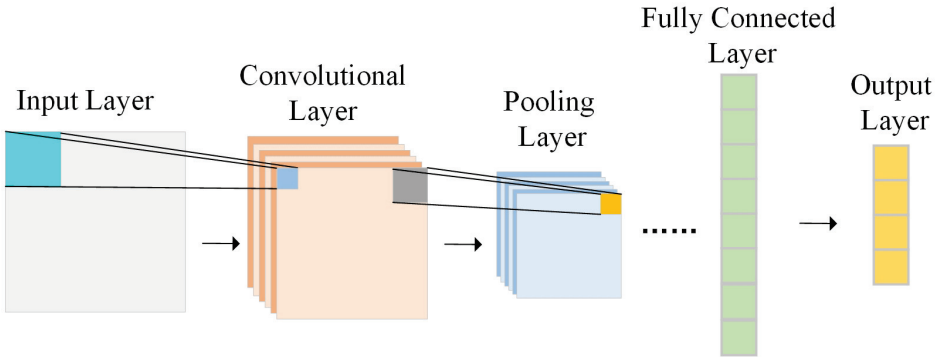

Figure 4. The structure of the CNN.

Multi-feature embedding is achieved using one-dimensional CNN, which is more suitable for furnace temperature data. The computation process of multi-feature embedding is as follows:

$$ME = Conv1d(X_t^N) \quad (6)$$

where ME denotes the multi-feature embedding operation, X_t^N denotes the one-dimensional convolution input, and $Conv1d(\cdot)$ denotes the one-dimensional convolution operation.

3.2. Reversible Instance Normalization

If the mean and variance, among other statistical properties, are observed to change over time in time-series data, it is an indication that a data distribution drift problem is present. The furnace temperature data, as typical time-series data, is analyzed using a window length of 30; the kernel density probability estimates for three historical windows are presented in Figure 5. It can be observed from Figure 5 that the mean and variance of the furnace temperature data are found to vary, indicating that a distribution drift problem is present in the furnace temperature data. Furnace temperature distribution drift is identified as a primary challenge hindering the accurate prediction of furnace temperature. RevIN is described as a normalization and denormalization method with learnable affine transformations, which is effectively used to address the issue of distribution drift in the data.

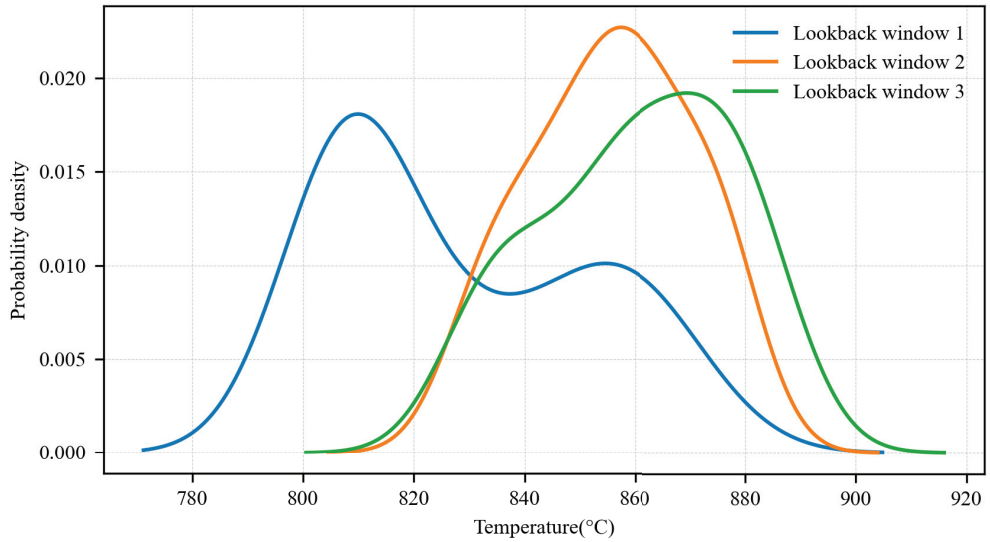

Figure 5. Kernel density probability estimates.

RevIN is composed of normalization and denormalization layers arranged in a symmetric structure. Furnace temperature prediction is treated as a multivariate time-series prediction task. Given the original input $X \in \mathcal{R}^{T_x \times l}$, the goal is to produce output $Y \in \mathcal{R}^{pre\_len \times 1}$, where T_x represents the length of the input sequence, l represents the number of variables, and pre_len represents the lengths of the prediction sequences to be generated. Firstly, instance normalization is applied to the input data X. The mean and standard deviation of the input data X are computed as follows:

$$\begin{cases} \mathrm{E}_t[X_{lt}] = \dfrac{1}{T_x}\displaystyle\sum_{j=1}^{T_x} X_{lj} \\ Var[X_{lt}] = \dfrac{1}{T_x}\displaystyle\sum_{j=1}^{T_x} (X_{lj} - \mathrm{E}_t[X_{lt}])^2 \end{cases} \tag{7}$$

Using these statistical measures, the input data X are normalized as Equation (8):

$$\hat{X}_{lt} = \gamma_l \left(\frac{x_{lt}^{(i)} - \mathrm{E}_t[X_{lt}]}{\sqrt{Var[X_{lt}] + \varepsilon}}\right) + \beta_l \tag{8}$$

where γ and β denote learnable affine parameter vectors and ε denotes the offset.

Subsequently, the prediction model receives the instance-normalized $\hat{X}$ as the input sequence for prediction. However, $\hat{X}$ exhibits statistics that differ from the distribution of the original input X, and capturing the original distribution of X is challenging by merely observing the instance-normalized $\hat{X}$. By performing denormalization at the output layer of the prediction model, the non-stationary information removed from the original input X is restored to the output of the prediction model. By applying the inverse normalization of Equation (8) to the output $\tilde{Y}$, obtained from the instance-normalized input $\hat{X}$, which does not contain non-stationary information, the non-stationary information is restored to the final output Y of the prediction model. The process of denormalization is as follows:

$$Y = \sqrt{Var[X_{lt}] + \varepsilon} \cdot \left(\frac{\tilde{Y} - \beta_l}{\gamma_l}\right) + \mathrm{E}_t[X_{lt}] \tag{9}$$

where Y is the final predicted value instead of $\tilde{Y}$.

RevIN is characterized by symmetric normalization and denormalization layers, which effectively handle non-stationary information in time-series data. Non-stationary infor-

mation in furnace temperature data can be removed by RevIN, and this information can be restored when needed, thus addressing the issue of distribution drift in the furnace temperature data. The application of RevIN is significant for alleviating the impact of furnace temperature data distribution drift and for improving the accuracy and stability of multi-step furnace temperature predictions.

By integrating RevIN, CNN, time coding, and Transformer, the RevIN-CNN-Transformer model is obtained. The proposed model effectively handles distribution drift in the furnace temperature data. The combination of local feature extraction by CNN and global feature extraction by Transformer is utilized to address the strong nonlinear characteristics in furnace temperature data. In addition, the temporal relevance of the proposed model is enhanced by time coding. The structure of the RevIN-CNN-Transformer model is shown in Figure 6.

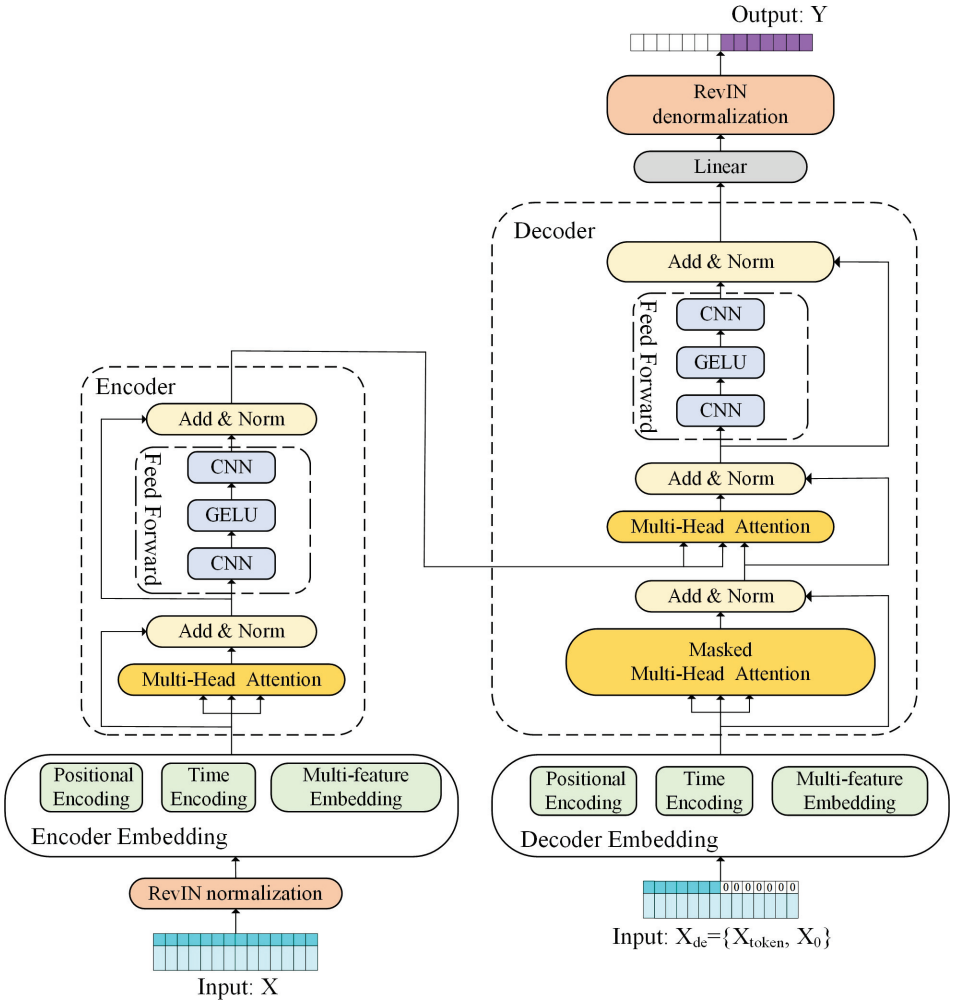

Figure 6. The structure of the RevIN-CNN-Transformer model.

The operating process of the RevIN-CNN-Transformer model is as follows:

Step 1: $X \in \mathcal{R}^{T_x \times l}$ is the input sequence, where T_x represents the length of the input sequence and l represents the number of variables. By applying RevIN normalization to X through Equation (8), $E(X)$ is obtained.

Step 2: Perform Encoder Embedding operation on $E(X)$.

(a) By applying positional encoding to $E(X)$ through Equation (4), $PE(X) \in \mathcal{R}^{T_x \times d_{\mathrm{mod}\,el}}$ is obtained, where $d_{\mathrm{mod}\,el}$ represents the dimensions of the prediction model.

(b) By applying time coding to $E(X)$ through Equation (5), $TE(X) \in \mathcal{R}^{T_x \times d_{\mathrm{mod}\,el}}$ is obtained.

(c) By applying multi-feature embedding to $E(X)$ through Equation (6), $ME(X) \in \mathcal{R}^{Tx \times d \bmod el}$ is obtained.

Then, by summing $PE(X)$, $TE(X)$, and $ME(X)$, $Z_0 = PE(X) + TE(X) + ME(X)$ is obtained.

Step 3: By applying the multi-head attention mechanism to Z_0, $Z_N = \text{MultiHead}(Z_0) \in \mathcal{R}^{Tx \times d \bmod el}$ is obtained.

Step 4: After passing Z_N through the feedforward network, the output of the encoder is $Z'_N = \text{GELU}(Conv1d(Z_N)) \in \mathcal{R}^{Tx \times d \bmod el}$.

Step 5: $X_{token} \in \mathcal{R}^{Label\_len \times l}$, where *Label_len* represents the lengths of known data used by the decoder during the prediction process. $X_0 \in \mathcal{R}^{pre\_len \times l}$, where *pre_len* represents the lengths of the prediction sequences to be generated. Therefore, the input to the decoder is $X_{de} = \{X_{token}, X_0\} \in \mathcal{R}^{Ty \times l}$, and $T_y = Label\_len + pre\_len$ represents the length of the target sequence fed into the decoder.

Step 6: Perform decoder embedding operation on X_{de}.

(a) By applying positional encoding to X_{de} through Equation (4), $PX_{de} \in \mathcal{R}^{Ty \times d \bmod el}$ is obtained.
(b) By applying time coding to X_{de} through Equation (5), $TX_{de} \in \mathcal{R}^{Ty \times d \bmod el}$ is obtained.
(c) By applying multi-feature embedding to X_{de} through Equation (6), $MX_{de} \in \mathcal{R}^{Ty \times d \bmod el}$ is obtained.

Then, by summing PX_{de}, TX_{de}, and MX_{de}, $Z'_0 = PX_{de} + TX_{de} + MX_{de}$ is obtained.

Step 7: By applying masked multi-head attention to Z'_0, $Z'_w = \text{MultiHead}(Z'_0) \in \mathcal{R}^{Ty \times d \bmod el}$ is obtained.

Step 8: By combining the encoder's output, Z'_w passes through the encoder–decoder attention, yielding $Z''_w = \text{MultiHead}(Z'_w, Z'_N) \in \mathcal{R}^{Ty \times d \bmod el}$.

Step 9: After passing Z''_w through the feedforward network, the output of the decoder is $Z''_N = \text{GELU}(Conv1d(Z''_w)) \in \mathcal{R}^{Ty \times d \bmod el}$.

Step 10: After passing Z''_N through the linear layer and then applying RevIN denormalization, the final output $Y \in \mathcal{R}^{pre\_len \times 1}$ is obtained.

4. Industrial Case

4.1. Dataset and Data Preprocessing

In order to verify the performance of the RevIN-CNN-Transformer model, it was applied to the multi-step prediction of furnace temperature in an industrial regenerative aluminum smelting plant. The aluminum plant was characterized by high-temperature smelting and a complex production process, with advanced technology and equipment utilized for large-scale aluminum production. Through the mechanistic analysis of the regenerative aluminum melting furnace, it is found that seven factors influence the furnace temperature. However, during the data collection, the variations in burner switching time and combustion air temperature are relatively small. Therefore, the influence of burner switching time and combustion air temperature is ignored during the prediction of furnace temperature. To construct the model, the selected auxiliary variables are shown in Table 2. These auxiliary variables are measured by sensors. The types and parameters of the sensors are shown in Table 3. The data were collected from the regenerative aluminum smelting furnace in the plant, spanning from 1 November to 29 November 2017. The data were sampled every 5 min, resulting in a dataset of 8000 samples. The dataset was divided as follows: 80% of the data were allocated to the training set, 10% to the validation set, and the remaining 10% to the test set. The comprehensive assessment of the performance of the RevIN-CNN-Transformer model in furnace temperature prediction was enabled by the division of the dataset.

Table 2. Auxiliary variables of the proposed model.

Index	Auxiliary Variable
1	12 # Gas flow rate
2	34 # Gas flow rate
3	12 # Combustion air flow rate
4	34 # Combustion air flow rate
5	12 # Combustion air pressure differential
6	34 # Combustion air pressure differential
7	12 # Combustion air valve opening
8	34 # Combustion air valve opening
9	B3 # Exhaust temperature

Table 3. Sensor types and parameters.

Sensor Type	Measurement Range	Accuracy	Response Time
Flow Meter	0–15 m^3/h	±1%	0.2 s
Differential Pressure Gauge	0–10,000 Pa	±0.5%	0.1 s
Valve Position Indicator	0–100%	±1%	0.1 s
Thermocouple	0–1200 °C	±0.5%	0.5 s

To eliminate the impact caused by differences in dimensions among variables and enable comparison on the same scale, standardization is performed. Z-score standardization is employed in this paper, with the specific expression in Equation (10):

$$x_i^* = \frac{x_i - \mu}{\sigma} \tag{10}$$

where x_i denotes the original data value, μ denotes the mean of the data, σ denotes the standard deviation of the data, and x_i^* denotes the standardized value.

To evaluate the performance of the proposed prediction model, the root mean squared error (RMSE), the mean absolute error (MAE), and the coefficient of determination (R^2) are selected as evaluation indices. Smaller values of RMSE and MAE are associated with higher prediction accuracy. Greater accuracy in the prediction results is indicated by a value of R^2 closer to 1. The three evaluation indices are defined as follows:

$$RMSE = \sqrt{\frac{1}{N_T}\sum_{i=1}^{N_T}(y_i - \hat{y}_i)^2} \tag{11}$$

$$MAE = \frac{1}{N_T}\sum_{i=1}^{N_T}|y_i - \hat{y}_i| \tag{12}$$

$$R^2 = 1 - \frac{\sum_{i=1}^{N_T}(y_i - \hat{y}_i)^2}{\sum_{i=1}^{N_T}(y_i - \bar{y})^2} \tag{13}$$

where N_T denotes the number of samples used for testing, y_i denotes the actual value of the furnace temperature, $\hat{y}_i$ denotes the predicted value of the furnace temperature, and $\bar{y}_i$ denotes the mean value of the actual furnace temperature.

4.2. Results and Analysis

The experiments in this paper are run on the Windows 11 operating system, configured with an Intel(R) Core(TM) i5-12490F CPU and a GeForce RTX 4060 GPU. The experimental environment uses the Pytorch framework, and Python version 3.10.13 is installed. Hyperparameters such as learning rate, epoch, and batch size are shown to have a significant impact on the performance of the prediction model; therefore, optimal settings

are necessary. The learning rate is identified as one of the key hyperparameters that need to be adjusted during the training of the prediction model. A learning rate that is too high may prevent convergence and cause oscillations, while a rate that is too low may slow convergence and waste training time. The performance metrics of the prediction model under different learning rates can be obtained through the trial and error method, as shown in Table 4. From Table 4, it is shown that the optimal learning rate for the proposed model should be set to 0.0001. The optimal settings for the two hyperparameters, epoch and batch size, are also found through the trial and error method, with optimal values being 15 and 12, respectively.

Table 4. Model performance at different learning rates.

Learning Rate	MAE	RMSE	R^2
0.01	44.612	52.854	0.415
0.001	2.487	3.570	0.997
0.0001	1.984	2.865	0.998
0.00001	3.041	4.188	0.996

The loss function adopted by the proposed model is the mean squared error (MSE). Under the optimal settings of hyperparameters, the loss curves for the training and validation sets are shown in Figure 7. It can be observed from Figure 7 that the loss curves for both the training and validation sets tend to stabilize after a certain number of iterations, indicating that the errors of the prediction model on the training and validation sets are stabilized at a lower level. The error of the prediction model tends to zero and stabilizes, demonstrating that the prediction model converges.

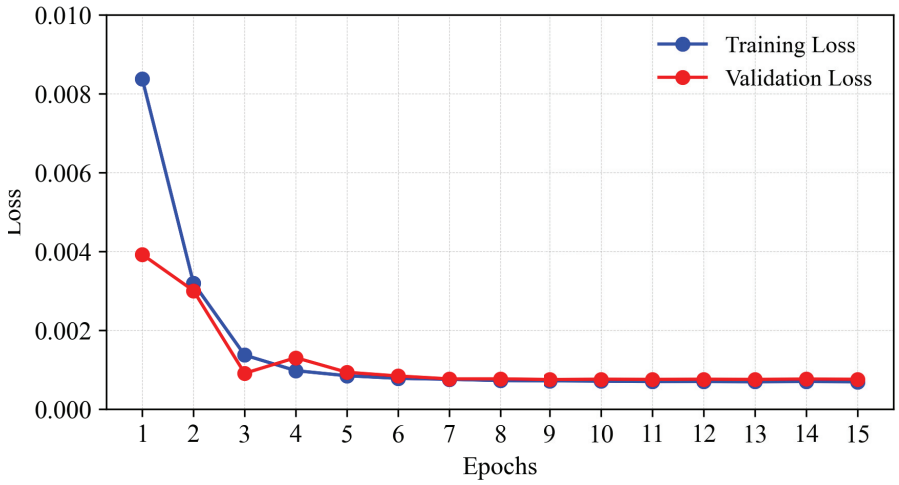

Figure 7. Training and validation loss curves.

To comprehensively evaluate the performance of the proposed model, comparative experiments and ablation experiments are conducted. The comparative experiments are primarily used to assess the performance advantages of the proposed model relative to some existing deep-learning models. The ablation experiments are used to analyze the contribution of each component of the proposed prediction model to the overall performance.

4.2.1. Comparative Experiments

To verify the superiority of the proposed model, the ARIMA model, the Transformer model [22], the Informer model [35], and the Autoformer model [36] are used for experimental comparison. The performances of the RevIN-CNN-Transformer model, the ARIMA model, the Transformer model, the Informer model, and the Autoformer model are compared in the furnace temperature prediction task with 1-step, 4-step, and 8-step prediction

steps. The prediction results of the five models with 1-step, 4-step, and 8-step prediction steps are shown in Figure 8, Figure 9, and Figure 10, respectively.

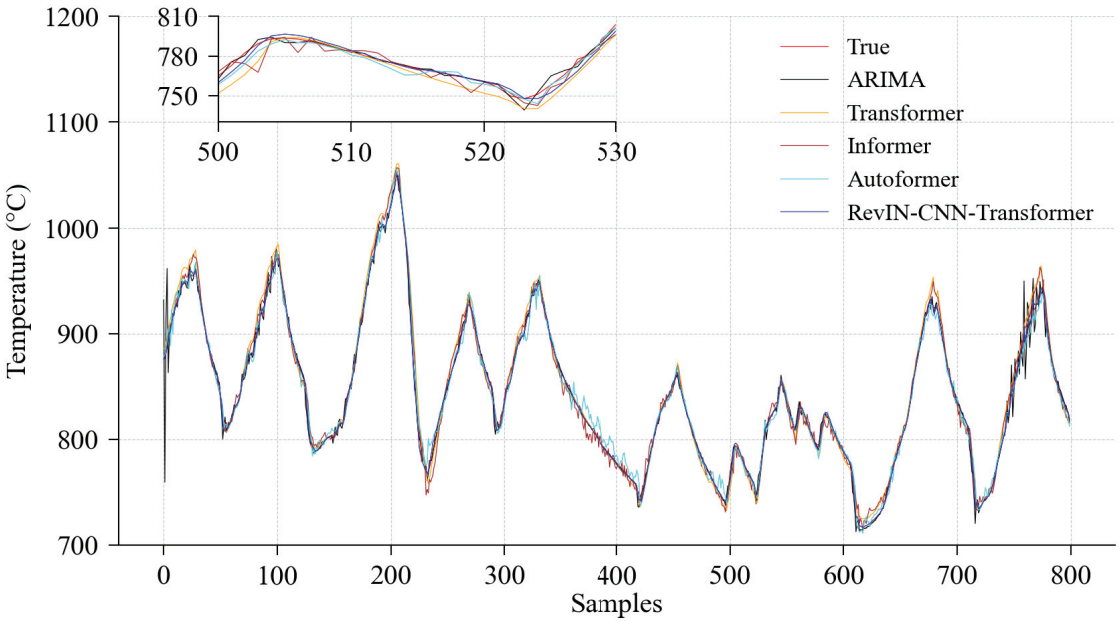

Figure 8. The 1-step prediction results of the five prediction models.

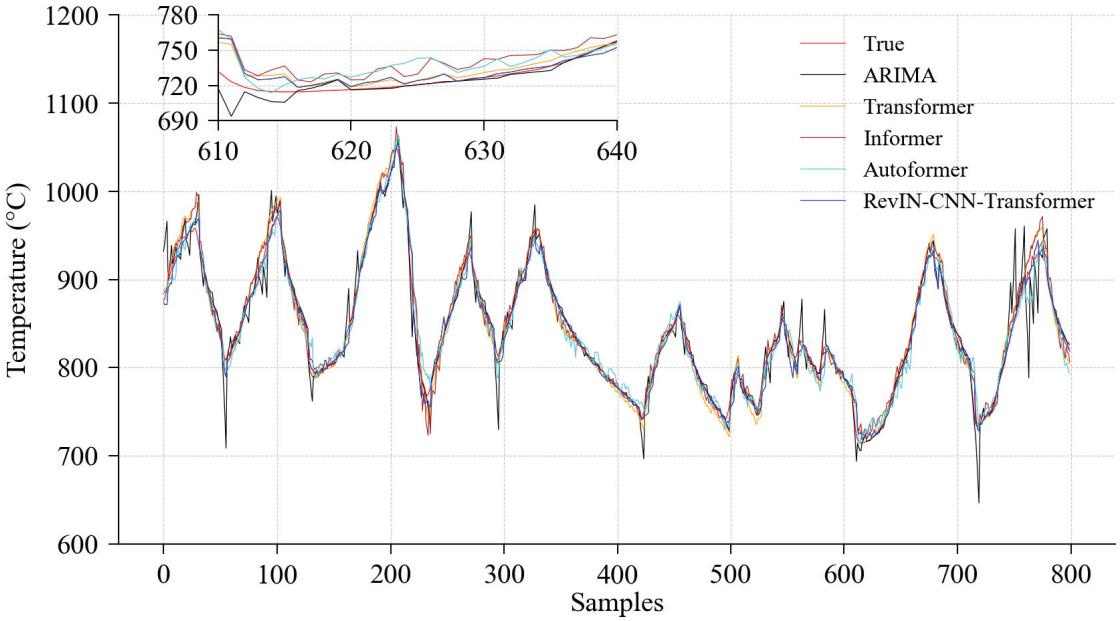

Figure 9. The 4-step prediction results of the five prediction models.

In a magnified view of the prediction results from Figure 8, the prediction curve of the RevIN-CNN-Transformer model is shown to fit the actual values accurately and to follow the fluctuations of the actual curve closely. As shown in Figures 9 and 10, the decrease in the performances of the five models as the prediction step increases and the increase in the fluctuation of the prediction curves are observed. However, the prediction results of the RevIN-CNN-Transformer model are significantly better than those of the other prediction models. The comparative experimental results demonstrate that better performance is achieved by the RevIN-CNN-Transformer model in the multi-step furnace temperature prediction task. The evaluation index results for the five models at 1-step, 4-step, and 8-step furnace temperature prediction steps are shown in Table 5.

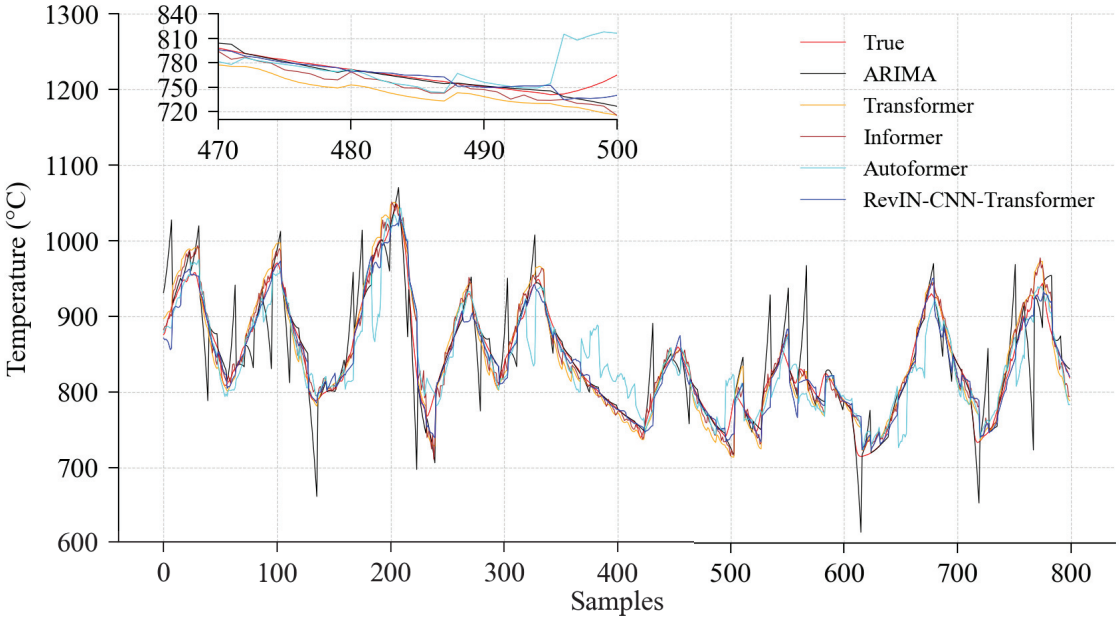

Figure 10. The 8-step prediction results of the five prediction models.

Table 5. The results of the evaluation indices for the models under different prediction steps.

Prediction Step	Evaluation Metrics	ARIMA	Transformer	Informer	Autoformer	RevIN-CNN-Transformer
1-step	MAE	3.181	6.312	6.061	5.107	1.984
	RMSE	7.592	8.283	7.810	6.889	2.865
	R2	0.988	0.986	0.987	0.990	0.998
4-step	MAE	8.063	9.648	8.691	8.897	5.755
	RMSE	16.249	12.126	11.849	11.892	8.351
	R2	0.949	0.969	0.971	0.970	0.985
8-step	MAE	18.376	14.872	12.129	19.943	10.600
	RMSE	32.735	19.112	16.766	27.491	15.998
	R2	0.810	0.924	0.941	0.842	0.946

It can be seen from Table 5 that the RevIN-CNN-Transformer model performs better than the other four prediction models across the three prediction steps. Among the three prediction steps, the smallest values of MAE and RMSE and the highest value of R^2 are exhibited by the RevIN-CNN-Transformer model, indicating that higher prediction accuracy and better fitting performance are achieved by the proposed model.

The comparison of the reduction rates of MAE and RMSE for the other four prediction models relative to the RevIN-CNN-Transformer model under 1-step, 4-step, and 8-step prediction steps is shown in Figure 11.

The better prediction performance of the RevIN-CNN-Transformer model compared to the other prediction models for 1-step, 4-step, and 8-step prediction steps is shown in Figure 11. In the 1-step prediction, reductions of 38 to 69% in MAE and 58 to 65% in RMSE are achieved by the RevIN-CNN-Transformer model. In the 4-step prediction, reductions of 29 to 40% in MAE and 30 to 49% in RMSE are achieved by the proposed model. In the 8-step prediction, the proposed model achieves reductions of 13 to 47% in MAE and 5 to 51% in RMSE. The RevIN-CNN-Transformer model has smaller MAE and RMSE values compared to the other four prediction models, indicating that smaller prediction errors, lower dispersion, and better prediction performance are obtained.

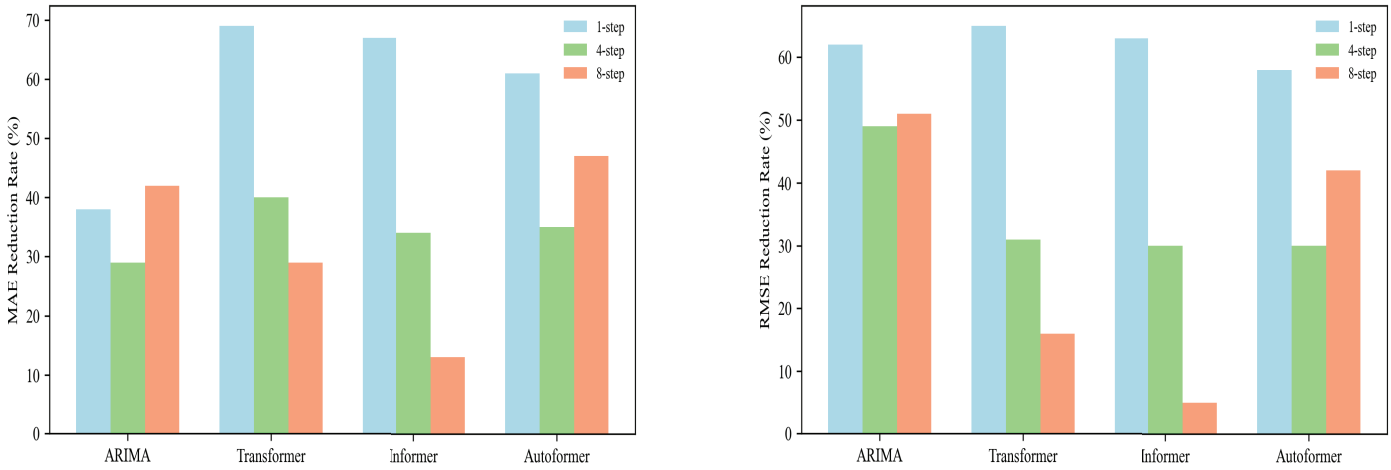

(**a**) (**b**)

Figure 11. The comparison of the reduction rates of evaluation indices for the four models under different prediction steps: (**a**) MAE reduction rates. (**b**) RMSE reduction rates.

4.2.2. Ablation Experiments

To validate the effectiveness of each component in the proposed prediction model, systematic ablation experiments are conducted. The impact of removing key components of the prediction model on prediction performance is assessed. All ablation experiments are conducted on the same dataset with the same training parameters. The evaluation indices of MAE, RMSE, and R^2 are used to ensure the comparability of the ablation experiment results. The CNN and RevIN are added separately to the Transformer model to explore their effects. The impact of removing the time-coding module from the RevIN-CNN-Transformer model is analyzed. All ablation experiments are conducted on the furnace temperature prediction task with a 4-step prediction horizon, and the results are shown in Figure 12.

The evaluation indices of the ablation experiments for the RevIN-CNN-Transformer model are presented in Table 6.

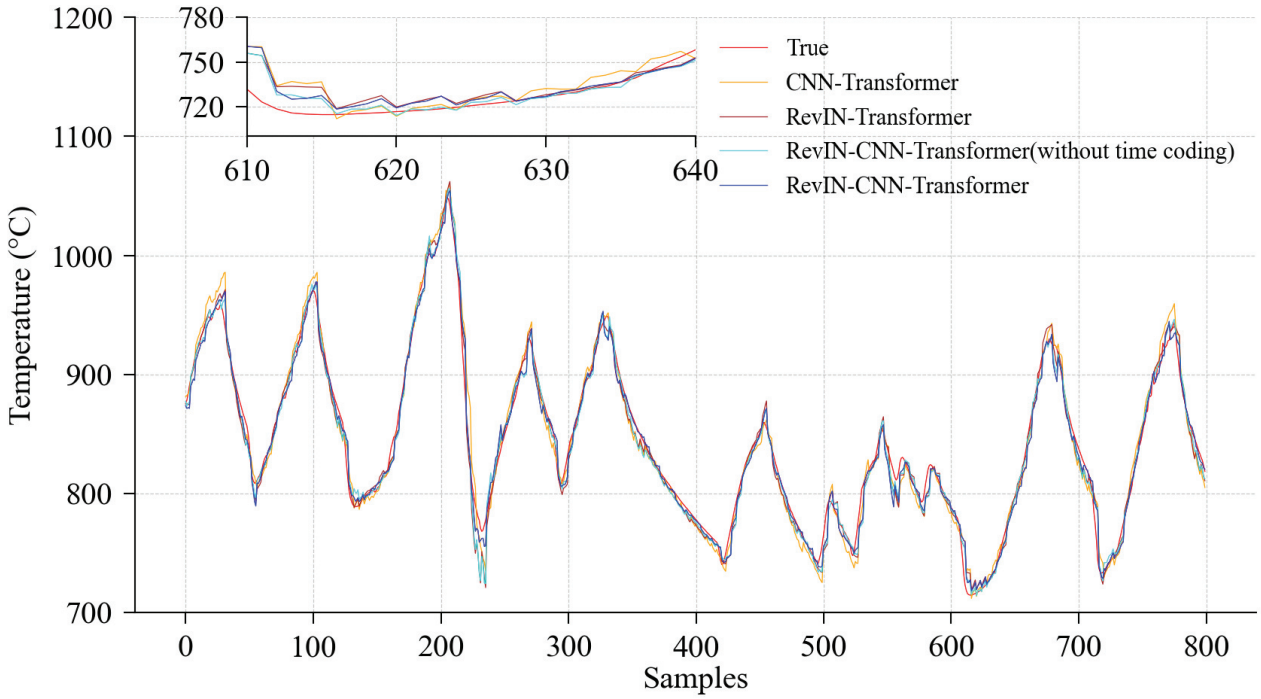

Figure 12. The results of the ablation experiments.

Table 6. The results of the evaluation indices for the ablation experiments of the prediction model.

Prediction Model	MAE	RMSE	R^2
CNN-Transformer	8.118	10.681	0.976
RevIN-Transformer	6.856	9.743	0.980
RevIN-CNN-Transformer (without time coding)	6.317	9.268	0.982
RevIN-CNN-Transformer	5.755	8.351	0.985

It can be seen from Table 6 that the performance of the RevIN-CNN-Transformer model is significantly improved by the introduction of the CNN and RevIN modules. Specifically, the issue of distribution drift in the furnace temperature data is effectively addressed by the RevIN module. The ability of the RevIN-CNN-Transformer model to focus on local information is enhanced by the CNN module through the extraction of local features from the furnace temperature data. The RevIN-CNN-Transformer model is enabled to better understand the overall trend of the furnace temperature and effectively capture the details within the temperature data through the introduction of the CNN and RevIN modules, thus improving the accuracy and stability of the predictions. Additionally, the temporal correlation of the RevIN-CNN-Transformer model is enhanced by the time-coding module. The performance of the proposed model in handling complex and multivariate coupling furnace temperature prediction tasks is significantly improved by the combination of the Transformer, CNN, RevIN, and time-coding modules.

5. Conclusions

A multi-step furnace temperature prediction model based on RevIN-CNN-Transformer is proposed to address the issues of strong nonlinear characteristics and distribution drift of furnace temperature for the regenerative aluminum melting process. The ability of the predictive model to learn time-related information is significantly enhanced by applying time coding to the input data. A significant improvement in the furnace temperature prediction is achieved by the proposed model, which utilizes the local feature extraction capabilities of CNN and the global feature extraction capabilities of Transformer. In addition, the issue of decreased prediction performance due to data distribution drift is effectively addressed by the introduction of RevIN. The experimental results from the furnace temperature dataset of an aluminum smelting plant show that time-related information is effectively extracted from the furnace temperature data by the proposed model. The proposed model surpasses the evaluation indices of the other models for multi-step prediction. The strong nonlinear characteristics and distribution drift issues of furnace temperature are addressed by the proposed prediction model, and favorable application results are achieved in the multi-step furnace temperature prediction. Compared to single-step prediction, multi-step prediction provides operators with more long-term predictive information, allowing them sufficient time to make adjustments, thereby improving production efficiency and reducing energy consumption. Although the errors of multi-step prediction may accumulate as the number of prediction steps increases, the opportunity for operators to have sufficient time for adjustments holds practical significance in industrial applications.

Author Contributions: Conceptualization, J.D. and P.L.; methodology, J.D. and P.L.; software, P.L. and H.S.; validation, P.L., H.S. and H.L.; formal analysis and investigation, P.L., H.S. and H.L.; data curation, P.L. and H.L.; writing—original draft preparation, J.D. and P.L.; writing—review and editing, J.D. and P.L.; visualization, H.L. and H.S.; supervision, J.D. and P.L.; project administration, J.D.; funding acquisition, J.D. All authors have read and agreed to the published version of the manuscript.

Funding: This research was funded by the National Natural Science Foundation of China (No. 62341302, No. 62273111).

Data Availability Statement: The data presented in this study are available on request from the corresponding author.

Conflicts of Interest: The authors declare no conflicts of interest. The funders had no role in the design of the study; in the collection, analyses, or interpretation of data; in the writing of the manuscript; or in the decision to publish the results.

References

1. Qiu, L.; Feng, Y.; Chen, Z.; Li, Y.; Zhang, X. Numerical simulation and optimization of the melting process for the regenerative aluminum melting furnace. *Appl. Therm. Eng.* **2018**, *145*, 315–327. [CrossRef]
2. Bozkurt, Ö.; Kaya, M.F. A CFD Assisted Study: Investigation of the Transformation of A Recuperative Furnace to Regenerative Furnace For Industrial Aluminium Melting. *Eng. Mach. Mag.* **2021**, *62*, 245–261. [CrossRef]
3. Chen, X.; Dai, J.; Luo, Y. Temperature prediction model for a regenerative aluminum smelting furnace by a just-in-time learning-based triple-weighted regularized extreme learning machine. *Processes* **2022**, *10*, 1972. [CrossRef]
4. Yin, L.; Zhou, H. Modal decomposition integrated model for ultra-supercritical coal-fired power plant reheater tube temperature multi-step prediction. *Energy* **2024**, *292*, 130521. [CrossRef]
5. Xue, P.; Jiang, Y.; Zhou, Z.; Chen, X.; Fang, X.; Liu, J. Multi-step ahead forecasting of heat load in district heating systems using machine learning algorithms. *Energy* **2019**, *188*, 116085. [CrossRef]
6. Khosravi, K.; Golkarian, A.; Barzegar, R.; Aalami, M.T.; Heddam, S.; Omidvar, E.; Keesstra, S.D.; López-Vicente, M. Multi-step ahead soil temperature forecasting at different depths based on meteorological data: Integrating resampling algorithms and machine learning models. *Pedosphere* **2023**, *33*, 479–495. [CrossRef]
7. Zhao, Y.; Ma, Z.; Han, X. Research on multi-step mixed predictiom model of coal gasifier furnace temperature based on machine learning. *Proc. J. D Conf. Ser.* **2022**, *2187*, 012070. [CrossRef]
8. Yan, M.; Bi, H.; Wang, H.; Xu, C.; Chen, L.; Zhang, L.; Chen, S.; Xu, X.; Chen, Q.; Jia, Y.; et al. Advanced soft-sensing techniques for predicting furnace temperature in industrial organic waste gasification. *Process. Saf. Environ. Prot.* **2024**, *190*, 1253–1262. [CrossRef]
9. Dai, J.; Chen, N.; Yuan, X.; Gui, W.; Luo, L. Temperature prediction for roller kiln based on hybrid first-principle model and data-driven MW-DLWKPCR model. *ISA Trans.* **2020**, *98*, 403–417. [CrossRef]
10. Rasul, K.; Seward, C.; Schuster, I.; Vollgraf, R. Autoregressive denoising diffusion models for multivariate probabilistic time series forecasting. In Proceedings of the 38th International Conference on Machine Learning, Online, 18–24 July 2021; Volume 139, pp. 8857–8868.
11. Magadum, R.B.; Bilagi, S.; Bhandarkar, S.; Patil, A.; Joshi, A. Short-term wind power forecast using time series analysis: Auto-regressive moving-average model (ARMA). In *Recent Developments in Electrical and Electronics Engineering: Select Proceedings of ICRDEEE 2022*; Springer: Singapore, 2023; Volume 979, pp. 319–341.
12. Kumar, R.; Kumar, P.; Kumar, Y. Multi-step time series analysis and forecasting strategy using ARIMA and evolutionary algorithms. *Int. J. Inf. Technol.* **2022**, *14*, 359–373. [CrossRef]
13. Lin, W.; Zhang, B.; Li, H.; Lu, R. Multi-step prediction of photovoltaic power based on two-stage decomposition and BILSTM. *Neurocomputing* **2022**, *504*, 56–67. [CrossRef]
14. Wang, Y.; Xu, Y.; Song, X.; Sun, Q.; Zhang, J.; Liu, Z. Novel method for temperature prediction in rotary kiln process through machine learning and CFD. *Powder Technol.* **2024**, *439*, 119649. [CrossRef]
15. Kong, X.; Du, X.; Xue, G.; Xu, Z. Multi-step short-term solar radiation prediction based on empirical mode decomposition and gated recurrent unit optimized via an attention mechanism. *Energy* **2023**, *282*, 128825. [CrossRef]
16. Hu, Y.; Man, Y.; Ren, J.; Zhou, J.; Zeng, Z. Multi-step carbon emissions forecasting model for industrial process based on a new strategy and machine learning methods. *Process. Saf. Environ. Prot.* **2024**, *187*, 1213–1233. [CrossRef]
17. Aljuaydi, F.; Wiwatanapataphee, B.; Wu, Y.H. Multivariate machine learning-based prediction models of freeway traffic flow under non-recurrent events. *Alex. Eng. J.* **2023**, *65*, 151–162. [CrossRef]
18. Feng, K.; Yang, L.; Su, B.; Feng, W.; Wang, L. An integration model for converter molten steel end temperature prediction based on Bayesian formula. *Steel Res. Int.* **2022**, *93*, 2100433. [CrossRef]
19. Huang, Q.; Lei, S.; Jiang, C.; Xu, C. Furnace temperature prediction of aluminum smelting furnace based on KPCA-ELM. In Proceedings of the 2018 Chinese Automation Congress (CAC), Xi'an, China, 30 November–2 December 2018; pp. 1454–1459.
20. Liu, Q.; Wei, J.; Lei, S.; Huang, Q.; Zhang, M.; Zhou, X. Temperature prediction modeling and control parameter optimization based on data driven. In Proceedings of the 2020 IEEE Fifth International Conference on Data Science in Cyberspace (DSC), Hong Kong, China, 27–30 July 2020; pp. 8–14.
21. Zhang, Z.; Dai, H.; Jiang, D.; Yu, Y.; Tian, R. Multi-step ahead forecasting of wind vector for multiple wind turbines based on new deep learning model. *Energy* **2024**, *304*, 131964. [CrossRef]
22. Vaswani, A.; Shazeer, N.; Parmar, N.; Uszkoreit, J.; Jones, L.; Gomez, A.N.; Kaiser, L.; Polosukhin, I. Attention is all you need. In Proceedings of the 31st International Conference on Neural Information Processing Systems, Long Beach, CA, USA, 4–9 December 2017; pp. 6000–6010.
23. Dettori, S.; Matino, I.; Colla, V.; Speets, R. A deep-learning-based approach for forecasting off-gas production and consumption in the blast furnace. *Neural Comput. Appl.* **2022**, *34*, 911–923. [CrossRef]
24. Duan, Y.; Dai, J.; Luo, Y.; Chen, G.; Cai, X. A Dynamic Time Warping Based Locally Weighted LSTM Modeling for Temperature Prediction of Recycled Aluminum Smelting. *IEEE Access* **2023**, *11*, 36980–36992. [CrossRef]

25. Chen, C.J.; Chou, F.I.; Chou, J.H. Temperature prediction for reheating furnace by gated recurrent unit approach. *IEEE Access* **2022**, *10*, 33362–33369. [CrossRef]
26. Ji, Z.; Tao, W.; Ren, J. Boiler furnace temperature and oxygen content prediction based on hybrid CNN, biLSTM, and SE-Net models. *Appl. Intell.* **2024**, *54*, 8241–8261. [CrossRef]
27. Ma, S.; Li, Y.; Luo, D.; Song, T. Temperature Prediction of Medium Frequency Furnace Based on Transformer Model. In Proceedings of the International Conference on Neural Computing for Advanced Applications, Jinan, China, 8–10 July 2022; Volume 1637, pp. 463–476.
28. Han, Y.; Han, L.; Shi, X.; Li, J.; Huang, X.; Hu, X.; Chu, C.; Geng, Z. Novel CNN-based transformer integrating Boruta algorithm for production prediction modeling and energy saving of industrial processes. *Expert Syst. Appl.* **2024**, *255*, 124447. [CrossRef]
29. Tan, P.; Zhu, H.; He, Z.; Jin, Z.; Zhang, C.; Fang, Q.; Chen, G. Multi-step ahead prediction of reheat steam temperature of a 660 MW coal-fired utility boiler using long short-term memory. *Front. Energy Res.* **2022**, *10*, 845328. [CrossRef]
30. Wan, Z.; Kang, Y.; Ou, R.; Xue, S.; Xu, D.; Luo, X. Multi-step time series forecasting on the temperature of lithium-ion batteries. *J. Energy Storage* **2023**, *64*, 107092. [CrossRef]
31. Chen, Y.; Chen, X.; Xu, A.; Sun, Q.; Peng, X. A hybrid CNN-Transformer model for ozone concentration prediction. *Air Qual. Atmos. Health* **2022**, *15*, 1533–1546. [CrossRef]
32. Fan, W.; Wang, P.; Wang, D.; Wang, D.; Zhou, Y.; Fu, Y. Dish-ts: A general paradigm for alleviating distribution shift in time series forecasting. In Proceedings of the AAAI Conference on Artificial Intelligence, Washington, DC, USA, 7–14 February 2023; Volume 37, pp. 7522–7529.
33. Du, Y.; Wang, J.; Feng, W.; Pan, S.; Qin, T.; Xu, R.; Wang, C. Adarnn: Adaptive learning and forecasting of time series. In Proceedings of the 30th ACM International Conference on Information & Knowledge Management, Queensland, Australia, 1–5 November 2021; pp. 402–411.
34. Kim, T.; Kim, J.; Tae, Y.; Park, C.; Choi, J.H.; Choo, J. Reversible instance normalization for accurate time-series forecasting against distribution shift. In Proceedings of the Tenth International Conference on Learning Representations, Vienna, Austria, 4 May 2021.
35. Zhou, H.; Zhang, S.; Peng, J.; Zhang, S.; Li, J.; Xiong, H.; Zhang, W. Informer: Beyond efficient transformer for long sequence time-series forecasting. In Proceedings of the AAAI Conference on Artificial Intelligence, Online, 2–9 February 2021; Volume 35, pp. 11106–11115.
36. Chen, M.; Peng, H.; Fu, J.; Ling, H. Autoformer: Searching transformers for visual recognition. In Proceedings of the IEEE/CVF International Conference on Computer Vision, Montreal, BC, Canada, 11–17 October 2021; pp. 12270–12280.

processes

MDPI

Article

Filling Process Optimization of a Fully Flexible Machine through Computer Simulation and Advanced Mathematical Modeling

Kai Zhao [1], Qiuhua Shi [2], Shuguang Zhao [2], Fang Ye [3,*] and Mohamed Badran [4,*]

[1] School of Information Engineering, North China University of Water Resources and Electric Power, Zhengzhou 450046, China; benzhihong2022@126.com
[2] School of Aerospace Engineering, Zhengzhou University of Aeronautics, Zhengzhou 450046, China; shiqiuhua@ncwu.edu.cn (Q.S.); sguang0504@163.com (S.Z.)
[3] School of Public Economics and Administration, Shanghai University of Finance and Economics, Shanghai 200433, China
[4] Department of Mechanical Engineering, School of Sciences and Engineering, The American University in Cairo, New Cairo 11835, Egypt
* Correspondence: yefang5905@126.com (F.Y.); mobadran@aucegypt.edu (M.B.)

Abstract: It is possible to optimize the yogurt and flavor filling process through a fully flexible machine that can accommodate different types of yogurt and flavors, allowing for rapid adjustment of filling parameters such as volume, speed, and feed rate. Previously, researchers focused on developing a yogurt filling machine and presented their findings across varied machine configurations. The contribution of this study comprises two key elements: configuring the machine to achieve full flexibility, wherein yogurt and any flavor can be filled at any designated filling station, and devising a novel mathematical model to optimize the newly configured machine settings. A real-life problem within the context of yogurt filling has been solved using the proposed model and results have been compared with the previously published models. It has been found that the proposed model for the fully flexible machine settings outperformed the previously published models, achieving a significant margin of improvement.

Keywords: combinatorial optimization; filling process optimization; makespan minimization; mathematical modelling; scheduling and sequencing; yogurt filling machine

1. Introduction

Optimizing the filling process of machines by customizing the machine settings allows the process to be optimized to achieve optimal results. In this approach, machine settings are adjusted to suit the specific needs of the product filling and the production line on which the machine operates. By utilizing fully flexible machine settings, manufacturers can improve the filling process's accuracy, efficiency, and consistency, leading to significant cost savings, minimizing the processing time and improved product quality. With machines capable of filling containers of different volumes, the machine's settings may be adjusted to ensure that each container is filled correctly and efficiently. As a result, there can be significant reductions in product waste, an increase in productivity, and an increase in profitability. Optimizing the filling process through fully flexible machine settings can enhance the efficiency and quality of the manufacturing process while reducing costs [1].

An objective of the parallel machine scheduling is to minimize the makespan or the time it takes to complete all jobs by simultaneously scheduling jobs on multiple identical machines. J. Lee et al. [2] worked on the makespan minimization of the parallel machine scheduling problem and to obtain optimal solutions, a mathematical model was presented. A NP-hard problem was considered. First, a feasible solution was obtained and the solution was then improved in a constructive way. A real problem from industry was considered to test the performance of the proposed algorithm and was found very efficient for most

practical cases. To minimize two objectives simultaneously, S. Wang et al. [3] considered a scheduling problem of identical parallel machines. The two objectives considered in the problem were the minimization of the makespan and the energy. The reasons for working on these objectives were that a minimum makespan results in high utilization of the machines and energy being the major portion of the total cost of the manufacturing company. The contributions of the research include the derivation of a bi-objective scheduling problem of identical parallel machines from a real-world manufacturing company, adaption of an augmented ε-constraint method and comparison and validation of the performance of the proposed method. D. Hu et al. [4] studied a scheduling problem on parallel machines and the problem formulated as a mixed-integer linear programming model with the objective to minimize the makespan. Two genetic algorithms were developed and their performances were then evaluated. While implementing genetic algorithm, the results showed that a greedy assignment scheme works better than a random assignment scheme. S. Ozpeynirci et al. [5] worked on the integration of scheduling and tool assignment problems through mixed-integer programming approach with the objective to minimize the makespan. A tabu search algorithm was developed for finding near-optimal solution in a reasonable computational time instead of NP-hard which requires extremely higher computational time with the increase in the problem size. E. Canakoglu et al. [6] proposed a new mathematical model for resource constrained parallel machine problem with additional covering constraints and with the objective to minimize makespan. The proposed methodology efficiently resulted in a high number of jobs as compared to the number of machines. The proposed tabu search algorithm resulted in a balanced workload distribution over the employees and attained low mean absolute deviation value.

A combinatorial optimization procedure seeks to find the best solution from a finite number of potential solutions. A set of constraints is typically described by a combinatorial structure optimized according to the objective function. A combinatorial optimization problem is finding the optimal combination of elements that optimizes the objective function. A comprehensive introduction to combinatorial optimization has been provided by B. Korte et al. [7], which discusses both the theoretical foundations and practical algorithms for solving optimization problems. A new crossover operator for genetic algorithms has been proposed by Arram et al. [8]. The operator is intended to improve the performance of genetic algorithms in the context of combinatorial optimization. Using graph-based neural networks and combinatorial optimization, Gannouni et al. [9] developed a novel approach to production scheduling. Using a real-world production scheduling problem, the method's performance was assessed. Compared with traditional scheduling methods, the proposed approach significantly reduces setup waste and generates feasible schedules that meet production requirements. Penna et al. [10] proposed modeling the timetable scheduling problem with job shop scheduling techniques. They explained how to formulate the problem as a job shop scheduling problem, where events and activities are considered jobs, and time slots and locations are considered machines. Job-shop scheduling was presented by El-Kholany et al. [11] as one of the most well-known combinatorial optimization problems, which involves the allocation of resources and sequencing of operations to minimize the makespan or time needed to complete the work. Several factors were highlighted, including the complexity of the problem and the necessity for effective problem-solving methods.

Several factors and variables must be considered to optimize the filling process, such as the type of container, product characteristics, filling equipment, packing procedures, and operational parameters that affect the process. A study by Kopanos et al. [12] highlighted the difficulty of production scheduling in food processing due to multiple product types, limited resources, processing time constraints, and interdependencies. It emphasized the need for mathematical models and algorithms. Wang et al. [13] proposed a mathematical model and a mixed-integer linear programming (MILP) formulation could be developed to achieve the shortest possible makespan about parallel-batching machines as well as non-identical job sizes. Chen et al. [14] presented an approach to optimize factor settings

in a pharmaceutical filling process, identifying the most critical factors and determining their optimal settings to optimize efficiency and quality. Based on the integrated nature of the problem, Ferreira et al. [15] investigated how to simultaneously determine the production quantity for different flavors of soft drinks and schedule production operations to meet customer demands while considering various constraints. Several optimization opportunities were identified and potential strategies were proposed by H. Wang et al. [16] for enhancing the performance of the system. It was concluded that automated drug-filling systems require modifications to their hardware, software, workflow, and operational procedures to be optimized.

As part of the operations management and production planning, scheduling and sequencing are closely related concepts. To maximize resource utilization, meet deadlines, and reduce workflow overhead, these activities aim to establish the order and timing of tasks or activities. Among the essential factors of efficient scheduling are reducing production costs and improving overall operational effectiveness, as highlighted by Strohhecker et al. [17]. Heuristics have been proposed for loading and sequencing to minimize the total completion time, each with algorithmic logic and decision rules. In a complex environment such as an industrial setting, G. Da Col et al. [18] acknowledged that job shop scheduling is a complex problem that must be addressed to maximize resource utilization, minimize job completion times, and increase productivity. Baldo et al. [19] presented an optimization approach for scheduling problems. They developed a mathematical model that incorporated the various constraints and objectives of the brewery industry, including production capacity, variations in demand, and storage constraints. As demonstrated by the experimental results, the optimization approach effectively solved the brewery industry's lot sizing and scheduling problems. Basso et al. [20] formulated and solved the bottling scheduling problem in the wine industry heuristically. It was believed that the findings contributed to improving scheduling processes, resource utilization, and operational efficiency in the wine industry. A scheduling model was proposed by Niaki et al. [21] to optimize the production process and improve resource utilization in the yogurt industry to minimize production time, maximize resource utilization, and accurately deliver products promptly.

In the mathematical modelling for process optimization, S. Rezig et al. [22] proposed a new approach and the contribution includes linear optimization mathematical model for production planning and to show the importance of the mathematical models for industrial issues. To express the effectiveness of the proposed model, a problem was solved and the results were presented. Toledo et al. [23] proposed a mixed-integer linear programming model for the description of an industrial problem relevant to soft drinks. An integrated solution approach was presented as the decisions made in one stage had consequences on another stage of the problem. Using CPLEX software (v. 20.1.0), the goal was to obtain the optimal solutions within one hour of running the problem on the computer. P. Kumar et al. [24] worked on the optimization and the performance analysis of soft drink bottle filling system using the Particle Swarm Optimization (PSO) technique. Equations were derived and different effects were studied. The performance was optimized using the PSO technique when the results were discussed with managers of the plant. For the minimization of the total weighted number of tardy jobs, S. Guo et al. [25], presented job scheduling with different weights on a single machine. The problem aimed at finding a feasible schedule. A real-life problem of lot sizing and production scheduling in the beverage industry was presented by M. Samouilidou et al. [26], where the production facility considered was identified as multistage and multiproduct. The objective was to generate an optimal production schedule which can satisfy a demand. The results showed that the optimal schedule leaded to better productivity of the plant and reduced the utilization and cost on the resources of labors.

Under the "Vision 2023" program of the Kingdom of Saudi Arabia, efforts have been started for many years for the digital transformation of all sectors of the country. To compete with global challenges, it was essential to renovate and standardize manufacturing and production industries. To upgrade the Industry 4.0 knowledge of the students, B.

Salah et al. [27] worked on the learning methodology of the students at the University. The proposed methodology translated the potential of the students from theoretical to applied side. It was expected to induce a robust curriculum consisting of mechatronics and digitalized instrumentation relevant to Industry 4.0. The students were involved in different activities relevant to Industry 4.0 including 3D printing and familiarity with different components of the yogurt filling machine. It can be noted that many components were fixed in the yogurt filling machine, the filling process was performed but it was not an optimized filling process. There was a need to make a mathematical model and the filling process be optimized. B. Salah et al. [28] made changes in the settings of the yogurt filling machine and the filling of yogurt and all three flavors was performed at two different points. A mathematical model was developed with the objective of minimizing the filling time or maximizing the speed of the conveyor belt subject to constraints on the maximum allowable speed of the conveyor belt and feed rates of the filling nozzles. A real-life problem was solved and optimized results were achieved. The results were then used in the one-dimensional rules to find a rule which is better than the other ones. J. Chen et al. [29] modified the machine settings and proposed the filling of yogurt and flavors from a single point. The mathematical model was slightly modified and the simultaneous filling resulted in reduced filling time when the same earlier presented problem was solved through the proposed model. The results of the model were used as input in the one-dimensional rules. The results also showed that the model in [29] is 1.05-fold faster than the model presented in [28]. Y. Cui et al. [30] further modified the machine settings and proposed dedicated filling points for each of the three flavors. Due to dedicated filling points, it was not possible to mix more than one flavor with yogurt as customer may demand. The objective function of the model in [30] was similar to that of [29]; however, the constraints were slightly different from the earlier presented models. The same problem considered in [28,29] was solved using the modified model for dedicated filling points for each flavor, resulted in 2.55- and 2.41-fold faster than the models presented in [28,29], respectively. B. Salah et al. [31] combined several concepts of Industry 4.0 and proposed a control system for system improvement and remodeling of the yogurt filling machine. A new controller called Raspberry Pi 4 Model B (Raspberry Pi Trading Ltd., Cambridge, UK) was added in the system for controlling the NFC signal. For the purpose of minimizing the human intervention, the concepts of Industry 4.0 were implemented throughout the yogurt filling machine successfully.

The existing machine in Case I [28] was filling yogurt and flavors at two different points, and the filling times of yogurt and flavors were considered equal. Due to the filling at two distinct points, there was a possibility of filling the yogurt and flavors at a single point and reducing the processing time further. Hence, Case II [29] was presented, and yogurt and flavors were filled under a unified head nozzle. The limitations of Case II [29] include the non-simultaneous filling of flavors into different cups. As customers can order assorted flavors mixed with yogurt and further reduce their waiting time, Case III [30] was introduced, with dedicated filling points for the other flavors. Case III [30] made filling the yogurt and flavors possible simultaneously, minimizing the processing time.

In this research article, the settings of the yogurt filling machine are further modified, where the yogurt and all three flavors can be filled at any of the three filling points. Through the machine settings, it was possible to fill the yogurt and any of the three flavors from any filling point in the machine and hence the system is made fully flexible. A new mathematical model has been presented with the objective to minimize the filling time subject to constraints relevant to the speed of the conveyor belt, the yogurt and flavor filling times and the idle times of yogurt and flavor filling nozzles. A real-life problem has been solved to test the model considering the customer order dependent and independent variables. It has been found that the new model produced better results than the previously published models for the yogurt filling machine.

The different sections in this article are as follows. Section 1 presents the introduction and brief literature survey of fully flexible machines, parallel machine scheduling,

combinatorial optimization, filling process optimization, sequencing and scheduling, and yogurt filling machines. In contrast, Section 2 provides the problem description. The proposed mathematical model for the fully flexible parallel machines is explained in Section 3, whereas Section 4 illustrates the solution procedure by providing an example. The results and discussion appear in Section 5; the conclusion and further recommendations are written in Section 6.

2. Problem Description

To address the limitations of the existing yogurt filling machines regarding flexibility and efficiency, the newly developed system can ideally switch between multiple flavors, production volumes, and packaging sizes while maintaining a higher level of productivity. Figure 1a illustrates the unified head containing four filling nozzles, which fill predetermined volumes of base yogurt and three different flavors into the cups. The cups, initially empty, are positioned at the entry point and subsequently moved to the filling area employing a conveyor belt. Once the filling process is completed, the cups are directed to the exit point, where a robotic arm removes them from the system. Figure 1b illustrates the rear view of the machine, highlighting a panel attached with sensors, switches, and buttons. At the same time, the diaphragm pumps are engaged to facilitate the transfer of yogurt and flavors from the tanks to the filling nozzles.

(**a**) (**b**)

Figure 1. The automatic yogurt filling machine: (**a**) the The front view of the machine with a unified head nozzle and conveyor belt and (**b**) the The control panel, filling tanks, and pumps of the machine. Source: B. Salah et al. [28].

The main components used in the fully flexible yogurt filling machine are yogurt and flavor filling nozzles, conveyor belt, filling point allocation system, cup detection and orientation system, flavor and yogurt supply system, automated cleaning and sanitizing system, Human–Machine Interface (HMI), Industry 4.0 technologies, quality control system, Raspberry Pi 4 Model B Controller and NFC Signal.

The machine settings were changed, and the system was fully flexible to reduce the processing time further. The complete flexibility of the machine can be achieved by fixing three unified heads working in parallel at various positions. Figure 2 shows three machines that can fill any flavor at any time. The empty cups are loaded on the conveyor belt and moved towards the filling points. Two conveyor belts work under each unified head, with two nozzles in each. The stationary conveyor belt is represented by zero, while the belt in motion is represented by 1. The unified head relates to all tanks of assorted flavors and yogurt through small pipes where large volumes of flavors and yogurt are available to fill the cups with the required quantities. The cups then move towards the exit point, where a robotic arm is used to remove them from the system.

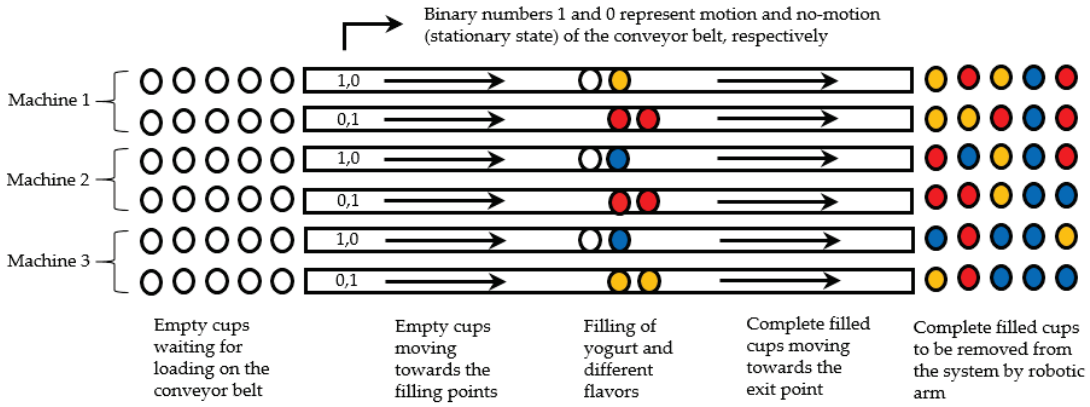

Figure 2. Three fully flexible parallel unified heads with two conveyor belts for each head in the system fill the required volumes of yogurt and flavors in cups.

The limitations of the b. Salah et al. [28] model include limited flexibility, inefficient use of resources and lack of optimization, while the limitations of the j. Chen et al. [29] model consist of limited simultaneous filling, inability to handle assorted flavors and limited flexibility, whereas the limitations of the y. Cui et al. [30] model comprise dedicated filling points, inability to mix flavors, limited scalability. The current proposed model overcomes these limitations by allowing filling of yogurt and any flavor at any of the three filling points, enabling simultaneous filling of yogurt and multiple flavors, optimizing filling time and conveyor belt speed, adapting to changing customer demands and assorted flavor requests and working in parallel to fill the cups with required volumes.

The fully flexible yogurt filling machine has been designed as an innovative equipment to streamline the yogurt and flavor filling process. This system consists of three unified heads, each equipped with two nozzles, enhancing flexibility and efficiency. The machine is designed to simultaneously manage various yogurt filling requirements due to the integration of multiple heads and nozzles. As given in Table 1, all combinations allow operators to access the information quickly and efficiently they need and determine which combinations are possible. This reduces the time they need to spend thinking and makes it easier to find the desired combination.

Table 1. All flavors and yogurt filling combinations through three unified heads (Head-I, II, and III), each with two nozzles (N-I and N-II).

Yogurt	Blueberry						Strawberry						Mango					
	Head-I		Head-II		Head-III		Head-I		Head-II		Head-III		Head-I		Head-II		Head-III	
	N-I	N-II	N-I	N-II	N-I	N-II	N-I	N-II	N-I	N-II	N-I	N-II	N-I	N-II	N-I	N-II	N-I	N-II
1	0	0	0	0	0	0	0	0	0	0	0	0	0	0	0	0	0	0
	0	0	0	0	0	0	0	0	0	0	0	0	0	0	0	0	0	0
	1	0	0	0	0	0	1	0	0	0	0	0	1	0	0	0	0	0
	0	1	0	0	0	0	0	1	0	0	0	0	0	1	0	0	0	0
	0	0	1	0	0	0	0	0	1	0	0	0	0	0	1	0	0	0
	0	0	0	1	0	0	0	0	0	1	0	0	0	0	0	1	0	0
	1	0	1	0	0	0	1	0	1	0	0	0	1	0	1	0	0	0
	0	1	0	1	0	0	0	1	0	1	0	0	0	1	0	1	0	0
	0	0	0	0	1	0	0	0	0	0	1	0	0	0	0	0	1	0
	0	0	0	0	0	1	0	0	0	0	0	1	0	0	0	0	0	1
	1	0	0	0	1	0	1	0	0	0	1	0	1	0	0	0	1	0
	0	1	0	0	0	1	0	1	0	0	0	1	0	1	0	0	0	1
	0	0	1	0	1	0	0	0	1	0	1	0	0	0	1	0	1	0

Table 1. *Cont.*

Yogurt	Blueberry						Strawberry						Mango					
	Head-I		Head-II		Head-III		Head-I		Head-II		Head-III		Head-I		Head-II		Head-III	
	N-I	N-II	N-I	N-II	N-I	N-II	N-I	N-II	N-I	N-II	N-I	N-II	N-I	N-II	N-I	N-II	N-I	N-II
1	0	0	0	1	0	1	0	0	0	1	0	1	0	0	0	1	0	1
	1	0	1	0	1	0	1	0	1	0	1	0	1	0	1	0	1	0
	0	1	0	1	0	1	0	1	0	1	0	1	0	1	0	1	0	1

Several advantages are associated with fully flexible yogurt filling machines, making them a desirable possibility for mixing yogurt with assorted flavors. Some benefits of using a fully flexible yogurt filling machine include improved flexibility, product variety, customization, efficiency and productivity, cost savings, and adaptability to market trends. Automation also reduces the risk of human error and increases efficiency, leading to lower production costs.

There are few benefits of the proposed machine settings. The economic benefits include increased efficiency and improved productivity while the operational benefits include flexibility and reduced idle time. Similarly, the maintenance benefits include reduced downtime, extended equipment life, simplified maintenance and reduced energy consumption. Few other benefits are improved customer satisfaction and competitive advantage in the market.

The use of fully flexible yogurt filling machines has many advantages, but they also have certain limitations. Some limitations are that they are more expensive than traditional filling machines, are complex to operate and maintain, require appropriate training and expertise from the operator, have increased maintenance requirements, had compatibility issues, and require floor space.

3. Mathematical Modelling

Considering the primary goal of minimizing the makespan of the system while deciding the optimal allocation of all jobs to the available machines, a linear programming model has been developed. A variety of constraints and equations have been taken into consideration in the development of the model. The model formulation has several essential components, including indices, parameters, and decision variables. The linear programming model allows for the planning and allocating jobs to machines based on constraints and equations. Together, these elements form the foundation for adequate scheduling and allocation of jobs.

The mathematical modeling process is divided into two stages. A model for the filling speed of conveyor belts, filling time, idle time and job processing time is developed in the first stage. The purpose of this stage is to represent and analyze the dynamics of the filling process in as much detail as possible. In the second stage, the model is intended to address the problem of parallel machines to identify and explain the optimal combinations of filling times for different types of orders. Formulating and solving the second stage allows the model to determine the most efficient schedule and allocation of resources, ultimately improving the efficiency of the filling system.

Stage I

Indices

a	volume of yogurt	$a \in A$
b	yogurt type	$b \in B$
c	volume of flavor	$c \in C$
d	flavor type	$d \in D$
e	total volume of yogurt and flavor(s)	$e \in E$
f	filling machine in the system	$f \in F$
g	belt number in a machine	$g \in G$
h	different types of total volumes	$h \in H$

i	number of machines	$i \in I$
j	number of jobs	$j \in J$

Parameters

L_t	total length centimeter (cm)
l	half of the total length of the conveyor belt centimeter (cm)
V_{abcde}	yogurt volume in the total volume of a cup milliliter (mL)
v_{abcde}	flavor volume in the total volume of a cup milliliter (mL)
$S_{\max}$	conveyor belt maximum allowable speed centimeter per second (cm/s)
P_j	processing time of job j on any machine second (s)
P_{ij}	processing time of job j on machine i second (s)
C_i	completion time of a set of jobs on machine i second (s)
$C_{\max}$	maximum completion time of a set of jobs assigned to any machine second (s)
m_{fg}	binary number used for stationary and moving states of the conveyer belts unit less
T_b	yogurt nozzle idle time second (s)
T_d	flavor nozzle idle time second (s)
t_b	filling time of yogurt second (s)
t_d	filling time of flavor second (s)
S_a	actual speed of the belt centimeter per second (cm/s)
S_c	calculated speed of the belt centimeter per second (cm/s)
C	a number used in filling time calculations, where $MinP_j \leq C \leq \sum_{j=1}^{J} P_j$ second (s)

Decision and Resulting Variables

X_{ij}	1 if machine i is used to process job j, or else 0 unit less
δ_{abcde}	yogurt valve feed rate milliliter per second (mL/s)
α_{abcde}	strawberry flavor valve feed rate milliliter per second (mL/s)
β_{abcde}	blueberry flavor valve feed rate milliliter per second (mL/s)
γ_{abcde}	mango flavor valve feed rate milliliter per second (mL/s)

The following are few equations used in the mathematical calculations of the yogurt filling process.

$$S_a = \min\left\{\min\left(l\frac{\delta_{abcde}}{V_{abcde}}, l\frac{\alpha_{abcde}}{v_{abcde}}, l\frac{\beta_{abcde}}{v_{abcde}}, l\frac{\gamma_{abcde}}{v_{abcde}}\right), S_{\max}\right\} \; a \in A, b \in B, c \in C, d \in D, e \in E \tag{1}$$

$$t_\delta = \frac{V_{abcde}}{\delta_{abcde}} \; a \in A, b \in B, c \in C, d \in D, e \in E \tag{2}$$

$$t_\alpha = \frac{v_{abcde}}{\alpha_{abcde}} \; a \in A, b \in B, c \in C, d \in D, e \in E \tag{3}$$

$$t_\beta = \frac{v_{abcde}}{\beta_{abcde}} \; a \in A, b \in B, c \in C, d \in D, e \in E \tag{4}$$

$$t_\gamma = \frac{v_{abcde}}{\gamma_{abcde}} \; a \in A, b \in B, c \in C, d \in D, e \in E \tag{5}$$

$$S_c = \frac{l}{t_\delta} \tag{6}$$

$$T_\delta = \frac{l}{S_{\max}} - \frac{l}{S_c} \text{ if } \frac{l}{S_{\max}} - \frac{l}{S_c} > 0 \text{ otherwise } 0 \tag{7}$$

$$T_\alpha = \max(t_\delta, t_\alpha, t_\beta, t_\gamma) - t_\alpha \tag{8}$$

$$T_\beta = \max(t_\delta, t_\alpha, t_\beta, t_\gamma) - t_\beta \tag{9}$$

$$T_\gamma = \max(t_\delta, t_\alpha, t_\beta, t_\gamma) - t_\gamma \tag{10}$$

$$\sum_{f=1}^{F} m_{fg} = 1 \; g \in G \tag{11}$$

$$\sum_{f=1}^{F}\sum_{g=1}^{G} m_{fg} = 3 \tag{12}$$

$$P_j = \frac{V_{abcde}}{\delta_{abcde}}, \frac{v_{abcde}}{\alpha_{abcde}}, \frac{v_{abcde}}{\beta_{abcde}}, \frac{v_{abcde}}{\gamma_{abcde}}\ a \in A, b \in B, c \in C, d \in D, e \in E \tag{13}$$

Equation (1) is used to find the actual speed of the conveyor belt while Equations (2)–(5) are utilized to find the filling time of the required volumes of yogurt, flavor 1, flavor 2 and flavor 3, respectively. Equation (6) is used to find the calculated speed of the conveyer belt whereas Equations (7)–(10) calculate the idle times of the yogurt, flavor 1, flavor 2 and flavor 3 nozzles, respectively. Equation (11) states that one out of the two belts in a fully flexible machine should be in motion while Equation (12) enforces that three out of the six belts in the system must be in motion at any time during the filling process. Equation (13) finds the filling times of yogurt and flavors of any order.

In Stage II, the model is used to optimize the filling process. The solution of the model results in optimal values of the filling times for each order.

Stage II

$$\textbf{Minimize: } Z = C - \sum_{a=1}^{A}\sum_{b=1}^{B}\sum_{c=1}^{C}\sum_{d=1}^{D}\sum_{e=1}^{E}\left(\frac{V_{abcde}}{\delta_{abcde}} + \frac{v_{abcde}}{\alpha_{abcde}} + \frac{v_{abcde}}{\beta_{abcde}} + \frac{v_{abcde}}{\gamma_{abcde}}\right) \tag{14}$$

Subject to the following constraints and equations:

$$\sum_{j=1}^{J} P_j D_j X_{ij} \leq C\ i \in I \tag{15}$$

$$\sum_{i=1}^{I} X_{ij} = 1\ j \in J \tag{16}$$

$$X_{ij} \in \{0,1\}\ i \in I,\ j \in J \tag{17}$$

$$C_i = \sum_{j=1}^{J} P_j D_j X_{ij}\ i \in I \tag{18}$$

$$C_{\max} = \max_{i=1}^{I} C_i \tag{19}$$

$$\delta_{abcde} \leq Maximum\ \delta_{abcde}\ a \in A, b \in B, c \in C, d \in D, e \in E \tag{20}$$

$$\alpha_{abcde} \leq Maximum\ \alpha_{abcde}\ a \in A, b \in B, c \in C, d \in D, e \in E \tag{21}$$

$$\beta_{abcde} \leq Maximum\ \beta_{abcde}\ a \in A, b \in B, c \in C, d \in D, e \in E \tag{22}$$

$$\gamma_{abcde} \leq Maximum\ \gamma_{abcde}\ a \in A, b \in B, c \in C, d \in D, e \in E \tag{23}$$

$$\frac{l}{S_a} - \frac{V_{abcde}}{\delta_{abcde}} \geq 0\ a \in A, b \in B, c \in C, d \in D, e \in E \tag{24}$$

$$\frac{l}{S_a} - \frac{v_{abcde}}{\alpha_{abcde}} \geq 0\ a \in A, b \in B, c \in C, d \in D, e \in E \tag{25}$$

$$\frac{l}{S_a} - \frac{v_{abcde}}{\beta_{abcde}} \geq 0\ a \in A, b \in B, c \in C, d \in D, e \in E \tag{26}$$

$$\frac{l}{S_a} - \frac{v_{abcde}}{\gamma_{abcde}} \geq 0\ a \in A, b \in B, c \in C, d \in D, e \in E \tag{27}$$

The objective function 14 linked with all constraints and equations of the model is used to minimize the processing and filling times of the cups assigned to different filling stations of the system. Constraint 15 states that the processing time of the jobs assigned to any machine in the system should be less than or equal to the total completion time. Equation (16) states that a job must be assigned to any of the machines in the system for filling while Equation (17) is used for binary restrictions. Equation (18) states that the processing time on any machine is equal to the summation of the filling times of the jobs

assigned to that machine. Equation (19) shows that the makespan is equal to the maximum value of the processing times of any of the available machines used in the filling of the yogurt and flavors. Inequalities (20)–(23) restrict the feed rates to be less than or equal to the maximum allowable values of the feed rates of yogurt, flavor 1, flavor 2 and flavor 3, respectively. Inequalities (23)–(26) states that either the filling times of yogurt, flavor 1, flavor 2 and flavor 3 are equal or less than to the time in which an empty cup reaches the filling point from the entry point or a completely filled cup moves from the filling point to the exit point, respectively.

Using a linear programming model, the machine can be programmed to optimize the filling process, allowing it to allocate resources more efficiently, reduce the total time it takes to fill the cups and make better decisions in real time based on changes in demand or other factors. Furthermore, the model can be adapted to changing conditions, allowing it to ensure optimal performance. The cups can be filled with exact quantities of yogurt and flavors using automated filling machines in a much shorter time.

4. Solution Procedure

Once the set of orders from customers is received, various quantities of yogurt and flavors are combined in a cup. Typically, the yogurt content outweighs the flavor(s) by a significant margin. In this case, a minimum of 75% of yogurt can be ordered in a cup and a maximum of 25% of any flavor or combination of flavors can be ordered in a cup. Ensuring the total volume falls within the permissible upper and lower limits is essential. The upper limit of total volume of a cup is 1500 mL while the minimum limit of total volume is 250 mL. Table 2 illustrates the demand of customers for 18 total volumes of yogurt and flavors, including the respective yogurt and flavor percentages. Notably, previous studies only involved a single flavor mixed with the yogurt, whereas the current model allows for combining multiple flavors and thus the system is fully flexible. The last column of Table 2 shows the number of cups required in each order. Flavor I, II, and III are used to represent blueberry, strawberry, and mango flavors, respectively.

Table 2. Orders for yogurt mixed with flavors and the percentages of yogurt and flavors.

Order No.	Total Volume of Cup (mL)	Percentage of Yogurt and Flavor(s) in the Total Volume of Cup (%)				Number of Cups
		Yogurt	Flavor I	Flavor II	Flavor III	
1	1500	75	10	10	5	5
2	1500	80	0	10	10	9
3	1500	85	10	5	0	10
4	1250	85	15	0	0	10
5	1250	90	0	10	0	5
6	1250	95	0	0	5	10
7	1000	80	10	0	10	5
8	1000	85	0	10	5	8
9	1000	90	10	0	0	10
10	750	75	10	5	10	8
11	750	80	10	0	10	8
12	750	85	10	0	5	11
13	500	85	0	5	10	7
14	500	90	5	5	0	10
15	500	95	0	5	0	12
16	250	80	10	0	10	20
17	250	85	0	10	5	17
18	250	90	5	5	0	35

Table 2 provides the parameters influenced by customer orders. In contrast, Table 3 displays the parameters independent of customer orders. Considering the values of these parameters resolves the problem, leading to an optimal solution.

Table 3. Customer order independent parameters.

S. No.	Parameter	Value	Unit
1	Conveyor belt maximum allowable speed	10	cm/s
2	Conveyor belt total length	50	cm
3	Maximum volume that a customer can order in a single cup	1500	mL
4	Minimum volume that a customer can order in a single cup	250	mL
5	Volume of yogurt container	300	L
6	Volume of the containers of flavors	75	L
7	Yogurt valve maximum feed rate	100	mL/s
8	Flavor valve maximum feed rate	33.34	mL/s

The LP problem was solved using the LP_Solve tool (v. 5.5.2.5), employing a computer with a Core i7 processor running at 1.99 GHz. The computations were conducted within a reasonable time, yielding the desired results. LP_Solve, a solver tool for MILP, was utilized for this purpose. The speed of the conveyor belt and the feed rates of the yogurt and flavor valves are directly interconnected. Table 4 shows how the model optimizes the conveyor belt speed to maximize the feed rates, resulting in the highest possible values. The speed of the belt relies on the feed rates and consistently remains below the maximum allowable limit. Consequently, the calculated conveyor belt speed is essential in filling. Typically, the flavor percentages are lower than the yogurt percentage in the total volume required, causing the flavors to be filled before the yogurt. This leads to idle time for the flavor nozzles while waiting to fill the subsequent cup. On the other hand, the yogurt valves operate at full capacity mostly without any idle time. The idle time of yogurt value occurs when a cup is filled earlier than the arrival of next cup to the filling point. This happens in case when the calculated speed exceeds the maximum allowable speed of the conveyer belt. The processing times for the entire order quantity of cups are provided in the last column of Table 4.

Table 4. The solution of the proposed model, the values of the decision variables, the filling times of different nozzles and the processing time of cups.

Order No.	Feed Rate (mL/s)				Filling Time of Nozzle (s)				Processing Time (s)
	δ_{abcde}	α_{abcde}	β_{abcde}	γ_{abcde}	Yogurt	Flavor I	Flavor II	Flavor III	
1	100	33.34	33.34	33.34	11.25	4.50	4.50	2.25	11.25
2	100	0	33.34	33.34	12.00	0.00	4.50	4.50	12.00
3	100	33.34	33.34	0	12.75	4.50	2.25	0.00	12.75
4	100	33.34	0	0	10.63	5.62	0.00	0.00	10.63
5	100	0	33.34	0	11.25	0.00	3.75	0.00	11.25
6	100	0	0	33.34	11.88	0.00	0.00	1.87	11.88
7	100	33.34	0	33.34	8.00	3.00	0.00	3.00	8.00
8	100	0	33.34	33.34	8.50	0.00	3.00	1.50	8.50
9	100	33.34	0	0	9.00	3.00	0.00	0.00	9.00
10	100	33.34	33.34	33.34	5.63	2.25	1.12	2.25	5.63
11	100	33.34	0	33.34	6.00	2.25	0.00	2.25	6.00
12	100	33.34	0	33.34	6.38	2.25	0.00	1.12	6.38

Table 4. *Cont.*

Order No.	Feed Rate (mL/s)				Filling Time of Nozzle (s)				Processing Time (s)
	δ_{abcde}	α_{abcde}	β_{abcde}	γ_{abcde}	Yogurt	Flavor I	Flavor II	Flavor III	
13	100	0	33.34	33.34	4.25	0.00	0.75	1.50	4.25
14	100	33.34	33.34	0	4.50	0.75	0.75	0.00	4.50
15	100	0	33.34	0	4.75	0.00	0.75	0.00	4.75
16	100	33.34	0	33.34	2.00	0.75	0.00	0.75	2.00
17	100	0	33.34	33.34	2.13	0.00	0.75	0.37	2.13
18	100	33.34	33.34	0	2.25	0.37	0.37	0.00	2.25

The speed of the conveyor belt is inversely proportional to the volume of yogurt and flavor(s) in a cup. For large volumes, the speed of the belt is small where for small volumes, the speed of the belt increases. As can be seen in Table 5, the calculated speed increases as the volume decreases. The speed of the belt can be increased till the maximum allowable limit which is 10 cm/s. The actual speed is equal to the maximum speed of the belt in case when the calculated speed is exceeding the maximum allowable speed. There is no idle time of yogurt nozzle when the speed of the belt is less than the maximum speed limit. When the speed of the belt is less than the maximum limit, an empty cup reaches in a time equal to the filling time of the cup under the nozzle. When the speed of the belt exceeds 10 cm/s, an empty cup reaches in a time more than the filling time of the cup under the nozzle and thus the yogurt nozzle remains idle till the empty cup reaches under the nozzle. The volume of flavor is very less than the yogurt volume, and the flavor is normally filled earlier than the yogurt, thus once the required volume of flavor is filled then the flavor nozzle remains idle till the next cup reaches for filling.

Table 5. The calculated, maximum allowable and actual speed of the conveyor belt and the idle times yogurt and flavor nozzles.

Order No.	Speed of the Conveyor Belt (cm/s)			Idle Time of Yogurt and Flavors Nozzles (s)			
	S_c	S_{max}	S_a	Yogurt	Flavor I	Flavor II	Flavor III
1	4.44	10	4.44	0.00	6.75	6.75	9.00
2	4.17	10	4.17	0.00	12.00	7.50	7.50
3	3.92	10	3.92	0.00	8.25	10.50	12.75
4	4.71	10	4.71	0.00	5.00	10.63	10.63
5	4.44	10	4.44	0.00	11.25	7.50	11.25
6	4.21	10	4.21	0.00	11.88	11.88	10.00
7	6.25	10	6.25	0.00	5.00	8.00	5.00
8	5.88	10	5.88	0.00	8.50	5.50	7.00
9	5.56	10	5.56	0.00	6.00	9.00	9.00
10	8.89	10	8.89	0.00	3.38	4.50	3.38
11	8.33	10	8.33	0.00	3.75	6.00	3.75
12	7.84	10	7.84	0.00	4.13	6.38	5.25
13	11.76	10	10.00	0.75	4.25	3.50	2.75
14	11.11	10	10.00	0.50	3.75	3.75	4.50
15	10.53	10	10.00	0.25	4.75	4.00	4.75
16	25.00	10	10.00	3.00	1.25	2.00	1.25
17	23.53	10	10.00	2.88	2.13	1.38	1.75
18	22.22	10	10.00	2.75	1.88	1.88	2.25

Since each machine is fully flexible, thus any ordered cup can be fulfilled using any of the available machines. In the parallel machine problem ($P_3||C_{max}$), it is essential to minimize customer waiting time and deliver the complete set of orders simultaneously by ensuring that the processing time combinations on the different available machines are almost similar. Figure 3 illustrates the processing of orders across the three available parallel working machines, resulting in the total processing times of machines 1, 2, and 3 as 417.000 s, 416.625 s, and 416.875 s, respectively. The total work content amounts to 1250.500 s on the three machines, with an average machine load of 416.833 s and a makespan value (C_{max}) of 417.000 s.

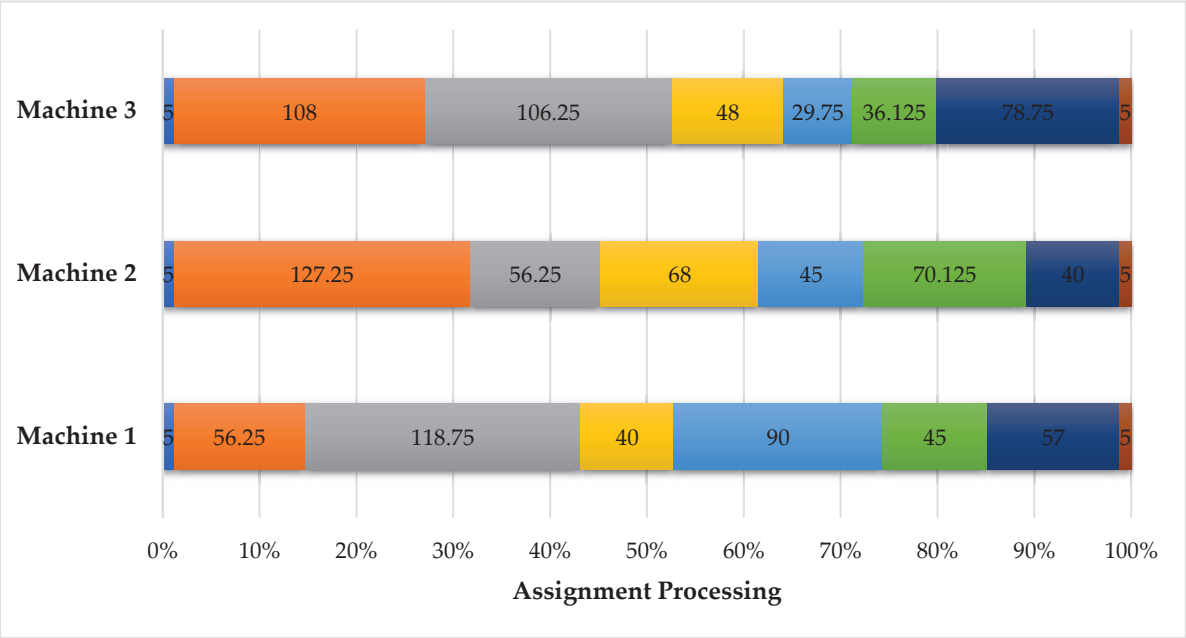

Figure 3. Gantt chart for optimal solution of $P_3||C_{max}$ problem; blue color is for "reaching the cup from entry to filling point"; Orange, Grey, Yellow, Sky Blue, Light Green, Dark Blue colors represent first, second, third, 4th, 5th, and 6th order processed on each machine, respectively. The last dark orange color represents "the time taken by the cup from filling to exit point".

At any machine, the first empty cup when reaches to the filling point, it takes 5 s to reach. As there is no filling started, the conveyor belt moves over the length of 50 cm of the belt with maximum allowable speed (10 cm/s). Similarly, when all cups are filled, the last cup moves with maximum speed to the leave the system. Equation (28) is used for this relation and 5 s at the start and end used at each machine.

$$P_{ij} = \frac{l}{S_{\max}} + \sum_{j=1}^{J} P_j + \frac{l}{S_{\max}} \; i \in I \tag{28}$$

5. Results and Discussion

In this section, two types of analysis have been performed. The first one is to change the feed rate of the yogurt valve from 100 mL/s, with an increment of 25 units, to 200 mL/s and check its impact on the yogurt filling time, the speed of the belt, the idle time of yogurt nozzle and the filling time of yogurt nozzle. In the second type of analysis, the processing times for similar orders of the proposed and previously published models are compared, and the differences among them are shown.

5.1. The Effect of Change in the Feed Rate of the Yogurt Valve on the Filling Time of Yogurt in a Cup, the Speed of the Conveyor Belt, the Idle Time of the Yogurt Nozzle and the Processing Time of an Order

For the analysis purpose, the feed rates of all nozzles of the flavors are kept at 100 mL/s, and the maximum speed of the conveyor belt is equal to 10 cm/s. The feed rates of yogurt valves are changed to find their impact on the yogurt filling time, the speed of the belt, the idle time of yogurt nozzle and the filling time of yogurt nozzle Also, the results of the proposed model are compared with those of the previously published models. Feed rates for each order are evaluated for the belt speed, which is precisely equal to its maximum permissible value and has no idle time for the yogurt valve in most cases.

The increase in the feed rates of yogurt nozzles decreases the filling time of yogurt. As depicted in Figure 4, the yogurt filling time is the largest for all orders when the feed rate of the nozzle is considered equal to 100 mL/s. The filling time decreases with the increase in the value of the yogurt feed rate and is the lowest when the feed rate of the nozzle reaches 200 mL/s. For large volumes, the change in the yogurt filling time per 25 mL/s change in yogurt feed rate is higher when compared to smaller demanded volumes of yogurt, and vice versa.

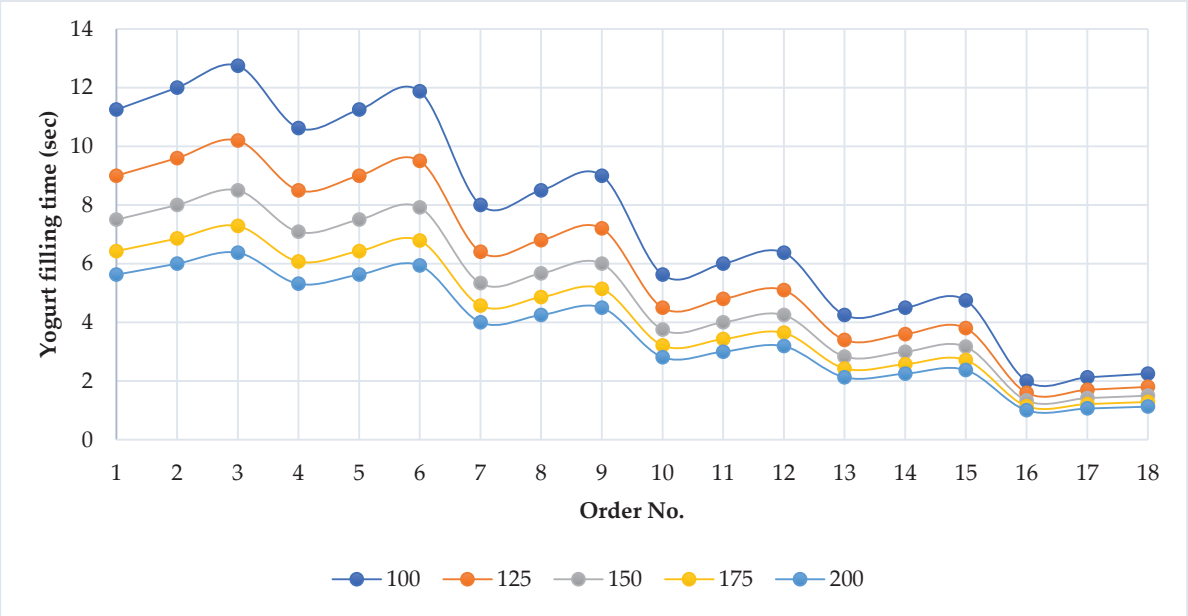

Figure 4. The impact of the feed rate of yogurt nozzle on the filling time of yogurt in a cup.

The increase in the feed rates of yogurt nozzles increases the speed of the conveyor belt. As shown in Figure 5, the speed of the conveyor belt is slowest when the feed rate of the nozzle is considered equal to 100 mL/s. The speed increases with the increase in the value of the yogurt feed rate and is the fastest for all orders when the feed rate of the nozzle reaches 200 mL/s. For large volumes, the change in the yogurt filling time per 25 mL/s change in yogurt feed rate is minor when compared to smaller demanded volumes of yogurt, and vice versa. For small required volumes, the change in the speed of the conveyor belt is higher than the large volumes in the set of orders. It can be noted that, in this analysis, the maximum allowable speed of the belt is not considered and the speed exceeds the limit.

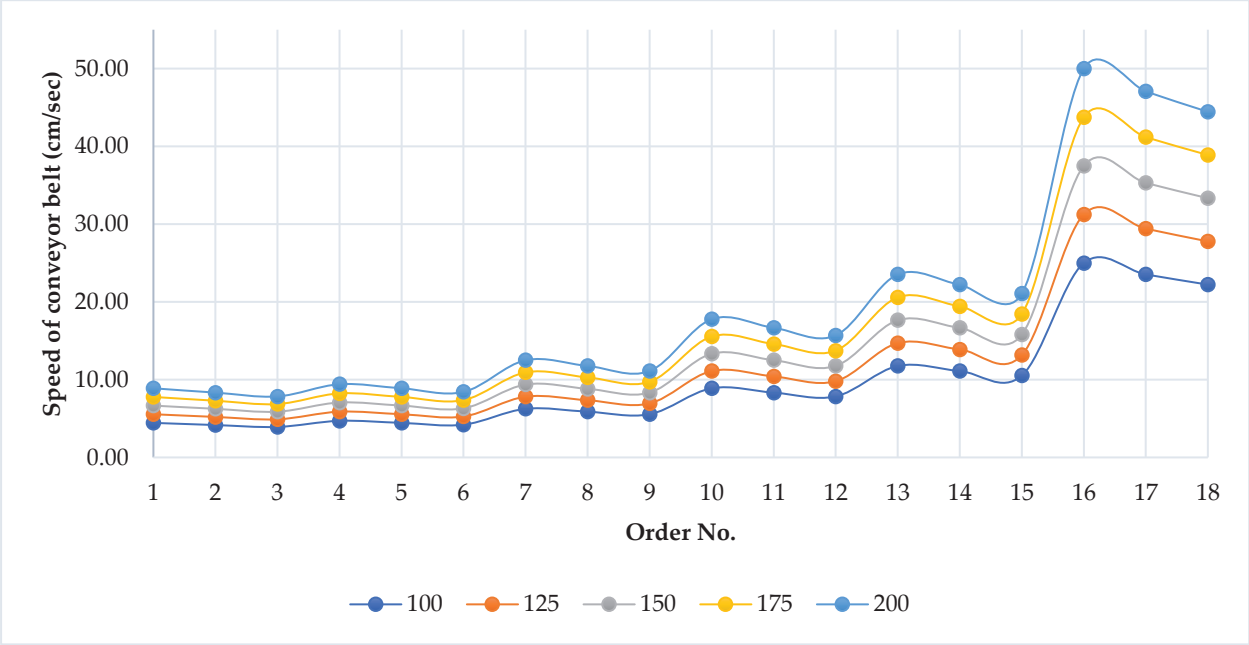

Figure 5. The impact of the yogurt nozzle's feed rate on the speed of the conveyor belt when upper limit of the speed (10 cm/s) is not considered.

In Figure 6, the upper limit of the speed of the belt is considered equal to 10 cm/s. The speed of the belt is lowest for feed rate equal to 100 mL/s. As the feed rate is increased by 25 units till 200 mL/s, the speed of the belt increases. For small volumes, the calculated speed may increase the upper limit, but is actually kept at 10 cm/s during the filling processing. When the calculated speed is more than 10 cm/s and the belt is actually run at 10 cm/s, the cup under filling is filled earlier at 100 mL/s than the next empty cup reaches to the filling point. During this time, the yogurt nozzle remains idle and waits for the empty cup to reach to the filling point.

Figure 6. The impact of the yogurt nozzle's feed rate on the speed of the conveyor belt when upper limit of the speed (10 cm/s) is considered.

Keeping the maximum speed of the conveyor belt at 10 cm/s, the required amount of yogurt is filled in the cup through the yogurt nozzle. For most of the orders, the speed of the conveyor belt is less than or equal to the maximum allowable limit. However, in many

cases, the speed of the conveyor belts exceeds the allowable limit for different values of the feed rates, as shown in Figure 7.

Figure 7. The impact of the yogurt nozzle's feed rate on its idle time.

For a 100 mL/s feed rate, the speed of the belt is less than or equal to 10 cm/s for the orders starting from 1 to 12. These are orders of higher volumes of yogurt than orders starting from 13 to 20. As the volumes of the orders 13–20 decreases, the speed of the belt exceeds 10 cm/s but is kept at 10 cm/s. Due to keeping the speed of the belt at 10 cm/s and the feed rate of yogurt nozzle at 100 mL/s, the cup is filled earlier than the arrival of the empty cup to the filling point and hence the yogurt nozzle waits for the arrival of empty cup and remains idle. It can be noted that for large volumes of yogurt, the filling time is more and thus the speed of the belt is slow and vice versa.

As the speed of the belt is equal to half of the length of belt divided by the time in which an empty cup reaches to the filling point from entry point or reaches to exit point from filling point. This time is normally equal to the filling time of the cup. Where the calculated speed exceeds 10 cm/s and the conveyor belt is run at 10 cm/s, this time is greater than the filling time of the cup. The filling time can be represented by the relationship given in Inequality (29) as follows.

$$\text{Filling time} \geq \frac{l}{S_a} \tag{29}$$

The relationship given in Inequality (29) can be used when the speed of the conveyor belt is less than or equal to the maximum allowable limit (10 cm/s). In case when the actual speed of the conveyor belt is equal to 10 cm/s, i.e., the conveyor belt is run at 10 cm/s, the relationship given in the Equation (30) are used.

$$\text{Filling time} + \text{idle time} = \frac{l}{S_{\max}} \tag{30}$$

As can be seen in Figure 8, for orders with the calculated speed of the belt less than 10 cm/s, the filling time is more than 5 s, while for orders with a calculated speed greater than or equal to 10 cm/s and when the belt is actually run at 10 cm/s, the sum of the filling and idles times of the yogurt nozzle is exactly equal to 5 s.

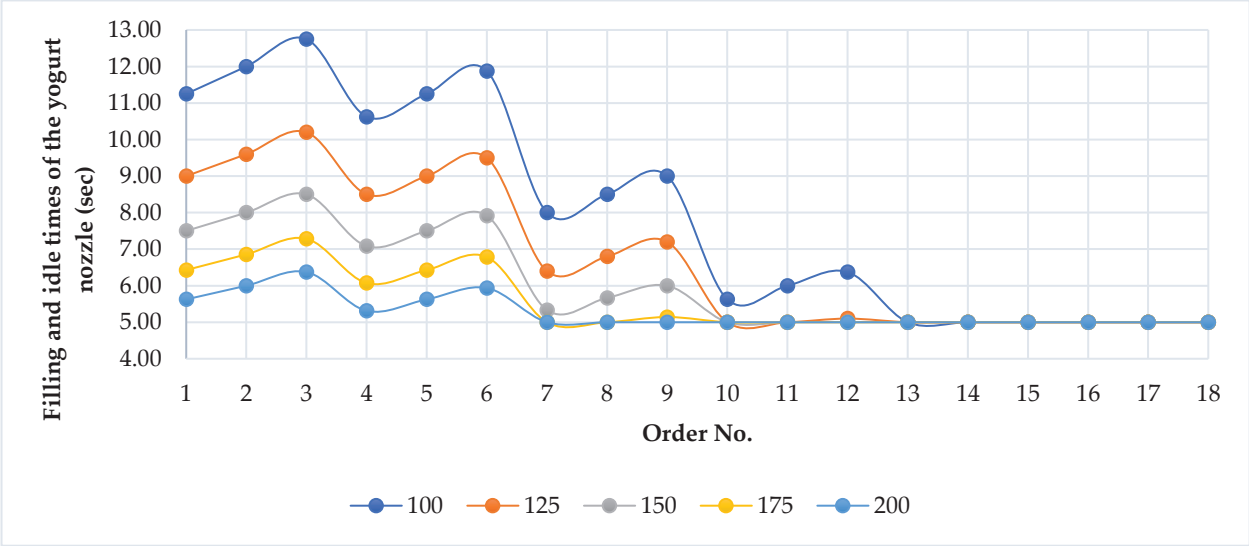

Figure 8. The impact of the yogurt nozzle's feed rate on the filling and idle times of the yogurt nozzle.

It can be noted that for large volumes, the filling time is higher than that for smaller volumes of the yogurt. The filling time decreases with the increase in the feed rate of the yogurt nozzle.

5.2. Comparison of the Proposed Model with the Previously Published Models

The proposed model is compared with the previously published models, i.e., B. Salah et al. [28], J. Chen et al. [29] and Y. Cui et al. [30], as can be seen in Figure 9. During the comparison, the yogurt feed rate was kept at 100 mL/s. When processing all orders at the above value of the parameter, the B. Salah et al. [28] model takes longer than the other models. However, the current proposed model takes less time than all other models.

In the set of orders, few require more than one flavor to be mixed with the yogurt. As there are dedicated filling points for each flavor in the case of Y. Cui et al. [30], for each flavor, the cup is initially passed through the dedicated line where the filling nozzle is available to fill the required flavor. The additional time to fill the second or third flavor in the cup is added to the initial processing time. Therefore, the processing time of Y. Cui et al. [30] study is more than that of Chen et al. [29] in most cases.

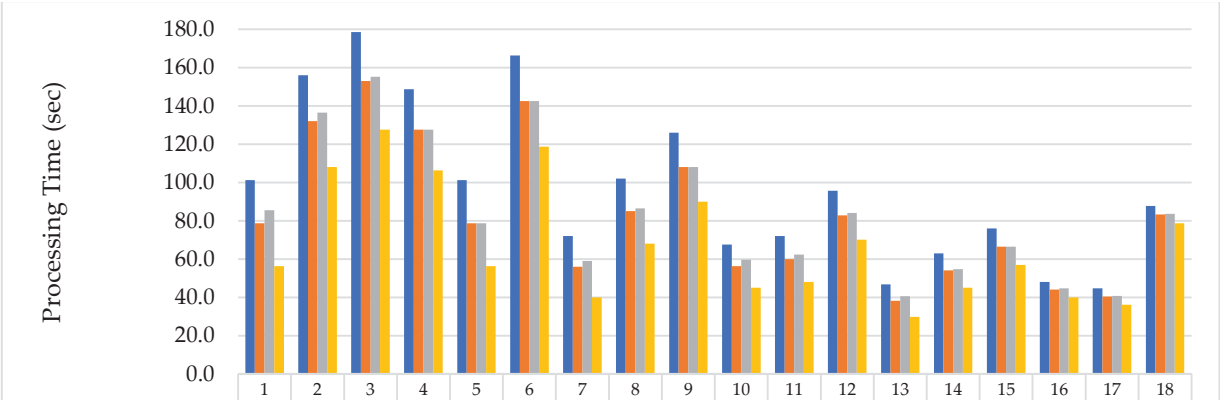

	1	2	3	4	5	6	7	8	9	10	11	12	13	14	15	16	17	18
B. Salah et al. 2021	101.3	156.0	178.5	148.8	101.3	166.3	72.0	102.0	126.0	67.5	72.0	95.6	46.8	63.0	76.0	48.0	44.6	87.8
J. Chen et al. 2022	78.8	132.0	153.0	127.5	78.8	142.5	56.0	85.0	108.0	56.3	60.0	82.9	38.3	54.0	66.5	44.0	40.4	83.3
Y. Cui et al. 2022	85.5	136.5	155.2	127.5	78.8	142.5	59.0	86.5	108.0	59.6	62.2	84.0	40.5	54.7	66.5	44.7	40.7	83.6
The Proposed Model	56.3	108.0	127.5	106.3	56.3	118.8	40.0	68.0	90.0	45.0	48.0	70.1	29.8	45.0	57.0	40.0	36.1	78.8

Figure 9. Comparison of the previously published models (B. Salah et al. [28], J. Chen et al. [29] and Y. Cui et al. [30]) with the proposed model at a yogurt feed rate of 100 mL/s.

The increase in the yogurt nozzle's feed rate decreases processing time. As shown in Figure 10, the previously published models have been compared with the proposed models, and as the feed rates are increased, the average processing time for all orders decreases. The proposed model results in the lowest average processing times for all orders, while B. Salah et al. [28] results in the highest values.

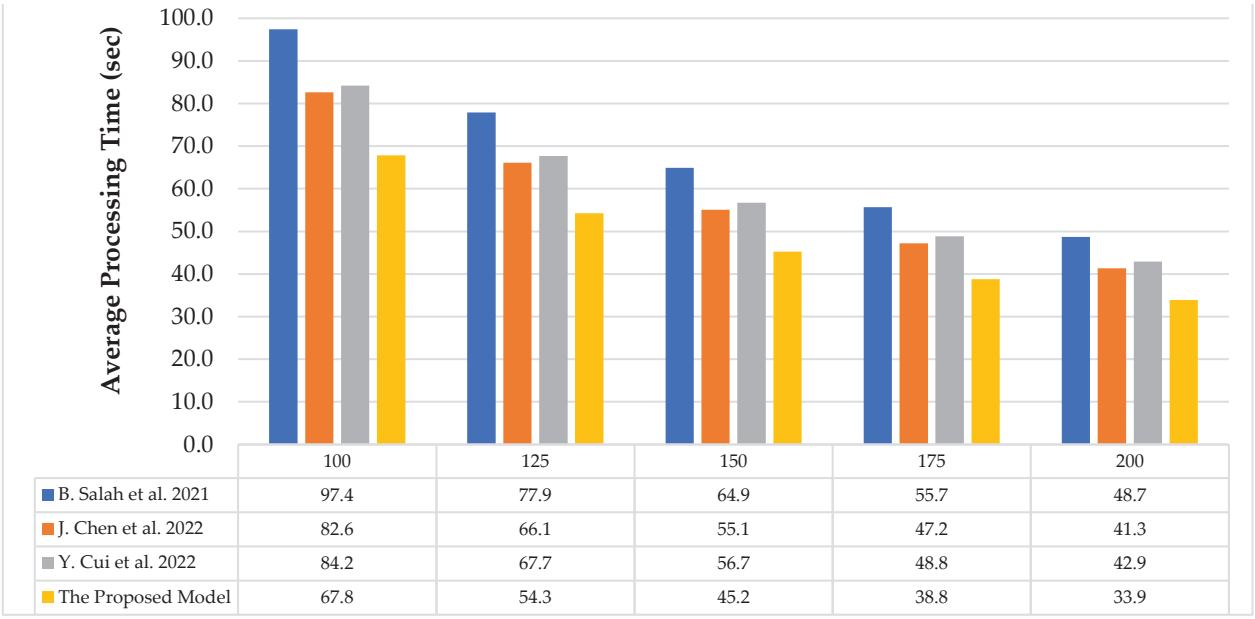

	100	125	150	175	200
B. Salah et al. 2021	97.4	77.9	64.9	55.7	48.7
J. Chen et al. 2022	82.6	66.1	55.1	47.2	41.3
Y. Cui et al. 2022	84.2	67.7	56.7	48.8	42.9
The Proposed Model	67.8	54.3	45.2	38.8	33.9

Figure 10. A comparison of the previously published models (B. Salah et al. [28], J. Chen et al. [29] and Y. Cui et al. [30]) with the proposed model based on the average processing time for a yogurt feed rate of 100 mL/s.

Solving the problem of 18 orders on the 3 parallel working machines, with a maximum allowable feed rate of the yogurt nozzle of 100 mL/s and the maximum allowable speed of the belt of 10 cm/s, the processing times recorded by the B. Salah et al. [28], J. Chen et al. [29] and Y. Cui et al. [30] model are 97.4 s, 82.6 s and 84.2 s, respectively, while the proposed model takes 67.8 s to complete the filling process of all cups demanded by customers. This means that the proposed model is 1.43-, 1.21- and 1.24-fold faster than B. Salah et al. [28], J. Chen et al. [29] and Y. Cui et al. [30] models, respectively.

6. Conclusions

This article compares the processing times of the different machine settings of the yogurt filling machine. Previously published articles on process optimization have been reported by changing the machine settings and revising the mathematical model accordingly. In the current study, the machine's settings are changed to fully flexible, where the yogurt and all flavors are filled in the cup at any filling point of the machine. A mathematical model has been developed for the proposed machine settings, where each filling point in the machine works in parallel to fill the required volumes of yogurt and flavors simultaneously. To compare the model with the previously published models on the machine, a real-life problem is solved, where the customer demand comprises 18 orders for different volumes of yogurt and flavors. The total processing times of machines 1, 2, and 3 are 417.000 s, 416.625 s, and 416.875 s, respectively. The total work content amounts to 1250.500 s on the three machines, with an average machine load of 416.833 s and a makespan value (C_{max}) of 417.000 s. After comparison with previous published models, the proposed model is 1.43-, 1.21- and 1.24-fold faster than the B. Salah et al. [28], J. Chen et al. [29] and Y. Cui et al. [30] models, respectively.

Implementing the fully flexible yogurt filling machine model in real-world settings may face challenges such as technical complexity, equipment modifications, operator

training, maintenance and repair, diverse customer demand and significant investment in equipment, software, and training. Addressing these challenges is important to successfully implementing the proposed model and realizing its benefits in real-world yogurt filling machine operations.

In the future, to further automate the yogurt filling machine and reduce human intervention, some of the technologies that can be employed are Machine Learning, Internet of Things, Advanced Conveyor Belt Systems and Industry 4.0 technologies.

Author Contributions: Conceptualization, K.Z.; formal analysis, S.Z. and M.B.; funding acquisition, M.B.; investigation, F.Y.; methodology, K.Z. and M.B.; project administration, F.Y.; resources, Q.S. and F.Y.; software, S.Z.; supervision, Q.S.; validation, Q.S.; writing—original draft, K.Z. and S.Z.; writing—review and editing, M.B. All authors have read and agreed to the published version of the manuscript.

Funding: The Article Processing Charges (APC) were funded by an internal mini-grant Type B by The American University in Cairo. The research work is also supported by Key Scientific Research Project of Colleges and Universities in Henan Province, China No. 23A460013 and Henan Province Science and Technology Project No. 212102110218.

Data Availability Statement: Data is contained within the article.

Acknowledgments: The authors acknowledge the support of the American University in Cairo, Egypt for funding the APC.

Conflicts of Interest: The authors declare no conflict of interest.

References

1. He, F.; Shen, K.; Lu, L.; Tong, Y. Model for improvement of overall equipment effectiveness of beer filling lines. *Adv. Mech. Eng.* **2018**, *10*, 1687814018789247. [CrossRef]
2. Lee, J.H.; Jang, H. Uniform parallel machine scheduling with dedicated machines, job splitting and setup resources. *Sustainability* **2019**, *11*, 7137. [CrossRef]
3. Wang, S.; Wang, X.; Yu, J.; Ma, S.; Liu, M. Bi-objective identical parallel machine scheduling to minimize total energy consumption and makespan. *J. Clean. Prod.* **2018**, *193*, 424–440. [CrossRef]
4. Hu, D.; Yao, Z. Genetic algorithms for parallel machine scheduling with setup times. In Proceedings of the 2nd International Conference on Information Science and Engineering, Hangzhou, China, 4–6 December 2010; IEEE: Piscataway, NJ, USA, 2010; pp. 1233–1236.
5. Özpeynirci, S.; Gökgür, B.; Hnich, B. Parallel machine scheduling with tool loading. *Appl. Math. Model.* **2016**, *40*, 5660–5671. [CrossRef]
6. Çanakoğlu, E.; Muter, İ. Identical parallel machine scheduling with discrete additional resource and an application in audit scheduling. *Int. J. Prod. Res.* **2021**, *59*, 5321–5336. [CrossRef]
7. Bernhard, K.; Vygen, J. *Combinatorial Optimization: Theory and Algorithms*, 3rd ed.; Springer: Berlin/Heidelberg, Germany, 2008.
8. Arram, A.; Ayob, M. A novel multi-parent order crossover in genetic algorithm for combinatorial optimization problems. *Comput. Ind. Eng.* **2019**, *133*, 267–274. [CrossRef]
9. Gannouni, A.; Samsonov, V.; Behery, M.; Meisen, T.; Lakemeyer, G. Neural combinatorial optimization for production scheduling with sequence-dependent setup waste. In Proceedings of the IEEE International Conference on Systems, Man, and Cybernetics (SMC), Toronto, ON, Canada, 11–14 October 2020; IEEE: Piscataway, NJ, USA, 2020; pp. 2640–2647.
10. Fuentes-Penna, A.; Gómez-Espinosa, L.C.; Borja, A.P.P. An introduction to Job Shop Scheduling to model the Timetabling Scheduling Problem. *Int. J. Comb. Optim. Probl. Inform.* **2022**, *13*.
11. El-Kholany, M.M.; Gebser, M.; Schekotihin, K. Problem decomposition and multi-shot ASP solving for job-shop scheduling. *Theory Pract. Log. Program.* **2022**, *22*, 623–639. [CrossRef]
12. Kopanos, G.M.; Puigjaner, L.; Georgiadis, M.C. Efficient mathematical frameworks for detailed production scheduling in food processing industries. *Comput. Chem. Eng.* **2012**, *42*, 206–216. [CrossRef]
13. Wang, J.Q.; Fan, G.Q.; Zhang, Y.; Zhang, C.W.; Leung, J.Y.T. Two-agent scheduling on a single parallel-batching machine with equal processing time and non-identical job sizes. *Eur. J. Oper. Res.* **2017**, *258*, 478–490. [CrossRef]
14. Chen, G.; Ezekiel, A.; Bardhan, T.K. Optimization of factor settings for pharmaceutical filling process by factorial design of mixed levels. *Ind. Syst. Eng. Rev.* **2013**, *1*, 110–122. [CrossRef]
15. Ferreira, D.; Morabito, R.; Rangel, S. Solution approaches for the soft drink integrated production lot sizing and scheduling problem. *Eur. J. Oper. Res.* **2009**, *196*, 697–706. [CrossRef]
16. Wang, H.; Yoon, S.W. Evaluation and optimization of automatic drug dispensing/filling system. In Proceedings of the 3rd Annual World Conference of the Society for Industrial and Systems Engineering, San Antonio, TX, USA, 20–22 October 2014.

17. Strohhecker, J.; Hamann, M.; Thun, J.H. Loading and sequencing heuristics for job scheduling on two unrelated parallel machines with long, sequence-dependent set-up times. *Int. J. Prod. Res.* **2016**, *54*, 6747–6767. [CrossRef]
18. Da Col, G.; Teppan, E.C. Industrial-size job shop scheduling with constraint programming. *Oper. Res. Perspect.* **2022**, *9*, 100249. [CrossRef]
19. Baldo, T.A.; Santos, M.O.; Almada-Lobo, B.; Morabito, R. An optimization approach for the lot sizing and scheduling problem in the brewery industry. *Comput. Ind. Eng.* **2014**, *72*, 58–71. [CrossRef]
20. Basso, F.; Varas, M. A MIP formulation and a heuristic solution approach for the bottling scheduling problem in the wine industry. *Comput. Ind. Eng.* **2017**, *105*, 136–145. [CrossRef]
21. Niaki, M.K.; Nonino, F.; Komijan, A.R.; Dehghani, M. Food production in batch manufacturing systems with multiple shared-common resources: A scheduling model and its application in the yoghurt industry. *Int. J. Serv. Oper. Manag.* **2017**, *27*, 345–365. [CrossRef]
22. Rezig, S.; Ezzeddine, W.; Turki, S.; Rezg, N. Mathematical Model for Production Plan Optimization—A Case Study of Discrete Event Systems. *Mathematics* **2020**, *8*, 955. [CrossRef]
23. Toledo CF, M.; Kimms, A.; França, P.M.; Morabito, R. A mathematical model for the synchronized and integrated two-level lot sizing and scheduling problem. *J. Oper. Res. Soc. Under Rev.* **2006**.
24. Kumar, P.; Tewari, P. Performance analysis and optimization for CSDGB filling system of a beverage plant using particle swarm optimization. *Int. J. Ind. Eng. Comput.* **2017**, *8*, 303–314. [CrossRef]
25. Guo, S.; Lang, H.; Zhang, H. Scheduling of Jobs with Multiple Weights on a Single Machine for Minimizing the Total Weighted Number of Tardy Jobs. *Mathematics* **2023**, *11*, 1013. [CrossRef]
26. Samouilidou, M.E.; Diakoumi, E.; Georgiadis, G.P.; Dikaiakos, A.; Georgiadis, M.C. Lot-sizing and Production Scheduling of a Beverage Industry. In *Computer Aided Chemical Engineering*; Elsevier: Amsterdam, The Netherlands, 2023; Volume 52, pp. 95–100.
27. Salah, B.; Khan, S.; Ramadan, M.; Gjeldum, N. Integrating the concept of industry 4.0 by teaching methodology in industrial engineering curriculum. *Processes* **2020**, *8*, 1007. [CrossRef]
28. Salah, B.; Khan, R.; Ramadan, M.; Ahmad, R.; Saleem, W. Lab Scale Implementation of Industry 4.0 for an Automatic Yogurt Filling Production System—Experimentation, Modeling and Process Optimization. *Appl. Sci.* **2021**, *11*, 9821. [CrossRef]
29. Chen, J.; Khan, R.; Cui, Y.; Salah, B.; Liu, Y.; Saleem, W. The effect of changes in settings from multiple filling points to a single filling point of an industry 4.0-based yogurt filling machine. *Processes* **2022**, *10*, 1642. [CrossRef]
30. Cui, Y.; Zhang, X.; Luo, J. Filling Process Optimization through Modifications in Machine Settings. *Processes* **2022**, *10*, 2273. [CrossRef]
31. Salah, B.; Alsamhan, A.M.; Khan, S.; Ruzayqat, M. Designing and Developing a Smart Yogurt Filling Machine in the Industry 4.0 Era. *Machines* **2021**, *9*, 300. [CrossRef]

processes

MDPI

Article

Numerical Simulations for the Mechanical Behavior of a Type-B Sleeve under Pipeline Suspension

Haiping Tang [1,*], Yaping Ding [2], Guangyou Qiu [3], Ziguang Liu [1] and Zhibin Deng [1]

[1] College of Civil Aviation Safety Engineering, Civil Aviation Flight University of China, Deyang 618307, China; 18790896558@163.com (Z.L.); dengzb84@163.com (Z.D.)
[2] Department of Transportation and Municipal Engineering, Sichuan College of Architectural Technology, Chengdu 610399, China; dingsccat@126.com
[3] Dehong Oil and Gas Transportation Branch of Southwest Oil and Gas Pipeline Co., Ltd. of Pipe China, No. 6 Jinkongque Street, Mangshi 678400, China; qiugyou@163.com
* Correspondence: tang14187@cafuc.edu.cn

Abstract: The type-B sleeve is widely used for reinforcing defective pipelines. Due to the impact of suspension on pipeline safety, the behavior of the type-B sleeve structure has garnered increasing attention. In this study, we establish a numerical model of a defective pipeline reinforced with a type-B sleeve while accounting for the effects of the internal natural gas pressure and gravitational load. We investigate the influence of the sleeve length, suspended pipeline length, internal pressure, and sleeve position on the mechanical behavior of the type-B sleeve. The maximum values for Mises stress and axial strain were both observed near the edge of the suspended segment of the pipeline. For the type-B sleeve structure, the high Mises stress zone was at the bottom of the fillet weld; the axial strain near the fillet weld alternated between tension and compression along the axial direction. With an increase in internal pressure and suspended pipeline length, the Mises stress and axial strain of the type-B sleeve became more prominent. For sleeve length in the ranges of 1 to 3 m, the changes in the stress and strain did not exceed 10 MPa and 0.5×10^{-3}, respectively. However, the Mises stress and axial strain on the type-B sleeve structure were independent of the position of the defect on the pipeline. This study provides an important reference for type-B sleeve protection during suspension and other similar practical engineering applications.

Keywords: type-B sleeve; suspended pipeline; mechanical behavior; numerical simulation

1. Introduction

Long-distance natural gas pipelines play an important role in energy transportation. However, defects such as corrosion and cracks often lead to a decrease in the strength of the pipeline, causing accidents and severe economic losses [1–3]. Timely reinforcement at defective locations is the main way to prevent such accidents. In general, the type-A sleeve, type-B sleeve, and composite sleeve are widely used in enhancing the strength of the defective pipeline [4–6]. However, the type-B steel sleeve, which attaches to the pipe by fillet welds, has significant advantages due to the axial sealing and high strength and has been widely employed in engineering practice [7,8].

As Figure 1 indicates, the local structure of a reinforced pipeline includes the sleeve, fillet welds, and the defective pipeline. Once the defective pipeline penetrates, the enclosed space formed by fillet weld and sleeve can prevent leakage. An experiment by Battelle laboratory [9] demonstrated that the blasting capacity of the pipeline repaired by the type-B sleeve reached or even exceeded the design pressure, which is highly useful for improving the bearing capacity. Yi et al. [10] investigated the burst pressure of a corroded X80 steel pipeline with a type-B repair sleeve and revealed that the local defective region exhibits the highest levels of stress, followed by the fillet weld. Unfortunately, buried pipelines are also subjected to additional geological loads, in addition to the internal pressure [11].

Wherever the foundation subsides, the bending moment increases at the cross-section of the buried pipeline. The stress caused by the settlement greatly affects the operational safety of pipelines. Therefore, the mechanical behavior of pipelines has always been a research concern [12,13]. The bending moment generated by a suspended pipeline can be particularly substantial, with the severe stress and strain concentrations on the structure of the type-B sleeve. Therefore, studying the mechanical behavior of pipelines suspended by geological subsidence is of great significance.

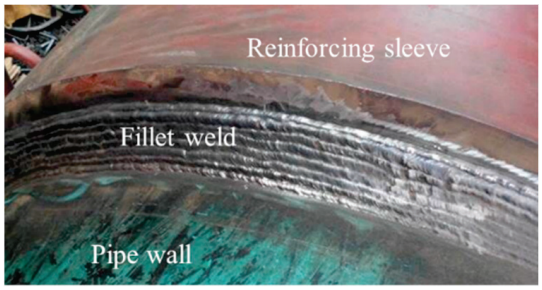

Figure 1. Type-B sleeve on a pipeline.

Previous studies have mainly focused on the mechanical behavior of pipelines with type-B sleeves under internal pressure. Due to rapid developments, the application of high-grade and large-diameter pipelines in gas transportation pipeline engineering continues to increase, such as the West–East Gas Transmission Project and the China–Russia Eastern Gas Pipeline. Compared to being only subjected to internal pressure, the mechanical behavior of type-B sleeves under pipeline suspension can be much more complex [14].

Therefore, in this study, we investigated the stress and strain experienced by type-B sleeves under buried gas pipeline suspension using Abaqus finite element analysis software. Particularly, the effects of pipeline suspension length, type-B sleeve position and length, internal pipeline pressure, and defect location on the mechanical behavior of type-B sleeves were studied. This study provides a theoretical foundation for designing and assessing pipelines reinforced with type-B sleeves.

2. Finite Element Model of Sleeve Repair Pipeline

2.1. Finite Element Model Parameters

To establish the finite element model, the structural dimensions were determined according to the "ASME B31.8—Gas Transmission and Distribution Piping Systems" specification. As shown in Figure 2, the relations between the dimensions of the type-B sleeve can be calculated as follows.

$$t_s = 1.4t \tag{1}$$

$$l_f = 1.4t + g_a \tag{2}$$

where t is the pipeline wall thickness; t_s is the sleeve wall thickness; g_a = 2.5 mm is the gap between the sleeve wall and pipeline wall; l_f is the length of the fillet weld leg; R is the internal diameter of the pipeline.

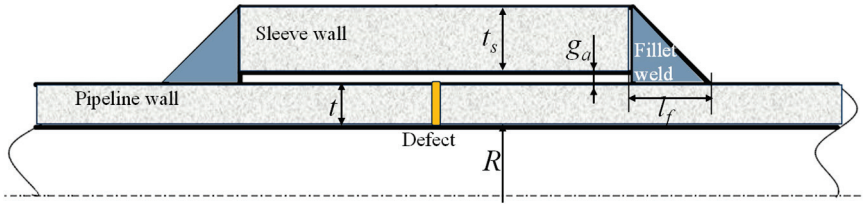

Figure 2. The diagrammatic sketch of type-B sleeve.

We selected the API 5L X80 pipeline with a diameter of 1422 mm and a wall thickness of 24 mm for simulation. Before suspension, the pipeline burial depth was set to 2.5 m

according to the "SY/T 6649-2018 Defect Repair of Oil & Gas Pipeline" Specification, and the sleeve wall thickness and the fillet weld leg length were calculated by Equations (1) and (2). The type-B sleeve is used to reinforce the strength of the defective pipeline wall. Therefore, the defect is considered in the finite element model, and its diameter is set to 20 mm. As Figure 3 demonstrates, the test pipeline can be divided into suspended and buried sections. To reduce the effect of the soil model on the mechanical behavior of the type-B sleeve, the soil model dimensions fixed its dimensions while appropriately increasing the height to 20 m × 6 m × 10 m [15].

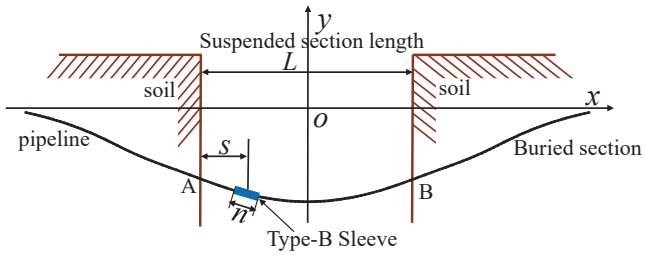

Figure 3. Diagram of the suspended pipeline.

2.2. Materials Properties

In general, the type-B sleeve uses the same material as the pipeline steel, and the weld of the sleeve is adopted based on equal strength matching with the pipeline steel. Therefore, the material properties of X80 steel are assigned to pipeline, sleeve, and fillet weld. For the API 5L X80 steel pipeline used in this study, the stress–strain curve of X80 pipeline steel is shown in Figure 4, and the Ramberg–Osgood model was used to describe the nonlinear model [16,17]. This is described by Equation (3), and the X80 pipeline streel properties are listed in Table 1.

$$\varepsilon = \frac{\sigma_t}{E}\left[1 + \alpha\left(\frac{\sigma_t}{\sigma_y}\right)^{n-1}\right] \tag{3}$$

where ε is the true strain of X80 steel; σ_t is tensile strength of X80 steel (MPa); σ_y is the yield strength of X80 steel (MPa); E is Young's modulus of X80 steel (GPa); n is the strain hardening exponent of X80 steel; α is the hardening coefficient of X80 steel.

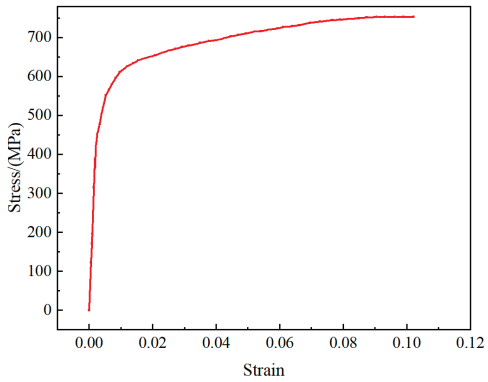

Figure 4. The stress–strain constitutive of the X80 pipeline steel.

Table 1. The property parameters of X80 pipeline steel.

Type	Density (kg/m^3)	Young's Modulus (MPa)	Poisson's Ratio	Yield Strength (MPa)	Tensile Strength (MPa)
X80 steel	8000	210	0.3	572	742

The mechanical behavior of the clay soil chosen in this study could be represented by the ideal elastic–plastic Mohr–Coulomb model [17]. The characteristic parameters of soil are listed in Table 2.

Table 2. Material properties of soil.

Type	Density (kg/m^3)	Elasticity Modulus (MPa)	Poisson's Ratio	Friction Angle (°)	Cohesion (kPa)	Dilatation Angle (°)
Clay	1950	50	0.3	22.5	30	0

2.3. Finite Element Model with Pipeline–Soil Interaction

To investigate the mechanical behavior of the suspended pipeline repaired by a type-B sleeve, the finite element model was established using the software Abaqus, which is shown in Figure 5a. The surface-to-surface interaction is used to describe the pipeline–soil contact relationship. In this model, we designated the pipeline's external surface and internal soil surface as the master surface and slave surface, respectively. Hard contact was applied to simulate the normal direction of the contact surface, while a penalty function method with a coefficient of 0.3 was employed to describe the tangential direction of the contact surface. Considering the quality of the grid and the geometric features of the finite element model, structured grid and hex elements were used to generate the mesh. Meanwhile, to ensure precision and computational efficiency, the element type was set as C3D8R. As shown in Figure 5b, due to the stress concentration at fillet weld and defects, the meshes were refined to improve the calculating precision.

During the suspension, the pipeline is supported by the soil. Therefore, the lateral and axial directions of the soil are less impacted by the loads of the suspended pipeline. To simulate actual working conditions, symmetric constrains were adopted at the plane of the soil and pipeline. The lower surface of the soil was fully fixed to maintain model stability, while its upper and suspended surfaces were free of constraints, which is shown in Figure 5c. Mechanical equilibrium is maintained between the pipeline soil before subsidence. Therefore, the natural gas pressure was employed, and a gravitational acceleration of $g = -9.8\ m/s^2$ along the Y-axis was applied to the model.

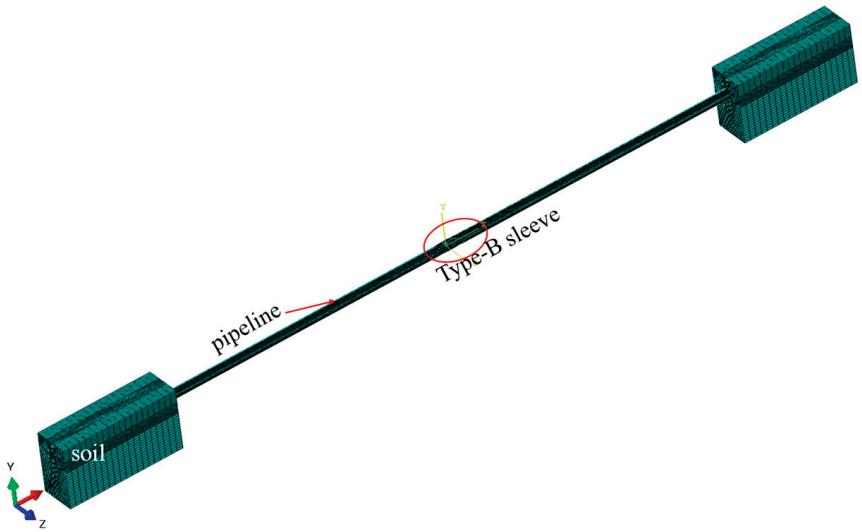

(**a**)

Figure 5. *Cont.*

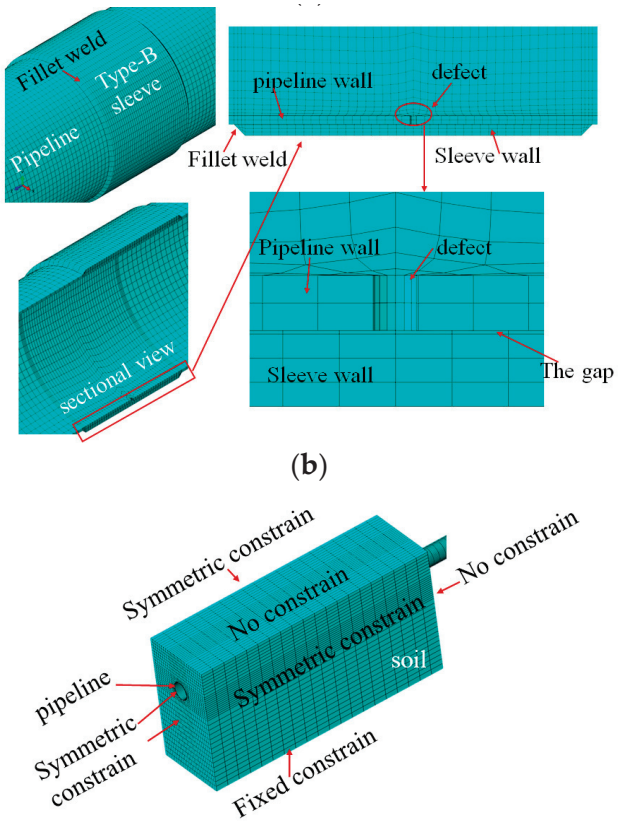

Figure 5. The numerical model of the suspended pipeline. (**a**) The finite model. (**b**) The enlarged view of the type-B sleeve model. (**c**) The boundary conditions.

2.4. Model Verification

When the length of the suspended pipeline is 300 m, the internal pressure is 12 MPa, and the length of the type-B sleeve is 1 m, the effect of the grid size of the type-B sleeve on the numerical results is calculated. As Table 3 lists, it can be found that the numerical simulation stabilized when the mesh size of the type-B sleeve is 33 mm, and the whole model consists of 333,152 elements.

Table 3. Mesh sensitivity results.

Gride Size (mm)	Gride Number	Maximum Displacement of Pipeline (m)	Maximum Mises Stress of Pipeline (Mpa)	Maximum Mises Stress of Type-B Sleeve (Mpa)
83	101,592	6.181	609	443
62.5	195,200	6.175	611	450
50	195,968	6.173	612	450
33	333,152	6.171	613	453
25	342,752	6.171	613	453
20	466,752	6.171	613	453

It is very difficult to verify the numerical model by experiment; thus, the numerical model was verified analytically. As shown in Figure 3, for the buried segment of the pipeline at each point, the gravity of the pipeline is equal to the support force of the soil, and the compression deformation of the soil is equal to the deflection of the pipeline. Equation (4) is presented according to Winkler elastic foundation beam theory [12].

$$EI\frac{d^4y}{d^4x} = q - ky \tag{4}$$

where q is the weight per unit length of pipeline; E is the elastic modulus of X80 pipeline steel; I is the cross-sectional moment of inertia of pipeline; y is the deflection of pipeline; k is the elastic resistance coefficient of soil.

The equilibrium equation on the pipeline cross-section can be given in Equations (5)–(7) [18].

$$\frac{dM(x)}{dx} = Q(x) \tag{5}$$

$$\frac{dQ(x)}{dx} = q \tag{6}$$

$$EIy'' = -M(x) \tag{7}$$

where $Q(x)$ is the shearing force, and $M(x)$ is the bending moment on the cross-section of the pipeline. The general solution can be expressed as Equation (8) [12]:

$$y = e^{\lambda x}(c_1 \cos \lambda x + c_2 \sin \lambda x) + e^{-\lambda x}(c_3 \cos \lambda x + c_4 \sin \lambda x) \tag{8}$$

where λ is the root of the characteristic equation; c_1, c_2, c_3, c_4 are the specific coefficients.

For the suspended segment of the pipeline, the differential equation of deflection can be represented as Equation (9) [19]:

$$EI\frac{d^2y}{d^2x} = M_B + S_B(y - y_B) + \frac{1}{2}qx^2 - \frac{1}{2}qLx \tag{9}$$

where M_B is the bending moment at point B in Figure 3, L is the length of the suspended pipeline, y_B is the displacement of point B in the Y-axis direction, and S_B is the equivalent axial tensile load calculated as:

$$S_B = \frac{\pi p d^2}{4} \tag{10}$$

where d is the outside diameter of the pipeline, and p is the internal pressure of the pipeline.

As Figure 6 indicates, both our numerical finite element model for pipeline suspended displacement and the theoretical results of Shang B. et al. [18] revealed the maximum settlement displacement to be at the middle of the pipeline. The analytical and numerical solutions for maximum settlement displacement were 5.8224 m and 6.1705 m, respectively. The error is 5.983% and lower than 6%. Therefore, the error meets the allowable range, and the accuracy of our model can be verified.

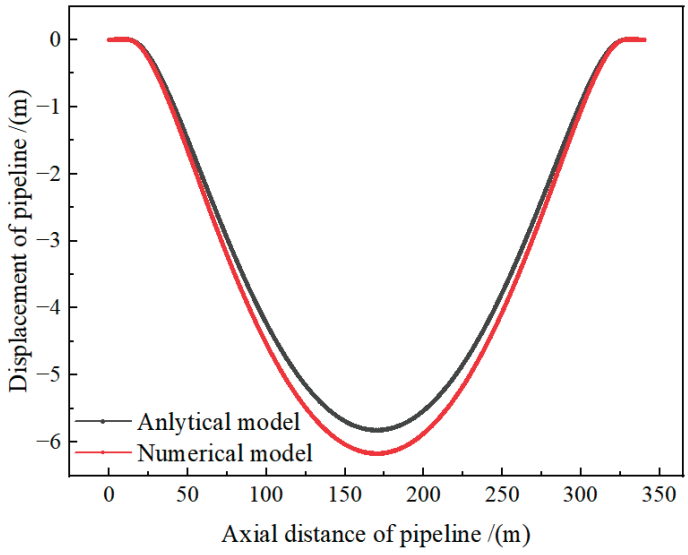

Figure 6. Comparison of the theoretical and numerical model.

3. Results and Discussion

3.1. The Influence of the Types of Defects

The types of defects on the pipeline are shown in Figure 7. If the defect on the type-B-sleeve reinforced pipeline penetrates the pipeline wall, natural gas will fill the space formed by the outer wall of the pipeline, the inner wall of the sleeve, and the fillet weld. Therefore, we conducted a comparative analysis of the mechanical behaviors of the reinforced pipeline under penetrating and non-penetrating defect conditions.

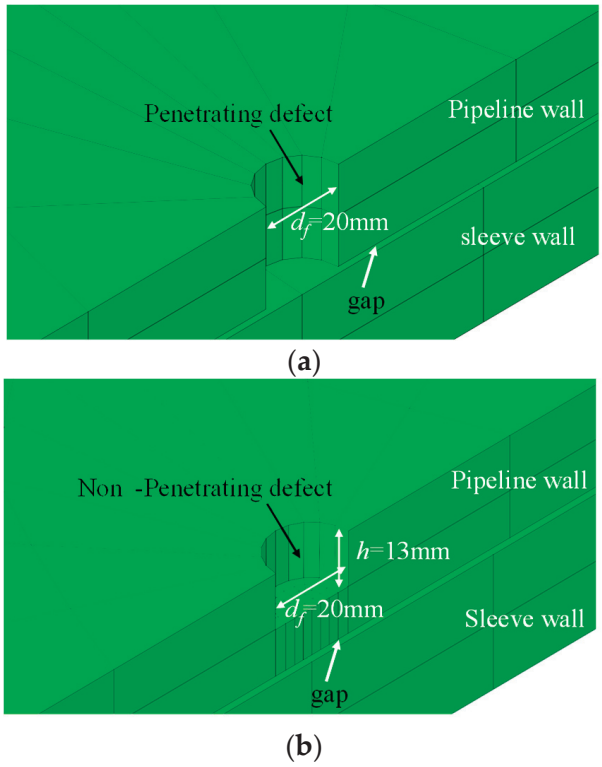

Figure 7. Diagrammatic representation of defect on the pipeline. (**a**) The penetrating defect. (**b**) The non-penetrating defect.

For the suspended pipeline length of 300 m, internal pressure of 12 MPa, non-penetrating defect depth of 13 mm, type-B sleeve with a length of 1 m, and located at the middle of the suspended pipeline, the mechanical behavior was calculated. As Figure 8 depicts, high Mises stress (M_S) zones for penetrating and non-penetrating pipelines were located at junctional regions of the suspended segment of the pipeline. The peak M_S value is measured to be 613 Mpa, exceeding the yield strength repaired type-B sleeve. However, the M_S on the type-B sleeve with a penetrating defect is a notable difference from that with a non-penetrating defect.

As Figure 9a shows, high stress concentration was observed at the bottom of the fillet weld for both these types of defective pipelines, with a slightly higher value for the pipeline with penetrating defects (453 Mpa) compared to the one with non-penetrating defects (415 Mpa). The Mises stress distribution on the type-B sleeve was further compared, and a similar trend was observed; as shown in Figure 9b, stress on the sleeve with penetrating defects was larger than that on the one with non-penetrating defects.

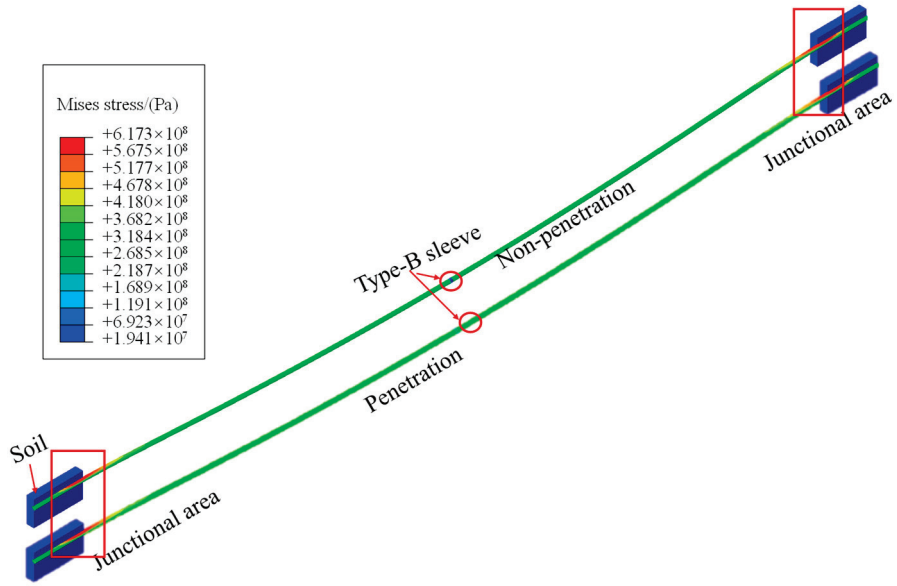

Figure 8. The Mises stress distribution on the pipeline.

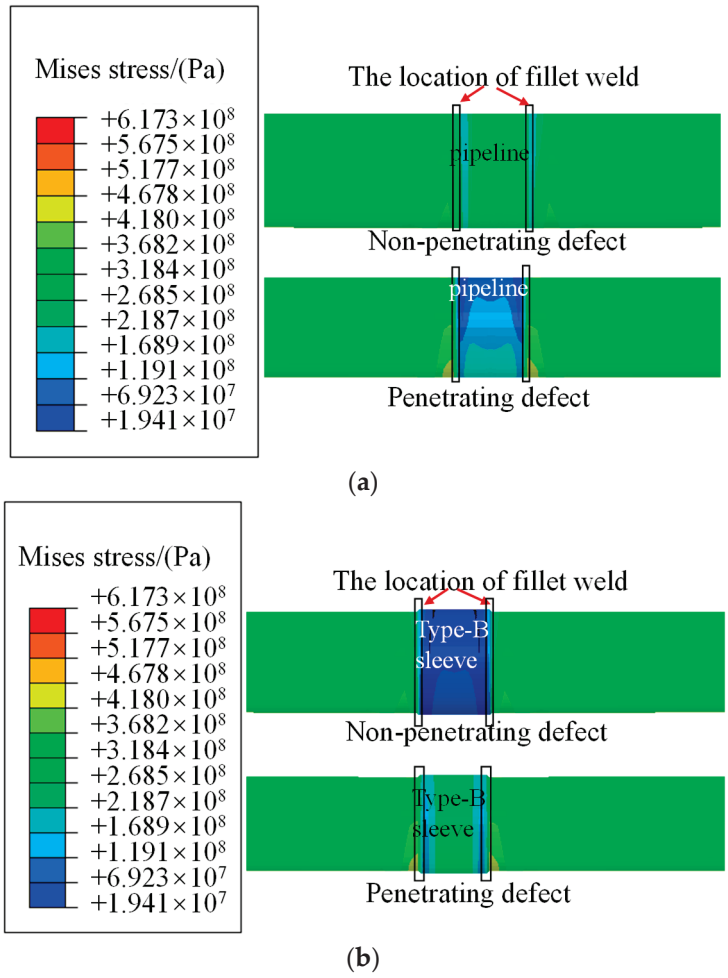

Figure 9. Mises stress distribution. (**a**) The Mises stress distribution on the pipeline. (**b**) The Mises stress distribution on the type-B sleeve.

As seen in Figure 10, the axial strain (ε_a) distribution along the defective pipeline revealed high tensile strain near the bottom of the fillet weld, with the maximum ε_a of the

penetrating defect reaching 1.732×10^{-3}, i.e., higher than that of the non-penetrating defect (1.53×10^{-3}). Figure 10a shows that regardless of whether or not the defect penetrates the pipeline wall, the axial strain value and distribution on the pipeline between the two fillet welds were mostly similar. For the type-B sleeve, Figure 10b demonstrates that although the magnitude of the axial strain varied, the distribution pattern essentially remained consistent. The axial strain changed from tension to compression upon moving from the pipeline to the type-B sleeve. However, for the pipeline with penetrating defects, the compressive strain value at the fillet weld zone exceeded -6×10^{-4}, i.e., significantly higher than that at the fillet weld zone of the pipeline with non-penetrating defects (-2.17×10^{-5}). Comparing the results for the two situations indicates that the failure risk increased for the type-B sleeve with the defect penetrating the pipeline wall. Therefore, we chose the pipeline with penetrating defects for the subsequent simulations. Furthermore, the M_S and ε_a values at the bottom of the type-B sleeve were higher and more complex than those at its top. Therefore, as Figure 11 shows, the axial paths along the bottom of the type-B sleeve and circumferential paths along the fillet weld are chosen to investigate the mechanical behavior of the type-B structure.

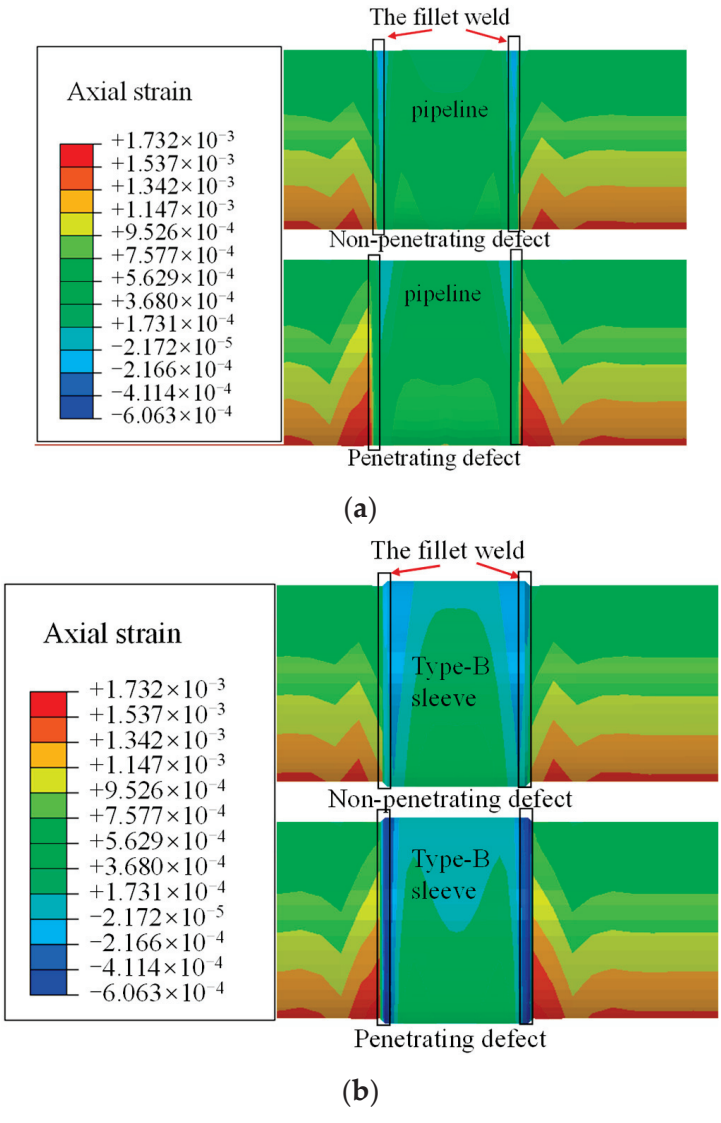

Figure 10. The axial strain distribution. (**a**) The axial strain on the pipeline. (**b**) The axial strain on the type-B sleeve.

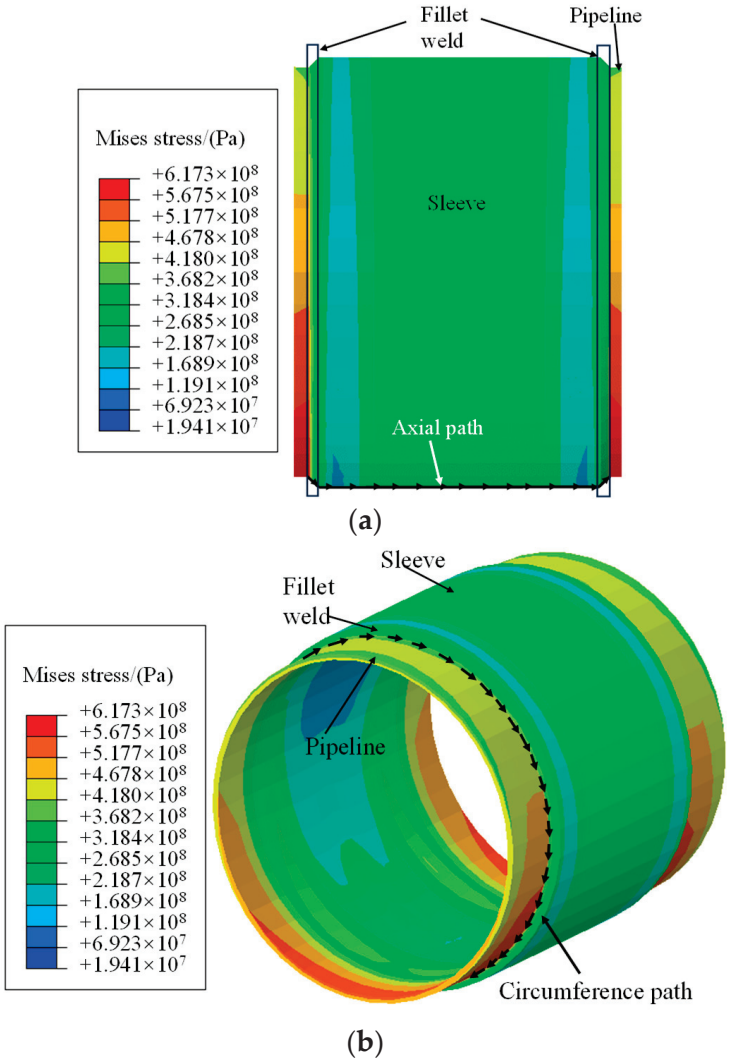

Figure 11. The selected path. (**a**) Axial path. (**b**) Circumferential path.

3.2. Effect of Type-B Sleeve Location

Figure 3 shows that the type-B sleeve location on the suspended pipeline is defined as the distance between the symmetric plane of the type-B sleeve and soil, which is represented by *s*. The effect of the type-B sleeve location on the M_S and ε_a along the axial path is shown in Figure 12. The Mises stress is found to be the highest at the fillet weld. As shown in Figure 12a, along the axial path, the M_S on the fillet weld increases from 339 MPa at s = 0 man to 453 Mpa at s = 150 m. For the type-B sleeve, at s = 0 m, the M_S is 395.8 Mpa, i.e., higher than any other sleeve location, while the M_S remains nearly constant at the central region of the sleeve for all locations. The load acting on the sleeve is transmitted through fillet welds during pipeline suspension. Due to the length of the sleeve being much shorter than the suspended pipeline length, the difference in load values between the two ends of the type-B sleeve is not significant. Therefore, little distinction is observed in the axial strain and Mises stress at the central regions of the type-B sleeve.

Figure 12b shows the axial stain along the axial path and reveals that the two fillet welds experienced asymmetric stresses when the type-B sleeve was not placed at the center of the suspended pipeline, resulting in unequal loads on both fillet weld locations. At s = 0 m, the ε_a along the axial path is compressive. Except for s = 0, the peak axial compressive strain (-0.529×10^{-3}) at both sleeve ends for all sleeve locations remains quite similar within an error of 0.04×10^{-3}. The strain alternated between tension and

compression at both sleeve ends. For s = 150 m, the highest axial tensile strain increases to 1.662×10^{-3}.

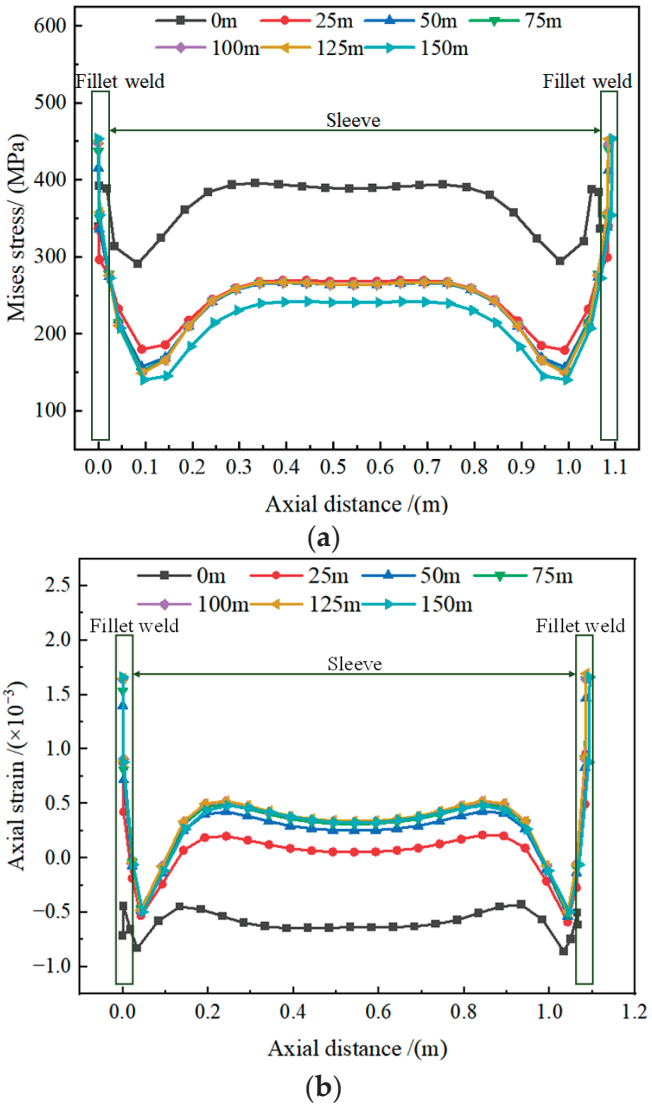

Figure 12. The Mises stress distribution along the axial distance. (**a**) Mises stress along the axial reference path. (**b**) Axial strain along the axial reference path.

The Mises stress and axial strain at the fillet weld along the circumferential paths are shown in Figure 13. Figure 13a shows that when the distance s increases, the stress at the top (bottom) of the fillet weld tends to decrease (increase). At s = 0 m, the peak M_S at the top of the fillet weld is 602 MPa, exceeding the yield strength stress of the API 5L X80 pipeline steel. Along the circumferential path, as shown in Figure 13b, the peak axial tensile strain is observed to be 5.5×10^{-3} for s = 0 m, which decreases to 2.2×10^{-3} at s = 150 m. Therefore, when the sleeve position settles closer to the edge of the suspended portion of the pipeline, the failure risk of the sleeve construction increases.

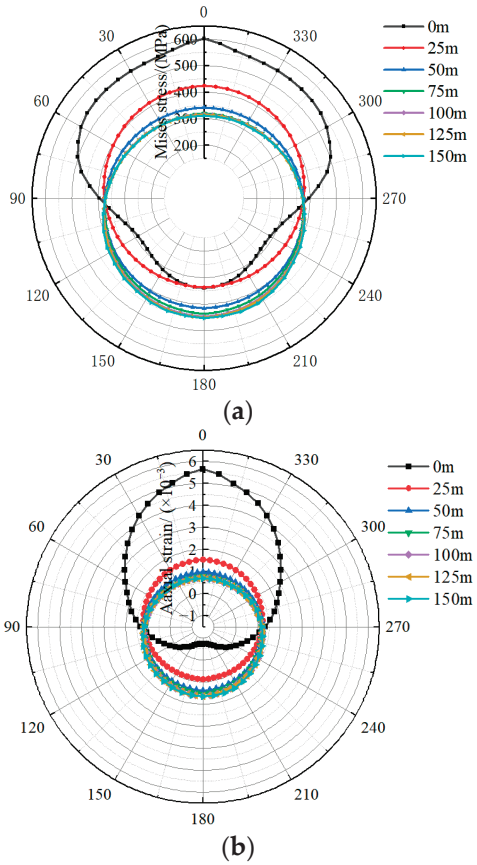

Figure 13. The Mises stress and axial strain along the circumferential path. (**a**) The Mises stress distribution. (**b**) The axial strain distribution.

3.3. Effect of the Sleeve Length

Figure 14 illustrates the influence of the length of the type-B sleeve on the M_S and ε_a along the axial path. It can be seen from Figure 14a that the peak Mises stress is at the fillet weld; the M_S value in the middle region of the sleeve is not affected by the length of the sleeve. When the length of the type-B sleeve increases from 1 to 3 m, the Mises stress at the (i) fillet weld increases from 453 MPa to 468 Mpa, and (ii) the adjacent to the fillet weld position grows from 130 Mpa to 175 Mpa. This is due to the axial force and shear force on the cross-section experiencing negligible change with the sleeve length increasing from 1.0 to 3.0 m. Moreover, the large diameter and wall thickness weaken the load on the fillet weld and sleeve.

Figure 14b shows that except sleeve length of 1.5 m, the maximum axial tensile strain and compressive strain have a positive and negative correlation with the sleeve length, respectively. At the sleeve length of 1 m, the peak axial tensile strain and compressive strain are 0.7×10^{-3} and -0.56×10^{-3}, respectively. When the length of the type-B sleeve increases to 3 m, the axial tensile strain increases to 1.72×10^{-3} and compressive strain reduces to -0.25×10^{-3}. In particular, at a sleeve length of 1.5 m, the peak tensile and compressive ε_a are 1.57×10^{-3} and -0.15×10^{-3}, respectively.

Along the circumferential path, near the bottom of the fillet weld, the Mises stress increased from 453 to 468 MPa as the sleeve length increased from 1.0 to 3.0 m, which is shown in Figure 15a. However, the stress values near the top of the fillet weld are less affected by the sleeve length; the M_S increased from 311 Mpa for a sleeve length of 1.0 m to 314 Mpa for a sleeve length of 3.0 m. Figure 15b demonstrates that the axial strain at the top of the fillet weld is 0.69×10^{-3} at the sleeve length of 1 m, i.e., only marginally greater than the axial strain at other sleeve lengths. At the bottom of the fillet weld, the ε_a increases from 1.66×10^{-3} to 1.72×10^{-3} as the length of the type-B sleeve increases from 1 to 3 m.

The results indicate that stress and strain can be reduced to a certain extent by selecting the appropriate sleeve length, thereby increasing the bearing capacity of the type-B sleeve.

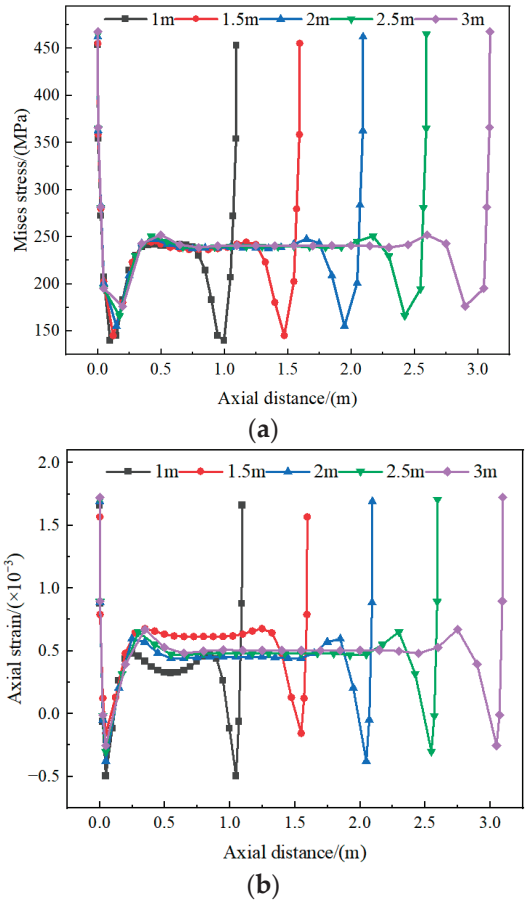

Figure 14. The Mises stress and axial strain distributed along the axial path. (**a**) The Mises stress along the axial path. (**b**) The axial strain along the axial path.

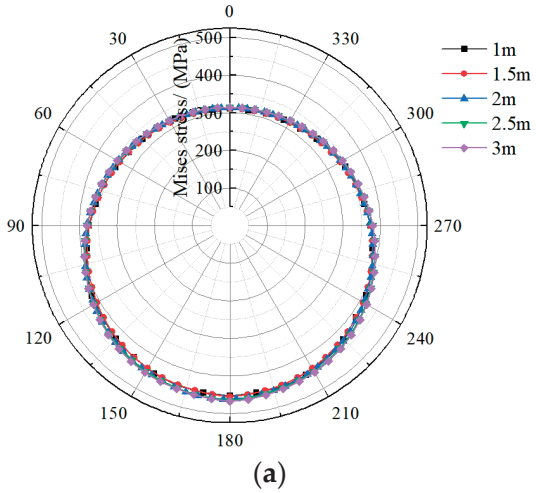

Figure 15. *Cont.*

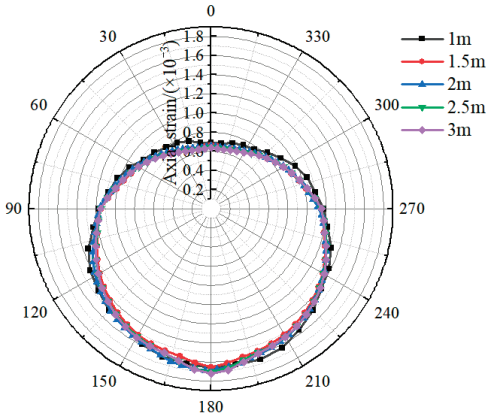

(**b**)

Figure 15. The Mises stress and axial strain along the circumferential path. (**a**) The Mises stress distribution along the circumferential path. (**b**) The axial strain distribution along the circumferential path.

3.4. Effect of the Defect Location

Figure 16 illustrates the location of the defect on the pipeline, which is represented by θ. Figure 17 shows the effect of the defect's position on the mechanical behavior of the type-B sleeve along the axial path. As illustrated in Figure 17a, the peak Mises stress is observed at the fillet weld of the type-B sleeve. When the defect position varies from 0° to 180°, the M_S at every position of the axial path remains virtually constant. The peak M_S at the fillet weld is 447 MPa, while the M_S at the middle region of the sleeve remains 241 Mpa.

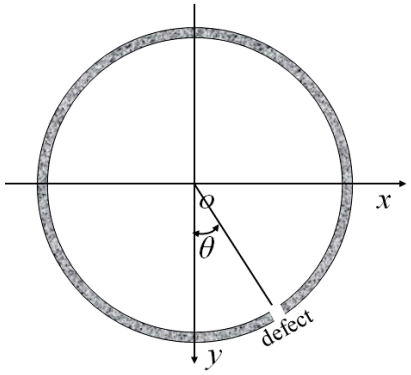

Figure 16. The defect location (θ) on the pipeline.

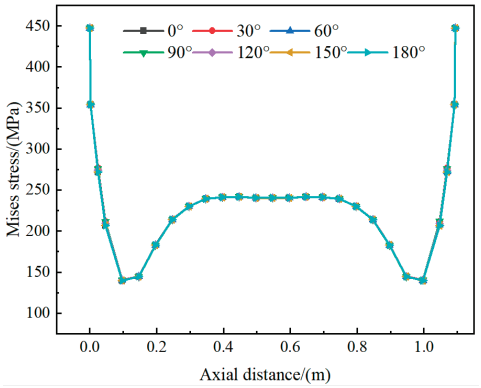

(**a**)

Figure 17. *Cont.*

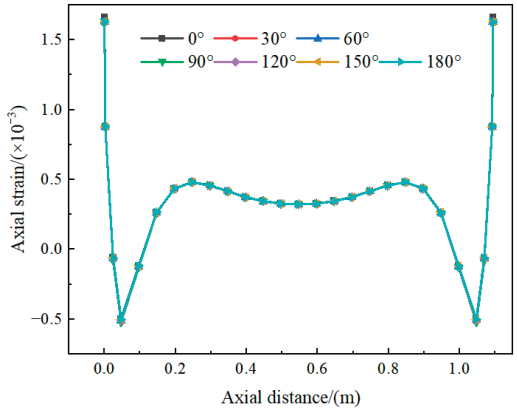

(**b**)

Figure 17. The Mises stress and axial strain distribution along the axial path. (**a**) The Mises stress distribution along the axial path. (**b**)The axial strain distribution along the axial path.

Along the axial reference path, for $\theta = 0°$, the ε_a at the fillet weld was 1.66×10^{-3}, which is shown in Figure 17b. However, an axial strain difference of only 0.03×10^{-3} is observed at the fillet weld between the defect at $\theta = 0°$and other positions, i.e., except for at $\theta = 0°$, the ε_a values appear to be the same at every point along the axial path. Therefore, the defect location on the pipeline is determined to have little relation with the load acting on the type-B sleeve.

The influence of defect location on the Mises stress and axial strain of the fillet weld along the circumferential path is shown in Figure 18. It can be found in Figure 18a that only minor changes are observed in M_S at each point on the circumferential path as the defect position shifts from 0° to 180°. For $\theta = 0°$, the M_S at the top and bottom of the fillet weld are 311 MPa and 453 Mpa, respectively. The relationship between the axial strain of the fillet weld and the defect location is shown in Figure 18b. It can be seen that ε_a at 90° and 270° on the circumferential path slightly fluctuates with the change in the defect position. For $\theta = 0°$ and 180°, the ε_a is 1.45×10^{-3} and 1.40×10^{-3}, respectively. In general, the load on the sleeve remains unchanged when the defect location changes. Therefore, the stress and strain distribution indicate that the location of the defect on the pipeline has little effect on the mechanical behavior of the type-B sleeve.

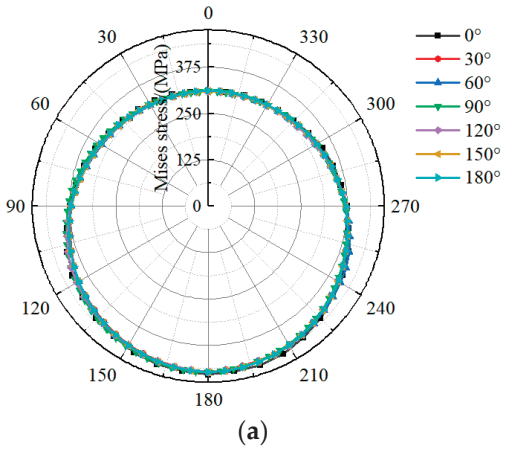

(**a**)

Figure 18. *Cont.*

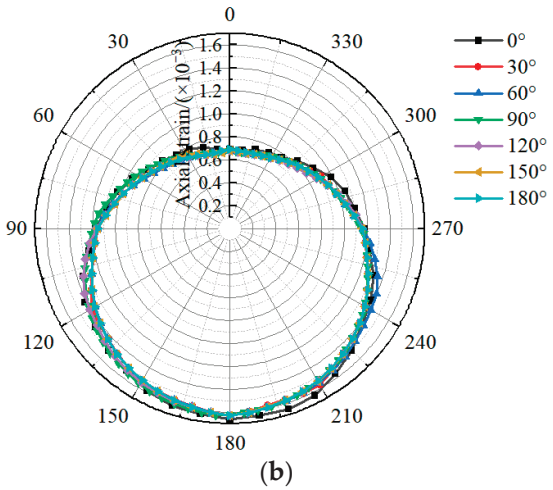

(**b**)

Figure 18. The Mises stress and strain of fillet weld along the circumferential path. (**a**) Mises stress distribution. (**b**) Axial strain distribution.

3.5. Effect of the Internal Pressure

Figure 19a illustrates the Mises stress at each point of the axial path with increasing internal pressure. As the internal pressure increases from 2 MPa to 12 Mpa, the M_S (i) at the fillet weld increases from 255 Mpa to 453 Mpa, and (ii) in the middle section of the sleeve increases from 77 Mpa to 241 Mpa.

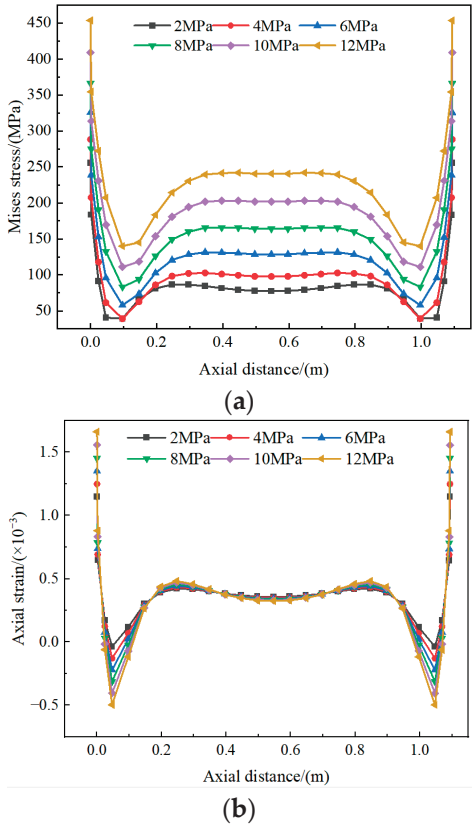

(**a**)

(**b**)

Figure 19. The effect of internal pressure on Mises stress and axial strain along the axial path. (**a**) Mises stress distribution. (**b**) Axial strain distribution.

Figure 19b shows that the axial strain at the ends of the sleeve increases with the internal pressure growing along the axial path, while that in the middle region of the type-B sleeve remains at 0.35×10^{-3}. At the fillet weld, the peak ε_a of the axial path is 1.15×10^{-3}

for the 2 MPa, which increases to 1.66 × 10^{-3} as the internal pressure reaches 12 Mpa. When the pressure is less than 2 Mpa, the axial strain is tensile along the axial path and gradually transitions from tensile to compressive at both ends of the sleeve as the internal pressure exceeds 2 Mpa.

Figure 20a shows that the Mises stress at every point on the circumferential path increases with growing internal pressure. When the internal pressure increases from 2 Mpa to 12 Mpa, the M_S at (i) the top of the fillet weld increases from 84 Mpa to 311 Mpa, and (ii) the bottom of the fillet weld increases from 255 Mpa to 453 Mpa. Similarly, for 2 Mpa, the ε_a at the top and bottom of the fillet weld are 0.32 × 10^{-3} and 1.15 × 10^{-3}, respectively, which increases 1.15 × 10^{-3} and 1.66 × 10^{-3}, respectively, as the pressure reaches 12 Mpa. Therefore, it is clear that the internal pressure has less impact on the axial strain at the top of the weld than at its bottom.

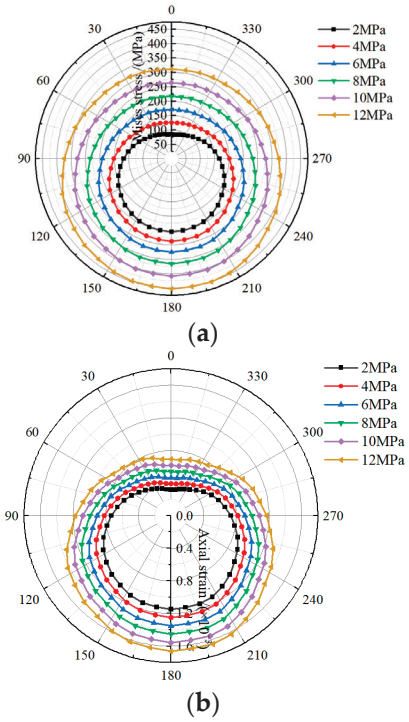

Figure 20. The Mises stress and axial strain along the circumferential path. (**a**) Mises stress distribution. (**b**) Axial strain distribution.

As Equations (11)–(13) show, the internal pressure applied on the pipeline and type-B sleeve is an important factor affecting the stress and strain. Radial stress, axial stress, and the circumferential stress caused by internal pressure can be expressed as:

$$\sigma_r = -p \tag{11}$$

$$\sigma_{ap} = \mu p(d - 2t)/2t \tag{12}$$

$$\sigma_c = \frac{p(d - 2t)}{2t} \tag{13}$$

where the σ_r, σ_{ap}, and σ_c are radial stress, axial stress, and circumferential stress, respectively; t is the pipeline wall thickness; μ is the Poisson's ratio.

3.6. Effect of the Suspended Pipeline Length

Figure 21a shows that the Mises stress at the fillet weld is 386 MPa for a suspended pipeline length of 100 m, which increases to 503 Mpa at a suspended pipeline length of 600 m. It also can be observed that the M_S at every point of the middle region of the type-B sleeve is equal between the suspended pipeline lengths of 200 to 500 m. Furthermore, the

M_S along the axial path also follows a similar trend for the suspended pipeline lengths of 100 and 600 m.

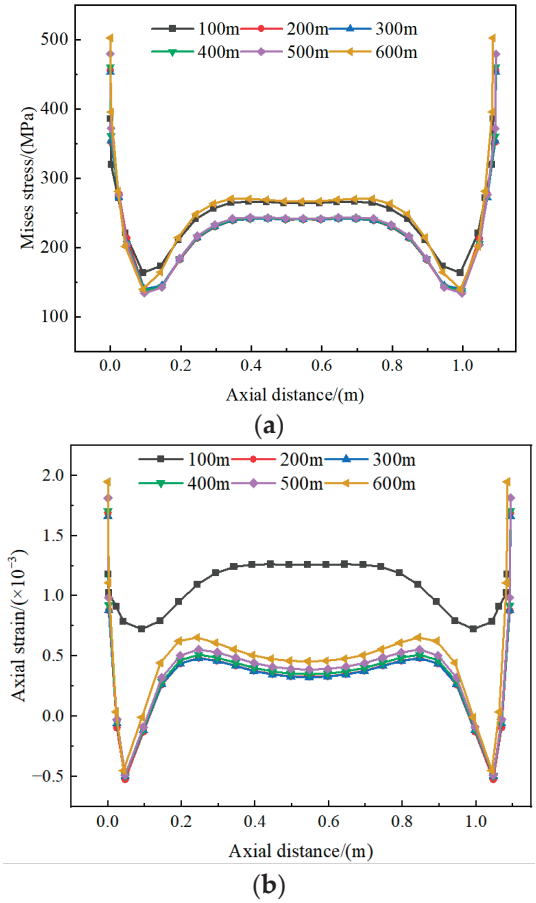

Figure 21. The Mises stress and axial strain distribution along the axial path. (**a**) Mises stress distribution; (**b**) Axial strain distribution.

As depicted in Figure 21b, along the axial path, the peak axial strain is observed at the fillet weld, and its value increases from 1.18×10^{-3} to 1.94×10^{-3} when the suspended pipeline length increases from 100 m to 600 m. When the suspended pipeline length is 100 m, the axial strain along the axial path remains tensile. However, tensile and compressive strains distribute along the axial path when the length of the suspended pipeline exceeds 200 m. The axial compressive strain value decreases only by 0.07×10^{-3} as the suspended pipeline length increases from 200 to 600 m.

Figure 22 illustrates the relationship between suspended pipeline length and Mises stress and axial strain along the circumferential path. It is found that as the suspended pipeline length increases from 100 m to 600 m, the M_S at the top and bottom of the fillet weld increases from 288 MPa to 416 Mpa and 386 Mpa to 502 Mpa, respectively (Figure 22a). Thus, the influence of suspended pipeline length on the Mises stress at the top of the fillet weld is higher than that at its bottom.

In Figure 22b, the ε_a distribution along the fillet weld reveals that the longer the suspended pipeline length, the greater the ε_a at each point of the fillet weld. When the suspended pipeline length is 100 m, the axial strain at the top point of the circumferential path is compressive, with a value of -0.39×10^{-3}. The axial strain at the bottom of the fillet weld increases from 1.27×10^{-3} to 1.95×10^{-3} as the suspended pipeline length increases from 100 m to 600 m.

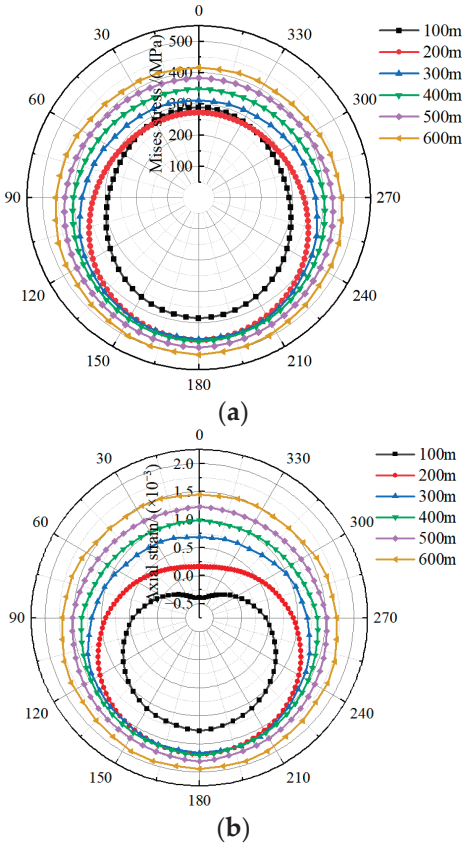

Figure 22. The Mises stress and axial strain distribution of fillet weld along the circumferential path. (**a**) Mises stress distribution; (**b**) Axial strain distribution.

The results show that the length of the suspended pipeline has an important effect on the mechanical behavior of the type-B sleeve, but an increase in suspended pipeline length may not always be harmful to the middle region of the sleeve.

4. Conclusions

In this study, a numerical model of a pipeline reinforced with a type-B sleeve was established while considering the effect of the pipeline–soil interaction and penetrating defect, and its mechanical behavior was investigated under suspension. The primary conclusions of our study are detailed as follows.

The strength of the defective pipeline significantly improved after repairing it with a sleeve. The Mises stress (i) around the defect decreased, and (ii) at the fillet weld increased after the type-B sleeve installation.

Due to the effects of the bending moment and shear force generated by suspension, peak Mises stress and axial strain values were observed at the ends of the suspended section of the pipeline, which were unaffected by the position of the type-B sleeve. Therefore, the closer the sleeve position is to the end of the suspended section, the greater the risk of failure.

A comparison of the Mises stress and axial strain distribution in the type-B sleeve structures revealed that the fillet weld is the most prone to failure. Natural gas pressure and suspended pipeline length are the key load factors affecting the mechanical behavior of the welds.

As the length of the sleeve increased from 1 to 3 m, the additional peak Mises stress and tensile axial strain values on the sleeve did not exceed 14 MPa and 0.06×10^{-3}, respectively.

When settlement occurs, the maximum Mises stress and axial strain values were observed at the fillet weld for the type-B sleeve structure; the axial strain alternated between tension and compression. Both Mises stress and axial strain experienced an increase with

the increasing suspended pipeline length, inter-al pressure, and type-B sleeve length, but they were almost independent of the defect location on the pipeline.

The results of this study suggest that reducing natural gas transportation pressure and optimizing sleeve structure parameters can diminish the risk of sleeve failure due to suspension.

Author Contributions: Conceptualization, G.Q.; Methodology, H.T. and Y.D.; Software, H.T., Y.D. and G.Q.; Validation, Z.L. and Z.D.; Formal analysis, Y.D.; Investigation, H.T.; Resources, G.Q. and Z.D.; Data curation, H.T. and G.Q.; Writing—original draft preparation, H.T. and Y.D.; writing—review and editing, H.T. and G.Q.; Visualization, H.T.; Supervision, Y.D.; Project administration, H.T. and Z.D.; Funding acquisition, H.T. All authors have read and agreed to the published version of the manuscript.

Funding: This work is supported by Key Projects of Civil Aviation Flight Academy of China (Grant: J2021-104) and Civil Aviation Administration Education Talent Program (Grant: MHJY2023025). The authors appreciated the support of Key Projects of Sichuan Vocational and Technical College of Architecture (Grant: 2022KJ04).

Data Availability Statement: Data are contained within the article.

Conflicts of Interest: Guangyou Qiu was employed by the Pipe China The remaining authors declare that the research was conducted in the absence of any commercial or financial relationships that could be construed as a potential conflict of interest. The authors declare that they have no known competing financial interests or personal relationships that could have appeared to influence the work reported in this paper.

References

1. Zhang, Y.M.; Yi, D.K.; Xiao, Z.M.; Huang, Z.H. Engineering critical assessment for offshore pipelines with 3-D elliptical embedded cracks. *Eng. Fail. Anal.* **2015**, *51*, 37–54. [CrossRef]
2. Zheng, Q.; Xu, Q.; Shu, Z.; Yang, D.; Chen, W.; Akkurt, N.; Zhang, H.; Lin, L.; Zhang, X.; Ding, Y. A review of advances in mechanical behaviors of the underground energy transmission pipeline network under loads. *Gas Sci. Eng.* **2023**, *117*, 205074. [CrossRef]
3. Zhang, J.; Gu, X.; Zhou, Y.; Wang, Y.; Zhang, H.; Zhang, Y. Mechanical properties of buried gas pipeline under traffic loads. *Processes* **2023**, *11*, 3087. [CrossRef]
4. Lim, K.S.; Azraai, S.N.A.; Yahaya, N.; Md Noor, N.; Zardasti, L.; Kim, J.J. Behaviour of steel pipelines with composite repairs analysed using experimental and numerical approaches. *Thin-Walled Struct.* **2019**, *139*, 321–333. [CrossRef]
5. Kec, J.; Černý, I.; Poloch, A.; Kyselá, B.; Poupa, M. Oil transmission pipelines with corrosion defects reinforced by two types of sleeves: Comparison efficiency of sleeves. *Procedia Struct. Integr.* **2022**, *37*, 598–605. [CrossRef]
6. Alexander, C.; Vyvial, B.; Wilson, F. Pipeline repair of corrosion and dents: A comparison of composite repairs and steel sleeves. In Proceedings of the 2014 10th International Pipeline Conference, Calgary, AB, Canada, 29 September–3 October 2014.
7. Huang, Z.; Tang, H.; Ding, Y.; Wei, Q.; Xia, G. Numerical simulations of temperature for the in-service welding of gas pipeline. *J. Mater. Process. Technol.* **2017**, *248*, 72–78. [CrossRef]
8. Vafaei, M.; Mashhuriazar, A.; Omidvar, H.; Sajuri, Z. In-service welding of X70 steel gas pipeline: Numerical and experimental investigations. *J. Mater. Res. Technol.* **2023**, *26*, 6907–6918. [CrossRef]
9. Arif, A.; Al-Nassar, Y.; Al-Qahtani, H. Optimization of Pipe Repair Sleeve Design. *J. Press. Vessel. Technol.* **2012**, *134*, 051702. [CrossRef]
10. Shuai, Y.; Wang, X.; Wang, J.; Yin, H.; Cheng, Y.F. Modeling of mechanical behavior of corroded X80 steel pipeline reinforced with type-B repair sleeve. *Thin-Walled Struct.* **2021**, *163*, 107708. [CrossRef]
11. Sabapathy, P.N.; Wahab, M.A.; Painter, M.J. The prediction of burn-through during in-service welding of gas pipelines. *Int. J. Press. Vessel. Pip.* **2000**, *77*, 669–677. [CrossRef]
12. Yu, C.; Han, C.; Xie, R.; Wang, L. Mechanical behavior analysis of buried pipeline under stratum settlement caused by underground mining. *Int. J. Press. Vessel. Pip.* **2020**, *188*, 104212. [CrossRef]
13. Liu, M.; Ortega, R. Assessment of impact to buried pipelines due to tunneling-induced settlement. *J. Pipeline. Syst. Eng. Pract.* **2023**, *14*, 04023020. [CrossRef]
14. Ma, C.; Cheng, X.; Xu, T. Research on local buckling failure range of X80 buried steel pipeline under oblique-reverse fault. *Soil Dyn. Earthq. Eng.* **2023**, *164*, 107592. [CrossRef]
15. Zhang, J.; Xie, R. Mechanical Behavior analysis of suspended Pipelines caused by ground subsidence. *J. Pipeline. Syst. Eng. Pract.* **2021**, *12*, 04021030. [CrossRef]
16. Shuai, Y.; Wang, X.; Cheng, Y. Buckling resistance of an X80 steel pipeline at corrosion defect under bending moment. *J. Nat. Gas. Sci. Eng.* **2021**, *93*, 104016. [CrossRef]

17. Cheng, X.; Ma, C.; Huang, R.; Huang, S.; Yang, W. Failure mode analysis of X80 buried steel pipeline under oblique-reverse fault. *Soil Dyn. Earthq. Eng.* **2019**, *125*, 105723. [CrossRef]
18. Shang, B.; Li, C.; Lu, H. Stress analysis of suspended gas pipeline segment. *J. Pipeline Syst. Eng. Pract.* **2017**, *8*, 04017003. [CrossRef]
19. Zhang, B.; Chen, F.; Wang, Q. Analytical model of buried beams on a tensionless foundation subjected to differential settlement. *Appl. Math. Model.* **2020**, *87*, 269–286. [CrossRef]

processes

MDPI

Article

Improving Ammonia Emission Model of Urea Fertilizer Fluidized Bed Granulation System Using Particle Swarm Optimization for Sustainable Fertilizer Manufacturing Practice

Norhidayah Mohamad [1,*], Nor Azlina Ab. Aziz [1], Anith Khairunnisa Ghazali [1] and Mohd Rizal Salleh [2]

[1] Faculty of Engineering & Technology, Multimedia University, Melaka 75450, Malaysia; azlina.aziz@mmu.edu.my (N.A.A.A.); anith.ghazali@mmu.edu.my (A.K.G.)
[2] Faculty of Manufacturing Engineering, Universiti Teknikal Malaysia Melaka, Hang Tuah Jaya, Durian Tunggal, Melaka 76100, Malaysia; rizal@utem.edu.my
* Correspondence: norhidayah.mohamad@mmu.edu.my

Abstract: Granulation is an important class of production processes in food, chemical and pharmaceutical manufacturing industries. In urea fertilizer manufacturing, fluidized beds are often used for the granulation system. However, the granulation processes release ammonia to the environment. Ammonia gas can contribute to eutrophication, which is an oversupply of nitrogen and acidification to the ecosystems. Eutrophication may cause major disruptions of aquatic ecosystems. It is estimated that global ammonia emissions from urea fertilizer processes are approximately at 10 to 12 Tg N/year, which represents 23% of overall ammonia released globally. Therefore, accurate modeling of the ammonia emission by the urea fertilizer fluidized bed granulation system is important. It allows for the system to be operated efficiently and within sustainable condition. This research attempts to optimize the model of the system using the particle swarm optimization (PSO) algorithm. The model takes pressure (Mpa), binder feed rate (rpm) and inlet temperature (°C) as the manipulated variables. The PSO searches for the model's optimal coefficients. The accuracy of the model is measured using mean square error (MSE) between the model's simulated value and the actual data of ammonia released which is collected from an experiment. The proposed method reduces the MSE to 0.09727, indicating that the model can accurately simulate the actual system.

Keywords: particle swarm optimization; ammonia emission; granulation; urea fertilizer

1. Introduction

Granulation is an important step in the manufacturing process of food, chemicals and pharmaceuticals. It is used to make the individual solute particles in fluid mixtures flock together in bigger entities called grains or granules. Granulation occurs through the creation of bonding between the solid powder particles. The bonding of the powder particles can be induced through the application of a binding agent. The transformation of the powder particles into granules allows the tableting process to produce tablets of required quality at the required tablet press speed range [1,2]. The granulation process is also instrumental in urea fertilizer production. Urea fertilizer stands out as the most widely utilized solid nitrogenous fertilizer globally due to its excellent water solubility [3,4]. Compared to other nitrogenous fertilizers, urea provides a higher quantity of nitrogen to plants and soil owing to its concentrated nitrogen content of 46%. In Malaysia, urea fertilizer subsidies are provided by the government to assist farmers in gaining better productivity [5]. The effectiveness of urea-based fertilizer in improving productivity and yield of maize and paddy is reported in [6] and [7], respectively.

Although urea is proven to be a good fertilizer, its usage and production pose risks to the environment, including the release of ammonia gas. A study conducted at paddy field of Jiangxi Province China from 2019 to 2021 observed that ammonia volatilization

increases after fertilization [8]. Another study from China, which was conducted at the Jiangsu Province from 2000 to 2017 in [9], reported that among the main cause of ammonia emissions by agriculture sector is the nitrogen fertilizer. Specifically, urea and ammonium bicarbonate from nitrogen fertilizer contribute around 80% of the ammonia emissions. In addition to the emission from the application of the fertilizer itself, the urea granulation process also contributes to ammonia emissions. Figure 1 shows the reaction process of fluid bed granulation where the ammonia gas is released during the mixing of urea powder with the urea binder solution. The ammonia gas is formed when the urea solution is heated under high pressure. The ammonia gas is released to the environment through the output ventilation from the fluid bed granulation's chamber.

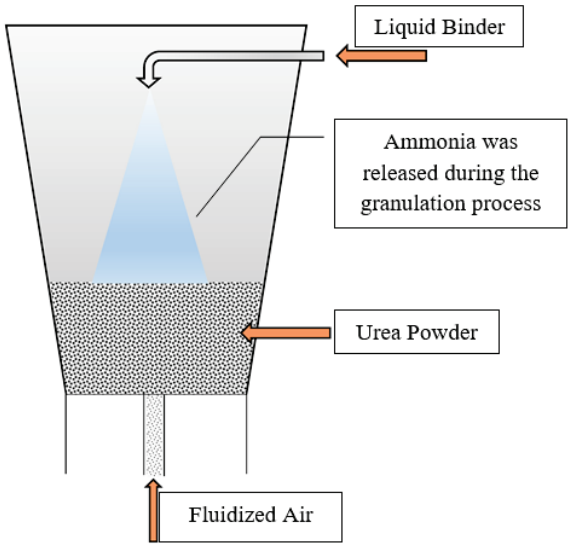

Figure 1. Schematic of fluidized bed granulation process.

The ammonia gas can be highly poisonous and has a multitude of impacts on a variety of live beings [10]. For humans, inhaling ammonia vapor poses risks such as irritation and corrosive damage to the skin, eyes and respiratory tracts. Inhalation of very high levels can even be fatal. When dissolved in water, the elevated levels of ammonia are also toxic to a wide range of aquatic organisms. Ammonia can also contribute to eutrophication, an oversupply of nitrogen and acidification to the ecosystems.

Optimal manufacturing of urea fertilizer is important. It not only helps to improve effectiveness of the urea absorption for better plant growth [11], but also minimizes the negative impact to the environment including the amount of ammonia gas pollution. Therefore, this research focuses on minimizing the amount of ammonia gas released by the urea fertilizer fluidized bed granulation system without affecting the quality of urea granules. This is achieved through the utilization of optimal modeling of the fluidized bed granulation system. Mathematical modeling is popularly used across all fields to represent a system or a process. For example, the modeling of capacitance of a supercapacitor is discussed in [12], the spraying process of an electrostatic oiling machine is modeled in [13] and the model of reservoir operation is reported in [14].

Here, urea fertilizer fluidized bed granulation system model parameters are optimized using particle swarm optimization (PSO) with three manipulated variables, namely pressure (Mpa), binder feed rate (rpm) and inlet temperature (°C). The readers are referred to our earlier work [15] for details on the previously developed model using the Response Surface Method (RSM). The developed model is using a quadratic polynomial model. RSM is popularly used for modeling. It is useful in finding empirical relations and the effect of each parameter and their interactions on the responses considered [16]. In [17], an attempt was made to study radial gas mixing in a fluidized bed using RSM to determine

the relationship between radial gas mixing and operating conditions in the bubbling or slugging fluidization regimes.

In this work, the modeling problem is formulated as a 10-dimensional minimization problem with PSO [18] is used as the optimizer. PSO is frequently used in optimization of a mathematical model. PSO is used for parameter optimization of a simulated biological system in [19]. In another work [20], PSO is used to model the pH of a hydroponics system for better plant growth. PSO is also used for optimizing the susceptible, infected and resistant (SIR) models of infections in [21]. In [22,23], PSO is used for the optimization of parameters of a controller system model. Meanwhile, PSO is used for modeling of a single link flexible manipulator in [24]. These works show that PSO is a powerful algorithm towards optimizing and improving mathematical models. PSO is a black box modeling technique that is simpler compared to the traditional method [24]. Additionally, the traditional modeling method is more suitable for a linear system [22]. The success of PSO in optimum modeling of various systems and its advantages motivates this research. The optimized model of the fluidized bed granulation system is validated by comparing the simulation data with the experiment data. The model's best mean square error (MSE) is 0.09727, which shows the high accuracy of the model.

This work is presented in four sections. The methodology is presented in Section 2. The experimental setting is discussed in Section 3. This is followed by the results and discussion section. Lastly, the work is concluded, and future direction is discussed in Section 5.

2. Related Works

Mathematical modeling of fertilizer systems had been adopted by existing works for various perspectives. For example, Lipin et al. [25] created an inclusive model to forecast nutrient release from controlled release fertilizers (CRF) that incorporates all three release stages: (1) the initial stage of liquid infiltration in the coating layer, (2) the constant release stage where solid fertilizer exists in the core and (3) the gradual decay release stage when there is no more solid fertilizer in the core. This model consists of the computation of three coefficients: the water and nutrient diffusion coefficients within the coating layer as well as the coating material's limiting water absorption capacity. It provides the capacity to predict the rate of nutrient release, the cumulative release pattern for all release phases and coating types, presuming a diffusion-based release mechanism. The model reveals accurate simulation of nitrogen release from polymer-coated particles by investigating various coated urea types. It also predicts moisture content profiles and nutrient solution concentration profiles within the coated layer for lag, linear and decay times, as well as nutrient concentration in the aquatic environment.

Guo et al. [26] proposed mathematical models to describe the synthesis of urea–formaldehyde fertilizers with varying nitrogen release properties. This research employs a central composite design (CCD) of response surface methodology to investigate the impact of reaction times, temperatures and molar ratios on the solubility of nitrogen in hot or cold water. The results indicate that the solubility of nitrogen in water, whether cold or hot, from urea–formaldehyde fertilizers is mostly influenced by the molar ratios of urea to formaldehyde. Additionally, mathematical models based on quadratic polynomials are developed for urea–formaldehyde. The model is beneficial towards precise synthesis of urea–formaldehyde fertilizers. Similarly, nutrient release by spherical coated fertilizer granules was modeled in [27]. The model takes into consideration the granule's radius, contact area and diffusivity towards the fertilizer saturation and release time.

Meanwhile, an approach that focused on modeling the effectiveness of ridge–furrow film mulching and nitrogen fertilizer towards improving maize production quality was proposed in [28]. The model was developed using data collected in Loess Plateau, China. The authors reported that optimization of the model parameters contributes towards accurate modeling the maize grain filling process at different application rates of the fertilizer. The effectiveness of nitrogen, phosphorus and potassium fertilizer application

for growth of HB16 winter cauliflower is modeled in [29]. The model can determine the optimal fertilizer usage for achieving production target. This helps sustainable agriculture practice and avoids waste.

A review paper by Irfan et al. [30] highlighted the importance of mathematical modeling in developing more efficient fertilizers and understanding the release of nutrients from controlled release fertilizers (CRFs). The research emphasized how mathematical modeling may be used to anticipate and visualize nutrient release characteristics. It also stressed the need to have an extensive knowledge of the physiological and chemical processes that lead to nutrient release. Two categories of models are differentiated: mechanistic models and empirical models. The mechanistic models look into the coating material and nutrient contained inside the granule, while empirical models focus on moisture and temperature. On the other hand, Haydar et al. [31] in their review focused on the model for physiochemical parameters for slow and controlled release nanofertilizers such as the water retention and absorption capacity, the swelling ratio, the loading and nutrient use efficiency and several other parameters. The models offer quick predictions without the need to conduct actual experiment, thus providing time- and cost-effective solutions.

Swain et al. [32] investigated the performance of six machine learning algorithms, support vector machine, artificial neural network, random forest, M5 tree (M5P), reduced error pruning tree (REPTree) and surface response, in predicting and optimizing nitrate leaching from urea super granules (USGs). They explored various factors such as binding materials, binding agents and coating curing times as primary predictors. Some algorithms exhibited high efficacy in predicting nitrate leaching, but there is potential to enhance these models further by incorporating advanced optimization methods like genetic algorithms and particle swarm optimization. High prediction accuracy helps in determining the best amount of fertilizer to be used which is cost effective as well as reducing risk of pollution via nitrate leaching.

In contrast to the works reviewed above, the work by Duffuan [33] explored another angle of modeling for ammonia and urea fertilizer manufacturing. The author explored the modeling of federate with respect to the cost of the fertilizer manufacturing operation. The author reported that the model can help in choosing the best setting that helps in reducing the operational cost of the fertilizer plant.

Although there has been notable advancement in fertilizer modeling such as the release of nutrients, there is still limited work that focuses on modeling the manufacturing process of fertilizer, especially modeling the impacts of the manufacturing process on environment, specifically ammonia release. Moreover, in optimizing the models, an optimal model is expected to make a significant contribution to formulating the best sustainable manufacturing practice.

3. Materials and Methods

3.1. The Mathematical Model of Fluidized Bed Granulation System

The mathematical model is developed based on the lab scale fluidized bed granulation shown in Figure 2a, whilst the schematic diagram of the system is shown in Figure 2b. In the schematic diagram, Section (1) is the granulator chamber, Section (2) is the ammonia measure channel and Section (3) is the binder feed line.

A quadratic polynomial model is used to model the system in the study using RSM [15]. The general form of the quadratic equation model is shown in Equation (1) below,

$$Y = \alpha_0 + \sum_{i=1}^{n} \alpha_i X_i + \sum_{i=1}^{n} \alpha_{ii} X_i^2 + \sum_{i=1}^{n-1} \sum_{j=i+1}^{n} \alpha_{ij} X_i X_j, \quad (1)$$

where Y is the objective function or response which is the amount of ammonia release while X_i are operating parameters or factors. The number of parameters is represented by

n. In this work, there are three parameters: pressure (Mpa), binder feed rate (rpm) and inlet temperature (°C). Thus, the Equation (1) can be written as Equation (2):

$$Sim = a + bx + c\left(x^2\right) + dy + e\left(y^2\right) + f(z) + g\left(z^2\right) + hxy + ixz + jyz \quad (2)$$

Based on Equation (2), the symbols of x, y and z represent the temperature, binder volume and pressure, respectively. Sim is the predicted ammonia released by the model. The coefficient values a, b, c, d, e, f, g, h, i and j in Equation (2) are chosen here by PSO.

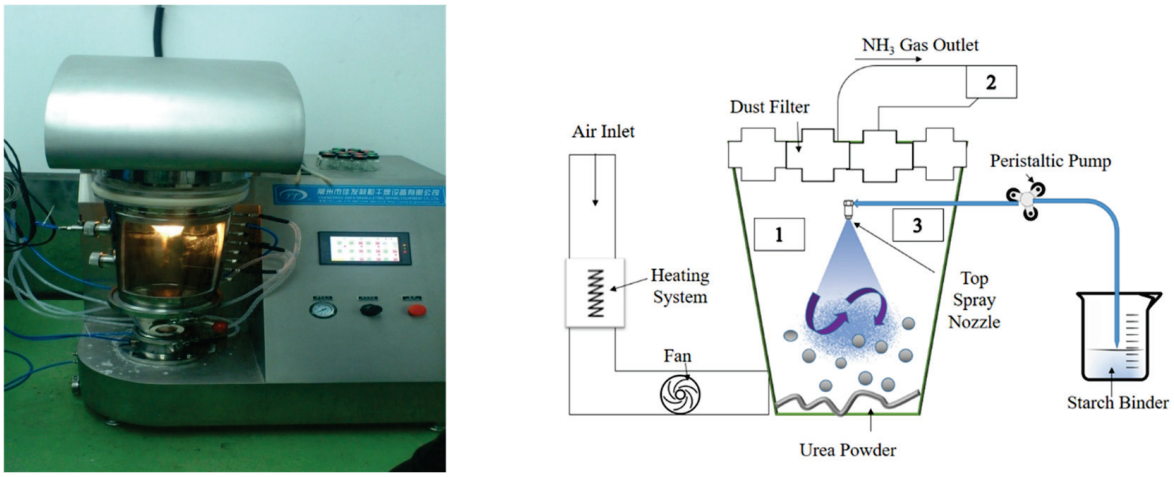

Figure 2. (**a**) Lab scale fluidized bed granulation system. (**b**) Schematic diagram of the system.

3.2. Model Optimization Using PSO

PSO is a swarm intelligence algorithm where a group of particles work together to search for the optimal solution. In this case, these are the coefficient values of the polynomial equation.

The algorithm of PSO starts with random initialization of the population. Here, the particles are randomly initialized between 0 and 1. After random initialization, the algorithm enters the iterative procedure of velocity and position update. The particle's velocity, v_{id}, is updated according to Equation (3).

$$v_{id} = \omega v_{id} + c_1 r1_{id}(p_{id} - x_{id}) + c_2 r2_{id}\left(p_{gd} - x_{id}\right) \quad (3)$$

$$\omega = -\frac{\omega_{max} - \omega_{min}}{\max\_iter} + \omega_{max} \quad (4)$$

Subscripts i and d in the equation represent particle number and parameter numbers, respectively. Since the model here has 10 coefficients to be optimized, $d = \{1, 2, 3, \ldots, 10\}$. c_1 and c_2 are cognitive and social coefficients. They control the influence of the particle's own best experience p_{id} and the swarm's best solution so far, p_{gd}. Typically, both values are set to 2, giving balance influence. Inertia weight ω controls the momentum of the particle from previous search. Linear decreasing inertia weight is adopted in this work to encourage exploration during the initial search process and later switch to fine tuning. The equation for inertia weight update is shown Equation (4), where ω_{max} and ω_{min} are the maximum (start) and minimum (end) values of inertia weight and max_$iter$ is the number of iterations of the algorithm. PSO is a stochastic algorithm. The randomness of the algorithm is presented by random values $r1_{id}$ and $r2_{id}$ between 0 and 1.

Velocity is used to update the particle's position, x_{id}, which is shown in Equation (5).

$$x_{id} = x_{id} + v_{id} \quad (5)$$

The particle *i*th position represents a potential solution. The iterative procedure of updating the particle's velocity, position and fitness evaluation continues until the stopping condition is reached, which is the maximum iteration number. The PSO algorithm is shown in Figure 3.

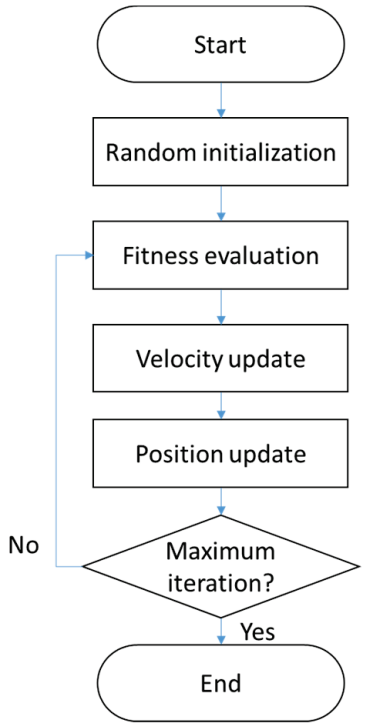

Figure 3. PSO algorithm.

3.3. Particle Encoding

The PSO particles are encoded according to the modeling problem to be optimized here. Each dimension of a particle represents a parameter in the model (Equation (2)). Particle encoding is illustrated in Figure 4.

x_{i1}	x_{i2}	x_{i3}	x_{i4}	x_{i5}	x_{i6}	x_{i7}	x_{i8}	x_{i9}	x_{i10}
a	b	c	d	e	f	g	h	i	j

Figure 4. Encoding of particle *i*.

3.4. Fitness Function

The fitness of quality of the solution proposed by PSO is evaluated using mean square error (MSE) shown in Equation (6).

$$MSE = \frac{1}{N}\sum_{k=1}^{N}(Y_{act\_k} - Sim_k)^2 \quad (6)$$

In Equation (6), N represents the amount of data from the experiment conducted to measure the ammonia released, Y_{act}, by the lab scale fluidized bed granulation system. The objective of PSO is to minimize MSE to a value closer to 0.

4. Experimental Setting

Based on the design of the experiment (DOE), the potential ammonia released was collected for modeling the fluidized bed granulation system. The data were obtained through continuously injecting the binder liquid into the blended urea powder at a temperature between 40 °C and 95 °C. The injected blended urea powder was agglomerated and

transformed into urea granules. Approximately 75% of the binder liquid that was heated under the vacuum chamber at these pressure ranges produced a vapor and formed urea granules. The remaining urea powder and air supplied from the fluidized bed granulation were then removed from the machine into the ventilation outlet using the fan. The urea with the water solution then was discharged as ammonia to the atmosphere.

The urea powder in the chamber emitted as ammonia when it was exposed to the high pressure and temperature. The binder feed rate was set to two settings: 4 rpm and 6 rpm. The fluidized bed pressure was set to 200 kPa, 400 kPa and 600 kPa. The mixture was heated and temperature was consistently increasing throughout the urea granulation process, which released ammonia into the environment. The ammonia readings were continuously collected for every single minute interval. In total, 238 readings were recorded. The collected readings are reported in units of ppm. The readings showed that there was gradual increase in the amount of ammonia gas released from this process until it reached a temperature of 65 °C, and a downward trend was also shown afterward due to the depletion of urea binder reagents. The collected ammonia released value was used for the data points of modeling the system.

PSO was implemented using MATLAB. The parameters used for the modeling are shown in Table 1. The algorithm was run 30 times; average and best results were recorded.

Table 1. PSO parameter values.

Parameter	Value
No. of particles	30
Max. iteration, max_*iter*	5000
ω	0.9–0.5 (linear decreasing)
$[c_i,\ c_2]$	[2, 2]

5. Results and Discussion

The MSE of the swarm's best at the end of iteration for each run is recorded. The average of MSE for the 30 runs is 24.2435. The best solution found by PSO among all the run has an MSE of 0.0973, which is close to zero. The error range between the ammonia predicted by the best model and the actual data collected during the experiment is [0.0026, 0.9468]. The small MSE indicates the accuracy of the model in simulating the actual fluidized bed granulation system while the small range shows the stability of the model over various settings of the fluidized bed granulation system. The best MSE and the average MSE observed are presented in Table 2. The coefficients' values that offer the best MSE are shown in Table 3.

Table 2. MSE of the model.

Results	Value
Best MSE	0.0973
Average MSE	24.2435
Error range of the best model	[0.0026, 0.9468]

Table 3. Fit summary for model value.

a	*b*	*c*	*d*	*e*	*f*	*g*	*h*	*i*	*j*
0.0069	0.4576	1.0702	−2.9929	1.0510×10^{-10}	-6.6921×10^{-5}	−0.18571	-9.3845×10^{-7}	7.8564×10^{-6}	4.5556

Figures 5 and 6 show the surface plot of predicted ammonia release using the best model over temperature under different feed rate and pressure values. The data collected via the experiment are plotted in blue. The results show that the predicted values of ammonia gas released are significantly close with the actual data from the experiment. It is obvious from the graph that the predicted value from the model had a small discrepancy with the experimental data.

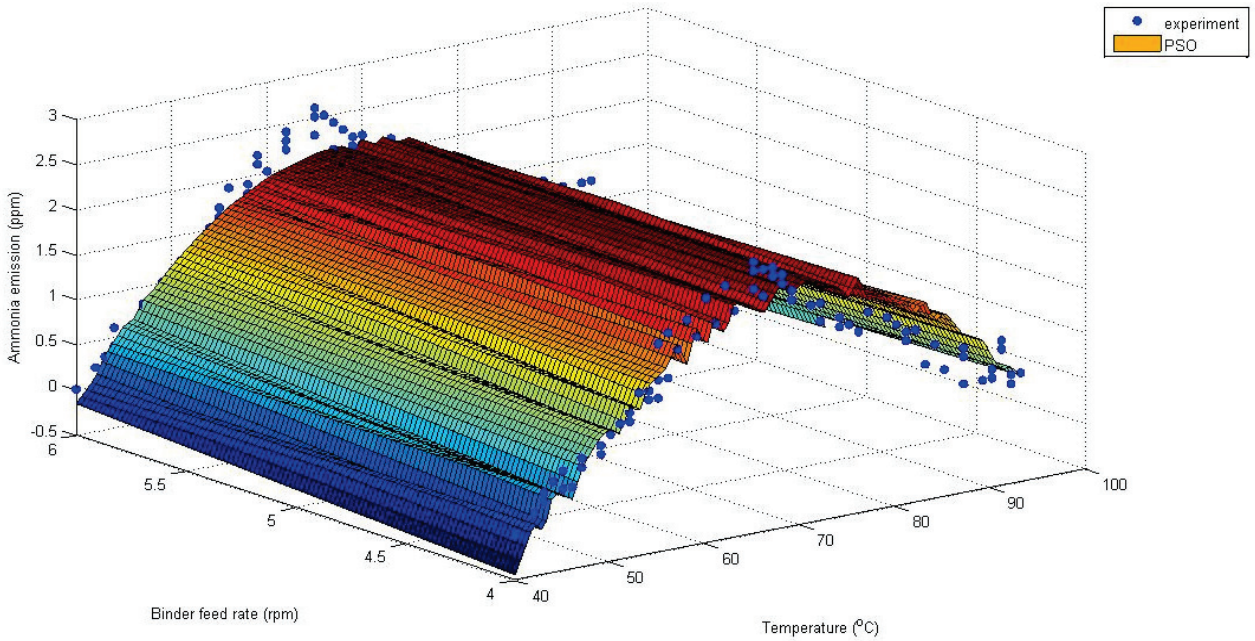

Figure 5. Ammonia emission predicted (PSO) and actual (experiment) vs. temperature over two different binder feed rates.

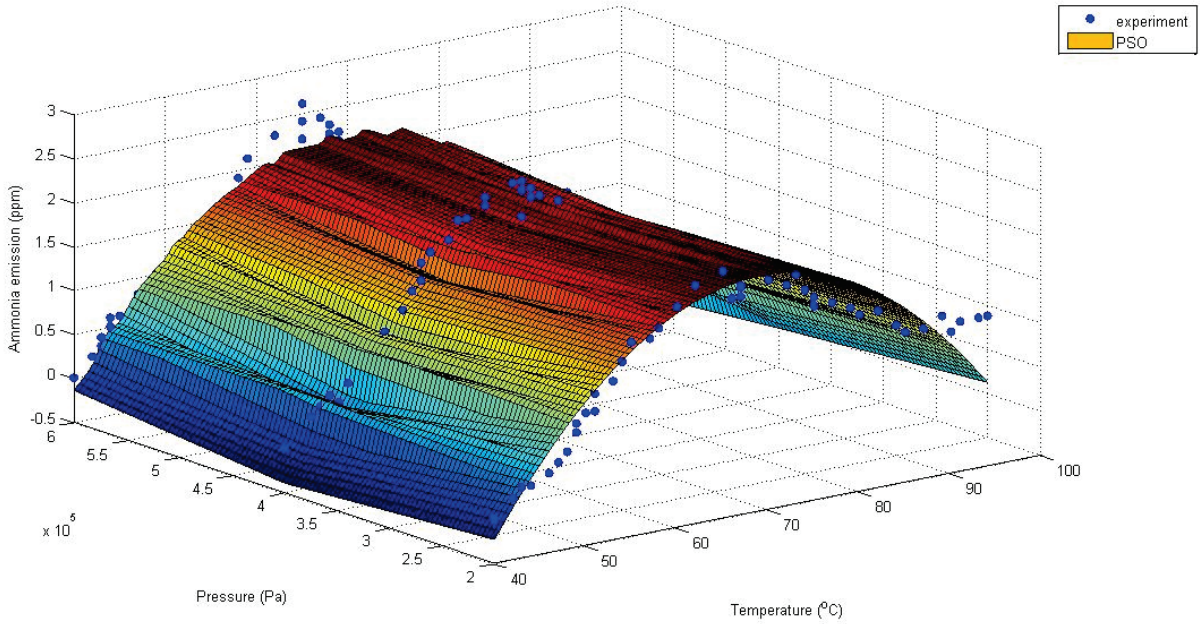

Figure 6. Ammonia emission predicted (PSO) and actual (experiment) vs. temperature over three different pressures.

Figure 7 shows a two-dimensional graph of the best model's predicted ammonia release in comparison with the actual value collected from the experiment for a clearer

view on the fitting of the quadratic model based on the optimized parameters. It can be seen that the model has a good fit for prediction of ammonia emission of less than 2 ppm. The error is higher for greater values of ammonia emission.

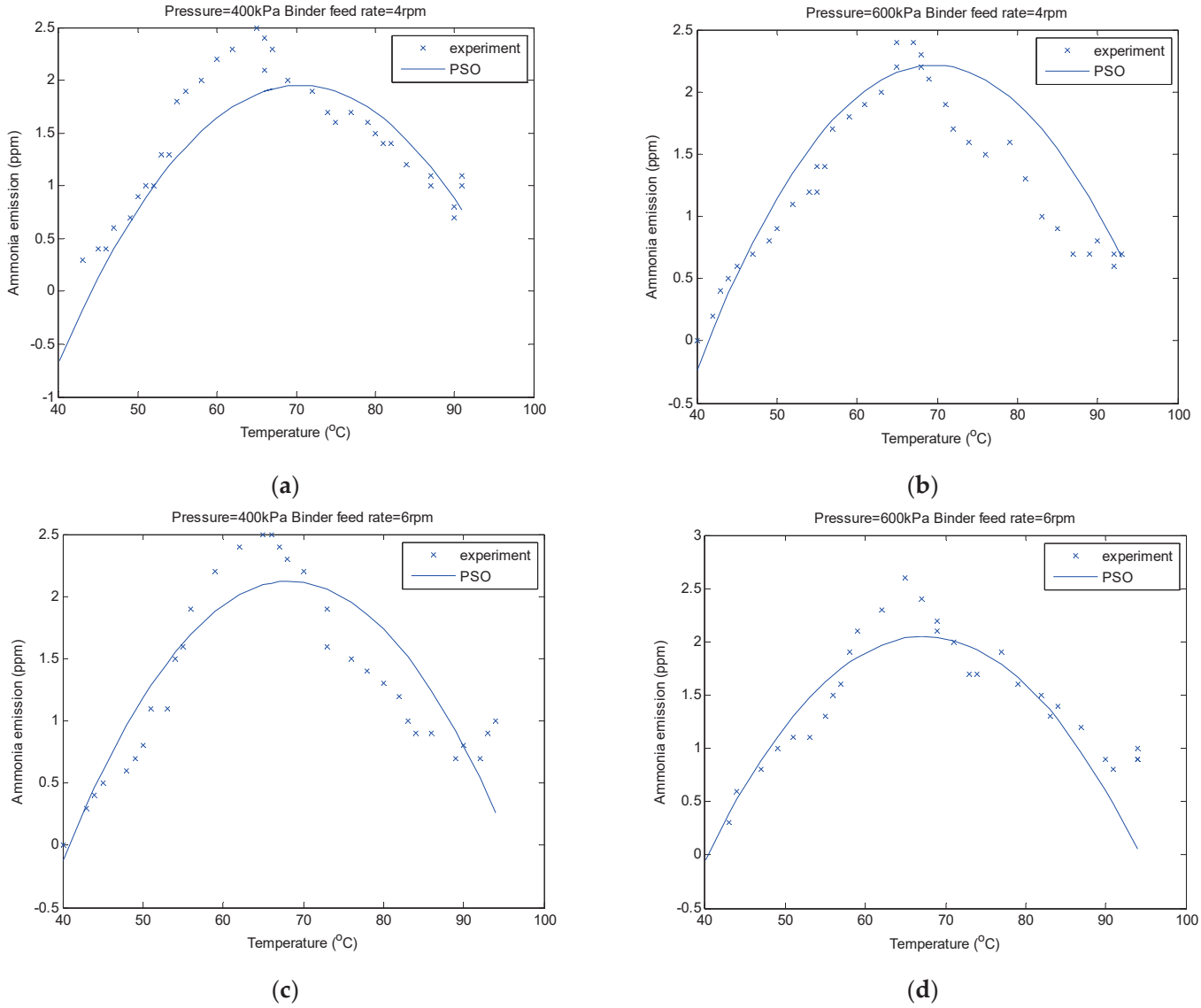

Figure 7. Ammonia emission predicted (PSO) and actual (experiment) vs. temperature over different pressure and feed rate settings (**a**) 400 kPa, 4 rpm (**b**) 600 kPa, 4 rpm, (**c**) 400 kPa, 6 rpm (**d**) 600 kPa, 6 rpm.

The swarm behavior can be observed via the convergence curve of the MSE vs. iteration in Figure 8. It is observed that both average and the best solution's MSE values gradually decrease. No premature convergence is observed. This is contributed by the chosen inertia weight. The decreasing inertia weight allows the swarm to balance between exploration and exploitation, which contributes towards minimizing the MSE efficiently.

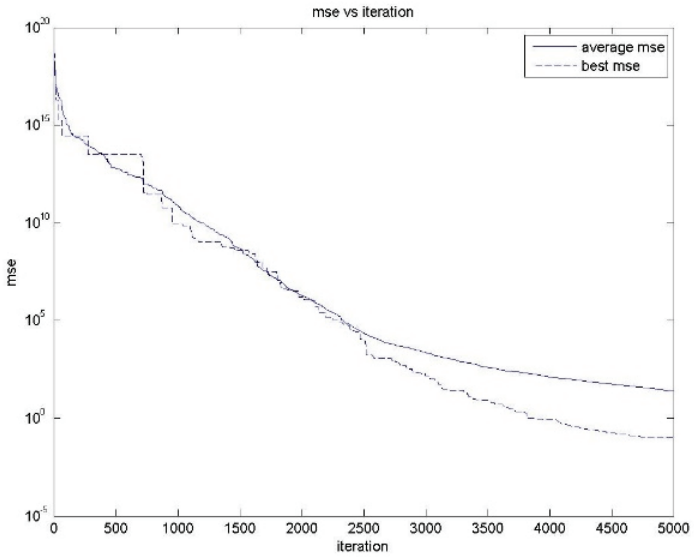

Figure 8. MSE vs. iteration.

6. Conclusions

PSO is employed in this research to optimize the model of the top-spray fluidized bed granulator. Three significant variables, namely binder feed rate, pressure and temperature, are selected for investigating the proposed optimization of the fluidized bed granulation model. The quadratic polynomial model is used for modeling and PSO is applied to search for the optimal coefficients. The optimized model performances are measured and validated using the MSE with respect to the actual experimental data. The best MSE is small and close to zero, 0.0973. Hence, it can be concluded that the developed model can be used to predict the minimum amount of ammonia gas released accurately with slight variation of the actual value.

The findings of this research show that PSO can be efficiently applied in designing an optimal mathematical model of a fertilizer's fluidized bed granulation system. The mathematical model can be used for improved, sustainable and healthy green manufacturing of bio-fertilizer. Specifically, the developed model enables sustainable production of the urea fertilizer with advanced parameter setting. The manufacturing with optimal parameter setting allows for fertilizer production with least ammonia emission and low risk of environmental pollution.

Based on the no-free lunch theorem, there is possibility that other optimization algorithms can solve this parameter optimization better than the PSO with linearly decreasing inertia applied here. Hence, in future studies, we will investigate the application of other optimization algorithms in solving this problem. Additionally, with more data, machine learning techniques such as artificial neural networks or regression can be considered alongside PSO to improve predictive capabilities. A dynamic model that considers temporal fluctuations, sensitivity analysis to identify crucial parameters and multi-objective optimization that takes into account things like production cost and the energy use could help to improve the system even more. Accounting for uncertainties, experimental validation and the use of sophisticated control methods such as model predictive control are to be considered for better sustainable manufacturing practice.

Author Contributions: N.M. and N.A.A.A. contributed to experimental design, analysis writing and editing. N.A.A.A., A.K.G. and M.R.S. contributed to validation, review, visualization and investigation. Project administration was prepared by N.M. All authors have read and agreed to the published version of the manuscript.

Funding: This research is funded by the Ministry of Higher Education of Malaysia under the Fundamental Research Grant Scheme (FRGS/1/2012/TK06/MMU/03/7) and the Multimedia University IR Fund (MMUI/230034).

Data Availability Statement: The data utilized in this study can be accessed for research purposes by contacting the corresponding author.

Acknowledgments: We extend our gratitude to Multimedia University and Universiti Teknikal Malaysia Melaka for their support in facilitating this research.

Conflicts of Interest: The authors declare no conflicts of interest.

References

1. Fries, L.; Antonyuk, S.; Heinrich, S.; Niederreiter, G.; Palzer, S. Product design based on discrete particle modeling of a fluidized bed granulator. *Particuology* **2014**, *12*, 13–24. [CrossRef]
2. Moraga, S.V.; Villa, M.P.; Bertín, D.E.; Cotabarren, I.M.; Piña, J.; Pedernera, M.; Bucalá, V. Fluidized-bed melt granulation: The effect of operating variables on process performance and granule properties. *Powder Technol.* **2015**, *286*, 654–667. [CrossRef]
3. Swify, S.; Mažeika, R.; Baltrusaitis, J.; Drapanauskaitė, D.; Barčauskaitė, K. Review: Modified Urea Fertilizers and Their Effects on Improving Nitrogen Use Efficiency (NUE). *Sustainability* **2024**, *16*, 188. [CrossRef]
4. Korsakov, K.; Stepanov, A.; Pozdnyakov, L.; Yakimenko, O. Humate-Coated Urea as a Tool to Decrease Nitrogen Losses in Soil. *Agronomy* **2023**, *13*, 1958. [CrossRef]
5. Alam, M.M.; Toriman, M.E.B.; Siwar, C.; Molla, R.I.; Talib, B. The impacts of agricultural supports for climate change adaptation: Farm level assessment study on paddy farmers. *Am. J. Environ. Sci.* **2011**, *7*, 178–182. [CrossRef]
6. Swify, S.; Avizienyte, D.; Mazeika, R.; Braziene, Z. Nitrogen Uptake and Maize Productivity. *Plants* **2022**, *11*, 3020. [CrossRef] [PubMed]
7. Akter, A.; Islam, M.R.; Islam, M.R.; Islam, A.; Hasan, S.L.; Uddin, S.; Rahman, M.M. Methods of Urea Fertilizer Application Influence Growth, Yield, and Nitrogen Use Efficiency of Transplanted Aman Rice. *Water* **2022**, *14*, 3539. [CrossRef]
8. Luo, W.; Li, Y.; Yang, Z.; Wang, Y.; Chen, J.; Xiao, X.; Chen, Y.; Wei, C.; Zou, Z. Water and Nitrogen Balance under Various Water and Fertilizer Regulation Modes. *Agronomy* **2023**, *13*, 2870. [CrossRef]
9. Huang, J.; Xiong, R.; Fang, L.; Li, T.; Shen, W. Estimation of interannual trends of ammonia emissions from agriculture in Jiangsu Province from 2000 to 2017. *Atmospheric Ocean. Sci. Lett.* **2020**, *13*, 268–273. [CrossRef]
10. Wyer, K.E.; Kelleghan, D.B.; Blanes-Vidal, V.; Schauberger, G.; Curran, T.P. Ammonia emissions from agriculture and their contribution to fine particulate matter: A review of implications for human health. *J. Environ. Manag.* **2022**, *323*, 116285. [CrossRef]
11. Zhang, Y.; Li, D.; Zhang, K.; Xiao, F.; Li, Y.; Du, Y.; Xue, Y.; Zhang, L.; Gong, P.; Song, Y.; et al. The Effects of Long-Term Application of Stabilized and Coated Urea on Soil Chemical Properties, Microbial Community Structure, and Functional Genes in Paddy Fields. *Agronomy* **2023**, *13*, 2190. [CrossRef]
12. Heng, Y.A.; Ling, C.P. Modeling of Capacitance in A Supercapacitor. *J. Eng. Technol. Appl. Phys.* **2019**, *1*, 20–25. [CrossRef]
13. Landauer, J.; Kugi, A.; Steinböck, A. Mathematical modelling of an electrostatic oiling machine for steel strips. *Math. Comput. Model. Dyn. Syst.* **2023**, *29*, 69–94. [CrossRef]
14. Major, T.F.; Lara, A.; Cunge, J.A. Mathematical modelling of Yacyreta-Apipe Scheme on the Rio Parana. *Houille Blanche* **1985**, *71*, 519–528. [CrossRef]
15. Norhidayah, M.; Shaaban, A.; Dimin, M.F.; Norazlina, M.Y.; Rostam, O. Optimization of Biodegradable Urea Production Process to Minimize Ammonia Release Through Response Surface Method Experimental Design. *J. Adv. Res. Appl. Sci. Eng. Technol.* **2015**, *2*, 9–18.
16. Rao, M.S.; Venkaiah, N. Parametric Optimization in Machining of Nimonic-263 Alloy using RSM and Particle Swarm Optimization. *Procedia Mater. Sci.* **2015**, *10*, 70–79. [CrossRef]
17. Chyang, C.S.; Qian, F.P.; Chiou, H.Y. Radial gas mixing in a fluidized bed with a multi-horizontal nozzle distributor using response surface methodology. *Chem. Eng. Technol.* **2007**, *30*, 1700–1707. [CrossRef]
18. Shi, Y.; Eberhart, R. A Modified Particle Swarm Optimizer. In Proceedings of the IEEE International Conference on Evolutionary Computation, Anchorage, AK, USA, 4–9 May 1998; pp. 69–73.
19. Mosayebi, R.; Bahrami, F. A modified particle swarm optimization algorithm for parameter estimation of a biological system. *Theor. Biol. Med Model.* **2018**, *15*, 17. [CrossRef]
20. Saaid, M.F.; Yassin, A.I.M.; Tahir, N.M. Particle Swarm Optimization (PSO) Model for Hydroponics pH Control System. *TEM J.* **2021**, *10*, 1694–1699. [CrossRef]
21. Putra, S.; Mu'Tamar, K. Zulkarnain Estimation of Parameters in the SIR Epidemic Model Using Particle Swarm Optimization. *Am. J. Math. Comput. Model.* **2019**, *4*, 83. [CrossRef]
22. Alfi, A.; Modares, H. System identification and control using adaptive particle swarm optimization. *Appl. Math. Model.* **2011**, *35*, 1210–1221. [CrossRef]
23. Alızada, M.; Ozturk, S. PID and Fuzzy Logic Control of Ball and Beam System Using Particle Swarm Optimization. *World J. Eng. Technol.* **2023**, *11*, 859–873. [CrossRef]
24. Alam, M.S.; Tokhi, M.O. Dynamic modelling of a single-link flexible manipulator system: A particle swarm optimisation approach. *J. Low Freq. Noise Vib. Act. Control.* **2007**, *26*, 57–72. [CrossRef]
25. Lipin, A.A.; Lipin, A.G.; Wójtowicz, R. Modelling nutrient release from controlled release fertilisers. *Biosyst. Eng.* **2023**, *234*, 81–91. [CrossRef]

26. Guo, Y.; Zhang, M.; Liu, Z.; Tian, X.; Zhang, S.; Zhao, C.; Lu, H. Modeling and Optimizing the Synthesis of Urea-formaldehyde Fertilizers and Analyses of Factors Affecting these Processes. *Sci. Rep.* **2018**, *8*, 4504. [CrossRef] [PubMed]
27. Basu, S.K.; Kumar, N. Mathematical model and computer simulation for release of nutrients from coated fertilizer granules. *Math. Comput. Simul.* **2008**, *79*, 634–646. [CrossRef]
28. Fang, H.; Gu, X.; Jiang, T.; Yang, J.; Li, Y.; Huang, P.; Chen, P.; Yang, J. An optimized model for simulating grain-filling of maize and regulating nitrogen application rates under different film mulching and nitrogen fertilizer regimes on the Loess Plateau, China. *Soil Tillage Res.* **2020**, *199*, 104546. [CrossRef]
29. Li, G.; Xie, Z.; Yao, X.; Chen, X. Study on the mathematical model of the effects of NPK on winter cauliflower. *Math. Comput. Model.* **2011**, *54*, 1128–1137. [CrossRef]
30. Irfan, S.A.; Razali, R.; KuShaari, K.Z.; Mansor, N.; Azeem, B.; Versypt, A.N.F. A review of mathematical modeling and simulation of controlled-release fertilizers. *J. Control. Release* **2018**, *271*, 45–54. [CrossRef]
31. Haydar, M.S.; Ghosh, D.; Roy, S. Slow and controlled release nanofertilizers as an efficient tool for sustainable agriculture: Recent understanding and concerns. *Plant Nano Biol.* **2024**, *7*, 100058. [CrossRef]
32. Swain, S.S.; Khura, T.K.; Sahoo, P.K.; Chobhe, K.A.; Al-Ansari, N.; Kushwaha, H.L.; Kushwaha, N.L.; Panda, K.C.; Lande, S.D.; Singh, C. Proportional impact prediction model of coating material on nitrate leaching of slow-release Urea Super Granules (USG) using machine learning and RSM technique. *Sci. Rep.* **2024**, *14*, 3053. [CrossRef] [PubMed]
33. Duffuaa, S.O. A mathematical optimization model for chemical production at Saudi Arabia Fertilizer Company. *Top. Catal.* **1991**, *15*, 652–656. [CrossRef]

processes

MDPI

Article

Determinants for Supplier Selection Based on Hybrid Grey Theory: Case Study of the Vietnamese Coffee Industry

Nguyen-Nhu-Y Ho *, Phuong Mai Nguyen, Cong Thanh Tran and Huy Hung Ta *

International School, Vietnam National University Hanoi, Hanoi 10000, Vietnam; mainp@vnu.edu.vn (P.M.N.); thanhtc@vnu.edu.vn (C.T.T.)

* Correspondence: hngny@vnu.edu.vn (N.-N.-Y.H.); hungth@vnu.edu.vn (H.H.T.); Tel.: +84-2-3557-5992 (ext. 33) (H.H.T.)

Abstract: Coffee is not merely a refreshing beverage but also invigorates people, provides relaxation, contributes to human health, and fosters closer social connections. Coffee is one of the most widely consumed beverages worldwide and the most traded commercial commodity. Moreover, the rapid development of the Vietnamese coffee industry caused some concerns due to its insufficient performance and the fierce competition within the industry. It is significant to establish an efficient supply network; notwithstanding, supplier selection has always been a challenge for companies. Therefore, this paper employs a hybrid model to determine the supplier selection criteria, a vital factor for a manufacturer under practical operating conditions. Firstly, a combined model of Grey forecasting and the Grey Fourier series is applied to forecast future rainfall and temperature data for six consecutive years. Secondly, based on the criteria, strategies, and buyer requirements, the single-objective linear programming model helps identify the outperformed suppliers. The results found that prices and location change are determinants of supplier selection, and supplier shortage is an enormous barrier for the industry. In this study, these price forecasts allow supply chain management to make informed decisions about inventory levels, transportation routes, and resource allocation to ensure smooth operation and optimize coffee supply chain management.

Keywords: coffee industry; Grey forecasting; Grey Fourier series; supplier selection; single-objective linear programming

1. Introduction

In recent times, the global supply chain has faced numerous challenges. Trade tensions between the U.S. and China have resulted in stalled goods. As the pandemic subsides, the ongoing tension between Russia and Ukraine escalates transportation costs. The disruption in the global supply chain has led to a sharp increase in food prices, posing a risk of instability in many developing countries, including Vietnam.

Vietnam is located in the tropical belt of the Northern Hemisphere and has the proper climate for growing coffee trees with special flavor. With extensive and widespread cultivation of coffee across the country's land, Vietnam's harvested coffee area has expanded from 15,000 to nearly 640,000 hectares over the last three decades [1]. In the year of 2019, this industry produced approximately 1.6 million tons of green beans, which contributed to an export value of approximately U.S. $2.85 billion, accounting for about 3% of the national GDP. In recent years, the industry has been the world's second-largest exporter of coffee, after Brazil. The coffee industry has been one of the spearhead economic sectors in Vietnam, mainly produces Robusta coffee, accounts for 60% of Robusta worldwide, and is regarded as having the highest levels of productivity in the globe at the lowest price [2].

Coffee trees commonly grow in tropical regions where abundant rainfall, warm temperatures, and no frost are [3,4]. Franca et al. (2005) and Silva (2005) believed that factors such as the climate, soil, rainfall, and a suitable system of cultivation and irrigation in

certain localities must be regarded as vital values for good coffee tastes [5,6]. The Arabica coffee is a perennial plant and evergreen in nature, the best coffees are grown at altitudes above 1000 m where the annual rainfall remains below 1500 mm with favorable environmental quality such as rainfall, altitude, latitude, and longitude [7].

In North Vietnam, the climate is strongly influenced by northeastern winds, which, combined with heavy rainfall and cold weather, are not conducive to the growth and development of coffee [8,9]. Notwithstanding, coffee from this area has a distinctive taste, which is highly appreciated by customers worldwide similar to coffee from Sao Paulo, Brazil [10]. In particular, coffee trees in Son La and Dien Bien provinces are grown at relatively high latitudes. It is not needed for frequent irrigation, but their coffee has a rigorous quality standard and is considered specialty coffee [11]. The hot climate of middle Vietnam, Quang Tri is well-suited for Arabica coffee plantation with a deep aroma [12]. Dak Mil rural district, located in the central highlands region of Vietnam, close to the equator, the characteristic of the hot wet climate and is suitable for Robusta coffee trees [13,14]. This area has up to 19,000 hectares of coffee planting trees, accounting for one-third of the coffee output of the whole Dak Nong province [15]. The coffee trees can be grown in various soils, such as reddish-brown soil, golden-brown soil, and gray soil [16,17]. Compared to all soil types, Bazan red soil can prolong the life cycle of coffee trees, and it has a significant effect on the taste and color of coffee [18,19].

It is important to investigate the supply network of unprocessed coffee products from the three largest cities located from the north to the south of Vietnam, which are Hanoi capital, Da Nang, and Ho Chi Minh City. Figure 1 shows the general scenario of the Vietnamese agriculture industry and illustrates the connection between the government, agricultural companies, and farmers, which is the fundamental nature of the product lifecycle from coffee bean growers to end customers.

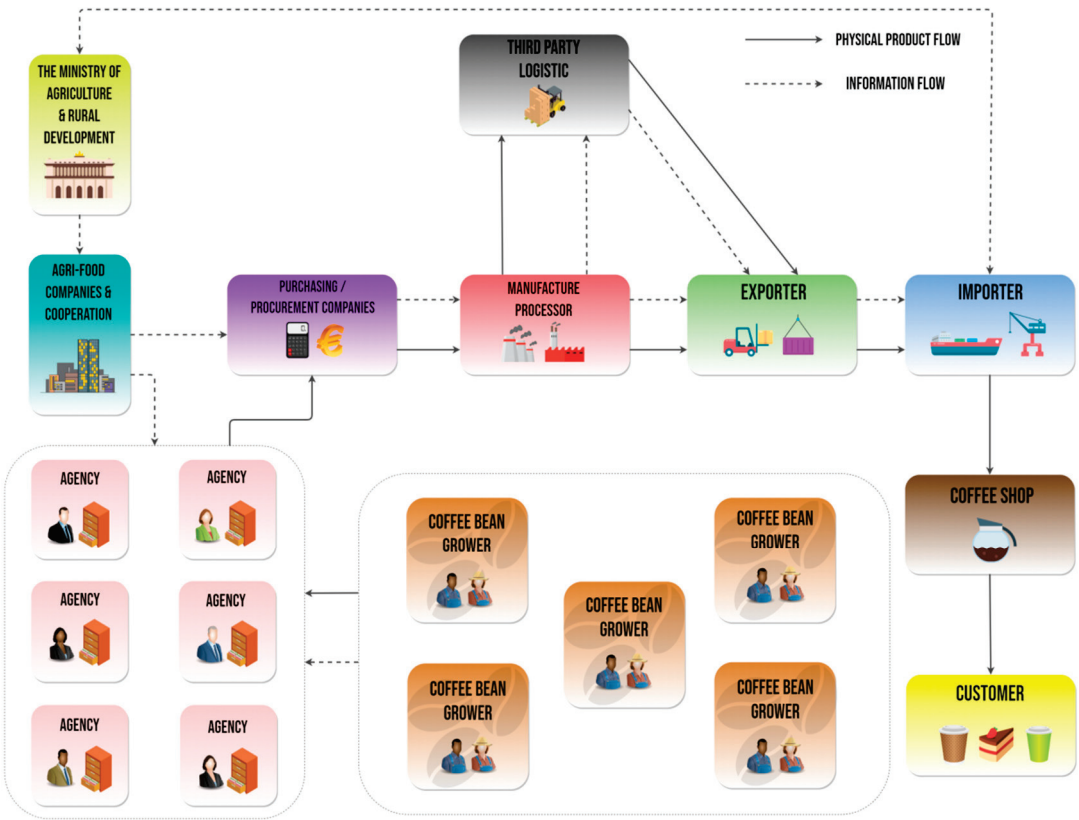

Figure 1. A framework of Vietnamese coffee supply network.

Currently, Vietnam has about 150 coffee-exporting agencies, and these companies commonly buy green bean coffee from self-organizing logistics systems and purchasing

agents [20]. The agricultural export crop contract is signed by the government to provide an outline of the food supply chain system from multiple angles and then inform the food companies and cooperative farms in Vietnam. The coffee bean growers, the agents, and the exporters formed the bottlenecks of Vietnamese coffee supply networks. The farmers harvest and dry green coffee beans before delivering them to the agencies. The agents negotiate with the larger ones or directly contact the manufacturer processor. The intermediate coffee bean suppliers select the types of coffee beans and deliver them to the manufacturers to produce the final products on a large scale. With the cooperation of its special network, the processing manufacturers order vast quantities from the local agents, create a feasible schedule to avoid late deliveries, and then check the export allotment quota for the crop. All procedures for concluding contracts for supplier selection must be executed carefully in terms of costs and regulations. Third-party logistic providers transfer the product to the buyers, who are importers and wholesalers, and the importer countries. Companies used to purchase the products directly from their long-term relations with the coffee growers or agencies; consequently, this led to restrictions on providing high-quality products and created an inefficient supply network within their industry.

According to Scherr et al. (2015) despite its large scale and diversity of coffee commodities across the nation, the industry is being threatened by very weak governance involving an amorphous combination of institutions, agencies, and farmers [21]. In addition, Keshky et al. (2020) coffee value chain is a vulnerable industry facing difficulties from external shocks such as natural disasters and trade protectionism, which may cause disruption of the global value chain [22]. Any inaccuracy in the supplier selection process can lead to substandard performance. Meanwhile, successful supplier selection will benefit the long-term development of the Vietnamese coffee industry by reducing operational and environmental costs and improving product quality.

Lin and Wu (2011) proved that the procurement activities of purchasing firms can support decision-making by identifying potential alternatives and selecting the best products in favor of the buyer's objectives [23]. Hammani et al. (2014) Supplier selection for the success of companies and industries is crucial for competitiveness in a fierce market-competition environment [24]. The selection of suppliers is crucial in developing a reliable supply chain and is devoted to effectively contributing to the mutual co-business development profits [24]. Global sourcing often aims to exploit the performance in the supply of products; it is also a prevailing trend among companies specializing in production-oriented agribusiness seeking new sources for competitive advantage [1].

Global sourcing often aims to exploit the performance of the supply of products. It is also a prevailing trend among companies specializing in production-oriented agribusiness seeking new sources for competitive advantage [25]. Manufacturers might optimize their value chain production and associated processes by adopting and selecting coffee bean vendors. Selecting suppliers aims to significantly optimize prices due to the effective use of energy and resources with less cost wastage.

Kittichotsatsawat et al. (2021) found that significant coffee problems were identified, such as high cultivation costs, a lack of standards to produce high-quality coffee, and unplanned incoming material (coffee cherries) that led to continuous losses and disappearing customer confidence. Vietnam also has the same problem as Thailand; however, transportation cost is the most important factor in determining the price and selecting the vendor cost in coffee manufacturing [26]. The coffee bean-growing regions in Vietnam are mainly dependent on collectors and traders. Engaging in the agriculture value chain helps ensure that the participants share rights and responsibilities, regulate market supply and demand, and trace the origin of products. It meets agricultural development needs, enhances production efficiency, and increases income for farmers and businesses. An effective and optimized supplier selection process is of pivotal importance for manufacturing organizations and all organizations in the age of the industrial revolution. Choosing the right supplier can help reduce purchasing risks, maximize value, and increase total quality management production.

This research aims to help manufacturers optimize their value chain's production and associated processes by selecting coffee bean vendors to reduce supply chain disruption. It proposes the selection criteria for optimizing supplier selection, for which previous research has not finished incorporating environmental factors into the conventional supplier selection model. The agricultural industry is inherently vulnerable to environmental challenges. The data was used in agrarian management of weather and climate change to predict the yield of croppers. Moreover, this study provides an empirical initiative based on a mixed model of grey forecasting in conjunction with the Grey Fourier series, a powerful method for accurately anticipating future values for this industry. In addition, a mathematical analysis based on binary linear programming is utilized to identify the necessary criteria for choosing desirable suppliers for coffee manufacturing. Overall, this study is intended to enhance the supplier domestic network, increase competitive ability, and help coffee growers improve productivity in cultivation.

2. Literature Review

The Vietnamese coffee industry has been experiencing significant growth and expansion in recent years. This growth has led to an increased demand for high-quality coffee beans, requiring the industry to have efficient supplier selection and order allocation processes (Siregar et al., 2019). One of the critical factors affecting the quality and price of coffee beans is the level of rainfall and temperature [27]. According to Dang et al. (2022), there have been increasing discussions in supplier selection research on enhancing supplier capabilities toward green and sustainable practices [28]. The supply networks and the competitiveness of a particular industry depend on supplier selection capacity to find solutions to address the urgent economic, political, and war crises. Agarwal and Vijayvargy (2011) emphasized that higher cooperation and coordination among the partners of the supply chain is a key issue, which requires strategies suitable for system optimal performance [29]. The selection of qualified suppliers must match the adequate evaluation criteria to ensure the right supplier is chosen. In other words, Li et al. (2020) once the qualified supplier becomes a critical cell of a well-managed and established supply network, the linkage between the buyer and supplier will significantly affect the well-run supply chain. In agribusiness supply chains, supplier selection behavior can be regarded as industrial buying behavior because of the need to purchase inputs from various sources [30]. Such organizational buying behavior is a complex decision-making and communication process involving numerous internal and external participants in the purchasing organization [31]. Suppliers are not the greatest assets in an organization, but poor choices can make them the most significant liability. Liao (2012) suggested that selecting the right agricultural product suppliers significantly decreases purchasing costs, improves competitive advantage, and enhances customer satisfaction [32]. Liu (2013) defined smaller independent food retailers with less negotiating power as having selection criteria and technological specifications for their suppliers. They tend to work with existing vendors to develop and co-create technological compatibility and specifications [33]. Thus, in today's rapidly changing world, the significance of accurate weather forecasts and vendor cost estimation in supply chain management cannot be overstated. Precise weather forecasts provide vital information for supply chain managers to anticipate and respond to potential risks and threats. These forecasts allow them to make informed decisions about inventory levels, transportation routes, and resource allocation to ensure the smooth operation of the supply chain. Additionally, accurate vendor cost estimation helps supply chain managers select the best vendors based on price uncertainty in the future. This allows them to optimize costs and maintain competitiveness in the market. Furthermore, accurate weather forecasts and vendor cost estimation play a crucial role in preserving the resilience and competitiveness of the coffee supply chain.

Grey system theory was initially introduced by Professor Deng based on mathematical analysis in 1982. The model has been famous among worldwide researchers due to its outperformed ability to solve unknown problems and deal with uncertain values [33].

Peng mentions with a few parameters required to apply the Grey model, it has been applied to many industries by providing various available solutions [34]. Building upon Deng's model, Odan et al., (2012) proved that linear statistical forecasting methods are widely used because they are easy to implement and fully understand the indicators [35]. However, in the real world, data have varying degrees of nonlinearity, which may not be adequately handled by linear applications. Many nonlinear methods were proposed in applied economic cases to improve forecasting performance. According to Hsu et al. (2009) obtained good performance on the various prediction applications using the Fourier series to refine the residual state transition matrices [36]. Wang and Phan (2015) illustrated the empirical idea that using Fourier series techniques can filter out high-frequency terms, which are considered to be noise, but achieve better performance [37]. González et al., (2008) and Romera and Seifert (2009) agreed that some data from the series would be used to fit a Fourier series made up of the peak frequencies of the spectrum plot of the fluctuation series [38,39]. Rahmawati and Salimi (2022) decided on the local, freshly roasted coffee for the domestic market [40]. However, this research didn't have a different delivery location. This Fourier series is used to forecast fluctuations that are different from those used for fitting. Demand forecasting is calculated by adding the trend prediction and is used to predict fluctuations in coffee vendors. The underlying reason for this approach is examining supplier selection from the manufacturers' perspective and an increasingly integrated and more complex production-distribution system.

3. Methodology

Formerly, companies made supplier selection decisions based on competitive prices. Studies in the field of supplier selection rose sharply after the 1960s. Therefore, the determinants of the selection criteria became significant issues that needed to be addressed. Supplier selection is a complex decision-making problem that should include both quantitative and qualitative criteria needed for suppliers' performance effectively. Some researchers have agreed that a combination of factors should fit the technical requirements and the company's targets.

A new approach based on the Grey model is employed to foresee future values. Grey model forecasting G.M. (1,N) is extensively used in many applications. The discrete Grey models are a class of new models initially developed that are characterized by poor information and a lack of information. The fields covered by Grey theory include systems analysis, data processing, modeling, prediction, decision-making, and control. Thus, the G.M. (1,1) is one of the most frequently models used in a series of Grey forecasting [33]. The paper adopted Curzi (2015) to describe the procedure in which price, rainfall, and temperature indicators from standard disaggregate trade data are used to anticipate future information [41]. Based on previous studies, Zeithaml (1988) designed a way to test the general wisdom that price and quality are positively related [42].

Based on the research of Amid et al., (2009), the study develops the single-objective linear programming model, which is a useful approach for supplier selection in the agriculture industry [43]. To specify the weight or goal priorities towards the best selection, a mathematics analysis of single-objective linear programming was applied to solve these problems, which is an outperformed application appropriate for the purpose of this study. The findings contribute to the existing literature by comparing analytical statistics and building the equation in order to obtain the average coffee price. The single linear programming model is applied to an actual case study for supplier selection in the coffee industry, where companies try to reduce manufacturing costs. Competitive price is regarded as one of the most important factors affecting consumers' buying decisions. Thus, we assumed a temperature mean of T_1 and a rainfall mean of T_2 to assess the impact of factors affecting the quality of the coffee bean and then calculate the coffee price in the Vietnamese market. P means the average price of the Vietnamese coffee bean. This section describes the procedure

that infers, using T_1 and T_2, information from standard disaggregate trade data based on the statistics formulation:

$$P = \beta_0 + \beta_1 T_1 + \beta_2 \ln(T_2) \quad (1)$$

where

$$T_2 = \ln(T_2) \quad (2)$$

3.1. Grey Forecasting

In this case, data were collected over six consecutive years, from 2017 to 2022. The authors applied the Grey model in this study to forecast the effect of price on coffee in the future. The Grey system theory, developed by Deng in 1982, is an important methodology that focuses on the study of problems involving small samples and poor information.

Theorem 1: *Let $X^{(0)}$, $X^{(1)}$, and $Z^{(1)}$ be the same as above except that $X^{(0)}$ is non-negative. If $\hat{a} = (a, b)^T$ is a parameter sequence and:*

$$Y = \begin{bmatrix} x^{(0)}(2) \\ x^{(0)}(3) \\ \vdots \\ x^{(0)}(n) \end{bmatrix}, \quad B = \begin{bmatrix} -z^{(1)}(2) & 1 \\ -z^{(1)}(3) & 1 \\ \vdots & 1 \\ -z^{(1)}(n) & 1 \end{bmatrix}, \quad (3)$$

The least squares estimate sequence of the G.M. (1,1) model Equation (2) satisfies $\hat{a} = \left(B^T B\right)^{-1} B^T Y$. Continuing all the notations from Theorem 1, if $[a, b]^T = \left(B^T B\right)^{-1} B^T Y$, then $\frac{dx^{(1)}}{dt} + ax^{(1)} = b$ is a whitenization equation of the G.M. (1,1) model in Equation (3). The time response sequence of the G.M. (1,1) model in Equation (5) is given below.

$$\hat{X}^{(1)}(k+1) = \left(x^{(0)}(1) - \frac{b}{a}\right) e^{-ak} + \frac{b}{a}, k = 1, 2, \ldots, \quad (4)$$

The parameters $(-a)$ and b of the GM (1,1) model are referred to as the development coefficient and Grey action quantity, respectively. The former reflects the development states of $\hat{x}^{(1)}$ and $\hat{x}^{(0)}$. In general, the variables that act upon the system of interest should be external or pre-defined. Because G.M. (1,1) is a model constructed from a single sequence, it uses only the behavioral sequence (referred to as output sequence or background values) of the system without considering any externally acting sequences (referred to as input sequences or driving quantities). The Grey action quantity in the G.M. (1,1) model is a value derived from the background value. It reflects changes contained in the data, and Its exact intention is Grey. For this quantity, rainfall and temperature realize the extension of the relevant intention. Its existence distinguishes Grey systems modeling from general modeling. It is also an important test to separate the thoughts of Grey systems and those of Grey boxes.

3.2. Grey Fourier Series

González et al. (2010) [38] separated the thoughts of Fourier series systems and those of forecasting boxes, which is also an important test.

Theorem 2: *Let $X^{(0)}$ be the original series of m entries, and v is the predicted series obtained from NGBM (1,1). Based on the predicted series v, a residual series named ε is defined as follows:*

$$\varepsilon = \{e(k)\}, \quad k = 2, 3, \ldots m$$

where

$$e(k) = x(k) - v(k) \quad k = 2, 3, \ldots m \quad (5)$$

According to the definition of the Fourier series, the residual sequence of NGBM (1,1), can be approximately expressed as follows:

$$\hat{\varepsilon}(k) = \frac{1}{2}a_{(0)} + \sum_{i-1}^{z}\left[\left[a_i\cos\left(\frac{2\pi i}{m-1}(k)\right)\right] + b_i\sin\left(\frac{2\pi i}{m-1}(k)\right)\right] \quad k = 1, 2, 3, \ldots m \tag{6}$$

where

$$Z = \frac{(m-1)}{2} - 1 \tag{7}$$

is called the minimum deployment frequency of the Fourier series and Z only be taken integer number.

Therefore, the residual series is rewritten as follows:

$$\varepsilon = PC \tag{8}$$

where

$$P = \begin{bmatrix} \frac{1}{2}\cos\left(\frac{2\pi i\times 1}{m-1}\times 2\right)\sin\left(\frac{2\pi i\times 1}{m-1}\times 2\right) & \ldots & \frac{1}{2}\cos\left(\frac{2\pi i\times Z}{m-1}\times 2\right)\sin\left(\frac{2\pi i\times Z}{m-1}\times 2\right) \\ \frac{1}{2}\cos\left(\frac{2\pi i\times 1}{m-1}\times 3\right)\sin\left(\frac{2\pi i\times 1}{m-1}\times 3\right) & \ldots & \frac{1}{2}\cos\left(\frac{2\pi i\times Z}{m-1}\times 3\right)\sin\left(\frac{2\pi i\times Z}{m-1}\times 3\right) \\ \vdots & \ldots & \vdots \\ \frac{1}{2}\cos\left(\frac{2\pi i\times 1}{m-1}\times m\right)\sin\left(\frac{2\pi i\times 1}{m-1}\times 3\right) & \ldots & \frac{1}{2}\cos\left(\frac{2\pi i\times Z}{m-1}\times m\right)\sin\left(\frac{2\pi i\times Z}{m-1}\times m\right) \end{bmatrix} \tag{9}$$

$$C = [a_0, a_1, b_1, a_2, b_2, \ldots, a_z, b_z]^T \tag{10}$$

The parameters $a_0, a_1, b_1, a_2, b_2, \ldots, a_z, b_z$ are obtained by using the ordinary least squares (O.L.S.) method whose results are in the following equation:

$$C = \left(P^T P\right)^{-1} P^T \varepsilon^T \tag{11}$$

Once the parameters are calculated, the modified residual series is then achieved based on the following expression:

$$\hat{\varepsilon}(k) = \frac{1}{2}a_0 + \sum_{i=1}^{z}\left[a_i\cos\left(\frac{2\pi i}{m-1}(k)\right) + b_i\sin\left(\frac{2\pi i}{m-1}(k)\right)\right] \tag{12}$$

From the predicted series v, and $\hat{\varepsilon}$ the Fourier modified series $\hat{v}$ of series v is determined by the following:

$$\hat{v} = \{\hat{v}_1, \hat{v}_2, \hat{v}_3, \ldots, \hat{v}_k, \ldots, \hat{v}_m\}$$

where

$$\hat{v} = \begin{cases} \hat{v}_1 = v_1 \\ \hat{v}_k = v_k + \hat{\varepsilon}_k \end{cases} \quad k = 2, 3, \ldots, k \tag{13}$$

There are some common approaches for evaluating the performance of the volatility model for forecasting. This study adopted two criteria to evaluate the forecasting model of the coffee price. Model characteristics include periodicity, randomness, and tendency. According to Liu et al. (2023), to obtain the tendency of the series and the context of the development of natural disasters, this study is not only used to improve the background value using integration but also to increase the accuracy by correcting the model's periodical errors [44]. The mean absolute percentage error (MAPE) is defined as follows:

$$MAPE = \frac{1}{n}\sum_{k=2}^{n}\left|\frac{x^{(0)}(k) - \hat{x^{(0)}}(k)}{x^{(0)}(k)}\right| \times 100\% \tag{14}$$

where $x^{(0)}(k)$: the actual value in time period k, and $\hat{x}^{(0)}(k)$: the forecast value in the time period.

The grade of MAPE is divided into four levels shown in Table 1.

Table 1. The MAPE grade level [22].

MAPE	≤10%	10–20%	20–50%	>50%
Grade levels	Excellent	Good	Qualified	Unqualified

We ensure no space for errors during the forecasting calculation because forecasting accuracy is important to solve mathematical concerns for future values with incomplete information. Therefore, in this paper, the MAPE is employed to measure the accuracy of the method for constructing fitted time series values. When MAPE values are small, the predicted values are close to the actual values.

3.3. Single-Objective Linear Programming Model

Decision variables are as follows:

Kij Quantity weight total purchase of agency i supplied by supplier j (in Ton)
Qij 0–1 variable determined by whether agency i is provided by supplier j (=1 if supplied)

Parameters:

Pij Price of supplier j
Ci Capacity of supplier j
tij Transportation cost agency i from supplier j
Di Total demand for agency i
qij Percent of defective parts for agency i supplied by supplier j
mij Minimum order quantity for agency i required by supplier j
M A large positive number

Single-objective Linear programming supplier selection with functions is based on a formulation for which Z is a minimization objective whereby Z represents the total transportation cost of the product.

$$\text{Min } Z = \sum_i \sum_j p_{ij}K_{ij} + \sum_i \sum_j t_{ij}K_{ij} \tag{15}$$

Subject to:

$$\sum_{i=1}^{3} XK_{ij} \leq C_j \quad \forall j \tag{16}$$

$$\sum_{j=1}^{5} K_{ij} \geq D_i \; \forall i \tag{17}$$

$$K_{ij} \geq m_{ij}K_{ij} \quad \forall i, j \tag{18}$$

$$K_{ij} \leq MK_{ij} \; \forall i, j \tag{19}$$

$$K_{ij} \geq 0 \quad \forall i, j \tag{20}$$

$$Q_{ij} \in \{1, 0\} \; \forall i, j \tag{21}$$

Constraint set (15) serves as the capacity constraint for each vendor, and set (16) serves as the overall capacity restriction. Constraint set (17) enforces the fulfillment of the demanded quantity for each part. Constraint set (18) specifies the minimum order quantity for all vendors. The constraint set (19) prevents conflict between the decision variables. Constraint set (20) preserves the non-negativity, and set (21) imposes the integrality on the decision variables.

4. Results and Analysis

This paper assumes that the proper and qualified sellers must meet all buyers' requirements. The selected criteria are the factors of temperature and rainfall. Each criterion will

contribute to the appropriate sourcing evaluation in the model's objective function for the industrial food chain. This is in conjunction with some criteria used to form the model constraints so that the feasible region can be located; in this real case, these are rainfall and temperature. Thus, we assumed that temperature means X_1 and rainfall means X_2 to assess the impact of factors affecting the quality of coffee beans and then calculate the coffee price in the Vietnamese market. P is the average price of Vietnamese coffee beans. The data on temperature, rainfall, and price for coffee from 2017 to 2022 undertaken from five meteorological regions in Vietnam are calculated by the authors. Based on the data from the Vietnam General Statistics Office [45], the SPSS 21.0 software was applied to identify the unstandardized coefficients β_0, β_1, β_2. This β_0, β_1, β_2 index help identify the target price, which is the elasticity of substitution. After running the software regression model, values of prices are obtained as shown in Table 2.

Table 2. The coefficients of the regression model for price forecasting.

Unstandardized Coefficients	Value
β_0	832.217
β_1	34.022
β_2	68.472

Source: Author's calculation.

Based on indicators of rainfall and temperature collected through five different meteorological regions from the regression model, the study develops a prediction model for the value of rainfall and temperature, which is used to calculate the future prices for the next section. All data are computed in the formulation:

4.1. Grey Forecasting

The sequence of raw data $X^{(0)} = \left(x^{(0)}(1), x^{(0)}(2), x^{(0)}(3), x^{(0)}(4), x^{(0)}(5), x^{(0)}(6)\right)$ = (21.11, 21.61, 21.85, 21.49, 22.6, 22.35) simulate this sequence $X^{(0)}$ using the following three G.M. (1,1) models and comparing the accuracy of the simulation:

From Equation (2) $x^{(0)}(k) + az^{(1)}(k) = b$, compute the accumulation generation of $X^{(0)}$ as follows:

$$X^{(1)} = \left(x^{(1)}(1), x^{(1)}(2), x^{(1)}(3), x^{(1)}(4), x^{(1)}(5)\right) = (21.11,\ 42.72,\ 64.57,\ 86.06,\ 109,\ 131.01)$$

We check the quasi-smoothness from $\sigma^{(1)}(k) = \frac{x^{(0)}(k)}{x^{(1)}(k-1)}$. It follows that $\sigma^{(1)}(2) = 0.49$, $\sigma^{(1)}(3) = 0.33$, $\sigma^{(1)}(4) = 0.25$, and $\sigma^{(1)}(5) = 0.2$, $\sigma^{(1)}(6) = 0.17$. Therefore, $k > 5$, $\sigma^{(1)}(k) \in \left]0.1; 1\right]$ with $\sigma = 0.9$, that is, the law of quasi-exponentially and the condition of quasi-smoothness is stratified. Thus, we can establish a G.M. (1,1) model for $X^{(1)}$. Using the adjacent neighbors of sequence, let $Z^{(1)} = \left(z^{(1)}(1), z^{(1)}(2), \ldots, z^{(1)}(n)\right)$ be the sequence generated from $X^{(1)}$ by the adjacent neighbor means sequence.

$$Z^{(1)} = \left(x^{(1)}(1), x^{(1)}(2), x^{(1)}(3), x^{(1)}(4), x^{(1)}(5)\right) = (32.91,\ 54.64,\ 76.31,\ 110,\ 132.01)$$

In addition, matrix B and constant vector Y_N are accumulated as follows:

$$B = \begin{bmatrix} -32.92 & 1 \\ -54.64. & 1 \\ -76.32 & 1 \\ -98.36 & 1 \\ -120.83 & 1 \end{bmatrix} \quad Y_N = \begin{bmatrix} 21.61 \\ 21.85 \\ 21.49 \\ 22.6 \\ 22.35 \end{bmatrix}$$

Using the least squares estimation, we obtain the sequence of parameters $\hat{a} = [a, b]^T$ as follows $\hat{a} = \left(B^T B\right)^{-1} B^T Y = \begin{bmatrix} -0.0102 \\ 21.201 \end{bmatrix}$. We establish the following model $\frac{dx^{(1)}}{dt} - 0.0102x^{(1)} = 21.201$ and its time response form $\hat{x}(k+1) = \left(x^{(0)}(1) - \frac{b}{a}\right)e^{-a(k)} + \frac{b}{a} = -21.21e^{-0.0102} + 0.00048$. Substituting different values of k into the equation: $k = 1X^{(1)}(1) = 21.11$.

Compute the simulated values of $X^{(0)}$ using the original series according to the accumulated generating operation by using $\hat{x}^{(0)}(k+1) = \alpha^{(1)}\hat{x}^{(1)}(k+1) - \hat{x}^{(1)}(k)$.

4.2. Grey Fourier Series

Let x be the original series of m entries and v is the predicted series (1,1). Base on the predicted series v, a residual series named ε is defined as:

$$e(k) = \{-1.0236, -1.9879, -2.9386, -4.0563, -4.7969\} \tag{22}$$

According to the definition of the Fourier Series, the residual sequence of NGBM (1,1), can be approximately expressed as follows:

$$\hat{\varepsilon}(k) = -0.5065 + \sum_{i=1}^{z}\left[-1.0413cos\left(\frac{2\pi i}{m-1}(k)\right) - 0.1308sin\left(\frac{2\pi i}{m-1}(k)\right)\right]$$

where

$$Z = \frac{(m-1)}{2} - 1$$

is called the minimum deployment frequency of Fourier series and Z only be taken integer number.

Therefore, residual series is rewritten as follows:

$$\varepsilon = PC$$

$$P = \begin{bmatrix} \frac{1}{2}cos\left(\frac{2\pi i\times 1}{m-1}\times 2\right)\sin\left(\frac{2\pi i\times 1}{m-1}\times 2\right) & \dots & \frac{1}{2}cos\left(\frac{2\pi i\times Z}{m-1}\times 2\right)\sin\left(\frac{2\pi i\times Z}{m-1}\times 2\right) \\ \frac{1}{2}cos\left(\frac{2\pi i\times 1}{m-1}\times 3\right)\sin\left(\frac{2\pi i\times 1}{m-1}\times 3\right) & \dots & \frac{1}{2}cos\left(\frac{2\pi i\times Z}{m-1}\times 3\right)\sin\left(\frac{2\pi i\times Z}{m-1}\times 3\right) \\ \frac{1}{2}cos\left(\frac{2\pi i\times 1}{m-1}\times 4\right)\sin\left(\frac{2\pi i\times 1}{m-1}\times 4\right) & \dots & \frac{1}{2}cos\left(\frac{2\pi i\times Z}{m-1}\times 4\right)\sin\left(\frac{2\pi i\times Z}{m-1}\times 4\right) \\ \frac{1}{2}cos\left(\frac{2\pi i\times 1}{m-1}\times 5\right)\sin\left(\frac{2\pi i\times 1}{m-1}\times 5\right) & \dots & \frac{1}{2}cos\left(\frac{2\pi i\times Z}{m-1}\times 5\right)\sin\left(\frac{2\pi i\times Z}{m-1}\times 5\right) \\ \frac{1}{2}cos\left(\frac{2\pi i\times 1}{m-1}\times 6\right)\sin\left(\frac{2\pi i\times 1}{m-1}\times 6\right) & \dots & \frac{1}{2}cos\left(\frac{2\pi i\times Z}{m-1}\times 6\right)\sin\left(\frac{2\pi i\times Z}{m-1}\times 6\right) \end{bmatrix}$$

The parameters $a_0,\ a_1, b_1, a_2, b_2,\ \dots, a_z, b_z$ are obtained by using the ordinary least squares (O.L.S.) method whose results are in the following equation:

$$C = \left(P^T P\right)^{-1} P^T \varepsilon^T$$

Once the parameters are calculated, the modified residual series as than achieved based on the following expression:

$$\hat{\varepsilon}(k) = -0.5065 + \sum_{i=1}^{z}\left[-1.0413cos\left(\frac{2\pi i}{m-1}(k)\right) - 0.1308sin\left(\frac{2\pi i}{m-1}(k)\right)\right]$$

From the predicted series v, and $\hat{\varepsilon}$, the Fourier modified series $\hat{v}$ of series v is determined. Where

$$\hat{v} = \begin{cases} \hat{v}_1 = 21.11 \\ \hat{v}_2 = 21.5351 \end{cases}$$

- Based on the actual results by applying the Grey forecasting and Grey Fourier series, it was found that the Grey Fourier series has a higher frequency spectra uncertainty

than Grey forecasting. Hence, this study adapts the Grey Fourier series for estimating the uncertain quantitative level of rainfall and temperature data for six consecutive years.

- By the same calculation and procedures, based on the actual data from 2017 to 2022, this study obtained all the forecasted values of all Vietnamese coffee companies from 2023 to 2028, which are shown in Table 3. The forecasting of rainfall and temperature from 2023 to 2028 and Figure 2 comparing the results of Grey forecasting model and Fourier series.

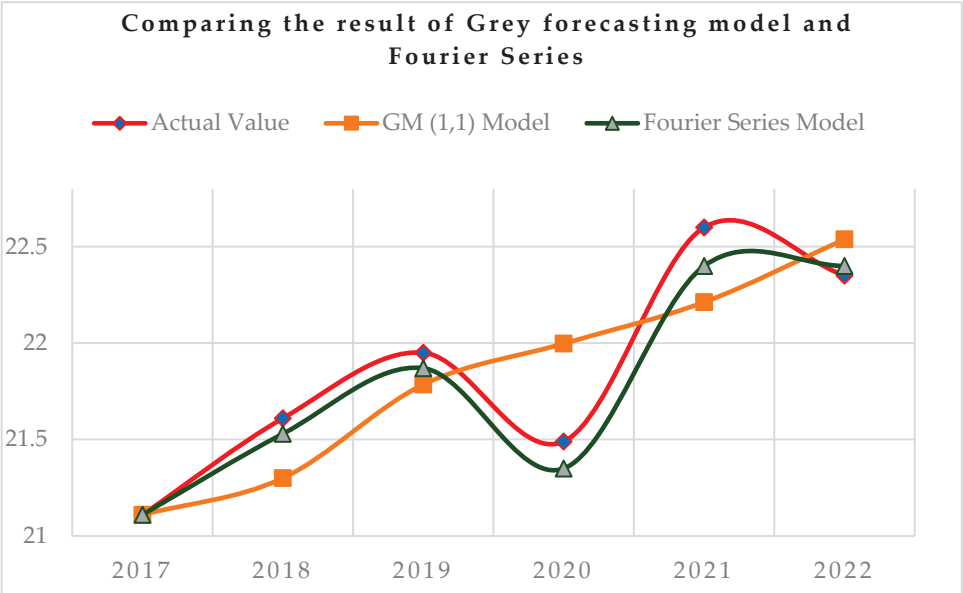

Figure 2. Comparing the result of the Grey forecasting model and Fourier series.

Table 3. The forecasting of rainfall and temperature from 2022 to 2027.

Year	S1		S2		S3		S4		S5	
	X1	X2	X1	X2	X1	X2	X1	X2	X1	X2
2023	22.89	7.48	20.85	7.74	20.39	7.41	23.20	7.34	24.61	7.57
2024	23.12	7.51	20.59	7.75	20.40	7.40	23.42	7.34	24.59	7.54
2025	23.36	7.55	20.33	7.76	20.41	7.39	23.65	7.33	24.58	7.50
2026	23.60	7.58	20.08	7.77	20.43	7.38	23.87	7.32	24.56	7.47
2027	23.84	7.62	19.83	7.78	20.44	7.37	24.10	7.32	24.54	7.44
2028	24.08	7.65	19.58	7.79	20.45	7.36	24.33	7.31	24.52	7.40

Source: Author's calculation.

- From the results of the forecasting, the authors found the coffee price for each supplier in the year 2023, which will help the manufacturer obtain various overviews of different coffee prices. In order to ensure there is no space for errors or mistakes during the forecasting calculation, MAPE is applied to measure the accuracy of the prediction model. The results are shown in Table 4 below.

Table 4. The MAPE for each supplier.

Average MAPE	S1		S2		S3		S4		S5	
	X1	X2	X1	X2	X1	X2	X1	X2	X1	X2
	0.861	0.600	1.669	0.540	0.301	0.359	0.856	0.203	1.006	0.479
					Average = 0.6874					

Source: Author's calculation.

Subsequently, MAPE is employed to measure the accuracy of the average Vietnamese coffee using the price for the forecasting year 2023. Table 5 shows that all MAPEs are smaller than 10%, which is considered as a good performance.

Table 5. The accuracy of the Grey Fourier series forecasting.

	S1	S2	S3	S4	S5
Average MAPEPrice's 2022	4.372	0.265	0.853	4.139	6.059
			Average = 3.14		

Source: Author's calculation.

As the results show in Table 5, the average MAPE of five growers in the year 2023 is 3.14% compared with the average real price, which is regarded as an excellent calculation. It strongly confirms that the Fourier series is highly accurate. Therefore, the study moves to the next stages of the calculation for the average price in 2023 using the Linear program: $P = \beta_0 + \beta_1 T_1 + \beta_2 \ln(T_2)$.

As the results of the statistical methods presented in Table 6, the study obtains a comprehensive estimation of the price. Once the estimation is obtained, the model of Single-objective Linear programming is proposed to select the proper suppliers.

Table 6. The average coffee price forecasting for 2023.

Price	2023
S1	2144
S2	2055
S3	2033
S4	2139
S5	2182

Source: Author's calculation.

4.3. Single-Objective Linear Programming Model

To judge the applicability of the single-objective linear programming model, actual data collected from a Vietnamese coffee manufacturer is used for this research.

The manufacturing procurement practices of the components required to produce a specific type of coffee have been purchased from several agencies. In this research, Arabica coffee is supplied by five potential vendors to five agents. It assumes that the expected demand for each agency is 2000, 1600, and 2900; then the minimum order quantities imposed by each supplier should be 150, 200, 150, 200, and 250. In this situation, the coffee bean price in the year 2022 was forecasted by the Grey model and given in Table 7.

Table 7. Transportation cost for each grower.

Growers j \ Supplier i	Transportation Cost USD/Ton to Supplier 1	Transportation Cost USD/Ton to Supplier 2	Transportation Cost USD/Ton to Supplier 3
1	142	163	281.6
2	142	163	281.6
3	186	135	220
4	210	164	220
5	210	164	158.4

Source: Author's calculation.

In this case study, for the optimal transfer of coffee beans from each grower to suppliers, three manufacturers from large cities collected and processed into the final products before delivering them to customers. Various transportation costs are incurred and shown in Table 7.

The results illustrated in Table 8 pointed out that the objective of minimum transportation cost is 14,805,470 USD for 6500 tons of coffee beans from five growers. In order to minimize cost and obtain the best choice, supplier 1 will buy 650 tons of coffee beans from grower 1; 1000 tons of coffee beans from grower 2; and 350 tons of coffee beans from grower 4. Supplier 2 will buy 250 tons of coffee beans from grower 3; 950 tons of coffee beans from grower 4; and 400 tons of coffee beans from grower 5. Then, supplier 3 will buy 700 tons of coffee beans from grower 1; an amount of 200 tons of coffee beans from grower 2; an amount of 1000 tons of coffee beans from grower 3; and 1000 tons of coffee beans from grower 5. In other words, the decision-makers prefer a supplier with a targeting price, optimal transport, and grower capacity. This paper indicates that price and location change are determinative factors for supplier selection. The empirical model of supplier selection is accurate and powerful for manufacturers to reduce business and transportation costs. In addition, it also helps to maintain the quality of products, provide targeting strategies for firms, and enhance the performance of the entire industry.

Table 8. The results of the supplier selection model.

Growers j \ Supplier i	1	2	3
1	650	0	700
2	1000	0	200
3	0	250	0
4	350	950	800
5	0	400	1200
Total	2000	1600	2900

Source: Author's calculation.

The research framework is undertaken in three main stages. In the first stage, supplier criteria are evaluated through existing literature reviews; the level of rainfall and temperature are identified as the most critical parameters affecting the quality and price of coffee beans. By applying the combination of the price regression function with Grey (1,1) and Fourier series, the result shows the Fourier series is more accurate in estimating the variation level of rainfall and temperature. Therefore, the Fourier series is used to anticipate the variation level of rainfall and temperature in six consecutive years (2023–2028) based on the historical data (2017–2022). In the second stage, the regression model of forecasting price is fully calculated. In the final stage, single-objective linear programming is useful for dealing with multi-criteria decision-making problems where the weight of criteria and assumptions for the between optimal price and cost.

5. Conclusions

The comprehensive selection criteria based on the hybrid model help improve the company's decision of choosing the right supplier. An appropriate supplier makes a great difference in enhancing and costing optimization, diversifying export capacity, and capturing opportunities for the growth of the Vietnamese coffee industry. The model of statistical analysis plays an important role in assessing the value of rainfall and temperature. As a result, it indicates that it undoubtedly has a tremendous impact on the average price of coffee beans. The combination method of Grey forecasting and the Grey Fourier series associated with the model of Binary Linear programming provides the predicted price of Vietnamese coffee beans, which is driven to an optimal solution helpful to address the current problems. The anticipation of the future price is solved carefully by applying the Grey Fourier series model. In addition, the findings prove that price and location change are determinants for the decision of supplier selections, and the supplier shortage is causing a huge problem for the coffee industry. The main objective of this paper was to demonstrate the empirical analysis based on mathematics perspectives aimed at optimizing the development of coffee domestic supply networks. The research provides businesses

and manufacturers with empirical solutions for determining future risks and improving the capacities to react against external risks.

The integrated approach also provides empirically worthwhile results for the overall development of the agriculture supply chain. The research framework offers feasible solutions for determining qualitative and quantitative factors affecting the success of purchasing and supply management professionals. The study improves the Vietnamese coffee supply network under fluctuating uncertainties such as climate change, price breaks, and government policy toward agricultural products. As a result, big data combined with forecasting the price of coffee beans can enhance supplier selection networks and improve coffee grower productivity, ultimately bringing greater profits to this sector. As this research is the first to propose the approach of Grey theory and single-objective linear programming to be applied in the agriculture industry, there are still some limitations, restrictions, and difficulties in combining these methods. In addition, the researchers could not investigate different variables, which could generate a more accurate result. Therefore, future studies are required with different assumptions.

Author Contributions: Conceptualization, N.-N.-Y.H. and P.M.N.; methodology and formal analysis, N.-N.-Y.H.; data collection, H.H.T. and C.T.T.; writing—original draft preparation, N.-N.-Y.H. and H.H.T.; writing—review and editing, P.M.N., C.T.T. and H.H.T.; visualization, N.-N.-Y.H.; supervision, N.-N.-Y.H. and P.M.N. All authors have read and agreed to the published version of the manuscript.

Funding: This research is funded by the International School, Vietnam National University, Hanoi, Vietnam.

Data Availability Statement: Data are contained within the article.

Conflicts of Interest: The authors declare no conflict of interest.

References

1. Thuy, H. Coffee Industry Adapts to Comply with New EU Regulations. Available online: https://vietnamagriculture.nongnghiep.vn/coffee-industry-adapts-to-comply-with-new-eu-regulations-d368066.html (accessed on 19 December 2023).
2. Tu, L.V. Country Coffee Profile: Vietnam. 2019. Available online: http://www.vicofa.org.vn/country-coffee-profile-vietnam-bid385.html (accessed on 18 December 2023).
3. Murthy, P.S.; Naidu, M.M. Protease production by Aspergillus oryzae in solid-state fermentation utilizing coffee by-products. *World Appl. Sci. J.* **2010**, *8*, 199–205.
4. Saw, A.K.-C.; Yam, W.-S.; Wong, K.-C.; Lai, C.-S. A comparative study of the volatile constituents of southeast Asian Coffea arabica, Coffea liberica and Coffea robusta green beans and their antioxidant activities. *J. Essent. Oil Bear. Plants* **2015**, *18*, 64–73. [CrossRef]
5. Franca, A.S.; Oliveira, L.S.; Mendonça, J.C.; Silva, X.A. Physical and chemical attributes of defective crude and roasted coffee beans. *Food Chem.* **2005**, *90*, 89–94. [CrossRef]
6. Silva, E.A.d.; MazzaferaII, P.; BruniniI, O.; SakaiI, E.; ArrudaI, F.B.; Mattoso, L.H.C.; Carvalho, C.R.L.; Pires, R.C.M. The influence of water management and environmental conditions on the chemical composition and beverage quality of coffee beans. *Braz. J. Plant Physiol.* **2005**, *17*, 229–238. [CrossRef]
7. Feria-Morales, A.M. Examining the case of green coffee to illustrate the limitations of grading systems/expert tasters in sensory evaluation for quality control. *Food Qual. Prefer.* **2002**, *13*, 355–367. [CrossRef]
8. Brosnan, T.; Sun, D.-W. Inspection and grading of agricultural and food products by computer vision systems—A review. *Comput. Electron. Agric.* **2002**, *36*, 193–213. [CrossRef]
9. Luong, Q.V.; Tauer, L.W. A real options analysis of coffee planting in Vietnam. *Agric. Econ.* **2006**, *35*, 49–57. [CrossRef]
10. Qin, X.; Miranda, V.S.; Machado, M.A.; Lemos, E.G.M.; Hartung, J.S. An Evaluation of the genetic diversity of *Xylella fastidiosa* isolated from diseased citrus and coffee in São Paulo, Brazil. *Phytopathology* **2001**, *91*, 599–605. [CrossRef]
11. Schmitter, P.; Dercon, G.; Hilger, T.; Le Ha, T.T.; Thanh, N.H.; Lam, N.; Vien, T.D.; Cadisch, G. Sediment induced soil spatial variation in paddy fields of Northwest Vietnam. *Geoderma* **2010**, *155*, 298–307. [CrossRef]
12. Greenfield, G. *Vietnam and the World Coffee Crisis: Local Coffee Riots in a Global Context*; National Coffee Growers Association: Bogotá, Colombia, 2002.
13. Lee, S.-C. Coffee middlemen in Dak Lak, Vietnam: A key stakeholder of coffee value chain as an intermediary of changes in local economies. *J. Econ. Geogr. Soc. Korea* **2013**, *16*, 372–388.
14. Kim, D.-C.; Hoang, T.Q. Development of coffee production and land mobility in Dak Lak, Vietnam. *J. Econ. Geogr. Soc. Korea* **2013**, *16*, 359–371.

15. Tan, S.B.H. Coffee frontiers in the Central Highlands of Vietnam: Networks of connectivity. *Asia Pac. Viewp.* **2000**, *41*, 51–67. [CrossRef]
16. Agergaard, J.; Fold, N.; Gough, K.V. Global–local interactions: Socioeconomic and spatial dynamics in Vietnam's coffee frontier. *Geogr. J.* **2009**, *175*, 133–145. [CrossRef]
17. Kilcher, L. How organic agriculture contributes to sustainable development. *J. Agric. Res. Trop. Subtrop.* **2007**, *89*, 31–49.
18. Tsai, D.-M.; Chen, W.-L. Coffee plantation area recognition in satellite images using Fourier transform. *Comput. Electron. Agric.* **2017**, *135*, 115–127. [CrossRef]
19. Toledo, P.R.; Pezza, L.; Pezza, H.R.; Toci, A.T. Relationship between the different aspects related to coffee quality and their volatile compounds. *Compr. Rev. Food Sci. Food Saf.* **2016**, *15*, 705–719. [CrossRef] [PubMed]
20. Vietnam Coffee. Available online: https://giacaphe.com/%E2%80%93 (accessed on 10 March 2022).
21. Scherr, S.J.; Mankad, K.; Jaffee, S.; Negra, C. *Steps Toward Green: Policy Responses to the Environmental Footprint of Commodity Agriculture in East and Southeast Asia*; EcoAgriculture Partners: Washington, DC, USA, 2015.
22. Keshky, E.; Basyouni, S.S.; Al Sabban, A.M. Getting through COVID-19: The pandemic's impact on the psychology of sustainability, quality of life, and the global economy–A systematic review. *Front. Psychol.* **2020**, *11*, 585897. [CrossRef] [PubMed]
23. Lin, P.-C.; Wu, L.-S. How supermarket chains in Taiwan select suppliers of fresh fruit and vegetables via direct purchasing. *Serv. Ind. J.* **2011**, *31*, 1237–1255. [CrossRef]
24. Hammami, R.; Temponi, C.; Frein, Y.A. Scenario-based stochastic model for supplier selection in global context with multiple buyers, currency fluctuation uncertainties, and price discounts. *Eur. J. Oper. Res.* **2014**, *233*, 159–170. [CrossRef]
25. Liu, L.; Cao, W.; Shi, B.; Tang, M. Large-scale green supplier selection approach under a q-rung interval-valued orthopair fuzzy environment. *Processes* **2019**, *7*, 573. [CrossRef]
26. Kittichotsatsawat, Y.; Jangkrajarng, V.; Tippayawong, K.Y. Enhancing coffee supply chain towards sustainable growth with big data and modern agricultural technologies. *Sustainability* **2021**, *13*, 4593. [CrossRef]
27. Siregar, E.; Nazir, N.; Asben, A. The Analysis of Strategic Partnership to Supply Mandailing Arabica Coffee for Export Quality Markets. In *IOP Conference Series: Earth and Environmental Science*; IOP Publishing: Bristol, UK, 2019; Volume 347, p. 012046.
28. Dang, T.T.; Nguyen, N.A.T.; Nguyen, V.T.T.; Dang, L.T.H. A two-stage multi-criteria supplier selection model for sustainable automotive supply chain under uncertainty. *Axioms* **2022**, *11*, 228. [CrossRef]
29. Agarwal, G.; Vijayvargy, L. An application of supplier selection in supply chain for modeling of intangibles: A case study of multinational Food Coffee industry. *Afr. J. Bus. Manag.* **2011**, *5*, 11505. [CrossRef]
30. Li, T.; Tan, Q.; Liu, W. Game theoretical perspectives on pricing decisions in asymmetric competing supply chains. *Discret. Dyn. Nat. Soc.* **2020**, *2020*, 9352013. [CrossRef]
31. Liao, C.-N. Applying fuzzy-MSGP approach for supplier evaluation and selection in food industry. *Afr. J. Agric. Res.* **2012**, *7*, 726–740.
32. Liu, A.H.; Bui, M.; Leach, M. Considering technological impacts when selecting food suppliers: Comparing retailers' buying behavior in the united states and Europe. *J. Business-to-Business Mark.* **2013**, *20*, 81–98. [CrossRef]
33. Ju-Long, D. Control problems of grey systems. *Syst. Control Lett.* **1982**, *1*, 288–294. [CrossRef]
34. Peng, Y.; Ning, L. Study on quality decisions in supply chain considering the lagged time and retailers competition. *Discret. Dyn. Nat. Soc.* **2020**, *2020*, 7482967. [CrossRef]
35. Odan, F.K.; Odan, F.K. Reis, and Management, Hybrid water demand forecasting model associating artificial neural network with Fourier series. *J. Water Resour. Plan. Manag.* **2012**, *138*, 245–256. [CrossRef]
36. Hsu, Y.-T.; Liu, M.-C.; Yeh, J.; Hung, H.-F. Forecasting the turning time of stock market based on Markov–Fourier grey model. *Expert Syst. Appl.* **2009**, *36*, 8597–8603. [CrossRef]
37. Wang, C.-N.; Phan, V.-T. An improved nonlinear grey bernoulli model combined with fourier series. *Math. Probl. Eng.* **2015**, *2015*, 740272.
38. González-Romera, E.; Jaramillo-Morán, M.; Carmona-Fernández, D. Monthly electric energy demand forecasting with neural networks and Fourier series. *Energy Convers. Manag.* **2008**, *49*, 3135–3142. [CrossRef]
39. Vieli, F.J.G.; Seifert, E. Fourier inversion of distributions supported by a hypersurface. *J. Fourier Anal. Appl.* **2009**, *16*, 34–51. [CrossRef]
40. Rahmawati, D.U.; Salimi, N. Sustainable and resilient supplier selection: The case of an Indonesian coffee supply chain. *J. Supply Chain Manag. Sci.* **2022**, *3*, 16–36. [CrossRef]
41. Curzi, D.; Pacca, L. Price, quality and trade costs in the food sector. *Food Policy* **2015**, *55*, 147–158. [CrossRef]
42. Zeithaml, V.A. Consumer perceptions of price, quality, and value: A means-end model and synthesis of evidence. *J. Mark.* **1988**, *52*, 2–22. [CrossRef]
43. Amid, A.; Ghodsypour, S.; O'brien, C. A weighted additive fuzzy multiobjective model for the supplier selection problem under price breaks in a supply Chain. *Int. J. Prod. Econ.* **2009**, *121*, 323–332. [CrossRef]

44. Liu, L.; Liu, S.; Fang, Z.; Jiang, A.; Shang, G. The recursive grey model and its application. *Appl. Math. Model.* **2023**, *119*, 447–464. [CrossRef]
45. General Statistics Office of Vietnam. Available online: https://www.gso.gov.vn/don-vi-hanh-chinh-dat-dai-va-khi-hau/ (accessed on 14 March 2022).

processes

MDPI

Article

Northern Lights: Prospecting Efficiency in Europe's Renewable Energy Sector

Yen-Hsing Hung and Fu-Chiang Yang *

Department of Industrial Engineering and Management, National Kaohsiung University of Science and Technology, Kaohsiung 80778, Taiwan
* Correspondence: fuchiang@nkust.edu.tw

Abstract: Northern European nations are at the forefront of renewable energy adoption but face challenges in optimizing energy conversion efficiency. There is a lack of detailed understanding of how behavioral factors affect the efficiency of renewable energy conversion in these countries. This study aims to evaluate and compare the renewable energy conversion efficiency of Northern European countries, intending to inform strategic policy making and identify best practices for technology deployment in the renewable energy sector. Employing a Data Envelopment Analysis (DEA) model, the study integrates behavioral economic parameters—specifically, the aversion loss and gain significance coefficients—to assess the efficiency of renewable energy conversion, accounting for psychological factors in decision making. A comprehensive sensitivity analysis was conducted, varying the gain significance coefficient while maintaining the aversion loss coefficient at constant levels. This experiment was designed to observe the impact of behavioral parameters on the efficiency ranking of each country. The analysis revealed that Latvia consistently ranked highest in efficiency, irrespective of the gain significance valuation, whereas Iceland consistently ranked lowest. Other countries demonstrated varying efficiency rankings with changes in gain significance, indicating different behavioral economic influences on their renewable energy sectors. Theoretically, the study enhances the DEA framework by integrating behavioral economics, offering a more holistic view of efficiency in renewable energy. Practically, it provides a benchmarking perspective that can guide policy and investment in renewable energy, with sensitivity analysis underscoring the importance of considering behavioral factors. The research offers a practical tool for policymakers and energy stakeholders to align renewable energy strategies with behavioral incentives, aiming to improve the adoption and effectiveness of these initiatives.

Keywords: Northern European; Data Envelopment Analysis; renewable energy; behavioral coefficient

1. Introduction

The transition towards renewable energy (RE) sources has emerged as a critical global mandate, driven by the escalating environmental concerns and the geopolitical instability that impacts fossil fuel markets [1]. The global energy landscape is undergoing a significant transformation, with renewable energy's share in the power sector expected to increase from 25% in 2019 to over 30% by 2024, according to the International Energy Agency (IEA) [2]. This shift is further emphasized by the urgent need to reduce greenhouse gas emissions, where the energy sector accounts for approximately two-thirds of global emissions, underscoring the critical role of renewable energy in achieving climate goals [3].

Compounding these environmental imperatives is the geopolitical volatility associated with traditional energy sources [4]. A dependence on Russia's oil and gas industry, for example, has been a stark reminder of the vulnerabilities many regions face concerning energy security and autonomy. In 2021, Europe imported approximately 40% of its natural

gas and 27% of its oil from Russia, highlighting the region's exposure to geopolitical risks and the urgency of diversifying energy sources [5].

In this context, the Northern European countries—Denmark, Estonia, Finland, Iceland, Ireland, Latvia, Lithuania, Norway, Sweden, and the United Kingdom—stand out for their proactive approach to embracing renewable energy [6]. Blessed with abundant natural resources, these nations have demonstrated a strong commitment to renewable energy, at least 20% of their energy consumption coming from renewable sources as of 2020 [7]. Their efforts are not only aimed at enhancing national energy security but also at contributing to global sustainability objectives [8]. However, transitioning to renewable energy is fraught with challenges, particularly regarding the need for substantial advancements in the efficiency of renewable energy conversion technologies and systems to meet growing energy demands sustainably [9,10].

Despite an increasing focus on renewable energy, a significant research gap persists in understanding and quantifying the efficiency of renewable energy conversion processes, especially within the Northern European context. This gap is critical as it influences the development of effective policies and the optimization of renewable energy systems for maximum productivity and sustainability. A review of the existing literature reveals a proliferation of studies on renewable energy deployment, yet few delve into the nuanced analysis of conversion efficiency in the Northern European region [11–14]. This lack of detailed efficiency metrics hinders the ability to fully leverage the potential of renewable resources, necessitating a more focused and analytical approach to assess and enhance the performance of renewable energy technologies.

The urgency of addressing these challenges cannot be overstated. As the world moves towards a more sustainable and secure energy future, the insights gained from evaluating the efficiency of renewable energy conversion in the Northern European countries could provide valuable lessons for global energy policy and technology development. This underscores the need for comprehensive research that not only identifies the current state of renewable energy efficiency but also proposes innovative solutions to improve it, thereby supporting the global transition towards a more resilient and sustainable energy system.

This study is motivated by the need to bridge these gaps through a comprehensive evaluation of the efficiency of renewable energy conversion in Northern European countries. It aims to provide actionable insights for policymakers and industry stakeholders to foster the development of more efficient, resilient, and sustainable energy systems. To achieve this, the study sets forth two primary objectives: a practical objective to evaluate the efficiency of renewable energy conversion for policy development, and a theoretical objective to propose and apply a robust Data Envelopment Analysis (DEA) model enhanced with prospect theory. This dual approach will facilitate a more nuanced understanding of the efficiency landscapes and the decision-making processes governing renewable energy investments and operations in the Northern European region.

This article is structured as follows: Section 1 outlines the study's background, motivation, and aims. Section 2 conducts a thorough literature review, identifying prior research and research gaps. Section 3 details the study's methodologies, particularly the use of a data analysis envelopment model enhanced with prospect theory. Section 4 delivers the numerical findings, analyzing renewable energy conversion efficiency in the Nordic countries. Section 5 wraps up the research, summarizing the main insights, policy implications, and directions for further investigation.

2. Literature Review

2.1. Renewable Energy Studies in Northern Eupopean

The research landscape on renewable energy in Europe encompasses studies that span various aspects, including policy frameworks, economic impacts, technological advancements, and environmental sustainability [15,16]. Campos et al. (2020) underscore the evolving role of RE prosumers within the EU, influenced by policies that transition consumers to active energy participants [17]. This study identifies France, Germany, the

Netherlands, and the United Kingdom as leaders in creating favorable conditions for collective prosumers, marking a significant move towards energy democratization and sustainability. Economic relationships between growth, carbon emissions, and renewable energy consumption have been explored by Radmehr, Riza et al. in their 2021 study, alongside Simionescu et al. (2023), both of which reveal strong spatial correlations across EU countries [13,18]. They highlight a bidirectional link between economic growth and renewable energy consumption, offering vital insights for policy development aimed at sustainable growth.

From an environmental perspective, the 2020 study by Destek and Aslan emphasizes the varied impacts of different renewable energy sources on carbon emissions, suggesting the need for policies tailored to the characteristics of each energy type [19]. Johannsen et al.'s 2023 research on decarbonizing the European industrial sector further stresses the potential of existing technologies, energy savings, and electrification for achieving environmental goals [20]. Potrč et al. (2021) and Tutak et al. (2022) investigate the socio-economic benefits of the EU's renewable energy transition, aiming for a carbon-neutral status by 2050 [3,21,22]. Their findings point to the significant potential of wind and solar power and the positive effects of renewable energy on economic growth and emission reductions. In terms of technology innovation, Panchenko et al. (2023) delve into "green" hydrogen production's future, emphasizing its importance in moving towards cleaner energy sources and enhancing energy independence [23]. This highlights the sector's continuous innovation and technological progress.

Despite the breadth of research, a notable gap exists in the detailed analysis of renewable energy conversion efficiency, especially within Northern European countries. This study seeks to address this by evaluating the efficiency of renewable energy conversion in these regions, employing a data analysis envelopment model with prospect theory enhancements. This comprehensive approach aims to shed light on efficiency dynamics, guiding policy and technological advancements in Northen Europe.

2.2. Data Envelopment Analysis Studies

The exploration of DEA across a diverse array of sectors, with a notable emphasis on the renewable energy domain, showcases its broad applicability and efficiency in performance evaluations and efficiency assessments. In 2020, the work of Kaffash brought to light DEA's growing significance within the insurance sector, highlighting its capacity to evaluate the operational efficiency of insurance firms amidst rapidly evolving market conditions and technological advancements [24]. This pivotal insight not only underscores the adaptability of DEA but also sets the stage for its application in critical areas such as the assessment of renewable energy efficiency, marking a significant leap towards broader utility in various industrial domains. Building upon this foundation, the research conducted by Tao Xu et al. further reinforces the importance of DEA in the energy sector, illuminating its widespread adoption for conducting detailed energy efficiency studies spanning the years from 2011 to 2019 [25]. In a similar vein, the work of Fotova Čiković and Lozić (2022) [26], along with Dutta et al. (2022) [27], ventures beyond traditional applications, extending DEA's reach into the realms of Information and Communication Technology (ICT) and supply chain management, respectively. These studies collectively highlight DEA's instrumental role in streamlining processes and bolstering sustainability efforts, attributes that are directly translatable and immensely beneficial to renewable energy initiatives.

The innovative approach introduced by Le and Nhieu represents a significant advancement in the application of DEA, marrying the methodology with behavioral insights and fuzzy Multi-Criteria Decision-Making (MCDM) techniques in 2022. This novel integration facilitates the selection of offshore wind and wave energy projects, demonstrating DEA's flexibility and effectiveness in navigating the intricate decision-making landscapes inherent in renewable energy projects [28]. Additionally, research by Kyrgiakos et al. (2023) showcases DEA's application within the agricultural sector with a focus on sustainabil-

ity, offering valuable insights into how the methodology can be leveraged to evaluate renewable energy initiatives through a comprehensive sustainability framework [29]. The groundbreaking work of Tavana et al. (2023) and Chia-Nan Wang et al. (2024) marks a significant evolution in DEA's application, incorporating behavioral theories and hybrid decision-making frameworks to refine and enhance the evaluation of renewable energy projects [30–32].

These developments not only underscore the methodological advancements within DEA but also spotlight the promising potential of applying DEA within Europe's renewable energy sector. Specifically, these advancements point towards the optimization of offshore energy exploitation and the meticulous selection of projects, guided by a thorough analysis of efficiency metrics. Such applications of DEA promise to offer comprehensive insights and robust frameworks for evaluating the sustainability and efficiency of renewable energy projects, thereby contributing significantly to the advancement of Europe's renewable energy objectives.

The comprehensive review underscores the significant strides made in the application of DEA across various sectors, highlighting its evolving role in enhancing efficiency and performance evaluations. Notably, although DEA's adaptability and effectiveness have been demonstrated in fields ranging from insurance to agriculture, its application within the renewable energy sector, particularly in Northern European countries, remains underexplored. This identified gap in the detailed analysis of renewable energy conversion efficiency in these regions presents a critical area for further research.

The current study aims to bridge this gap by employing a data analysis envelopment model, enhanced with prospect theory, to evaluate the efficiency of renewable energy conversion in Northern Europe. This endeavor seeks not only to understand the efficiency dynamics but also to inform policy and technological advancements in the region. The methodological advancements within DEA, highlighted by the research reviewed, underscore the potential for DEA's application in optimizing offshore energy exploitation and in the careful selection of renewable energy projects. By conducting a thorough analysis of efficiency metrics, this approach promises to offer comprehensive insights and robust frameworks for evaluating the sustainability and efficiency of renewable energy projects.

3. Methodology

3.1. Traditional DEA Model

In 1978, a groundbreaking achievement in operations research and efficiency assessment was marked by the introduction of the pioneering DEA model by Charnes and his collaborators, commonly known as the CCR (Charnes, Cooper and Rhodes) model. This model revolutionized the evaluation of technical efficiency across various sectors, operating on the premise of constant returns to scale, a fundamental concept in optimization [33]. However, as real-world applications unfolded, the limitation of universal applicability became apparent, leading to further advancements in DEA methodologies. In response, Banker and his team introduced the BCC (Banker, Chames and Cooper) model, accounting for variable returns to scale and enhancing flexibility and realism in analysis [34]. The comprehensive DEA framework, comprising both CCR and BCC models, serves as a vital tool for evaluating the performance of Decision-Making Units (DMUs) managing multiple inputs to produce diverse outputs. Technical efficiency (E_k) for each DMU (kth) is calculated using a mathematical model (1), which considers intricate input–output relationships, enabling not only efficiency quantification but also identification of improvement areas and resource optimization. The DEA methodology remains integral in addressing efficiency

challenges across industries, evolving continually to meet the needs of decision makers and analysts alike.

$$\begin{aligned} &maximize\ E_k = \rho + \sum_{t=1}^{T} u_t m_{tk} \\ S.t. \\ &\sum_{j=1}^{J} v_j n_{jk} = 1 \\ &\rho + \sum_{t=1}^{T} u_t m_{ti} - \sum_{j=1}^{J} v_j n_{ji} \le 0\ i = 1, \ldots, I \\ &u_t, v_j \ge 0 \qquad j = 1, \ldots, J; t = 1, \ldots, T \\ &\rho \text{ is free} \end{aligned} \tag{1}$$

In this model, u_t and v_j represent the weights assigned to the tth output and the jth input, respectively, playing a crucial role in determining the relative importance of each input and output in the efficiency assessment process. Moreover, the values of n_{ji} and m_{ti} hold significance, where n_{ji} denotes the value of the jth input for the ith DMU and m_{ti} signifies the value of the tth output for the same DMU, serving as the actual data for inputs and outputs used in the efficiency calculation. These values form the foundation upon which DEA evaluates the performance of DMUs. The primary objective of DEA is to ascertain the effectiveness of each DMU, with a DMU being deemed effective when its technical efficiency (E_k) equals 1. This signifies that the DMU is operating optimally, utilizing its inputs fully to generate the desired outputs without inefficiencies, thereby serving as a benchmark for others to emulate, indicative of exceptional performance and operating at the frontier of its production possibility.

3.2. Prospect Theory

Introduced by Kahneman and Tversky in 1979 [35], prospect theory has emerged as a foundational concept in behavioral economics, permeating numerous disciplines [36,37]. This theory delineates three key principles governing human decision making. Firstly, individuals evaluate gains and losses in relation to a reference point rather than absolute values, shaping their perception of outcomes—a concept known as reference dependence. Secondly, the theory highlights loss aversion, revealing that individuals are typically more sensitive to losses than equivalent gains, resulting in an asymmetrical impact on decision-making processes. Finally, prospect theory suggests diminishing sensitivity, indicating that individuals exhibit risk-seeking behavior in scenarios of potential losses but tend to be risk averse when facing potential gains, underscoring how the marginal utility of wealth decreases as wealth increases.

These principles collectively underpin the prospective value function, graphically represented by an asymmetrical S-shaped curve. This function embodies reference dependence, loss aversion, and diminishing sensitivity, providing a visual framework for understanding decision-making processes. Mathematically expressed as Equation (2), the value function ($f(\Delta t)$) incorporates parameters such as γ, δ, and θ to quantify decision makers' attitudes towards risk and loss aversion. By leveraging these parameters, the equation offers a quantitative model for analyzing human behavior influenced by prospect theory, facilitating predictive insights across diverse decision-making scenarios [38]. In Equation (2), Δt represents the difference in value with respect to the reference point. If Δt is positive, this difference is considered a gain and it is calculated into the value function corresponding to the level of concern the decision maker has for gains (γ). Conversely, if Δt is negative, it is included in the value function based on the decision maker's level of concern

about losses (δ). Furthermore, losses can also be mitigated depending on the psychological behavior of the decision maker calculated through the loss aversion coefficient (θ).

$$f(\Delta t) = \begin{cases} (\Delta t)^{\gamma} & ,\forall \Delta t \geq 0;\ 0 < \gamma < 1 \\ -\theta(-\Delta t)^{\delta} & ,\forall \Delta t < 0;\ 0 < \delta < 1 \end{cases} \tag{2}$$

3.3. The Behavioral DEA Model

Chen et al. have innovatively applied prospect theory principles to the domain of DEA, introducing a novel approach to assessing efficiency with a consideration of risk [39]. This novel behavioral DEA model unfolds through distinct steps tailored to capture the cognitive intricacies inherent in decision making under risk and uncertainty.

The initial step involves the normalization of inputs and outputs (x_{ji} and y_{ij}, respectively), as delineated by Equations (3) and (4). Normalization plays a pivotal role in enabling a fair comparison among varied decision-making units, effectively accommodating the inherent biases and subjectivity inherent in human decision-making processes.

$$x_{ji} = \frac{n_{ji}^{max} - n_{ji}}{n_{ji}^{max} - n_{ji}^{min}}\ i = 1, \ldots, I; j = 1, \ldots, J \tag{3}$$

$$y_{ti} = \frac{m_{ti} - m_{ti}^{min}}{m_{ti}^{max} - m_{ti}^{min}}\ i = 1, \ldots, I; t = 1, \ldots, T \tag{4}$$

The second step entails the identification of reference points to integrate the psychological aspects emphasized by prospect theory into the model. Both positive and negative reference points are identified to comprehend how individuals perceive and respond to gains and losses. These reference points, as depicted in Equations (5) and (6), serve as crucial benchmarks against which gains and losses are assessed, aligning with the reference dependence principle elucidated in prospect theory.

The positive reference points (n_j^+ *and* m_t^+):

$$n_j^+ = \min_i(x_{ji}); m_t^+ = \max_i(y_{ti}) \tag{5}$$

The negative reference points (n_j^- *and* m_t^-):

$$n_j^- = \max_i(x_{ji}); m_t^- = \min_i(y_{ti}) \tag{6}$$

In the third and final step, the behavioral DEA model is formulated, as delineated in Model (7). This model integrates the normalized inputs and outputs, reference points, and the principle of diminishing sensitivity, which reflects individuals' responses to gains and losses. The coefficient φ holds significance within this framework, representing the relative weight assigned to gains compared to losses. A value of 0.5 for φ denotes an equal consideration of gains and losses, indicating a balanced approach by decision makers. In model (7), the objective function is divided into two parts. The first parentheses are the gains, and the second parentheses describe the losses of each DMUs. The basis of this objective function is developed from the idea of expected value discussed in Equation (2).

Meanwhile, the constraints of the model comply with the principles of the traditional DEA model as presented in Model (1).

$$\begin{aligned}
&Maximize\ Z = \varphi\left(\rho + \sum_{t=1}^{T} u_{tk}\left(y_{tk} - m_t^-\right)^{\gamma} + \sum_{j=1}^{J} v_{jk}\left(n_j^- - x_{jk}\right)^{\gamma}\right)\\
&\quad -(1-\varphi)\left(\rho + \sum_{t=1}^{T} u_{tk}\theta\left(m_t^+ - y_{tk}\right)^{\delta} + \sum_{j=1}^{J} v_{jk}\theta\left(x_{jk} - n_j^+\right)^{\delta}\right)\\
&Subject\ to\\
&\quad \sum_{j=1}^{J} v_{jk} n_{jk} = 1\\
&\quad \rho + \sum_{t=1}^{T} u_{ti} m_{ti} - \sum_{j=1}^{J} v_{ji} n_{ji} \le 0 \quad i = 1, \ldots, I\\
&u_{ti},\ v_{ji} \ge 0, \rho \text{ is free} \quad j = 1, \ldots, J; t = 1, \ldots, T; i = 1, \ldots, I
\end{aligned} \tag{7}$$

4. Numerical Results

4.1. Problem Description

The pursuit of renewable energy efficiency in Northern European countries, including Denmark, Estonia, Finland, Iceland, Ireland, Latvia, Lithuania, Norway, Sweden, and the United Kingdom, has been underscored by the unique challenges and opportunities presented by their geographical and socio-economic conditions. Despite these countries' commendable strides towards integrating renewable energy into their national grids, there remains a significant problem: the optimization of renewable energy efficiency varies widely across this region. Moreover, the pressing need to transition from fossil fuel dependency to sustainable energy sources has highlighted the urgency of addressing these efficiency variances. The challenge, therefore, lies in identifying and implementing strategies that can elevate the efficiency of renewable energy conversion processes, ensuring that these nations not only meet but exceed their ambitious sustainability targets. This backdrop sets the stage for the proposed study, aiming to delve into the efficiency dynamics of renewable energy conversion within these Northern European countries, employing a comprehensive DEA model to uncover insights that could guide future enhancements in the sector.

In the assessment of renewable energy conversion efficiency within the Northern European context, a set of indicators has been meticulously selected according to references for integration into the proposed behavioral DEA model, where each is assigned a specific role as either an input or an output [14,40–46]. As shown in Figure 1, traditional energy production (Input 1), quantified through the gigawatt-hours (GWh) of electricity generated from fossil fuels, has been included as an input to serve as a foundational comparison point for the efficiency of renewable sources. This is augmented by the inclusion of the population size (Input 2) of the region, which is utilized to contextualize the demand for energy, thereby providing a backdrop against which the necessity for energy solutions is understood. Furthermore, the environmental repercussions of energy production processes are encapsulated through an indicator that represents the economic impact of particulate emissions (Input 3), calculated as a percentage of the Gross National Income (GNI), thereby underscoring the environmental costs associated with energy production.

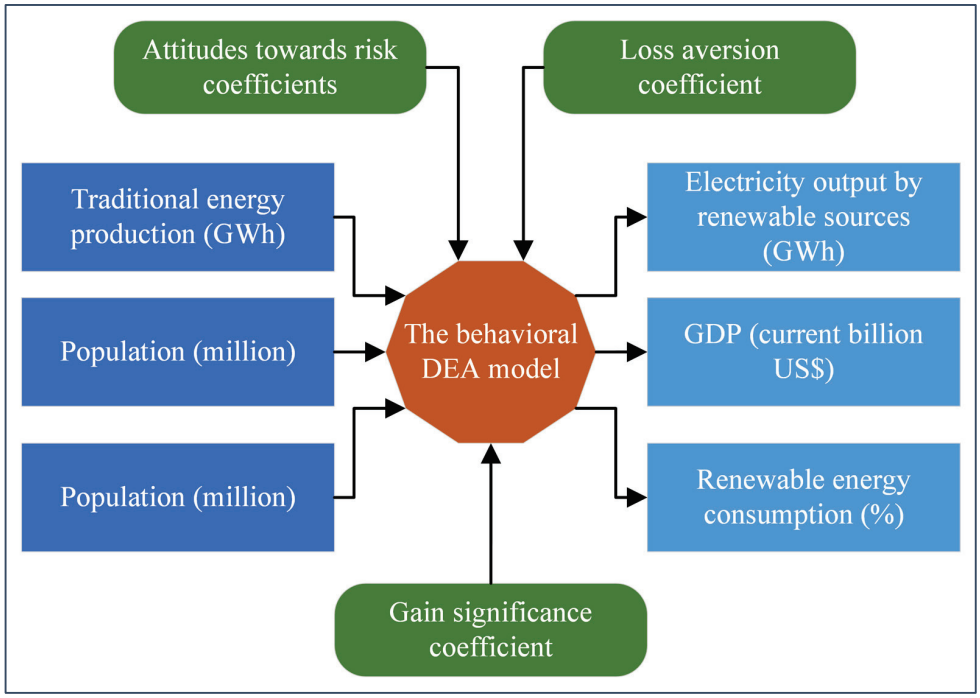

Figure 1. The behavioral DEA model application.

On the spectrum of outputs within our model, the focus is directed towards the electricity output derived from renewable sources (Output 1), also measured in GWh, to directly gauge the volume of clean energy generated. The economic impact of energy production and consumption is captured through the Gross Domestic Product (GDP) (Output 2), expressed in current US dollars, which serves as a linkage between energy efficiency and economic prosperity. Moreover, the proportion of renewable energy within the total energy consumption (Output 3) mix is incorporated as an output indicator, reflecting the degree of adoption and integration of renewable sources into the energy landscape, thereby making strides towards achieving sustainability goals.

4.2. Data Collection and Behavioral DEA Application

The study leverages an array of robust data sources to underpin its analysis of renewable energy efficiency in Northern European countries, notably drawing from the World Bank [47], the International Energy Agency (IEA) [48,49], and the International Renewable Energy Agency databases [50,51]. These repositories are renowned for their comprehensive and reliable datasets on global energy statistics.

The comprehensive process of data gathering and its subsequent synthesis have been meticulously documented in Table 1. This initial step set the foundation for the analysis, whereupon the collected data pertaining to the inputs and outputs were subjected to a normalization process, as delineated by Equations (3) and (4), with the normalized figures being systematically presented in Table 2. Following this preparatory phase, the study advanced to the application of the behavioral DEA model, as specified in model (7), which serves as the analytical tool for assessing the efficiency levels across the surveyed countries. The intricate process of efficiency calculation, employing the behavioral DEA model, takes into consideration a set of predefined psychological behavioral parameters. These parameters—φ set at 0.5, θ at 2.25, γ at 0.85, and δ at 0.92—play a crucial role in the model, reflecting the psychological dimensions incorporated into the efficiency analysis.

Table 1. The renewable energy performance indicators in Northern European 2021.

Country	Traditional Energy Production (GWh)	Population (Million)	Particulate Emission Damage Savings (% of GNI)	Electricity Output by Renewable Sources (GWh)	GDP (Current Billion US$)	Renewable Energy Consumption (% of Total Final Energy Consumption)
	Input 1	**Input 2**	**Input 3**	**Output 1**	**Output 2**	**Output 3**
Denmark	6158.38	5.86	0.04	26,095.91	405.69	39.70
Estonia	4233.78	1.33	0.03	2878.53	37.19	40.00
Finland	9582.00	5.54	0.01	38,175.37	296.47	47.49
Iceland	2.46	0.37	0.02	19,611.73	25.60	82.79
Ireland	19,651.08	5.03	0.02	11,613.51	513.39	13.69
Latvia	2128.40	1.88	0.13	3717.82	39.44	43.75
Lithuania	1316.50	2.80	0.09	2621.70	66.80	31.70
Norway	897.80	5.41	0.01	156,101.28	503.37	61.29
Sweden	1375.00	10.42	0.01	115,737.00	639.71	58.40
United Kingdom	132,429.85	67.03	0.05	122,178.14	3141.51	13.50

Table 2. The normalized performance data.

Country	Input 1	Input 2	Input 3	Output 1	Output 2	Output 3
Denmark	0.954	0.968	0.928	1.000	0.852	0.984
Estonia	0.918	0.986	0.922	1.000	0.930	0.977
Finland	0.753	0.810	0.969	0.943	0.920	0.000
Iceland	0.153	0.002	0.232	0.111	0.059	0.007
Ireland	0.122	0.004	0.087	0.000	0.157	0.004
Latvia	0.378	0.382	0.491	1.000	0.003	0.437
Lithuania	0.954	0.968	0.928	1.000	0.852	0.984
Norway	0.918	0.986	0.922	1.000	0.930	0.977
Sweden	0.753	0.810	0.969	0.943	0.920	0.000
United Kingdom	0.153	0.002	0.232	0.111	0.059	0.007

The results derived from this sophisticated calculation are then graphically represented in Figure 2, offering a visual depiction of the efficiency outcomes across the countries under study. This visual representation not only highlights the efficiency scores determined by the behavioral DEA model but also illustrates the impact of incorporating psychological behavioral parameters into the analysis, as corroborated by references [35,52,53]. Through this detailed approach, the study endeavors to provide a nuanced understanding of efficiency in the context of renewable energy utilization among Northern European countries, accounting for the behavioral factors that influence decision-making processes within this domain.

The efficiency results for renewable energy conversion in Northern European countries present a diverse picture, with efficiency scores ranging notably from as low as 0.046 to an exceptional high of 4.311. Different from traditional DEA models, the DEA model proposed in this study considers the effects of gains and losses at the same time. When the decision maker's psychology focuses on losses more than gains (reflected through the psychological behavior coefficient), the value of the objective function in the proposed DEA model can be negative. This leads to the proposed DEA model being unsolvable. To overcome this problem, a positive constant is added to the objective function, as ρ in model (7). This is to ensure that the proposed DEA model can solve and describe the difference in efficiency between DMUs. Therefore, the efficiency of DMUs by the proposed DEA model can be larger than 1. Furthermore, this also addresses the situation where two or more DMUs have an efficiency of 1. This makes it impossible to rank or provide more detailed assessments.

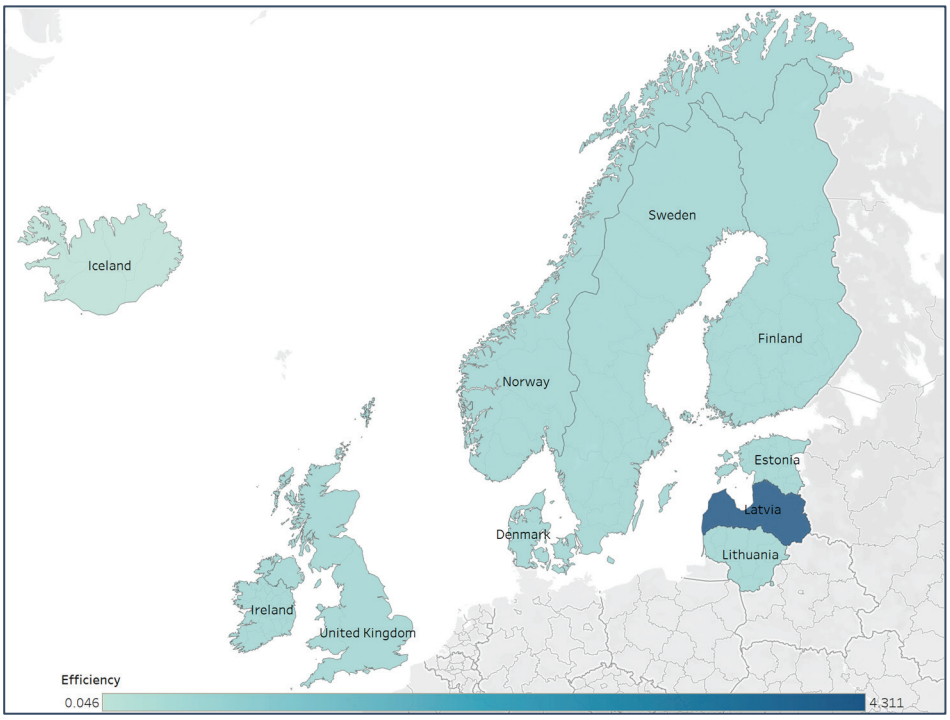

Figure 2. The renewable energy efficiency in Northern European with default psychological behavioral parameters.

The majority of the countries, including Denmark, Estonia, Finland, and Ireland, display a median efficiency score of 0.500. This uniformity suggests these countries are at an average efficiency level, potentially utilizing half of their renewable energy capacity when benchmarked against best practices within the data set. Lithuania, Norway, and Sweden are marginally below this median mark with a score of 0.499, indicating they are very close to their peers in terms of efficiency and might require minimal interventions to enhance their performance. In stark contrast, Iceland's efficiency score stands at 0.046, signaling a significant efficiency gap compared to other countries in the study. This low score may reflect unique national challenges that hinder efficient renewable energy conversion, necessitating a detailed investigation into potential technological, infrastructural, or policy improvements. On the other end of the spectrum, Latvia's outlier score of 4.311 is remarkably high, exceeding the conventional DEA score range and suggesting a highly effective renewable energy sector, though this anomalous value could also prompt a verification of data integrity and model specifications to confirm its accuracy.

The United Kingdom slightly exceeds the median with a score of 0.508, hinting at a relatively more efficient renewable energy conversion process compared to most of its regional counterparts. The consistency in the median scores and Latvia's extraordinary efficiency call for a critical review of the DEA model's structure, including input–output specification, scale assumptions, and orientation choices. These results underscore the need for both a comprehensive understanding of the factors driving Latvia's efficiency and a focused analysis of Iceland's renewable energy strategies to address its efficiency shortfall.

4.3. The Loss Aversion Sensitivity Analysis

In this section, a sensitivity analysis is performed to examine the influence of the aversion loss coefficient (θ) and gain significance coefficient (φ) on the efficiency of the countries. Accordingly, the behavioral DEA model was solved many times with different values of the aversion loss coefficient and gain significance coefficient. The ranking results of the solutions are summarized in Figures 3 and 4.

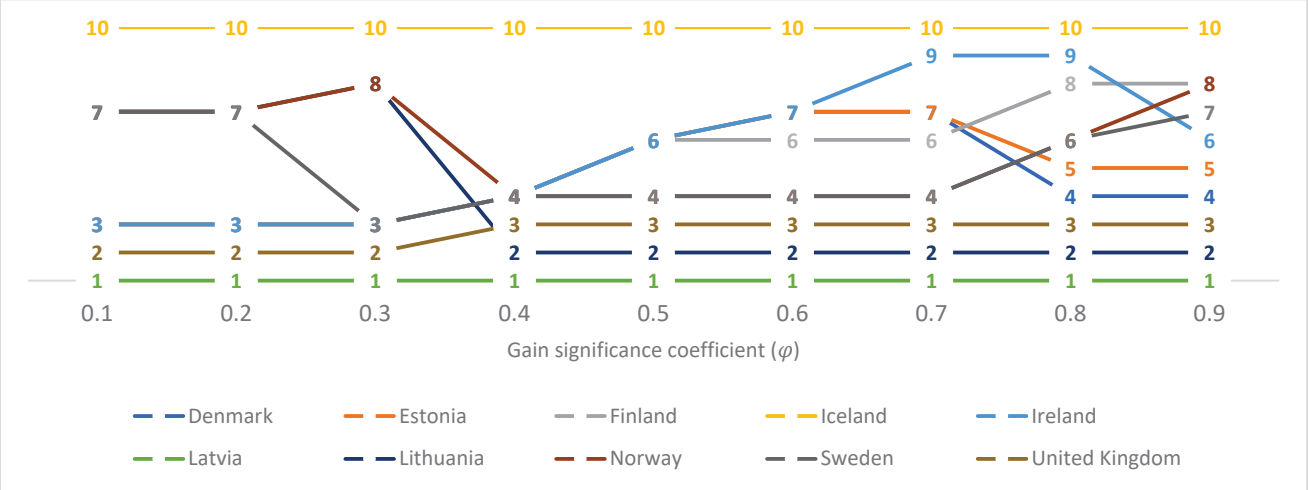

Figure 3. The ranking results with $\theta = 1$.

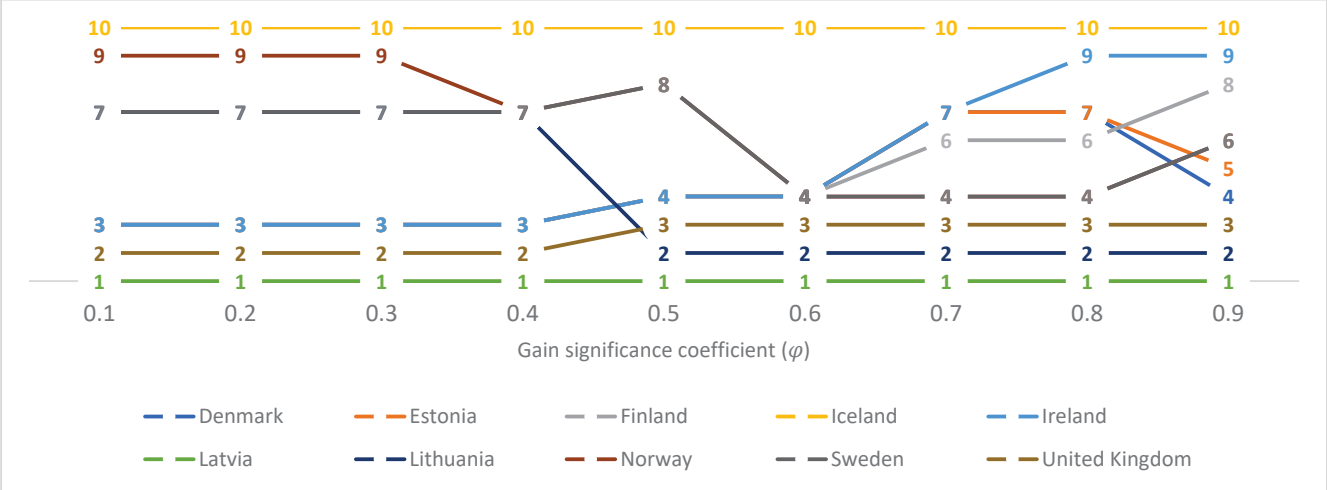

Figure 4. The ranking results with $\theta = 2$.

The ranking results in Figure 3, anchored by an aversion loss coefficient (θ) fixed at 1, reveal the dynamic effects of varying the gain significance coefficient (φ) on the perceived efficiency of renewable energy conversion in Northern European countries. Throughout the range of φ from 0.1 to 0.9, Latvia consistently emerges as the most efficient, suggesting that its renewable energy sector is robust against changes in the valuation of gains. Conversely, Iceland persistently ranks at the bottom, indicating that its renewable energy efficiency is lower compared to its regional counterparts, regardless of the psychological weighting of gains. As φ increases, depicting a higher valuation of gains, the rankings of countries like Finland improve, pointing to a positive response in its renewable energy sector to the increasing importance of gains. This could reflect a scenario where Finnish policies or technologies gain greater efficacy under conditions where gains are more significantly valued. Meanwhile, the rankings of Sweden and Norway exhibit a distinct variability, improving at intermediate φ values but decreasing at higher φ values, suggesting a non-linear response to the changing valuation of gains. The United Kingdom displays a moderate change in rankings with varying φ, suggesting a moderate sensitivity to the valuation of gains in its renewable energy efficiency. Notably, Lithuania's efficiency ranking fluctuates considerably across the spectrum of φ, indicating a more complex relationship between the efficiency of its renewable energy sector and the valuation of gains. These ranking shifts underscore the nuanced impact that behavioral factors can have on the evaluation

of energy policy and technology effectiveness. Countries that demonstrate fluctuating efficiency with changes in φ may require a more tailored approach to policy making that aligns with the behavioral tendencies of their energy sectors. The consistency of Latvia's top-ranking position suggests that it could serve as a model for best practices, whereas Iceland's consistently lower ranking points to a need for strategic policy interventions to enhance its renewable energy efficiency.

With the aversion loss coefficient (θ) set at 2, indicating a stronger aversion to losses, the sensitivity analysis of the gain significance coefficient (φ) provides an intriguing view into the rankings of renewable energy efficiency across Northern European countries.

The results show that with a higher aversion to loss, the countries' rankings are influenced variably by the gain significance, as shown in Figure 4. For instance, Latvia's top rank is consistent across all levels of φ, suggesting that its renewable energy sector's performance is perceived as efficient regardless of the psychological weight placed on gains. This could signify a robust energy policy or a highly effective implementation of renewable energy technologies in Latvia. Iceland, on the other hand, maintains the lowest rank across the board, indicating persistent challenges or inefficiencies in its renewable energy sector. This consistently low ranking could be due to factors such as less favorable natural conditions for renewable energy generation, less developed infrastructure, or policies that are not as conducive to promoting renewable energy efficiency. The rankings for countries like Lithuania and Norway show variability when the gain significance coefficient changes, indicating a fluctuating perception of efficiency as the emphasis on gains shifts. This may suggest that these countries' renewable energy sectors respond differently to psychological factors, and hence, could benefit from policies that align more closely with behavioral incentives. Sweden and the United Kingdom exhibit interesting patterns; their rankings remain relatively stable at lower φ values, but as φ increases, indicating a higher valuation of gains, their rankings improve. This suggests that these countries might have a good potential for efficiency gains that are not fully realized or valued at lower φ levels.

The changes in rankings for Denmark, Estonia, and Finland as φ increases suggest that these countries' renewable energy efficiencies may be more sensitive to the valuation of gains. For policy implications, these countries might consider strategies that emphasize the positive aspects of renewable energy investment and focus on the benefits rather than the costs.

4.4. Discussion

This study provides significant insights into the renewable energy conversion efficiency across Northern European countries by integrating behavioral economics into a DEA framework. By applying sensitivity analysis to the gain significance coefficient (φ) while holding the aversion loss coefficient (θ) coefficient, the research highlights the influence of behavioral factors on efficiency rankings among the countries studied. The innovative incorporation of behavioral economics into the DEA model has elucidated the role of psychological factors in energy policy and technology adoption, potentially transforming how policymakers and industry stakeholders approach renewable energy deployment. The sensitivity analysis reveals that the perception of efficiency is affected by the valuation placed on gains, a finding that could influence the design of incentive structures and policy measures aimed at boosting renewable energy use. For instance, the consistent high efficiency of Latvia across various levels of φ suggests that its renewable energy policies are well-aligned with both economic and behavioral incentives. Conversely, the consistently low ranking of Iceland indicates potential areas for policy intervention, perhaps suggesting a need for strategies that better leverage behavioral incentives to drive efficiency improvements. A notable finding is the fluctuation in rankings for countries like Lithuania and Norway at different levels of φ. This variability could reflect a unique interplay between existing renewable energy policies and the behavioral tendencies within these countries, signaling an opportunity for tailored policy adjustments that could enhance the efficiency of renewable energy conversion.

5. Conclusions

This study embarked on an exploration of renewable energy efficiency within Northern European countries, a region at the forefront of the global shift towards sustainable energy sources. Recognizing the imperative to transition from fossil fuel dependency to renewable alternatives, this study aimed to quantify and compare the efficiency of renewable energy conversion across Denmark, Estonia, Finland, Iceland, Ireland, Latvia, Lithuania, Norway, Sweden, and the United Kingdom. The primary objective was to evaluate the efficiency of renewable energy conversion, using a robust analytical framework that could inform policy and technology enhancements. The study sought to uncover how different countries perform relative to each other within the context of behavioral factors that influence energy policy and investment decisions.

A DEA model, enhanced with behavioral economics through the inclusion of the aversion loss coefficient (θ) and gain significance coefficient (φ), was employed. This approach allowed for the assessment of renewable energy conversion efficiency while accounting for the psychological dimensions that can impact decision-making processes within energy sectors. The sensitivity analysis revealed distinct patterns of efficiency rankings among the countries, with notable consistency for some and significant variability for others across different values of φ. Latvia consistently ranked as the most efficient, whereas Iceland was persistently at the lower end of the efficiency spectrum. These rankings shifted for other countries with changes in φ, indicating different levels of responsiveness to the psychological valuation of gains in renewable energy investment.

Theoretically, this study expands the DEA methodology by weaving in behavioral economics, providing a richer understanding of the factors driving efficiency in renewable energy. Practically, it offers a comparative analysis that can serve as a benchmarking tool for policymakers and energy sector stakeholders. It lays the groundwork for developing tailored strategies that align renewable energy initiatives with behavioral incentives, potentially enhancing the adoption and effectiveness of these initiatives.

Although the results are robust, the study acknowledges limitations. The DEA model used does not account for the dynamic nature of energy markets or the evolving policy landscape, which could significantly impact efficiency. Furthermore, cultural factors and individual country policies are not specifically accounted for, which may influence the interpretation of the behavioral parameters used in the model. Given these considerations, further research is warranted. Future studies could expand upon this work by incorporating dynamic models that track efficiency over time, explore the impact of individual renewable energy types, and consider country-specific behavioral factors. Qualitative analyses could also be valuable, providing a richer context for the quantitative findings and helping to understand the nuanced influences on renewable energy efficiency.

Author Contributions: Conceptualization, Y.-H.H. and F.-C.Y.; methodology, Y.-H.H. and F.-C.Y.; validation, Y.-H.H. and F.-C.Y.; formal analysis, Y.-H.H.; investigation, Y.-H.H. and F.-C.Y.; resources, Y.-H.H. and F.-C.Y.; data curation, Y.-H.H. and F.-C.Y.; writing—original draft preparation, Y.-H.H. writing—review and editing, Y.-H.H. and F.-C.Y.; visualization, Y.-H.H.; supervision, F.-C.Y.; project administration, F.-C.Y.; funding acquisition, F.-C.Y. All authors have read and agreed to the published version of the manuscript.

Funding: This research received no external funding.

Data Availability Statement: Data are contained within the article.

Conflicts of Interest: The authors declare no conflicts of interest.

Abbreviations

Notation/Acronyms	Description
DEA	Data Envelopment Analysis
RE	Renewable energy
IEA	The International Energy Agency
EU	the European Union
ICT	Information and Communication Technology
MCDM	Multi-Criteria Decision-Making
CCR model	Charnes, Cooper and Rhodes model
BCC model	Banker, Chames and Cooper model
DMUs	the Decision-Making Units
GWh	gigawatt-hours
GDP	the Gross Domestic Product
US	The United States
E_k	Technical efficiency of kth DMU
I	Number of DMUs
J	Number of input indicators
T	Number of output indicators
u_t	The weight assigned to the tth output of DEA model
v_j	The weight assigned to the jth input DEA model
m_{ti}	The value of the tth input for the ith DMU
n_{ji}	The value of the jth input for the ith DMU
ρ	The non-negative adjustment constants
Δl	The difference in value with respect to the reference point according to Prospect theory
γ	The decision-makers' attitudes towards gains
δ	The decision-makers' attitudes towards losses
θ	The loss aversion coefficient
x_{ji}	The normalized value of n_{ji}
y_{ti}	The normalized value of m_{ti}
n_j^+	The positive reference points for inputs
m_t^+	The positive reference points for outputs
n_j^-	The negative reference points for inputs
m_t^-	The negative reference points for outputs
φ	The gain significance coefficient
Z	The behavior DEA model's objective function value

References

1. Jordana, J.; Saz, A.; Marx, A.; Holesch, A.; Vandendriessche, M.; Coen, D.; Levi-Faur, D.; Rogers, C.; Zürn, M.; Tokhi, A.; et al. *Trends in Global Governance and Future Scenarios 2030*; Institut Barcelona d'Estudis Internacionals (IBEI): Barcelona, Spain, 2023.
2. The Global Power Mix Will Be Transformed by 2028. 2023. Available online: https://www.iea.org/energy-system/renewables (accessed on 11 November 2023).
3. Brodny, J.; Tutak, M. Assessing the energy security of European Union countries from two perspectives—A new integrated approach based on MCDM methods. *Appl. Energy* **2023**, *347*, 121443. [CrossRef]
4. Duarte, P.A.B.; FLeandro, J.B.S.; Galán, E.M. *The Palgrave Handbook of Globalization with Chinese Characteristics: The Case of the Belt and Road Initiative*; Springer Nature: Berlin/Heidelberg, Germany, 2023.
5. Where Does the EU's Gas Come from? 2024. Available online: https://www.consilium.europa.eu/en/infographics/eu-gas-supply (accessed on 1 February 2024).
6. Cross, S.; Hast, A.; Kuhi-Thalfeldt, R.; Syri, S.; Streimikiene, D.; Denina, A. Progress in renewable electricity in Northern Europe towards EU 2020 targets. *Renew. Sustain. Energy Rev.* **2015**, *52*, 1768–1780. [CrossRef]
7. Renewable Energy Targets. 2023. Available online: https://energy.ec.europa.eu/topics/renewable-energy/renewable-energy-directive-targets-and-rules/renewable-energy-targets_en (accessed on 11 May 2023).
8. Bahgat, G. Europe's energy security: Challenges and opportunities. *Int. Aff.* **2006**, *82*, 961–975. [CrossRef]
9. Bigerna, S.; Bollino, C.A.; Micheli, S. *The Sustainability of Renewable Energy in Europe*; Springer: Berlin/Heidelberg, Germany, 2015.
10. Parhamfar, M.; Sadeghkhani, I.; Adeli, A.M. Towards the application of renewable energy technologies in green ports: Technical and economic perspectives. *IET Renew. Power Gener.* **2023**, *17*, 3120–3132. [CrossRef]

11. Durakovic, G.; del Granado, P.C.; Tomasgard, A. Powering Europe with North Sea offshore wind: The impact of hydrogen investments on grid infrastructure and power prices. *Energy* **2023**, *263*, 125654. [CrossRef]
12. Dogan, E.; Hodžić, S.; Šikić, T.F. Do energy and environmental taxes stimulate or inhibit renewable energy deployment in the European Union? *Renew. Energy* **2023**, *202*, 1138–1145. [CrossRef]
13. Simionescu, M.; Rădulescu, M.; Cifuentes-Faura, J. Renewable Energy Consumption-Growth Nexus in European Countries: A Sectoral Approach. *Eval. Rev.* **2023**, *47*, 287–319. [CrossRef] [PubMed]
14. Gyamfi, B.A.; Kwakwa, P.A.; Adebayo, T.S. Energy intensity among European Union countries: The role of renewable energy, income and trade. *Int. J. Energy Sect. Manag.* **2023**, *17*, 801–819. [CrossRef]
15. Do, T.C.; Dang, T.D.; Dinh, T.Q.; Ahn, K.K. Developments in energy regeneration technologies for hydraulic excavators: A review. *Renew. Sustain. Energy Rev.* **2021**, *145*, 111076. [CrossRef]
16. Ha, K.; Truong, H.V.A.; Dang, T.D.; Ahn, K.K. Recent Control Technologies for Floating Offshore Wind Energy System: A Review. *Int. J. Precis. Eng. Manuf. Green Technol.* **2021**, *8*, 281–301. [CrossRef]
17. Inês, C.; Guilherme, P.L.; Esther, M.-G.; Swantje, G.; Stephen, H.; Lars, H. Regulatory challenges and opportunities for collective renewable energy prosumers in the EU. *Energy Policy* **2020**, *138*, 111212. [CrossRef]
18. Radmehr, R.; Henneberry, S.R.; Shayanmehr, S. Renewable Energy Consumption, CO_2 Emissions, and Economic Growth Nexus: A Simultaneity Spatial Modeling Analysis of EU Countries. *Struct. Chang. Econ. Dyn.* **2021**, *57*, 13–27. [CrossRef]
19. Destek, M.A.; Aslan, A. Disaggregated renewable energy consumption and environmental pollution nexus in G-7 countries. *Renew. Energy* **2020**, *151*, 1298–1306. [CrossRef]
20. Johannsen, R.M.; Mathiesen, B.V.; Kermeli, K.; Crijns-Graus, W.; Østergaard, P.A. Exploring pathways to 100% renewable energy in European industry. *Energy* **2023**, *268*, 126687. [CrossRef]
21. Potrč, S.; Čuček, L.; Martin, M.; Kravanja, Z. Sustainable renewable energy supply networks optimization—The gradual transition to a renewable energy system within the European Union by 2050. *Renew. Sustain. Energy Rev.* **2021**, *146*, 111186. [CrossRef]
22. Tutak, M.; Brodny, J. Renewable energy consumption in economic sectors in the EU-27. The impact on economics, environment and conventional energy sources. A 20-year perspective. *J. Clean. Prod.* **2022**, *345*, 131076. [CrossRef]
23. Panchenko, V.; Daus, Y.; Kovalev, A.; Yudaev, I.; Litti, Y. Prospects for the production of green hydrogen: Review of countries with high potential. *Int. J. Hydrogen Energy* **2023**, *48*, 4551–4571. [CrossRef]
24. Kaffash, S.; Azizi, R.; Huang, Y.; Zhu, J. A survey of data envelopment analysis applications in the insurance industry 1993–2018. *Eur. J. Oper. Res.* **2020**, *284*, 801–813. [CrossRef]
25. Xu, T.; You, J.; Li, H.; Shao, L. Energy Efficiency Evaluation Based on Data Envelopment Analysis: A Literature Review. *Energies* **2020**, *13*, 3548. [CrossRef]
26. Čiković, K.F.; Lozić, J. Application of Data Envelopment Analysis (DEA) in Information and Communication Technologies. *Teh. Glas.* **2022**, *16*, 129–134. [CrossRef]
27. Dutta, P.; Jaikumar, B.; Arora, M.S. Applications of data envelopment analysis in supplier selection between 2000 and 2020: A literature review. *Ann. Oper. Res.* **2022**, *315*, 1399–1454. [CrossRef]
28. Le, M.-T.; Nhieu, N.-L. An Offshore Wind–Wave Energy Station Location Analysis by a Novel Behavioral Dual-Side Spherical Fuzzy Approach: The Case Study of Vietnam. *Appl. Sci.* **2022**, *12*, 5201. [CrossRef]
29. Kyrgiakos, L.S.; Kleftodimos, G.; Vlontzos, G.; Pardalos, P.M. A systematic literature review of data envelopment analysis implementation in agriculture under the prism of sustainability. *Oper. Res.* **2023**, *23*, 1–38. [CrossRef]
30. Tavana, M.; Soltanifar, M.; Santos-Arteaga, F.J.; Sharafi, H. Analytic hierarchy process and data envelopment analysis: A match made in heaven. *Expert Syst. Appl.* **2023**, *223*, 119902. [CrossRef]
31. Wang, C.-N.; Nhieu, N.-L.; Tran, H.-V. Wave Energy Site Location Optimizing in Chile: A Fuzzy Serial Linear Programming Decision-Making Approach. *Environ. Dev. Sustain.* 2024; *early access*.
32. Wang, C.; Nguyen, H.; Nhieu, N.; Hsu, H. A prospect theory extension of data envelopment analysis model for wave-wind energy site selection in New Zealand. *Manag. Decis. Econ.* **2023**, *45*, 539–553. [CrossRef]
33. Charnes, A.; Cooper, W.W.; Rhodes, E. Measuring the efficiency of decision making units. *Eur. J. Oper. Res.* **1978**, *2*, 429–444. [CrossRef]
34. Banker, R.D.; Charnes, A.; Cooper, W.W. Some Models for Estimating Technical and Scale Inefficiencies in Data Envelopment Analysis. *Manag. Sci.* **1984**, *30*, 1078–1092. [CrossRef]
35. Kahneman, D.; Tversky, A. Prospect Theory: An Analysis of Decision under Risk. *Econometrica* **1979**, *47*, 263. [CrossRef]
36. Liang, H.; Xiong, W.; Dong, Y. A prospect theory-based method for fusing the individual preference-approval structures in group decision making. *Comput. Ind. Eng.* **2018**, *117*, 237–248. [CrossRef]
37. Wang, L.; Wang, Y.-M.; Martínez, L. A group decision method based on prospect theory for emergency situations. *Inf. Sci.* **2017**, *418–419*, 119–135. [CrossRef]
38. Le, M.-T.; Nhieu, N.-L. A Behavior-Simulated Spherical Fuzzy Extension of the Integrated Multi-Criteria Decision-Making Approach. *Symmetry* **2022**, *14*, 1136. [CrossRef]
39. Chen, X.; Liu, X.; Wang, W.; Gong, Z. Behavioral DEA model and its application to the efficiency evaluation of manufacturing transformation and upgrading in the Yangtze River Delta. *Soft Comput.* **2019**, *24*, 10721–10738. [CrossRef]
40. Tian, J.; Yu, L.; Xue, R.; Zhuang, S.; Shan, Y. Global low-carbon energy transition in the post-COVID-19 era. *Appl. Energy* **2022**, *307*, 118205. [CrossRef]

41. IRENA. *Renewable Energy Country Profiles*; International Renewable Energy Agency: New York, NY, USA, 2022.
42. Gunny, A.A.N.; Shahimin, M.F.M.; Mohamed, A.R.; Jalil, M.F.A. Current Status of Renewable Energy Development. In *Renewable Energy from Bio-Resources in Malaysia*; Springer: Singapore, 2022; pp. 1–19.
43. Wang, C.-N.; Nhieu, N.-L. Integrated DEA and hybrid ordinal priority approach for multi-criteria wave energy locating: A case study of South Africa. *Soft Comput.* **2023**, *27*, 18869–18883. [CrossRef]
44. Wang, C.-N.; Nhieu, N.-L.; Nguyen, H.-P.; Wang, J.-W. Simulation-Based Optimization Integrated Multiple Criteria Decision-Making Framework for Wave Energy Site Selection: A Case Study of Australia. *IEEE Access* **2021**, *9*, 167458–167476. [CrossRef]
45. Le, M.-T.; Nhieu, N.-L.; Pham, T.-D.T. Direct-Use Geothermal Energy Location Multi-Criteria Planning for On-Site Energy Security in Emergencies: A Case Study of Malaysia. *Sustainability* **2022**, *14*, 15132. [CrossRef]
46. Wang, C.-N.; Pham, T.-D.T.; Nhieu, N.-L.; Huang, C.-C. Smart Technology Prioritization for Sustainable Manufacturing in Emergency Situation by Integrated Spherical Fuzzy Bounded Rationality Decision-Making Approach. *Processes* **2022**, *10*, 2732. [CrossRef]
47. The World Bank. World Bank Open Data. Available online: https://databank.worldbank.org/ (accessed on 11 November 2023).
48. IEA. *Energy Statistics Data*; International Energy Agency: Paris, France, 2022.
49. IEA. *World Energy Investment 2022*; International Energy Agency (IEA): Paris, France, 2022.
50. IRENA. *Global Atlas for Renewable Energy*; International Renewable Energy Agency: Abu Dhabi, United Arab Emirates, 2022.
51. IRENA. *Renewable Energy Statistics 2022*; International Renewable Energy Agency (IRENA): Abu Dhabi, United Arab Emirates, 2022.
52. Tversky, A.; Kahneman, D. Advances in prospect theory: Cumulative representation of uncertainty. *J. Risk Uncertain.* **1992**, *5*, 297–323. [CrossRef]
53. Wang, C.-N.; Nhieu, N.-L.; Dao, T.-H.; Huang, C.-C. Simulation-Based Optimized Weighting TODIM Decision-Making Approach for National Oil Company Global Benchmarking. *IEEE Trans. Eng. Manag.* **2022**, *71*, 1215–1229. [CrossRef]

processes

MDPI

Article

Finite Element Simulation of a Multistage Square Cup Drawing Process for Relatively Thin Sheet Metal through a Conical Die

Walid M. Shewakh [1,2,*] and Ibrahim M. Hassab-Allah [3]

[1] Department of Industrial Engineering, Faculty of Engineering, Jazan University, Jazan 82817, Saudi Arabia
[2] Mechanical Production Department, Faculty of Technology and Education, Beni-Suef University, P.O. Box 62521, Beni-Suef 62511, Egypt
[3] Mechanical Design and Production Engineering Department, Faculty of Engineering, Assiut University, Assiut 71516, Egypt; ibrahim.abdeldaiam@aun.edu.eg
* Correspondence: wshewakh@jazanu.edu.sa

Abstract: A new manufacturing process has been developed that involves drawing circular sheets of thin metal through a conical die to create square cups. This technique produces deep square cups with a height-to-punch-side length ratio of approximately 2, as well as high dimensional accuracy and a nearly uniform height. The study investigated how various factors, including the sheet material properties and process geometric parameters, affect the limiting drawing ratio (LDR). The researchers used finite element analysis to determine the optimal die design for achieving a high LDR and found that the proposed technique is advantageous for producing long square cups with high dimensional accuracy.

Keywords: square cup drawing; limiting deep drawing ratio (LDR); punch shape factor; FE simulation; conical dies; deep drawing

1. Introduction

Square cups made of thin sheet metal are widespread across various industrial fields. They are utilised in automotive engineering, production lines, container construction, building construction, household appliances, and packaging industries. This process offers numerous benefits, including high productivity and the ability to create complex shapes. However, the process involves a complicated deformation mechanism, and the quality of the deformed cups and process efficiency depends on various parameters, such as punch shape factors, die geometry, blank shapes, sheet thickness, blank holding force, blank materials, friction, and lubrication. Hence, identifying the impacts of these parameters on the square cup deep drawing process can help develop better control strategies for optimising the process.

During the square cup deep drawing process, blanks are typically held against the die's face using a rigid blank holder plate to prevent wrinkles in the flange. However, this approach can lead to non-axisymmetric metal flow rates along the straight walls and around the corners, resulting in uneven material distribution around the cup walls. This flow non-uniformity can create local contact zones with an increased surface pressure due to the increased sheet thickness in the corner zones, leading to deformation concentration in the cup corners and cup fracture [1–4]. Controlling the material flow rate into the die cavity is crucial to prevent these issues; this can be achieved by optimising the blank holder force, which can help regulate the metal flow and improve the quality of the square cup drawing process.

Various solutions have been proposed to address the non-uniformity of the metal flow into the die cavity, including changing the material properties of the sheet metal, altering the frictional state, optimising the blank shape, and designing flexible blank holding

systems. Many innovative blank-holding systems have recently been proposed to improve performance and deep drawability.

There are three distinct approaches to enhancing the drawability of square cups. The first involves enhancing the material properties of the sheet metal used in the forming process. The second approach improves process parameters, including the friction and lubrication conditions, tool geometries, optimum blank shape, material properties, and form temperature. Finally, the third category centres on altering the deformation zone's stress state and instability condition. This third approach is recommended for increasing the limiting drawing ratio of square cups.

Pliable blank holder systems, introduced by Doege et al. [5,6], are designed with elastically deformable thin steel plates to allow for deflection. This innovative design ensures that pressure is evenly distributed across the blank regardless of changes in thickness. Yagami et al. [7] utilised separate segmented binders, each operated using a hydraulic cylinder with a unique binder force profile. Meanwhile, Hassan et al. [8] proposed a method for deep drawing with friction aided by a segmented blank holder. This holder is constructed with stiff segments connected by elastic joints. Lastly, Gavas et al. [9] suggested a blank holder system equipped with a spiral spring at the side in contact with the blank to be drawn. These techniques have been found to improve the material flow and formability.

In their paper, Venkatesh and Goh (1998) [10] explored the Guerin and Marform processes, which utilise rubber pads as pressure media and emphasise the innovation and development of new techniques. While these techniques can yield a superior surface finish and are versatile enough to accommodate a range of component materials, their cost-effectiveness is limited to short production runs and not well suited to mass production. It should be noted that the LDR achieved using these methods is larger than what is commonly achieved through conventional means, and they require a greater forming force to achieve successful deep drawing. In 1995, Sato et al. [11] proposed a multi-axial loading technique utilising a punch and four side tools for drawing thick deep square cups. This method leads to an increased LDR compared to the conventional method when working with thick sheets, as the thinning of the drawn cups at the punch profile radius is reduced. However, the maximum load required is still higher than the conventional methods, and the process is more complex. Lang et al. (2004) [12] conducted a study and found that hydromechanical deep drawing with hydraulic counter pressure offers several advantages compared to conventional square cup forming methods. This process creates high drawing ratio parts (3.44) with an impeccable surface quality and precise dimensions, even for intricate shapes. However, it requires significant forming forces and specialised equipment and only works with thin sheet materials. Explosive forming is a technique commonly used for shaping large, complex forms and has been utilized to create square cups. Wijayathunga and Webb (2006) [13] found that the process is complicated, and the drawing ratio is limited, which requires extensive experimentation and FE simulation to achieve uniform square cups with a considerable drawing ratio. Mustafa et al. (2007) [14] developed a test set to assess the drawability limits of gradually rectangular-shaped containers in a multi-point deep drawing process for 3D sheet metal parts. They used a multi-point forming technology with a given tool geometry and drawing velocity. The authors discovered that this technique reduces the die production costs, offers flexible usage, and achieves even deformation distribution. However, the setup process is complicated, and pitting defects may occur due to the concentrated load at individual punches during forming, leading to localised deformation and limiting the drawability of the sheet metal. In 2015, Walid et al. [15] introduced a modern method of producing a square shape by changing the geometric shape of the die, using a conical die with a square aperture and square punch. This method aims to obtain a product with the highest drawing ratio limit compared to the traditional method of using a square die and punch to produce a square shape. Furthermore, this method eliminates the defects associated with the traditional method.

Hassan et al. (2012) [16] introduced a divided blank holder featuring a tapered base and eight tapered segments, aiming to enhance the deep drawability of square cups. Their

study showed the superiority of deep drawing compared to the traditional methods when working with thin sheets and foils. However, they found that the deep drawability significantly decreased when working with thicker sheets. Hezam et al. (2009) [17] developed an innovative method to enhance the deep drawability of square cups, utilising a conical die equipped with a square aperture at its end, allowing for the seamless flow of the metal from the circular sections to the square aperture and throat of the die. The technique has shown promising results in increasing the drawing ratio, particularly for thicker sheets. However, further research is needed to optimise the setup dimensions and operating conditions to achieve the highest possible LDR. Additionally, gaining a better understanding of the process and its deformation characteristics is crucial, as the quality of the deformed cups and the efficiency of the process depend on optimal selection of the forming parameters. Adnan (2022) [18] compared two methods for producing complex shapes: direct and indirect. They found that the indirect method outperformed the direct method in terms of a lower drawing force, better thickness distribution, and more favourable stress and strain distribution. However, the direct method may not be suitable for complex shapes requiring multiple drawing stages, as it can be challenging to ensure proper centering between the die and the product.

Despite advancements in deep drawing techniques, they still have limitations compared to the traditional methods. Most techniques yield limiting drawing ratios of around 2, which only allows for a cup height-to-diameter ratio of approximately 1. Maximising the deep drawability in square cup drawing processes is critical to reducing manufacturing costs and time. The sheet metal's drawability depends on its ability to flow effortlessly in the plane of the sheet's flange region and resist deformation in the thickness direction. Given the limitations mentioned earlier, there is still a need to overcome them, improve the material flow, and increase the deep drawability. This study aims to design a new technique for creating a square cup by drawing a circular blank of relatively thin sheet metal (0.75 to 1.5 mm) through a conical die. The technique offers several advantages, including a simple deformation mechanism, simplified drawing tools, and reduced power requirements for forming. Since single-action presses can be used to perform the process, drawing beads or blank holder forces are unnecessary. The study used finite element analysis to investigate the sheet metal's deformation behaviour during the drawing process.

2. The Proposed Method for Square Cup Drawing of a Thin Sheet

Deep drawing of square cups without a blank holder is possible using the proper die geometry, such as a conical die and a suitable punch with a suitable side length/sheet thickness ratio (L_p/t_o). Hassab-Allah et al. [19] designed a new technique for square cup drawing of relatively thick sheets ($L_p/t_o < 30$). In the study in [20], some restrictions and optimum circumstances have been reported for deep drawing using a conical die. It was shown that fewer drawing stages and simple die sets needed for producing long square cups can be obtained with very high drawing ratios. Furthermore, deep drawing can be carried out in single-action presses. Unfortunately, when using the same technique described in [21] for drawing a square cup of a relatively thin sheet, i.e., drawing with high values of L_p/t_o ($L_p/t_o > 30$), wrinkling commonly occurred at the early stage of drawing due to the compressive hoop stresses induced in the flange of the cup. This is because the strength of a relatively thin sheet blank is insufficient to restrict buckling due to its buckling stiffness. The maximum drawing ratio in the deep drawing of square cups, without a blank holder, is restricted for thin sheets by the wrinkling or buckling of the flange or the cup walls. If wrinkles are avoided at the beginning of the deep drawing process, relatively high deep drawing ratios can be obtained. As a result of the wrinkling tendency, the flange's inherent stiffness at the beginning of the drawing stage can be enhanced by using an auxiliary drawing tool. In the proposed method, the forming of wrinkles at the early stage of drawing and during the drawing process can be avoided by using a tapered punch, as shown in Figure 1. The proposed technique is based on the same idea of deep drawing without a blank holder through a conical die except using an extra drawing tapered punch.

The square cup can be drawn by pushing the circular blank without a blank holder through a conical die. The conical die used in the proposed method contains a square aperture at the die exit; see Figure 1. The advantage of using a conical die is a decrease in the frictional force compared with that in the conventional deep drawing process since the sheet is in contact with the tool on one side only. Furthermore, the load resulting from bending and unbending is reduced owing to the more favourable shape of the die. However, in the conventional square cup deep drawing process, the blank is bent through a right angle as it passes over the die entry radius and then has to be unbent as it is straightened. Therefore, in the drawing through a conical die, the force available for plastic deformation is greater, and the maximum blank size is increased. Figure 2 shows the forming sequences during the square cup drawing through a conical die. During the cupping stage, in Figure 2a, the outer perimeter of the circular blank is forced into compression by the cupping action. The conical surface of the die cavity supports the outer edge of the blank during cupping, thus frequently preventing wrinkling. In the cupping stage, the blank is bent simply around the corners of the tapered punch, and the blank flange comes into contact with the die wall and conforms to its profile. Unlike the conventional deep drawing process, no unbending action is taken, producing a less work-hardened partially drawn frustum conical cup; see Figure 2a. The remaining ductility in the partially drawn frustum cup walls leads to considerable forming that can be achieved after the cupping stage without inter-stage annealing. The motion of the square and tapered punches are coupled during the cupping stage. At the end of the cupping stage, the circular blank was deformed into a frustum conical cup; see Figure 2a. The tapered punch acts as the blank holder with constant gap clearance during the square cup drawing stage. However, there is no need to apply force or pressure over the tapered punch; the tapered punch must be fixed at its end position. The flat-headed square punch pushes the bottom of the partially drawn frustum conical cup into the square aperture at the die exit, drawing it into a square cup; see Figure 2b. The plastic instability caused by compressive hoop stresses may also occur in the unsupported cup wall area between the tapered punch and die during the cupping stage. This plastic instability can be enhanced using a suitable end diameter for the tapered punch. The half cone angle of both the die and the tapered punch is also important in controlling the wrinkling in the unsupported cup wall area during the cupping stage, especially in the case of a relatively thin sheet. The best selection of half cone angle can enhance the buckling stiffness and increase the limiting drawing ratio.

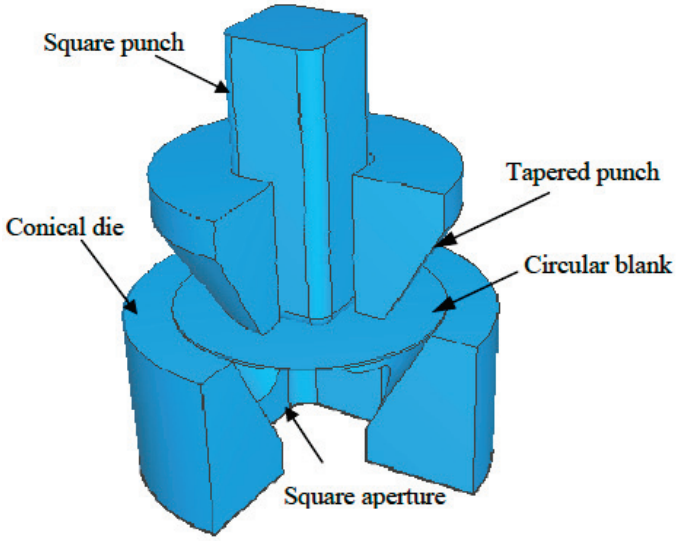

Figure 1. Pictorial representation of the drawing set and circular blank used for the square cup drawing process.

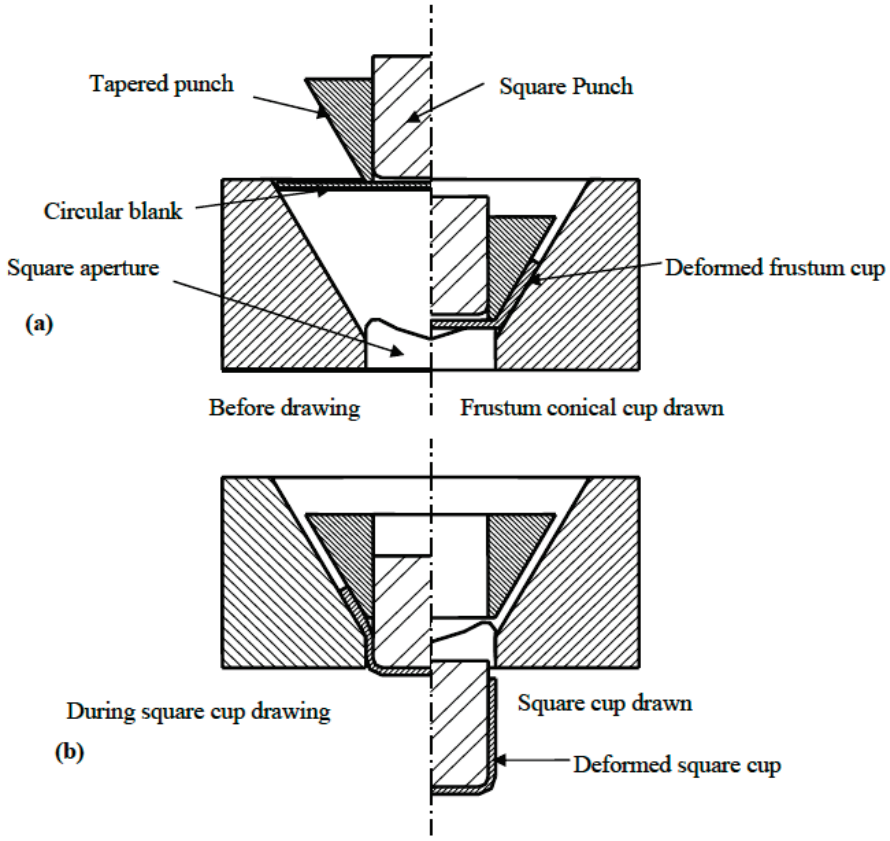

Figure 2. Sequences of square cup drawing through a conical die. (**a**) frustum conical cup drawing; (**b**) square cup drawing.

3. FEM Simulation of the Proposed Process

The geometrical parameters of the drawing die set are shown in Figure 3. Because many process parameters can influence the square cup's deep drawing, it is difficult to find the optimal process parameters and manufacture the drawing tools. Therefore, FE simulation was adopted to investigate the influences of those parameters. In the present work, the FE simulations have been carried out with the explicit elastic–plastic FE code DYNAFORM-PC. Figure 4 shows the mesh system for the complete tooling and sheet blank set used in the square cup's deep drawing. Owing to the geometric symmetry conditions, only a quarter model of the square cup was analysed. A quarter of the circular blank was initially meshed with 541 nodes and 500 elements, as shown in Figure 5. The remeshing generation module was adopted to completely describe the deformed blank's contour during the drawing process. For the FE simulation, the drawing tools are considered rigid, and the corresponding meshes used to define the tooling geometry are not for stress analysis. Due to the high elastic modulus of the drawing tools, a perfectly rigid surface is assumed, which is an acceptable approximation since the elastic deflection of the drawing tools is relatively negligible compared with the excessive plastic deformation of the blank. Rigid shell elements have been used to simulate the drawing tool surfaces to decrease the computing times. The drawing tools, tapered punch, square punch, and die were modelled using rigid 4-node shell elements with surface-to-surface contact for the interface between the circular blank and the drawing tools, while the circular blank was modelled using 4-node deformable shell elements.

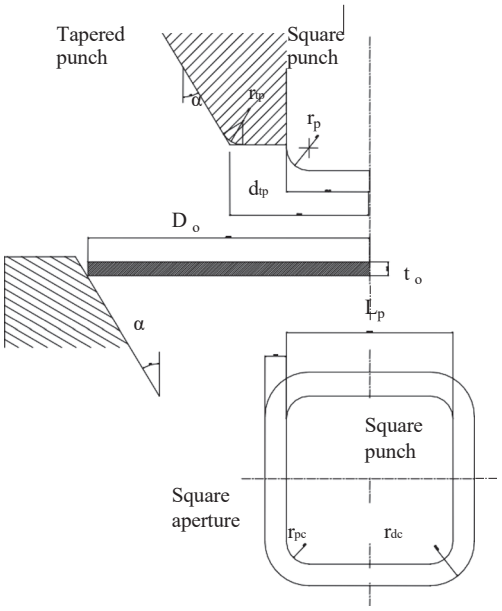

Figure 3. Geometrical description of the tooling for the deep drawing of square cup.

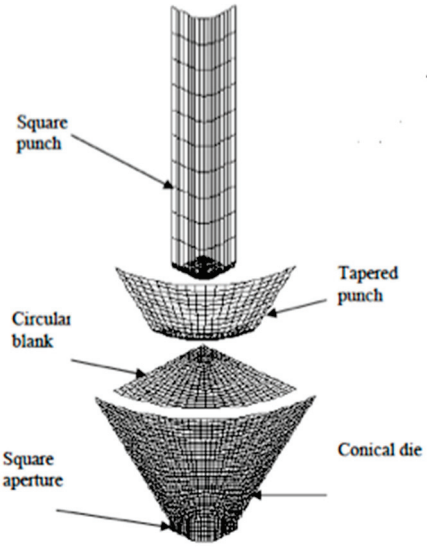

Figure 4. Quarter FE meshes for the blank and drawing tools.

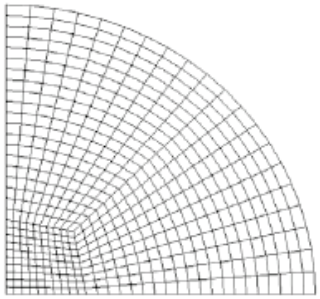

Figure 5. Initial FE mesh system for the quarter blank.

The deep drawing process is simulated by moving the tapered and square punches down to push the circular blank into the die cavity. The speed of both punches is set to be 5 m/s, while the conical die is completely fixed. The tapered and square punches are moved together at the beginning of the drawing process until the frustum conical cup is

drawn, as shown in Figure 2a. After that, only the square punch is further moved down to complete the drawing of the square cup, as shown in Figure 2b. The strain-hardening behaviour of the blank material is described in the FE simulations according to the power law (Hollomon's law): $\sigma = 500\ \varepsilon^n$ with different values for the strain-hardening exponent n of 0.1, 0.2, 0.25, 0.3, 0.4, and 0.5. The anisotropic behaviour of sheet metal has been represented using the average normal anisotropy (Lankford value R) with different values, 1.25, 1.5, 1.75, 2, and 2.25, to study the benefit of its values in the drawing of square cups.

The elastic properties of the blank material are Young's modulus E = 210 GPa and Poisson's ratio $\nu = 0.3$. To study the effect of the initial sheet thickness and the drawing set geometric parameters on the limiting drawing ratios, different values of initial sheet thicknesses (t_o = 0.75, 1, 1.25, and 1.5 mm) and die half cone angles (α = 20, 25, 30, 35, and 40°) were used in the FE simulation models. Square flat-headed punches with a side length L_p of 45 mm; punch nose radius r_p of 5 mm; and different values of corner radii r_{pc} = 4.5, 9, 13.5, 18 and 22.5 mm, which are equivalent to square punch shape factors r_{pc}/L_p = 0.1, 0.2, 0.3, 0.4, and 0.5, were used. The gap clearance (c) between the square punch and conical die aperture was kept constant, equal to 1.25. The same clearance value was used for the gap between the tapered punch and conical die. The square die aperture has a corner radius $r_{dc} = r_{pc} + c$. The used geometrical parameters of the tapered punch are a nose radius of 10 mm and different values of end diameter d_{tp} = 63, 67.5, 72, and 76.5 mm (which give tapered punch diameter ratios d_{tp}/L_p = 1.4, 1.5, 1.6, and 1.7, respectively). The drawing ratio (DR) is defined as the ratio of the initial diameter of a circular blank (D_o) to the square punch side length (L_p). The limiting drawing ratio (LDR) is the maximum drawing ratio of the blanks that can be drawn without failure. Constraints on the thickness variation must be applied to obtain a drawn cup without defects such as ruptures or wrinkles. Obtaining a square cup without defects requires some restrictions on the cup wall thickness strain to avoid plastic instability. The limitation constraints on the sheet thickness variation can be expressed using the following criteria [20,21]:

$$-25\% \leq \frac{t - t_0}{t_0} \leq +15\% \quad (1)$$

where to and t are the initial and current sheet thicknesses. The law of constant friction is assumed at the drawing tools–workpiece interface, and the coefficient of friction remains constant during the process. Contact with Coulomb friction law is used, in which the average friction coefficients between the contacting surfaces of the blank and the square punch, tapered punch, and die are taken to be 0.25, 0.05, and 0.05, respectively.

4. Results and Discussion

4.1. Effect of Sheet and Geometric Parameters of the Drawing Sets on the LDR

In this part of the FE simulation results, the effect of the process geometric parameters, sheet thickness, half cone angle, tapered punch diameter ratio (d_{tp}/L_p), and square punch shape factor (r_{pc}/L_p) on both the deformation characteristic and deep drawability of sheet metal are investigated. In order to examine the effect of these geometric parameters on the limiting deep drawing ratios, blanks of different sheet thicknesses and different outer diameters were drawn through deep drawing tool sets of different geometric parameter values. The drawing continued with an increasing blank outer diameter until defects such as ruptures or wrinkles occurred. The values of the blank outer diameter increased until either one of the two modes of failures occurred, i.e., the sheet thickness at the punch corner reached a predetermined critical value (75% of its initial value) or thickening at the blank outer circumferential reached a predetermined critical value (115% of its initial value). The maximum value of the blank outer diameter drawn into a square cup without failure was used as the formability index, and the limiting drawing ratio (LDR) was calculated based on its value. Figure 6 shows the predicted limiting deep drawing ratio variation with the initial sheet thickness. It can be noted that the LDR increases with an increase in the initial sheet thickness due to the increase in buckling stiffness with the increase in blank thickness,

which suppresses the occurrence of wall wrinkling. In this proposed technique, only the blank buckling stiffness suppresses the wrinkling because there is no blank holder.

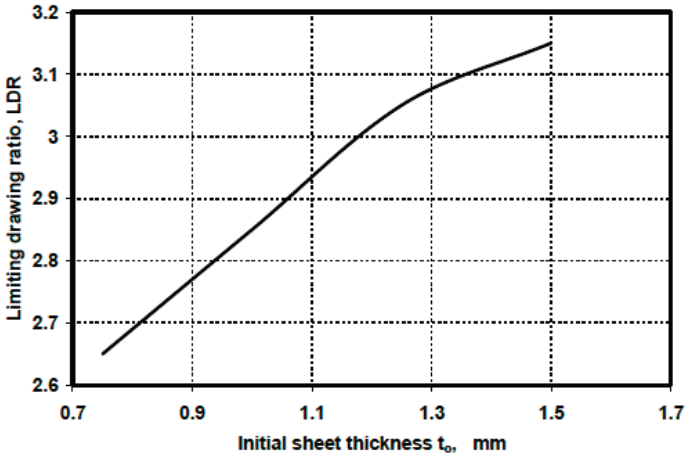

Figure 6. Variation in predicted LDR with the initial sheet thickness t_o (d_{tp}/L_p = 1.6, α = 30°, n = 0.25, R = 2, K = 500 MPa, r_{pc}/L_p = 0.2, $\mu_d = \mu_{tp}$ = 0.05, and μ_p = 0.25).

The half cone angle α significantly impacts the limiting drawing ratio, as demonstrated in Figure 7. Increasing the half cone angle leads to a drastic increase in the limiting drawing ratio. However, for die half cone angles greater than 35°, the limiting deep drawing ratio decreases with an increasing α due to premature and severe wrinkling. It is worth noting that an optimal half cone angle exists for drawing square cups, falling within the range of 30° to 35°. This type of premature and severe wrinkling occurs at the unsupported region and cannot be suppressed since the blank is not in place. This initial wall wrinkling typically starts at the blank circumferential, see Figure 8. Figure 9 illustrates how LDR's predicted limiting drawing ratio varies with the tapered punch diameter ratio dtp/Lp. The LDR increases as dtp/Lp increases until it reaches 1.6 and then decreases with further increases in d_{tp}/L_p. The decreasing limiting deep drawing ratio for high values of $d_{tp}/L_p > 1.6$ is due to the cup wall wrinkling formed at the edge of the cup wall near the end of the drawing stage, as shown in Figure 10.

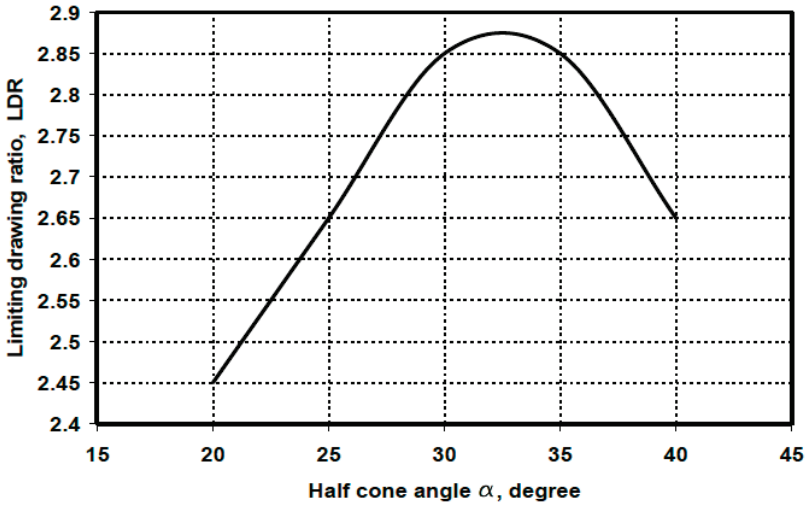

Figure 7. Variation in predicted LDR with the half cone angle α (d_{tp}/L_p = 1.6, t_o = 1 mm, n = 0.25, R = 2, K = 500 MPa, r_{pc}/L_p = 0.2, $\mu_d = \mu_{tp}$ = 0.05, and μ_p = 0.25).

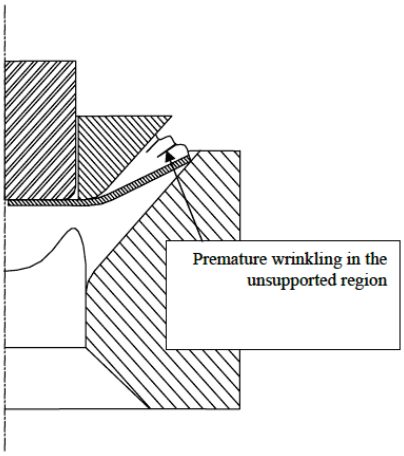

Figure 8. Premature wrinkling of the blank to be drawn over the die surfaces with large half-cone angle.

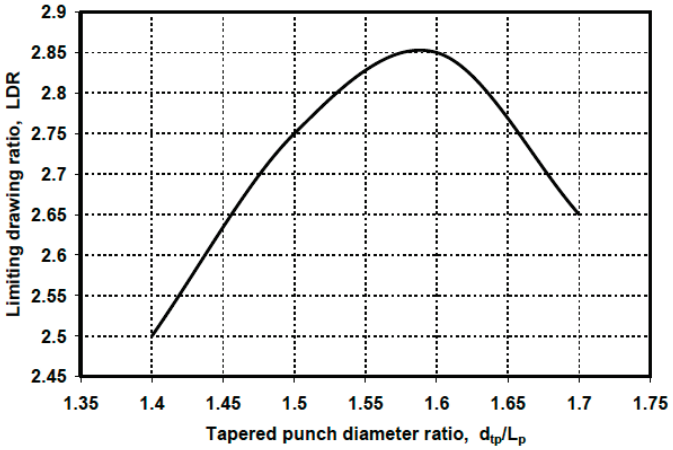

Figure 9. Variation in predicted LDR with the punch diameter ratio d_{tp}/L_p ($\alpha = 30°$, R = 2,. n = 0.25, K = 500 MPa, $r_{pc}/L_p = 0.2$, $\mu_d = \mu_b = 0.05$, t = 1 mm, and $\mu_p = 0.25$).

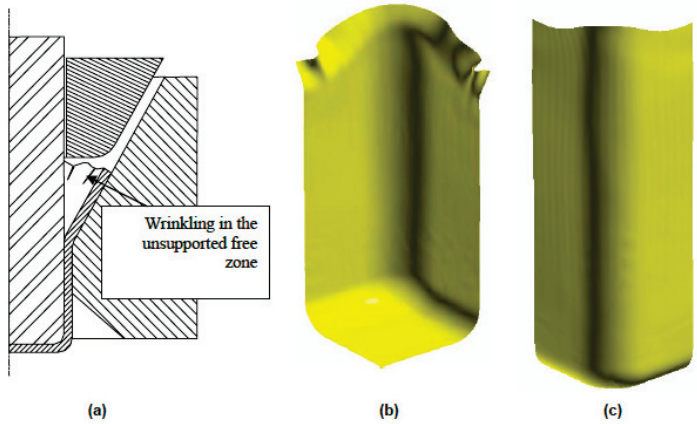

Figure 10. Cup wall wrinkling at the end of deep drawing process; (**a**) drawing tool set with high d_{tp}/L_p shows cup wall wrinkling in the unsupported free zone, (**b**) simulated drawn cup with wrinkles at the edge of cup wall, and (**c**) simulated successfully drawn cup, free from wrinkles.

In the cases of deep drawing with high values of d_{tp}/L_p, i.e., large tapered punch end diameter d_{tp} values, the distance between the tapered punch head (at their end stroke) and the square die aperture is insufficient. So, the wall of a partially drawn cup in the unsupported free zone, in Figure 10a, becomes unstable due to circumferential compressive

stresses. Therefore, the partially drawn cup becomes free to wrinkle if the circumferential compressive stress developed in the cup wall exceeds the buckling stress limit for the material to be drawn. The simulation results show that wrinkling occurred at the top of the cup wall, and the simulated shape of the wrinkled drawn cup is shown in Figure 10b. It can be seen that the wrinkles are located along the side walls of the cup. Consequently, increasing the end diameter of the tapered punch will cause more severe wrinkling. A common characteristic of these two types of wall wrinkling shown in Figures 8 and 10a is that wrinkles are found at the draw wall, occurring in the unsupported free zones. The successfully simulated drawn cup is shown in Figure 10c. It is worth noting that the successfully obtained cup has a nearly uniform cup height all around the cup cross-section. The limiting drawing ratio is greatly affected by the punch shape factor, r_{pc}/L_p [4]. Figure 11 shows the predicted limiting drawing ratio (LDR) variation with the punch shape factor. It is clear that the limiting drawing ratio (LDR)increased drastically with the increasing punch shape factor; similar results are reported in [4]. The decreasing limiting drawing ratio for small punch corner radius values (i.e., small punch shape factor values) can be attributed to the severe wrinkles formed at the die corner due to the excessive metal flow in small corner regions, and the corner zone cannot absorb all the excessive material that will pass through it. The limiting drawing ratio increased with an increasing punch shape factor until $r_{pc}/L_p = 0.2$, and a further increase in r_{pc}/L_p leads to a decrease in the limiting drawing ratio. The decreasing limiting drawing ratio for larger values of $r_{pc}/L_p \geq 0.2$ is attributed to the increased deformation concentration at the punch corners. This leads to severe thinning at the punch corners, and the cup wall becomes insufficient to sustain the drawing loads. Wrapping the sheet metal to be drawn over the rounded corner square head reduces the deformation concentration at the punch nose. The increase in the corner radius leads to an increase in the deformation concentration. In contrast, the extra decrease in the corner radius causes the flow of the sheet metal and wrinkling at the die corner. Therefore, an optimum punch corner radius value prevents both walls from wrinkling at the die corner and the deformation concentration over the punch nose. For the process parameters in Figure 11, the optimum punch shape factor equals 0.2, i.e., the optimum punch corner radius is 9 mm. Deep drawing with a shape factor $r_{pc}/L_p = 0.5$ represents the conventional deep drawing for a circular cup. From Figure 11, it is worth noting that the drawing with a 0.2 punch shape factor increased the LDR by about 6% compared to the LDR obtained using conventional circular cup deep drawing.

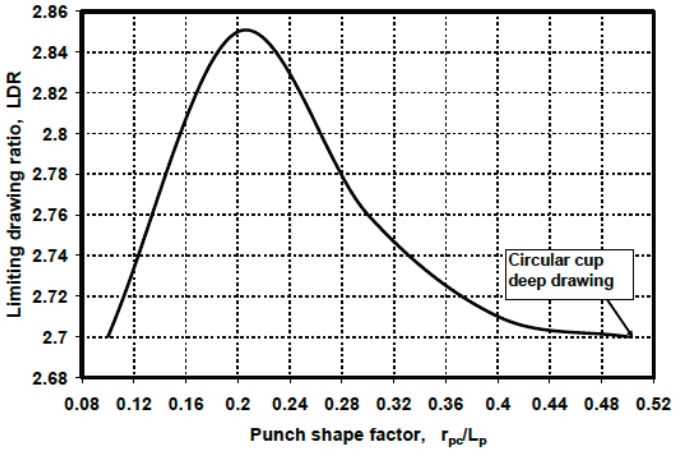

Figure 11. Variation in predicted LDR with the punch shape factor r_{pc}/L_p ($d_{tp}/L_p = 1.6$, $\alpha = 30^\circ$, t = 1 mm, R = 2, n = 0.25, K = 500 MPa, $\mu_d = \mu_{tp} = 0.05$, and $\mu_p = 0.25$).

4.2. Effect of Sheet Material Properties on the LDR

The results displayed in Figure 12 exhibit the relationship between the predicted limiting drawing ratio (LDR) and the average standard anisotropy R-value. The LDR increased as the average R-value increased, indicating that high R-values can effectively minimise

the thinning at the corner wall regions of the punch profile edge and the thickening at the cup wall. These findings demonstrate the benefits of utilising high R-values in drawing square cups.

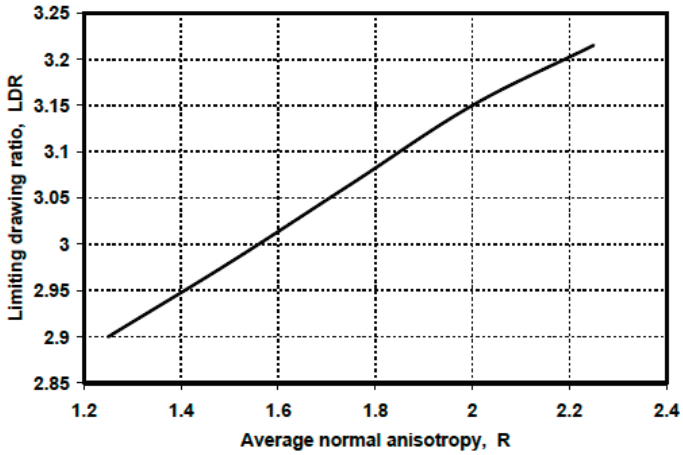

Figure 12. Variation in predicted LDR with the average normal anisotropy R-value (d_{tp}/L_p = 1.6, α = 30°, t_o = 1.5 mm, n = 0.25, K = 500 MPa, r_{pc}/L_p = 0.2, $\mu_d = \mu_{tp}$ = 0.05, and μ_p = 0.25).

Additionally, Figure 13 highlights the predicted LDR variation with the strain-hardening exponent n. It is worth noting that the LDR increased as n increased until n = 0.25. Increasing the strain-hardening exponent within the first zone of the curve (0.1 < n < 0.25) can prevent the instability caused by wrinkling at the beginning of the drawing operation. However, increasing the strain-hardening value (n > 0.25) decreased the LDR due to an increase in the thinning over the punch head corner. Based on the process parameters illustrated in Figure 13, an optimum strain-hardening exponent of n = 0.25 exists for drawing square cups.

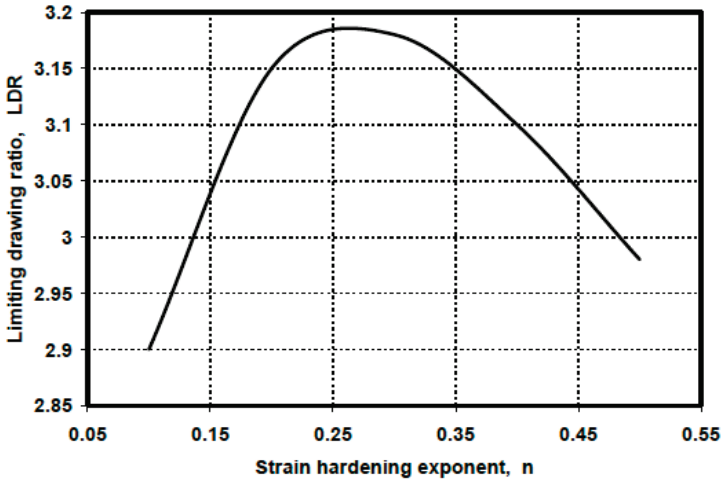

Figure 13. Variation in predicted LDR with the strain-hardening exponent n (d_{tp}/L_p = 1.6, α = 30°, t_o = 1.5 mm, R = 2, K = 500 MPa, r_{pc}/L_p = 0.2, $\mu_d = \mu_{tp}$ = 0.05, and μ_p = 0.25).

5. Conclusions

A novel technique using metal was proposed for drawing relatively thin sheets into square cups through conical dies. The DYNAFORM-PC finite element code was utilised to perform the simulation. The package used to simulate sheet metal forming was based on LS-DYNA. The analysis aimed to investigate the deformation behaviour and defect prediction during the process. The results of this investigation revealed the following:

1. The proposed technique significantly increases the limit drawing ratio (LDR) and improves the flow of blank material within the die throat.
2. The proposed technique can significantly reduce the loads required for drawing instead of conventional deep drawing.
3. For anisotropic sheet metal, orienting the circular blank to be drawn where the cup diagonal corresponds to the direction of the greatest R-value and greatest yield stress can further improve the LDR.
4. An optimum die design to obtain a high limiting drawing ratio was determined using the FE analysis.
5. There is no need for draw beads, a blank holding force, or blank design optimization.

Author Contributions: Conceptualization, I.M.H.-A.; Software, I.M.H.-A.; Validation, W.M.S.; Formal analysis, W.M.S. All authors have read and agreed to the published version of the manuscript.

Funding: This research was funded by the Deputyship for Research and Innovation, the Ministry of Education in Saudi Arabia, project number ISP-2024.

Data Availability Statement: The data presented in this study are available on request from the corresponding author.

Conflicts of Interest: The authors declare that they have no known competing financial interests or personal relationships that could have appeared to influence the work reported in this paper.

References

1. Marumo, Y.; Saiki, H.; Mori, T. Combined effects of strain hardening characteristics and the geometry on the deep-drawability of square aluminum cup. *J. Mater. Process. Technol.* **1999**, *89–90*, 30–36. [CrossRef]
2. Marumo, Y.; Saiki, H. Evaluation of the forming limit of aluminum square cups. *J. Mater. Process. Technol.* **1998**, *80–81*, 427–432. [CrossRef]
3. Kuwabara, T.; Akiyama, K.; Nakayama, Y. Square shell drawing characteristics of aluminum alloy sheet A5182-O. *J. Mater. Process. Technol.* **1993**, *38*, 737–749. [CrossRef]
4. Kawai, N.; Mori, T.; Hayashi, H.; Kondoh, F. Effects of punch cross-section on deep drawability of square shell of square shell of aluminum sheet. *J. Eng. Indus.* **1987**, *109*, 355–361. [CrossRef]
5. Doege, E.; Eland, L.E.; Ropers, C. Pliable blank holder systems for the optimization of process conditions in deep drawing. In *Advanced Technology of Plasticity 99, Proceedings of the 6th International Conference on Technology of Plasticity Nuremberg, 19–24 September 1999*; Springer: Berlin/Heidelberg, Germany, 1999; pp. 177–182.
6. Doege, E.; El, L.E. Design and application of pliable blank holder systems for the optimization of process conditions in sheet metal forming. *J. Mater. Process. Technol.* **2001**, *111*, 182–187. [CrossRef]
7. Yagami, T.; Manabe, K.; Yang, M.; Koyama, H. Intelligent sheet stamping process using segment blank holder modules. *J. Mater. Process. Technol.* **2004**, *155–156*, 2099–2105. [CrossRef]
8. Hassan, M.A.; Abouel-Kasem, A. A novel friction aided deep drawing process for producing deep square cups. In Proceedings of the Eight Cairo University Conference MDP-8 on Mechanical Design and Production, Cairo, Egypt, 4–6 January 2004; pp. 961–968.
9. Gavas, M.; Izciler, M. Design and application of blank holder system with spiral spring in deep drawing of square cups. *J. Mater. Process. Technol.* **2006**, *171*, 274–282. [CrossRef]
10. Venkatesh, V.; Goh, T. A note on mathematical models of cup drawing by the Guerin and Marform processes. *J. Mech. Work. Technol.* **1998**, *13*, 273–278. [CrossRef]
11. Sato, E.; Shimizu, T.; Sano, T.; Fuchizawa, S. Effect of multi-axial loading path on limiting drawing ratio. *J. Mater. Process. Technol.* **1995**, *63*, 60–65. [CrossRef]
12. Lang, L.; Danckert, K.; Nielsen, B.; Zhou, X. Investigation into the forming of a complex cup locally constrained by around die based on an innovative hydromechanical deep drawing method. *J. Mater. Process. Technol.* **2004**, *167*, 191–200. [CrossRef]
13. Wijayathunga, V.; Webb, D. Experimental evaluation and finite element simulation of explosive forming of a square cup from a brass plate assisted by a lead plug. *J. Mater. Process. Technol.* **2006**, *172*, 139–145. [CrossRef]
14. Yaşar, M.; Korkmaz, Z.; Gavas, M. Forming sheet metals by means of multi-point deep drawing method. *Mater. Des.* **2007**, *28*, 2647–2653. [CrossRef]
15. Shewakh, W.M.; Hassan, M.A.; Hassab-Allah, I. Square-Cup Deep Drawing of Relatively Thick Sheet Metals Through a Conical Die without Blank Holder. *Int. J. Mater. Form. Mach. Process.* **2015**, *2*, 31–46.
16. Hassan, M.; Ahmed, K.; Takakura, N. A developed process for deep drawing of metal foil square cups. *J. Mater. Process. Technol.* **2012**, *212*, 295–307. [CrossRef]
17. Hezam, L.; Hassan, M.; Hassab-Allah, I.; El-Sebaie, M. Development of a new process for producing deep square cups through conical dies. *Int. J. Mach. Tools Manuf.* **2009**, *49*, 773–780. [CrossRef]

18. Mohammed, A.I. Effect of Forming Method on the Behavior of the Drawing Process of a Complex Shape. *Iraqi J. Ind. Res.* **2022**, *9*, 1–11. [CrossRef]
19. Hassab-Allah, I.M.; Hezam, L.M.A.; El-Sebaie, M.G. A novel forming technology for drawing square cups. In Proceedings of the Production Engineering & Design for Development, PEDD7, Cairo, Egypt, 7–9 February 2006; pp. 948–960.
20. Naceur, H.; Guo, Y.; Batoz, J. Blank optimization in sheet metal forming using an evolutionary algorithm. *J. Mater. Process. Technol.* **2004**, *151*, 183–191. [CrossRef]
21. Sheng, Z.; Jirathearanat, S.; Altan, T. Adaptive FEM simulation for prediction of variable blank holder force in conical cup drawing. *Int. J. Mach. Tools Manuf.* **2004**, *44*, 487–494. [CrossRef]

processes

MDPI

Article

Method of Analyzing Technological Data in Metric Space in the Context of Industry 4.0

Karolina Czerwińska and Andrzej Pacana *

The Faculty of Mechanical Engineering and Aeronautics, Rzeszow University of Technology, 35-959 Rzeszow, Poland; k.czerwinska@prz.edu.pl
* Correspondence: app@prz.edu.pl; Tel.: +48-17-8651390

Abstract: The purpose of this article was to develop a method of analyzing the manufacturing process with variables indicating product competitiveness and technological capabilities in metric space as a cognitive source. The presented method will facilitate the identification of key development factors within the manufacturing processes that have the greatest impact on the adaptation of the manufacturing enterprise to Industry 4.0. The presented method of manufacturing process analysis integrates a number of tools (SMART method, brainstorming, BOST analysis, 3 × 3 metrics) that enable the implementation of statistical analysis. The model developed makes it possible to apply known mathematical methods in areas new to them (adaptation in the manufacturing area), which makes it possible to use scientific information in a new way. The versatility of the method allows it to be used in manufacturing companies to identify critical factors in manufacturing processes. A test of the developed method was carried out in one of the foundry enterprises, which allowed us to build a series of importance factors affecting effective production management. The methodology is addressed to the management of manufacturing enterprises as a method to assist in analyzing data and building (on the basis of improved manufacturing processes) a competitive strategy.

Keywords: 3 × 3 matrix; BOST survey; statistical analysis; process improvement; quality 4.0; industry 4.0; mechanical engineering

1. Introduction

Both increasing globalization and changes in the area of competition and economy determine the need to undertake changes in the management of a production enterprise. For this reason, enterprises, which are fundamental subjects of the economy, are increasingly required to have the ability to adapt their management methods and work organization to the thoroughly transforming conditions of their operation [1,2]. The ability to adapt to prevailing conditions in the environment (the dynamics of change, the structure of the organization, the complexity of processes) and the requirements of the market economy affects the results of operations and the development prospects of production facilities. The adaptation of enterprises becomes apparent in the form of implementation of various restructuring and innovative projects. The economic system creates specific operating conditions for organizations that enable enterprises to achieve their development goals. At the same time, the market economy places demands and challenges on guaranteeing the relative stability of operations [3–5].

As part of survival and continued stable operation in the market, increased development is a necessary process leading to changes in the structure and level of components of the enterprise. Development is determined by internal and external factory determinants of market success [6,7]. Internal factors are considered to be those that can be directly influenced by the enterprise. This group of factors determines the development of the enterprise. Among the internal factors, the most common are intellectual and capital-based factories [8]. On the other hand, conditions and external factors are those which the enterprise has little opportunity to influence. Intrinsic factors are defined as the broadly defined

environment of the enterprise. From the environment, the enterprise meets its needs while, at the same time, drawing on its resources [9–11].

Businesses operate in a certain external environment, that is, in a specific area in conjunction with other organizations and with the state. The environment shapes opportunities and possibilities but also creates constraints and places requirements [12]. On the other hand, it also happens that businesses indirectly (through their functioning) influence the external environment and shape its nature to a greater or lesser extent. Such a situation occurs in the case of business entities, or a group of entities characterized by high bargaining power; their decisions can trigger changes in the entire sector [13,14]. The external environment of modern companies is transforming into an increasingly volatile and complex one, and at the same time, it forces rapid and ruthless adaptation to new conditions. As a result, the level of dependence of companies on external conditions is increasing. Organizations wishing to operate in the market and ensure competitive advantage should have the ability to flexibly adapt to market changes. The need to undertake adequate and adaptive activities changes the scope and logic of organizations and the way they are managed and improved [15]. In the literature on the subject [16–18], an approach is encountered which testifies to the fact that actuating enterprises are oriented to conform to the changes that take place in the internal and external spheres, which has not only become a determinant of the survival of economic entities but also affects both the bluntness and level of their development. Only this type of adaptive enterprise will allow for the long-term multiplication of capital value and the realization of one of the main goals of the essence of the functioning of companies, namely, the maximization of market value, which, in the long term, allows for profit maximization [19]. Such a state of affairs is possible thanks to continuous restructuring changes, which enable the implementation of important transformations in the organizational, technical, production, and economic planes. Development processes translate into an increase in the efficiency of the undertaken activities, which directly shapes the rate of their creation of enterprise value and its market position [20]. There are many benefits in terms of developing competitiveness with the initiation of Industry 4.0.

The fourth-generation industry covers the entire value-added chain with its scope. As a result, it requires new strategies and business models, and at the same time, it implies the integration of industrial areas with the use of information technology [21,22]. Industry 4.0 promotes efficiency improvements, cost reductions, and shortens test phases and production. It makes it possible to extend the useful life of products. It makes it possible to produce individual pieces of products without limiting profitability to mass production only [23]. Industry 4.0 is supposed to be a guarantee for maintaining competitiveness in countries with high wages, energy conservation, and an aging population, while allowing manufacturing companies to adapt their offerings to the dynamically changing needs of the market and the demands of high quality [24,25]. However, before the operation of enterprises in accordance with the idea of Industry 4.0 develops its full potential and begins to bring positive effects to the economy, it will be crucial to look for new, progressive solutions. These solutions should concern the management of the organization, especially the technical area through effective control of the internal factors that shape the market position [26,27].

The purpose of the developed model was to identify the factors with the greatest impact on the technological capabilities and market position of manufacturing companies in the context of the idea of Industry 4.0 through the analysis of technological data within the metric space. The methodology used a 3×3 matrix within which the results of surveys were located, and statistical analyses were performed in order to propose a new use of scientific information and to realize in-depth analyses to support the management of the technological and organizational space. The proposed analysis model is characterized by a wide application dimension. It can be implemented in any manufacturing enterprise whose development intentions are geared towards Industry 4.0 concepts. Integration of the model in a manufacturing enterprise allows us to identify the most important factors in

the context of the development and success of the enterprise. This procedure will make it possible to develop effective plans for the development of the enterprise in the context of the idea of Industry 4.0. The next section of this study performs a literature review, which was carried out as part of our identification of the research gap in the topic under consideration. Section 3 describes the concept and assumptions of the developed data analysis model in metric space. Section 4 presents the verification of the model and its results. Section 5 is devoted to the summary of the study.

2. Literature Review

Adequately carried out management in specific internal and external conditions makes it possible to ensure a high level of competitiveness of the enterprise, which ensures a stable market position [28]. The competitiveness of a specific enterprise is most often studied in comparison with other comparable companies operating within the same sector. In the present approach, the aspect of competitiveness is understood as the result of the actions taken, which are related to customer acquisition [29]. Competitive superiority can be closely related to a well-thought-out and realistic strategy of technical development adequate to the concept of Industry 4.0 [30,31].

Constantly changing trends and market conditions force companies to seek new and progressive solutions in the field of organizational management [32], especially in the technical area through effective control of the internal factors shaping market position [33]. The management of enterprises focused on the implementation of developmental changes increases the possibility of implementing revolutionary solutions, resulting in increased competitiveness, often in a positive way. For this reason, various methods of analyzing the level of competitiveness are proposed in the literature. These methods are based on the analysis of multi-criteria indicators [34,35], the integration of several methods (historical method, content analysis, system analysis, formalization method) [36], and rough set methods used to assess the benefits of resources [37]. Proprietary methods relating to multi-faceted competitive analysis are also being developed. An example of this is the hybrid GIANN method, which combines multi-attribute utility theory with the concepts of entropy and information extraction and computational modeling via a multi-layer perceptron artificial neural network [38]. Models directed at recognizing the correlation between the technological level and competitive success of companies are also being developed [39]. Ejaz proposed a theoretical linear model identifying the digital technologies used, which have been shown to be a source of manufacturing competitiveness. This study sheds light on the limitations of measuring or defining the competitiveness factor at the company, regional, or national level. With regard to methods for measuring the level of competitiveness, it also distinguishes between methods that target cross-enterprises of a certain size, an example of which is a concept aimed at small manufacturing companies, which combines a context-free perspective with the contingency theory of quality management (Baldrige's quality excellence model) [40]. The indicated concept allows for the identification of internal factors with a significant impact on the competitiveness of an enterprise. The indicated methods refer to analyses based on internal factors.

With regard to external factors, methods for analyzing the level of competitiveness and market position most often involve market (marketing) research [41,42], and sometimes, marketing research is combined with comparative analysis [43]. Map-based methods (a novel dynamic mapping platform) are also proposed for analyzing changes in competitive positions [44]. Authors Fluhrer and Brahma [45] also present a concept of competitive level positioning in which data are analyzed using qualitative structuring. There is also research on hybrid brand positioning strategies undertaken to identify the most effective strategy [46].

Based on the literature review, studies on technology data analysis and competitive level analysis were grouped. The extracted areas are shown in Table 1.

Table 1. Research areas of technological data analysis and level of competitiveness.

Factor	Group	Covered Position in the Context of the Subject of the Study	Representatives (Literature Items)
Internal and external factors	Comparative studies	Examined against other comparable companies operating within the same sector. Lack of separation of factors.	Campos, T.L.R., Nunhes, T.V., Harney, B., de Oliveira, O.J. [22]
	Analyses of multi-criteria indicators	Expert analysis of the results obtained through the use of multi-criteria indicators that demonstrate the commercial success and competitiveness of the company.	Ginevicius, R., Gedvilaite, D., Stasiukynas, A., Suhajda, K. [34]
		Integration of macro and micro indicators at the level of the balanced scorecard (an analytical tool) in order to make management decisions about business operations and the level of competitiveness.	Datsenko, G., Kotseruba, N., Krupelnytska, I., Kudyrko, O., Lobacheva, I., Otkalenko, O. [35]
Internal factors	Integrating several methods of analysis	The following methods were used: the historical method and the content analysis method were used to examine the theory of enterprise development; the system analysis method was used to substantiate the conceptual vision of commercial enterprise development; and the formalization method was used to create a core model of enterprise development. The goal was to identify internal key determinants of competitiveness.	Hrosul, V., Zubkov, S., Mkrtchyan, T. [36]
	Approximate set methods	The weight of each evaluation indicator was determined with the application of significance in rough set theory, using the linear weighting method to determine the final result. It then systematically explains the main ideas and methods of rough set theory in evaluating favorable resources of enterprises.	Li, Z.G., Lou, W.F., Li, Y.S. [37]
	Neural networks	Consideration of multi-attribute utility theory with the concepts of entropy and information extraction, and computational modeling through the multi-layer perceptron artificial neural network.	Schaefer, J.L., Tardio, P.R., Barierle, I.C., Nara, E.O.B. [38]
	Linear models	A linear model identifying the digital technologies used which have been shown to be sources of manufacturing competitiveness.	Ejaz, M.R. [39]
	Context-free perspective combined with contingency theory of quality management	Using a pooled cross-sectional design and structural equation modeling to test the validity and reliability of the Baldrige model to measure quality management practices.	Parast, M.M., Safari, A., [40]
External factors	Market (marketing) research	Survey research using a proprietary questionnaire.	Anawade, Pa., Sharma, D.S. [41]
		A novel influence analysis technique called Grey Influence Analysis (GINA), which can be used to analyze the influence relationships between a set of factors when there are a large number of responses.	Rajesh, R. [42]
	Combining marketing research with benchmarking	Factor analysis, cluster analysis, and regression analysis were used.	Lin, S., Xu, S.Y., Liu, Y., Zhang, L.Y. [43]
	Dynamic mapping	EvoMap—a novel dynamic mapping framework that identifies company trajectories from high-frequency and potentially noisy data.	Matthe, M., Ringel, D.M., Skiera, B. [44]
	Competitive level positioning	Analyzed data using qualitative structuring, resulting in a newly developed and empirically based typology of SME positioning strategies.	Fluhrer, P., Brahm, T. [45]
		Exploring hybrid brand positioning strategies in emerging markets based on two positioning elements: brand country of origin (COO) and brand globality.	Hong, R.Y., Zhang, Z., Zhang, C., Hu, Z.H. [46]

Previous work has mainly relied on the survey method, on multi-variate competitive analysis, on multi-attribute utility theory, and even neural networks. The aforementioned methods, although beneficial, require preparation for their application. The integrated methods proposed in the model have the advantage of being easy to apply. Through this, the potential area of application (wide implication range) can be increased.

So far, the combination of methods used in the developed model has not taken place, and the advantages that characterize the integrated methods allow us to assume that the proposed model will be effective for companies using it.

The research highlighted the division of methods into two main groups: methods that are mainly based on the analysis of internal factors; and methods whose analysis is based on external factors. It is relatively rare to find methods that refer to internal and external success factors in terms of competitiveness. The realized analyses led to the identification of the gaps which will be considered in the study: (1) the lack of a model that integrates internal and external factors in the area of technological capabilities and market position (Industry 4.0) in a single model; (2) the lack of a model that recognizes the key factors (internal and external) underpinning the success of a manufacturing enterprise; and (3) the lack of a model that, based on an analysis of the internal and external factors of a manufacturing enterprise, indicates a development strategy to increase the competitiveness of the enterprise. The study presents a structured model for proceeding with the analysis of data in the metric space on the degree of utilization of technological capabilities and competitiveness indicative of market position in the context of Industry 4.0. The presented model supports the management and development processes of enterprises and, at the same time, fills the identified research gaps.

3. Method of Data Analysis in Metric Space

The market position of manufacturing plants is influenced by the level of technological sophistication and innovation, as well as the quality of finished products. Therefore, a key issue in the context of effective management is data analysis, particularly the relationship between the technological capabilities and competitiveness of products. Figure 1 shows the assumptions of the developed data analysis model for adapting the production process to the requirements of Industry 4.0.

The developed model was divided into three steps: survey preparation, diagnostic testing, and statistical analysis. The individual steps of the method are as follows:

Stage 1—survey preparation

Given the distinctive features of the tools used in the method of data analysis in metric space, the main production process carried out in a manufacturing company should be considered the proper subject of the study. In addition, it is necessary to identify the key data for the study from the selected process.

The selection of a team of experts is an important step in the implementation of the presented method of analysis; it means the selection of people responsible for the implementation of the presented method in the context of obtaining the intended results. Individual members of the expert team should be selected from the management team. The members of the team should have experience and a wide range of knowledge regarding the selected subject of research, as well as competition and the situation in the market within which the company operates.

In the framework of the implementation of the developed model, it is recommended to define a research objective that will be linked to the results of the analysis. The definition of the goal should be based on the SMART technique—one of the most effective techniques for properly defining the desired results and the path to achieve them. The name SMART is an acronym referring to the five key characteristics that a well-defined goal should meet (S—"specific"; M—"measurable"; A—"attractive"; R—"realistic"; and T—"time-based") [47,48]. Setting goals in accordance with the SMART principle allows you to start implementing them right away, to stay motivated to see your actions through to the end, and to be able to easily assess progress and accurately determine when the established

goal has been achieved. The SMART principle folds into a precise approach to defining the study's objectives, motivates action, and further prompts multi-faceted consideration of the study's purpose [49,50]. One of the planes is the analysis of production processes in the context of the implications of the Industry 4.0 concept. The definition of an adequate research objective (using the SMART technique) will facilitate the realization of the analysis of the current state of affairs in the relationship between technological capabilities and market position and will make it possible to indicate further courses of action in terms of effective adaptation to the Industry 4.0 concept in the diagnosed development conditions.

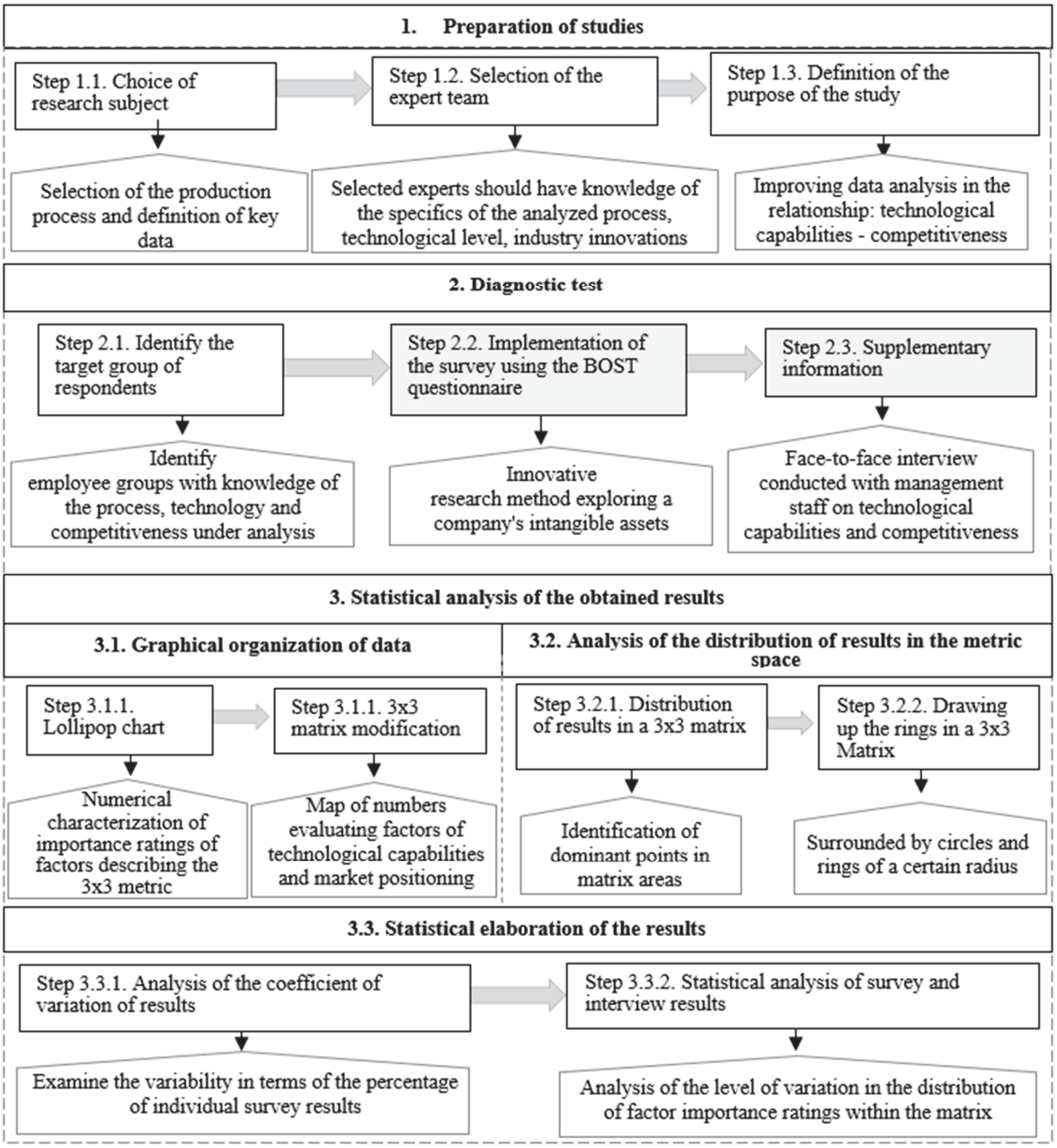

Figure 1. Concept of the method of data analysis in metric space.

The SMARTER method can also be used to identify and build a valid survey objective. This method is a development of the SMART method by including additional features (E—"exciting"; and R—"recorded") that the study objective must meet. Another modification of the SMART method is the SMART UP method, which indicates that the stated goal, according to the acronyms, should be U—"under control" and P—"positive" [48].

In the study, the SMART method was chosen to build a correct objective due to its considerable popularity in scientific works. This method is the best choice in the context of defining the goal of the study because it supports setting the goal in a way that allows it to be achieved. An important determinant of our choice of the SMART method was also the fact that this concept helps monitor progress and adjust plans in response to changing conditions. In addition, the method clearly indicates what the goal should be (meeting 5 characteristics: "specific" "measurable", "attractive", "realistic", and "time-based"). Related methods, which are an extension of the SMART method, are only a development of it, which are not required in the context of the research topic undertaken.

Stage 2—Diagnostic survey

Managerial staff of the production department, technology department, quality control department, and product marketing department were selected for the survey. A total of 28 people participated in the survey. The group of employees is responsible for the control and improvement of the studied extrusion process and product—the suction manifold. The indicated number of respondents is due to the fact that the research carried out within the framework of the study is a pilot study and concerns the selected manufacturing process. The enterprise employs about 1300 people and the group of respondents thus represents 21.54% of the managerial staff associated with the studied production area.

The survey was conducted in the fourth quarter of 2023. The survey was mandatory, and the return rate was 100%. The survey questions were subject to validation.

We carried out a survey using the BOST (acronym from the author's first and last name—Stanislaw Borkowski) method in the employee version [51]. The employee version takes into account a set of factors relating to the elements of the Toyota house roof and principles 1, 2, 3, 4, 6, 7, and 14 [52]. The model developed includes Toyota's first management principle, which indicates that management decisions should be based on a long-term philosophy, even at the expense of short-term financial goals [53,54]. The use of the BOST method was considered the best solution for further research because the model allows for the collection and further analysis of data using a standardized questionnaire in which the questions relate to spheres that coincide with those studied within the implications of the model (technological capabilities and market position of the company). One aspect that confirms the best choice of this method is the factors included in it; these allude to providing the best quality products while implementing processes in the shortest possible time, as well as at the lowest cost, which can be considered important aspects in terms of achieving success.

The benefit of the BOST method is its transparent nature and the speed of its implementation. The usefulness of the BOST method is also manifested in its ability to use a standardized set of competitive factors in the study, which contributes to the success of the research.

The BOST method sets the direction for further research by determining the factors describing the Toyota management principle 1 in the context of determining their impact on the technological capabilities and market position of the enterprise against the background of the idea of Industry 4.0. The BOST method takes into account the intangible resources of enterprises such as customer well-being, product innovation, cooperation with cooperators, the self-reliance responsibility of employees, the development of technology, and the nurturing of the enterprise culture. This BOST survey is described in more detail in the work of [51]. In addition, in order to ensure a broader scope of analysis, the survey includes such factors as trust in relations with employees, the size of the market offer, the quality of the goods sold, the price of the goods offered, own research and development work, the purchase of research and development work, as well as factors relating directly to the idea of Industry 4.0: automation, advanced digital technologies, capital (understood in material terms, i.e., machinery and equipment), entrepreneurship, and the combination of physical and virtual spheres of production. The procedure of taking into account a larger number of factors makes it possible to carry out a multi-faceted analysis of the foundry pre-casting companies.

After conducting a survey using the BOST survey, a face-to-face interview should be conducted with employees. The interview should be carried out in the form of a dialogue that allows the researcher to obtain information from the respondent that will be useful in the context of achieving the set research objective. With regard to the presented model, the subject of the interviews should concern the technological level and market position of the company. The face-to-face interview was found to be the best within the discussed sequence of methodological steps because during the meeting, it is possible to better clarify questions that were not understood. In addition, this solution provides a better understanding of the answers and allows us to establish a deeper connection with our interviewee.

Step 3—Statistical analysis of the obtained results

As part of the graphical representation of the obtained results, it is necessary to create a numerical characterization of the data, i.e., assessments of the importance of the factors that describe the 3 × 3 matrix (technological capabilities and market position). In order to have a good understanding of the obtained assessments, initially, the result is presented using a lollipop chart. Then, on the substrate of the modified 3 × 3 matrix, one should place the individual pairs of results in the corresponding poms of the matrix, showing their distribution. Modification of the 3 × 3 matrix refers to the indication of the correlation between technological capabilities (the X axis) and market position (the Y axis) (in the original version, the Y axis indicates the competitiveness of the product). Figure 2 shows the characteristics of the modified 3 × 3 matrix with the designations of the nine strategies. Interventionary studies involving animals or humans, as well as other studies that require ethical approval, must list the authority that provided approval and the corresponding ethical approval code.

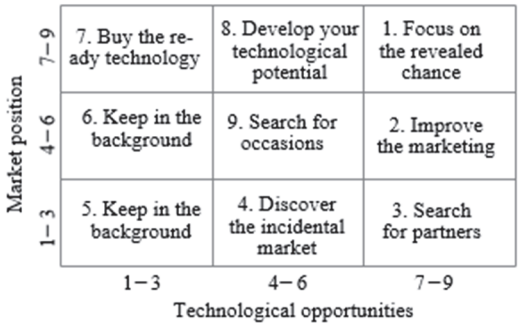

Figure 2. Characteristics of the 3 × 3 matrix in the modified version with the designation of its zones (management strategies).

The 3 × 3 matrix, in its original version, was used in the study [55], while its modifications were applied in [56–58]. Within the matrix, 9 areas indicative of the technological position of the analyzed production facility are separated. Each area of the 3 × 3 matrix proposes a specific development strategy that must be undertaken to achieve success. It is desirable to achieve field 1—"Focus on the revealed chance". This box indicates that all of the pairs of characteristics located there received scores in the range of 7–9. In the modified version, box 1, in addition to recommending a strategy, also indicates the pairs of factors that are among the most important (scores in the range of 7–9) and to which the most attention should be paid when improving production processes and creating development strategies in the context of the implications of Industry 4.0 in the enterprise and achieving market success.

The use of the 3 × 3 matrix in the technology data analysis model is predicated on the significant number of benefits it provides. The matrix is intuitive and user-friendly in nature. Each area in the matrix pre-presents a clearly defined approach to enterprise development, making it easy to interpret and apply. The biaxial approach of the 3 × 3 matrix provides an equalized assessment. In addition to its primary use, i.e., diagnosis of the enterprise's position, the matrix can serve as a strategic tool for planning and predicting development paths. Such predictability allows us to proactively plan transitions between areas of

the matrix by implementing the appropriate strategies indicated therein. The use of the 3 × 3 matrix in the framework of the stage under discussion is the most appropriate solution because it provides predictability of the development direction of the enterprise, which allows for the proactive planning of transitions between areas of the matrix by implementing the relevant strategies indicated therein.

The next step refers to the identification of dominant points (dominant pairs of results regarding technological capabilities and market position) within each of the 9 areas of the 3 × 3 matrix. The purpose of this step is to perform analyses of the zones of the 3 × 3 matrix as separate metric spaces. The dominant points are considered to be the numbers with the highest value. The dominant points are the centers of circles and rings with radii of 1–4. A radius value of 1 indicates the center of a specific area of the matrix.

The last step of the method concerns the analysis of the coefficient of variation, which is the quotient of the non-relative measure of variation and the corresponding mean. This coefficient indicates the ratio of the standard deviation to the mean value. It is classified as a measure of dispersion and helps determine the degree of variation in the value of a variable. The coefficient of variation is mainly useful in situations where comparisons are made between the variability of traits in two populations and when the researcher makes analyses from the range of variation between different measures [59,60]. The feature under study is the percentage of survey results placed within the resulting rings. In the classical approach, i.e., statistical analysis of survey and interview results, the study is concerned with analyzing the level of variation in the distribution of factor importance ratings within the matrix.

4. Model Verification and Results

The integration and thus model checking of the data analysis in the metric space was performed at one of the production companies in the foundry industry, which is located in the southeastern part of Poland.

The foundry industry, which is popular in Poland, especially in the southeastern part of the country, is one of the heavy industries with a significant negative impact on the environment. As part of the implementation of the idea of sustainable development, and under pressure from the European Union, this industry is being forced to undertake radical modernization. These changes must be implemented according to the adopted strategies. This activity can be helped by this study. Using modern developments as well as proven and integrated methodologies, it is possible to assist managers of foundry companies and beyond in adapting their companies to the requirements of modern Industry 4.0.

Stage 1—preparation of the study

As part of the test of the developed analysis model, the manufacturing process of an intake manifold used in automotive applications was considered as the subject of the study. The task of the manifold is to supply the fuel–air mixture or the air itself to the engine cylinders with the lowest possible flow resistance. The product created by the selected production process is one of the mainly produced products (in terms of number) in the company.

A panel of experts was selected from among the company's management staff, which included a quality control manager, a product marketing manager, and a technology department manager. The selection of the composition of the team of research experts took into account the predisposition of employees to meet the requirements of analyzing data on the technology used and the market situation, including the company's position in the market in the context of the idea of Industry 4.0.

The purpose of the implications of the developed model is to analyze the data of the current state of the production process of intake manifolds used in automotive applications and the market position. Thanks to the in-depth analysis of the factors affecting the process under study, it is possible to eliminate the sensitive factors affecting disruptions during innovation, which will effectively ensure an increase in technological capabilities and a high level of competitiveness of the product.

Stage 2—Diagnostic survey

Employees of managers and executives of the production department, technology department, quality control department, and product marketing department were selected for the survey. A total of 28 people participated in the survey. This group of employees is responsible for controlling and improving the extrusion process and the product, i.e., the suction manifold. The survey was conducted in the fourth quarter of 2023. The indicated number of respondents is due to the fact that the research carried out in the study is a pilot study. The survey was mandatory, and the return rate was 100%. The survey questions were subject to validation. The enterprise employs about 1300 people.

Selected managerial and executive employees, thinking about the company where they work, were asked to answer the following question: what factors determine the development concept of your company? They were to rate the various factors of innovation on a scale of 1–9 (where 1—the least important factor; 9—the most important factor). Factors mentioned in the question in the context of technological capabilities are product innovation, independence of employees, responsibility of employees, development of technology, automation, advanced digital technologies, capital (understood in material terms, i.e., machinery and equipment), entrepreneurship, and the combination of physical and virtual spheres of production. Factors relating to market position are customer interest, cooperation with partners, trust in relations with employees, preservation of culture in the company, size of the market offer, quality of goods sold, price of goods offered, own research and development work, purchase of research, and development work.

Following the survey, face-to-face interviews were conducted with management staff to expand the knowledge gathered. The interviews covered their views on the competitiveness of the product and the company's market position. The issue of the ability to plan, create, and sell the product was raised, as well as operational competitiveness (capturing the technical skills that facilitate the functioning of the enterprise in a given market) and system competitiveness (testifying to the wide range of activities of the enterprise leading to the improvement and modernization of the implementation of the organization's processes in terms of Industry 4.0).

Stage 3—Statistical analysis of the obtained results

Based on the information obtained from the implementation of Stage 2, a numerical specification of the importance level ratings of the various factors indicating technological capabilities and market position was developed. The specification is shown in Figure 3.

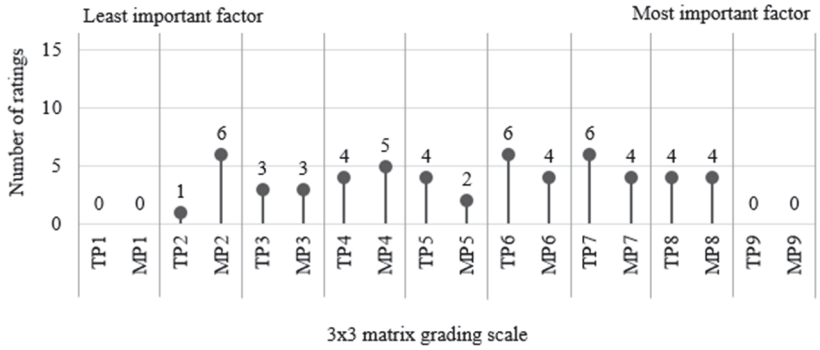

Figure 3. Describing the level of importance of assessments of factors indicating technological capabilities (TP) and market position (MP), taking into account the areas of the 3 × 3 matrix (horizontal axis digits).

The lollipop chart shows the structure of evaluations of the two factors (technological capabilities—TP; market position—MP) awarded by employees, divided into 9 areas of a 3 × 3 matrix. In Figure 3, the numbers indicated on the vertical axis correspond to the areas of a 3 × 3 matrix.

In the next step, a map of the numbers of indications and evaluations of the analyzed factors—technological capabilities (TP) and market position (MP) acquired in stage 2 of the analysis—was developed (Figure 4).

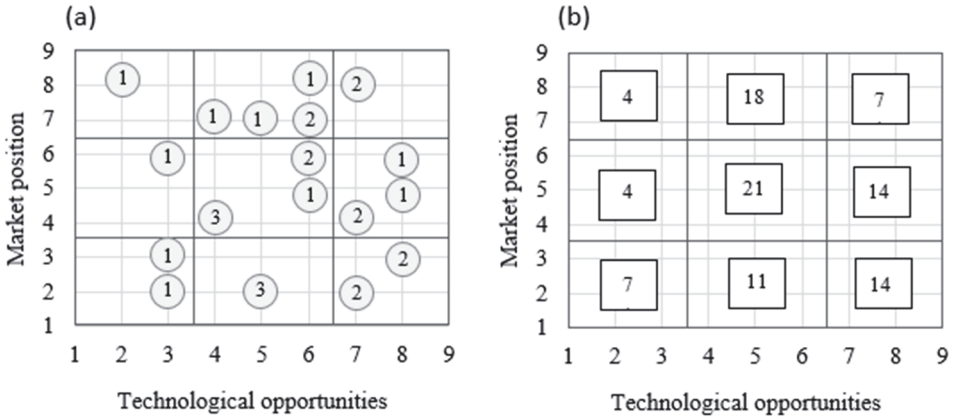

Figure 4. Analysis of the importance level assessments of pairs of factors indicating technological capabilities (TP) and market position (MP): (**a**) the unitary capture of pairs of factors; (**b**) factor structure in percentage terms.

The highest concentration of pairs of ratings is found in the middle part of the matrix. This fact indicates that the largest number of respondents gave grades 4–7 for the technological capabilities factor and grades 2–8 for the market position factor. With reference to part (b) of Figure 4, i.e., the percentage share of evaluation results, it can be seen that 21% of the evaluation pairs are located in part 9 (strategy: search for occasions) and 18% of the evaluation pairs in part 8 (strategy: develop your technological potential). Therefore, a practical recommendation is to intensify the company's activities in the area of the more efficient use of technological resources. The company should also increase its activity in shaping product competitiveness (making the product more attractive) and increasing its market position. Motivation to take the indicated actions in the analyzed area can be increased access to resources not previously owned, better use of the emerging opportunities of the environment, increased flexibility of activities, and increased positive image of the enterprise. Among respondents, 14% of employees believe that marketing activities should be improved, and new partners should be sought. Undertaking the indicated activities will move the results towards the desired field—field number 1.

Examining the distribution and structure of the results of the diagnostic survey within the 3 × 3 matrix, one can see the points with the highest value (dominant results). In each of the nine zones, the dominant points will be the centers of established circles with radii increasing sequentially by the value of 1. In the case where there is no dominant point in a zone, the center of the ring is taken as the point closest to zone 9 and the score of 9 points in both the x and y axes of the 3 × 3 matrix. The centers (midpoints) of the rings have a radius value of 1. Within the zones of the 3 × 3 matrix, the following points were considered as the centers of the rings: area "1" point with coordinates: (7;8); area "2" point with coordinates: (7;4); area "3" point with coordinates: (8;3); area "4" point with coordinates: (5;2); area "5" point with coordinates: (3;3); area "6" point with coordinates: (3;6); area "7" point with coordinates: (2;8); area "8" point with coordinates: (6;7); and area "9" point with coordinates: (6;6). In this way, it is possible to analyze assessment structures in metric space.

As part of further analyses, metric spaces were created in the form of rings appropriately superimposed on individual areas of a 3 × 3 matrix (Figure 5).

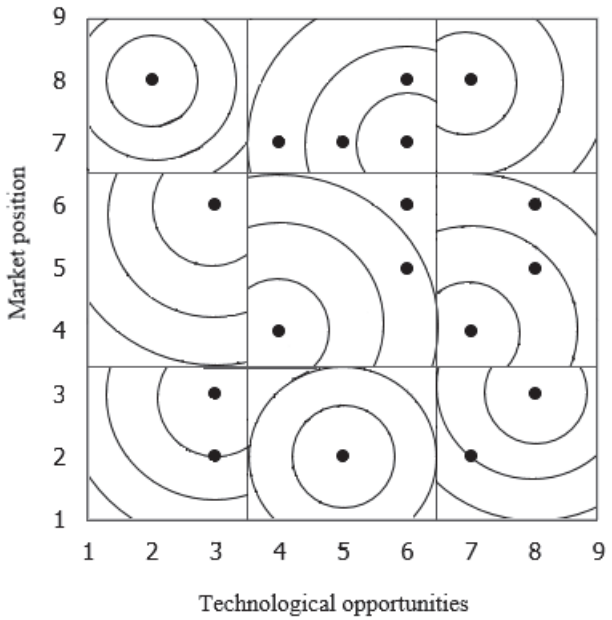

Figure 5. Positioning of rings against 3 × 3 matrix zones.

The percentage of individual pairs of factor evaluations that fell within the defined rings was also analyzed. This analysis is presented in Table 2.

Table 2. Layout of the structure of a set of rings against the background of the metric space.

Ring Structure		3 × 3 Matrix Zone								
		1	2	3	4	5	6	7	8	9
Location of rings within the zones of the 3 × 3 matrix	$0 \leq r < 1$	100	50	50	100	50	100	100	40	50
	$1 \leq r < 2$	0	25	50	0	50	0	0	40	0
	$2 \leq r < 3$	0	25	0	0	0	0	0	20	17
	$3 \leq r < 4$	0	0	0	0	0	0	0	0	33

One of the statistical measures of analysis is the coefficient of variation. This coefficient is a type of measure that describes the relationship that occurs between the analyzed distributions that differ both from each other and from the values of the characteristics around the central values. The basis for the analysis of the coefficient of variation of the percentage of the factors presented is a 3 × 3 matrix indicating the significance ratings of pairs of factors (technological capabilities, market position) in the form of points of a specific position. The values of coefficients of variation and the number of non-zero rings within the zones of the 3 × 3 matrix are indicated in Table 3.

Table 3. List of coefficients of variation of percentages of factor pairs within rings.

3 × 3 Matrix Zone	Coefficient of Variation of Percentages of Factor Pairs	Number of Non-Empty Rings
1	0	1
2	35	3
3	0	2
4	0	1
5	0	2
6	0	1
7	0	1
8	28	3
9	40	3

When interpreting the values of the coefficient of variation, it should be remembered that the smaller the coefficient of variation, the better. Within the considered zones of the 3 × 3 matrix, the values of the coefficient of variation of the percentage of points in the outlined rings are in the range of 0–40 (Table 3). The achieved values of the coefficient of variation indicate that six zones (zone 1 and 3–7) are homogeneous; they show no variability. In contrast, the remaining zones (zone 2, 8, and 9) are characterized by average variability.

Based on the data obtained (Table 3), it is possible to create a ranking of the separated zones of the 3 × 3 matrix using the topological matrix and the rings created. The zones were hierarchized on the basis of the value of the coefficient of variation of the importance ratings of the analyzed factors (technological capabilities and market position) placed in the 3 × 3 matrix. The developed series looks as follows:

$$(\text{“1”}, \text{“3”}, \text{“4”}, \text{“5”}, \text{“6”}, \text{“7”}) < \text{“8”} < \text{”2”} < \text{“9”}, \quad (1)$$

The ranking was determined according to the principle of interpreting the coefficient of variation; the less, the better—that is, starting with the smallest values. The brackets used in the series indicate the equal value of the coefficient of variation within the zones.

The result of the analysis shows the agreement of the respondents regarding the significant influence of the factors considered in the survey on the sphere of technological capability and market position. The obtained ranking of the level of variability in the area of zones of the 3 × 3 matrix indicates the level of importance of the factors influencing technological capabilities and market position. The key factors for the enterprise in the context of building competitiveness are the factors located in zone 9. Slightly less important are the factors from zone 2 and, in turn, from zone 8. The following pairs of factors were located within the aforementioned zones:

- Automation (a factor relating to technological capabilities) and quality of goods sold (a factor relating to market position)—zone 9.
- Application of advanced digital technologies (factor on technological capabilities) and own research and development (factor on market position)—zone 2.
- The development of technology (technological capabilities factor) and the price of goods offered (market position factor)—zone 8.

Among the factors with the greatest impact were those directly related to the concept of the fourth industrial revolution (automation, advanced digital technologies, and technology development). These factors are characterized by a significant impact on the competitiveness of the organization. The importance of the other analyzed factors from both the group of factors related to technological capabilities and market position was assessed at an equal (least significant) level, i.e., no variability was detected.

The obtained result indicates an unambiguous position in achieving the goal, maintaining a leading market position and achieving the desired field in the 3 × 3 matrix, which means embracing the strategy: “Search for occasions”. For the analyzed company, a strategy is recommended within the framework in which the directions of development will concern the factories of groups 9, 2, and 8.

Metric spaces appear in many areas of mathematics such as mathematical analysis, order theory, and algebraic geometry. Metric space is a concept that is located on the borderline between mathematical analysis and topology. Thanks to this concept, we are able to define, in a natural way, many concepts known from mathematical analysis in a broader class of objects and conduct analyses within this space. Typically, these analyses do not apply to manufacturing engineering and process improvement. However, the proposed model of data analysis in the area of metric space makes it possible to identify the factors with the greatest impact on the technological capabilities and market position of the enterprise in the context of the implications of the idea of Industry 4.0. In addition, the verification of the developed model of technological data analysis highlighted that sensibly conducted data analysis in metric space using complementary methods and techniques has

a significant positive impact on ensuring the continuity of adequate development directions of the enterprise.

The proposed method makes it possible to conduct analyses to support the management of technological and organizational space in manufacturing enterprises. The use of the model makes it possible to identify the key factors of development of a specific enterprise that testify to the technological capabilities, market position, and potential with respect to the implications of Industry 4.0. Thus, it will be possible to adopt adequate directions of development in the internal and external space. The proposed model for analyzing technological data is characterized by a broad application dimension.

The proposed model can be used by manufacturing companies. Each of them selects specific experts (respondents). The conclusions of the developed method will be dedicated to this specific enterprise. The development strategy established according to the methodology is not necessarily the right strategy for another enterprise with similar characteristics.

5. Conclusions

The optimal level of efficiency in the sphere of management of a manufacturing enterprise under certain internal and external conditions allows the organization to maintain high competitiveness, which determines its long-term development. The research carried out was aimed at developing an innovative model of data analysis within the metric space, allowing us to identify the factors with the greatest impact on the technological capabilities and market position of the enterprise against the backdrop of the idea of Industry 4.0. The methodology used a 3×3 matrix within which the results of the surveys were located, and statistical analyses were performed in order to propose a new use of scientific information and the implementation of in-depth analysis to support the management of the technological and organizational space. The proposed analysis model is characterized by a wide application dimension.

Adopting the topological metric to analyze the data contained in the 3×3 matrix by dividing its zones into rings, it is possible to calculate the value of the coefficient of variation within the standardized zones. This procedure makes it possible to create a ranking based on the values of the coefficients of variation of the importance ratings of the analyzed factors of the separated zones. The ranking indicates the level of agreement of respondents on the determination of the impact of individual factors on the technological capabilities and market position of the enterprise. In addition, verification of the developed data analysis model highlighted that judiciously conducted data analysis has a significant positive impact on ensuring the continuity of adequate development directions of the enterprise in both internal and external space. The resulting series of assessments of the importance of factors influencing technological capabilities and market position indicate the positive importance of automation and technical development in the manufacturing process. Factors directly related to the idea of Industry 4.0 (product innovation, technology development) were found to be the factors with the greatest impact on the competitiveness of the enterprise, which is influenced by the use of technological capabilities. In the evaluation of this group of factors, the lowest level of variation in the variation index parameter was identified. This shows that respondents clearly emphasize the importance of such activities in order to maintain a leading market position and move closer to the desired field in the 3×3 matrix, indicating "Search for occasions" strategies. This conclusion is in line with the paradigms of the fourth industrial revolution.

Future research directions will include the implication of the developed model of data analysis in the metric space to other manufacturing processes in the framework in which the leading products of the enterprise are produced in order to ensure the identification of the appropriate direction of improvement activities in the use of technological opportunities and to ensure market position. The actions taken contribute to technological development and increase the level of competitiveness of the studied enterprise. The next step in the development of the method will be to increase the number of analyzed factors relating to the sustainable development and management of the production enterprise. The

presented course of research implementation can support decision-making in the field of the management and development of production enterprises.

Author Contributions: Conceptualization, K.C. and A.P.; methodology, K.C. and A.P.; validation, K.C.; formal analysis, A.P.; data curation, K.C.; writing—original draft preparation, K.C. and A.P.; writing—review and editing, K.C. and A.P.; visualization, K.C. and A.P.; supervision, K.C. and A.P.; project administration, A.P. All authors have read and agreed to the published version of the manuscript.

Funding: This research received no external funding.

Data Availability Statement: Data are contained within the article.

Conflicts of Interest: The authors declare no conflicts of interest.

References

1. Baryshnikova, N.; Kiriliuk, O.; Klimecka-Tatar, D. Enterprises' strategies transformation in the real sector of the economy in the context of the COVID-19 pandemic. *Prod. Eng. Arch.* **2021**, *1*, 8–15. [CrossRef]
2. Furman, J.; Malysa, T. The role of visual management in the organization of safe work in production companies. *Prod. Eng. Arch.* **2023**, *29*, 195–200. [CrossRef]
3. Klimas, P.; Czakon, W.; Fredrich, V. Strategy frames in coopetition: An examination of coopetition entry factors in high-tech firms. *Eur. Manag. J.* **2022**, *40*, 258–272. [CrossRef]
4. Ligarski, M.J. Methodology of problem analysis in the quality management system with the use of systems approach. *Manag. Syst. Prod. Eng.* **2018**, *26*, 157–161. [CrossRef]
5. Klimecka Tatar, D.; Niciejewska, M. Small-sized enterprises management in the aspect of organizational culture. *Rev. Gest. Tecnol.—J. Manag. Technol.* **2021**, *21*, 4–24. [CrossRef]
6. Antonelli, C.; Crespi, F.; Scellato, G. Internal and external factors in innovation persistence. *Econ. Innov. New Technol.* **2013**, *22*, 256–280. [CrossRef]
7. Pacana, A.; Czerwińska, K. Analysis of the causes of control panel inconsistencies in the gravitational casting process by means of quality management instruments. *Prod. Eng. Arch.* **2019**, *25*, 12–16. [CrossRef]
8. Tikhonor, A.; Zelentsova, L. Analysis of External and Internal Factors of Business Competitiveness. *Qual.-Access Success* **2021**, *22*, 16–19.
9. Bilomistniy, O.; Bilomistna, I.; Galushko, Y. Influence external and internal factors to financial security of enterprise. *Financ. Credit. Act.—Probl. Theory Pract.* **2017**, *1*, 105–111. [CrossRef]
10. Nasim, K. Role of internal and external organizational factors in TQM implementation: A systematic literature review and theoretical framework. *Int. J. Qual. Reliab. Manag.* **2018**, *35*, 1014–1033. [CrossRef]
11. Pacana, A.; Czerwińska, K. Comparative tests of the quality of the piston combustion chamber for a diesel engine. *Teh. Vjesn.—Tech. Gaz.* **2020**, *27*, 1021–2024. [CrossRef]
12. Gawlik, R. Methodological aspects of qualitative-quantitative analysis of decision-making processes. *Manag. Prod. Eng. Rev.* **2016**, *7*, 3–11. [CrossRef]
13. Pietraszek, J.; Radek, N.; Goroshko, A.V. Challenges for the DOE methodology related to the introduction of Industry 4.0. *Prod. Eng. Arch.* **2021**, *26*, 190–194. [CrossRef]
14. Pacana, A.; Czerwińska, K. Model of Diagnosing and Searching for Incompatibilities in Aluminium Castings. *Materials* **2021**, *14*, 6497. [CrossRef] [PubMed]
15. De Valon, T.; Cegarra-Navarro, J.G.; Garcia-Perez, A.; Martinez-Martinez, A. Co-creating sustainable competitiveness in an unpredictable business reality. *Proc. Int. Conf. Bus. Excell.* **2022**, *16*, 47–58. [CrossRef]
16. Wolniak, R. The assessment of significance of benefits gained from the improvement of quality management systems in Polish organizations. *Qual. Quant.* **2013**, *47*, 515–528. [CrossRef]
17. Borowiecki, R.; Olesiński, Z.; Rzepka, A.; Hys, K. Development of teal organisations in economy 4.0: An empirical research. *Eur. Res. Stud. J.* **2021**, *24*, 117–129. [CrossRef]
18. Ritter, T.; Pedersen, C.L. Digitization capability and the digitalization of business models in business-to-business firms: Past, present, and future. *Ind. Mark. Manag.* **2020**, *86*, 180–190. [CrossRef]
19. Csiki, O.; Demeter, K.; Losonci, D. How to improve firm performance?—The role of production capabilities and routines. *Int. J. Oper. Prod. Manag.* **2023**, *43*, 1–26. [CrossRef]
20. Liu, Y.; Wang, X.; Yang, Y.D. The impact of strategic knowledge disclosure on enterprise innovation performance. *Manag. Decis. Econ.* **2023**, *44*, 2582–2592. [CrossRef]
21. Luo, Y.D.; Zahira, S.A. Industry 4.0 in international business research. *J. Int. Bus. Stud.* **2023**, *54*, 403–417. [CrossRef]
22. Pech, M.; Vanecek, D. Barriers of new technology introduction and disadvantages of industry 4.0 for industrial enterprises. *Serbian J. Manag.* **2022**, *17*, 197–206. [CrossRef]

23. Ghobakhloo, M.; Vilkas, M.; Stefanini, A.; Grybauskas, A.; Marcinkevicius, G.; Petraite, M.; Sarvari, P.A. Developing capabilities underlying to Industry 4.0 design principles within the manufacturing context. *J. Manuf. Technol. Manag.* **2023**, *34*, 1183–1207. [CrossRef]
24. Alsaadi, N. Modeling and Analysis of Industry 4.0 Adoption Challenges in the Manufacturing Industry. *Processes* **2022**, *10*, 2150. [CrossRef]
25. Salunkhe, O.; Berglund, A.F. Industry 4.0 enabling technologies for increasing operational flexibility in final assembly. *Int. J. Ind. Eng. Manag.* **2022**, *13*, 38–48. [CrossRef]
26. Rosario At Dias, J.C. Industry 4.0 and Marketing: Towards an Integrated Future Research Agenda. *J. Sens. Actuator Netw.* **2022**, *11*, 30. [CrossRef]
27. Ulewicz, R.; Czerwińska, K.; Pacana, A. A rank model of casting non-conformity detection methods in the context of Industry 4.0. *Materials* **2023**, *16*, 723. [CrossRef] [PubMed]
28. Jamwal, A.; Agrawal r Sharma, M.; Giallanza, A. Industry 4.0 Technologies for Manufacturing Sustainability: A Systematic Review and Future Research Directions. *Appl. Sci.* **2021**, *11*, 5725. [CrossRef]
29. Campos, T.L.R.; Nunhes, T.V.; Harney, B.; de Oliveira, O.J. Corporate sustainability in entrepreneurial settings: Green management and operational fairness as joint drivers of venture competitiveness. *J. Small Bus. Enterp. Dev.* **2023**, *30*, 342–368. [CrossRef]
30. Miskiewicz, R.; Wolniak, R. Practical application of the industry 4.0 concept in a steel company. *Sustainability* **2020**, *12*, 5776. [CrossRef]
31. Hong, P.; Jagani, S.; Pham, P.; Jung, E. Globalization orientation, business practices and performance outcomes: An empirical investigation of B2B manufacturing firms. *J. Bus. Ind. Mark.* **2023**, *38*, 2259–2274. [CrossRef]
32. Shi, L.; Gao, S.; Xu, A.R.; Zheng, K.X.; Ji, Y.P.; Dong, X.L.; Xing, L.Z. Influence of Enterprise's Factor Inputs and Co-Opetition Relationships to Its Innovation Output. *Sustainability* **2023**, *15*, 838. [CrossRef]
33. Brilinger, A.S.; Els, C.; Schafer, B.; Bender, B. Business model risk and uncertainty factors: Toward building and maintaining profitable and sustainable business models. *Bus. Horiz.* **2020**, *63*, 121–130. [CrossRef]
34. Ginevicius, R.; Gedvilaite, D.; Stasiukynas, A.; Suhajda, K. Complex Expert Assessment of the State of Business Enterprises. *Acta Polytech. Hung.* **2020**, *19*, 135–150. [CrossRef]
35. Datsenko, G.; Kotseruba, N.; Krupelnytska, I.; Kudyrko, O.; Lobacheva, I.; Otkalenko, O. Analytical Toolkit in Terms of Increasing Competitiveness Under Unstable Economic Conditions. *Financ. Credit. Act.—Probl. Theory Pract.* **2022**, *3*, 216–223. [CrossRef]
36. Hrosul, V.; Zubkov, S.; Mkrtchyan, T. The Development Core of Enterprise: Theoretical Aspect. *Balt. J. Econ. Stud.* **2021**, *7*, 73–81. [CrossRef]
37. Li, Z.G.; Lou, W.F.; Li, Y.S. Evaluation of Advantageous Resources in Enterprise Based on Rough Set Theory. In *Comprehensive Evaluation of Economy and Society with Statistical Science*; Aussino Academic Publishing House: Sydney, Australia, 2010; pp. 153–157.
38. Schaefer, J.L.; Tardio, P.R.; Barierle, I.C.; Nara, E.O.B. GIANN-A Methodology for Optimizing Competitiveness Performance Assessment Models for Small and Medium-Sized Enterprises. *Adm. Sci.* **2023**, *13*, 56. [CrossRef]
39. Ejaz, M.R. Smart Manufacturing as a Management Strategy to Achieve Sustainable Competitiveness. *J. Knowl. Econ.* **2023**. [CrossRef]
40. Parast, M.M.; Safari, A. Enhancing the quality and competitiveness of small businesses: A pooled cross-sectional analysis. *Int. J. Prod. Econ.* **2022**, *246*, 108410. [CrossRef]
41. Anawade, P.A.; Sharma, D.S. The Influence of Marketing Strategy on Business Results: An Empirical Study for Selected Small and Medium Enterprises (SMEs) of Nashik Municipal Corporation (NMC). *Int. J. Early Child. Spec. Educ.* **2022**, *14*, 5764–5769. [CrossRef]
42. Rajesh, R. An introduction to grey influence analysis (GINA): Applications to causal modelling in marketing and supply chain research. *Expert Syst. Appl.* **2022**, *212*, 118816. [CrossRef]
43. Lin, S.; Xu, S.Y.; Liu, Y.; Zhang, L.Y. Destination brand experience, brand positioning, and intention to visit: A multi-destination comparison study. *J. Vacat. Mark.* **2023**. [CrossRef]
44. Matthe, M.; Ringel, D.M.; Skiera, B. Mapping Market Structure Evolution. *Mark. Sci.* **2022**, *42*, 589–613. [CrossRef]
45. Fluhrer, P.; Brahm, T. Positioning in SMEs: Entrepreneurs' perceptions and strategies. *J. Res. Mark. Entrep.* **2023**, *25*, 431–454. [CrossRef]
46. Hong, R.Y.; Zhang, Z.; Zhang, C.; Hu, Z.H. Is brand globalness compatible with brand country-of-origin? An investigation of hybrid brand positioning strategies for emerging market brands. *Int. Mark. Rev.* **2022**, *40*, 49–79. [CrossRef]
47. Nelke, M. *Strategic Business Development for Information Centres and Libraries*; Chandos Information Professional Series; Chandos Publishing: Witney, UK, 2010; pp. 89–103.
48. Jung, K.; Morris, K.C.; Lyons, K.W.; Leong, S.; Cho, H. Mapping Strategic Goals and Operational Performance Metrics for Smart Manufacturing Systems. *Procedia Comput. Sci.* **2015**, *44*, 184–193. [CrossRef]
49. Delzenne, N.; Deuts Ne Lobo, D.N.; Grimble, G. Presentation and publication skills: How to develop a protocol and write a grant. *Clin. Nutr.* **2023**, *57*, 73–76. [CrossRef] [PubMed]
50. Schimpf, C.; Castellani, B. Approachable modeling and smart methods: A new methods field of study. *Int. J. Soc. Res. Methodol.* **2022**, *27*, 1–15. [CrossRef]
51. Borkowski, S. *Toyotaryzm, Wyniki Badań BOST*; Wydawnictwo, PTM: Warszawa, Poland, 2012.

52. Vanichchinchai, A. The effects of the Toyota Way on agile manufacturing: An empirical analysis. *J. Manuf. Technol. Manag.* **2022**, *33*, 1450–1472. [CrossRef]
53. Black, J.T. Design rules for implementing the Toyota Production System. *Int. J. Prod. Res.* **2007**, *45*, 3639–3664. [CrossRef]
54. Pacana, A.; Siwiec, D. Universal Model to Support the Quality Improvement of Industrial Products. *Materials* **2021**, *14*, 7872. [CrossRef] [PubMed]
55. Lowe, P. *Management of Technology: Perception and Opportunities*; Chapman & Hall: London, UK, 1995.
56. Borkowski, S.; Ingaldi, M.; Jagusiak-Kocik, M. The use of 3 × 3 matrix to evaluate a manufacturing technology of chosen metal company. *Manag. Syst. Prod. Eng.* **2014**, *15*, 121–125. [CrossRef]
57. Klimecka-Tatar, D.; Ingaldi, M. Assessment of the Technological Position of a Selected Enterprise in the Metallurgical Industry. *Mater. Res. Proc.* **2020**, *17*, 72–78. [CrossRef]
58. Ingaldi, M. Use of the SWOT ANALYSIS and 3 × 3 matrix to determine the technological posistion of the chosen metal company. *Acta Metall. Slovaca—Conf.* **2014**, *4*, 207–214. [CrossRef]
59. Altunkaynak, B.; Gamgam, H. Bootstrap confidence intervals for the coefficient of quartile variation. *Commun. Stat.-Simul. Comput.* **2019**, *48*, 2138–2146. [CrossRef]
60. Jalilibal, Z.; Amiri, A.; Castagliola, P.; Khoo, M.B.C. Monitoring the coefficient of variation: A literature review. *Comput. Ind. Eng.* **2021**, *161*, 107600. [CrossRef]

processes

MDPI

Article

Optimizing Production Schedules: Balancing Worker Cooperation and Learning Dynamics in Seru Systems

Weiguo Liu *, Weizhe Dai and Xuyin Wang

Business School, Northwest Normal University, Lanzhou 730070, China; daiwz001025@163.com (W.D.); humorgirlwxy@nwnu.edu.cn (X.W.)
* Correspondence: winterplum.home@nwnu.edu.cn

Abstract: This paper aims to investigate the seru scheduling problem while considering the dual effects of worker cooperation and learning behavior to minimize the makespan and order processing time. Given the complexity of this research problem, an improved shuffled frog leaping algorithm based on a genetic algorithm is proposed. We design a double-layer encoding based on the problem, introduce a single point and uniform crossover operator, and select the crossover method in probability form to complete the evolution of the meme group. To avoid damaging grouping information, the individual encoding structure is transformed into unit form. Finally, numerical experiments were conducted using numerical examples of large and small sizes for verification. The experimental results demonstrate the feasibility of the proposed model and algorithm, as well as the necessity of considering worker dual behavior in the seru scheduling problem.

Keywords: seru scheduling; worker cooperation; learning effects; shuffled frog leaping algorithm

1. Introduction

To efficiently and flexibly respond to the market and meet the diverse needs of consumers, the seru system has emerged. The seru system is an outcome produced by transforming the traditional assembly line disassembly, efficiently combining efficiency and flexibility [1,2]. It is known as the "ecological and economic" manufacturing model in the Japanese manufacturing industry [3]. After the application of seru systems by manufacturing companies such as Canon, Sony, and Panasonic, it has been found that seru systems also possess advantages such as reduced production costs, decreased production time, and minimal energy consumption [4–8]. Therefore, the seru system is deemed one of the most promising production methods in the era of Industry 4.0.

The current research on seru systems mainly focuses on seru construction and seru scheduling. Seru scheduling relies on the seru construction process to determine the order allocation and processing order of each seru unit. Additionally, seru scheduling is the key to reflecting the efficiency and flexibility of seru systems, and whether the advantages of seru systems can be fully utilized mainly depends on the core step of seru scheduling. In terms of seru scheduling, Zhan et al. [9] proposed the GP-SS scheduling rule to address the seru scheduling problem with resource conflicts. Jiang et al. [10] transformed the seru scheduling problem into an assignment problem. Li et al. [11] studied the on-line seru scheduling problem while considering resource conflicts. Wu et al. [12] devised a reinforcement learning-driven two-stage evolutionary algorithm to address the scheduling problem of a hybrid seru system considering worker transfer. Lian et al. [13] solved the energy-saving scheduling problem by considering seru reconfiguration. Zhang et al. [14] used the branch and bound algorithm to solve the seru scheduling problem. Shen et al. [15] designed a hybrid GA-PSO algorithm to solve the seru scheduling problem that considered worker learning effects and dynamic resource allocation. Zhang et al. [16–18] constructed scenarios for different seru scheduling problems that considered worker learning behavior

and demonstrated that considering worker learning behavior can help improve seru system performance. Jiang et al. [19] found that as the learning effect of workers increases, the production cost of the seru system will decrease. Based on the aforementioned research findings, the seru scheduling problem has been extensively explored from various angles and has achieved significant progress. However, due to the difficulty in measuring worker cooperation and learning behavior, few research studies on seru scheduling simultaneously considered worker dual behavior. The seru system is centered around workers, and the two most prominent behaviors are worker cooperation and learning behavior. Its production efficiency and performance largely depend on the workers' abilities and personal behavior. Therefore, how to effectively leverage the dual behavioral effects of workers to optimize the performance of the seru system is a crucial issue that needs to be addressed urgently.

In the production workshop, when workers repeatedly operate the same process or task, there will be a learning effect [20–22]. The learning effect refers to the phenomenon where the processing time of a single product decreases with the increase in cumulative production volume [23]. At the theoretical level, Wright [24] proposed the learning effect curve for the first time in the aviation manufacturing industry. Subsequently, learning effect models, such as the S-curve [25], Stanford-B [26], Dejong [27], and Plateau [28], were proposed based on different research scenarios. At the application level, Zhang et al. [29] considered learning effects in constructing problem scenarios in hybrid flow shop scheduling. Hu et al. [30] constructed a single-process workshop scenario that considers learning effects. Wang et al. [31] studied the joint decision-making problem of unit manufacturing systems considering learning and forgetting effects. Learning behavior is a common phenomenon in production and manufacturing, and constructing scenarios that consider learning behavior can shorten the gap between theory and practice, which is beneficial for enterprises to make low-cost and efficient production decisions. Due to human social needs, cooperative behavior may occur among workers. Good cooperative behavior can improve the work efficiency of workers; on the contrary, work efficiency will decrease [5,32,33]. In the current study, Sakamaki [32], Cao et al. [34], and Wang et al. [33] all proved that considering worker cooperation behavior in production scheduling can help improve production efficiency. It can be seen that worker behavior is a realistic influencing factor that cannot be ignored in production scheduling.

When solving the seru scheduling problem, scholars mainly relied on improved genetic algorithms [35–39] to solve problems and have achieved certain results, but the optimization algorithm has the limitation of the solving scale and the shortage of solving quality. Therefore, this paper intends to utilize the shuffled frog leaping algorithm, which has a simple idea, fewer experimental parameters, and strong global optimization ability, to solve the problem. The shuffled frog leaping algorithm combines the advantages of the Memetic algorithm and particle swarm optimization algorithm, with a strong global search ability. Some scholars have applied it to the field of production scheduling. Moreover, the hybrid leapfrog algorithm has not yet been applied in the research of seru production systems, so it is necessary to explore the application of the hybrid leapfrog algorithm to solve seru systems, which is a further expansion of the research field of seru production systems. Drawing from the preceding analysis, this paper will explore the seru scheduling problem while considering the dual behavior of workers. The objective is to minimize both the makespan and order processing time. The improved hybrid leapfrog algorithm serves as a breakthrough. The ultimate goal is to enhance the efficiency of the seru system, propose reasonable and effective worker and order-allocation plans, and provide managers with a theoretical basis and technical support for making informed scheduling decisions.

2. Problem Description

This article adopts a segmented seru as the basic unit, which is the corresponding process assembly assigned by workers within the unit. Within a seru unit, the assembly of a product is jointly completed by multiple workers. This article focuses on three subproblems: seru-worker, seru-order, and order-worker allocation. Assuming a seru system

that produces C product types, W versatile workers are allocated to N seru units for I order production. Producing each product requires k processes, each corresponding to a skill. Because workers are multi-skilled, there are multiple matching relationships between workers and processes. In the seru unit, a worker can be responsible for multiple processes of the product, which can be discontinuous, but the corresponding processing skills for the process need to be mastered by the worker.

Figure 1 describes the problem studied in this paper. In the figure, there are six processes, three orders, two products, and five workers to build two seru units. Taking seru1 as an example, if the distribution order is i_1 and i_3, and the product c_1 is produced, the corresponding operation set is $u_1 = (k_1, k_2, k_4, k_5)$, of which worker w_1 is responsible for operations k_1 and k_2, and worker w_5 is responsible for operations k_4 and k_5.

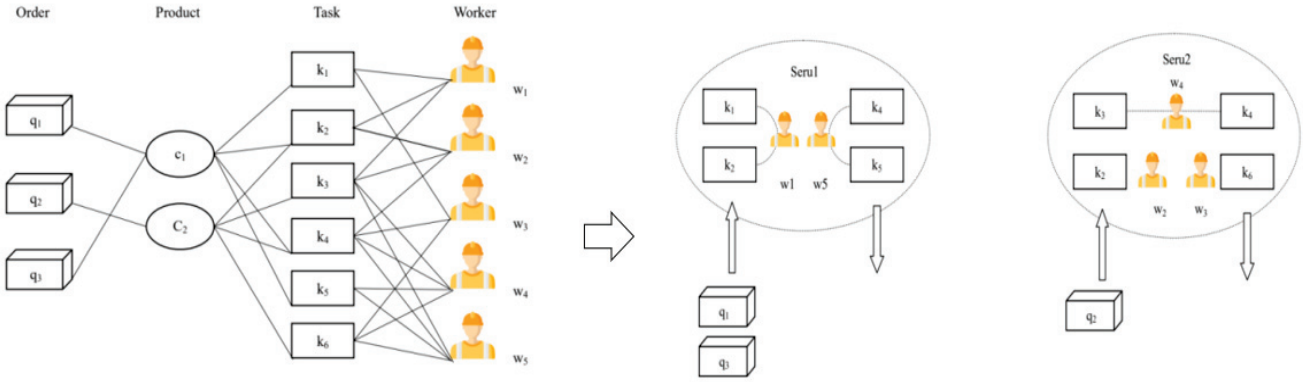

Figure 1. Problem description under seru production system.

3. Model Formulation

3.1. Model Assumptions

The research questions in this article include the following assumptions:

(1) The type and quantity of products in the order are known.
(2) Batch splitting is not considered, which means each order can only be produced within one seru unit.
(3) Each order encompasses only one type of product.
(4) The processing time of each task in each product is known and constant.
(5) The number of workers is constant.
(6) The worker movements between serus do not exist.

3.2. Modeling

This paper takes the model proposed by Wang et al. [33] as a reference, considering the influencing parameters of worker learning behavior effects, and modifies the model based on segmented units. According to the DeJong learning effect model and the characteristics of segmented units, it is necessary to calculate the cumulative number of products completed by each order worker before starting processing, as well as the cumulative number of products completed after this order is completed. This can be recorded as the upper and lower limits of the q variable cumulative completed products in the learning effect. The specific calculation formula is shown in Equations (1) and (2).

$$Q_{ijw}^{ub} = \begin{cases} Q_{jw} & , k = 1 \\ \sum_{r=1}^{j} \sum_{k=1}^{K} X_{irk} Q_{rw} C_{rp} \, C_{jp} & , k \neq 1 \end{cases} \quad (1)$$

$$Q_{ijw}^{lb} = \begin{cases} 1 & , k = 1 \\ \sum_{r=1}^{j-1} \sum_{k=2}^{K} Q_{rw} X_{ir(k-1)} X_{ijk} C_{rp} \, C_{jp} + 1 & , k \neq 1 \end{cases} \quad (2)$$

In the segmented seru unit, the cooperative behavior between workers is mainly the cooperation between workers and their left and right workers. Due to the coefficient of cooperative behavior, a_{wu} is inversely proportional to the processing time; that is, the higher the cooperation coefficient, the shorter the processing time. Based on this, $1 - a_{wu}$ can directly represent the impact on processing time. For the overall cooperation coefficient of workers, see Equation (3).

$$a_w = (1 - a_{wu})(1 - a_{pw})Y_{wi}Y_{ui}Y_{pi} \tag{3}$$

The quantity of products completed by worker w is shown in Equation (4)

$$Q_{jw} = \sum_{i=1}^{I} Y_{wi}R_{ij}S_j \tag{4}$$

Considering the factors influencing worker cooperation and learning behavior, the total processing time for worker w to complete process s of order j is shown in Equation (5).

$$T_{jw}^{s} = \sum_{q=Q_{ijw}^{lb}}^{Q_{ijw}^{ub}} T_p^s a_w \left(M + (1 - M)q^b\right) \tag{5}$$

The model in this article aims to minimize the maximum completion time and minimize the order processing time. The specific model construction is as follows:

$$f_1 = min\ makespan = min\left\{max_{\{j\in\{1,2,\ldots J\}\}}(FCB_j + ST_j + FC_j)\right\} \tag{6}$$

$$f_2 = min\sum_{j=1}^{J}\sum_{w=1}^{W}\left(\sum_{i=1}^{I}\sum_{k=1}^{K} FC_j Y_{wi}X_{ijk}\right) \tag{7}$$

s.t.

$$\sum_{i=1}^{I} Y_{wi} = 1\ , \mathrm{w} = 1, 2, \ldots, \mathrm{W} \tag{8}$$

$$W_{min} \le \sum_{w=1}^{W} Y_{wi} \le W_{max}\ , i = 1, 2, ..., I \tag{9}$$

$$\sum_{i=1}^{I} R_{ij} = 1, j = 1, 2, \ldots, J \tag{10}$$

$$FC_j = \frac{\sum_{i=1}^{I} X_{ijk}\sum_{w=1}^{W} Y_{wi}\sum_{p=1}^{P} U_{wp}C_{jp}\sum_{s=1}^{S} T_{jw}^{s}}{\sum_{i=1}^{I}\sum_{w=1}^{W} Y_{wi}R_{ij}} \tag{11}$$

$$ST_j = \sum_{r=1}^{J}\sum_{p=1}^{P} X_{ir(k-1)}Z_pC_{jp}(1 - C_{rp})\ , if\ k \ne 1, r \ne j, X_{ijk} = 1 \tag{12}$$

$$FCB_j = \sum_{r=1}^{j-1}\sum_{i=1}^{I}\sum_{k=1}^{j}(FC_r + ST_r)X_{ijk}X_{ir(k-1)} \tag{13}$$

$$\sum_{j=1}^{J}\sum_{k=1}^{K} X_{ijk}FC_j < T_i\ , i = 1, 2, ..., I \tag{14}$$

$$C_j = FC_j + ST_j + FCB_j < D_j \tag{15}$$

$$X_{ijk}\ , Y_{wi} \in \{0, 1\}$$

$$S_j \in Z\ , \forall i \tag{16}$$

$$-1 \le b \le 0\ , 0 \le M \le 1$$

where Equations (6) and (7) are objective functions that represent the minimizing makespan and order processing time, respectively. Equation (8) ensures that each worker can only work within one seru unit. Equation (9) represents the number of workers within each seru unit. Equation (10) indicates that each order can only be assigned to one seru unit without considering order splitting. Equation (11) represents the processing time of all products in seru i for order j. Equation (12) represents the preparation time of order j in seru i. Equation (13) represents the start time of order j in seru i. Equation (14) limits the processing time of all orders in seru i to be less than the available production time of

seru i. Equation (15) indicates that order j must be completed within the delivery date. Equation (16) represents other logical constraints in this model.

4. Improved Shuffled Frog Leaping Algorithm (SFLA)

The SFLA is a meta-heuristic algorithm that mimics the communication and cooperation among frogs during their foraging process [40]. It mainly includes four basic operations: population initialization, meme group partitioning, meme group evolution, and meme group reconstruction [41,42]. This paper proposes refinements to the hybrid leapfrog algorithm based on the characteristics of the research problem. The main contribution or improvement ideas are as follows: firstly, due to the multi-objective optimization problem in this study, there are Pareto optimality and non-dominated frontier solution sets, and the method of using a single objective function to evaluate the fitness of individuals is no longer applicable. To avoid subjective factors, this article introduces non-dominated sorting and crowding distance in the NSGA-II algorithm to evaluate individual strengths and weaknesses. Secondly, using non-dominated level grouping as the grouping result of the meme group, in order to improve the convergence speed of the algorithm, the optimal individuals from non-dominated levels are selected to form the optimal group. During the evolution process of the meme group, cross-operations are performed within the optimal group, which can better transmit optimal information. Thirdly, we introduce the single point crossover and uniform crossover operators in genetic algorithms, comprehensively utilize the advantages of the two operators, and randomly select crossover operations in the form of probability to increase population diversity.

4.1. Encoding Method

When encoding the order-scheduling problem in the seru production system, it is necessary to consider three sub-problems: worker-seru, order-seru, and order-worker. In the first two sub-problems, both workers and orders are the result of allocation in the seru unit. Due to the common feature of the seru unit, this paper proposes a double-layer gene-coding approach. The first layer of coding consists of $W + I$ gene loci, including the allocation results of two sub-problems: the first part consists of W gene loci, representing the allocation results of worker-seru; the second part consists of I gene loci, representing the allocation results of order-seru. The numbers on the first gene locus are all seru numbers. The second layer of coding represents the result of order-worker allocation. As the result of order-worker allocation is influenced by the results of the first two sub-problems, each order is considered as a unit, and the number of operations in the order is the number of gene bits under that order. Regarding the gene bits, the corresponding processing workers for that operation are represented. For example, the coding example in Figure 2 is a seru system consisting of 4 seru units, 12 workers, and 8 orders. In the first layer, the first 12 loci represent worker seru allocation, while the last 8 loci represent order seru allocation; the second layer is the worker corresponding to the process in the order. In the seru 1 unit, workers w_2, w_9, and w_{12} work together to complete production orders j_1 and j_5. In order 1, w_2 is responsible for processing J_{11} and J_{15}, w_9 is responsible for processing J_{12} and J_{14}, w_{12} is responsible for processing J_{13}, and other orders are assigned similarly.

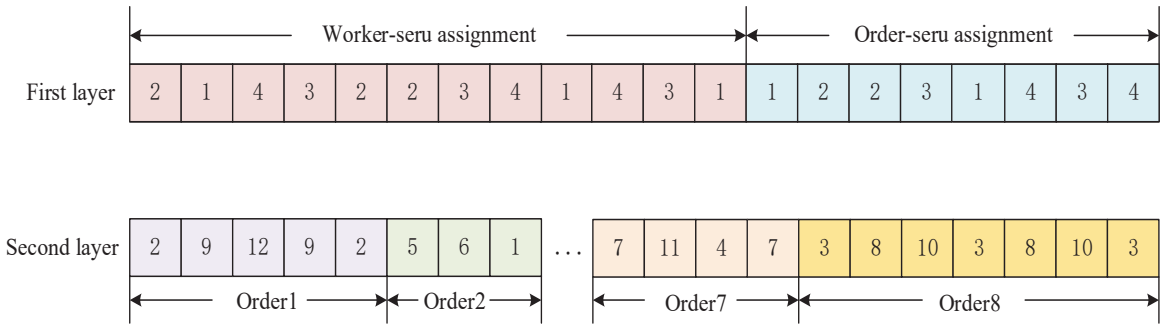

Figure 2. Encoding example diagram.

4.2. Population Initialization

Generate an initial population F consisting of N frogs in the feasible domain. Ensure that all solutions corresponding to frogs meet the coding requirements and are feasible solutions for the optimization problems. Specifically, for randomly generated frog individuals, the first layer of genes corresponds to the two parts of seru-worker and seru-order allocation. Adjust the random allocation results according to the constraints in the model. The second layer of gene coding is determined by the first layer of gene coding. The assigned order and corresponding worker must be in the same seru unit, and the worker must have the ability to process the process. Therefore, it is feasible to randomly produce initialized frog population individuals.

4.3. Division of Meme Groups

Divide the frog population into different meme groups based on non-dominated sorting and crowding distance at each level. Non-dominated sorting compares the corresponding function values of two individuals. If both objective function values of Frog 1 are better than Frog 2, it is considered that Frog 1 dominates Frog 2; if Frog 1 has an objective function value that is better than Frog 2 and another equal objective value, it is considered that Frog 1 dominates Frog 2. Count the number of non-dominated levels, denoted as Y_n. Memetic group division refers to the grouping of non-dominated levels.

4.4. Memetic Evolution

For better meme evolution, select the optimal individuals from different meme groups to form a group so that frog individuals can quickly transmit optimal information. This article uses a crossover operator to update individuals within the meme group. The crossover operation only applies to the first layer of genes, while the second layer of genes is determined based on the first layer of genes. In the improved shuffled frog leaping algorithm, each meme group has one frog with the best position and the worst position, which is the best position among all frogs. Here, the best frog individual in the group is the same as the best frog individual in the population.

During the first evolution of the meme group, a crossover operation is performed on F_b and F_w to generate a new solution. If the generated new solution is better than F_w, it is replaced. If the effect is not good, a secondary adjustment is made. The second adjustment is to randomly generate a new individual F_g to replace it. When making alternative comparisons, the fitness used in this article is the solution corresponding to the objective function one, as the solution corresponding to the objective function one is the maximum completion time of the seru production system, which better indicates the rationality of the scheduling plan.

Before performing the crossover operation, use Figure 3 to change the first-layer structure of the individual and transform it into a unit-combination form. The reason for the transformation form is, firstly, it can avoid cross operation from damaging grouping information; secondly, during the crossover process, this approach can better preserve some excellent genes of the parents; thirdly, the individual gene loci in the first layer are too

long. After transforming the form, each seru unit is treated as a whole for cross-operation, which shortens the length of individual genes in the form and can improve the algorithm's solving speed.

For the seru-worker section, this article adopts a single-point crossover operation, which is simple and easy to implement and can compensate for the slow speed of uniform crossover optimization. On two parent genes, each seru unit is treated as a single gene point, and gene points are randomly selected for crossover. The crossover operation involves all genes after that gene point. In the newly generated offspring genes, since the evolution of the meme group mainly involves updating the worst frog, during the single-point crossover operation, the right gene of the worst frog was replaced with the right gene of the best frog. In order to retain some of the genes in the optimal solution, the left gene in the duplicate gene was deleted. For missing gene loci, compensate for the missing genes in the worker coding order. The single-point crossover operation is shown in Figure 4.

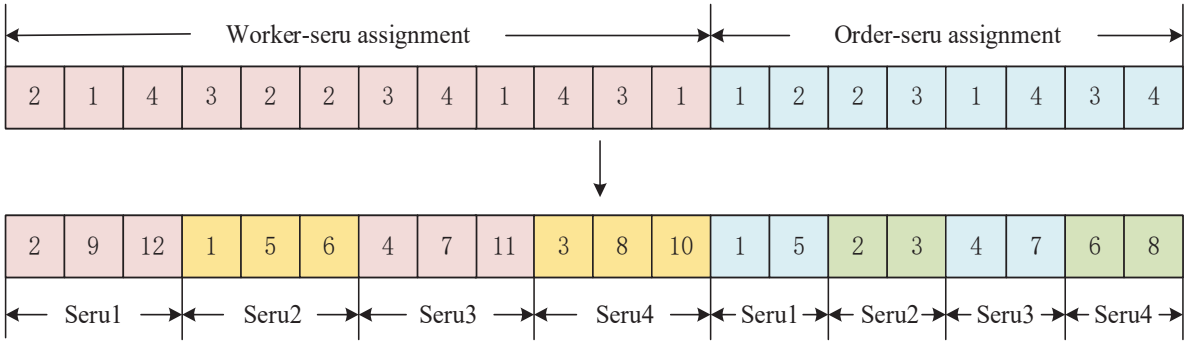

Figure 3. Individual first-layer gene transformation.

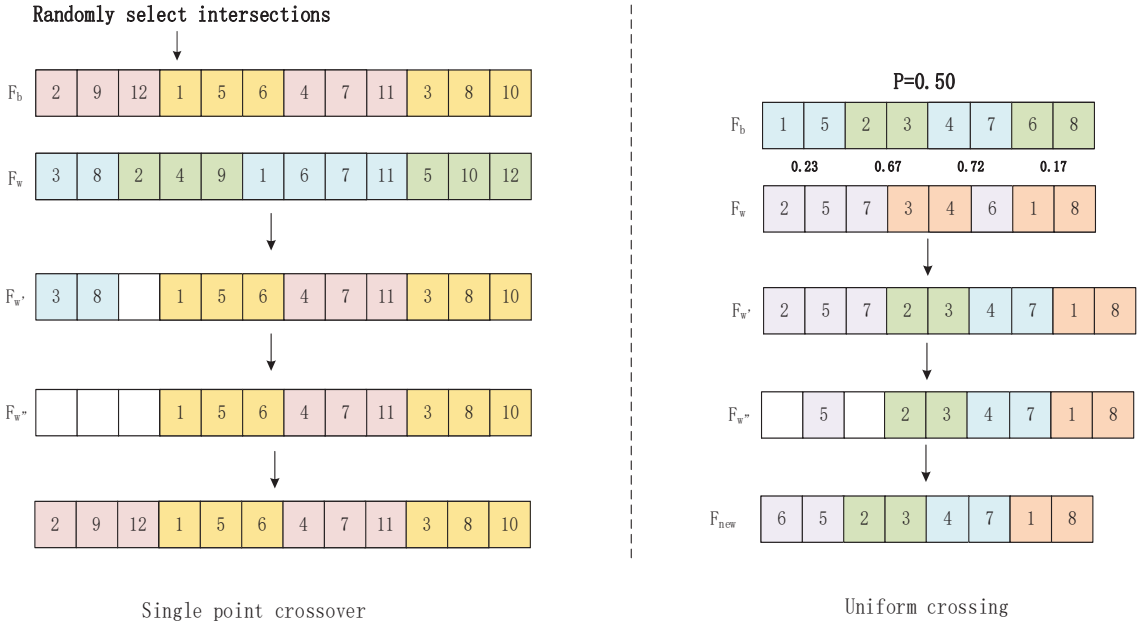

Figure 4. Cross-operation.

For the seru-order section, this article adopts the uniform crossover operation, which can compensate for the situation where a single point cross is prone to falling into local optima and increasing the diversity of the population. On two parent genes, treat each seru unit as a single gene point as a whole. For each gene point of the optimal frog individual in the parent generation, U_k is randomly generated to represent its selection probability, where $U_k \in (0, 1)$. The gene points on the parent gene are exchanged with a probability of $P = 0.5$. When the probability of corresponding gene points on the parent gene is $U_k > P$, a

gene-crossover operation is performed; otherwise, no crossover operation is performed. In the process of uniform crossover, the probability of gene points is compared in order from left to right, and the operations for repeated and missing values are the same as those in the single-point crossover. The uniform crossover operation is shown in Figure 4.

To comprehensively utilize the advantages of the two operators and randomly select crossover operations in the form of probability, the single-point crossover operation of the worker-seru part and the uniform crossover operation of the order-seru part are both carried out with a 50% probability; that is, if the random selection probability $P > 50\%$, the seru-worker part of the crossover operation will be carried out, and the seru-order part will be adjusted accordingly; if $P \leq 50\%$, proceed with the cross-operation of the seru-order section. The portion of the second gene worker order is adjusted according to changes in the first gene. The specific steps are as follows:

Step 1: Determine the optimal frog F_b and worst frog F_w in the meme group.

Step 2: Take probability P and perform single-point crossing ($P > 50\%$) or uniform crossing operation ($P \leq 50\%$) on F_b and F_w to obtain F_{new1}.

Step 3: Compare the fitness values of F_{new1} and F_w. If the fitness of F_{new1} is better than that of F_w, replace F_w with F_{new1}; otherwise, proceed to step 4.

Step 4: Randomly select another frog in the group to replace F_w.

Step 5: After updating the position of the worst frog, upgrade the cultural genome and re-rank the fitness. If the maximum number of evolutions has not been reached, return to step 1 to continue the local search until the maximum number of evolutions in the meme group is reached, ending the local search.

4.5. Algorithm Flow

The improved shuffled frog leaping algorithm proposed in this article uses non-dominated sorting and crowding distance in NSGA-II to evaluate the superiority and inferiority of individuals. To improve the convergence speed of the algorithm, the optimal individuals from each non-dominated level are selected to form a group and complete the evolution of the meme group. In the process of meme evolution, using crossover operators to update frog individuals can improve population diversity. The combination of single-point crossover and uniform crossover for meme evolution can further improve the convergence speed of the algorithm, effectively avoid reducing local optimal solutions, and improve the breadth and depth of the search. The detailed steps of SFLA are as follows:

Step 1: Frog population initialization. Randomly generate a population of S with N frogs.

Step 2: Frog population sorting. Sort the frog individuals in the population using non-dominated sorting and crowding distance, and record the frog F_g with the best fitness in population S.

Step 3: Meme grouping. The grouping of individual frogs is equivalent to a non-dominated ranking hierarchy, and the optimal solutions from each hierarchy are selected to form a meme group.

Step 4: Meme evolution. Independently perform meme evolution on the meme group and update the worst frog in the group.

Step 5: Meme group reconstruction. Mixed cultural genomes: after completing a local search in each meme group, reassemble population S to complete communication and communication between frogs, reorder according to step 2, update the optimal frog in each meme group, and record the frog F_g with the best fitness in population S.

Step 6: If the maximum evolution number (Gen) or convergence condition of the entire population has not been reached, return to step 3 to continue. Otherwise, stop the algorithm iteration and output the global optimal value.

The basic process of the improved shuffled frog leaping algorithm in this article is shown in Figure 5.

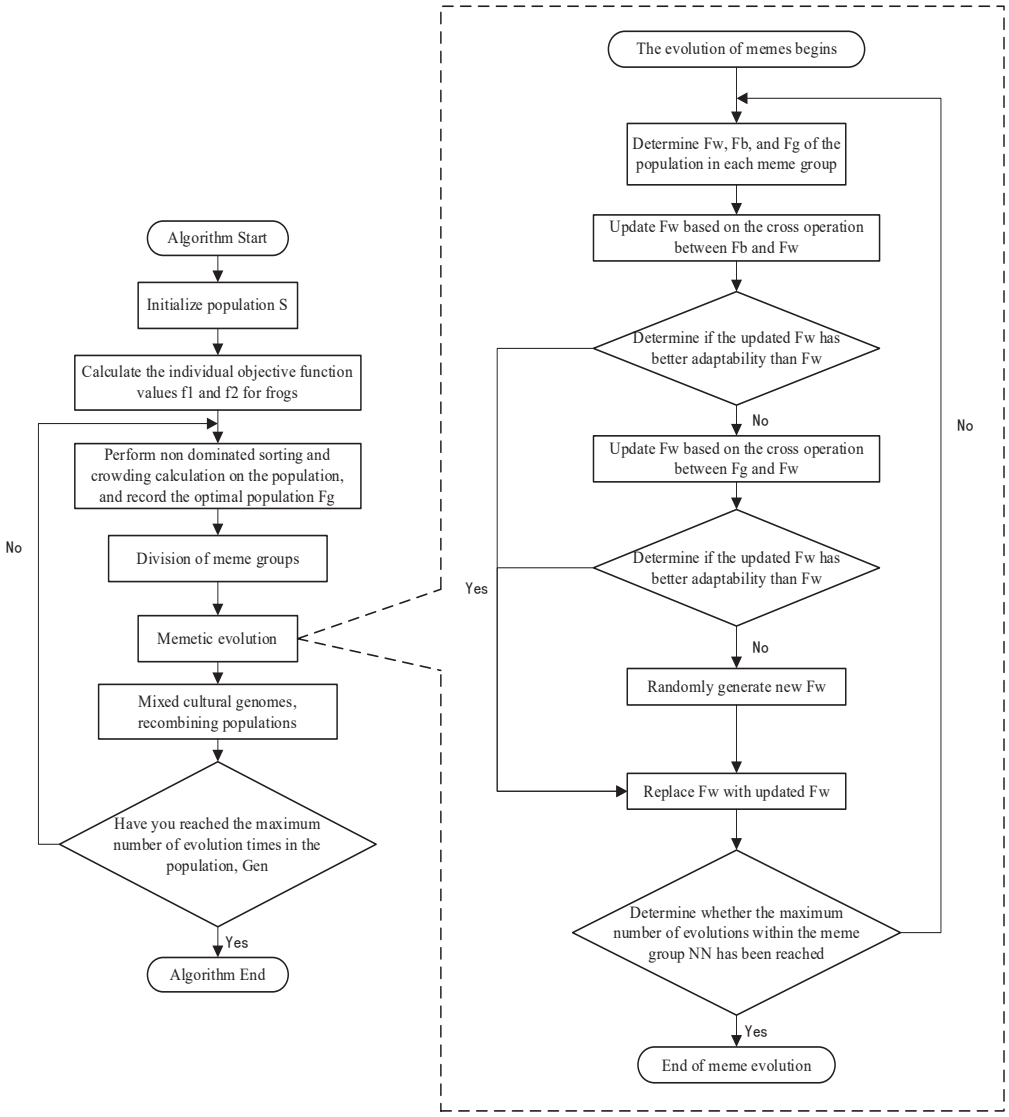

Figure 5. Flow diagram of improved SFLA.

5. Numerical Tests

To verify the rationality and applicability of the improved hybrid leapfrog algorithm designed in this article in solving the order-scheduling problem considering worker cooperation and learning effects in the seru production environment, MATLAB R2022a software was used to conduct experimental simulation verification on large-scale and small-scale examples.

The parameters set in Table 1 are for using the improved hybrid leapfrog algorithm to solve specific examples in this article. The experimental parameter settings of the size calculation examples in this article refer to the experimental settings of Lian et al.'s [1] calculation examples, and adjustments have been made based on this. In the production process of seru, due to different product types, the corresponding processes and standard processing times of the products may vary. The specific processes and standard processing times of the products are shown in Table 2. The specific processing skills of workers are shown in Table 3.

Small scale examples: Assuming there are 4 seru units and 12 workers in the production workshop, and 10 orders have arrived, order scheduling and allocation are required. The basic information on the orders is shown in Table 4. This article allocates orders based on the size of their delivery dates. The order of order allocation is Order 6, Order 1, Order 5, Order 7, Order 9, Order 4, Order 10, Order 2, Order 8, and Order 3.

Table 1. Example parameters.

Systemic Factors	Parameter Value
pop_size	100
m_frog	20
n_frog	5
Gen	50
a_{wu}	N(0, 0.01)
M	U(0, 1)
b	U(−1, 0)
worker_lowlim	2
worker_uplim	5
T_seru	2400

Table 2. Standard processing time for the corresponding process of the product.

	S1	S2	S3	S4	S5	S6	S7	S8
P1	2.92	2.79	3.36	-	3.72	2.94	3.12	3.08
P2	-	2.79	3.36	3.40	3.72	-	3.12	3.08
P3	2.92	2.79	3.36	3.40	3.72	2.94	3.12	3.08

Note: "-" indicates that the product does not require this processing step.

Table 3. The corresponding process for workers' processing skills.

	S1	S2	S3	S4	S5	S6	S7	S8
W1	√	-	√	-	√	√	√	√
W2	-	√	√	√	√	√	-	√
W3	√	√	-	√	√	-	√	√
W4	-	√	√	√	√	-	√	√
W5	√	√	√	√	√	-	√	-
W6	-	√	√	-	√	√	√	√
W7	√	√	√	-	-	√	√	√
W8	-	√	√	√	√	-	√	√
W9	√	√	√	√	√	√	√	√
W10	-	√	√	√	√	-	√	√
W11	√	√	√	-	√	√	√	√
W12	-	√	√	√	√	-	√	√

Note: "√" indicates that the worker has mastered the skill, "-" Indicates that the worker does not master the skill.

Table 4. Example of order basic information.

Order Number	J1	J2	J3	J4	J5	J6	J7	J8	J9	J10
Product type	1	3	2	2	3	2	1	1	2	2
Order	32	16	17	28	17	35	35	33	19	31
Delivery date	750	1200	1800	900	780	550	850	1750	870	960
Setup time	3.4	2.7	3.1	3.1	2.7	3.1	3.4	3.4	3.1	3.1

To verify the necessity of considering the effects of worker cooperation and learning behavior when solving order-scheduling problems in this article, a comparative experiment was conducted.

Example experiment 1: Research the necessity of considering the effects of learning behavior. The indicators for considering learning behavior are selected with an incompressible factor of M = 0.79 and a learning index of b = −0.7. Other variables and parameters are controlled to be consistent with the control group. In the control group, worker cooperation and learning behavior were not considered. The seru order-scheduling problem with and without considering worker learning effects is solved separately, and the results are shown in Figure 6. From the results, it can be seen that under the premise of this article, the order-scheduling scheme considering worker-learning effects obtains better solutions for

the maximum completion time and total processing time of worker orders in the seru production system; that is, considering worker-learning effects in the seru scheduling scheme can obtain better allocation results.

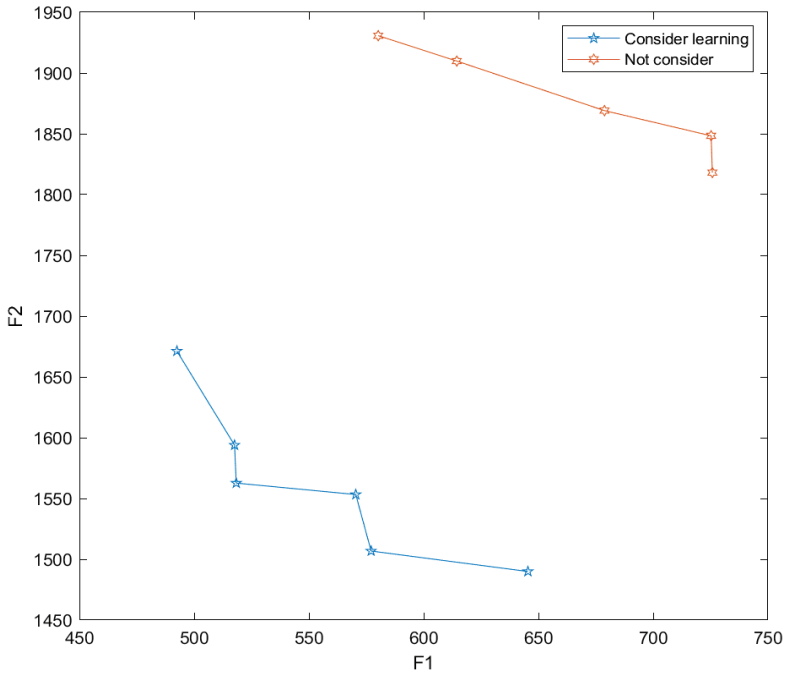

Figure 6. Comparison of results in example experiment 1.

When considering the learning effect of workers, this article adopts the DeJong learning effect model. In the DeJong learning effect model, changes in the incompressible factor M and learning index b will both affect the learning effect. To further explore the impact of worker learning effects on order scheduling, this article changes the incompressible factor and learning index that affect learning effects.

Example experiment 2: Changing the incompressibility factor and learning index. Selecting incompressible factors M with values of 0.79, 0.89, and 0.95, and controlling for the same other variables, the results obtained are shown in Figure 7. From the results of Figure 7, it can be seen that when the learning index remains unchanged and the incompressibility factor increases, the solutions obtained for both objective functions increase. The incompressible factor represents the impact of the automation level of the production line on the learning effect. A larger index indicates a greater degree of automation in the assembly line and a diminished learning ability of workers. This indicates that in the seru production system, an appropriate level of automation can improve the completion efficiency of orders. However, since the seru production system mainly relies on worker production, a higher level of automation is not conducive to the improvement in worker learning ability and affects the production time of orders. Selecting learning indices of -0.7, -0.8, and -0.9, controlling for the same other variables, the results are shown in Figure 8. From the results of Figure 8, it can be seen that when the control incompressibility factor remains constant and the learning index | b | is increased, the overall learning ability continues to increase, and the solutions obtained from the two objective functions tend toward the origin; that is, as the learning index | b | increases, the results become better. This further demonstrates the necessity of considering the worker-learning effect in order scheduling for a reasonable arrangement of order scheduling.

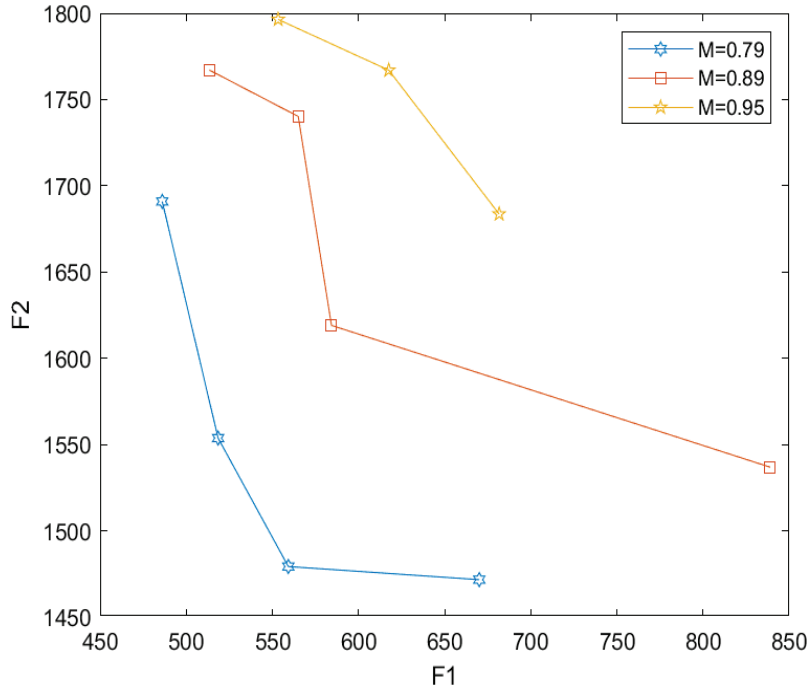

Figure 7. Comparison of results with different incompressibility factors in example experiment 2.

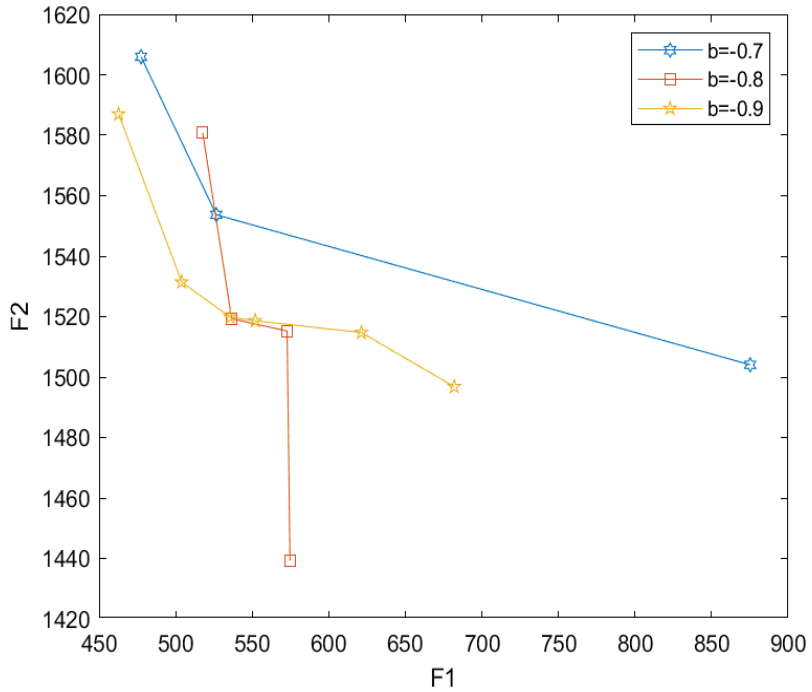

Figure 8. Comparison of results of different learning indices in example experiment 2.

Example experiment 3: Research on the necessity of considering the effects of worker cooperative behavior. The cooperation coefficient of randomly selected workers remains unchanged in the comparative experiment, and other variables and parameters are controlled to be consistent with the control group. In the control group, worker cooperation and learning behavior were not considered. The results are shown in Figure 9. In Figure 9, it can be seen that the order-scheduling scheme obtained by considering the cooperative behavior of workers has a better solution for the objective function of maximum completion time and total order processing time. Therefore, considering the cooperative behavior of workers is beneficial for the allocation of seru order scheduling.

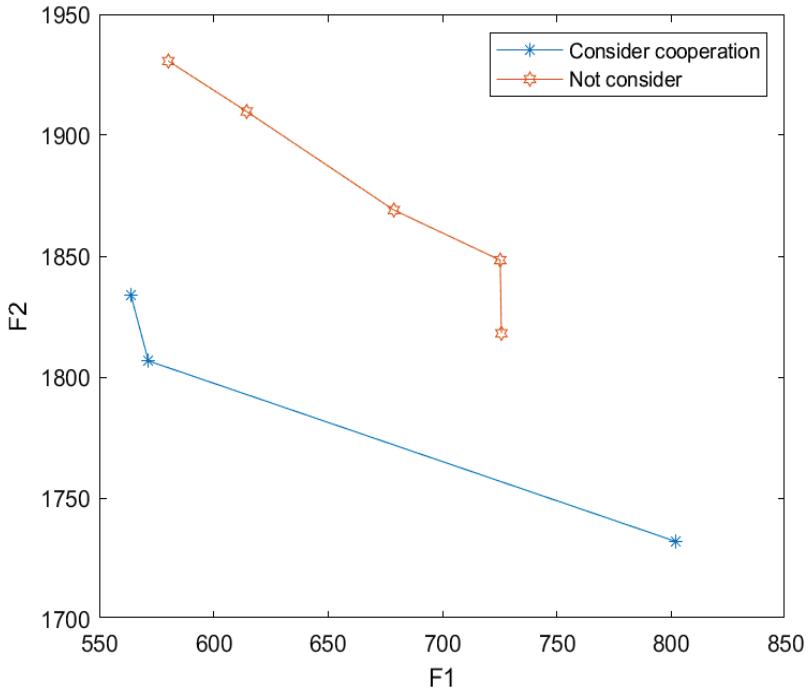

Figure 9. Comparison of results in example experiment 3.

To further explore the impact of worker behavior effects on seru scheduling and to consider the dual factors of worker cooperation and learning behavior effects on seru order scheduling, case experiment 4 was conducted.

Example experiment 4: The necessity of considering the dual behavioral effects of workers was studied, and the experimental results are shown in Figure 10. In Figure 10, it can be seen that the optimal solutions obtained by considering worker behavior effects are better than those obtained without considering worker behavior effects, indicating that considering worker behavior effects can improve the efficiency of the seru production system. In Figure 10, it can also be observed that the optimal solution obtained by considering the dual behavioral effects of workers is superior to the optimal solution obtained by solely considering the cooperative or learning behavioral effects of workers. This indicates that in actual production scheduling, considering both cooperative and learning behaviors of workers to develop order-scheduling schemes can better leverage the effects of worker behavior, maximize human production efficiency, and optimize the performance of the seru system.

To verify the effectiveness of the algorithm, this paper applies the GA algorithm and the improved shuffled frog leaping algorithm to solve the problem through small-scale examples. To provide a more intuitive reflection of the results, this article has expanded the production volume of orders. The same applies to other items, and Table 5 shows the order demand quantity table. Figure 11 shows the results obtained from running three algorithms five times. The GSFLA algorithm applies a crossover operator based on the traditional shuffled frog leaping algorithm. The crossover operator is the same as in this article, but the meme group evolution is different. The GSFLA algorithm applies the meme group evolution idea of the traditional shuffled frog leaping algorithm. In the graph, it can be seen that the algorithm in this study is superior to the GSFLA algorithm but has no significant advantage compared to the GA algorithm. However, the average single operation time of the algorithm in this paper is 0.95 s, and the average single operation time of the GA algorithm is 16.2 s, reducing the running time by 94%. Through the above comparison, it can be concluded that the algorithm in this study is effective, but there are still shortcomings in improvement. In the future, the idea of the genetic algorithm can be further referenced to improve the optimization ability.

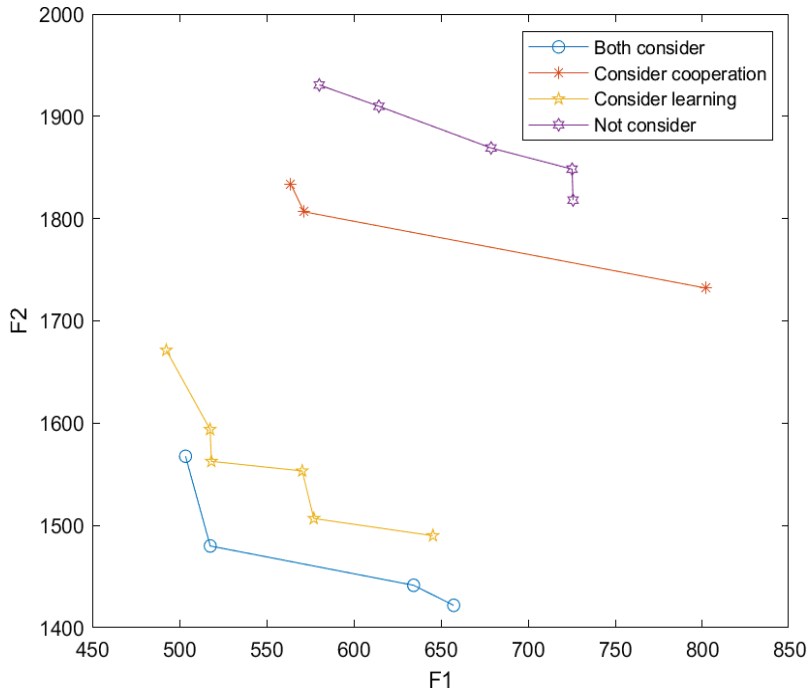

Figure 10. Comparison of results in example experiment 4.

Table 5. Order quantity information.

Order Number	J1	J2	J3	J4	J5	J6	J7	J8	J9	J10
Order	164	115	117	128	127	135	185	133	119	131

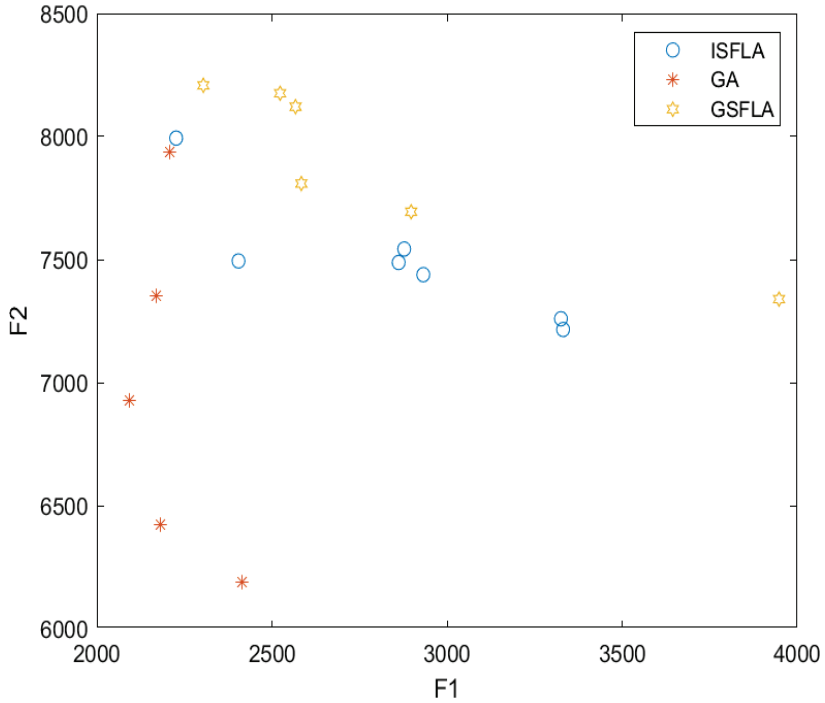

Figure 11. Non-dominated solution sets of three algorithms.

In the actual seru production scenario, the batch size of orders received by the workshop will be greater than that in small-scale examples, and the relationship between seru units and orders will also be more complex.

To further validate the effectiveness of the algorithm, this article intends to conduct large-scale numerical experiments, with specific experimental parameters shown in Table 6.

Table 6. Parameter information of large-calculation examples.

Parameter	Value Range
Seru	6
Worker	18
Order	25
Order quantity	[20, 40]
Workers' master skills	[6, 8]
Delivery lead time	[800, 2000]
Incompressible factor M	0.79
Learning Index b	−0.7

Table 7 shows the non-dominated solution set for the large-scale experiment. Table 8 and Figure 12 take the large example of non-dominant solution 1 as an example and list the Gantt charts of the optimal solution for the optimal solution and the optimal order-scheduling scheme. In summary, in the design process of production scheduling, enterprises can improve the efficiency of the seru production system by leveraging worker cooperation and learning behavior.

Table 7. Large example experiment's non-dominant solution set.

F1	F2
1182.22	5567.60
1203.59	4722.48
1483.43	4496.41
1524.19	4365.36
2084.35	4295.84

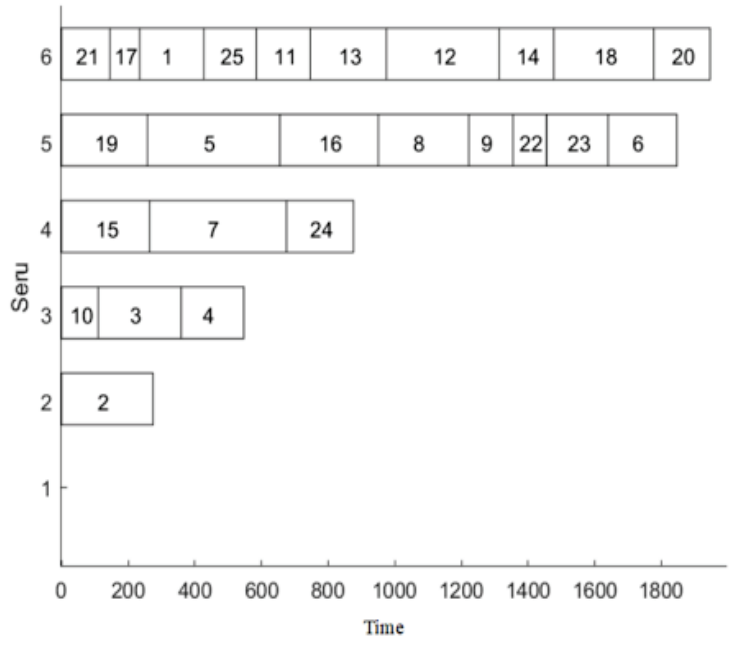

Figure 12. Gantt chart of order scheduling results in large-example experiments. Note: the numbers on the graph represent the order number.

Table 8. Large-example worker-allocation plan.

Worker	Seru	Worker	Seru
1	3	10	3
2	1	11	3
3	4	12	6
4	1	13	2
5	6	14	6
6	5	15	4
7	5	16	6
8	5	17	2
9	4	18	3

6. Conclusions

This article studies the order-scheduling problem while considering the effects of worker cooperation and learning behavior. In constructing the problem model, factors such as worker cooperation behavior, learning behavior, and preparation time for order processing are taken into account. A nonlinear programming model is established to minimize the maximum completion time and order processing time. To better solve the seru production scheduling problem, this paper introduces a hybrid frog jump algorithm with a strong global optimization ability to solve it. Based on the order-scheduling problem solved in this article and the characteristics of the model, the hybrid leapfrog algorithm is improved. The effectiveness of the model and algorithm has been demonstrated through small-scale and large-scale numerical experiments. The following conclusions can be drawn from the example experiment: (1) Both cooperative and learning behaviors of workers will have an impact on seru production, and learning behavior has a greater impact on seru production efficiency than cooperative behavior. (2) Considering the dual behavioral effects of workers can optimize the seru's production efficiency. (3) Positive cooperative behavior can promote seru production, but negative cooperative behavior can hinder seru production. Based on the aforementioned findings, we can offer several recommendations for business managers. Firstly, enterprises should focus on creating a conducive work environment, enhancing employee cooperation awareness, and facilitating communication and collaboration to improve workshop production efficiency. Secondly, when developing an order-scheduling plan, managers should take into account the learning tendencies of workers during the order-production process. They should also fully utilize the learning behavior effects of workers, gathering similar orders to improve worker skill proficiency and further improving the efficiency of seru production systems.

The order-scheduling problem addressed in this article, with known order requirements, does not consider the impact of dynamic factors such as random order arrival and new order arrival. It is limited to static order scheduling. Future research can focus more on dynamic factors and consider random order demands to better fit the actual seru production environment.

Author Contributions: Conceptualization, W.L. and W.D.; methodology, W.L. and W.D.; validation, W.D. and X.W.; formal analysis, W.D. and X.W.; investigation, W.D. and X.W.; data curation, W.D.; writing—original draft preparation, W.D.; writing—review and editing, W.L. and W.D. All authors have read and agreed to the published version of the manuscript.

Funding: This research was supported by the National Natural Science Regional Foundation of China (72061029 and 71861031).

Data Availability Statement: Data are contained within the article.

Conflicts of Interest: The authors declare no conflict of interest.

Notation

i	Index of seru, $i = 1, 2, \ldots, I$.
j	Index of order, $j = 1, 2, \ldots, J$.
w	Index of worker, $w = 1, 2, \ldots, W$.
p	Product types, $p = 1, 2, \ldots, P$.
k	Processing sequence of orders in seru, $k = 1, 2, \ldots, K$.
T_p^s	Standard processing time for process s of product p.
M	Incompressible factor ($0 \leq M \leq 1$).
b	Learning index ($-1 \leq b \leq 0$).
α_{wu}	Cooperation coefficient between worker w and worker n.
α_w	Cooperative influence factors of workers w.
S_j	Quantity of order j.
W_{min}	The lower limit for worker allocation within seru.
W_{max}	The upper limit for workers allocated within seru.
FCB_j	Start time of order j in seru i.
ST_j	Preparation time of order j in seru i.
FC_j	Processing time of order j in seru i.
Q_{jw}	Number of orders completed by worker w.
Q_{ijw}	The number of orders completed by worker w in seru i.
T_{jw}^s	The total processing time for worker w to complete process s in order j.
T_i	Available production time for seru i.
Z_p	Replacement time for product p.
D_j	Delivery date of order j.

$$Y_{wi} = \begin{cases} 1, \ if \ worker \ w \ is \ assigned \ to \ seru \ i \\ 0, \ otherwise \end{cases}$$

$$R_{ij} = \begin{cases} 1, \ if \ order \ j \ is \ processed \ in \ seru \ i \\ 0, \ otherwise \end{cases}$$

$$C_{jp} = \begin{cases} 1, \ if \ the \ product \ type \ of \ order \ j \ is \ p \\ 0, \ otherwise \end{cases}$$

$$X_{ijk} = \begin{cases} 1, \ if \ the \ processing \ position \ of \ order \ j \ in \ seru \ i \ is \ k \\ 0, \ otherwise \end{cases}$$

$$U_{wp} = \begin{cases} 1, \ If \ the \ type \ of \ product \ processed \ by \ worker \ w \ is \ p \\ 0, \ otherwise \end{cases}$$

References

1. Lian, J.; Liu, C.; Yin, Y. A multifunctional worker allocation model and algorithm considering worker heterogeneity under seru production mode. *Oper. Res. Manag.* **2019**, *28*, 81–89.
2. Zeng, S.; Wu, Y.; Yu, Y. Research on fairness oriented joint decision making of multifunctional work batch job allocation in seru production system. *Ind. Eng. Manag.* **2023**, *28*, 58–65.
3. Zhang, X.; Liu, C.; Li, W.; Evans, S.; Yin, Y. Effects of key enabling technologies for seru production on sustainable performance. *Omega* **2017**, *66*, 290–307. [CrossRef]
4. Liu, C.; Stecke, K.E.; Lian, J.; Yin, Y. An implementation framework for seru production. *Int. Trans. Oper. Res.* **2014**, *21*, 1–19. [CrossRef]
5. Treville, S.; Ketokivi, M.; Singhal, V.R. Competitive manufacturing in a high-cost environment: Introduction to the special issue. *J. Oper. Manag.* **2017**, *49–51*, 1–5. [CrossRef]
6. Yamada, H. *Waste Reduction*; Gentosha: Tokyo, Japan, 2009. (In Japanese)
7. Yu, Y.; Tang, J. Review of seru production. *Front. Eng. Manag.* **2019**, *6*, 183–192. [CrossRef]
8. Yin, Y.; Stecke, K.E.; Swink, M.; Kaku, I. Lessons from seru production on manufacturing competitively in a high cost environment. *J. Oper. Manag.* **2017**, *49*, 67–76. [CrossRef]
9. Zhan, R.; Zhang, J.; Cui, Z.; Peng, J.; Li, D. An automatic heuristic design approach for seru scheduling problem with resource conflicts. *Discret. Dyn. Nat. Soc.* **2021**, *2021*, 8166343. [CrossRef]
10. Jiang, Y.; Zhang, Z.; Gong, X.; Yin, Y. An exact solution method for solving seru scheduling problems with past-sequence-dependent setup time and learning effect. *Comput. Ind. Eng.* **2021**, *158*, 107354. [CrossRef]
11. Li, D.; Jiang, Y.; Zhang, J.; Cui, Z.; Yin, Y. An on-line seru scheduling algorithm with proactive waiting considering resource conflicts. *Eur. J. Oper. Res.* **2023**, *309*, 506–515. [CrossRef]
12. Wu, Y.; Wang, L.; Chen, J.F.; Zheng, J.; Pan, Z. A reinforcement learning driven two-stage evolutionary optimisation for hybrid seru system scheduling with worker transfer. *Int. J. Prod. Res.* **2023**, 1–20. [CrossRef]

13. Lian, J.; Li, W.; Pu, G.; Zhang, P. Bi-objective energy-efficient scheduling in a seru production system considering reconfiguration of serus. *Sustain. Comput. Inform. Syst.* **2023**, *39*, 100900. [CrossRef]
14. Zhang, X.; Zhang, Z.; Gong, X.; Yin, Y. An exact branch-and-bound algorithm for seru scheduling problems with sequence-dependent setup time. *Soft Comput.* **2023**, *27*, 6415–6436. [CrossRef]
15. Shen, L.; Zhang, Z.; Song, X.; Yin, Y. A hybrid GA-PSO algorithm for seru scheduling problem with dynamic resource allocation. *Int. J. Manuf. Res.* **2023**, *18*, 100–124. [CrossRef]
16. Zhang, Z.; Song, X.; Huang, H.; Yin, Y.; Lev, B. Scheduling problem in seru production system considering DeJong's learning effect and job splitting. *Ann. Oper. Res.* **2022**, *312*, 1–23. [CrossRef]
17. Zhang, Z.; Shen, L.; Gong, X.; Zhong, X.; Yin, Y. A genetic-simulated annealing algorithm for stochastic seru scheduling problem with deterioration and learning effect. *J. Ind. Prod. Eng.* **2023**, *40*, 205–222. [CrossRef]
18. Zhang, Z.; Song, X.; Gong, X.; Yin, Y.; Lev, B.; Zhou, X. An effective heuristic based on 3-opt strategy for seru scheduling problems with learning effect. *Int. J. Prod. Res.* **2023**, *61*, 1938–1954. [CrossRef]
19. Jiang, Y.; Zhang, Z.; Song, X.; Yin, Y. seru scheduling problems with multiple due-windows assignment and learning effect. *J. Syst. Sci. Syst. Eng.* **2022**, *31*, 480–511. [CrossRef]
20. Dong, P.; Yu, J. A Production Scheduling Model for Clothing Sewing Workshop Considering Learning Forgetting Effect. *Mod. Text. Technol.* **2023**, *31*, 81–91.
21. Janiak, A.; Kovalyov, M.Y.; Lichtenstein, M. Strong NP-hardness of scheduling problems with learning or aging effect. *Ann. Oper. Res.* **2013**, *206*, 577–583. [CrossRef]
22. Sun, L.H.; Cui, K.; Chen, J.H.; Wang, J.; He, X.C. Some results of the worst-case analysis for flow shop scheduling with a learning effect. *Ann. Oper. Res.* **2013**, *211*, 481–490. [CrossRef]
23. Biskup, D. A state-of-the-art review on scheduling with learning effects. *EuropeanJournal Oper. Res.* **2008**, *188*, 315–329. [CrossRef]
24. Wright, T.P. Factors affecting the cost of airplanes. *J. Aeronaut. Sci.* **1936**, *3*, 122–128. [CrossRef]
25. Carr, G.W. Peacetime cost estimating requires new learning curves. *Aviation* **1946**, *45*, 220–228.
26. Asher, H. Cost-Quantity Relationships in the Airframe Industry. Ph.D. Thesis, The Ohio State University, Columbus, OH, USA, 1956.
27. Dejong, J.R. The effects of increasing skill on cycle time and its consequences for time standards. *Ergonomics* **1957**, *1*, 51–60. [CrossRef]
28. Baloff, N. Extension of the learning curve—Some empirical results. *J. Oper. Res. Soc.* **1971**, *22*, 329–340. [CrossRef]
29. Zhang, H.; Xu, G.; Zhang, J. Research on multi-stage hybrid flow shop scheduling problem with learning effects. *J. Chongqing Norm. Univ. (Nat. Sci. Ed.)* **2021**, *38*, 87–95.
30. Hu, J.; Wu, Y.; Wang, Y.; Wu, Y. A Single Person Job Shop Scheduling Algorithm Considering Learning Effects. *Control Decis. Mak.* **2022**, *37*, 37–46.
31. Wang, J.; Liu, C.; Zhou, M. Improved bacterial foraging algorithm for cell formation and product scheduling considering learning and forgetting factors in cellular manufacturing systems. *IEEE Syst. J.* **2020**, *14*, 3047–3056. [CrossRef]
32. Sakamaki, H. *Canon Cellular Production Method*; Oriental Press: Beijing, China, 2006.
33. Wang, Y.; Tang, J. A Method for Constructing Unit Assembly Systems Considering Employee Collaboration. *Control Decis. Mak.* **2020**, *35*, 453–460.
34. Cao, H.; Kong, F. Collaborative simulation of U-shaped assembly line workers based on emotional model. *Comput. Integr. Manuf. Syst.* **2015**, *21*, 3209–3221.
35. Liu, F.; Fang, K.; Tang, J.; Yin, Y. Solving the rotating seru production problem with dynamic multi-objective evolutionary algorithms. *J. Manag. Sci. Eng.* **2022**, *7*, 48–66. [CrossRef]
36. Li, X.; Zhang, Z.; Sun, W.; Liu, Y.; Tang, J. Parallel dynamic NSGA-II with multi-population search for rescheduling of seru production considering schedule changes under different dynamic events. *Expert Syst. Appl.* **2023**, *238*, 121993. [CrossRef]
37. Miao, Q.; Bai, Z.; Liu, X.; Awais, M. Modelling and numerical analysis for seru system balancing with lot splitting. *Int. J. Prod. Res.* **2023**, *61*, 7410–7433. [CrossRef]
38. Pan, C.; Yan, H.; Zhan, Y.; Zhang, W. seru production scheduling based on multi-population multi-objective genetic algorithm. *Control Eng.* **2023**, *30*, 1567–1574.
39. Yilmaz, B.G.; Yilmaz, Ö.F.; Çevikcan, E. Lot streaming in workforce scheduling problem for seru production system under Shojinka philosophy. *Comput. Ind. Eng.* **2023**, *185*, 109680. [CrossRef]
40. Eusuff, M.M.; Lansey, K.E. Optimization of water distribution network design using the shuffled frog leaping algorithm. *J. Water Resour. Plan. Manag.* **2003**, *129*, 210–225. [CrossRef]
41. Cao, J.; Wang, L.; Lei, D. Distributed assembly hybrid flow shop scheduling based on frog jump algorithm. *J. Huazhong Univ. Sci. Technol. (Nat. Sci. Ed.)* **2023**. [CrossRef]
42. Meng, L.; Zhang, B.; Ren, Y.; Zhang, C. A Hybrid Frog Jump Algorithm for Solving Distributed Flexible Job Shop Scheduling. *J. Mech. Eng.* **2021**, *57*, 263–272.

processes

MDPI

Article

Structural Design and Analysis of a 100 kW Radial Turbine for an Ocean Thermal Energy Conversion–Organic Rankine Cycle Power Plant

Xin Feng, Haoyang Li, Jie Huang, Qingfen Ma *, Mao Lin, Jingru Li and Zhongye Wu

College of Mechanical and Electrical Engineering, Hainan University, Haikou 570228, China; huangjie@hainanu.edu.cn (J.H.)

* Correspondence: mqf0920@hainanu.edu.cn

Abstract: In this paper, a 100 kW radial inflow turbine is designed for an ocean thermal energy conversion (OTEC) power plant based on the organic Rankine cycle (ORC) with ammonia as the working fluid. Based on one-dimensional (1D) and three-dimensional computational fluid dynamics (3D-CFD) modeling, the mechanical structure design, static and modal analyses of the turbine and its components are carried out to investigate its mechanical performance. The results show the stress and strain distribution in the volute, stator and rotor, and their maximum values appear, respectively, at the inlet cutout, the tip of the stator outlet and the connection position between the rotor and the shaft. After optimization, all the stresses in the above components are below the allowable values. The frequencies from the first order to the sixth order of the rotor and whole turbine were obtained through modal analysis without prestress and under prestress. The maximum frequency of the rotor and whole turbine is 707.75 Hz and 40.22 Hz, both of which are far away from the resonance frequency range that can avoid resonance. Therefore, the structure of the designed turbine is safe, feasible and reliable so as to better guide actual production.

Keywords: ocean thermal energy conversion; radial turbine; static analysis; structural design; modal analysis

1. Introduction

The ocean has a large number of untapped resources, such as ocean thermal energy (OTE), wave energy, tidal energy and water resources [1]. Exploring ocean energy has become an effective way to solve the energy crisis and achieve sustainable development [2]. The ocean is the largest solar energy utilization device on Earth, absorbing solar energy that far exceeds human energy consumption. The Earth receives enough energy from the sun every year to supply its needs [1]. Ocean thermal energy conversion (OTEC) utilizes the temperature difference between warm surface seawater and deep cold seawater as the heat source to realize the utilization of ocean thermal energy [3], possessing the advantages of huge reserves [4], continuous stability, natural cleaning and other characteristics [5,6], with a power generation potential of about 150 million kW [7]. Compared with other ocean clean energy sources, OTE is considered to be the worthiest due to its advantages in terms of high energy density and small power generation fluctuations.

The power generation equipment of an OTEC plant is a turbine, and they can be mainly divided into two categories: axial turbines and radial turbines. Ammonia was the earliest working fluid used and is still the most common in OTEC-ORC systems due to its advantages in terms of its good economy, large unit refrigeration capacity and high heat release coefficient [8–10]. In OTEC systems, the available temperature difference is small [11], limiting the power output and efficiency. Therefore, a radial inflow turbine is generally used in OTEC systems due to its simple structure, good economy, and high efficiency. In order to improve the actual turbine performance under the conditions of low

temperature and pressure, the structural design and optimization of an OTEC radial inflow turbine should be studied.

Some researchers have conducted 1D design [12–15], 3D-CFD simulation [16–18] and other analyses. Nithesh et al. [19] adopted a comprehensive 1D meanline design method for a radial inflow turbine with a 2 kW output power and found that blade edge filleting is very important to improve blade performance. Kim et al. [20] studied and proposed a new method for the appropriate selection of the mass flow rate and loading coefficient and carried out meanline analysis and three-dimensional viscosity simulations in order to verify whether the proposed method can optimize the design of a radial inflow turbine. Nithesh et al. [21] designed a 2 kW radial inflow turbine for OTEC closed-cycle using R22 as the working fluid and conducted a three-dimensional simulation to analyze the importance of blade number and fillet. Wu et al. [22] optimized the design of the dual-pressure steam turbine in the OTEC system based on structural theory. Compared with the initial design point, the total output of the turbine after primary, secondary and third structural optimization increased by 0.69%, 1.82% and 2.02%, respectively. However, these researchers only focused on the analysis and optimization through 3D-CFD simulation for radial turbines, lacking structural design and analysis.

Many scholars have verified the simulation results by conducting experiments. However, their research focused more on building experimental platforms and compared the power output or isentropic efficiency. Structure design analysis and verification for turbines are scarcely carried out. Uusitalo et al. [23] experimentally investigated a small-scale high-temperature ORC, in which the turbine was discovered as having an identical value between the system design value and the mechanical power output of about 6 kW. Weiß et al. [24] designed two small-scale turbines, an axial impulse turbine and a radial cantilever turbine, with a maximum power output of about 12 kW, which had isentropic efficiencies of 73.45% and 76.8%, as experimented on in the ORC test bed. Although the structure and modal analysis [25] of gas turbines can be of significance in terms of reference, the operating conditions of high temperatures and pressures [26] are totally different from those of OTEC-ORC turbines. In addition, the blades of gas turbines are usually made of stainless steel from 12 Cr and Ti-6Al-4V [26], which is not compatible with the working scenarios of OTEC-ORC turbines.

From the above literature investigation, it can be found that the research on turbines mostly focuses on CFD simulation and optimization. There are few studies on the structural design and analysis, especially for OTEC-ORC turbines, which operate at low temperature and pressure and are necessary to meet the efficient, feasible and reliable requirements. Therefore, based on the 1D design and 3D CFD optimization of a 100 kW radial inflow turbine in the OTEC-ORC cycle using ammonia as the working fluid, the mechanical structure and modal analysis as well as stress and strain analysis on the key components and the whole turbine are carried out to ensure the safety, reliability and processability so as to better match the actual production needs and provide guidance for the research of OTEC radial inflow turbines.

2. Aerodynamic Parameter Calculation Based on 1D Design and 3D-CFD Simulation

The meridian plane diagram and the rotor velocity triangles are shown in Figure 1. The 3D-CFD model of the turbine is shown in Figure 2. Mesh software is employed for the volute and diffuser to create tetrahedral mesh, and TurboGrid 19.2 software with ATM (Automatic Topology and Mesh) is used for the nozzle and rotor to create hexahedral mesh with the schematic diagram shown in Figure 3. The number of grid nodes for this design is selected as 1.6×10^6 after a mesh independence test. The calculated thermodynamic and structural parameters are shown in Table 1.

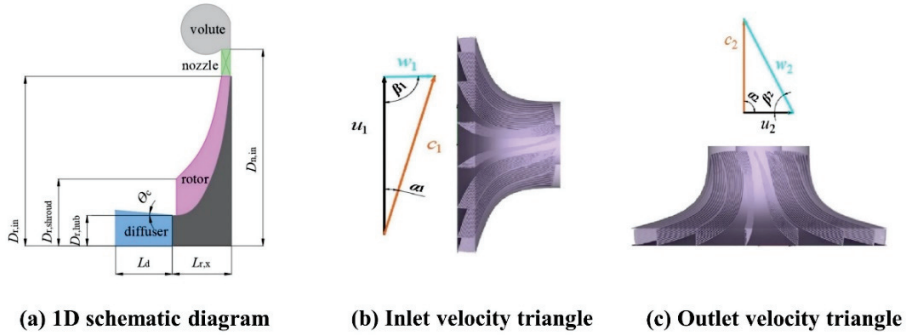

Figure 1. Schematic diagram and rotor velocity triangle of turbine structure.

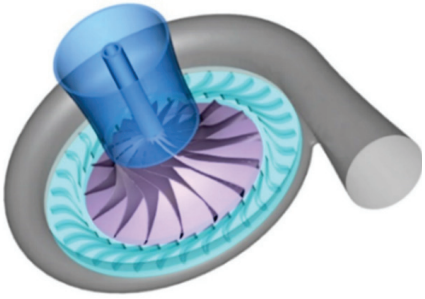

Figure 2. Three-dimensional (3D) model of the designed radial turbine.

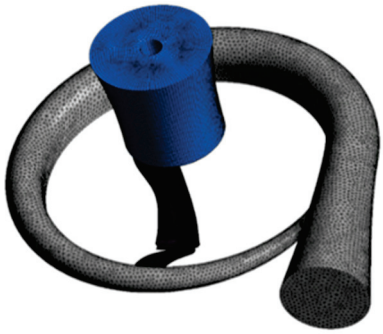

(**a**) Mesh of volute and diffuser.

(**b**) Mesh of nozzle and rotor.

Figure 3. Mesh diagram.

Steady-state, viscous flow simulation is performed using software CFX. The cubic equation of state by Peng–Robinson is used to calculate the thermodynamic parameters of the expansion process of the working fluid ammonia inside the turbine. Since the Reynolds number of the working fluid in the turbine is much greater than 10^5, the standard k-ε equation is used to solve the three-dimensional flow problem inside the turbine. The convection scheme of the momentum equation adopts high resolution, and the transport

equation adopts the first order. Because there is no mass transfer or change in chemical composition during the solution process, the energy equation is not considered. The convergence criterion is set as 10^{-6} for the residual target.

Table 1. Main parameters of the designed radial turbine.

Parameters	Units	Value	Parameters	Units	Value
M_{wf}	kg/s	4.09	$D_{r,shroud}$	m	0.208
P	kW	100	ψ	–	0.85
$T_{turb,in}$	°C	24	φ	–	0.95
$p_{turb,in}$	bar	7.3	$D_{n,in}$	mm	476.4
$T_{turb,out}$	°C	11.37	$D_{r,in}$	mm	415.8
$p_{turb,out}$	bar	6.0	$D_{n,out}$	mm	417.8
$\overline{D}$	–	0.366	$D_{r,shroud}$	mm	209.5
α_1	°	13°	$D_{r,hub}$	mm	48
β_2	°	60°	L_d	mm	257.8
Ω	–	0.437	$L_{r,x}$	mm	145.8
c_{2ss}	m/s	148.01	n	rpm	7000
c_1	m/s	157.79	N_r	–	15
u_1	m/s	153.18	N_n	–	32
w_1	m/s	35.5	$\eta_{t,isen}$	%	89.4
c_2	m/s	32.37	ζ_f	%	4.0%
u_2	m/s	56.06	ζ_l	%	2.0%
w_2	m/s	64.74	ζ_f	%	1.63%

3. Turbine Structural Design

The assembly of the turbine consists of four parts, namely the volute, stator, rotor and diffuser. This section conducts structural design, strength verification, connection and sealing design for these four parts.

3.1. Structural Design of Shaft

Torque is mainly transmitted through shafts when a rotor operates. Fatigue fracture is one of the main failure modes of shafts and tends to occur in places with smaller diameters. When the turbine operates, the main load is torque, and there is no external bending moment. Therefore, only the effect of torque is considered during design and verification.

The torsional strength should meet the requirements of Equation (1) [27].

$$\tau_T = \frac{T}{W_T} = \frac{9.55 \times 10^6 P}{0.2 d^3 n} \leq [\tau_T] \quad (1)$$

Wherein, τ_T (MPa), T (N·mm), and W_T (mm^3) are the torsional shear stress, torque on the shaft and torsional section coefficient, respectively. n (rpm), P (kW) and d (mm) are the shaft rotational speed, shaft power and the diameter of the shaft section. $[\tau_T]$ (MPa) is the allowable torsional shear stress.

The allowable torsional shear stress of AISI 1045 steel, the material of the shaft, is 35 MPa [28]. Therefore, the minimum diameter is calculated to be 26.91 mm and then rounded to 30 mm. As shown in Figure 4, a stepped shaft is used in the rotor structure, consisting of diameters of Φ30, Φ45, Φ50, Φ60, and Φ70, respectively, and their corresponding lengths are 28 mm, 25 mm, 123 mm, 34 mm, and 60 mm. The ends of the shaft also need to be chamfered to facilitate assembly and deburring.

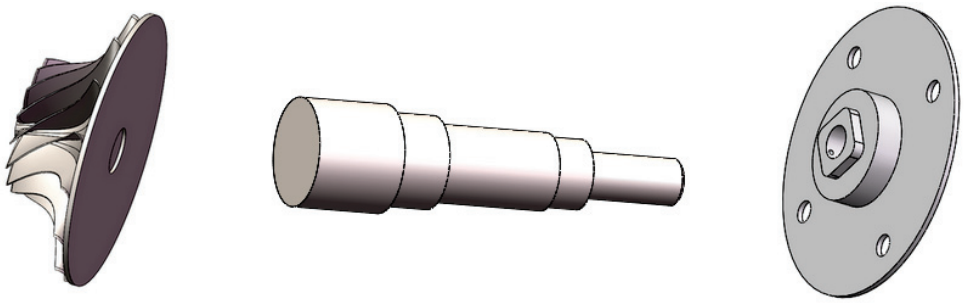

(**a**) Rotor. (**b**) Shaft. (**c**) Flange.

Figure 4. Structure of the shaft and assembled parts.

The torsional stiffness of the shaft is checked according to Equation (2) [27].

$$\varphi_{\mathrm{T}} = 5.73 \times 10^4 \frac{1}{LG} \sum_{\mathrm{i}=1}^{z} \frac{T_{\mathrm{i}} l_{\mathrm{i}}}{I_{p\mathrm{i}}} \leq [\varphi_{\mathrm{T}}] \tag{2}$$

$$I_p = \frac{\pi d^4}{32} \tag{3}$$

where φ_{T} (°/mm), G (MPa) and I_{p} (mm^4) are the torsion angle, the shear elastic modulus of the shaft material and the polar moment of inertia of the shaft section, respectively. L(mm) is the length of the stepped shaft subjected to torque. T_{i}, l_{i} and I_{pi} are the torque, length and polar moment of inertia on the i-th segment of the stepped shaft, respectively. z is the number of shaft segments on which the stepped shaft is subjected to torque. $[\varphi_{\mathrm{T}}]$ (°/mm) is the allowable torsion angle of the circular shaft.

The calculated value of φ_{T} is 0.0014°/mm, less than 0.5°/mm, which is the allowable circular shaft torsion angle of the precision transmission shaft. In addition to ensuring the torsional strength and rigidity, the shaft adopts mechanical sealing to effectively ensure the air tightness and achieve long reliable operation.

3.2. Calculation and Selection of the Bearing

As shown in Figure 5, it is a 3D assembly model of the turbine placed vertically. The bearing is required to not only bear radial load but also a certain axial load. Therefore, angular contact ball bearings S7312AC and S7309AC are employed according to the size of the shaft diameter. The contact angles of S7312AC and S7309AC are all 25°, the inner and outer diameters are 60 mm, 45 mm, and 130 mm, 100 mm, respectively, and their widths are 31 mm and 25 mm. The basic dynamic and static load ratings for each are 92.5 kN, 55.1 kN, and 62.6 kN, 37.1 kN. The maximum speeds are 7700 rpm and 10,000 rpm with oil lubrication.

Pitting corrosion damage is a common failure mode of rolling bearings. In order to ensure the effectiveness of the design, the fatigue life of the bearing must be verified. Using high-speed bearings makes the product of the average diameter of the bearing and the rotational speed greater than 0.6×10^6, which will generate a large amount of heat and can easily cause excessive wear and burns when bearings rotate. Therefore, in addition to ensuring that the bearing has sufficient fatigue life, its limit speed must also be checked to avoid the generation of excessive heat.

The axial force F_{ae} and radial force F_{re} on the shaft can be obtained from Formulas (3) and (4) [28].

$$F_{\mathrm{re}} = mg \tag{4}$$

$$F_{\mathrm{ae}} = 2T/d \tag{5}$$

$$T = 9.55 \times 10^6 P/n \tag{6}$$

The radial force F_r and the derived axial force F_d on the bearing can be obtained by Formula (7).

$$F_{r1} = \frac{4}{7}F_{re}, F_{r2} = \frac{3}{7}F_{re} \tag{7}$$

$$F_{d1} = 0.68F_{r1} \tag{8}$$

The axial forces F_{a1} and F_{a2} can be given by Formula (9) and Formula (10), respectively.

$$F_{a2} = F_{d2} \tag{9}$$

$$F_{a1} = F_{ae} - F_{d2} \tag{10}$$

The fatigue life of the bearing can be obtained from Formulas (11) and (12) [29]:

$$L_h = 10^6 \times (C/P)^{\varepsilon}/60n \tag{11}$$

$$P = f_p(XF_r + YF_a) \tag{12}$$

Here, P and C are the equivalent dynamic load and basic dynamic load, respectively. X and Y are the radial and axial dynamic load coefficient, respectively. When $F_a/F_r \leq 0.68$, X and Y take 1 and 0, respectively; otherwise, they take 0.41 and 0.87. f_p is the load coefficient. ε is the life index, and ε = 3 for ball bearings. The life of the bearings selected in this article is much longer than expected and meets the design requirements. Table 2 gives the specific calculation results.

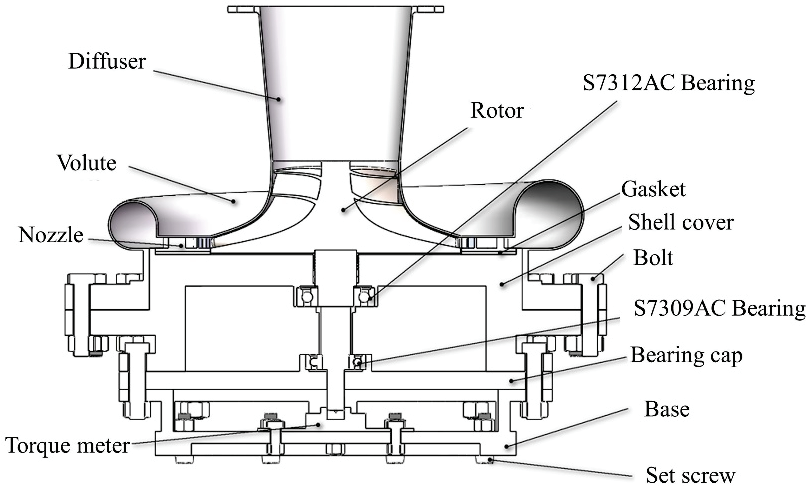

Figure 5. Three-dimensional (3D) structural model of the designed turbine.

Table 2. Bearing force analysis results.

	S7312AC	S7309AC
Radial force (N)	200.73	150.54
Derived axial force (N)	136.49	102.37
Axial force (N)	553.85	102.37
Equivalent dynamic load (N)	620.56	165.59
Bearing life (h)	7.89×10^6	8.77×10^7

In addition to checking the life of the bearing, we should also check the limit speed of the bearing to determine whether the bearing can operate stably. Equation (13) gives the check condition, which means the maximum speed should be less than or equal to the limit speed:

$$n_{max} \leq n_{lim} \tag{13}$$

The bearings adopt oil lubrication in this article. The corresponding limit speeds of the two bearings are 7700 rpm and 10,000 rpm, respectively. The design speed is 7000 rpm, which is smaller than the limit speed of the bearing and meets the requirements.

3.3. Structural Design of Volute and Diffuser

Figure 6 shows the structural model of volute, which makes the working fluid flow axially and symmetrically at the outlet. The connection with the outside is a flange connection. The material of the volute is stainless steel ZG10Cr13. According to GB 150-2011 Pressure Vessels, the wall thickness of volute can be calculated by Formula (14).

$$\delta = \frac{P_t D_v}{2[\sigma]\phi - P_t} \tag{14}$$

where P_t (MPa) and D_v (mm) are the theoretical design pressure and the minimum inner diameter of the volute. ϕ means the welding coefficient, and $[\sigma]$ (MPa) is the allowable stress of the material.

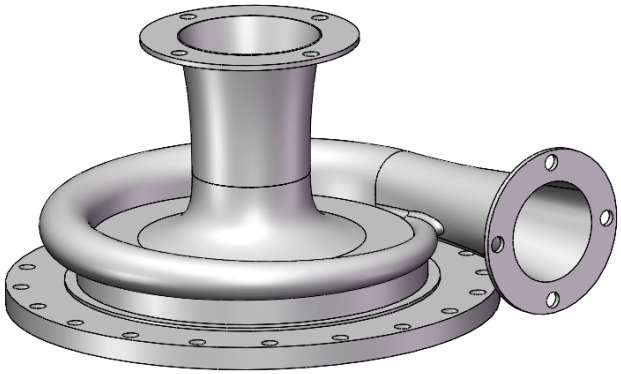

Figure 6. Volute structure diagram.

The equipment is prone to corrosion because of the environment where OTEC is utilized in high humidity and salt. Therefore, the wall thickness of the volute is designed to be 3 mm in this design in order to ensure the normal operation of the equipment.

In addition, the flange is also designed to be welded together with volute, which can facilitate the connection of volute with other components of the turbine. The specific design steps are as follows:

(1) The maximum working pressure of the designed turbine in this article is 7.3 bar, and the working temperature is 24 °C. Therefore, the nominal pressure is determined to be 1 MPa for safety.
(2) The type of flange is preliminarily determined to be Type A flat welding based on the above-mentioned parameters. The inner diameter of the volute is 596.4 mm, which is rounded and taken as 600 mm. The corresponding outer diameter of the flange and thickness is 780 mm and 42 mm. The hole diameter and number of the M27 bolt are 30 mm and 20. The outer diameter of the flange and the center diameter of the bolt hole adjust to 900 mm and 845 mm, respectively, in order to avoid the installation.
(3) The sealing structure is selected as a flat sealing surface, because the working fluid is gaseous ammonia that is not corrosive.
(4) According to the working temperature, the material of the flange is made of stainless steel ZG10Cr13, which is consistent with the volute material to ensure the uniformity of material, structure, performance and stress during the welding process. The gasket is made of asbestos rubber, and the material of the stud and nut are AISI 1035 steel and AISI 1025 steel, respectively.

The diffuser discharges the exhaust steam and should have good ability to divert flow. The conical diffuser is utilized in this article. In order to reduce the installation process

and reduce the risk of leakage, the diffuser and the volute are integrated into one body, so its thickness and the material are the same as the volute. The outlet of the diffuser is connected with flanges and pipes.

3.4. Structural Design of Stator and Rotor

In the design of the stator, the blades and base are processed separately. The stator blades can be processed by milling and positioned using positioning pins to prevent the stator from rotating. A boss is used to achieve circumferential positioning, and its structure is shown in Figure 7.

Figure 7. Stator structure.

In order to ensure the air tightness of the device, a gasket is utilized for sealing where the blades and the volute base contact. Because the OTEC turbine is operated under low temperature and pressure condition, comparing with the gas turbines operated at high temperature and pressure [25,26], the requirements for the material of an OTEC turbine stator and rotor is less strict, and aluminum alloy 6A04 is selected due to its good processing performance, light weight and high compressive strength. Thus, there is no need for stainless steel from 12Cr and Ti-6Al-4V [26], saving investment cost.

The installation accuracy of the rotor must be guaranteed because it is the key working component. Therefore, a 5 mm deep welding groove is left at the bottom of the rotor to ensure the concentricity between the shaft and rotor. Figure 8 shows a schematic diagram of the connection between the rotor and shaft. The blade thickness of the rotor is 2 mm, and the blade number is 15.

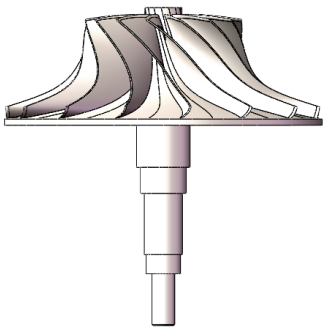

Figure 8. Schematic diagram of rotor and working shaft connection.

4. Structural Strength and Modal Analysis of Turbine

According to the calculation results of CFX, the corresponding constraints and loads are applied. ANSYS 19.2 software is used to analyze the strength of the volute, stator, rotor and shaft. The fluid pressure in the diffuser is low and the velocity is small, so no calibration is required.

4.1. Structural Strength Analysis

First, meshing and independence analysis are performed. Table 3 shows the results of independence analysis; the parameters with italic type are the final grid sizes. The meshing results of the main components are shown in Figure 9.

Table 3. Grid independence analysis.

Grid Size (mm)				Deformation (mm)			
Volute	**Stator**	**Rotor**	**Shaft**	**Volute**	**Stator**	**Rotor**	**Shaft**
5	4	8	1	1.373	0.00691	0.0977	0.00296
6	5	10	2	1.238	0.00678	0.0976	0.00295
8	10	11	3	0.886	0.00667	0.0971	0.00295
10	15	15	5	0.607	0.00638	0.0968	0.00293
20	20	20	10	0.197	0.00532	0.0945	0.00296

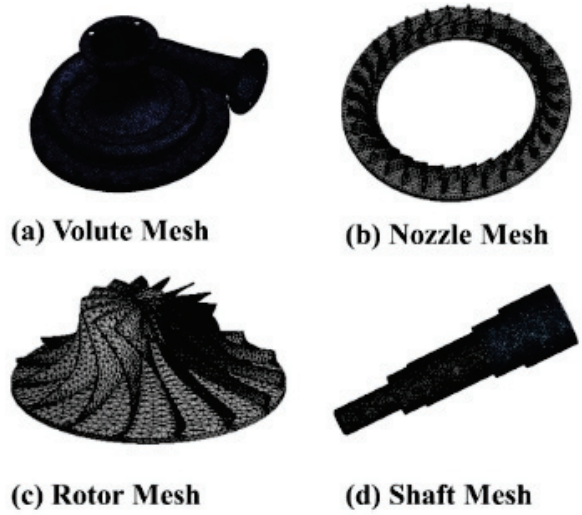

Figure 9. Meshing results of main components.

The stress and strain distribution of the volute are shown in Figure 10a,b. There is a stress concentration at the inlet cut of the volute. The maximum stress of 583 MPa exceeds the maximum allowable stress of the material of 350 MPa, and the maximum strain is 0.00303 mm/mm. Therefore, the volute structure is optimized by adding bosses to make the tip surface more rounded to reduce stress concentration. Figure 10c,d show the optimized stress and strain distribution of the volute. The maximum stress is 124.74 MPa, which meets the design standards. The optimized volute stress is reduced by 78.60%. The strain of the volute is 6.6×10^{-4} mm/mm, which is reduced by 78.22%.

The stator is a stationary component, and the bottom surface is fixedly constrained. Thus, it is mainly affected by gravity, aerodynamic and temperature load. Figure 11 shows the stress and strain distribution of the stator. The maximum stress point appears at the tip of the stationary blade cascade outlet. The maximum stress is 144.72 MPa, half of the material's allowable stress of 280 MPa, which is within the material's bearing capacity. It can be found that part of the blade outlet is more easily deformed than part of the inlet. The deformation is largest at the upper part of the stator blade outlet with a value of 0.0068 mm.

The rotor is the most critical component of the turbine. In this paper, the design speed of the rotor is 7000 rpm. Therefore, in addition to gravity, aerodynamic and temperature load, the inertial force caused by rotation must also be considered. The constraints are the axial constraints on the top end surface and the tangential and normal constraints on the outer diameter cylindrical surface. Figure 12 shows the stress and strain distribution of the rotor, in which we can find that the maximum stress point appears at the connection between the rotor and shaft. The maximum stress is 100.22 MPa, which is in line with the material's bearing capacity. In addition, there is also stress concentration at the root of the blade, which can easily cause the blade to break. The maximum strain of the rotor is 0.098 mm, which will occur at the entrance of the rotor because the pressure and inertial force are the largest there.

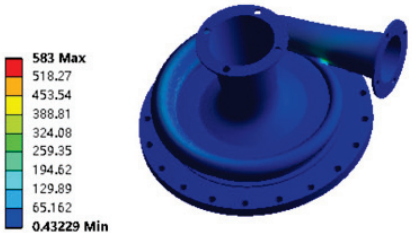

(**a**) Stress distribution.

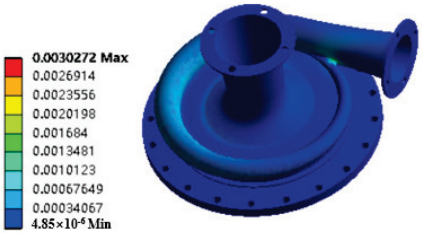

(**b**) Strain distribution.

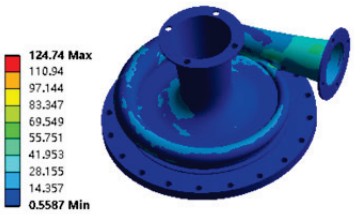

(**c**) Optimized stress distribution.

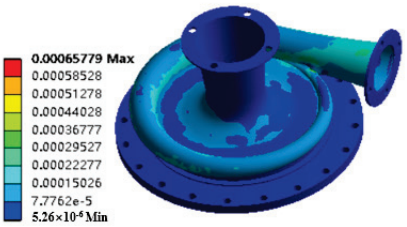

(**d**) Optimized strain distribution.

Figure 10. Stress and strain distribution on volute with optimization.

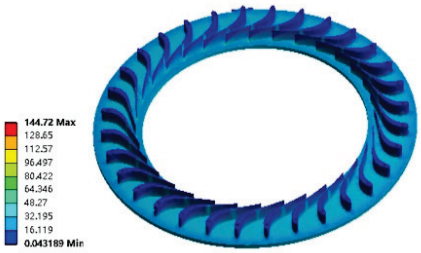

(**a**) Stress distribution.

(**b**) Strain distribution.

Figure 11. Stress and strain distribution on stator.

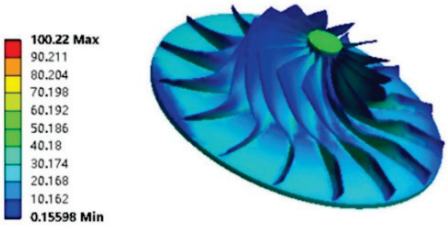

(**a**) Stress distribution.

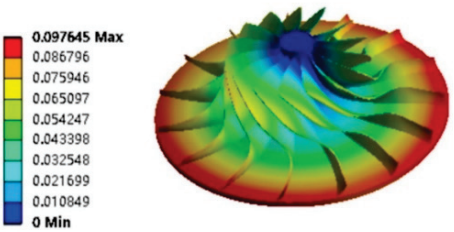

(**b**) Strain distribution.

Figure 12. Stress and strain distribution of the rotor.

The shaft is an important component for the turbine to transmit torque, and its strength needs to be checked. The material of the shaft is AISI 1045 steel. Figure 13 shows the strain and stress distribution on the shaft. The maximum stress and strain are 2.946 MPa and 0.0029 mm, respectively, which meet the design requirements.

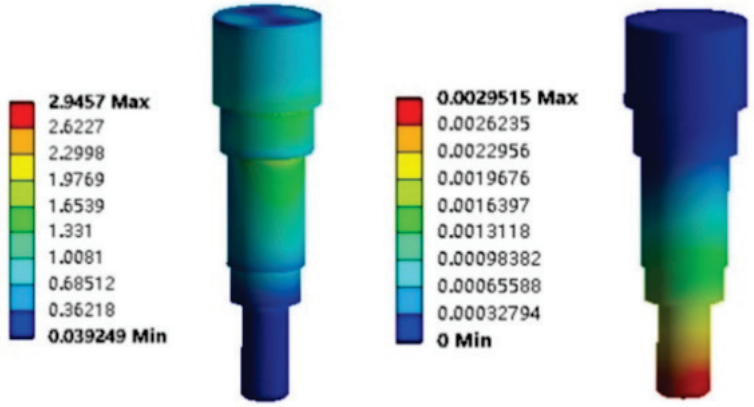

(**a**) Stress distribution. (**b**) Strain distribution.

Figure 13. Stress and strain distribution on the shaft.

4.2. Modal Analysis of the Turbine

The movement of rotating parts will inevitably produce vibrations. Through modal analysis, the vibration shape and natural frequency of the rotor can be determined, and the modal parameters in each order of states can be obtained. In addition, the vibration frequency in the assembled state will also be different, so the modal analysis of the complete machine will also be discussed in this section. Modal analysis can be divided into prestressed and non-prestressed states, which will be analyzed and discussed to avoid resonance.

The rotor must bear the effects of loads and constraints during operation, and its vibration frequency will be different from that without prestress. Therefore, the modal analysis under prestress is required. The rotational vibration frequency of the rotor can be obtained through the rotation speed by Formula (15) [30].

$$f = nN/60 \tag{15}$$

Here, n and N are the rotor speed and number of rotor blades, respectively.

If the vibration frequency differs within 15% of the rotational vibration frequency, the object will resonate. The rotational vibration frequency of the rotor in this article is 1750 Hz, and its resonance frequency range is 1487.5–2012.5 Hz

4.2.1. Modal Analysis without Prestress

Modal analysis of the rotor without prestress is performed because the proportion of low-order modal energy in structural vibration is much greater than that of high-order modal energy. The vibration shape diagrams of each order are shown in Figure 14. The vibration frequency of the rotor is 691.25–707.75 Hz. The maximum amplitude appears at the exit of the rotor blade.

When the rotor is running, it will also cause vibration of the turbine; thus, the non-prestressed modal analysis of the whole machine should be performed to ensure that the turbine does not resonate. Figure 15 shows the vibration shape of the radial turbine at each order. The maximum vibration frequency appears at the entrance and exit. Table 4 shows the free mode vibration frequencies of the rotor and turbine. The overall natural vibration frequencies are much smaller than the resonance frequency of the rotor. Therefore, there will be no resonance phenomenon in the rotor and assembly.

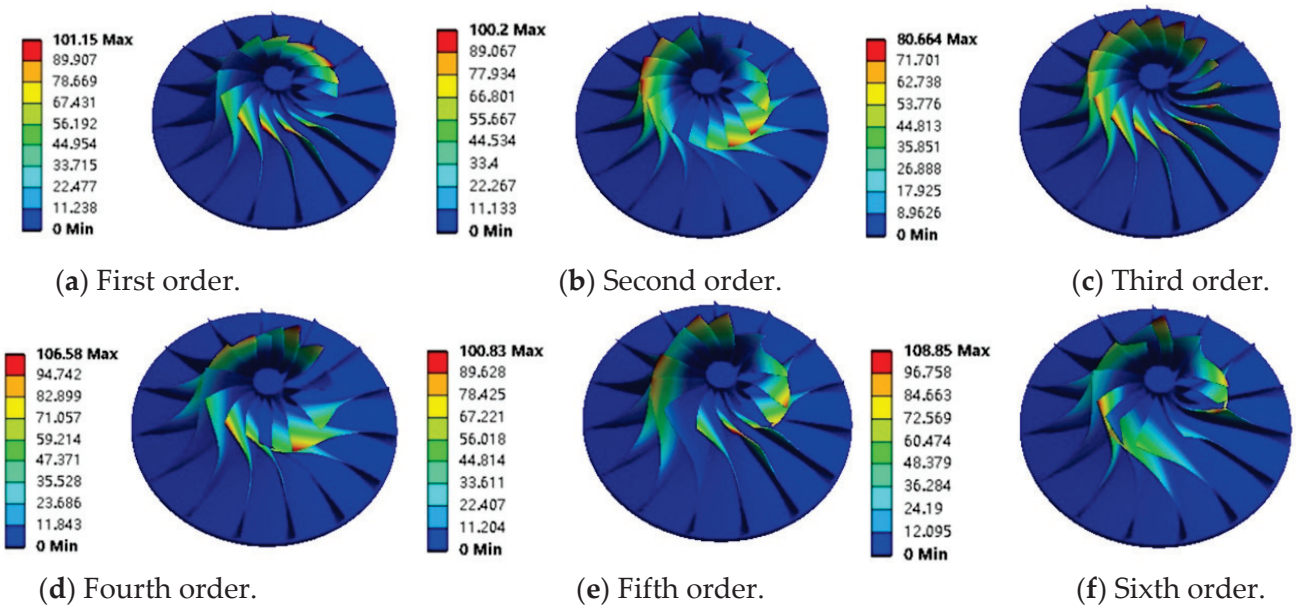

(**a**) First order. (**b**) Second order. (**c**) Third order.

(**d**) Fourth order. (**e**) Fifth order. (**f**) Sixth order.

Figure 14. Vibration shapes of the rotor in free mode.

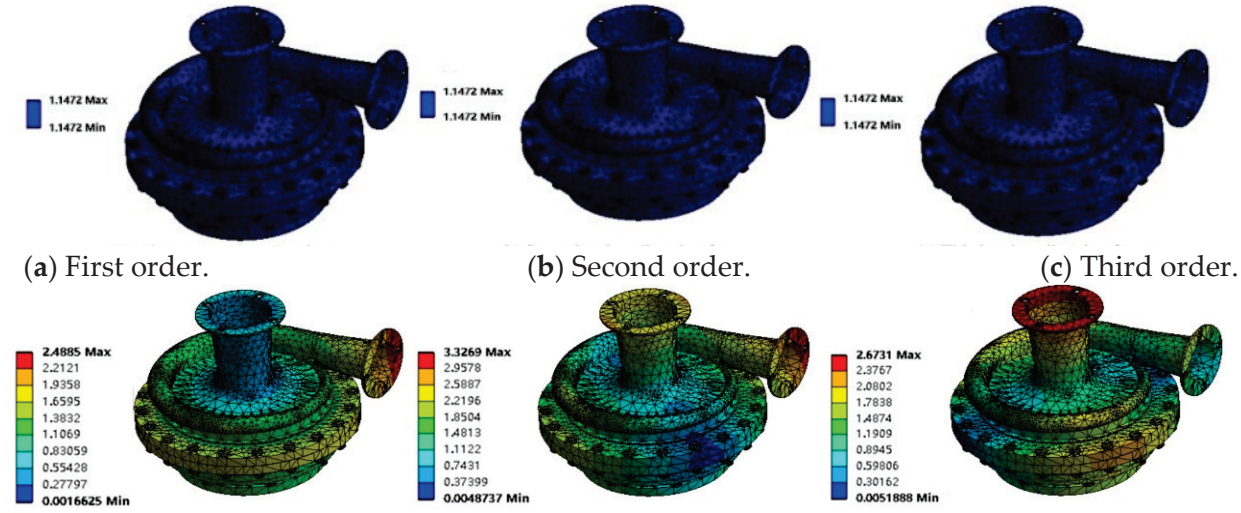

(**a**) First order. (**b**) Second order. (**c**) Third order.

(**d**) Fourth order. (**e**) Fifth order. (**f**) Sixth order.

Figure 15. Vibration shapes of the turbine in free mode.

Table 4. Each order frequency of rotor and turbine in free mode.

Orders	Vibration Frequency (Hz)	
	Rotor	Turbine
First order	691.25	0
Second order	691.38	5.00×10^{-4}
Third order	701.55	1.00×10^{-3}
Fourth order	703.98	19.55
Fifth order	704.33	39.68
Sixth order	707.75	40.22

4.2.2. Modal Analysis under Prestress

Each order frequency of the rotor and turbine with prestress is shown in Table 5. Figure 16 presents the vibration shapes. The maximum vibration frequency of the rotor is 721.52 Hz, and its maximum amplitude still appears at the exit of the rotor blade. Compared with the state without prestress, the vibration frequency of the rotor increases slightly, and the rotor does not show obvious stress stiffening. Therefore, it can be considered that the prestress has a small impact on the vibration frequency of the rotor.

Table 5. Each order frequency of rotor and turbine with prestress.

Orders	Vibration Frequency (Hz)	
	Rotor	Turbine
First order	704.22	208.57
Second order	704.35	268.69
Third order	715.14	294.44
Fourth order	717.63	334.01
Fifth order	717.98	348.07
Sixth order	721.52	371.44

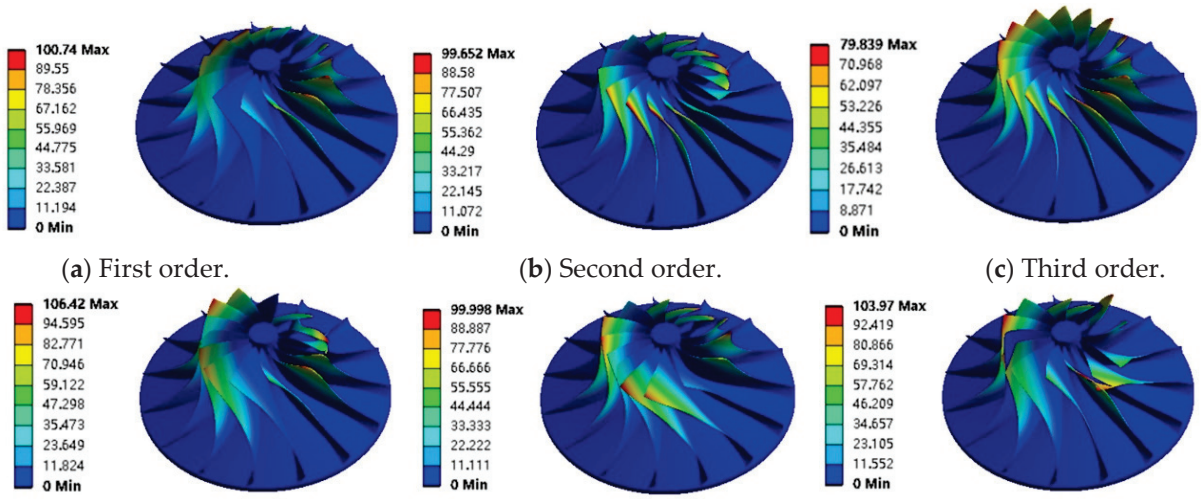

(**a**) First order. (**b**) Second order. (**c**) Third order.

(**d**) Fourth order. (**e**) Fifth order. (**f**) Sixth order.

Figure 16. Vibration shapes of the rotor with prestress.

Similarly, the entire turbine should also undergo prestressed modal analysis. The vibration frequency of the six orders with prestress of the overall structure are shown in Table 5. Although the overall vibration frequency is higher than the vibration frequency of the non-prestressed state, it is much smaller than the rotor rotation frequency. Therefore, the resonance of the turbine will not occur. Figure 17 shows the vibration shape of each order of the turbine. Compared with the free mode, in the 2nd, 3rd and 4th orders, the maximum amplitude of the whole machine appears at the exit of the diffuser. In the first and sixth order, the maximum amplitude of the turbine appears at the entrance of the volute.

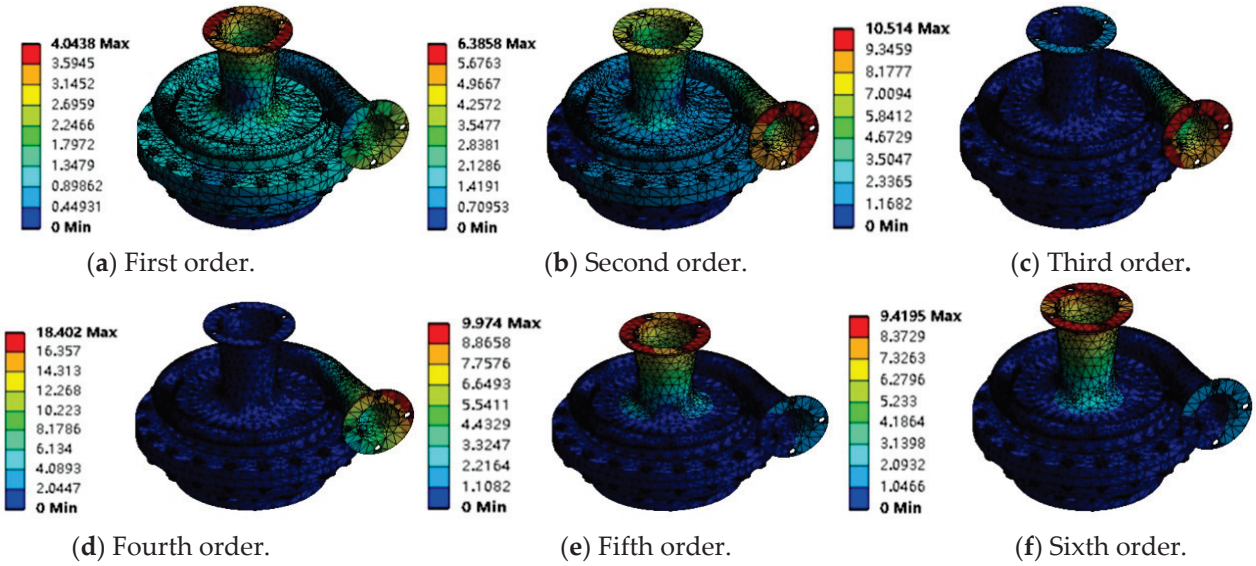

(**a**) First order. (**b**) Second order. (**c**) Third order**.**

(**d**) Fourth order. (**e**) Fifth order. (**f**) Sixth order.

Figure 17. Vibration shapes of the turbine with prestress.

5. Conclusions

A radial inflow turbine is designed for a 100 kW OTEC-ORC plant with ammonia as the working fluid. One-dimensional design and three-dimensional modeling are carried out to obtain thermodynamic and structural parameters of the turbine and key components. To ensure the safety, reliability and processability, structural and modal analysis on the key components, the rotor and the whole turbine are carried out. The results show that the designed structure can meet the requirements.

Through static analysis, the stress and strain distribution on the shaft, volute, stator and rotor are obtained. After optimization, the stress concentration occurs in the volute at the inlet and has the maximum stress with 292.37 MPa, which is lower than the allowable material strength and meets the design requirements. The maximum stress of the stator is 144.72 MPa, which appears at the outlet tip of the blade. The maximum stress of the rotor is 100.22 MPa, which occurs at the connection between the rotor and the shaft. Therefore, from the stress and strain viewpoint, the structural design performed in this paper meets the requirements well.

The frequencies of the rotor and the whole turbine are analyzed by modal analysis without prestress and under prestress, respectively. The maximum frequency of the rotor and whole turbine are 707.75 Hz and 40.23 Hz, which are all far away from the resonance frequency range. Therefore, resonance can be avoided in operation.

The radial turbine designed for OTEC under ambient conditions is efficient with an isentropic efficiency of 89.4%. After conducting mechanical structure and modal analysis, as well as stress and strain analysis on the key components and the equipment as a whole, the safety, reliability and processability of the designed turbine in the OTEC application have been proved, and the results are instructive for researchers and engineers to build an OTEC-ORC turbine prototype and experimental platform.

Although the designed turbine has been proven to be efficient and feasible for the OTEC-ORC by numerical simulation, the prototype may differ with the designed results due to the limitations of manufacturing level, which will influence the performance of the turbine. Furthermore, the turbine is possibly installed on a floating offshore platform; thus, its vibration characteristics will be affected by the movement of the platform, and the coupling effects should be monitored and then considered into the model simulation to optimize the mechanical structure.

Author Contributions: Conceptualization, Supervision, Writing—review and editing, Funding acquisition, Q.M.; Simulation, Data analysis, Writing—original draft, X.F., J.H. and H.L.; Reviewing and supervision, M.L.; Validation and editing, J.L. and Z.W. All authors have read and agreed to the published version of the manuscript.

Funding: This research was funded by the Hainan Provincial Natural Science Foundation of China (422CXTD509), the Hainan Province Science and Technology Special Fund (ZDYF2021GXJS021), and the National Natural Science Foundations of China (51769006).

Data Availability Statement: Data are unavailable due to privacy or ethical restrictions but will be provided when requested.

Conflicts of Interest: The authors declare no conflict of interest.

Nomenclature

c	Absolute speed, m/s	$\overline{D}$	Ration of wheel diameter
u	Tangential velocity, m/s	Ω	Reaction degree
w	Relative velocity, m/s	ξ	Loss
P	Power, kW	η	Efficiency
m	Mass flow rate, kg/s	τ	Shear stress
n	Rotational speed, rpm	ε	Life index of bearing
Re	Reynolds number	Subscripts	
T	Temperature	turb	Turbine
N	Number	in	Inlet
L	Length, mm	out	Outlet
d	Diameter, mm	1	Rotor inlet
G	Elastic modulus, Mpa	2	Rotor outlet
φ_{T}	Twist angle, °/mm	r	Rotor
I_{p}	Polar inertia moment, mm^4	n	Nozzle
F	Force, N	r	Radial
X	Radial dynamic load factor	a	Axial
Y	Axial dynamic load factor	u	peripheral
L_{h}	Bearing life, h	isen	Isentropic
Greek letter		Acronyms	
α	Absolute airflow angle	ORC	Organic Rankine Cycle
β	Relative airflow angle	OTEC	Ocean Thermal Energy Conversion
χ	Characteristic ratio	CFD	Computational fluid dynamics
ϕ	Nozzle velocity coefficient	1-D	One-dimensional
ψ	Rotor velocity coefficient	3-D	Three-dimensional

References

1. Khan, N.; Kalair, A.; Abas, N.; Haider, A. Review of ocean tidal, wave and thermal energy technologies. *Renew. Sustain. Energy Rev.* **2017**, *72*, 590–604. [CrossRef]
2. Hasan, A.; Dincer, I. A new integrated ocean thermal energy conversion-based trigeneration system for sustainable communities. *J. Energy Resour. Technol.* **2020**, *142*, 061301. [CrossRef]
3. Sun, F.; Ikegami, Y.; Jia, B.; Arima, H. Optimization design and exergy analysis of organic rankine cycle in ocean thermal energy conversion. *Appl. Ocean Res.* **2012**, *35*, 38–46. [CrossRef]
4. Hasan, A.; Dincer, I. An ocean thermal energy conversion based system for district cooling, ammonia and power production. *Int. J. Hydrogen Energy* **2020**, *45*, 15878–15887. [CrossRef]
5. Matsuda, Y.; Oouchida, R.; Sugi, T.; Goto, S.; Yasunaga, T.; Ikegami, Y. Power generation control of OTEC plant using double-stage Rankine cycle with target power output variation by simultaneous regulation of multiple flow rates. In Proceedings of the 2019 58th Annual Conference of the Society of Instrument and Control Engineers of Japan (SICE), Hiroshima, Japan, 10–13 September 2019; pp. 1412–1417.
6. Hernández-Romero, I.M.; Nápoles-Rivera, F.; Flores-Tlacuahuac, A.; Fuentes-Cortés, L.F. Optimal design of the ocean thermal energy conversion systems involving weather and energy demand variations. *Chem. Eng. Process.-Process Intensif.* **2020**, *157*, 108114. [CrossRef]
7. Dongna, M. Overview of ocean energy power generation. *Sci. Technol. Inf.* **2015**, *13*, 246–247.
8. Yoon, J.-I.; Son, C.-H.; Baek, S.-M.; Ye, B.H.; Kim, H.-J.; Lee, H.-S. Performance characteristics of a high-efficiency R717 OTEC power cycle. *Appl. Therm. Eng.* **2014**, *72*, 304–308. [CrossRef]

9. Mohd Idrus, N.H.; Musa, M.N.; Yahya, W.J.; Ithnin, A.M. Geo-Ocean Thermal Energy Conversion (GeOTEC) power cycle/plant. *Renew. Energy* **2017**, *111*, 372–380. [CrossRef]
10. Zhang, C.; Wu, Z.; Wang, J.; Ding, C.; Gao, T.; Chen, Y. Thermodynamic performance of a radial-inflow turbine for ocean thermal energy conversion using ammonia. *Renew. Energy* **2023**, *202*, 907–920. [CrossRef]
11. Liu, W.; Xu, X.; Chen, F.; Liu, Y.; Li, S.; Liu, L.; Chen, Y. A review of research on the closed thermodynamic cycles of ocean thermal energy conversion. *Renew. Sustain. Energy Rev.* **2020**, *119*, 109581. [CrossRef]
12. Alshammari, F.; Khedher, N.B.; Said, L.B. Development of an automated design and off-design radial turbine model for solar organic Rankine cycle coupled to a parabolic trough solar collector. *Appl. Therm. Eng.* **2023**, *230*, 120677. [CrossRef]
13. Xu, G.; Zhao, G.; Quan, Y.; Liang, R.; Li, T.; Dong, B.; Fu, J. Design and optimization of a radial-axial two-stage coaxial turbine for high-temperature supercritical organic Rankine cycle. *Appl. Therm. Eng.* **2023**, *227*, 120365. [CrossRef]
14. Yu, Z.; Wang, C.; Rong, F.; Liang, W. Optimal coupling design for organic Rankine cycle and radial turbine rotor using CFD modeling, machine learning and genetic algorithm. *Energy Convers. Manag.* **2023**, *275*, 116493. [CrossRef]
15. Ma, Q.; Gao, Z.; Huang, J.; Mahian, O.; Feng, X.; Lu, H.; Wang, S.; Wang, C.; Tang, R.; Li, J. Thermodynamic analysis and turbine design of a 100 kW OTEC-ORC with binary non-azeotropic working fluid. *Energy* **2023**, *263*, 126097. [CrossRef]
16. Uusitalo, A.; Zocca, M. Design and numerical analysis of supersonic radial-inflow turbines for transcritical ORC processes. *Energy Convers. Manag.* **2023**, *277*, 116609. [CrossRef]
17. Li, W.; Ni, Q.; Ling, X. Investigations on ORC radial inflow turbine three-dimensional geometry design and off-design performance prediction. *Case Stud. Therm. Eng.* **2023**, *44*, 102893. [CrossRef]
18. Gunawan, G.; Permana, D.I.; Soetikno, P. Design and numerical simulation of radial inflow turbine of the regenerative Brayton cycle using supercritical carbon dioxide. *Results Eng.* **2023**, *17*, 100931. [CrossRef]
19. Nithesh, K.G.; Chatterjee, D. Numerical prediction of the performance of radial inflow turbine designed for ocean thermal energy conversion system. *Appl. Energy* **2016**, *167*, 1–16. [CrossRef]
20. Kim, N.J.; Ng, K.C.; Chun, W. Using the condenser effluent from a nuclear power plant for Ocean Thermal Energy Conversion (OTEC). *Int. Commun. Heat Mass Transf.* **2009**, *36*, 1008–1013. [CrossRef]
21. Nithesh, K.G.; Chatterjee, D.; Oh, C.; Lee, Y.-H. Design and performance analysis of radial-inflow turboexpander for OTEC application. *Renew. Energy* **2016**, *85*, 834–843. [CrossRef]
22. Wu, Z.; Feng, H.; Chen, L.; Xie, Z.; Cai, C.; Xia, S. Optimal design of dual-pressure turbine in OTEC system based on constructal theory. *Energy Convers. Manag.* **2019**, *201*, 112179. [CrossRef]
23. Uusitalo, A.; Turunen-Saaresti, T.; Honkatukia, J.; Dhanasegaran, R. Experimental study of small scale and high expansion ratio ORC for recovering high temperature waste heat. *Energy* **2020**, *208*, 118321. [CrossRef]
24. Weiß, A.P.; Popp, T.; Müller, J.; Hauer, J.; Brüggemann, D.; Preißinger, M. Experimental characterization and comparison of an axial and a cantilever micro-turbine for small-scale Organic Rankine Cycle. *Appl. Therm. Eng.* **2018**, *140*, 235–244. [CrossRef]
25. Xu, M.; Cao, L.; Song, L. Structure and modal analysis of the last stage blade in steam turbine under low volume flow conditions. *Eng. Fail. Anal.* **2022**, *131*, 105820. [CrossRef]
26. Zhu, M. Design and analysis of steam turbine blades. *J. Phys. Conf. Ser.* **2019**, *1300*, 012056. [CrossRef]
27. Paul, S.; Charles, C. *Torsional Analysis of Structural Steel Members*; American Institute of Steel Construction: Chicago, IL, USA, 1997.
28. Lianggui, P. *Mechanical Design*, 9th ed.; Higher Education Press: Beijing, China, 2013; pp. 303–332.
29. Hua, Z. Analysis of the Support Structure of 60° Angular Contact Ball Bearings for Ball Screws. *Mech. Manag. Dev.* **2023**, *38*, 8–9. [CrossRef]
30. Jie, X. Modal analysis of local ventilator impeller for mining based on ANSYS. *Technol. Innov. Appl.* **2016**, *31*, 65.

MDPI AG
Grosspeteranlage 5
4052 Basel
Switzerland
Tel.: +41 61 683 77 34

Processes Editorial Office
E-mail: processes@mdpi.com
www.mdpi.com/journal/processes

Academic Open
Access Publishing

mdpi.com

ISBN 978-3-7258-6211-5